



nanomaterials

Silica and Silicon Based Nanostructures

Edited by
Céline Ternon

Printed Edition of the Special Issue Published in *Nanomaterials*

Silica and Silicon Based Nanostructures

Silica and Silicon Based Nanostructures

Editor

Céline Ternon

MDPI • Basel • Beijing • Wuhan • Barcelona • Belgrade • Manchester • Tokyo • Cluj • Tianjin



Editor

Céline Ternon
Grenoble INP, Institute of
Engineering
Univ. Grenoble Alpes
Grenoble
France

Editorial Office

MDPI
St. Alban-Anlage 66
4052 Basel, Switzerland

This is a reprint of articles from the Special Issue published online in the open access journal *Nanomaterials* (ISSN 2079-4991) (available at: www.mdpi.com/journal/nanomaterials/special_issues/silica_silicon).

For citation purposes, cite each article independently as indicated on the article page online and as indicated below:

LastName, A.A.; LastName, B.B.; LastName, C.C. Article Title. <i>Journal Name</i> Year , <i>Volume Number</i> , Page Range.
--

ISBN 978-3-0365-4766-4 (Hbk)

ISBN 978-3-0365-4765-7 (PDF)

© 2022 by the authors. Articles in this book are Open Access and distributed under the Creative Commons Attribution (CC BY) license, which allows users to download, copy and build upon published articles, as long as the author and publisher are properly credited, which ensures maximum dissemination and a wider impact of our publications.

The book as a whole is distributed by MDPI under the terms and conditions of the Creative Commons license CC BY-NC-ND.

Contents

About the Editor vii

Céline Ternon

Silica- and Silicon-Based Nanostructures

Reprinted from: *Nanomaterials* **2022**, *12*, 1270, doi:10.3390/nano12081270 1

Tabassom Arjmand, Maxime Legallais, Thi Thu Thuy Nguyen, Pauline Serre, Monica Vallejo-Perez and Fanny Morisot et al.

Functional Devices from Bottom-Up Silicon Nanowires: A Review

Reprinted from: *Nanomaterials* **2022**, *12*, 1043, doi:10.3390/nano12071043 3

Zheng Fan, Danfeng Cui, Zengxing Zhang, Zhou Zhao, Hongmei Chen and Yanyun Fan et al.

Recent Progress of Black Silicon: From Fabrications to Applications

Reprinted from: *Nanomaterials* **2020**, *11*, 41, doi:10.3390/nano11010041 59

Shruti Mendiratta and Ahmed Atef Ahmed Ali

Recent Advances in Functionalized Mesoporous Silica Frameworks for Efficient Desulfurization of Fuels

Reprinted from: *Nanomaterials* **2020**, *10*, 1116, doi:10.3390/nano10061116 85

Sankar Sekar and Sejoon Lee

Derivation of Luminescent Mesoporous Silicon Nanocrystals from Biomass Rice Husks by Facile Magnesiothermic Reduction

Reprinted from: *Nanomaterials* **2021**, *11*, 613, doi:10.3390/nano11030613 117

Saquib Ahmed M. A. Peerzade, Nadezhda Makarova and Igor Sokolov

Ultrabright Fluorescent Silica Nanoparticles for Dual pH and Temperature Measurements

Reprinted from: *Nanomaterials* **2021**, *11*, 1524, doi:10.3390/nano11061524 129

Caroline Keller, Antoine Desrues, Saravanan Karuppiah, Eléa Martin, John P. Alper and Florent Boismain et al.

Effect of Size and Shape on Electrochemical Performance of Nano-Silicon-Based Lithium Battery

Reprinted from: *Nanomaterials* **2021**, *11*, 307, doi:10.3390/nano11020307 147

Andika Pandu Nugroho, Naufal Hanif Hawari, Bagas Prakoso, Andam Deatama Refino, Nursidik Yulianto and Ferry Iskandar et al.

Vertically Aligned *n*-Type Silicon Nanowire Array as a Free-Standing Anode for Lithium-Ion Batteries

Reprinted from: *Nanomaterials* **2021**, *11*, 3137, doi:10.3390/nano11113137 163

Dapeng Zheng, Manuel Monasterio, Weipeng Feng, Waiching Tang, Hongzhi Cui and Zhijun Dong

Hydration Characteristics of Tricalcium Aluminate in the Presence of Nano-Silica

Reprinted from: *Nanomaterials* **2021**, *11*, 199, doi:10.3390/nano11010199 177

Mehrez E. El-Naggar, Nader R. Abdelsalam, Moustafa M.G. Fouda, Marwa I. Mackled, Malik A.M. Al-Jaddadi and Hayssam M. Ali et al.

Soil Application of Nano Silica on Maize Yield and Its Insecticidal Activity Against Some Stored Insects After the Post-Harvest

Reprinted from: *Nanomaterials* **2020**, *10*, 739, doi:10.3390/nano10040739 189

Rabia Akan and Ulrich Vogt

Optimization of Metal-Assisted Chemical Etching for Deep Silicon Nanostructures

Reprinted from: *Nanomaterials* **2021**, *11*, 2806, doi:10.3390/nano11112806 **209**

About the Editor

Céline Ternon

Céline Ternon graduated with PhD degrees from the University of Caen in 2002. Her doctoral research involved the growth, modelling and study of luminescent silica and silicon-based nanostructures. She joined the Grenoble INP Institute of Engineering, Univ. Grenoble Alpes in 2003, where she is currently associate professor, gender equality officer and head of the department Physical Engineering for Photonics and Microelectronics.

She conducts research at LMGP in France in the field of nanomaterials and nanotechnologies. Her research interest lies at the interface between material science and device application, with a particular interest for the field of biosensing. One of her main objective is to develop new processes allowing the easy manipulation and integration of the nanomaterials into devices. In 2010, she launched an original activity based on semiconducting randomly oriented nanowire networks also called nanonets. Since then, she has worked tirelessly to demonstrate the value of these extremely versatile and innovative materials. She has more than 50 peer-reviewed scientific papers and several pedagogical publications.



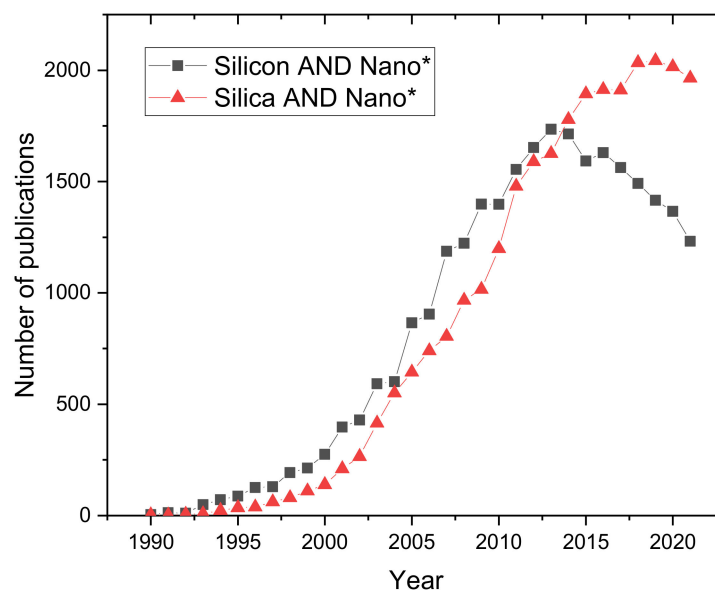
Editorial

Silica- and Silicon-Based Nanostructures

Céline Ternon

Univ. Grenoble Alpes, CNRS, Grenoble INP (Institute of Engineering Univ. Grenoble Alpes), LMGP, F-38000 Grenoble, France; celine.ternon@grenoble-inp.fr

As depicted in Figure 1, studies on silicon and silica-based nanostructures first appeared in the early 1990s, and their numbers grew until the mid-2010s. Since then, the level of scientific research has decreased for silica-based nanostructures and started to decrease for silicon-based nanostructures. An extensive literature review of silicon-based nanostructures clearly shows that the major areas affected by the decline in the number of studies are “applied physics” and “engineering electrical electronic”, whereas numerous applied fields are the subject of increased interest, particularly the applications of energy.



Citation: Ternon, C. Silica- and Silicon-Based Nanostructures. *Nanomaterials* **2022**, *12*, 1270. <https://doi.org/10.3390/nano12081270>

Received: 16 March 2022

Accepted: 25 March 2022

Published: 8 April 2022

Publisher's Note: MDPI stays neutral with regard to jurisdictional claims in published maps and institutional affiliations.



Copyright: © 2022 by the author. Licensee MDPI, Basel, Switzerland. This article is an open access article distributed under the terms and conditions of the Creative Commons Attribution (CC BY) license (<https://creativecommons.org/licenses/by/4.0/>).

Figure 1. Number of articles published per year about silicon or silica nanostructures, based on a search using the keywords “Silicon AND Nano*” or “Silica AND Nano*” on the website Web of Science. The star * at the end of nano means that all words beginning with “nano” are considered in the search (nanoparticles, nanowires . . .).

For silicon nanostructures, such a decrease in research is a sign that structures and technologies have been mastered and that the most popular applications, such as electronic devices, have been explored. Research teams are now exploring new areas and applications for these nanostructures.

The purpose of this Special Issue is to bring together state-of-the-art innovations in the field and allow the emergence of novel ideas and concepts for silicon- and silica-based nanostructures. The three reviews in this Special Issue [1–3] offer an original view of the last 10 years of research on silicon nanostructures, especially for black silicon [1], bottom-up nanowires [2], and mesoporous silicon [3]. Most interestingly, these reviews outline the areas of interest for the future of these materials. In line with this, some studies [4–10] clearly

illustrate the thematic shift of research into these materials, with a growing interest in eco-responsive areas, such as biomass synthesis [4], environmental sensors [5], batteries [6,7] or depollution [3].

In conclusion, we hope that the readers will enjoy the works and articles collated in this Special Issue, inspiring ideas and providing information to inform further studies of these fascinating nanomaterials, as well as generating new projects and topics.

Acknowledgments: I would like to thank all the authors who contributed their most recent research to this Special Issue. We would like to thank all those who contributed to the success of this Special Issue for their patience, help and dedication.



Conflicts of Interest: The authors declare no conflict of interest.

References

1. Fan, Z.; Cui, D.; Zhang, Z.; Zhao, Z.; Chen, H.; Fan, Y.; Li, P.; Zhang, Z.; Xue, C.; Yan, S. Recent Progress of Black Silicon: From Fabrications to Applications. *Nanomaterials* **2021**, *11*, 41. [CrossRef] [PubMed]
2. Arjmand, T.; Legallais, M.; Nguyen, T.T.T.; Serre, P.; Vallejo-Perez, M.; Morisot, F.; Salem, B.; TERNON, C. Functional devices from bottom-up Silicon nanowires: A review. *Nanomaterials* **2022**, *12*, 1043. [CrossRef]
3. Mendiratta, S.; Ali, A. Recent Advances in Functionalized Mesoporous Silica Frameworks for Efficient Desulfurization of Fuels. *Nanomaterials* **2020**, *10*, 1116. [CrossRef] [PubMed]
4. Sekar, S.; Lee, S. Derivation of Luminescent Mesoporous Silicon Nanocrystals from Biomass Rice Husks by Facile Magnesiothermic Reduction. *Nanomaterials* **2021**, *11*, 613. [CrossRef] [PubMed]
5. Peerzade, S.; Makarova, N.; Sokolov, I. Ultrabright Fluorescent Silica Nanoparticles for Dual pH and Temperature Measurements. *Nanomaterials* **2021**, *11*, 1524. [CrossRef] [PubMed]
6. Keller, C.; Desrues, A.; Karuppiyah, S.; Martin, E.; Alper, J.; Boismain, F.; Villevieille, C.; Herlin-Boime, N.; Haon, C.; Chenevier, P. Effect of Size and Shape on Electrochemical Performance of Nano-Silicon-Based Lithium Battery. *Nanomaterials* **2021**, *11*, 307. [CrossRef] [PubMed]
7. Nugroho, A.; Hawari, N.; Prakoso, B.; Refino, A.; Yulianto, N.; Iskandar, F.; Kartini, E.; Peiner, E.; Wasisto, H.; Sumboja, A. Vertically Aligned n-Type Silicon Nanowire Array as a Free-Standing Anode for Lithium-Ion Batteries. *Nanomaterials* **2021**, *11*, 3137. [CrossRef] [PubMed]
8. Zheng, D.; Monasterio, M.; Feng, W.; Tang, W.; Cui, H.; Dong, Z. Hydration Characteristics of Tricalcium Aluminate in the Presence of Nano-Silica. *Nanomaterials* **2021**, *11*, 199. [CrossRef] [PubMed]
9. El-Naggar, M.; Abdelsalam, N.; Fouda, M.; Mackled, M.; Al-Jaddadi, M.; Ali, H.; Siddiqui, M.; Kandil, E. Soil Application of Nano Silica on Maize Yield and Its Insecticidal Activity Against Some Stored Insects After the Post-Harvest. *Nanomaterials* **2020**, *10*, 739. [CrossRef] [PubMed]
10. Akan, R.; Vogt, U. Optimization of Metal-Assisted Chemical Etching for Deep Silicon Nanostructures. *Nanomaterials* **2021**, *11*, 2806. [CrossRef] [PubMed]

Review

Functional Devices from Bottom-Up Silicon Nanowires: A Review

Tabassom Arjmand^{1,2,3}, Maxime Legallais^{1,2}, Thi Thu Thuy Nguyen¹, Pauline Serre^{1,3}, Monica Vallejo-Perez¹, Fanny Morisot¹, Bassem Salem³  and Céline Ternon^{1,*} 

¹ Univ. Grenoble Alpes, CNRS, Grenoble INP (Institute of Engineering Univ. Grenoble Alpes), LMGP, F-38000 Grenoble, France; tabassom.arjmand@grenoble-inp.fr (T.A.); maxime.legallais@cea.fr (M.L.); thuthuynguyen2004@gmail.com (T.T.T.N.); pauserre@gmail.com (P.S.); monica.vallejop@gmail.com (M.V.-P.); morisoff@gmail.com (F.M.)

² Univ. Grenoble Alpes, CNRS, Grenoble INP (Institute of Engineering Univ. Grenoble Alpes), IMEP-LAHC, F-38000 Grenoble, France

³ Univ. Grenoble Alpes, CNRS, CEA/LETI-Minatec, Grenoble INP (Institute of Engineering Univ. Grenoble Alpes), LTM, F-38000 Grenoble, France; bassem.salem@cea.fr

* Correspondence: celine.ternon@grenoble-inp.fr

Abstract: This paper summarizes some of the essential aspects for the fabrication of functional devices from bottom-up silicon nanowires. In a first part, the different ways of exploiting nanowires in functional devices, from single nanowires to large assemblies of nanowires such as nanonets (two-dimensional arrays of randomly oriented nanowires), are briefly reviewed. Subsequently, the main properties of nanowires are discussed followed by those of nanonets that benefit from the large numbers of nanowires involved. After describing the main techniques used for the growth of nanowires, in the context of functional device fabrication, the different techniques used for nanowire manipulation are largely presented as they constitute one of the first fundamental steps that allows the nanowire positioning necessary to start the integration process. The advantages and disadvantages of each of these manipulation techniques are discussed. Then, the main families of nanowire-based transistors are presented; their most common integration routes and the electrical performance of the resulting devices are also presented and compared in order to highlight the relevance of these different geometries. Because they can be bottlenecks, the key technological elements necessary for the integration of silicon nanowires are detailed: the sintering technique, the importance of surface and interface engineering, and the key role of silicidation for good device performance. Finally the main application areas for these silicon nanowire devices are reviewed.

Keywords: nanowires; nanonets; transistor; integration process; silicon

Citation: Arjmand, T.; Legallais, M.; Nguyen, T.T.T.; Serre, P.; Vallejo-Perez, M.; Morisot, F.; Salem, B.; Ternon, C. Functional Devices from Bottom-Up Silicon Nanowires: A Review. *Nanomaterials* **2022**, *12*, 1043. <https://doi.org/10.3390/nano12071043>

Academic Editor: Yun-Mo Sung

Received: 9 February 2022

Accepted: 14 March 2022

Published: 22 March 2022

Publisher's Note: MDPI stays neutral with regard to jurisdictional claims in published maps and institutional affiliations.



Copyright: © 2022 by the authors. Licensee MDPI, Basel, Switzerland. This article is an open access article distributed under the terms and conditions of the Creative Commons Attribution (CC BY) license (<https://creativecommons.org/licenses/by/4.0/>).

1. Introduction

The study of nano-objects reveals a new world in which the observed properties may differ from those of bulk materials. When the size of structures reaches the nanoscale, the ratio of surface to volume of the structures increases drastically [1]. Since the number of atoms on the surface becomes comparable to the number in the volume, the physico-chemical properties of nanostructures are modified and even controlled by surface effects. These surface effects induce new properties compared to the bulk material that multiply the field of investigation. Over time, the study of nano-objects has increasingly become a scientific and technological revolution. Nanowires (NWs) can be defined as nanostructures that have diameters towards the nanometer scale (<100 nm).

Nanowires are still in an experimental stage and have not yet been used in real applications [2,3]. However, there is a graceful evolution in NW-based technology and investigations suggest that they can be used as the building blocks for the next-generation electronics and very sensitive biosensors [2,4,5]. Another possible real application of

nanowires is nano-electromechanical systems (NEMS) due to their high Young's moduli [2,6]. Nanorobots can also be aided by nanowires in the generation and conduction of their required energy [7].

In this review, we focus on synthesized silicon nanowires (bottom-up NWs) and do not consider nanowires formed by any etching techniques. These nanowires can be used vertically attached directly to their growth substrate [8,9], or detached from it to be transferred elsewhere and integrated into devices [10,11]. The mastery of the synthesis techniques allows obtaining nanowires of very small diameters, with controlled crystallinity and doping. In addition, surface engineering allows good control of their surface properties. Their quasi-one-dimensional characteristic gives them remarkable properties for many applications—such as electronic, optoelectronic, energy, and biomedical applications. In 1998, Morales and Lieber succeeded in synthesizing the first silicon and germanium nanowires with diameters of less than 20 nm for lengths greater than 1 μm [12]. This major breakthrough was an immediate success within the scientific community as a new field of research in nanoelectronics.

It is possible to make conducting (e.g., Ni, Pt, Au), semiconducting (e.g., Si, InP, GaN), and insulating (e.g., SiO_2 , TiO_2) nanowires which can find different possible real applications [2,13–15]. Among these nanowires, silicon nanowires (SiNWs) are considered as popular nanomaterials due to their exceptional electrical and mechanical properties and their conductivity can be controlled by the field effect behavior [2,16–18]. In addition, their synthesis is very well controlled due to broad study in the literature, their integration in transistors takes benefits from the technological knowledge related to the manufacture of MOSFET, particularly for the production of electrical contacts [19,20]. Finally, NWs have a very high length-to-diameter ratio called form factor. Because of this one-dimensional shape, which is comparable to some biological molecules, NWs are the ideal transducer for bio-detection. In 2001, Lieber's group was the first to highlight the promising potential of SiNWs as biosensors [21]. This technology still arouses curiosity today, and silicon nanowires are still potential candidates for field effect transistors and advanced sensors [22,23].

To appreciate the attractiveness of silicon nanowires (SiNWs) in a broad sense, we have shown in Figure 1 the result of a search on the Of Knowledge website with the keyword "Si or Silicon" AND "nanowire*" in the title. The first decade of the 21st century saw an explosion in the number of publications on silicon nanowires (Figure 1), as their potential appeared extremely promising. These publications are mainly concerned with the synthesis, formation, characterization, and integration into functional devices that are mostly composed of a single nanowire or several nanowires in parallel. From 2012 onwards, we observe a steady decrease in the number of publications. This can be attributed on the one hand to the less innovative aspect of the topic over the years with increasingly complete coverage of knowledge on this material. On the other hand, the difficulty of producing functional devices in a reproducible and efficient manner with technologies that are transferable to industry and at reasonable costs tends to blunt the appeal of these materials. A few years ago, and based on this observation, some groups [24–30] started to work on nanowire assemblies, also called nanowire networks and referred to as nanonets. Indeed, such assemblies benefit from advantageous nanometric properties, as well as easy connection to macroscopic objects thanks to their large dimension.

In this review, properties, growth, and transfer methods of SiNWs—either singularly, or in the form of a network—are reported. To have a better view of devices based on these materials, technological key parameters were discussed. Afterward, SiNW-based transistors are explored as building blocks for most of the applications depicted in different common forms—in particular, single NW field effect transistors (SiNW-FETs), nanonet field effect transistors (SiNN-FETs), and multi-parallel channel field effect transistors (MPC-FETs). Ultimately, it is shown that SiNWs, owing to their unique physical and chemical properties, are promising candidates for the wide range of applications that differ from those of bulk silicon material.

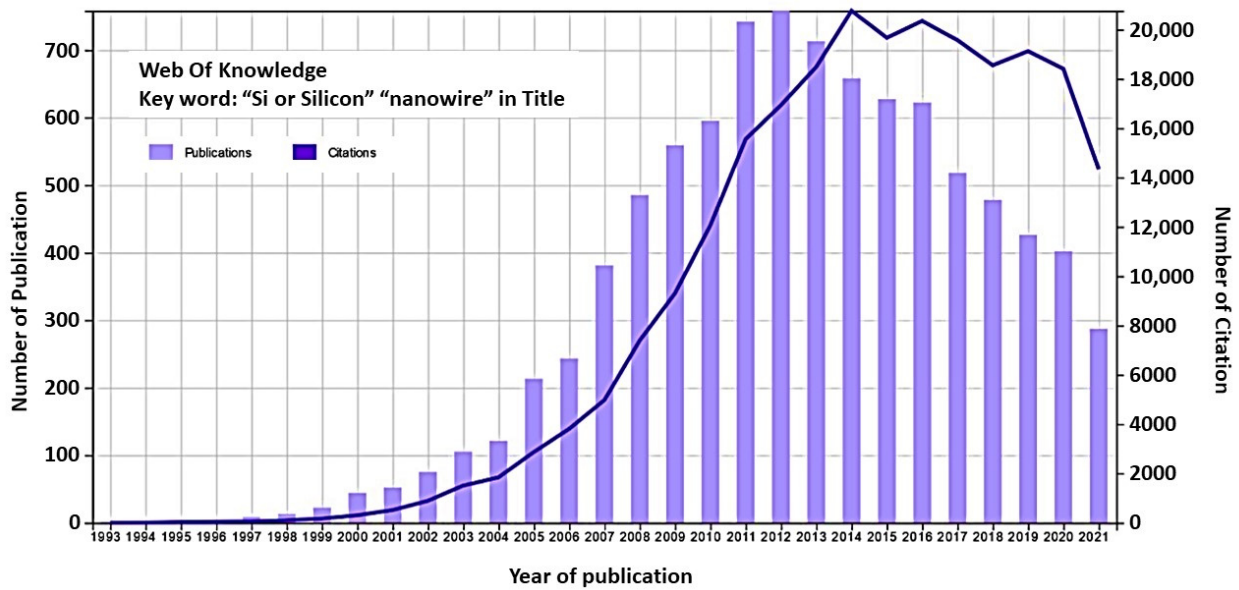


Figure 1. Number of articles published per year and the number of citations based on a search using the keyword “Si or Silicon Nanowire” on the website Of Knowledge.

2. From Nanowire-Based to Nanonet-Based Silicon Devices

There are a broad variety of nanowire-based devices—such as single nanowire, crossed nanowires, forest of upright nanowires, and two- and three-dimensional (2D and 3D) nanonet based devices—as schematically summarized in Figure 2. Crossed nanowire device architectures, more complex than single NW devices, can open up new opportunities that differentiate NW-based devices from conventional paradigms. Depending on the choice of NWs, the structure can yield a variety of critical device elements, including transistors and diodes [31]. Forest-like and 3D-NW structures, combining the properties of 1D and 3D nanostructures, could have more interesting properties than simple arrays of in-plane nanowires because of their higher porosity and specific surface area [32]. However, in this review, we will focus on single NW field effect transistors (SiNW-FETs), nanonet field effect transistors (SiNN-FETs), and multi-parallel channel field effect transistors (MPC-FETs).

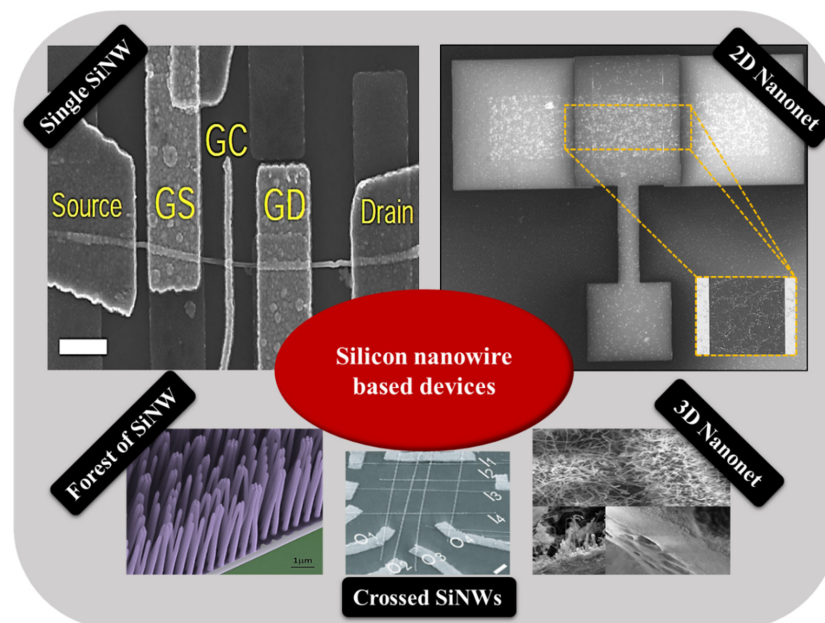


Figure 2. Different types of nanowire-based samples [33,34].

Today, single nanowire devices and parallel nanowire devices are well known to the scientific community and widely reported in the literature. Nanonet-based devices, on the other hand, are less well known, especially in the context of semiconductor nanowires. Nanonet, an acronym for NANOstructured NETwork, is a term that was introduced by George Grüner in 2006 [35,36]. It refers to a network of one-dimensional, randomly oriented nanostructures on the surface of a substrate. Two types of nanonets can be distinguished according to the thickness of the film formed. On one hand, three-dimensional nanonets have a thickness comparable to or larger than the length of the nanostructures (Figure 3a). On the other hand, two-dimensional nanonets are defined by a film thickness comparable to the diameter of the nanostructures (Figure 3b).

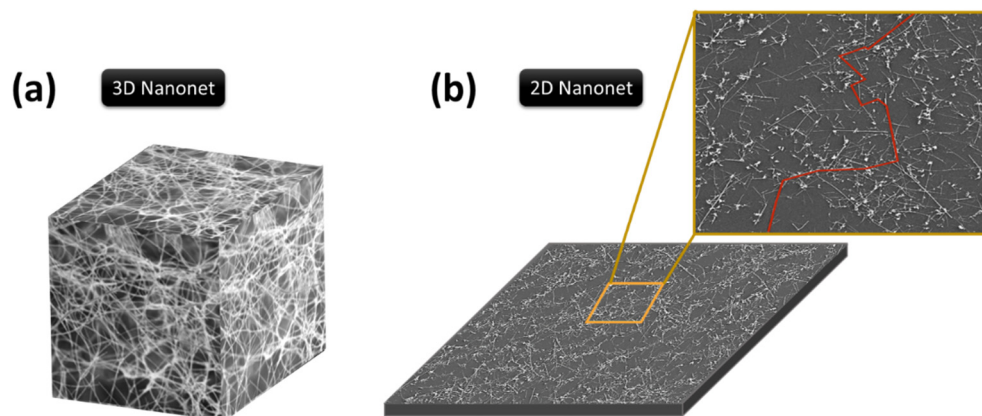


Figure 3. Schematic made by SEM images for representation of a nanonet (a) three-dimensional (3D nanonet) and (b) two-dimensional (2D nanonet). A top view and percolation path in red are highlighted in image (b).

Considering the electronic properties, such three-dimensional or two-dimensional networks are governed by percolation theory. Percolation is associated with a system in which randomly distributed objects of a given geometry may or may not form connections with each other [37,38]. A nanonet is then defined as percolating when a network of infinite size can communicate (e.g., conduct current) over the entire network via percolation paths that involve nanostructures and connections between nanostructures (Figure 3b). The density of nanostructures is a key parameter to control this communication (conduction in the current, etc.) via the interconnections between nanostructures. As a result, there is a critical density, called the percolation threshold, at which percolation pathways can be used to ensure communication in the nanonet. The manufacture of functional electrical devices from nanonets requires densities above the percolation threshold. Besides, nanonets are highly interesting because once the nanostructures are gathered to form the network, new properties appear and multiply the number of degrees of freedom. These properties are separated according to the intrinsic properties of the nanostructures and the macroscopic properties that come from the nanonet itself [36,39]. The particular properties of the nanonets are described in Section 4 in detail.

The literature on silicon nanonets remains scarce, despite the very well-controlled growth of NWs and excellent carrier mobility in bulk materials [40,41]. One of the plausible reasons for the lack of interest in these nanonets is the formation of an oxide that forms around the NWs when they are exposed to air. This native oxide is an electrical insulator and thus limits conduction across the junctions between NWs and the fabrication of long channel devices [42]. As a consequence, there is a deep-seated belief in the scientific community that it would be impossible to produce functional electrical devices based on Si-NW networks. To overcome this major disadvantage, Heo et al. [42] used intermediate metal contacts in the transistor channel to allow current to flow despite insulating junctions between SiNWs, but such a solution has a profound impact on the nanonet and the advantages arising from the geometry of the nanonets are probably lost. The Lieber group [43] also made devices

with arrays of silicon NWs; however, the length of the NWs remains close to the length of the channel and therefore the current can flow directly from one contact to another without using junctions between NWs. Furthermore, SiNNs have also been studied by the Unalan group for photodetection applications [44]. According to their observations, light makes it possible to reduce the height of the energy barrier at the level of the junctions between NWs, thus allowing the passage of current through the devices. However, even in that study, the length of the channel remains comparable to that of the NWs, limiting the junction number to one maximum. As a result, few NW/NW junctions are involved in the conduction of the nanonet, which prevents the full benefits of network geometry from being exploited.

Generally, semiconducting nanonets—in comparison with metallic ones—are much less studied and, most of the time, when dealing with NWs, the reported work is an isolated study that is not followed by any other publication [24,44–46]. We believe that the reason for this lies in the great sensitivity of semiconducting nanonets to their environment, which makes electrical properties unstable and weakly reproducible at first sight. However, Ternon's group has demonstrated that appropriate surface engineering and optimization of the effects resulting from the nanometric scale allow addressing this instability and low reproducibility. As a consequence, sensitivity can be controlled instead of endured [47]. As a result, they developed a process for sintering junctions that makes nanonets insensitive to oxidation in the long term [48] making their integration into electronic devices possible.

Among NWs, SiNWs are considered one of the most popular one-dimensional materials due to their functionality for nanoscale electronics without the need for complex and costly fabrication facilities. The main obstacles to the mass production of single NW devices, including high-resolution lithography technologies or elaborated process technology, are still valid. There are a huge number of papers on single SiNWs, but not all the other class of SiNW assemble like silicon nanonets, although they indicate being a good alternative for single NWs due to their easier integration and production in large-scale electronics. These types of materials combine the advantage of NWs, such as high sensitivity, with the ability to be transferred on any kind of substrates, whether rigid or flexible.

3. Silicon Nanowire Properties

3.1. Mechanical Properties

Mechanical properties of nanowires are of considerable significance in device processing since changes in temperature, induced strain, and external stress can change the electrical conductivity of the nanowire due to internal dislocations or flexoelectricity [49,50]. The processing of VLSI (very large-scale integration) induces compressive and tensile stresses via deposition of different materials which can cause failure in devices mainly due to delamination and electro-migration [51]. Moreover, due to the Si NW ability to relax strain, it presents the possibility to also combine lattice mismatched materials (e.g., Ge) in axial heterostructures without the formation of misfit dislocations. Nanowires, which are 1D systems, are expected to have interesting mechanical properties due to their high aspect ratio compared to bulk materials and reduced number of defects per unit length [6,51]. However, manipulating these materials for mechanical measurements is a challenging task [51,52]. The main methods which are used to investigate their mechanical properties are mechanical resonance, atomic force microscopy (AFM), and nanoindentation [18,52]. The resonance method is used only for the determination of the elastic properties and is not easy to measure the applied force. On the other hand, nanoindentation has very good force and displacement resolution and control [52].

Experiments based on the AFM-based nanoindentation showed that the stiffness of silicon nanowires is well described by the Herz theory [18]. Therefore, the wires with diameters in the range of 100 nm to 600 nm have elastic modulus values which are independent of the wire diameter and are more or less identical to those of bulk silicon [18]. This implies that the elastic characteristics of silicon nanowires with diameters larger than 100 nm are not affected by the finite size effect. Furthermore, the elastic modulus of nanowires with diameters of less than 100 nm was found to decrease with diameter [18]. In contrast, com-

putational studies do not support any size dependence of Young's modulus for SiNWs with a diameter greater than 10 nm [53,54]. In fact, some experimentalists disagree on the evolution of Young's modulus as a function of size [55]. In many cases, experimentally depicted structures and the analogous theoretically simulated models have different dimensions, surface contours, or passivation. Therefore, it has been speculated that the surface effects should have a certain influence on the difference between experimental and theoretical data. Importantly, the experimental proofs of possible sources of such misconceptions have been provided, at least for the resonance and tensile tests [56–60].

Moreover, NWs can be used in the field of sensors and nano-electromechanical systems (NEMS) [18,51]. This is because, according to their tensile strength and Young's modulus, they are very robust materials and have the ability to store elastic energy [51,61]. Then, nanoscale resonators can be built from silicon nanowires with high oscillation frequencies (100 MHz up to 1 GHz) because of their excellent elastic properties [18,51]. The detection of molecules at atomic resolution was achieved with these nanoscale resonators [18].

3.2. Electrical Properties

The small sizes of SiNWs make their electronic and electrical properties strongly dependent on growth direction, size, morphology, and surface reconstruction. A well-known example is the size dependence of the electronic bandgap width of SiNWs irrespective of wire direction. As the nanowire diameter, d , decreases below 10 nm, the band gap of the nanowire widens and deviates from that of bulk silicon gradually (Equation (1)) [62]. Moreover, the orientation of the NW axis and the surface have a great effect on the electronic properties of SiNWs [63].

$$\text{Band Gap} \propto \frac{1}{d^n}; 1 \leq n \leq 2 \quad (1)$$

Therefore, the electronic properties—such as the band gap, valley splitting, and effective mass—are also functions of the diameter [64]. These affect the transport properties of the nanowires [65]. Hydrogen and oxygen terminated SiNWs have also been studied to gain an understanding of their optical and electronic properties [66–68].

In the presence of perfect crystalline SiNW with four atoms per unit cell, three conductance channels are found corresponding to three s bands crossing the Fermi level [69]. Conductance variations are observed if one or two atoms are added or removed. Thus, the conductance is affected by the crystalline structure of the nanowire [23]. Furthermore, variations in the surface conditions, such as scattering phenomena of carriers in nanowires, cause changes in conductivity [23,51]; meanwhile, it is also seen that scattering phenomena are NW diameter dependent [23,70].

The large aspect ratio of nanowires makes their conductivity very sensitive to surface excitation by external charges [6,23,61]. As it is seen in Figure 4, a small surface perturbation can influence the entire section of the nanowire, whereas in the case of a thin film, only a fraction of its surface is influenced. This important property is the reason why silicon nanowires are so electrically sensitive to surface events. Thus, this phenomenon is the basis for the detection of single molecules and the use of silicon nanowires in biosensors [17,22,61,71].

It has been shown that threshold voltage (V_{th}) can be significantly tuned by the NW diameter (d) [72,73]. V_{th} is linearly proportional to d in an NW field effect transistor (NWFET) due to the greater influence of the surface scattering processes. NWFETs based on thin nanowires exhibit a steep subthreshold slope with a small threshold voltage, but low conductivity in comparison with NWFETs with larger diameters in which—due to high short-channel length effects—they experience a moderated subthreshold slope with a larger threshold voltage [74].

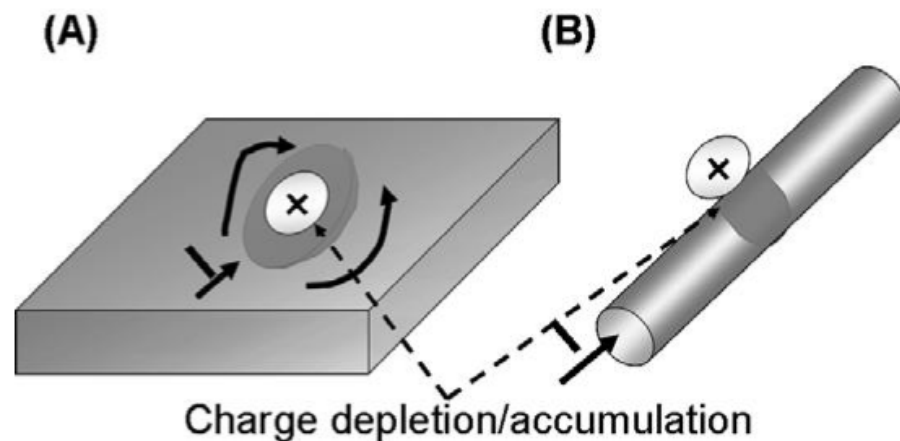


Figure 4. The major advantage of 1D nanostructures (B) over 2D thin film (A). Binding to 1D nanowire leads to depletion or accumulation in the ‘bulk’ of the nanowire as opposed to only the surface in the 2D thin-film case. Reproduced from [61].

Additionally, the free carrier concentration in silicon nanowires depends on the size of the structure. It was shown that the donor ionization energy of silicon nanowires increases with decreasing nanowire diameter. Therefore, the free carrier density can be profoundly modified at diameter values much larger (>10 nm) than those at which quantum and dopant surface segregation effects are set in [16].

Thus, silicon nanowires exhibit charge trapping behavior and transport properties, tunable by surface engineering, that make them attractive for use in electronic devices such as MIS (metal–insulator–semiconductor) structures and field effect transistors (FET). Therefore, SiNWs are attractive for designing a wide range of functional devices such as flash memory, logic devices, as well as chemical and biological sensors [51,62,75–78].

3.3. Surface Chemistry

As for bulk silicon, silicon nanowires are subject to surface oxidation when exposed to an oxidizing atmosphere such as air. This native oxide is of poor quality and is accompanied by many oxygen-derived defects. Moreover, native oxides are a contamination source by metallic impurities [79] and are poorly stable in aqueous media [80]. Native oxide can be easily removed by using either chemical reactants—such as buffer oxide etching (BOE) solution, diluted hydrofluoric acid (HF), HF vapor, and gaseous ammonia (NH_3)—or by physical etching method including argon (Ar) plasma etching. Most of these methods provide hydrogenated surfaces that are an interesting starting point for further functionalization in the frame of sensor applications [79,81].

In contrast to bulk silicon or thin films, the oxidation kinetics of H-terminated silicon nanowires is very slowed down regardless of the oxidation temperature (ambient–900 °C) compared to planar structures [82–85]. Moreover, it has been shown that—below 100 nm in diameter—the smaller the diameter of the nanowires, the slower the phenomenon [83]. This change in kinetics is commonly explained by compressive stress at the SiO_2/Si interface retarding the interfacial reaction [82,83]. Then, this effect becomes more significant for a more curved surface [86]. On this basis, Fazzini et al. propose that since oxidation retardation is inversely proportional to nanowire diameter, this property can be used to homogenize the diameter of a given nanowire population [87]. Such a slowing down of oxidation is an extremely interesting phenomenon when it comes to making functional devices. Indeed, this unwanted oxidation has detrimental effects on the electronic properties of nanowires. Preventing oxidation during silicon processing is an important task in all microelectronic processing. Thus, thanks to this slowing down of oxidation, silicon nanowires with a diameter lower than 10 nm can remain several days in the ambient air without oxidizing and can then be easily processed without any special precautions against oxidation [84].

3.4. Optical Properties

Remarkably, small diameter (<6 nm) SiNWs grown along most of the crystallographic orientations have a direct band gap [88], meaning that the maximum of the valence band and the minimum of the conduction band occur at the same point in the reciprocal space. This property has allowed envisaging the use of SiNWs as optically active materials for photonics applications [89]. Silicon nanowires exhibit strong antireflective properties and are capable of enhancing optical absorption over that of bare bulk crystalline silicon [90]. Nanowires can exhibit mechanical strain effects if exposed to light which has a wavelength comparable to their energy bandgap. This is due to their photoelastic properties [18].

In all, as yet it has been shown that SiNWs are found to possess such remarkable optical properties as visible photoluminescence (PL) [91,92], very low total reflection [92,93], enhancement of Raman scattering [92–94], coherent anti-Stokes light scattering [95], inter-band PL [93,96], and efficiency of generation of third harmonics whereby light is generated at a wavelength which is one-third of the pump wavelength [92,97].

3.5. Thermal Properties

SiNWs could have applications in nano- and micro-scale thermoelectric power generators [98,99]. Therefore, it is important to study their thermal conductivity. However, for a major increment in the Seebeck coefficient, nanowires with a diameter of less than 5 nm are required [100]. The optimal diameter of NWs for good thermoelectric properties is between 30 and 100 nm. The thermal conductivity can be very small if rough nanowires are fabricated, while electrical conductivity and the Seebeck coefficient are very close to the bulk silicon [101]. Two opposite phenomena compete within the nanowires with respect to the thermal conductivity. On the one hand, as the diameter of the nanowires decreases, the surface-to-volume ratio increases, which increases the surface scattering effects and thus decreases the thermal conductivity of the nanowires. On the other hand, it has been predicted that for very small diameters (<1.5 nm), by a quantum confinement phonons effect, the thermal conductivity increases [102,103].

One has to note that silicon nanowires, when used within applications or experiments, may have a curved-like shape and not be straight. As the phonon transport can be affected by their curvature, their thermal conductivity then changes. There is an additional obstructive mechanism to phonon transport, particularly in the ballistic regime, thanks to the deviation of phonon from the main heat flow direction due to its curvature. Therefore, thermal conductivity is reduced when the radius of the nanowire curvature increases [5]. The effect of the curvature on the thermal impedance has a greater effect when the radius of the curvature is one order smaller than the phonon mean free path [5].

This observation is interesting since the thermal conductivity of silicon nanowires can be controlled by the proper shaping of the wire. For instance, the thermal conductivity of NWs with large roughness is found to be significantly below the prediction [5,104]. This is important in the use of silicon nanowires in next-generation electronics because the shrinking of electronic devices towards the nanoscale region demands an increase in power dissipation per unit area [99,105].

4. Silicon Nanonet Properties

Two-dimensional (2D) nanonets are very promising because, by an averaging effect, the structure provides an increase in the reproducibility of nanonet properties by minimizing the disparities existing between the NWs. It also compensates for potential failures in operation to the extent that NWs from the network, which are not initially involved in conduction paths, can contribute to a new conduction path to bypass the failed NWs. Nanonets offer undisputed advantages thanks to the wise combination of the intrinsic properties of nanostructures with those of the nanonet. According to Zhao and Grüner, the 'nanonet' morphology can be regarded as a fourth material phase in addition to monocrystalline, polycrystalline, and amorphous structures [106]. Finally, because of the coexistence of NWs and junctions within a conduction path, it is expected that the switching of the

transistors from 'off' state to the 'on' state will be even more abrupt as the number of junctions increases [107]. However, to allow these advantages to be revealed and exploited, it is important that the dimensions of the nanonet be much larger than the length of the NWs and that the number of NWs involved in conduction is sufficiently large. Here, important parameters impacting nanonet-based devices besides ones from individual NWs are the morphological quality of the nanonets, the density of NWs within the nanonet, the size of the nanonet, and particularly the distance between the two electrodes of the device compared to the length of NWs. Such degrees of freedom in nanonet create vast opportunities in future applications.

4.1. Electrical Conductivity

Above the percolation threshold, the current is likely to flow through percolation paths (also called conduction paths) that involve nanostructures and connections between nanostructures. These junctions between nanostructures appear as an energy barrier for carriers and are therefore likely to be more resistive than nanostructures [36,108]. In that case, they can control conduction within the nanonet. As mentioned earlier, these junctions generate additional resistance, so they can enormously affect percolation transport in nanowire network [107,109]. Such a two-dimensional network is normally governed by the theory of percolation. Percolation is often defined as a system in which randomly distributed objects of a given geometry can form, or not form, connections between each other [37,110,111]. A nanonet is then defined as a percolating system when a network of infinite size can communicate (e.g., conduct current) over the entire network via percolation paths that involve nanostructures and connections between nanostructures. The density of nanostructures is a key parameter to control the communication in the medium via the interconnections between nanostructures. As a result, there is a critical density—called the percolation threshold—above which percolation paths allow for communication in the nanonet. The fabrication of functional electrical devices from nanonets requires the use of densities above the percolation threshold.

4.2. Porosity and Optical Transparency

Due to the very high aspect ratio of nanostructures, and by playing with the density and diameter of NWs, NNs can reach even 90% of optical transparency as illustrated in Figure 5.

Indeed, for low-density percolating networks, nanonets are essentially composed of voids. In the case of metallic NWs, this property makes nanonets particularly attractive as transparent electrodes [26]. With the same idea, in the case of semiconductor NWs, nanonets would be particularly attractive to form transparent transistors and transparent electronics in general. Moreover, the high porosity of the nanonet can allow the insertion of functional materials [108], which is of high value when dealing with biosensors.

4.3. Mechanical Strength and Flexibility

Based on the excellent flexibility in individual nanowires which is diameter dependent, and for diameters less than 100 nm is remarkable when these nanostructures are assembled as a nanonet, the entire network is capable of being subjected to mechanical deformation [112] (Figure 5) and can adapt to the substrate morphology [112,113]. The flexibility in the choice of nanostructures and the unique structure of the network suggests a broad spectrum of applications for nanonets, as we will see in the following.

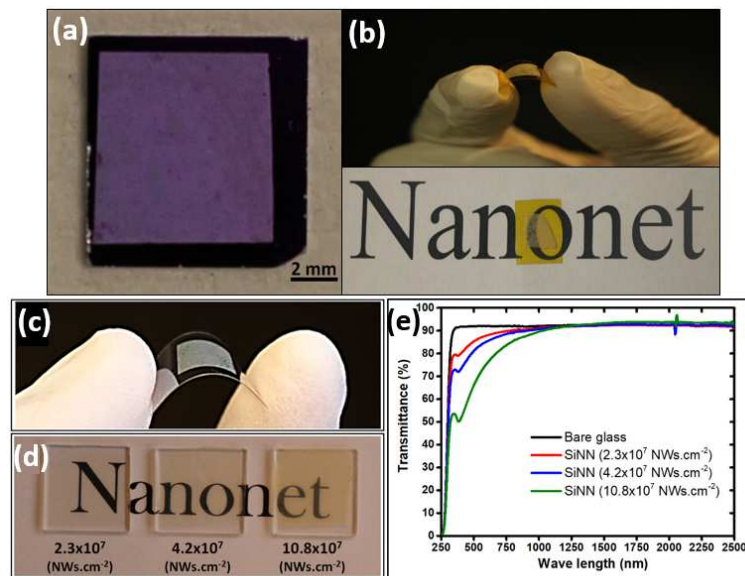


Figure 5. Silicon nanowire nanonets manufactured by vacuum filtration and then transferred to (a) Silicon/Si₃N₄, (b) Kapton, (c) plastic, and (d) glass substrates. (e) The transmittance of SiNN with the three densities were shown in image (e), the transmittance of the substrate (bare glass) is also reported. Reproduced from [114].

4.4. Fault Tolerance and Reproducibility

For electrical devices, conduction in a nanonet is ensured by multiple percolation paths that connect the two metallic contacts. Then, the number of conduction paths is greater but the presence of junctions within each path ultimately implies a reduction in current. Therefore, for a given electric field, the amount of current is generally lower in nanonet than in single nanowire devices (Figure 6). However, if one path is faulty, many other conduction paths remain and can guarantee the functionality of the device [36].

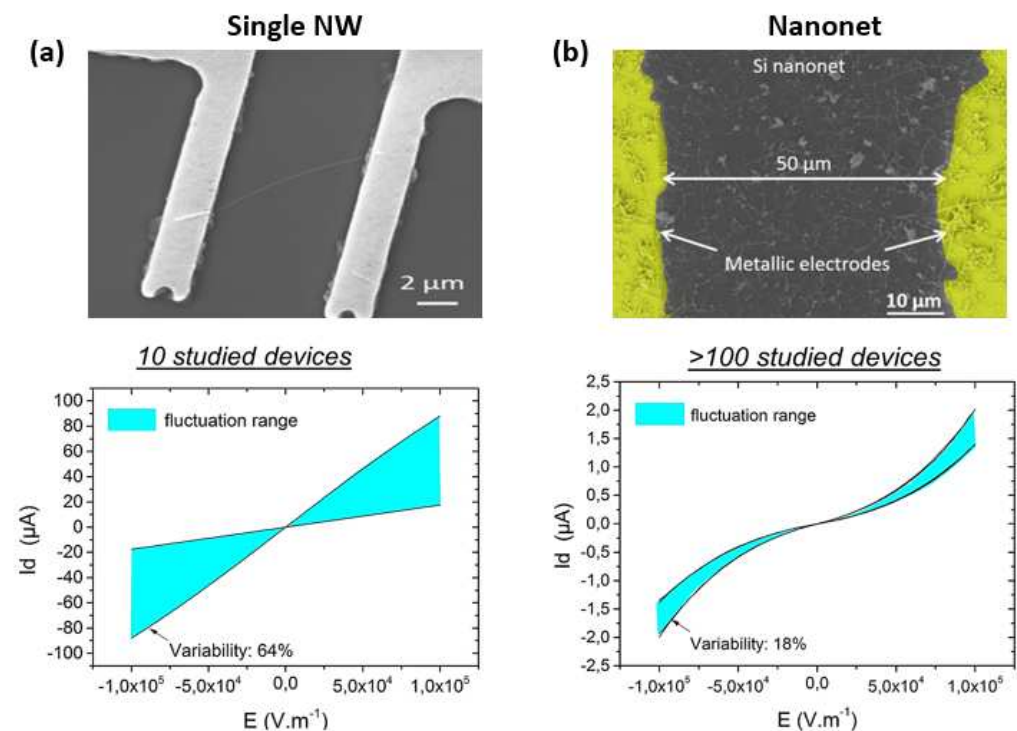


Figure 6. SEM image and fluctuation range in the current of (a) single nanowire and (b) nanonet-based resistors. Reproduced from ref. [28].

Moreover, the macroscopic properties of a given nanonet are the result of a considerable number (for $1 \times 1 \text{ cm}^2$ e.g., 10^6 – 10^8 NWs) of nanostructures which makes it possible to smooth out the disparities that may exist from one NW to another. Therefore, the properties of the nanonets show less disparity than those of the population of nanowires that constitute it. This can be demonstrated by studying the electrical characteristics of the single nanowire or nanonet devices based on the same nanowire population, as Pauline Serre has done. With a technological work based on heavily doped NWs (degenerated), she produced single SiNW resistors and Si NN resistors (Figure 6) [28,39]. By studying numerous devices (10 single SiNW resistors, >100 SiNN resistors), evidence of averaging effect is proven for nanonets. Indeed, the dispersion in the current of these two types of devices is clearly different: 64% for single NW resistors, against 18% for SiNN resistors. As a consequence, one of the main drawbacks of the single NW-based devices, lack of reproducibility, can be eliminated by the nanonet geometry.

5. Silicon Nanowire Growth

There are two major approaches to form nanowires. The ‘top-down’ approach starts from bulk silicon in the form of a substrate or thin film silicon with the use of SOI substrate with the objective to etch the material until reaching the formation of high aspect ratio structures called nanowires, but which section is not necessarily circular. Besides, the ‘bottom-up’ approach is used to grow nanowires, either vertically on the substrate or in-plane lying on the substrate. In the past few decades, there has been extensive research on synthetic nanowire strategies focused on a bottom-up approach to understand the growth of nanostructures, tune the geometrical dimensions during growth, and form heterostructures. Here, we focus on bottom-up approaches that give the opportunity to detach the NWs and to collect them with the objective to form a nanonet by assembling the NWs. Then, targeted bottom-up syntheses are additive and can be done in two phases: vapor and solution phase.

5.1. Vapor Phase

5.1.1. Low Pressure

In the frame of low-pressure chemical growth, silicon nanowires are synthesized using the vapor–liquid–solid (VLS) mechanism (see Figure 7A) on a silicon substrate $\langle 111 \rangle$ from a metal catalyst (Au [115,116], In [117], Pt [118], Sn [119], etc.) in a CVD reactor. To allow the NW growth, the catalyst must be present on the surface of the substrate in the form of nanoparticles. For this purpose, it is possible to disperse a solution of colloids on the surface of the substrate [11] or to deposit a thin film that forms nanoparticles by thermal dewetting [117]. Then the growth of the Si nanowires is carried out in the presence of silane, SiH_4 , used as a precursor to silicon. The Si atoms incorporate into the metallic droplets and when it reaches saturation, the excess silicon crystallizes at the interface between the droplet and the substrate. This process continues as long as the system is supplied with gaseous precursors and thus forms silicon nanowires.

Silicon nanowires can be doped during growth by adding boron (p-doping) or phosphorus (n-doping) in gaseous form. Phosphine, PH_3 , is used for n-type doping and diborane, B_2H_6 , for p-type doping [120]. The concentration of dopants in nanowires is directly related to the ratio between the concentration of dopant gas and the concentration of silane [121], which allows the doping of nanowires to be controlled with great precision during the growth. Two other gases can also be added during the synthesis of nanowires: hydrogen, H_2 , which is used as a carrier gas; and hydrogen chloride, HCl , which is used to prevent the diffusion of gold on the surface of the nanowires and thus inhibit the lateral and branch growth of the structures [121–123]. The silicon nanowires produced by VLS are of good crystal quality and can have a very high length at low costs. The length of the nanowires is controlled by the time of the growth and diameter of the nanowires depending on the size of the metallic nanoparticles [21].

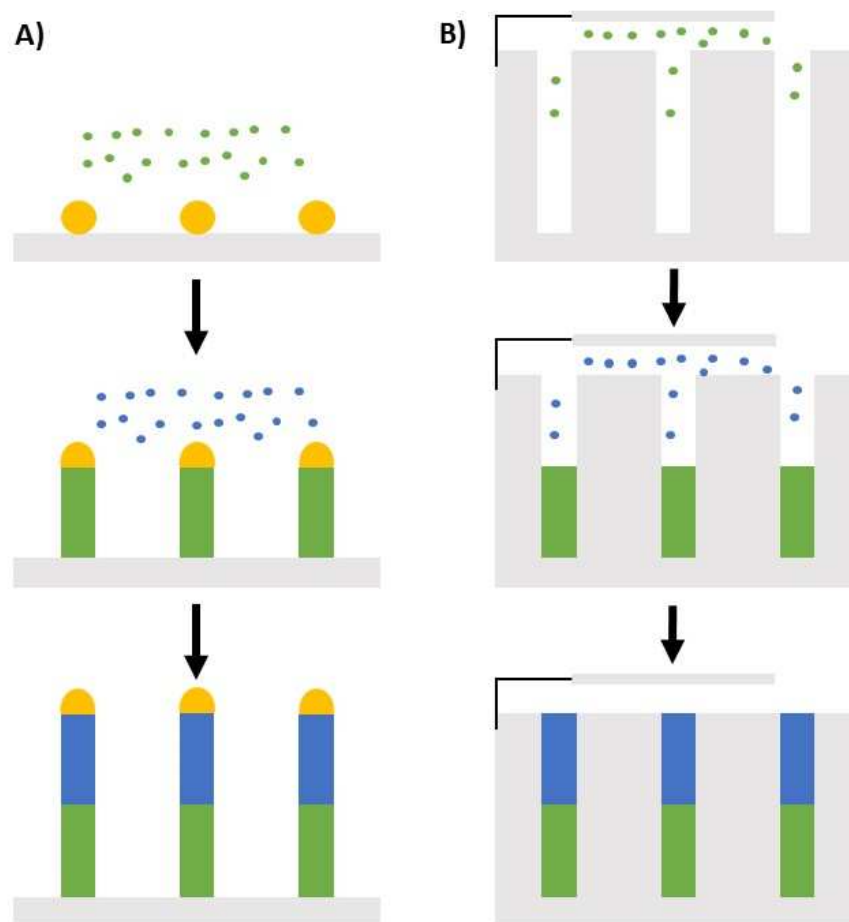


Figure 7. Schematic representation of two bottom-up synthesis methods. **(A)** Vapour-Liquid-Solid Chemical Vapor Deposition (VLS-CVD). Segmentation in composition is possible by the modulation of the gaseous precursor. **(B)** Electrochemical deposition in solution into anodic aluminum oxide. Segmentation is also possible.

5.1.2. High Pressure

The patented SyMMES technique [124] is similar to the CVD method and it aims to make its industrial scaling simpler, by limiting the hazard of the reactants, facilitating reactor design, and producing nanowires in large quantities.

In Figure 8, this method is shown for the solvent-free chemical synthesis of thin (10 ± 3 nm) SiNWs using diphenylsilane as a Si source and small (1–2 nm) gold nanoparticles (AuNP) as a catalyst in a sealed reactor at 420 °C and with a pressure < 10 bar. The catalyst nanoparticles are immobilized on micron-sized salt (NaCl) powder, which acts as a sacrificial 3D substrate which is easily removable by washing with water after NW growth. Pure SiNWs are obtained at a high production yield of 1 mg cm^{-3} of reactor volume and with a 70% chemical yield. In this method, n-type doping of the SiNWs is achieved by adding diphenylphosphine at concentrations of 0.025 to 1.5% as the dopant source [125]. Recently, the impact of the size/shape of SiNWs grown by this technique is also demonstrated on the electrochemical performance of conventional Li-ion batteries [126].

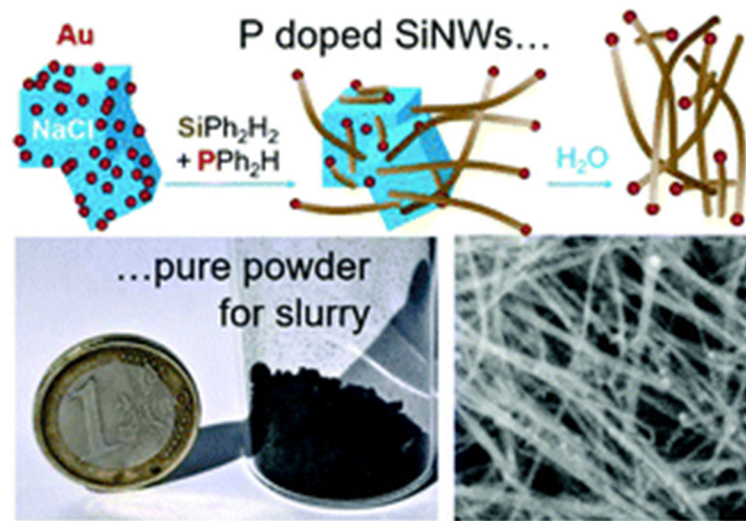


Figure 8. Schematic of the growth principle of SiNWs, and SEM image of as-grown silicon nanowires. Reproduced from [125].

5.2. Liquid (Solution) Phase

The first liquid phase technique for SiNW growth is the direct counterpart of the VLS technique. Then the solution–liquid–solid (SLS) mechanism is fully similar to that of VLS, except that nanowire precursors are dissolved into a high-boiling liquid, such as squalene ($C_{30}H_{62}$), and the catalysts are suspended therein, as described by Heitsch et al. [127].

The second method in liquid involves electrochemical phenomena. Here, anodic aluminum oxide (AAO) substrates are used for templated solution growth, using electrochemical deposition to fill the channels as shown in Figure 7B [128]. Drawing upon the solution-phase synthesis of nanoparticles, redox reactions can also be used to produce nanowires [129]. Seed particles are first grown by a rapid reduction of a dissolved precursor with a strong reducing agent such as sodium borohydride. Secondary growth is achieved with a weaker reducing agent, such as L-ascorbic acid, to prevent additional seed particle production. The nanowire anisotropy is achieved by controlling surface chemistry [123].

5.3. Summary on Growth

Table 1 gives a simple comparison between the different techniques used for SiNW growth. We studied the various methods currently used in bottom-up SiNW growth. Gold is the most widely used catalyst for SiNW growth by CVD under VLS mechanism, as it offers a good size control. However, the recent advances in the mentioned SiNW growth techniques are still in their early stages. The most appropriate method for the growth will ultimately be determined by a number of factors, including the desired application, as well as the available process control and associated costs. SiNW properties can be finely tuned for the desired application using the various growth methods available.

Table 1. Comparison between different NW growth methods including low pressure VLS (LP VLS), high pressure VLS (HP VLS), SLS, and electrochemical.

Method	Diameter Range	Crystallinity	Doping	Yield	Scalability	Homogeneity	Catalyst	Freestanding
LP VLS	>30 nm	Monocrystalline	Highly controlled	Medium	Good	Generally dispersed	Yes	No
HP VLS	<30 nm	Polycrystalline	Controlled	High	Very good	Homogeneous	Yes	Yes
SLS	Between 20 and 30 nm	Monocrystalline	Controlled	Medium	Good	Dispersed	Yes	No
Electrochemical	Limited by template	Polycrystalline	Controlled	High	Good	Highly homogeneous	Yes	No

6. SiNW Collective Handling

After growth, the nanowires are detached from the substrate and dispersed in solution to allow collective manipulation (colloidal suspension). Depending on the chosen assembly technique, it is possible to form arrays with a preferred orientation which are then not necessarily percolating or to form randomly oriented arrays. The common points of all these methods are the low thermal budget (less than 200 °C) and the easy scalability. In the frame of electronic application and functional device formation, the formation of the percolating network is mandatory. As a consequence, when the applied method leads to a preferential orientation, a two-step process has to be used to allow the crossing of the NWs that is required to allow charge carrier displacement.

6.1. Network with Preferential Orientation

6.1.1. Drop-Casting

The drop-casting is the simplest method to deposit NWs on top of a substrate. In this approach, a drop of a NW suspension is first deposited (literally 'drop-casted') on the surface. Second, a drying process is applied to evaporate the liquid. The clear advantage of this approach is its simplicity and versatility. There is also an opportunity to even mix different nanowires in a suitable solvent via ultrasonication before drop-casting. The main drawback is related to the homogeneity of the NW distribution on the substrate surface. Indeed, the drying process often induces shear forces that impact the NW positioning. As a consequence, drop-casting is well dedicated when the needs in terms of positioning or density are not too restrictive.

6.1.2. Fluidic Directed Assembly

In this method, nanowires can be assembled into parallel arrays with the control of average separation as well as complex crossed nanowires arrays. In this technique, the nanowires are suspended in a solution such as ethanol. Then, the suspension is sent through fluidic channel structures formed between poly(dimethylsiloxane) (PDMS) molds and a flat substrate. As a consequence, the NWs tend to align in the flow direction. In this way, by building the appropriate fluidic channel, parallel and crossed arrays of NWs can be readily achieved with single and sequential crossed flows (Figure 9), respectively, for the assembly [130]. The same result can be obtained with chemically patterned substrate that preferentially attracts the NWs in the functionalized region (Figure 9A).

The fluidic phase poses a challenge for single-nanowire control, accompanied to some extent by issues related to spacious microfluidic and large footprint electrodes [130].

6.1.3. Langmuir–Blodgett Assembly

Another promising method to produce aligned arrays of NWs on various substrates is the Langmuir–Blodgett (LB) technique [43,131–134]. In this technique, NW suspension is densely packed using a compression trough at an air–liquid interface. Dip coating can be then used to transfer the NWs onto receiver substrates by van der Waals, hydrophobic–hydrophilic, or electrostatic interactions when the substrate is lowered and withdrawn from the system, in the vertical direction as shown in Figure 10a.

This technique is frequently used in the assembly of highly ordered nanomaterials. By repeating the assembly process with a changed orientation of the substrate, hierarchical nanowire structures can also be produced as shown in Figure 10b–d [131].

The density of nanowires can be improved by adapting LB techniques to align the nanowires. Limitations of this technique include reorganization of the nanowires during dip coating that leads to overlapping features and gaps within the dense arrays of nanowires [43,133,134].

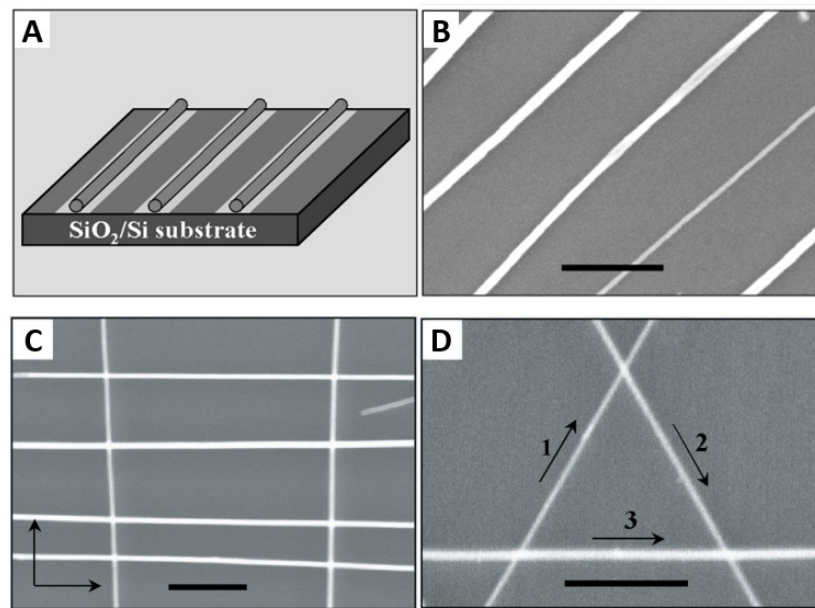


Figure 9. Assembly of periodic NW arrays and layer-by-layer assembly of crossed NW arrays. (A) Schematic view of the assembly of NWs onto a chemically patterned substrate. The light gray areas correspond to NH_2 -terminated surfaces, whereas the dark gray areas correspond to either methyl-terminated or bare surfaces. NWs are preferentially attracted to the NH_2 -terminated regions of the surface. (B) Parallel arrays of GaP NWs with 500-nm separation obtained with a patterned SAM surface. (C) Typical SEM images of crossed arrays of InP NWs obtained in a two-step assembly process with orthogonal flow directions for the sequential steps. Flow directions are highlighted by arrows in the images. (D) An equilateral triangle of GaP NWs obtained in a three-step assembly process, with 60° angles between flow directions, which are indicated by numbered arrows. The scale bars correspond to 500 nm in (B–D). Reproduced from [130].

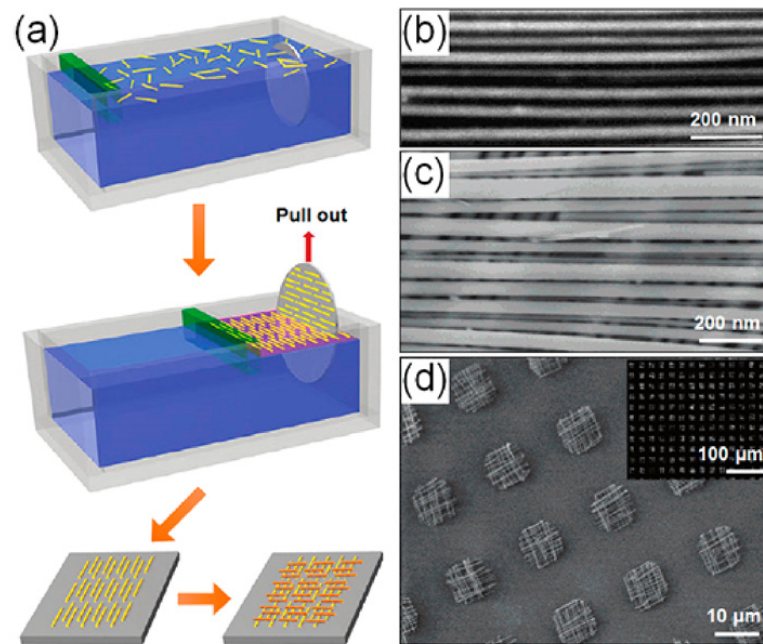


Figure 10. Langmuir–Blodgett assembly of nanowires. (a) Schematic illustration of the Langmuir–Blodgett assembly process. Reproduced from [134]. (b,c) SEM images of a high-density parallel nanowire array (b) and crossed nanowire array (c) on the substrates. (d) SEM images at different magnifications for patterned crossed nanowire arrays. Reproduced from [43].

6.1.4. Blown-Bubble Films

An approach with the potential for large scale transfer of well aligned NWs is the so-called blown-bubble film assembly (BBF) (Figure 11). This approach involves the preparation of homogeneous polymer suspension of NWs, followed by the expansion of polymer suspension using a circular die, and finally the breaking by an external force and the transfer of the bubble film to the desired substrate. By tuning the preliminary concentration, well aligned, and controlled density NWs over large areas are achievable [135–137].

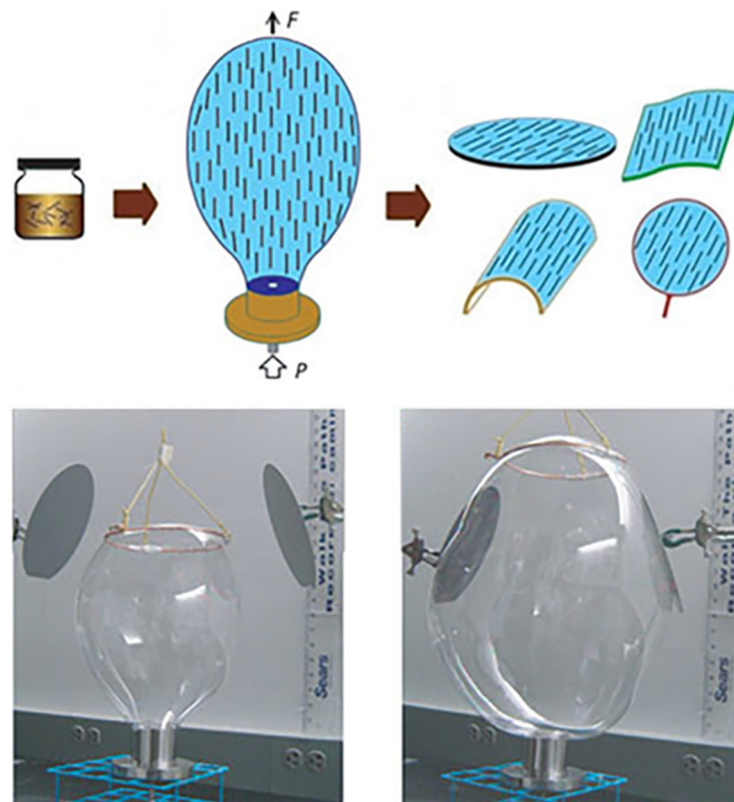


Figure 11. Illustration of blown bubble films method and photographs of the directed bubble expansion process in the early and final stages. Reproduced from [137].

Blow-bubble approach is inexpensive and can be adapted to patterning nanowires on many different types of substrates (e.g., flexible, flat, or curved). However, a challenge for these techniques is to control the viscosity of the bubble film in balance with a compatible surface coating on the nanowires, which has so far limited this demonstration to films of epoxy. Another challenge for this technique and for the alignment achieved using microfluidic flow is to precisely control the position of the deposited nanowires [43,136,137]. This method is highly attractive in a technology where device fabrication costs must be kept to a minimum and for transferring and aligning a variety of nanomaterials including SiNWs and CNTs [136,137].

6.1.5. Contact Printing

‘Printing’ has usually been used to describe a method by which a layer of ink is transferred from a stamp to a substrate through a reversing reaction [138,139]. Figure 12 contains an illustration of two different printing apparatuses. Printing methods thus include flexographic printing, offset printing, gravure printing, screen printing, and ink-jet printing. In the printing method, the choice of the solvents for ink preparation has been identified as an important parameter for active layer surface morphology [139–142].

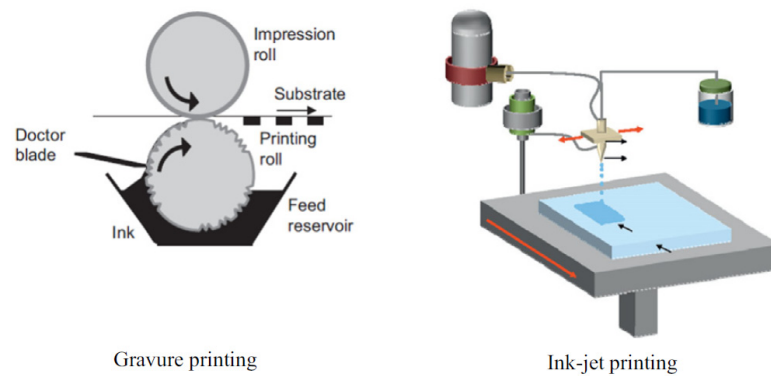


Figure 12. Illustration of printing apparatus. Reproduced from [139].

A simple but promising method is the contact printing (CP) technique developed by Javey et al. Here, the particularity is that the NWs are kept on their growth substrate until the transfer, no need to form a suspension. Therefore, during CP, nanowires are mechanically transferred by a shearing motion between the growth and the target substrate. In order to maximize the nanowire density and the alignment yield, the use of lubricants—such as mineral oil—is essential [143].

Yao et al. have significantly developed the nanowire alignment in CP by nanoscale combing technique [144,145]. In this technique, patterned resist windows opened by lithography are utilized to store the nanowires partially within the so-called anchoring regions [143,144,146], see Figure 13.

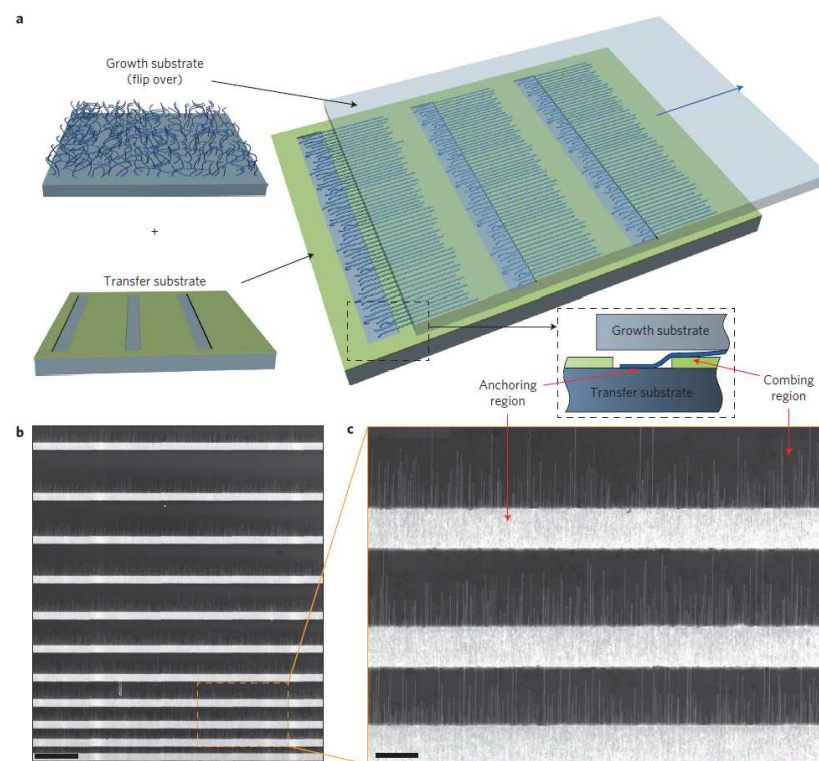


Figure 13. Schematics and demonstration of nano-combing. (a) Schematics of the nano-combing process. The blue arrow indicates the traveling direction of the growth substrate with respect to the target substrate, which yields a combing/aligning force that is parallel and opposite to the anchoring force. The dashed window at the right bottom shows a side view of the nano-combing process. (b,c) SEM images of silicon nanowires on the combing (resist) surface at different magnifications. The thickness of the resist (S1805) layer was 70 nm. Scale bars: 50 μm (b), 10 μm (c) Reproduced from [144].

Inspired by this CP technique, Robkopf and Strehle expand the current scope by focusing on the low-density nanowire assemblies and on dry friction to confine the nanowire deposition during CP [143]. Their motivation for dry friction was based on the fact that lubricants might act as a source of contamination in micro-device fabrication [147]. Therefore, they developed the concept of surface-controlled contact printing (SCCP) to avoid the need for lubricants, patterned resist, and post-print resist removal procedures. SCCP method is based on the frictional force between an individual nanowire on the growth substrate and the target surface, as shown in Figure 14. It has been shown that the material of the surface, the surface roughness, elevated structures, and nanoparticles can, in principle, be effective in the positioning of nanowires.

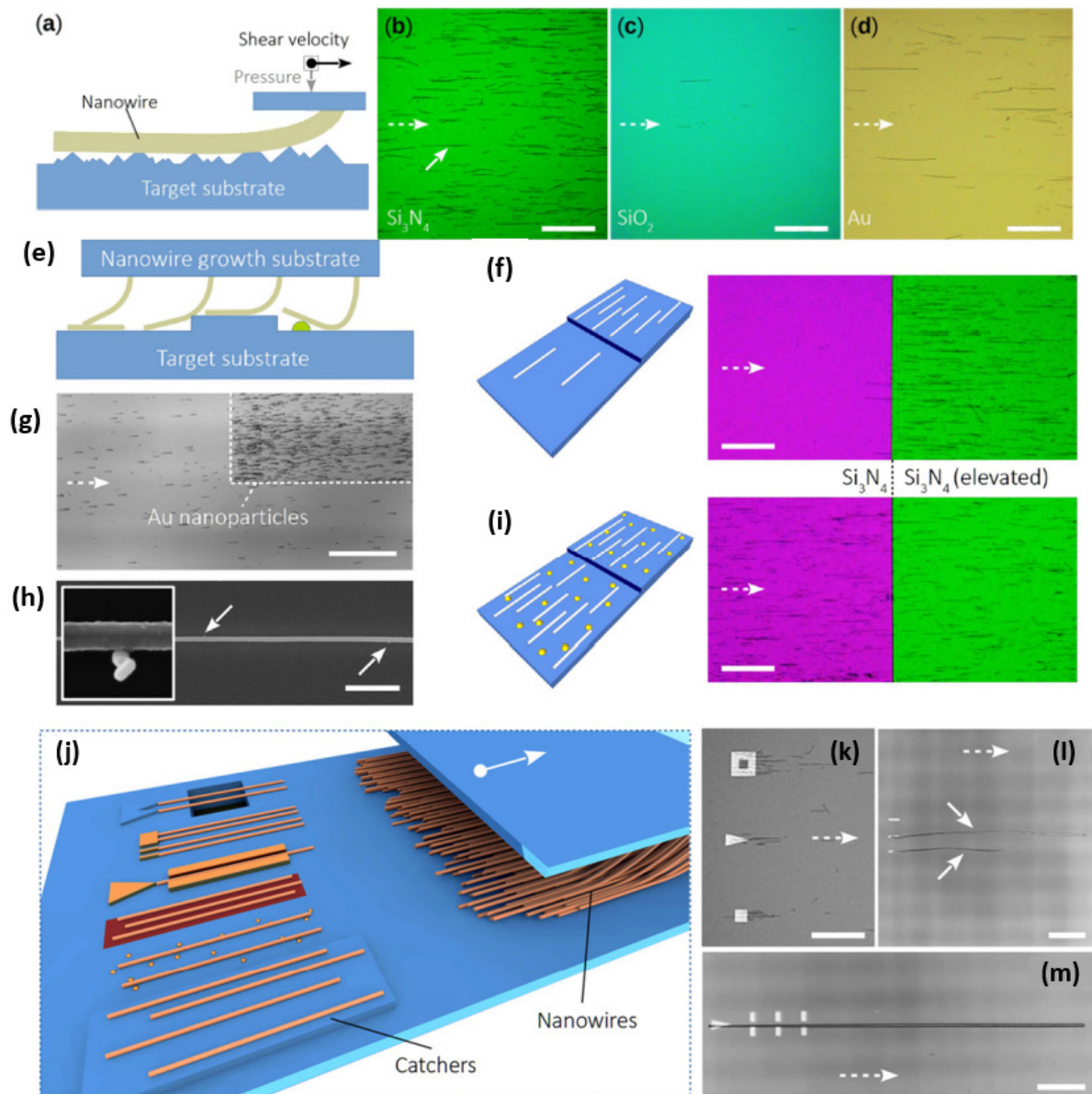


Figure 14. (a–d) Friction-based SCCP concept. (a) Schematic illustration of a nanowire in mechanical contact with a surface. The frictional force is predominantly influenced by the shear velocity vector, applied load, contact morphology, and materials of the nanowire and the target substrate. (b–d) Optical microscopy images of nanowires transferred in a lubricant-free manner (exemplified by the solid arrow in (a)) onto Si_3N_4 , SiO_2 , and Au surfaces. The dashed arrow represents the shear direction of the growth substrate. (e–i) Influence of local surface features on SCCP. (e) Schematic illustration showing the interaction of a nanowire with a previously deposited nanowire (left), the interactions of

nanowires with a step (center), and the interaction of a nanowire with a nanoparticle (right). (f) Schematic and optical images of an 80 nm step in Si_3N_4 , revealing that nanowires are preferentially deposited onto the elevated area. (g) Optical micrograph depicting an area decorated locally with Au nanoparticles of 50 nm in diameter. The nanoparticles increase the frictional force acting on the nanowires and, therefore, significantly increase the deposited nanowire density. (h) SEM image of a nanowire on a surface decorated with Au nanoparticles of 20 nm in diameter. The arrows indicate the positions of nanoparticles. The inset shows a magnified region containing a nanowire and Au nanoparticles. (i) The effect of the step, as shown in (f), is masked when Au nanoparticles (here, 50 nm in diameter) are present. The shear direction of the growth substrate is indicated in all images by a dashed arrow. The scale bars for (f–i) represent 100 μm , and that for (h) represents 1 μm . (j–m) Towards SCCP nano-device fabrication. (j) Schematic illustration of various catcher concepts, listed from front to back: elevated plateaux, nanoparticles, changes in surface roughness or material composition, catchers with selectivity or guiding rails, catchers for single and multiple-nanowire positioning, and catchers fabricated out of the substrate material with nanowires spanning a trench. (k) Catchers on SiO_2 of different lateral shapes, leading to an increased nanowire density adjacent to the catcher. The dashed arrow indicates the shear direction of the nanowire growth substrate. (l) Gold catchers on Si_3N_4 with the ability to position single nanowires (see white arrows). The width of a single structure is 300 nm. (m) Optical image of one triangular and six rectangular Au structures for single-nanowire positioning. When the triangular structure catches a single nanowire, the rectangular structures appear to assist, serving a function similar to that of a guiding rail, as revealed by experiments. Reproduced from [143].

Contact printing can be a promising alternative to transfer highly controllable single-NWs, but using lubricant is still necessary for that. SCCP provides further possibilities to control the positioning of nanowires by lubricant free or dry friction interaction. The reduction in nanowire densities and lower alignment yields are still some drawbacks of this method [143,144].

6.2. Random Networks

6.2.1. Vacuum Filtration

Vacuum filtration [148,149] is widely used in the literature as it allows the production of homogeneous nanostructured networks at low cost and over large areas. During solution filtration, the nanostructures are randomly trapped on the surface of a porous filter. In the frame of Si nanonet assembling, Pauline Serre [28] and Maxime Legallais [27] have shown that the process consists in five main steps that are: (1) dispersion of the silicon NWs in solution, (2) purification of the suspension by centrifugation, (3) analysis of the suspension by absorption spectroscopy, (4) assembly of the NWs into nanonets by vacuum filtration, and finally, (5) transfer of the nanonet onto a substrate, as shown in Figure 15.

Since the properties of nanonets are influenced by NW density, it is important to be able to control the density of nanonet. As the density of nanowires in nanonets is directly related to the number of nanowires in the suspension, the mastery of a technique of quantification of NWs is necessary. In Ternon's group, several techniques—such as Raman, infrared, fluorescence, and absorption spectroscopy—have been tested. Only the latter has made it possible to obtain a measurement that is directly proportional to the number of nanowires in the solution [28,36,150]. Then, for a given absorbance and a given NW geometry, the NN density is directly linked to the volume of the filtered suspension with high reproducibility. The greater the volume of filtered suspension, the greater the density in the nanonets (see Figure 16).

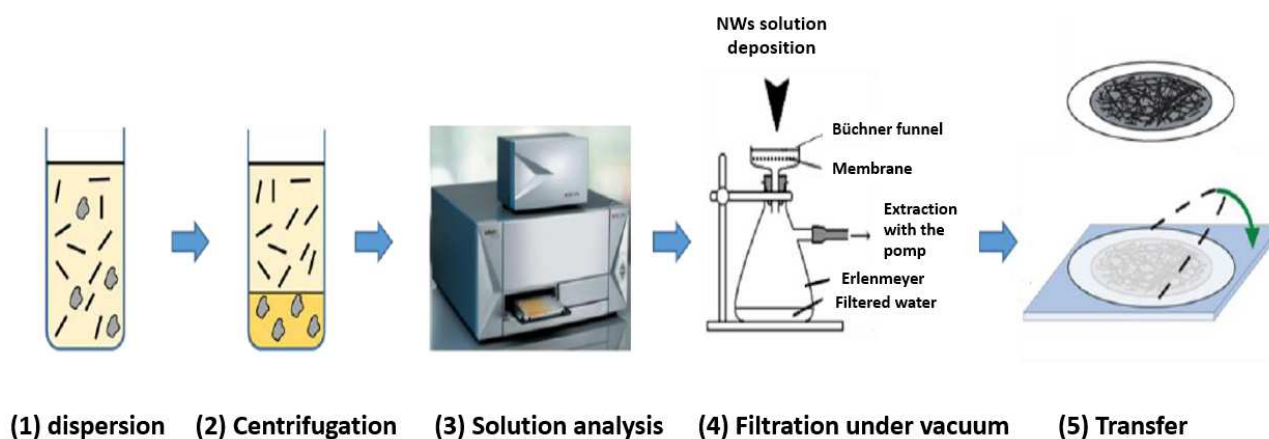


Figure 15. Overview of the protocol for manufacturing nanonets. This process consists of five main steps: (1) dispersion of the silicon NWs in solution, (2) purification of the NW suspension by centrifugation, (3) analysis of the suspension by absorption spectroscopy, (4) assembly of the NWs into nanonets by vacuum filtration, and (5) transfer of the nanonet onto a substrate. Reproduced from [27].

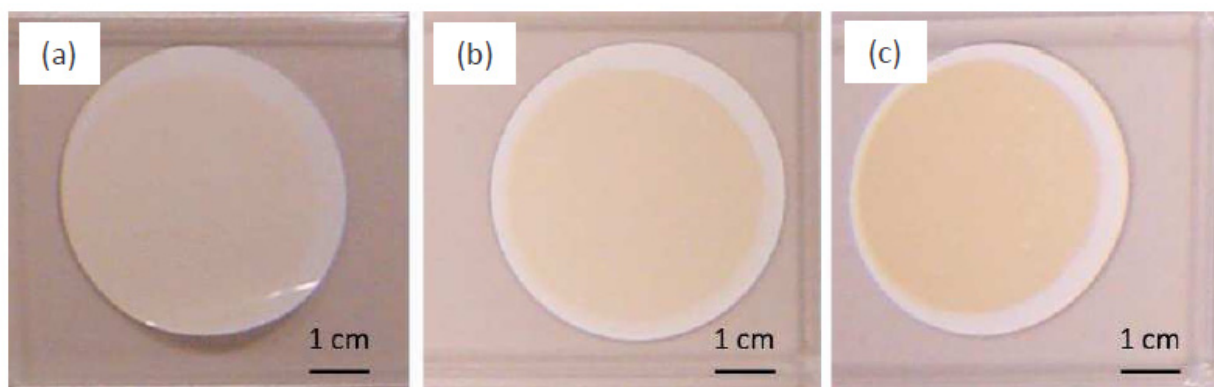


Figure 16. Membranes obtained after vacuum filtration of nanowires having the same arbitrarily fixed absorbance (0.06 at 400 nm) and different filtered volumes (a) 10 mL, (b) 20 mL, and (c) 35 mL. Reproduced from [28].

Once the nanowire solution has been analyzed, the silicon nanowires can be assembled by the filtration method with the schematic equipment in Figure 15 (step 4) [28,151,152]. The nanowire suspension is filtered for a few minutes through a nitrocellulose membrane. The progressive accumulation of the nanostructures on the filter surface decreases the flow velocity in these areas and induces an increase in flow in the areas devoid of nanostructures. These different flow velocities involved are at the origin of the self-assembly mechanism and the homogeneity of the nanonet.

When the nanowire suspension is not homogeneous—i.e., it contains aggregates from growth defects or clusters of NWs—it is possible to remove some of these elements by centrifugation as demonstrated by M. Legallais [27].

After filtration, NN can be transferred to the desired substrate either by the dissolution of the filter [148] or by direct contact [153]. For instance, Serre et al. [28] and Legallais et al. [27] demonstrated that this transfer can be carried out via a wet process by dissolving the membrane produced by vacuum filtration in an acetone bath. The adhesion of the nanonets to the surface of the substrates is simply due to van der Waals forces [27,28]. This process is well dedicated for SiNN [44,154] and can be adapted for a wide variety of nanostructures—such as NWs of zinc oxide [155], germanium [156], or carbon nanotubes (CNTs) [148,152]. Furthermore, the size of the nanonet is only conditioned by the size of the filter used and can therefore be easily enlarged. Finally, the formed nanonets can be

transferred onto different types of substrates either rigid or flexible, insulating or conductive, opaque or transparent, as shown in Figure 5, depending on the characterization and the intended application. Still, there is some difficulty such as finding a flexible substrate which is compatible with acetone.

Vacuum filtration is a low-temperature process in film production which affords films with some advantages such as surface uniformity and controllable thickness. Transferring NWs to a flexible substrate after being deposited on the filter depends on the substrate endurance towards acetone as most of the flexible substrates are attacked by it [27,157].

6.2.2. Spray Coating

One of the simple and efficient routes for the deposition of randomly dispersed nanowires or highly ordered and highly aligned even on a wide range of receiver substrates is spray coating. Spray coating is a technique in which nanowire suspension is electrostatically forced through a nozzle whereby a fine aerosol will be formed [158,159]. The spray coating system consisted of a hot plate for controlling the temperature of the substrate, a pressure flow spray nozzle element, a nozzle movement, and an angle control module. Normally, the spray coating system is designed by taking to account the viscosity of NW suspension, the NW suspension supply, and other process variables [158] (see Figure 17). Ossama Assad et al. [158] showed that by controlling these conditions and provided that the size of the generated droplet is comparable to the length of the single NW, the shear-driven elongation of the droplet results is likely in the alignment with the confined NW in the spraying direction.

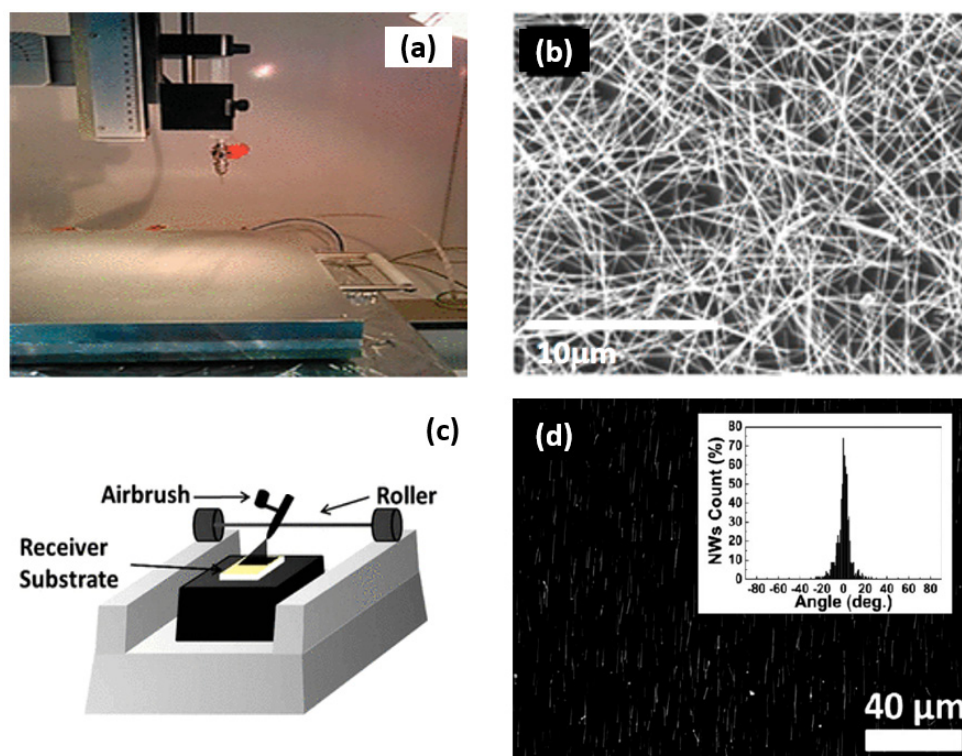


Figure 17. (a) Image of the electrostatic spray system step. Reproduced from [159]. (b) SEM image of the electrostatic spray deposited nanowire network. Reproduced from [159]. (c) Schematic of the spray coating apparatus. Reproduced from [158]. (d) representative dark-field optical image of spray-coated SiNWs on the SiO_x/Si substrate and the constituent analysis of 700 SiNWs with respect to the flow direction. Reproduced from [158]. Spray coating method can be controlled under conditions of temperature, droplet size, spray coating angle, and airflow which makes this method interesting either in the well-aligned or well controlled density in large size of nanonet with a small lack in control over the low density of nanonets.

Since this technique has no limitation in substrate size, it has great potential for large scale production and can replace spin-coating which is a conventional method [139]. However, the main concerns of utilizing the spray coating belong to higher film thickness and roughness.

As already mentioned, one of the key parameters in nanonet assembly is density. In spray coating, by controlling the concentration of the nanowire suspension or at the same time regulating the flow duration, it is possible to adjust the density of deposited NWs—e.g., for having high density deposited NWs, we should increase the spray coating duration. The level of density control over deposited NWs in this approach is similar to other techniques such as blown-bubble and contact transfer techniques, while in these two techniques we are dealing with just aligned nanowires.

Spray coating facilitates a low-cost uniform coverage over a large area which has a potential for immediate implementation in the industry and/or line production. In this technique, NWs film making by the spray coating method depends on the nozzle speed, diameter, and length of nanowires and is more beneficial for high densities and large-scale fabrication [158,159].

6.3. Advantages and Disadvantages of Each Technique

As already discussed, semiconductor NWs have demonstrated excellent performance for nanoscale electronics and due to their great mechanical flexibility, high yield, and low-cost bottom-up synthesis; they have outstanding potential to be used in flexible electronics. As the assembly of NWs remains a challenge for practical large-scale application, various innovative NW assembly technologies have been investigated [160]. As a result below in Table 2, there is a simple comparison between different techniques of transferring nanowires into a variety of substrates from rigid to flexible ones.

Table 2. Advantages and disadvantages of each NWs transferring technique.

Technique	NWs Uniformity	Random/ Aligned	Density (Percolation Regime)	NWs Layer Thickness (Low Density)	Versatile in Substrate	Scalability	Localized/ Large Scale	Complexity
Drop-casting	Low	Random/ Aligned	Low	Low	High	Low	Localized	Low
Fluidic directed	Medium	Aligned	Low	Low	Low	Low	Localized	Medium
Langmuir-Blodgett	High	Aligned	Medium	High	High	Medium	Localized/ Large scale	Medium
Blown-bubble	High	Aligned	Medium	Low	High	Low	Localized	
Contact printing	Medium	Aligned	Medium	Medium	Medium	Low	Localized	Medium
Vacuum filtration	High	Random	High	High	Medium	Medium	Large scale	Low
Spray coating	High	Random/ Aligned	Medium	Low	High	High	Large scale	Low

In order to fabricate devices based on a single SiNW, the best option in terms of simplicity and adaptability to varieties of substrates is drop-casting, but still this technique is not efficient and the number of devices out of each NW transfer is trivial and negligible. However, other techniques—such as Langmuir–Blodgett, blown-bubble, contact printing, and fluidic directed—are the best choices for multiple-parallel channel devices. Each technique has its advantages but still, Langmuir–Blodgett seems to be a better option over others. Finally, in order to have nanonet (assembly of randomly oriented nanowires), we deal with mostly two methods, vacuum filtration and spray coating in the other technique several transfer process in different angles are needed to produce arrays of nanowires with junctions so these latter methods are complex with low yield. Although in vacuum filtration technique, density regulation is much easier and the process is inexpensive, spray coating

can prevail over vacuum filtration because it is easily applicable on different substrates, at large scale, and it allows the selection of a random or aligned nanowire array.

Generally, though all these methods have an advantage over direct growth methods, these methods extend the assembly procedures, which increase the risk of additional contamination and destruction of the intrinsic properties.

7. Silicon Nanowire-Based Transistors

The small size and unprecedented ability to combine semiconductors with very different lattice parameters provide exciting new opportunities for devices. At the beginning of the 20th century, nanowire device researchers face the exciting challenge of deciding which devices, and thus which future applications, hold particular promise for this new class of material [161,162]. Among the many possibilities, the field effect transistor (FET) stands out as the modern workhorse of the semiconductor industry. Not surprisingly, most of the efforts in nanowire devices have focused on the fabrication of nanowire field effect transistors, as it is the building block of modern electronics and the most frequently fabricated device in history. FET is the dominant semiconductor device in digital and analog integrated circuits (ICs), and the most common power device [163]. It is a compact transistor that has been miniaturized and mass-produced for a wide range of applications.

Silicon transistor technology, especially metal–oxide–semiconductor (MOS) technology, is scaling down as predicted by Moore’s Law [18,164]. Originally, transistors had a three-dimensional active region (solid silicon substrate) then it was reduced to a two-dimensional geometry (silicon ultra-thin film on insulator (SOI)) to finally reach a one-dimensional structure with the introduction of nanowires (FinFET on SOI) [165,166], as schematically illustrated in Figure 18.

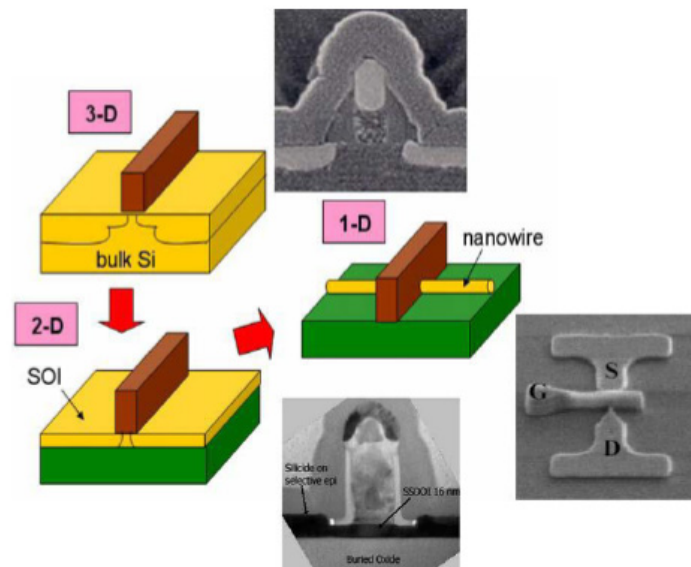


Figure 18. Continued scaling of silicon complementary metal–oxide–semiconductor (CMOS) transistor into nanometer regime requires the corresponding reduction in device active layer dimensionality. Reproduced from [6].

However, this scaling of the typical silicon transistor technology has almost reached its limits [22,51]. Despite the advanced capabilities of fabrication tools, many physical effects can prevent the tools from performing satisfactorily when the device size is scaled down to the nanoscale. In addition, transistor scalability, performance, and power dissipation are three fundamental issues facing aggressive miniaturization. Furthermore, the leakage mechanisms associated with the size reduction of conventional silicon transistors down to the nanoscale include direct gate dielectric tunneling, band-to-band tunneling, and short channel effects. Finally, silicon has almost reached its intrinsic switching speed limit. Other semiconducting materials with higher carrier mobility could solve the problem,

but the required power dissipation levels in the nanoscale structure do not allow further downscaling [6].

Nevertheless, one-dimensional (1D) structures are the smallest structures that can be used for efficient transport of electrons [6,61,167]. Semiconductor nanowires fall into this category and are obvious candidates to replace ultrathin-film SOI transistors [168]. Among semiconductor NWs, silicon nanowires have been studied more and are considered the most suitable for implementing nanowire transistors, as silicon dominates the semiconductor industry and its structure and doping can be precisely controlled [168]. However, the smaller the footprint of the manufactured devices, the higher the manufacturing cost and the more complicated it is to observe good reproducibility and homogeneity of the device characteristics. Nevertheless, being able to introduce nanometric structures into the devices is extremely interesting because it allows new properties and functionalities to emerge. In this, nanonet devices are extremely promising because they are made of nano components while having a large enough footprint to lower the cost and complexity of production. They are clearly not part of the miniaturization dynamics of the ‘More Moore’ trend, but rather contribute to the ‘More-than-Moore’ trend or even to a paradigm shift (Figure 19a).

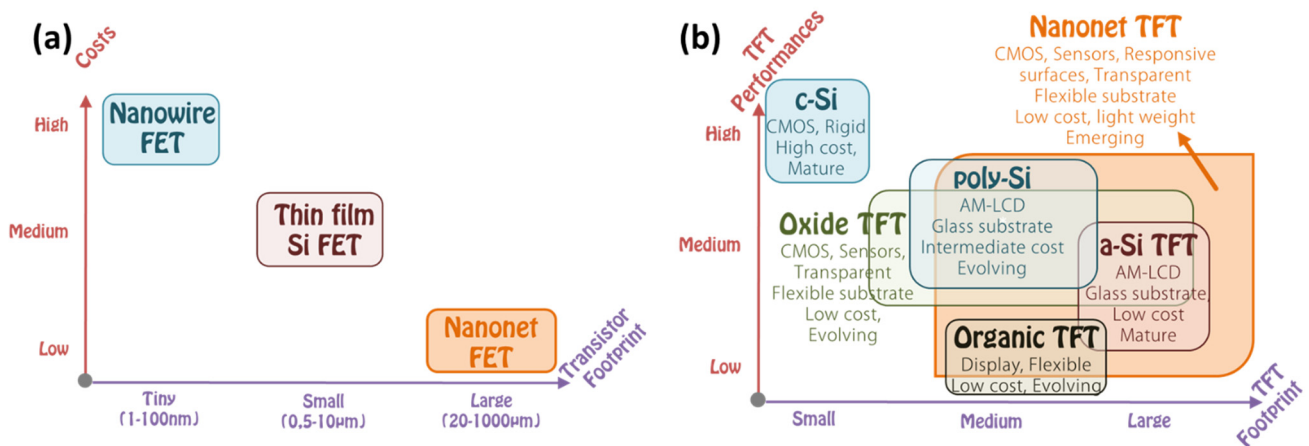


Figure 19. (a) Simple comparison between single SiNW-, thin film Si- and SiNN-FETs with respect to the industrial size and fabrication costs related. (b) Positioning (Nanonet TFT) in terms of thin-film transistor (TFT) performance versus footprint in comparison with the existing technologies (TFT based on: cSi: monocrystalline Si; poly-Si: polycrystalline Si; a-Si: amorphous Si; Organic: organic material; Oxide: metal oxide film).

Nanonet based transistors belong to the category of thin film transistors that provide numerous functionalities for various applications such as CMOS circuits, sensors, responsive surfaces, and flexible and transparent electronics. They compete not only with other materials such as oxides or organics but also with other forms of silicon, amorphous, polycrystalline, or monocrystalline. In this context, Figure 19b shows the performance of these devices according to their footprint.

In this section, we focus on nanowire transistors with the simplest geometry—namely, a source electrode, a drain electrode, a channel consisting of a single nanowire, parallel nanowires, or a nanonet, as well as a full back gate or localized top-gate. Thus, we will present the most basic integration processes and then the typical electrical characteristics.

7.1. Integration Process

7.1.1. Single Nanowire FETs (Single-SiNW-FETs)

Whether the approach is bottom-up or top-down, there is a phenomenal variety of integration processes and device geometries in the literature. There is a large number of studies presenting the fabrication of transistors with the simplest geometry, which we will describe in the rest of this paragraph [10,11,169], to the most complex transistors with variable doping along the nanowires and gate multiplicity allowing an electrostatic control

of the doping and thus the control of the nature of the channel (P or N) [170,171]. Even for the simplest geometry, there are integration subtleties that impact the properties of the manufactured transistor. A simple silicon nanowire transistor can be built as shown in Figure 20a. The two gold cubes represent the source (labeled S) and drain (labeled D) contacts of the transistor respectively whereas the gate is on the backside of the substrate. The dark blue cylinder represents the nanowire which is the channel of the transistor. The channel can be doped p-type or n-type. The top-gate of the transistor is shown in Figure 20b,c as a rectangular-like plate labeled with G. The gate can be placed in a semi-cylindrical shape on the top of the nanowire or all around the nanowire [168]. SiNW transistors manufactured with a gate that surrounds the whole nanowire (all-around-gate) allow better current control through the channel and thus higher current densities can be controlled compared to a planar device. What is more, the all-around-gate allows the devices to be shrunk even more (down to 10 nm) due to the excellent control of short-channel effects and leakage [51].

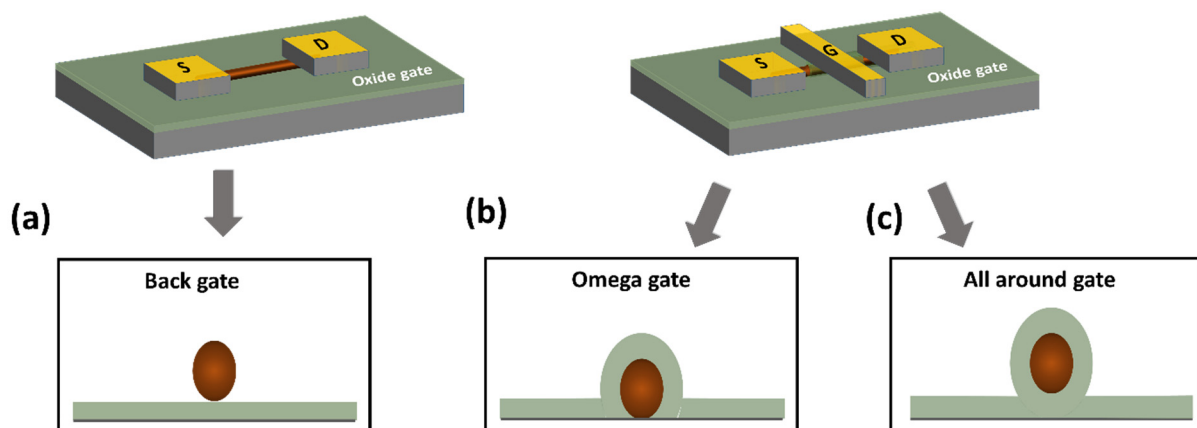


Figure 20. Schematic of NWFETS with (a) back gate, (b) semi-cylindrical top gate, and (c) cylindrical gate-all-around configurations. The nanowire is brown, gate-dielectric is light green, and source (S), drain (D), and top-gate (G) electrodes are gold. Insets show device cross section at the midpoint between source and drain.

The bottom-up approach, which is the subject of this paper, has caught our attention because it provides great flexibility in that nanowire growth and integration are two completely independent steps. Thus, it is easy to choose the material, length, diameter, type, and concentration of the dopants, and the orientation of the crystals because all these parameters can be adjusted during the synthesis. Today, the main limitation of this approach is the complexity of developing a method for large-scale transistor integration with high reproducibility.

For the simplest geometry (Figure 20a), the bottom-up processes start with as-grown SiNWs in both bottom-up (Figure 21i) as described in Section 5. Subsequently, the as-synthesized SiNWs have to be transferred onto the desired substrate, generally including the back-gate, by using the simple drop-casting or one of the methods described in Section 6 (Figure 21ii). In some works, SiNWs are passivated in order to preserve them from the environment sensibility, low efficiency, and short lifetime [27,172,173]. Thereafter, a photo- or electron-beam lithography process (Figure 21iii) followed by metallization (Figure 21iv) and lift-off (Figure 21v) are utilized to pattern metallic electrodes to the SiNWs [3,169,174]. Silicidation which is a process of the intermetallic compound formed by the reaction of metal and silicon can be performed in order to lower the access and/or series resistance of the device in contacts [11,175,176]. Eventually if desired, a top-gate can be added by an additional photolithography step.

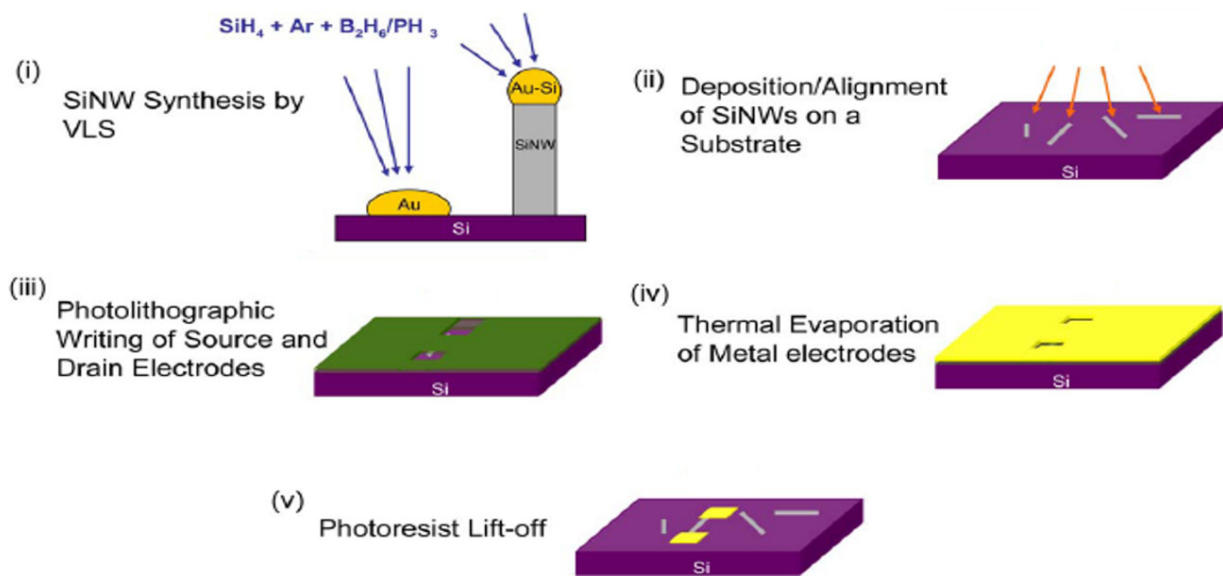


Figure 21. (i) The growth of SiNWs in CVD reaction via the VLS mechanism. (ii) Deposition/alignment of SiNWs on a silicon substrate. (iii) A photomask pattern to define source/drain electrodes. (iv) Thermal evaporation to deposit the source/drain contacts. (v) Lift-off the remaining photoresist with Remover PG. Adapted from [174].

Generally, this type of integration process, based on drop-casting, yields only a low success rate in obtaining nanowire devices without allowing large statistical studies. However, this is sufficient to study the fundamental properties of single SiNW devices. Furthermore, this method is clearly not suitable for the low-cost, mass production of SiNW devices. Therefore, the use of the techniques described in Section 6 that allow the assembly of SiNWs with controlled orientation and spacing over large areas is essential for the fabrication of complex logic circuits and high-performance devices.

7.1.2. Silicon Nanonet FETs (SiNN-FETs)

To qualify as a nanonet device, the geometry of the transistor must be such that the length of the channel is greater than the length of the nanowires so that no nanowires are able to bridge the two electrodes directly. The current flows from one contact (source) to another (drain) via percolation paths that involve NWs as well as junctions between NWs. Typical devices are illustrated in Figure 22.

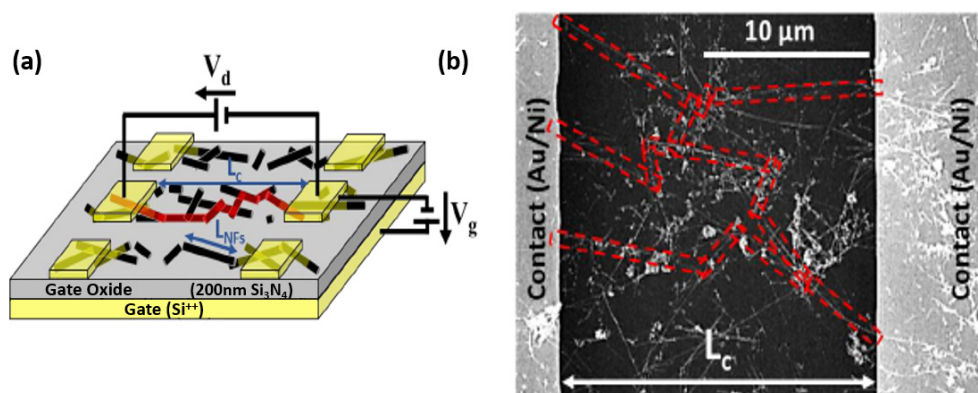


Figure 22. (a) Schematic and (b) SEM image of SiNN transistor studied. The schematic (a) refers to long channel transistors for which the length of the NWs (L_{NFs}) is less than the channel length (L_c). Conversely, the SEM image (b) refers to the possible conduction paths involving NW–NW junctions are indicated in red. Reproduced from [27].

Thus, the fabrication starts with the assembly of the nanonets on the surface of the substrate including the back gate according to one of the methods described in Section 6. Then the fabrication process of back-gated SiNN-FETs can be broken down into four main steps:

- Sintering of the NW–NW junctions and passivation of the NN to stabilize electrical properties (see Section 8.1 Sintering and Section 8.2 Surface and Interface).
- NN patterning to define the channel geometry (Figure 23i-0–i-5).
- Deposition of the source/drain contacts (Figure 23ii-0–ii-5).
- Silicidation of the source/drain contacts (see Section 8.3 Silicidation).

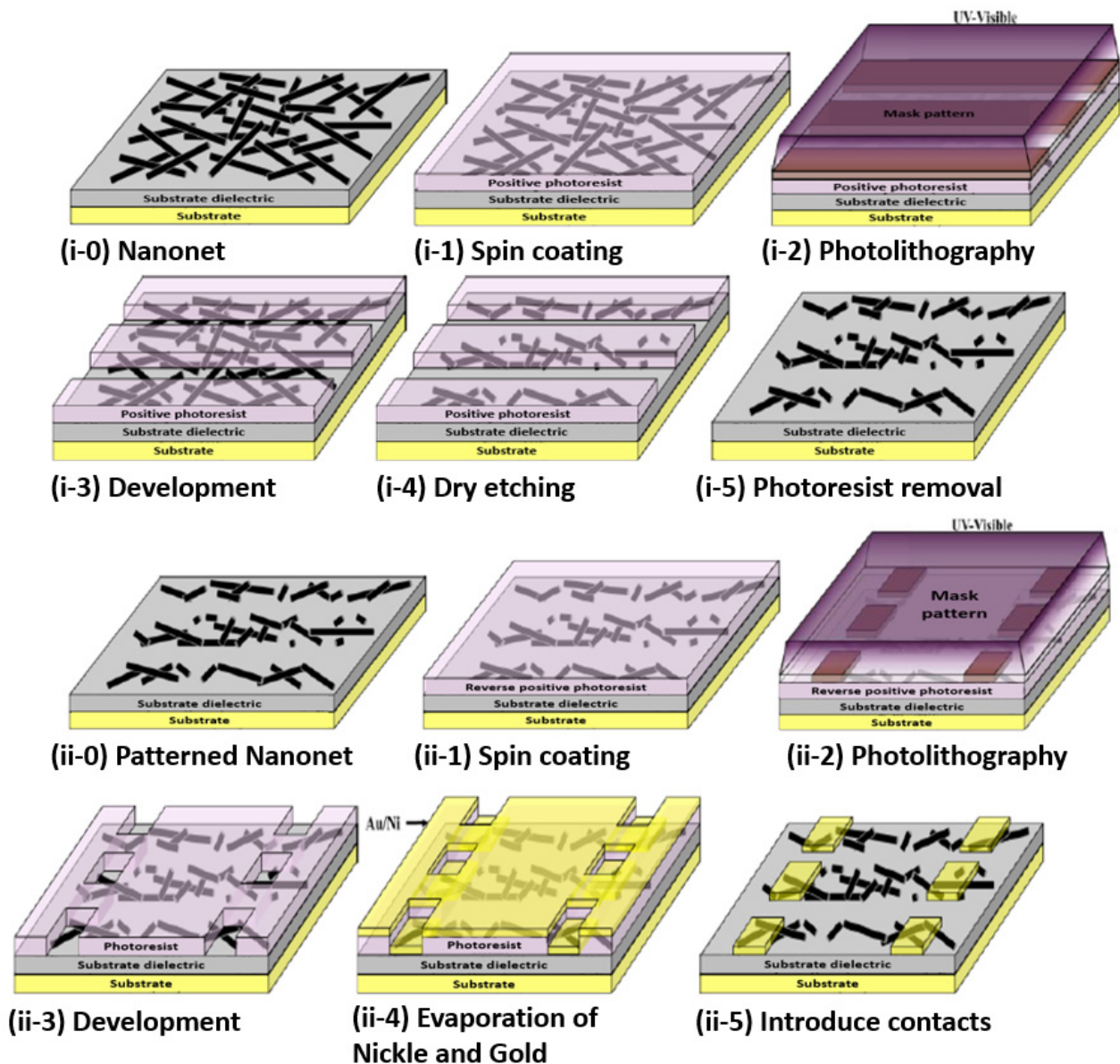


Figure 23. Main steps in the isolation of nanonets. (i-0) Fabrication of nanonets. (i-1) Deposition of the positive photoresist by the spin-coating technique. (i-2) Photolithography with the UV–visible through the mask. (i-3) Photoresist development. (i-4) Dry etching of the NWs by a sulfur hexafluoride plasma. (i-5) Photoresist removal. Main steps for the formation of source/drain contacts. (ii-0) Nanonet after isolation. (ii-1) Deposition of inversion photoresist using the spin-coating technique. (ii-2) Photolithography in the UV–visible through the mask aligned with the isolated nanonet. (ii-3) Photoresist development. (ii-4) Electron beam evaporation of nickel and gold. (ii-5) Revelation of the source/drain contacts after lifting of the photoresist (lift-off).

By doing the silicidation step, back-gate SiNN-based FETs are achieved. These steps can be modified due to the need and application. For example, one might need a local top-gate instead of a full back-gate hence some procedures will be added such as deposition of the gate oxide, lithography of top-gate, and metal evaporation step to introduce top-gate. In Figure 24, SiNN-based FETs with two different designs are demonstrated.

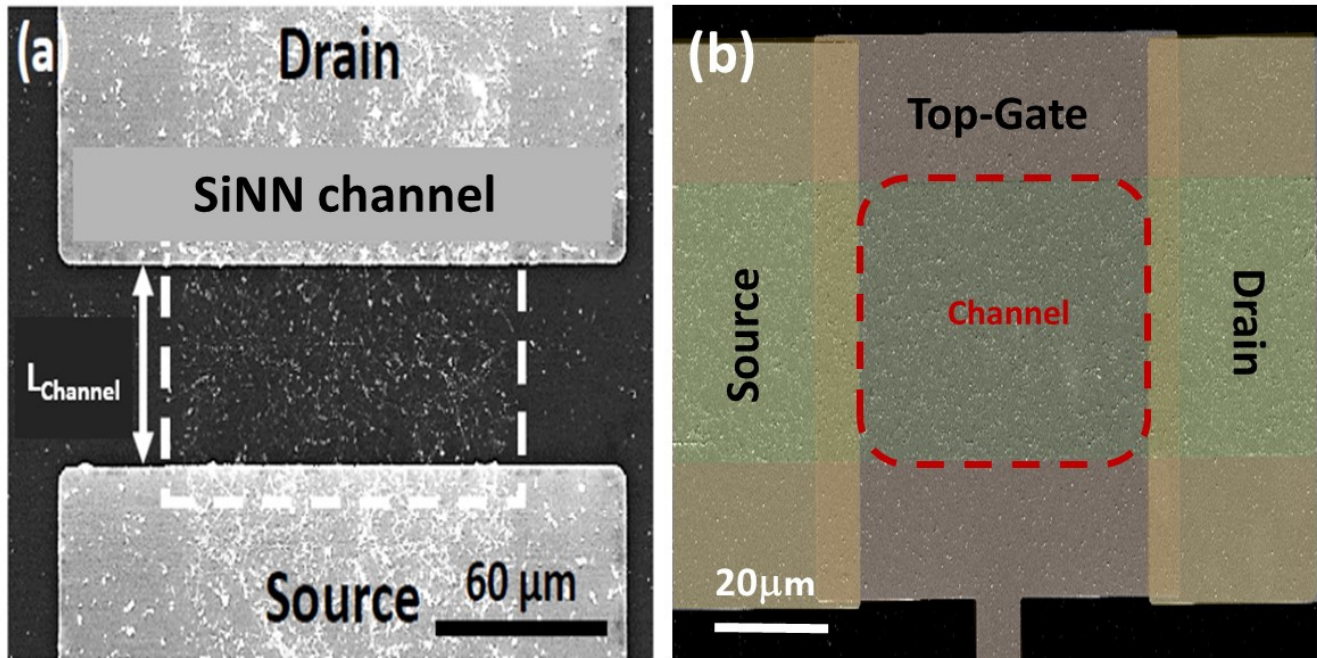


Figure 24. (a) SEM image final full back-gate FET based on SiNN. The length of the Si nanonet channel is 50 μm for a width of 120 μm . The square contacts measure 200 μm on each side. (b) SEM image final local top-gate FET based on SiNN. The length of the Si nanonet channel is 50 μm for a width of 100 μm . The square contacts measure 200 μm on each side. Although this integration process involves only simple and mastered steps, such integration has proven to be challenging since, to date, very few papers have presented the fabrication of this type of device. Moreover, to date, there are works based on the SiNN devices on rigid substrates, especially resistors and transistors but there is a great potential in the field of flexibility that is still unproven.

7.1.3. Multiple-Parallel-Channel FETs (MPC-FETs)

The realization of a multiple-parallel-channel field effect transistor (in reference to multiple parallel NWs as channels) can arise from two strategies. First, by choosing an appropriate technique (Section 6), it is possible to align nanowires parallel to each other and then apply the integration process presented for single nanowire transistors which will then result in an MPC FET since the channel will consist of nanowires in parallel (Figure 25a,b). The second strategy consists in producing a nanonet on the surface of the substrate and then applying the dedicated integration technique while choosing a geometry such that the length of the channel is smaller than the length of the NWs. As a consequence, several NWs are able to bridge the two electrodes, forming an MPC-FET (Figure 25c,d).

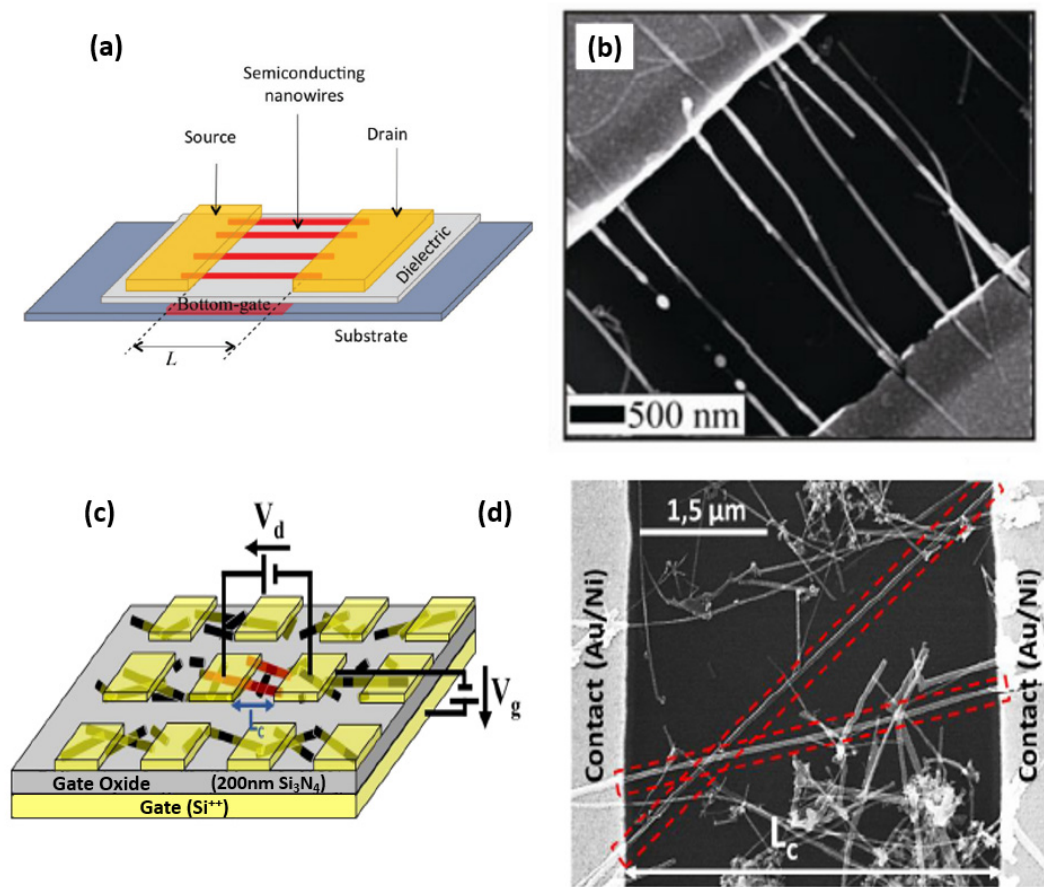


Figure 25. (a) Schematics of bottom-gate of multi parallel array silicon nanowires. Reproduced from [177] (b) SEM image of as fabricated parallel channels FETs with intruded NiSi₂ Schottky barrier contacts. Reproduced from [178]. (c) Refer to the schematic of the short channel transistor (Nanowire length higher than channel length) (d) SEM image of MPC-FETs based on short-channel SiNN and the possible conduction paths involving with without-NW-NW junctions are indicated in red. Reproduced from [27].

7.2. Electrical Characteristics of Single SiNW-, SiMPC-, and SiNN-FETs

The operation of a single SiNW-based transistor is similar to that of a typical FET transistor. If the SiNWs are p-type and a positive/negative voltage is applied to the gate (G), then the carriers are depleted/accumulated; conversely, if the SiNWs are n-type and positive/negative voltage is applied to the gate, then the carriers are accumulated/depleted (Figure 26). Therefore, the variation of the SiNW conductance via the field-effect action allows for the transistor action to be implemented with SiNWs [17,31].

P-type SiNWs have attracted greater interest than n-type ones. P-type SiNWs were fabricated and showed high performance characteristics. Their transconductance was about 10 times greater than typical planar devices and the holes' mobility was an order of magnitude larger too. Both the transconductance and mobility increased after surface modification of the SiNW. This implies that some of the electrical characteristics of the SiNW transistors can be controlled by proper surface modification as described in the next section. Therefore, the performance of SiNW transistors can exceed that of typical devices [51].

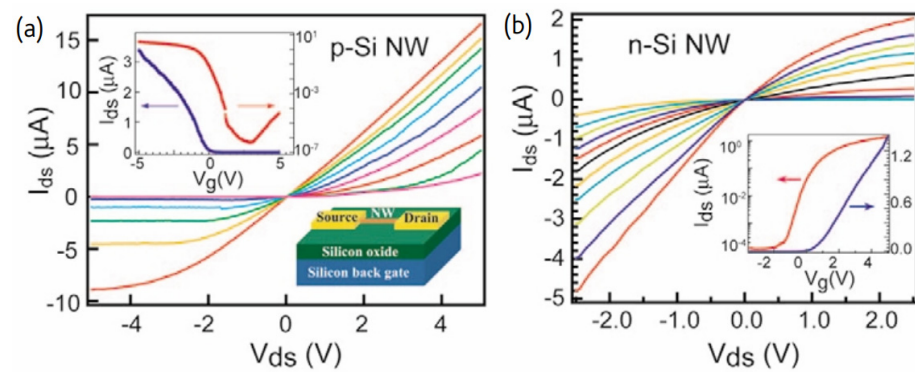


Figure 26. SiNW-FETs: a family of current versus drain-source voltage (I_{ds} - V_{ds}) plots for a representative (a) 20 nm p-Si NW device (channel length of 1 μm ; from red to pink, $V_g = -5$ V to 3 V); and (b) 20 nm n-Si NW device (channel length of 2 μm ; from yellow to red, $V_g = -5$ V to 5 V) in a standard back-gated NW-FET geometry as illustrated. Insets in (a,b) are current versus gate-voltage (I_{ds} - V_g) curves recorded for NWFETs plotted on linear (blue) and log (red) scales at $V_{ds} = -1$ V and 1 V, respectively. Reproduced from [31].

In addition, one of the major gains in 1D nanostructures is depletion or accumulation in the bulk of nanowires while in 2D structures such as thin film is happening only on the surface which causes lateral current shunting. This property provides sensing with label-free and direct detection when the nanowire is used as a sensor to make real-time detection possible [22,61]. Based on this advantage in nanowires, Li et al. [75] depicted an efficient strategy through surface functionalization to build a single silicon nanowire field-effect transistor-based biosensor that is capable of directly detecting protein adsorption/desorption at the single-event level (see Figure 27).

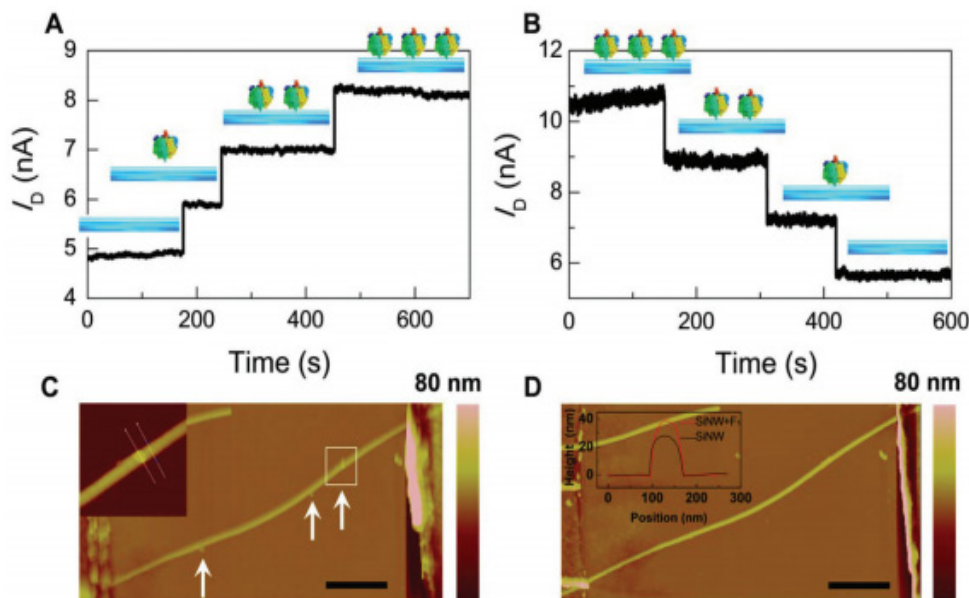


Figure 27. Sensing properties. (A,B) Real-time recordings of the absorption/desorption processes of F1-ATPases, showing the gradual changes in I_D with three steps. Drain voltage, $V_D = 0.1$ V and gate voltage, $V_G = 0$ V. (C,D) Corresponding AFM images after protein delivery ((C), inset shows an enlarged image of a single F1 protein) and after further EDTA treatment ((D) inset is the height profile of the bare silicon nanowire and the nanowire with an adsorbed F1 protein particle in (C) inset). The total height of F1 is ~ 12 nm including a ~ 2 nm linkage). The scale bar is 1 μm . Reproduced from [75].

As will be discussed in the following section, the contact resistance of SiNW-FETs affects their performance significantly. Devices with titanium (Ti) source-drain contacts

revealed variations in their transconductance and mobility after thermal annealing effects. Other materials for the contacts, such as silicide and nickel monosilicide, can reduce this variation in the performance of the device [11,51].

That is why the MPC-FETs and NN-FETs are particularly interesting, as they can maintain the nanosize of the components while increasing the amount of current for a given voltage [178].

In the case of MPC-FETs, fabricated from aligned parallel NWs, Figure 28 depicts the off-current as a function of the on-current for different inter-electrode (IE) spacing (2.5–5.5 μm). It can be seen that the current output can clearly exceed the μA range and that it increases when the inter-electrode (IE) spacing is reduced. However, the off-current increases when the on-current increases, and accordingly, the on/off current ratio drops with decreasing IE spacing. Since channel length (L_c) of individual nanowires varies in the parallel array due to dispersion in nanowire alignment as shown in Figure 28b, though a small number of nanowires with short channels will be found in the ensemble, affected by quasi short channel effect (SCE), these nanowires will degrade the total on/off current ratio. This apparent quasi short channel effect for parallel array devices at such a large electrode spacing is not observed for single nanowires [178].

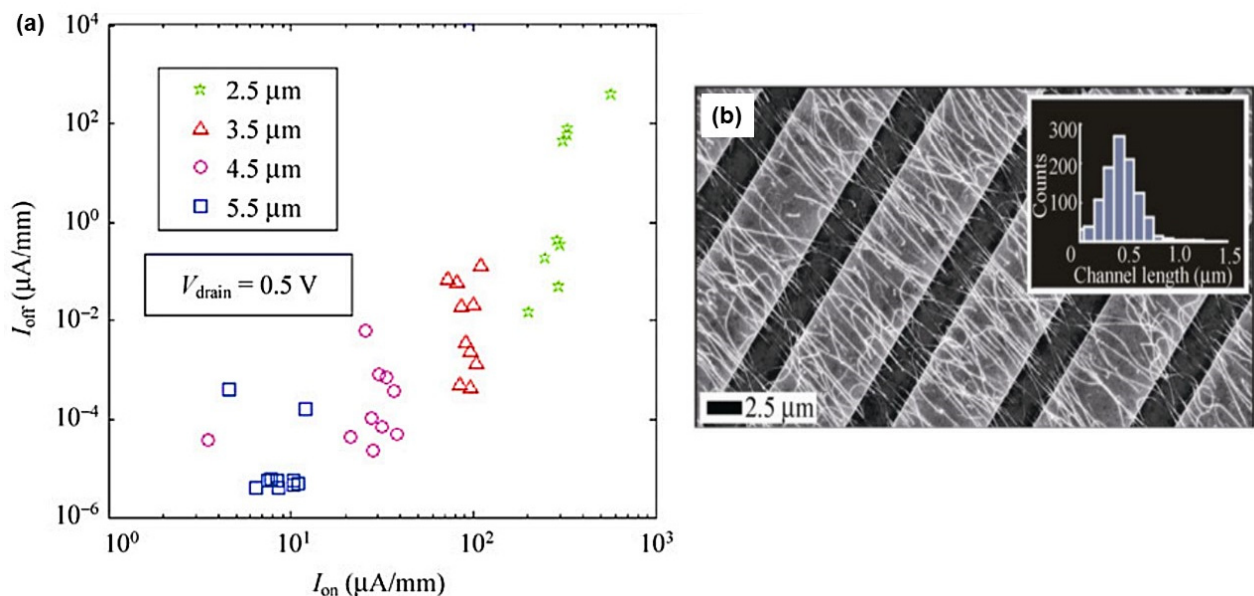


Figure 28. (a) Source-drain voltage V_{sd} versus a gate voltage V_g statistics of 36 nanowire parallel array FET devices. Each device consists of 500–1000 nanowires. Off-current versus on-current per mm electrode width for $V_{\text{sd}} = 0.5 \text{ V}$. The on/off ratio is shown for devices with four different inter-electrode spacing but the same silicidation process (green/stars 2.5 μm ; red/triangles 3.5 μm ; purple/circles 4.5 μm ; blue/sq. 5.5 μm). Reproduced from [178]. (b) High density nanowires are contacted by nickel electrodes. The inset displays the histogram of channel lengths of individual nanowires after silicidation for a device with 2.5 μm inter-electrode spacing. Reproduced from [178].

When MPC-FETs are obtained from a randomly oriented nanowire network, the same trend is observed: by decreasing the channel length, the on and off current increase (Figure 29A,B, 5 and 10 μm). Moreover, from this figure, one can notice a surprising and significant degradation of the subthreshold swing.

Then MPC-FETs are interesting to increase the on-current, but at the same time, off-current also increases and the commutation ability degrades. Such behavior can be explained by the intrinsic disparity of the nanowire population. Indeed, whatever the method of bottom-up synthesis of NWs, it is possible to observe variations of diameters, doping, or surface properties from one nanowire to another. Such variations are responsible for different electrical behaviors for each NW. Thus, there is a dispersion of on-current, off-current, sub-threshold slope, and threshold voltages [179,180]. While this is not a major

problem for the on-current, the existence of a single nanowire with a high off current will result in a high off current for the MPC FET. Similarly, if all of the nanowires making up the MPC-FET switch successively, this will result in the MPC FET switching over a wide range of gate voltages [72].

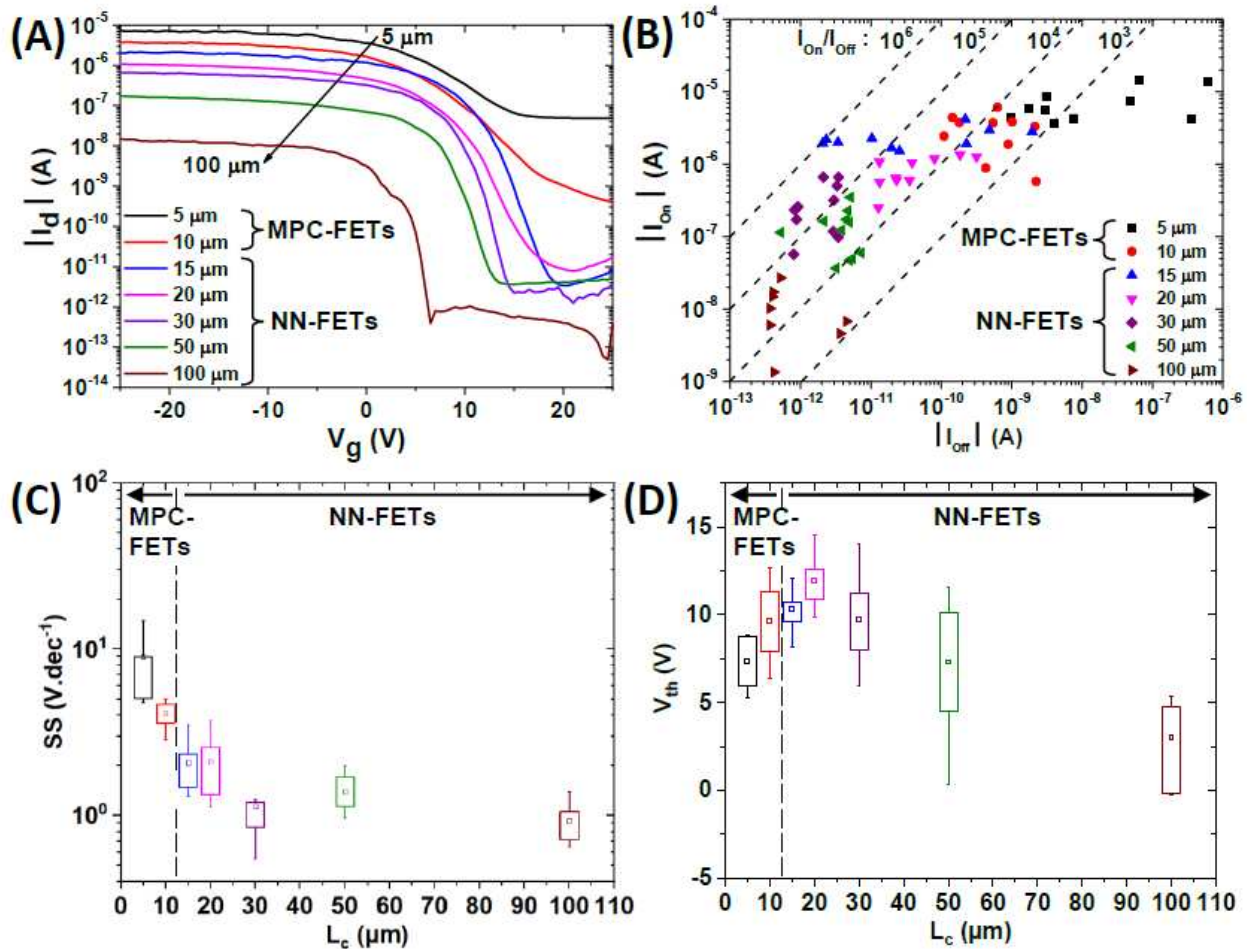


Figure 29. Study of transistor electrical properties for various channel lengths. (A) Typical transfer characteristics from 5 to 100 μm at $V_d = -4$ V. (B) On current (I_{on}) as a function of off current (I_{off}). The on current is defined as I_d at $V_g = -25$ V, $V_d = -4$ V, (C) subthreshold slope (SS), and (D) threshold voltage (V_{th}) for various channel lengths extracted for about seventy transistors. For (B) the on-to-off ratio (I_{on}/I_{off}) is indicated by the dashed lines. Reproduced from [72].

In this context, NN-FETs appear to be promising for reconciling high current, high I_{on}/I_{off} ratio, and fast switching, as illustrated in Figure 29 (15–100 μm). In Figure 29B, by measuring over 70 NN-based transistors with different channel lengths, an interesting trend in the I_{on}/I_{off} curve is observed. On one hand, the NN-FETs with the smallest length (15–20 μm) have a quite dispersed current while the current is almost stable. On the other hand, for the longer (>20 μm), current is almost fixed with a reduction in current by increasing the channel length. As a consequence, this leads to a drastic change in the on-to-off ratio and the observation of an optimum on-to-off ratio as high as 10^5 [72].

In order to have a better understanding of the differences inherent to these three types of nanowire-based devices, Figure 30 presents the transfer characteristics of a single-SiNW FET, an MPC FET, and an NN FET. All previous observations are summarized on that graph. The MPC-FET clearly exhibits the highest on-current, but all other transistor parameters are poor. In contrast, and against all expectations, the NN FET maintains very good performance with fast switching and very low off-current while exhibiting an on-current up to 100 times higher than that of the single nanowire device, even though its

channel is over 10 times longer. As a consequence, an NN-FET could be as interesting, and even more than a single SiNW-FET.

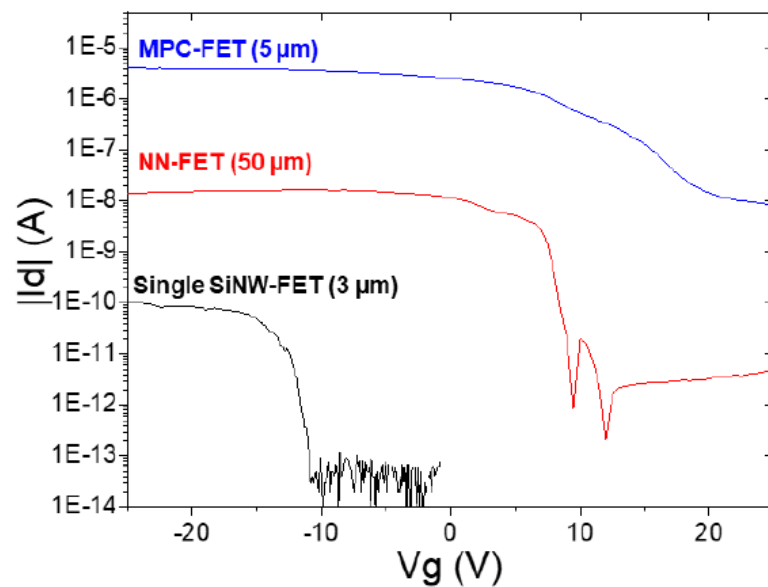


Figure 30. Typical transfer characteristic at $V_d = -1$ V for single SiNW-FET with $L_c = 3$ μm (black), MPC-FET with $L_c = 5$ μm (blue), SiNN-FET with $L_c = 50$ μm (red). Reproduced from [72].

The statistical summary in Figure 31 presents a comparison between the performance, in terms of $I_{\text{on}}/I_{\text{off}}$ ratio and subthreshold slope, of single SiNW FETs from the literature and SiNN as a function of channel length. It is important to mention that, for SiNN based transistors, each point on the graph results from measuring the performances of several devices (average and variability): on the order of 15 devices for channel lengths below 300 μm and 3 to 6 devices for longer ones.

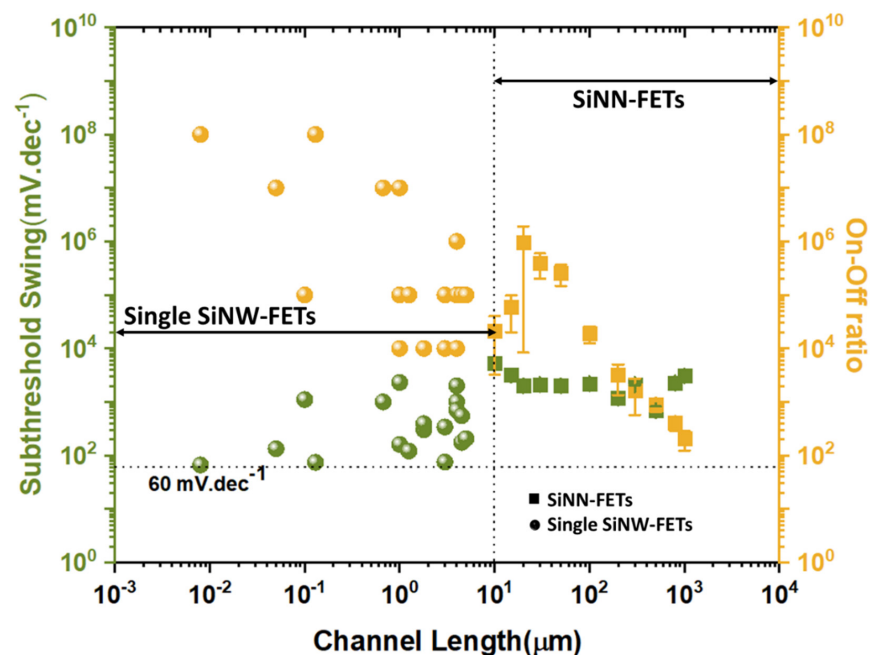


Figure 31. A comparison between single SiNW-FETs [11,33,175,181–190] and SiNN-FETs with respect to the channel length (SiNN density is about 0.6 NWs μm^{-2}). Squares of SiNN-FETs segment show the average of several devices’ performances in which bars are representative of deviation in measured parameters for a certain L_c .

Such a graph clearly shows that single-nanowire devices exhibit highly dispersed performance, even for a given channel length, while NN devices show much lower dispersion.

In conclusion, despite having lots of resistive junctions, SiNN based devices have good performance. Then the NW/NW junctions, which might initially appear to be a weakness of this type of system, are in fact an asset that allow good performance, good reproducibility, and high fault tolerance.

8. Technological Key Elements for SiNW-Based Device Integration

8.1. Sintering

When silicon is exposed to air, silicon dioxide (SiO_2)—commonly known as native oxide—is systematically formed on its surface. This oxidation is self-limiting at ambient temperature and the SiO_2 formed stops growing once it has reached a certain thickness of a few nanometers. According to high-resolution transmission electron microscopy (HRTEM) analyses, the NWs are covered with about 2 nm native oxide [28]. With a permittivity dielectric of 3.9, the silica layer—of amorphous structure—has good electrical insulating properties. The native thickness formed around the NWs is sufficient to inhibit the possible conduction by tunneling from one NW to another and makes it impossible to fabricate percolating devices with SiNNs [42]. Subsequently, Pauline Serre showed that in the absence of oxide, current can flow from one nanowire to the other via the junctions [39]. To do this, she studied the behavior of resistors based on NNs. Thus, as long as the devices are stored under nitrogen after deoxidation by hydrofluoric acid (HF) treatment, significant conduction is observed across the resistor. As soon as they are exposed to air, conductance decreases exponentially with air exposure time due to the progressive reoxidation of the NWs as shown in Figure 32a. Such a decrease in current observed in Figure 32a is explained by the progressive growth of SiO_2 at the junctions between NWs as indicated by the passage from step (1) to (1.a) in Figure 32b. With a time constant of 2.2 days, the silica shell formed is thick enough to electrically isolate the NW–NW junctions and prevent current flow through the nanonet. The use of the SiNNs is then jeopardized as a functional device under air. Nevertheless, when low-temperature annealing ($400\text{ }^\circ\text{C}$) is performed just after removal of SiO_2 by treatment with hydrofluoric acid (HF), the conductance shown in Figure 32a decreases by only 20% and then stabilizes for several months [48].

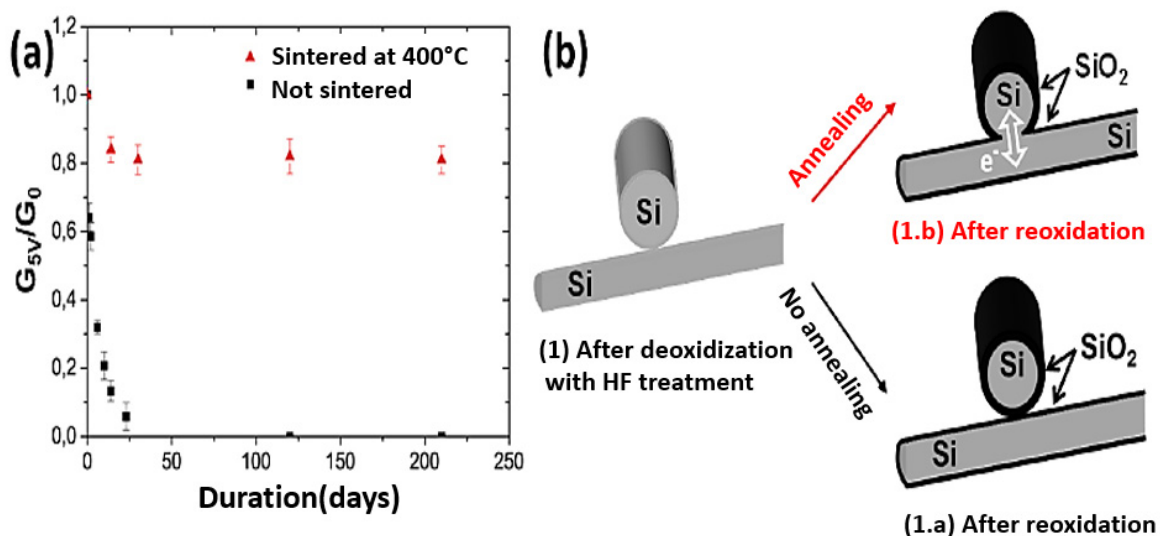


Figure 32. (a) Evolution of the conductance over time of Si nanonets based on not-annealed degenerated NWs and annealed at $400\text{ }^\circ\text{C}$ after deoxidation. The conductance at 5 V was normalized to the initial conductance just after deoxidation. (b) Diagrams illustrating, after deoxidation, the reoxidation under air of an NW–NW junction (1.a) without annealing or (1.b) with annealing at $400\text{ }^\circ\text{C}$ under nitrogen. Reproduced from [27].

HRTEM analysis, presented in Figure 33a.1 with its equivalent diagram (a.2), reveals the presence of a neck at the junction between two NWs. On this micrograph, the visible dislocation shows a continuity of crystalline planes between the two NWs. This crystal lattice continuity explains the stabilization of the current observed in Figure 32a even after several months of exposure to air. The 20% decrease in current after a few days is explained by the progressive reduction of the neck by the growth of the native oxide. However, when the reoxidation stops for a SiO₂ thickness of about 2 nm, the neck size stabilizes and the current is then constant even under air (Figure 32b, step (1.b)).

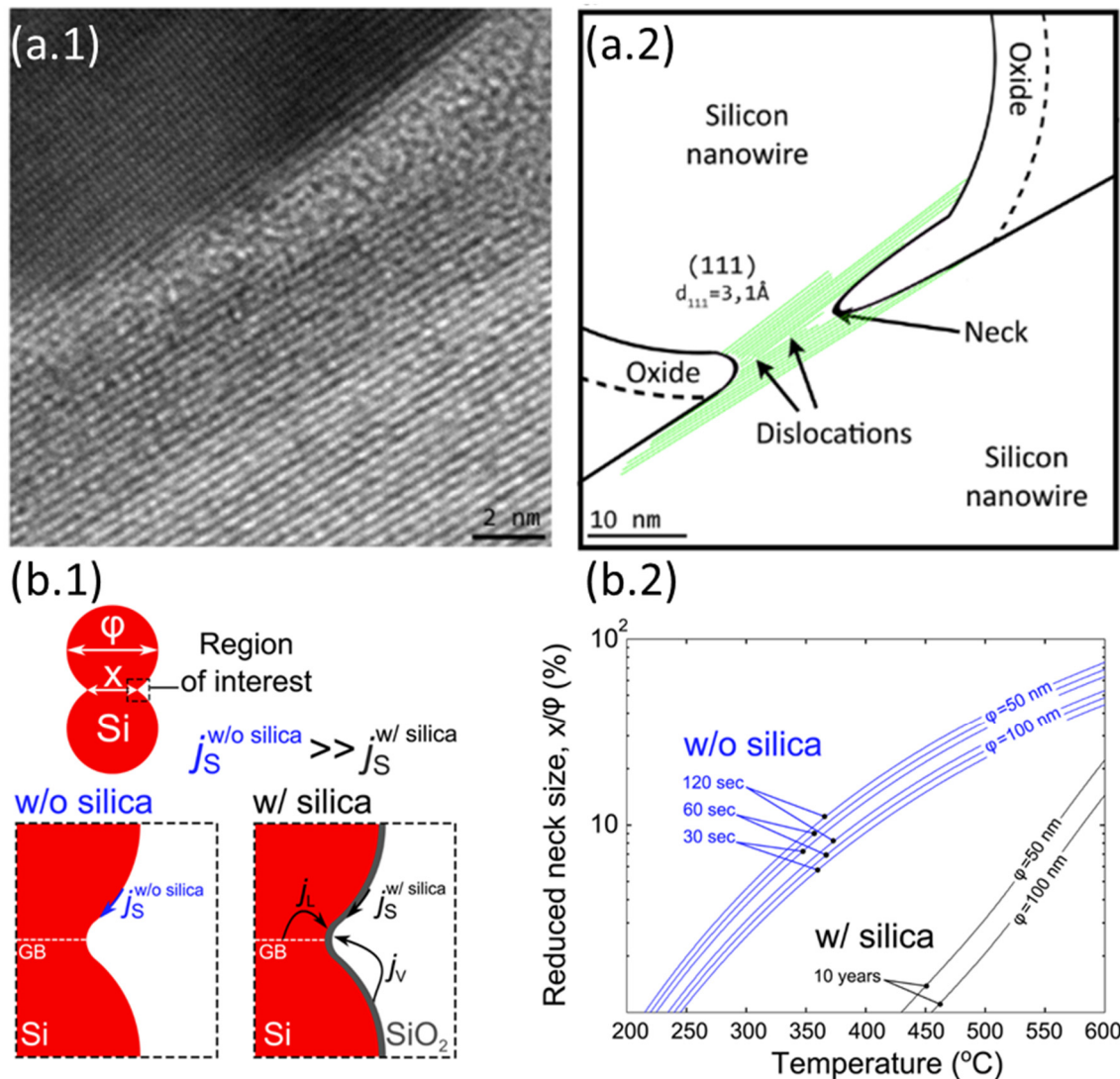


Figure 33. (a.1) High-resolution TEM image realized after re-oxidation of a junction between two NWs annealed at 400 °C under nitrogen. (a.2) Schematic representation of the TEM image showing the formation of a dislocation and a neck delimited by SiO₂ at the NW–NW junction. (b.1) Modeling of the sintering between two silicon nanoparticles with (w/) and without (w/o) the native oxide. Surface diffusion (j_s), volume diffusion from the grain boundary (j_L), and vapor diffusion (j_v) are the material transports considered. X and ϕ represent the shot size and diameter of the nanoparticles, respectively. (b.2) Sintering map representing the neck size relative to the initial nanoparticle size as a function of temperature for different annealing times. Reproduced from [48].

8.2. Surface and Interfaces

8.2.1. Modulation Thanks to Interface Surrounding the Channel

The quality of the interface surrounding the channel is a key parameter for all electronic devices such as FETs as it influences many parameters, from high to low frequency noise [191,192]. For example, a mechanism for filling or emptying traps at the NW/oxide interface leads to a memory effect as this gate dependency could compromise the operation of the transistor. According to the literature, the most commonly used oxides for passivation of silicon nanowires are silicon oxide (SiO_2), aluminium oxide (Al_2O_3), and hafnium oxide (HfO_2) [47,193]. It has been shown that Al_2O_3 offers better chemical stability than silicon oxide while maintaining excellent sensitivity in the case of using them as sensors [194,195].

In their early work, Legallais et al. studied SiNN FETs passivated by the native silicon dioxide layer which systematically grows when the silicon is exposed to air [47]. It is known this native SiO_2 provides poor-quality interfaces and induces the formation of a high density of dangling bonds at the interface. On the basis of the foregoing, they opted for an alumina encapsulation layer as it is fully compatible with the integration process and can be easily etched before contact deposition, using HF treatment [47]. Atomic layer deposition (ALD) was chosen for alumina deposition since it involves a self-limiting growth mechanism that enables the formation of high quality and homogenous thin film. Moreover, this technique provides a conformal coating and properly encapsulates SiNWs while preserving the sintered NW–NW junctions (Figure 34).

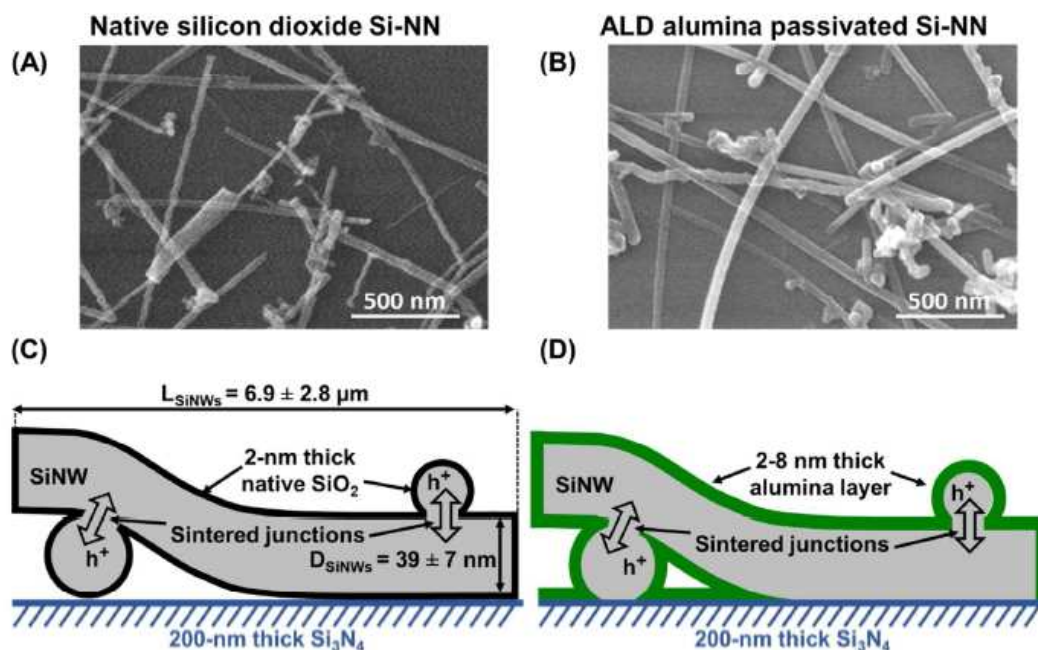


Figure 34. Comparison between sintered SiNN coated by (A,C) natively grown silicon dioxide and passivated by (B,D) alumina deposited using ALD. (A, B) Refer to top-view SEM images of nanonets, while (C, D) are sectional schemes of three coated SiNWs: one sectioned in the length and two according to the diameter. For (C), the mean and standard deviation of SiNW length (L_{SiNWs}) and diameter (D_{SiNWs}) are indicated. For (D), due to conformal coating with ALD, alumina is deposited simultaneously on SiNWs and onto the substrate whereas SiNW–SiNW junction and underneath SiNW portions are considered alumina-free. Reproduced from [47].

As native SiO_2 has a high density of dangling bonds at the interface, this interruption in the periodic lattice structure acts as interface traps for carriers. These traps are responsible for the reduction of transistor performances. On the contrary, alumina provides a better quality interface and improved electrical characteristics, as clearly shown in Figure 35A,B.

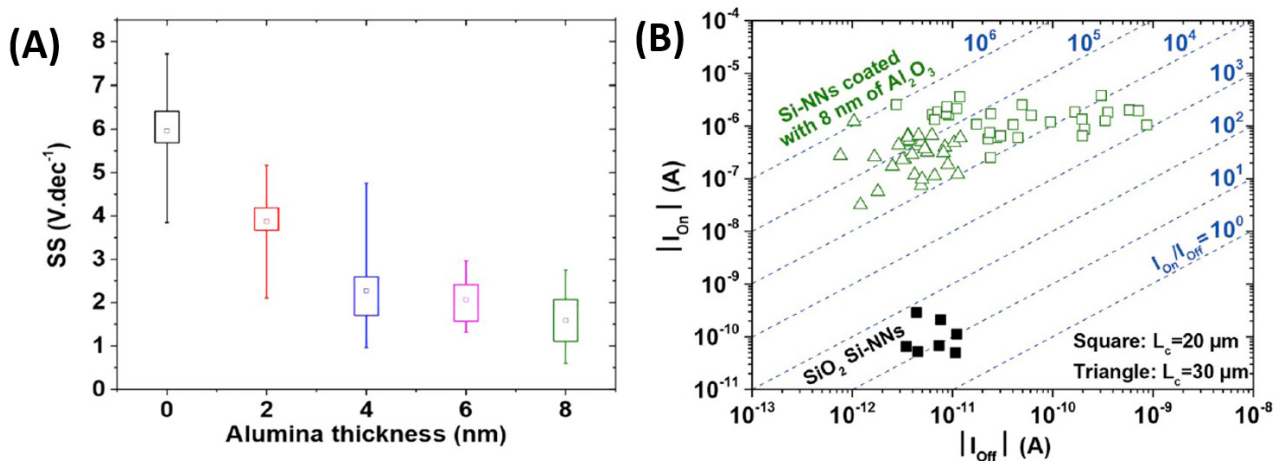


Figure 35. (A) Effect of the alumina thickness on the subthreshold slope (SS). 0 nm of alumina corresponds to a 2-nm thick layer of native SiO₂. For all transistors, the channel length (L_c) is 20 μm and the drain voltage (V_d) was set at -4 V. The boxes show the 25th and 75th percentiles, whereas the whiskers represent the 5th and 95th percentiles. The empty square in the boxes shows the mean value. (B) Reproducibility of the on and off current for transistors based on native SiO₂ SiNNs (full symbol) and 8-nm alumina encapsulated SiNNs (empty symbol) for 20 μm (square) and 30 μm (triangle) long channel. For native SiO₂ SiNN based devices, no current is observed when the channel length is 30 μm. The on-to-off ratio ($I_{on} = I_{off}$) is indicated by the dashed line. I_{on} and I_{off} were extracted at -25 V and $+25$ V, respectively. Reproduced from [47].

As a result, this study shows that proper material engineering of nanonets via alumina encapsulation can drastically enhance the electrical characteristics of back-gate FETs.

At the same time, although silicon nanowires are considered promising for future biomedical sensors, their limited stability under physiological conditions is a challenge for sensor development. Solving this issue by surface engineering as described above opens up new possibilities for sensor improvements [81,196,197].

However, as with thin films, the nanostructures composing the nanonet can be functionalized with, for example, molecules or proteins. DNA sensors based on SiNN have been achieved by chemically modifying the surface of nanonet with 3-aminopropyltriethoxysilane (APTES) silanization [28] or (3-glycidyloxypropyl)trimethoxysilane (GOPS) [198]. Particularly, GOPS functionalization enables DNA electrical detection with SiNN-FETs [199]. Additionally, silicon nanonet field effect transistors (SiNN-FETs) were biomodified using thrombin-binding aptamer (TBA-15) [200] with the aim to detect thrombin protein. As an illustration, Figure 36 shows the shift in threshold voltage induced by aptamer probes grafting on the SiNN surface. As a result, again it has been demonstrated that the surrounding material can drastically change the characteristics of the SiNN-FETs.

8.2.2. Modulation Thanks to Functionalization under the Channel

As previously stated, the complex electronic mechanisms involved in electronic devices are highly dependent not only on the energy barriers to conquer but also on the interface traps, which can induce modification of the charge carrier density thus changing the performances of the devices. The phenomena are poorly understood, and the roots of changes are numerous ranging from the neutralization of surface defects, the modification of the surface energy, and even the creation of interface dipoles. Celle et al. focused on the control of the chemical nature of the interface between the gate oxide and the semiconductor, the place where the conduction channel is established in FETs (back gate-bottom contact structure Figure 37) [201].

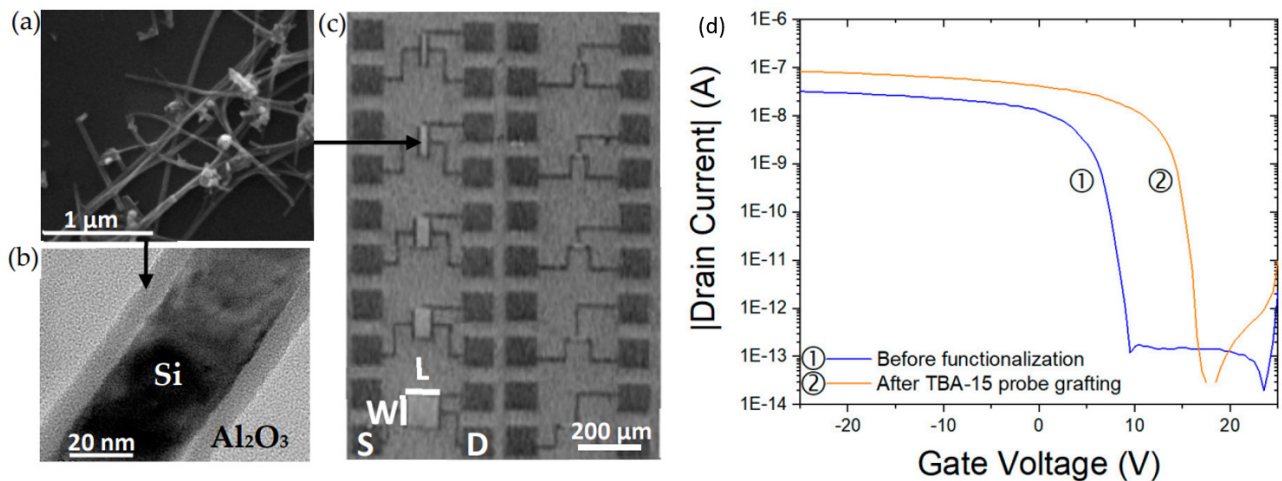


Figure 36. (a) SEM image of the Si nanonet (NN) after transfer on heavily doped Si substrate covered with a 200 nm thick Si₃N₄. (b) High-resolution TEM (HRTEM) image displaying an Al₂O₃ passivated Si nanowire. (c) Optical image of Al₂O₃ passivated SiNN field effect transistors (FETs) presenting different channel geometries. (d) Transfer characteristics were obtained for an L = 100 μm, W = 100 μm NN-FET at a drain voltage of V_{ds} = −2 V before and after functionalization with thrombin-binding aptamer (TBA-15). Reproduced from [200].

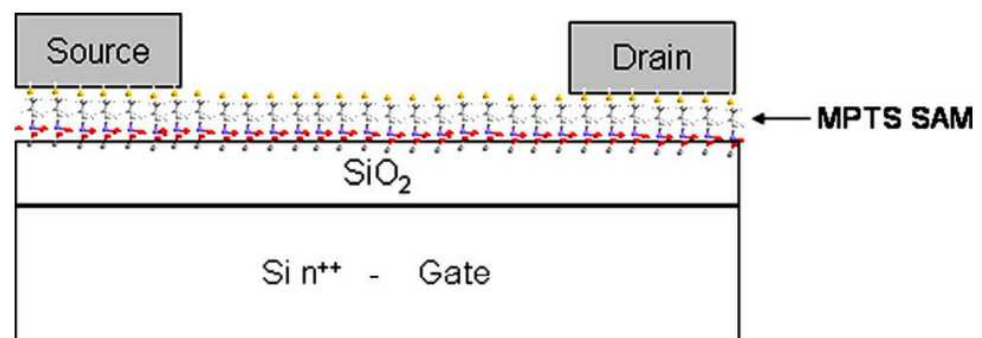


Figure 37. Schematic structure of the devices with MPTS as anchoring layer for gold electrodes. Reproduced from [201].

They show that thiolated self-assembled monolayer (SAMs) can be used to anchor source-drain gold electrodes on the substrate, leading to excellent electronic performances of the organic field-effect transistor (OFET) on the same level as those using a standard electrode process. It has been demonstrated that the threshold voltage is tunable while keeping the other electrical properties nearly unchanged by functionalization of the surface of the substrate under the channel (Figure 38). These self-assembled monolayers strongly modify the OFET characteristics, leading notably to charge carrier mobility [201,202].

SAMs are known to generate a built-in electric field, which modifies the carrier density in the transistor channel. For instance, it is seen that fluorinated SAMs have the tendency to generate a local electric field that accumulates holes, and on the contrary, devices with 3-aminopropyl-triethoxysilane (APTS), or triarylamine triethoxysilane derivative (TAATS) accumulate electrons, leading to the need for a very large negative gate bias to turn on organic semiconductor which is polytriarylamine (PTAA), into hole accumulation mode. They have shown that this local electric field is related to the dipole moment of the molecules [201,202].

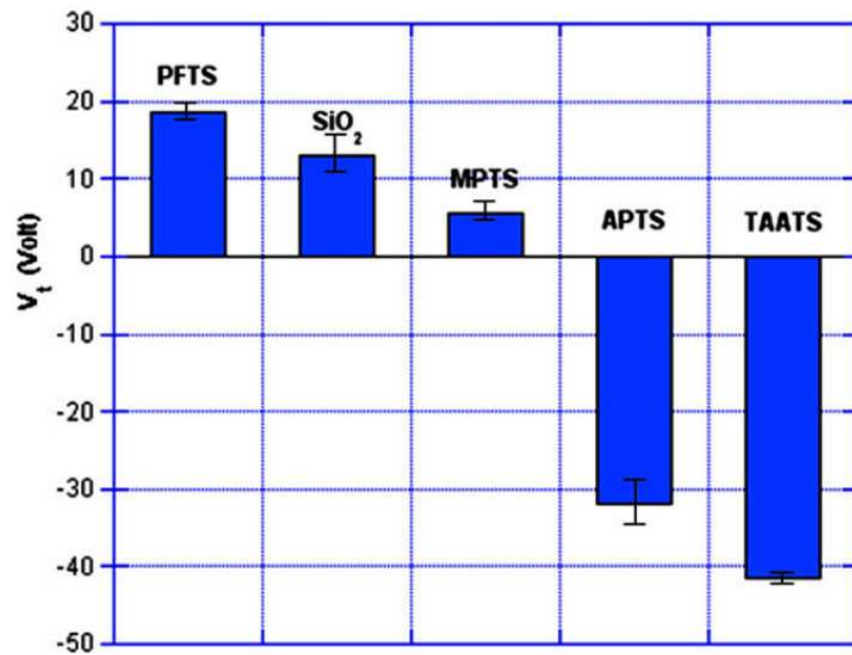


Figure 38. V_t as a function of the channel modification. Reproduced from [201].

8.3. Silicidation

Silicidation was commonly used since the 1980s in MOSFETs in forming an alloy between metal and silicon during an annealing process in order to decrease the electrical contact resistance between the two materials. During this step, solid-state reactions occur by diffusion and/or nucleation processes of the thermally activated species. Depending on the experimental annealing conditions, different stable crystalline phases called silicides can form and are denoted M_xSi_y with M the metal used. Silicon has the particularity of associating with many metals, some of which are grouped in Table 3. Historically, the silicides TiSi_2 , CoSi_2 , and more recently NiSi have been the most used by the microelectronics industry for their low electrical resistivity ranging from 10 to 25 $\mu\Omega\cdot\text{cm}$ [203]. Nevertheless, Ti- and Co-based alloys require higher temperature annealing which may be responsible for the deactivation of the dopants contained in the silicon and implies an increase in contact resistance at the interface between silicide and Si [204]. Moreover, for some Co silicides, Si is the dominant diffusion species, which causes the formation of gaps or voids in the silicon. Following this phenomenon, the diffusion of Si gaps can also become considerable. Thus, simultaneous flows of matter in one direction and of vacancies in the other lead to the appearance of porosities within the silicon, a phenomenon commonly known as the Kirkendall effect. This is probably one of the reasons why a high increase in the electrical resistance of Co silicides is observed when the channel length of MOSFETs is below 50 nm [205,206].

Table 3. Properties of different silicides used in the microelectronics industry. Table adapted from references [205,207,208]. Φ_{bh} corresponds to the barrier height on N-type silicon.

Silicide	Formation Temperature ($^{\circ}\text{C}$)	Crystalline Structure	Resistivity ($\mu\Omega\cdot\text{cm}$)	Φ_{bh} (eV)
TiSi_2	650	Orthorhombic	13–16	0.60
CoSi_2	450	Cubic	18–20	0.64
PtSi	300	Orthorhombic	28–35	0.87
NiSi	400	Orthorhombic	10.5–18	0.75

For the reasons stated above, NiSi silicide is today widely used due to its low electrical resistivity (10.5–18 $\mu\Omega\cdot\text{cm}$) as well as its lower formation temperature (400 $^{\circ}\text{C}$). Further-

more, Ni-based silicidation is a diffusion process in which Ni is the dominant diffusion species [206]. While, contrary to Co silicides, the gaps generated during thermal annealing are located in the metallic contact and avoid the appearance of porosities within the silicon. Nevertheless, the complexity of the Ni-Si phase diagram presented in Figure 39 indicates the difficulty to control, during annealing, the formation of the desired NiSi phase. Indeed, many crystalline and stable phases at room temperature are likely to form [209]. Note that the variations in resistivity from one phase to another are very large, ranging from 7 to 150 $\mu\Omega\cdot\text{cm}$ (Table 4).

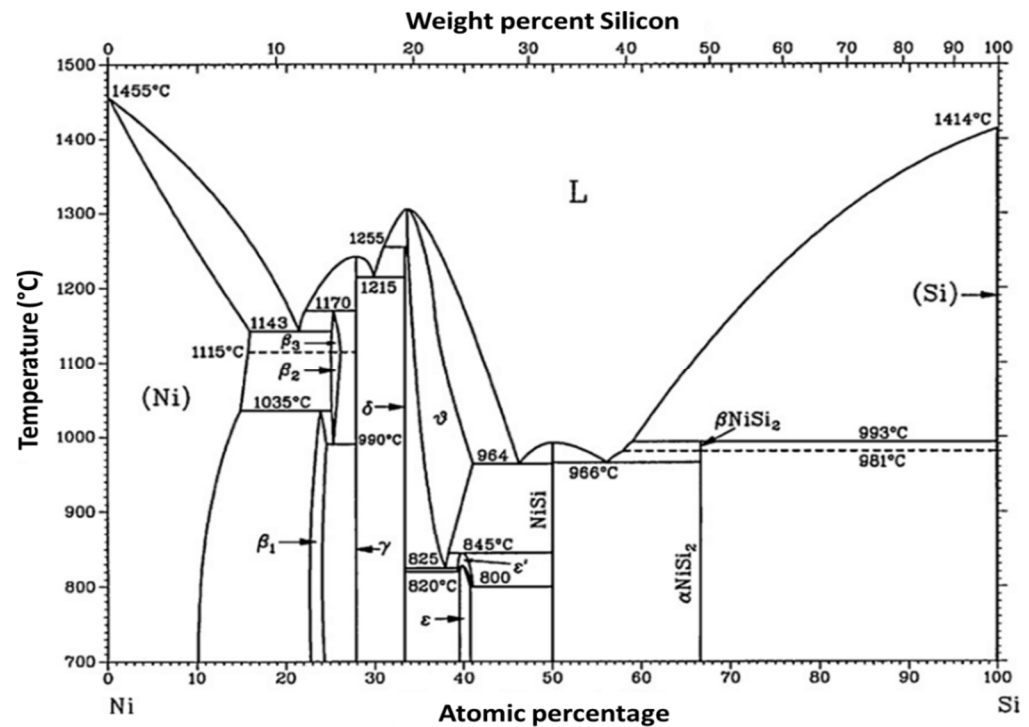


Figure 39. Binary phase diagram of the nickel–silicon pair. Reproduced from [209].

Table 4. Formation temperature, crystallographic structure, electrical resistivity, unit cell volume per Si atom ($V_{\text{Ni}_x\text{Si}_i/\text{Si}}$), and the ratio of this volume to that of Si ($V_{\text{Ni}_x\text{Si}_i/\text{Si}}/V_{\text{Si}}$) of each room temperature stable Ni_xSi_y silicide [205,208]. UNK is the acronym for unknown.

Phase	Formation Temperature (°C)	Crystalline Structure	Resistivity ($\mu\Omega\cdot\text{cm}$)	$V_{\text{Ni}_x\text{Si}_i/\text{Si}}$ (\AA^3)	$V_{\text{Ni}_x\text{Si}_i/\text{Si}}/V_{\text{Si}}$
Ni	-	Cubic	7–10	-	-
Ni_3Si	UNK	Cubic	80–90	43.08	2.15
$\text{Ni}_{31}\text{Si}_{12}$	UNK	Hexagonal	90–150	39.46	1.97
Ni_2Si	200	Orthorhombic	24–30	32.15	1.61
Ni_3Si_2	UNK	Orthorhombic	60–70	28.73	1.44
NiSi	400	Orthorhombic	10.5–18	24.12	1.21
NiSi_2	800	Cubic	34–50	19.75	0.99
Si	-	Cubic	Depend on doping	20.01	1

Currently, the silicidation process [210] (a portmanteau for ‘self-aligned silicide’) is used to achieve simultaneous silicidation of the source, drain. This technique consists in forming the Ni_2Si phase by diffusion of Ni during the first annealing between 270 and 350 °C. Then, after etching the excess of unreacted nickel, the NiSi silicide is formed after second annealing between 400 and 550 °C [211]. According to Ottaviani, NiSi can only be formed after consumption of the entire metal reservoir, which explains the need to etch the excess Ni after the first annealing [212].

It was shown that the NiSi phase can form a low resistive Si-Ni interface for a thermal budget compatible with the specifications of today's microelectronics industry.

Silicidation of Silicon Nanowires with Nickel

For silicon nanowires, the formation of a silicide also makes it possible to form an abrupt interface over the entire cross-section of the nanowire between the silicide and the nanowire, which facilitates the injection of the carriers. Indeed, the nickel penetrates over the entire volume of the SiNW and then diffuses longitudinally. Otherwise, for non-silicided nanowires, the injection of the carriers is less efficient since it is done radially through the edges of the SiNWs. In addition, Chou et al. studied the kinetics of NiSi formation between 450 and 750 °C by in-situ transmission electron microscopy analyses [213,214].

Nevertheless, the NiSi phase is often accompanied by a Ni-rich phase that forms at lower temperatures [215–217]. Other crystallographic studies have shown the possibility of obtaining Ni-rich phases such as Ni₃₁Si₁₂ and Ni₂Si for temperatures between 400 and 450 °C [176,218]. More surprisingly, NiSi₂ silicide has been stabilized at low temperatures between 440 and 550 °C while it forms at about 800 °C for bulk materials [175,176,218–220]. In order to evaluate the phases likely to form for a given temperature, Figure 40 represents the minimum and maximum temperatures of formation of the different Ni_xSi_y silicides in silicon nanowires from references reported in the literature.

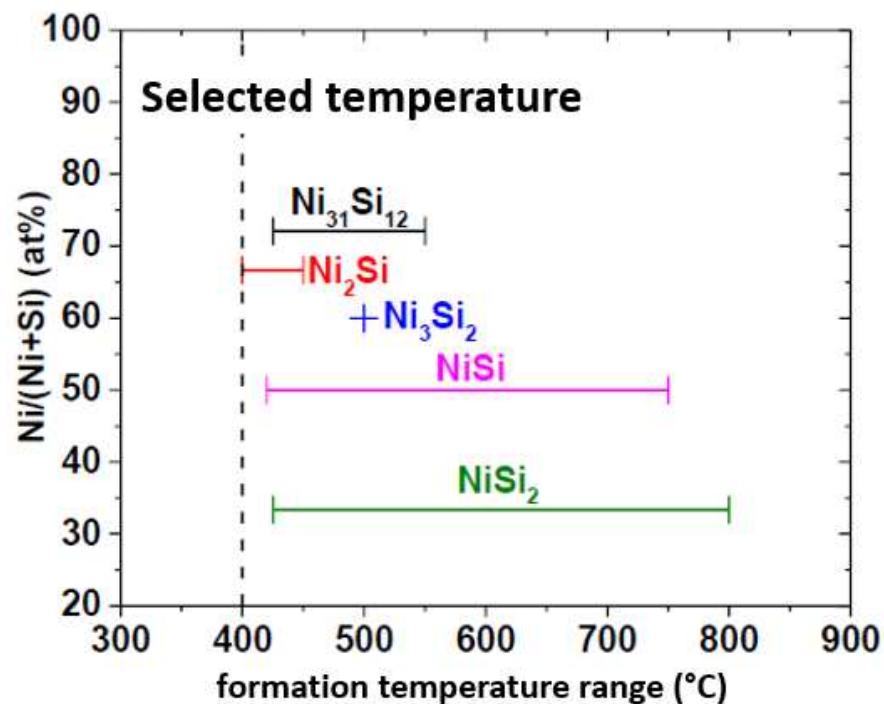


Figure 40. Temperature range of formation of different Ni_xSi_y silicides in SiNWs reported in the literature from 15 references [175,176,182,213,214,216–224].

According to Figure 40 based on SiNWs, for an annealing temperature of about 400–450 °C, we can see that the Ni₃₁Si₁₂, Ni₂Si, NiSi, and NiSi₂ phases are likely to form, i.e., a variation in electrical resistivity between 10.5 and 150 μΩ.cm (Table 4). Thus, obtaining the NiSi phase in SiNWs is complex and the silicidation involves many parameters such as the crystal orientation [176,218], the diameter of the nanowire [217], the thickness of the nickel film [225], or the thickness of the oxide surrounding the nanowire [221]. According to the work of Ogata et al. [220], the diffusion length of silicide in SiNW evolves with the square root of the annealing time.

According to the literature carried out previously, the desired NiSi silicide of low electrical resistivity is formed at a temperature of about 400 °C for massive materials

(Table 4). In the context of NW silicidation, the complex growth mechanisms involved do not allow to conclude on an optimal temperature and time for the formation of the NiSi phase despite a rich literature on this subject. Nevertheless, according to the work of Ternon et al. [48] and the studies of Byon et al. [182], an optimum of the electrical properties can be distinguished for annealing at 400 °C which is consistent with the NiSi formation temperature. Moreover, this temperature does not exceed the maximum temperature allowed for integration on the back-end of a reading circuit.

To complete the silicidation study, the impact of silicide existence on the electrical characteristics of SiNWs was also considered [226]. The main advantage of silicide contacts over non-silicided contacts is better device performance by modifying the nature of the metal–semiconductor interface, thus reducing series resistance [11,214,215,227]. Guillaume Rosaz showed that the NiSi silicide, formed at 400 °C in the nanowires, lowers the height of the Schottky barrier, thus favoring the injection of the carriers. The performance of the transistors is significantly improved by an increase in current accompanied by a decrease in subthreshold swing [3,11]. The thermally activated intrusion of nickel into the SiNW is an inexpensive and robust, but not fully controlled, process. They demonstrated that the silicidation reaction seems to be self-limited (see Figure 41c).

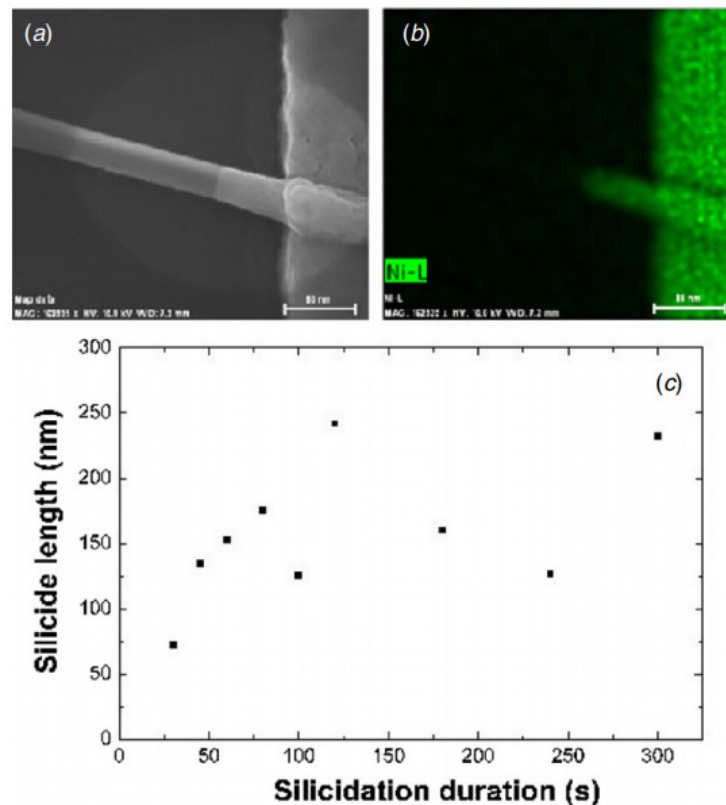


Figure 41. (a) SEM view of a silicided contact after annealing at 400 °C under nitrogen gas during 300 s. The scale bar is 80 nm. (b) EDX picture of the contact presented in (a). Green color indicates the presence of nickel. One can notice the propagation of the nickel in the SiNW after the annealing step leading to the formation of a silicide. (c) Length of the silicided section obtained at 400 °C under nitrogen gas in an RTA furnace as a function of the annealing time. Reproduced from [11].

The silicide region lessens the resistance of the contacts in two ways. First, the low sheet resistance of the silicide layer reduces the in-plane contact resistance, and second, the silicide reaction leads to an intimate and more reliable metal–semiconductor (MS) contact and transforms the contact surface initially on the surface of the NW into a contact surface on the cross-section of the NW. As a result, in terms of performance, the most substantial properties of a silicide material are its low electrical resistivity and its lower Schottky

barrier height [227,228]. Byon et al. also studied the impact of silicidation on the electrical properties of transistors and observed an optimum between 400 and 450 °C after successive annealing from 250 to 500 °C [182].

Figure 42 presents the transfer characteristics before and after annealing of a 20 μm channel SiNN-FET elaborated with a density of $42 \times 10^6 \text{ NWs cm}^{-2}$ (drain-source bias of -4 V). Before annealing, the device exhibits and the state of 9 nA and 0.7 pA respectively, resulting in an on/off ratio of 10^4 . After annealing, the state reaches 170 nA while the state remains constant, corresponding to an enlarged on/off ratio $>10^5$. Such improvement by one order of magnitude confirms the formation of a low resistive phase, enhancing hole injection at the metal/SiNW contact.

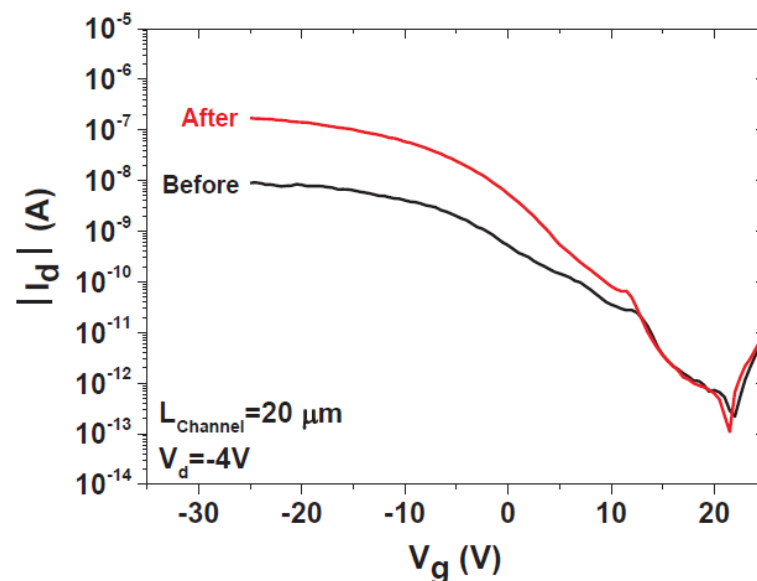


Figure 42. Transfer characteristics before and after silicidation (400 °C, for 60 s) of a 20 μm channel Si nanonet FET elaborated with 18 mL of filtered SiNW solution (with $42 \times 10^6 \text{ NWs cm}^{-2}$ corresponding density). The drain-source bias was set at -4 V . Reproduced from [226].

9. Applications

Silicon nanowires can be exploited in many ways in electronic devices and can find numerous real applications such as displays, data storage, 3-D computing, lasers, smart cards, wearable electronics, high efficiency programming, ring oscillators [6,31,168]. They have so far shown promising applications in areas ranging from biological sensors, thermo-electric converters, opto-mechanical devices, piezoelectric sensors, and solar cells among others. Describing all the potential applications in detail is far beyond the scope of this review. However, dealing with devices without describing applications would leave a taste of unfinished business. As a consequence, in this section, without being exhaustive, we choose to summarize some basic applications for the simplest SiNW-based devices (resistor, transistors, and diodes).

9.1. Photodetectors

Optical properties of SiNWs have allowed envisaging the use of SiNWs as optically active materials for photonics application. The ease of bandgap conversion from indirect to direct band due to dimension, crystallography, mechanical strain, and alloying allows SiNWs to be used in the optical applications—e.g., photodetectors (PDs) and light emitters (LEs). Since silicon nanowires have a superior ability to tune absorption with morphology, Um et al. reported that SiNWs with a coating of an indium oxide layer on it, lead to efficient carrier separation and collection, resulting in an improvement of quantum efficiency and by controlling the nanowire radii, can create a multispectral detector [229].

9.2. Memories

A self-alignment technique can be used to position the silicon nanowires, which could allow for lower production costs than current flash memory cards. SiNW-based memory devices showed better stability at higher temperatures, no power consumption in the off-state, and very small switching energy (10^{-14} J) [230].

With the advent of new CMOS compatible fabrication methods for silicon nanowires, it is now feasible to build memory and memristive devices. The SiNW-FET based dielectric charge-trapping flash-like memories have been fabricated and fully characterized by Zhu et al. (Figure 43c,d) [231].

These non-volatile memory devices exhibited fast programming/erasing speed, excellent retention, and endurance, indicating the advantages of integrating the multilayer of charge-storage stacks on the nanowire channel. Such high-performance flash-like non-volatile memory can be integrated into the microprocessor chip as the local memory which requires high density and good endurance [231–233].

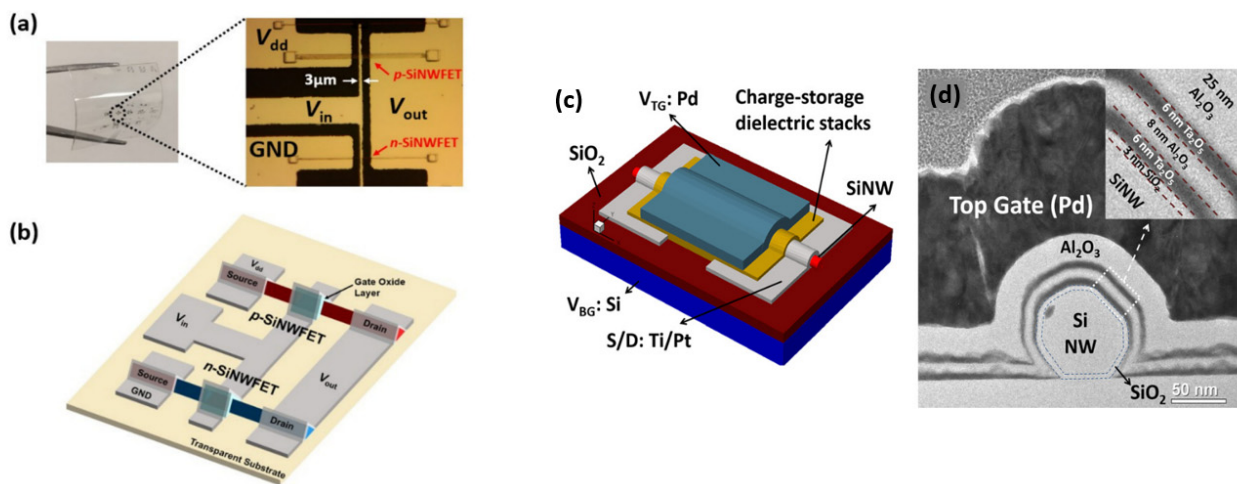


Figure 43. (a) Optical images and (b) schematic illustration of the SiNW CMOS inverter on a transparent substrate. Reproduced from [234]. (c) Schematic of a SiNW-FET-based charge-trapping non-volatile flash memory; (d) TEM image of the cross section of a MATATOS device. Inset demonstrates the typical thickness of the top gate stack. Reproduced from [231].

9.3. Biosensors

Sensors are important tools for life sciences and biochemistry. The use of sensors in these areas leads to the detection and diagnosis of diseases and to the discovery of new drugs [17,71]. Microelectronic sensors based on thin film transistors and ion-sensitive field-effect transistors (ISFETs) are used since the 1970s. They offered a cheap solution over the chemical sensors and could be integrated on a chip [71]. Nevertheless, the microelectronic sensors did not have the required characteristics to be used as biosensors because of their undesired sensitivity to temperature and light and because their parameters were not fixed over time. Additionally, solid-state electrodes were not reliable and this led to the use of chemical sensors [71]. Currently, the detection of biomolecules at low concentrations is achieved with fluorescent labeling and optical detection methods. However, this technique is expensive and time-consuming and thus silicon nanowires may be an alternative solution [71,235].

Silicon nanowires can almost act as perfect biosensors due to their inherent properties [235]. When used as sensors, their characteristics include ultrahigh sensitivity because the molecule being sensed depletes or accumulates the charges in the bulk of the nanowire [17,235]. In addition, direct label-free detection allows the molecules to be detected in real time which eliminates the time consuming labeling chemistry [17,23,71].

Another important characteristic is that they are non-radioactive and that sensor arrays can allow detection of different molecules in the same solution [23,71].

Although SiNW sensors have great characteristics there are factors that can affect their performance. These include the surrounding environment of the nanowire and the electrostatic screening action of the ions in the solution. The performance of a sensor can be characterized by sensitivity, settling time, and selectivity. A simulation with a silicon nanowire with a length between 2 and 20 μm showed how the sensitivity can be influenced by several factors. The results showed that the sensitivity increases with reduced dopant density and decreased diameter and length. However, it is not possible to reduce these quantities as much as needed to achieve the maximum desired sensitivity due to the dopant fluctuations effect. Furthermore, this simulation revealed that the dielectric constant of the surrounding environment affects the sensitivity of SiNW. If the surrounding media is air then the sensor has greater sensitivity if it is designed to operate in the depletion mode. Finally, parasitic ions in the surrounding solution of the sensor screen the charge of the target molecule and reduce sensitivity [71].

Experimental applications of SiNW sensors include the detection of proteins, DNA, pH, drug discovery, single viruses, glucose, and arrays for parallel molecule detection, as shown in Figure 44 [17,61,236].

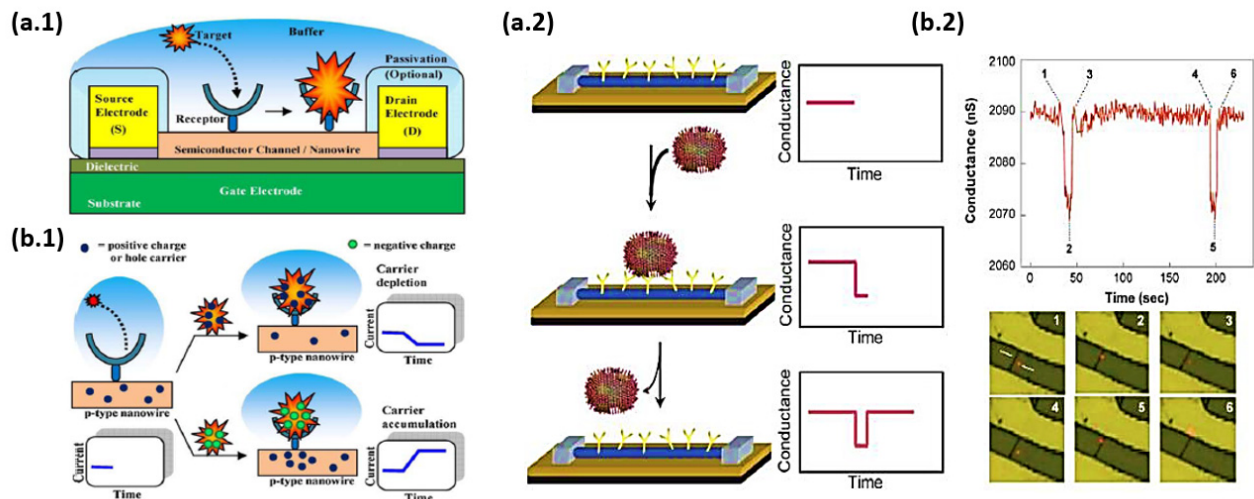


Figure 44. (a.1) The illustration of a nanoscale FET biosensor with a cross-sectional view. (b.1) When positively charged target molecules bind the receptor modified on a p-type NW, positive carriers (holes) are depleted in the NW, resulting in a decrease in conductance. Conversely, negatively charged target molecules captured by the receptor would make an accumulation of hole carriers, causing an increase in conductance. Reproduced from [174]. (a.2) Schematic of a single virus binding and unbinding to the surface of a SiNW device modified with antibody receptors and the corresponding time-dependent change in conductance. (b.2) Simultaneous conductance and optical data recorded for a Si nanowire device after the introduction of influenza A solution. The images correspond to the two binding/unbinding events highlighted by time points 1–3 and 4–6 in the conductance data, with the virus appearing as a red dot in the images. Reproduced from [17].

9.4. Gas Sensor

Silicon nanowires can find applications as gas sensors too. As an example, this was demonstrated for H_2 sensing when the surface of an n-type SiNW was coated with palladium nanoparticles (Pd particles). Good selectivity was demonstrated as no response was observed when exposed to NH_3 or N_2O gases. However, when H_2 gas flowed over the sensor, the current flowing through was increased, as shown in Figure 45. Furthermore, the SiNW sensor responded faster (2.3 s) than an ordinary macroscopic Pd wire sensor (more than 10 s) [236].

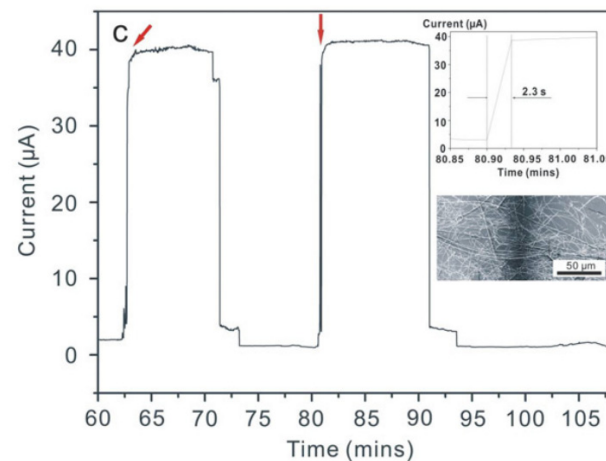


Figure 45. Real time current response of Pd coated SiNWs in 5% H₂. The inset images show the enlarged current response (**upper**) and an SEM image (**below**) of the device. Note that, the sensor was inside a chamber with a pressure of 0.01 Torr, and a voltage of 2 V was applied across it. Reproduced from [236].

9.5. Thermoelectric Application

Thermoelectric devices can convert heat directly into electrical power, and vice versa, and they have a broad range of applications: energy recovery and green energy harvesting; energy micro-harvesting (scavenging) for the capillary supply of small systems, such as sensor nodes for Internet of Things (IoT); powering of systems in remote and harsh environments typical, for example, of spatial exploration; localized and optimized cooling of small systems, where the reliability and the compactness can play a fundamental role [101, 237,238]. Unfortunately, the available materials with thermoelectric properties good enough for an acceptable thermal-to-electrical conversion efficiency limit all of the potentialities offered by thermoelectric devices at the current state of the art.

The observed high electrical and low thermal conductivity of highly doped SiNWs arrays, shows that SiNWs arrays represent a promising material for thermoelectric applications. Hence, it could make a significant contribution in the fundamental fields of energy micro-harvesting (scavenging) and macro-harvesting [101,237,238].

10. Conclusions

Semiconductor nanowires, especially silicon nanowires, have aroused a lot of scientific interest over the past 25 years and have been considered a promising material for nanoscale devices and integrated circuits. Key parameters in realizing application through a bottom-up paradigm include chemical composition, structure, size, morphology, and doping which have been fully controlled in semiconductor NW systems. Among semiconductor NWs, silicon NWs—owing to their unique physical and chemical properties—show promise for a wide range of applications, including FETs. However, such devices based on single SiNWs face complicated fabrication processes and low reproducibility of their electrical characteristics which originate from various issues such as dispersion in length, diameter, and doping of individual nanowires, wire surface passivation, poorly controlled gate length, or silicidation with the silicide length and quality arising from annealing step.

Researchers tried to solve these issues with multi-channel SiNW-based devices which have better stability and reproducibility in comparison with single SiNW-based devices. Apart from increased on-current in MPC-FETs, some other parameters include on-to-off ratio or subthreshold swing degrade. This degradation occurs due to intrinsic disparities of all parameters which have already been mentioned for single SiNWs such as length, diameter, doping, and surface properties.

Silicon nanonets are networks of randomly oriented silicon nanowires. Due to its flexibility, transparency, and reproducibility, this material is highly attractive as an alterna-

tive to amorphous silicon or organic materials for various macro-electronic applications involving sensors and displays. Based on the easy integration process simply relying on standard photolithography, it has demonstrated successful workability, reproducibility, and excellent air stability along with interesting performance for device channel length ranging from micrometer to millimeter scales. SiNN-FETs also displayed good stability and reproducibility which differentiates them from single SiNW- and MPC-FETs and which are the results of averaging effect over thousands of nanowires and their junctions.

According to literature, the nanonet-based thin film transistor technology has the respective advantages of poly-Si, a-Si, or organic material, without their particular drawbacks, along with being flexible. Moreover, low-cost and large-scale technology is an important asset of this material, in comparison to the issues surrounding the poly-Si option. Furthermore, using nanostructures—such as a network of nanowires—allows electronics to be smaller, more powerful, and more efficient. Finally, in conclusion, nanonets can address the need for cost-effective, reproducible, and efficient systems to exploit nanoscale properties while being easily manipulated and compatible with large-scale integration and opening up many opportunities, both in terms of applications and fundamental studies, in short, a new field of research.

Funding: This work has received funding from the EU H2020 RIA project Nanonets2Sense under grant agreement no. 688329 and ANR in the framework of Convergence project, Flag ERA (ERANET—JTC2016).

Conflicts of Interest: The authors declare no conflict of interest. The funders had no role in the design of the study; in the collection, analyses, or interpretation of data; in the writing of the manuscript, or in the decision to publish the results.

References

1. Ramgir, N.S.; Yang, Y.; Zacharias, M. Nanowire-Based Sensors. *Small* **2010**, *6*, 1705–1722. [CrossRef] [PubMed]
2. Wu, B.; Heidelberg, A.; Boland, J. Mechanical properties of ultrahigh-strength gold nanowires. *Nat. Mater.* **2005**, *4*, 525–529. [CrossRef] [PubMed]
3. Rosaz, G. Intégration 3D de Nanofils Si et SiGe Pour la Réalisation de Transistors Verticaux à Canal. 2012. Available online: <https://www.theses.fr/2012GRENT108> (accessed on 9 February 2022).
4. Lu, W.; Xiang, J. Semiconductor Nanowires: From Next-Generation Electronics to Sustainable Energy. *R. Soc. Chem.* **2015**, *39*. Available online: <http://stacks.iop.org/0022-3727/39/i=21/a=R01> (accessed on 8 February 2022).
5. Liu, L.-C.; Huang, M.-J.; Yang, R.; Jeng, M.-S.; Yang, C.-C. Curvature effect on the phonon thermal conductivity of dielectric nanowires. *J. Appl. Phys.* **2009**, *105*, 104313. [CrossRef]
6. Yu, B.; Meyyappan, M. Nanotechnology: Role in emerging nanoelectronics. *Solid-State Electron.* **2006**, *50*, 536–544. [CrossRef]
7. How Nanowires Work. 2014, pp. 1–5. Available online: <https://science.howstuffworks.com/nanowire.htm> (accessed on 11 January 2022).
8. Ternon, C.; Dupas, F.; Stein, S.; Aguirre, C.; Dhalluin, F.; Baron, T. Carbon Nanotube Sheet as Top Contact Electrode for Nanowires: Highly Versatile and Simple Process. *J. Nanosci. Nanotechnol.* **2015**, *15*, 1669–1673. [CrossRef] [PubMed]
9. Rosaz, G.; Salem, B.; Pauc, N.; Potié, A.; Gentile, P.; Baron, T. Vertically integrated silicon-germanium nanowire field-effect transistor. *Appl. Phys. Lett.* **2011**, *99*, 193107. [CrossRef]
10. Arjmand, T.; Legallais, M.; Haffner, T.; Bawedin, M.; Ternon, C.; Salem, B. Development of a robust fabrication process for single silicon nanowire-based omega gate transistors on polyamide substrate. *Semicond. Sci. Technol.* **2020**, *36*, 025003. [CrossRef]
11. Rosaz, G.; Salem, B.; Pauc, N.; Gentile, P.; Potié, A.; Solanki, A.; Baron, T. High-performance silicon nanowire field-effect transistor with silicided contacts. *Semicond. Sci. Technol.* **2011**, *26*, 085020. [CrossRef]
12. Morales, A.M.; Lieber, C.M. A Laser Ablation Method for the Synthesis of Crystalline Semiconductor Nanowires. *Science* **1998**, *279*, 208–211. [CrossRef]
13. Yu, P.; Wu, J.; Liu, S.; Xiong, J.; Jagadish, C.; Wang, Z.M. Design and fabrication of silicon nanowires towards efficient solar cells. *Nano Today* **2016**, *11*, 704–737. [CrossRef]
14. Chen, L.; Lu, W.; Lieber, C.M. Chapter 1. Semiconductor Nanowire Growth and Integration. In *Semiconductor Nanowires: From Next-Generation Electronics to Sustainable Energy*; Royal Society of Chemistry: London, UK, 2014; pp. 1–53. [CrossRef]
15. Appenzeller, J.; Member, S.; Knoch, J.; Björk, M.T.; Riel, H.; Schmid, H.; Riess, W. Toward nanowire electronics. *IEEE Trans. Electron Devices* **2008**, *55*, 2827–2845. [CrossRef]
16. Björk, M.T.; Schmid, H.; Knoch, J.; Riel, H.; Riess, W. Donor deactivation in silicon nanostructures. *Nat. Nanotechnol.* **2009**, *4*, 103–107. [CrossRef] [PubMed]
17. Patolsky, F.; Lieber, C.M. Nanowire nanosensors. *Mater. Today* **2005**, *8*, 20–28. [CrossRef]

18. Sohn, Y.-S.; Park, J.; Yoon, G.; Song, J.; Jee, S.-W.; Lee, J.-H.; Na, S.; Kwon, T.; Eom, K. Mechanical Properties of Silicon Nanowires. *Nanoscale Res. Lett.* **2009**, *5*, 211–216. [CrossRef] [PubMed]
19. Dasgupta, N.P.; Sun, J.; Liu, C.; Britzman, S.; Andrews, S.C.; Lim, J.; Gao, H.; Yan, R.; Yang, P. 25th Anniversary Article: Semiconductor Nanowires—Synthesis, Characterization, and Applications. *Adv. Mater.* **2014**, *26*, 2137–2184. [CrossRef]
20. Schmidt, V.; Wittemann, J.V.; Senz, S.; Gösele, U. Silicon Nanowires: A Review on Aspects of their Growth and their Electrical Properties. *Adv. Mater.* **2009**, *21*, 2681–2702. [CrossRef]
21. Cui, Y.; Wei, Q.; Park, H.; Lieber, C.M. Nanowire Nanosensors for Highly Sensitive and Selective Detection of Biological and Chemical Species. *Science* **2001**, *293*, 1289–1292. [CrossRef]
22. Shao, M.; Ma, D.D.D.; Lee, S. Silicon Nanowires—Synthesis, Properties, and Applications. *Eur. J. Inorg. Chem.* **2010**, *2010*, 4264–4278. [CrossRef]
23. Dhahi, T.S.; Bin Hashim UD, A.; Ahmed, N.M.; Mat Taib, A. A review on the electrochemical sensors and biosensors composed of nanogaps as sensing material. *J. Optoelectron. Adv. Mater.* **2010**, *12*, 1857–1862.
24. Sun, C.; Mathews, N.; Zheng, M.; Sow, C.H.; Wong, L.H.; Mhaisalkar, S.G. Aligned Tin Oxide Nanonets for High-Performance Transistors. *J. Phys. Chem. C* **2009**, *114*, 1331–1336. [CrossRef]
25. Morisot, F.; Nguyen, V.H.; Montemont, C.; Maindron, T.; Munoz-Rojas, D.; Mouis, M.; Langlet, M.; Ternon, C. Al₂O₃, Al doped ZnO and SnO₂ encapsulation of randomly oriented ZnO nanowire networks for high performance and stable electrical devices. *Nanotechnology* **2019**, *30*, 385202. [CrossRef] [PubMed]
26. Langley, D.; Giusti, G.; Mayousse, C.; Celle, C.; Bellet, D.; Simonato, J.-P. Flexible transparent conductive materials based on silver nanowire networks: A review. *Nanotechnology* **2013**, *24*, 452001. [CrossRef] [PubMed]
27. Legallais, M. Conception, Etude et Modélisation d’une Nouvelle Génération de Transistors à Nanofils de Silicium Pour Applications Biocapteurs. Ph.D. Dissertation, Université Grenoble Alpes, Grenoble, France, 2017.
28. Pauline, S. Etude des Propriétés Structurales et électriques de Réseaux Aléatoires de Nanofils de Silicium. 2014. Available online: <https://tel.archives-ouvertes.fr/tel-01162345/> (accessed on 9 February 2022).
29. De, S.; Coleman, J.N. The effects of percolation in nanostructured transparent conductors. *Mrs Bull.* **2011**, *36*, 774–781. [CrossRef]
30. Acharya, S.; Panda, A.B.; Belman, N.; Efrima, S.; Golan, Y. A Semiconductor-Nanowire Assembly of Ultrahigh Junction Density by the Langmuir–Blodgett Technique. *Adv. Mater.* **2006**, *18*, 210–213. [CrossRef]
31. Li, Y.; Qian, F.; Xiang, J.; Lieber, C.M. Nanowire electronic and optoelectronic devices. *Mater. Today* **2006**, *9*, 18–27. [CrossRef]
32. Kharisov, B.I.; Kharissova, O.V.; García, B.O.; Méndez, Y.P.; de la Fuente, I.G. State of the art of nanoforest structures and their applications. *RSC Adv.* **2015**, *5*, 105507–105523. [CrossRef]
33. Zhong, Z.; Wang, D.; Cui, Y.; Bockrath, M.W.; Lieber, C.M. Nanowire Crossbar Arrays as Address Decoders for Integrated Nanosystems. *Science* **2003**, *302*, 1377–1379. [CrossRef]
34. Mongillo, M.; Spathis, P.; Katsaros, G.; Gentile, P.; De Franceschi, S. Multifunctional Devices and Logic Gates with Undoped Silicon Nanowires. *Nano Lett.* **2012**, *12*, 3074–3079. [CrossRef]
35. Gruner, G. Carbon nanonets spark new electronics. *Sci. Am.* **2007**, *296*, 76–83. [CrossRef]
36. Gruner, G. Carbon nanotube films for transparent and plastic electronics. *J. Mater. Chem.* **2006**, *16*, 3533–3539. [CrossRef]
37. Hammersley, J.M. Percolation processes. *Math. Proc. Camb. Philos. Soc.* **1957**, *53*, 642–645. [CrossRef]
38. Kirkpatrick, S. Percolation and Conduction. *Rev. Mod. Phys.* **1973**, *45*, 574–588. [CrossRef]
39. Serre, P.; Mongillo, M.; Periwal, P.; Baron, T.; Ternon, C. Percolating silicon nanowire networks with highly reproducible electrical properties. *Nanotechnology* **2014**, *26*, 15201. [CrossRef]
40. Hill, D.J.; Teitsworth, T.S.; Ritchie, E.T.; Atkin, J.M.; Cahoon, J.F. Interplay of Surface Recombination and Diode Geometry for the Performance of Axial p–i–n Nanowire Solar Cells. *ACS Nano* **2018**, *12*, 10554–10563. [CrossRef]
41. Sze, S.; Irvin, J. Resistivity, mobility and impurity levels in GaAs, Ge, and Si at 300° K. *Solid-State Electron.* **1968**, *11*, 599–602. [CrossRef]
42. Heo, K.; Cho, E.; Yang, J.-E.; Kim, M.-H.; Lee, M.; Lee, B.Y.; Kwon, S.G.; Lee, M.-S.; Jo, M.-H.; Choi, H.-J.; et al. Large-Scale Assembly of Silicon Nanowire Network-Based Devices Using Conventional Microfabrication Facilities. *Nano Lett.* **2008**, *8*, 4523–4527. [CrossRef]
43. Whang, D.; Jin, S.; Wu, Y.; Lieber, C.M. Large-Scale Hierarchical Organization of Nanowire Arrays for Integrated Nanosystems. *Nano Lett.* **2003**, *3*, 1255–1259. [CrossRef]
44. Mulazimoglu, E.; Coskun, S.; Gunoven, M.; Butun, B.; Ozbay, E.; Turan, R.; Unalan, H. Silicon nanowire network metal-semiconductor-metal photodetectors. *Appl. Phys. Lett.* **2013**, *103*, 83114. [CrossRef]
45. Rabbani, M.G.; Patil, S.R.; Verma, A.; Villarreal, J.E.; Korgel, B.A.; Nekovei, R.; Khader, M.M.; Darling, R.B.; Anantram, M.P. Zero-bias photocurrents in highly-disordered networks of Ge and Si nanowires. *Nanotechnology* **2015**, *27*, 045201. [CrossRef]
46. Dalal, S.H.; Unalan, H.; Zhang, Y.; Hiralal, P.; Gangloff, L.; Flewitt, A.; Amaratunga, G.A.J.; Milne, W.I. Synthesis of ZnO nanowires for thin film network transistors. *Carbon Nanotub. Assoc. Devices* **2008**, *7037*, 172–178. [CrossRef]
47. Legallais, M.; Nguyen, T.T.T.; Cazimajou, T.; Mouis, M.; Salem, B.; Ternon, C. Material engineering of percolating silicon nanowire networks for reliable and efficient electronic devices. *Mater. Chem. Phys.* **2019**, *238*, 121871. [CrossRef]
48. Ternon, C.; Serre, P.; Lebrun, J.-M.; Brouzet, V.; Legallais, M.; David, S.; Luciani, T.; Pascal, C.; Baron, T.; Missiaen, J.-M. Low Temperature Processing to Form Oxidation Insensitive Electrical Contact at Silicon Nanowire/Nanowire Junctions. *Adv. Electron. Mater.* **2015**, *1*, 1500172. [CrossRef]

49. Shu, L.; Liang, R.; Rao, Z.; Fei, L.; Ke, S.; Wang, Y. Flexoelectric materials and their related applications: A focused review. *J. Adv. Ceram.* **2019**, *8*, 153–173. [CrossRef]
50. Liang, X.; Hu, S.; Shen, S. Effects of surface and flexoelectricity on a piezoelectric nanobeam. *Smart Mater. Struct.* **2014**, *23*, 035020. [CrossRef]
51. Wu, X.; Kulkarni, J.S.; Collins, G.; Petkov, N.; Alméjida, D.; Boland, J.J.; Erts, D.; Holmes, J.D. Synthesis and Electrical and Mechanical Properties of Silicon and Germanium Nanowires. *Chem. Mater.* **2008**, *20*, 5954–5967. [CrossRef]
52. Feng, G.; Nix, W.D.; Yoon, Y.; Lee, C.J. A study of the mechanical properties of nanowires using nanoindentation. *J. Appl. Phys.* **2006**, *99*, 74304. [CrossRef]
53. Lee, B.; Rudd, R.E. First-principles calculation of mechanical properties of Si(001) nanowires and comparison to nanomechanical theory. *Phys. Rev. B* **2007**, *75*, 195328. [CrossRef]
54. Park, S.; Kim, J.; Park, J.; Lee, J.; Choi, Y.; Kwon, O. Molecular dynamics study on size-dependent elastic properties of silicon nanocantilevers. *Thin Solid Films* **2005**, *492*, 285–289. [CrossRef]
55. Zhu, Y.; Xu, F.; Qin, Q.; Fung, W.Y.; Lu, W. Mechanical Properties of Vapor–Liquid–Solid Synthesized Silicon Nanowires. *Nano Lett.* **2009**, *9*, 3934–3939. [CrossRef]
56. Sadeghian, H.; Yang, C.-K.; Gavan, K.B.; Goosen, J.; Van Der Drift, E.W.J.M.; Van Der Zant, H.S.J.; Bossche, A.; French, P.J.; Van Keulen, F. Some considerations of effects-induced errors in resonant cantilevers with the laser deflection method. *J. Micromech. Microeng.* **2010**, *20*, 105027. [CrossRef]
57. Steighner, M.S.; Snedeker, L.P.; Boyce, B.L.; Gall, K.; Miller, D.C.; Muhlstein, C. Dependence on diameter and growth direction of apparent strain to failure of Si nanowires. *J. Appl. Phys.* **2011**, *109*, 33503. [CrossRef]
58. Sadeghian, H.; Yang, C.-K.; Goosen, J.; Bossche, A.; Staufer, U.; French, P.J.; Van Keulen, F. Effects of size and defects on the elasticity of silicon nanocantilevers. *J. Micromech. Microeng.* **2010**, *20*, 064012. [CrossRef]
59. Röhlig, C.-C.; Niebelschütz, M.; Brueckner, K.; Tonisch, K.; Ambacher, O.; Cimalla, V. Elastic properties of nanowires. *Phys. Status Solidi* **2010**, *247*, 2557–2570. [CrossRef]
60. Kim, Y.-J.; Son, K.; Choi, I.-C.; Park, W.I.; Jang, J.-I. Exploring Nanomechanical Behavior of Silicon Nanowires: AFM Bending Versus Nanoindentation. *Adv. Funct. Mater.* **2010**, *21*, 279–286. [CrossRef]
61. Wanekaya, A.K.; Chen, W.; Myung, N.V.; Mulchandani, A. Nanowire-Based Electrochemical Biosensors. *Electroanalysis* **2006**, *18*, 533–550. [CrossRef]
62. Zhao, X.; Wei, C.-M.; Yang, L.; Chou, M.-Y. Quantum Confinement and Electronic Properties of Silicon Nanowires. *Phys. Rev. Lett.* **2004**, *92*, 236805. [CrossRef] [PubMed]
63. Lu, A. Theoretical Study of Electronic and Electrical Properties of Silicon Nanowires. Public Health, 2007. Available online: http://lbms03.cityu.edu.hk/theses/c_ftt/phd-ap-b22687658f.pdf (accessed on 9 February 2022).
64. Sacconi, F.; Persson, M.P.; Povolotskyi, M.; Latessa, L.; Pecchia, A.; Gagliardi, A.; Balint, A.; Fraunheim, T.; Di Carlo, A. Electronic and transport properties of silicon nanowires. *J. Comput. Electron.* **2007**, *6*, 329–333. [CrossRef]
65. Saitta, A.M.; Buda, F.; Fiumara, G.; Giaquinta, P.V. Ab initio molecular-dynamics study of electronic and optical properties of silicon quantum wires: Orientational effects. *Phys. Rev. B* **1996**, *53*, 1446–1451. [CrossRef]
66. Matsuda, Y.; Tahir-Kheli, J.; Goddard, W.A. Surface and Electronic Properties of Hydrogen Terminated Si [001] Nanowires. *J. Phys. Chem. C* **2011**, *115*, 12586–12591. [CrossRef]
67. Haick, H.; Hurley, P.T.; Hochbaum, A.I.; Yang, P.; Lewis, N.S. Electrical Characteristics and Chemical Stability of Non-Oxidized, Methyl-Terminated Silicon Nanowires. *J. Am. Chem. Soc.* **2006**, *128*, 8990–8991. [CrossRef] [PubMed]
68. Yuan, G.D.; Zhou, Y.B.; Guo, C.S.; Zhang, W.J.; Tang, Y.B.; Li, Y.Q.; Chen, Z.H.; He, Z.B.; Wang, P.F.; Bello, I.; et al. Tunable Electrical Properties of Silicon Nanowires via Surface-Ambient Chemistry. *ACS Nano* **2010**, *4*, 3045–3052. [CrossRef] [PubMed]
69. Zhao, J.; Buia, C.; Han, J.; Lu, J.P. Quantum transport properties of ultrathin silver nanowires. *Nanotechnology* **2003**, *14*, 501–504. [CrossRef]
70. Wiecha, P.R.; Cuche, A.; Arbouet, A.; Girard, C.; Colas des Francs, G.; Lecestre, A.; Paillard, V. Strongly Directional Scattering from Dielectric Nanowires. *ACS Photonics* **2018**, *4*, 2036–2046. [CrossRef]
71. Nair, P.R.; Alam, M.A. Design Considerations of Silicon Nanowire Biosensors. *IEEE Trans. Electron Devices* **2007**, *54*, 3400–3408. [CrossRef]
72. Legallais, M.; Nguyen, T.T.T.; Cazimajou, T.; Mouis, M.; Arjmand, T.; Salem, B.; Ternon, C. Role played by the nanowire/nanowire junctions in the electrical properties of semiconductor percolating silicon nanowire networks. *J. Appl. Phys.* **2020**, *128*, 204501. [CrossRef]
73. Basori, R.; Samanta, S. Diameter dependent threshold voltage modification of resistive state switching in organometallic single nanowire devices (diameter~10–100 nm). *Appl. Phys. Lett.* **2018**, *113*, 123507. [CrossRef]
74. Nguyen, B.M.; Taur, Y.; Picraux, S.T.; Dayeh, S.A. Diameter-independent hole mobility in Ge/Si core/shell nanowire field effect transistors. *Nano Lett.* **2014**, *14*, 585–591.
75. Li, J.; He, G.; Ueno, H.; Jia, C.; Noji, H.; Qi, C.; Guo, X. Direct real-time detection of single proteins using silicon nanowire-based electrical circuits. *Nanoscale* **2016**, *8*, 16172–16176. [CrossRef]
76. Feng, S.; Yu, D.; Zhang, H.; Bai, Z.; Ding, Y. The growth mechanism of silicon nanowires and their quantum confinement effect. *J. Cryst. Growth* **2000**, *209*, 513–517. [CrossRef]

77. Baek, E.; Das, N.R.; Cannistraci, C.V.; Rim, T.; Bermúdez, G.S.C.; Nych, K.; Cho, H.; Kim, K.; Baek, C.-K.; Makarov, D.; et al. Intrinsic plasticity of silicon nanowire neurotransistors for dynamic memory and learning functions. *Nat. Electron.* **2020**, *3*, 398–408. [CrossRef]
78. Zhang, H.; Kikuchi, N.; Ohshima, N.; Kajisa, T.; Sakata, T.; Izumi, T.; Sone, H. Design and Fabrication of Silicon Nanowire-Based Biosensors with Integration of Critical Factors: Toward Ultrasensitive Specific Detection of Biomolecules. *ACS Appl. Mater. Interfaces* **2020**, *12*, 51808–51819. [CrossRef] [PubMed]
79. Ahoulou, S.; Perret, E.; Nedelec, J.-M. Functionalization and Characterization of Silicon Nanowires for Sensing Applications: A Review. *Nanomaterials* **2021**, *11*, 999. [CrossRef]
80. Calistri-Yeh, M.; Kramer, E.J.; Sharma, R.; Zhao, W.; Rafailovich, M.H.; Sokolov, A.J.; Brock, J.D. Thermal Stability of Self-Assembled Monolayers from Alkylchlorosilanes. *Langmuir* **1996**, *12*, 2747–2755. [CrossRef]
81. Steinbach, A.M.; Sandner, T.; Nilsen, M.; Hua, X.; Sivakumar, R.; Geiger, D.; Moeinian, A.; Strehle, S. The Electronic Properties of Silicon Nanowires during Their Dissolution under Simulated Physiological Conditions. *Appl. Sci.* **2019**, *9*, 804. [CrossRef]
82. Bashouti, M.Y.; Sardashti, K.; Ristein, J.; Christiansen, S. Kinetic study of H-terminated silicon nanowires oxidation in very first stages. *Nanoscale Res. Lett.* **2013**, *8*, 41. [CrossRef]
83. Liu, B.; Wang, Y.; Ho, T.-T.; Lew, K.-K.; Eichfeld, S.M.; Redwing, J.M.; Mayer, T.S.; Mohney, S.E. Oxidation of silicon nanowires for top-gated field effect transistors. *J. Vac. Sci. Technol. A: Vacuum Surfaces Films* **2008**, *26*, 370. [CrossRef]
84. Ma, D.D.D.; Lee, C.S.; Au, F.C.K.; Tong, S.Y.; Lee, S.T. Small-diameter Silicon Nanowire Surfaces. *Science* **2003**, *299*, 1874–1877. [CrossRef]
85. Bashouti, M.Y.; Sardashti, K.; Ristein, J.; Christiansen, S.H. Early stages of oxide growth in H-terminated silicon nanowires: Determination of kinetic behavior and activation energy. *Phys. Chem. Chem. Phys.* **2012**, *14*, 11877–11881. [CrossRef]
86. Büttner, C.C.; Zacharias, M. Retarded oxidation of Si nanowires. *Appl. Phys. Lett.* **2006**, *89*, 263106. [CrossRef]
87. Fazzini, P.-F.; Bonafos, C.; Claverie, A.; Hubert, A.; Ernst, T.; Respaud, M. Modeling stress retarded self-limiting oxidation of suspended silicon nanowires for the development of silicon nanowire-based nanodevices. *J. Appl. Phys.* **2011**, *110*, 033524. [CrossRef]
88. Harris, C.; O'Reilly, E. Nature of the band gap of silicon and germanium nanowires. *Phys. E Low-Dimens. Syst. Nanostruct.* **2006**, *32*, 341–345. [CrossRef]
89. Guichard, A.R.; Barsic, D.N.; Sharma, S.; Kamins, T.; Brongersma, M.L. Tunable Light Emission from Quantum-Confined Excitons in TiSi₂-Catalyzed Silicon Nanowires. *Nano Lett.* **2006**, *6*, 2140–2144. [CrossRef] [PubMed]
90. Kumar, C. *UV-VIS and Photoluminescence Spectroscopy for Nanomaterials Characterization*; Springer: Berlin, Germany, 2013; pp. 1–599. [CrossRef]
91. Sivakov, V.A.; Voigt, F.; Berger, A.; Bauer, G.; Christiansen, S.H. Roughness of silicon nanowire sidewalls and room temperature photoluminescence. *Phys. Rev. B* **2010**, *82*, 125446. [CrossRef]
92. Gonchar, K.A.; Zubairova, A.A.; Schleusener, A.; Osminkina, L.A.; Sivakov, V. Optical Properties of Silicon Nanowires Fabricated by Environment-Friendly Chemistry. *Nanoscale Res. Lett.* **2016**, *11*, 357. [CrossRef]
93. Osminkina, L.A.; Gonchar, K.A.; Marshov, V.S.; Bunkov, K.V.; Petrov, D.V.; Golovan, L.A.; Talkenberg, F.; Sivakov, V.A.; Timoshenko, V. Optical properties of silicon nanowire arrays formed by metal-assisted chemical etching: Evidences for light localization effect. *Nanoscale Res. Lett.* **2012**, *7*, 524. [CrossRef]
94. Gonchar, K.A.; Golovan, L.A.; Timoshenko, V.Y.; Sivakov, V.A.; Christiansen, S. Effects of light localization in photoluminescence and Raman scattering in silicon nanostructures. *Bull. Russ. Acad. Sci. Phys.* **2010**, *74*, 1712–1714. [CrossRef]
95. Golovan, L.; Gonchar, K.; Osminkina, L.; Timoshenko, V.; Petrov, G.; Yakovlev, V. Coherent anti-Stokes Raman scattering in silicon nanowire ensembles. *Laser Phys. Lett.* **2011**, *9*, 145–150. [CrossRef]
96. Gonchar, K.A.; Osminkina, L.A.; Sivakov, V.; Lysenko, V.; Timoshenko, V. Optical properties of nanowire structures produced by the metal-assisted chemical etching of lightly doped silicon crystal wafers. *Semiconductors* **2014**, *48*, 1613–1618. [CrossRef]
97. Zaboltnov, S.V.; Kholodov, M.M.; Georgobiani, V.A.; Presnov, D.E.; Golovan, L.A.; Kashkarov, P.K. Photon lifetime correlated increase of Raman scattering and third-harmonic generation in silicon nanowire arrays. *Laser Phys. Lett.* **2016**, *13*, 35902. [CrossRef]
98. Li, Y.; Wang, G.; Akbari-Saatlu, M.; Procek, M.; Radamson, H.H. Si and SiGe nanowire for micro-thermoelectric generator: A review of the current state of the art. *Front. Mater.* **2021**, *8*, 611078. [CrossRef]
99. Zhan, T.; Yamato, R.; Hashimoto, S.; Tomita, M.; Oba, S.; Himeda, Y.; Mesaki, K.; Takezawa, H.; Yokogawa, R.; Xu, Y.; et al. Miniaturized planar Si-nanowire micro-thermoelectric generator using exuded thermal field for power generation. *Sci. Technol. Adv. Mater.* **2018**, *19*, 443–453. [CrossRef] [PubMed]
100. Pennelli, G.; Macucci, M. Optimization of the thermoelectric properties of nanostructured silicon. *J. Appl. Phys.* **2013**, *114*, 214507. [CrossRef]
101. Pennelli, G.; Dimaggio, E.; Masci, A. Silicon Nanowires: A Breakthrough for Thermoelectric Applications. *Materials* **2021**, *14*, 5305. [CrossRef] [PubMed]
102. Paulo, A.S.; Bokor, J.; Howe, R.T.; He, R.; Yang, P.; Gao, D.; Carraro, C.; Maboudian, R. Mechanical elasticity of single and double clamped silicon nanobeams fabricated by the vapor-liquid-solid method. *Appl. Phys. Lett.* **2005**, *87*, 53111. [CrossRef]
103. Ponomareva, I.; Srivastava, D.; Menon, M. Thermal Conductivity in Thin Silicon Nanowires: Phonon Confinement Effect. *Nano Lett.* **2007**, *7*, 1155–1159. [CrossRef]

104. Feser, J.P.; Sadhu, J.S.; Azeredo, B.P.; Hsu, K.H.; Ma, J.; Kim, J.; Seong, M.; Fang, N.; Li, X.; Ferreira, P.M.; et al. Thermal conductivity of silicon nanowire arrays with controlled roughness. *J. Appl. Phys.* **2012**, *112*, 114306. [CrossRef]
105. Pop, E. Energy dissipation and transport in nanoscale devices. *Nano Res.* **2010**, *3*, 147–169. [CrossRef]
106. Zhao, Y.; Grüner, G. Nanonet as a scaffold with targeted functionalities. *J. Mater. Chem.* **2012**, *22*, 24983–24991. [CrossRef]
107. Cazimajou, T.; Mouis, M.; Legallais, M.; Nguyen, T.; Ternon, C.; Salem, B.; Ghibaudo, G. Analysis of the role of inter-nanowire junctions on current percolation effects in silicon nanonet field-effect transistors. *Solid-State Electron.* **2019**, *168*, 107725. [CrossRef]
108. Hu, L.; Hecht, D.S.; Grüner, G. Carbon Nanotube Thin Films: Fabrication, Properties, and Applications. *Chem. Rev.* **2010**, *110*, 5790–5844. [CrossRef]
109. Fata, N.; Mishra, S.; Xue, Y.; Wang, Y.; Hicks, J.; Ural, A. Effect of junction-to-nanowire resistance ratio on the percolation conductivity and critical exponents of nanowire networks. *J. Appl. Phys.* **2020**, *128*, 124301. [CrossRef]
110. Pike, G.E.; Seager, C.H. Percolation and conductivity: A computer study. I. *Phys. Rev. B* **1974**, *10*, 1421–1434. [CrossRef]
111. Seager, C.H.; Pike, G.E. Percolation and conductivity: A computer study. II. *Phys. Rev. B* **1974**, *10*, 1435–1446. [CrossRef]
112. Cao, Q.; Kim, H.-S.; Pimparkar, N.; Kulkarni, J.P.; Wang, C.; Shim, M.; Roy, K.; Alam, M.A.; Rogers, J.A. Medium-scale carbon nanotube thin-film integrated circuits on flexible plastic substrates. *Nature* **2008**, *454*, 495–500. [CrossRef] [PubMed]
113. Ternon, C.; Serre, P.; Rey, G.; Holtzinger, C.; Periwai, P.; Martin, M.; Baron, T.; Stambouli, V.; Langlet, M. High aspect ratio semiconducting nanostructure random networks: Highly versatile materials for multiple applications. *Phys. Status Solidi (RRL)—Rapid Res. Lett.* **2013**, *7*, 919–923. [CrossRef]
114. Nguyen, T.T.T.; Cazimajou, T.; Legallais, M.; Arjmand, T.; Nguyen, V.H.; Mouis, M.; Salem, B.; Robin, E.; Ternon, C. Monolithic fabrication of nano-to-millimeter scale integrated transistors based on transparent and flexible silicon nanonets. *Nano Futur.* **2019**, *3*, 25002. [CrossRef]
115. Den Hertog, M.I.; Rouviere, J.L.; Dhalluin, F.; Gentile, P.; Ferret, P.; Ternon, C.; Baron, T. Gold Catalyzed Silicon Nanowires: Defects in the Wires and Gold on the Wires. In *Microscopy of Semiconducting Materials 2007*; Cullis, A.G., Midgley, P.A., Eds.; Springer Proceedings in Physics; Springer: Dordrecht, The Netherlands, 2008; Volume 120. [CrossRef]
116. Surawijaya, A.; Anshori, I.; Rohiman, A.; Idris, I.; Iskandar, F.; Abdullah, M. Gold Nanoparticles Assisted Silicon Nanowire Growth using Vapor Liquid Solid Method. *AIP Conf. Proc.* **2011**, *1415*, 36–38. [CrossRef]
117. Kumar, R.R.; Rao, K.N.; Phani, A. Growth of silicon nanowires by electron beam evaporation using indium catalyst. *Mater. Lett.* **2012**, *66*, 110–112. [CrossRef]
118. Jeong, H.; Park, T.; Seong, H.; Kim, M.; Kim, U.; Choi, H. Growth kinetics of silicon nanowires by platinum assisted vapour–liquid–solid mechanism. *Chem. Phys. Lett.* **2009**, *467*, 331–334. [CrossRef]
119. Djoumi, S.; Kail, F.; Chahed, L.; i Cabarrocas, P.R. Growth Study of Silicon Nanowires Synthesized Via Plasma-Assisted VLS Using Tin Catalysts. *Mod. Concepts Mater. Sci.* **2020**, *2*, 1–2. [CrossRef]
120. Brouzet, V.; Salem, B.; Periwai, P.; Rosaz, G.; Baron, T.; Bassani, F.; Gentile, P.; Ghibaudo, G. Fabrication and characterization of silicon nanowire p-i-n MOS gated diode for use as p-type tunnel FET. *Appl. Phys. A* **2015**, *121*, 1285–1290. [CrossRef]
121. Cui, Y.; Lieber, C.M. Functional Nanoscale Electronic Devices Assembled Using Silicon Nanowire Building Blocks. *Science* **2001**, *291*, 851–853. [CrossRef]
122. Duan, X.; Niu, C.; Sahi, V.; Chen, J.; Parce, J.W.; Empedocles, S.; Goldman, J.L. High-performance thin-film transistors using semiconductor nanowires and nanoribbons. *Nature* **2003**, *425*, 274–278. [CrossRef] [PubMed]
123. Gentile, P.; Solanki, A.; Pauc, N.; Oehler, F.; Salem, B.; Rosaz, G.; Baron, T.; Den Hertog, M.; Calvo, V. Effect of HCl on the doping and shape control of silicon nanowires. *Nanotechnology* **2012**, *23*, 215702. [CrossRef] [PubMed]
124. Burchak, O.; Chenevier, P.; Reiss, P. Procédé de Préparation de Nanofils de Silicium. Patent WO2015189827A1, 17 December 2015.
125. Burchak, O.; Keller, C.; Lapertot, G.; Salaün, M.; Danet, J.; Chen, Y.; Bendiab, N.; Pépin-Donat, B.; Lombard, C.; Faure-Vincent, J.; et al. Scalable chemical synthesis of doped silicon nanowires for energy applications. *Nanoscale* **2019**, *11*, 22504–22514. [CrossRef]
126. Keller, C.; Desrues, A.; Karuppiyah, S.; Martin, E.; Alper, J.; Boismain, F.; Villevieille, C.; Herlin-Boime, N.; Haon, C.; Chenevier, P. Effect of Size and Shape on Electrochemical Performance of Nano-Silicon-Based Lithium Battery. *Nanomaterials* **2021**, *11*, 307. [CrossRef]
127. Heitsch, A.T.; Fanfair, D.D.; Tuan, H.-Y.; Korgel, B.A. Solution–Liquid–Solid (SLS) Growth of Silicon Nanowires. *J. Am. Chem. Soc.* **2008**, *130*, 5436–5437. [CrossRef]
128. Qin, L.; Park, S.; Huang, L.; Mirkin, C.A. On-Wire Lithography. *Science* **2005**, *309*, 113–116. [CrossRef]
129. Um, H.-D.; Kim, N.; Lee, K.; Hwang, I.; Seo, J.H.; Young, J.Y.; Duane, P.; Wober, M.; Seo, K. Versatile control of metal-assisted chemical etching for vertical silicon microwire arrays and their photovoltaic applications. *Sci. Rep.* **2015**, *5*, 11277. [CrossRef]
130. Huang, Y.; Duan, X.; Wei, Q.; Lieber, C.M. Directed Assembly of One-Dimensional Nanostructures into Functional Networks. *Science* **2001**, *291*, 630–633. [CrossRef] [PubMed]
131. Jia, C.; Lin, Z.; Huang, Y.; Duan, X. Nanowire Electronics: From Nanoscale to Macroscale. *Chem. Rev.* **2019**, *119*, 9074–9135. [CrossRef] [PubMed]
132. Park, J.; Shin, G.; Ha, J.S. Controlling orientation of V2O5 nanowires within micropatterns via microcontact printing combined with the gluing Langmuir–Blodgett technique. *Nanotechnology* **2008**, *19*, 395303. [CrossRef] [PubMed]
133. Tao, A.; Kim, F.; Hess, C.; Goldberger, J.; He, R.; Sun, Y.; Xia, A.Y.; Yang, P. Langmuir–Blodgett Silver Nanowire Monolayers for Molecular Sensing Using Surface-Enhanced Raman Spectroscopy. *Nano Lett.* **2003**, *3*, 1229–1233. [CrossRef]

134. Liu, X.; Long, Y.-Z.; Liao, L.; Duan, X.; Fan, Z. Large-Scale Integration of Semiconductor Nanowires for High-Performance Flexible Electronics. *ACS Nano* **2012**, *6*, 1888–1900. [CrossRef]
135. Yu, G.; Cao, A.; Lieber, C.M. Large-area blown bubble films of aligned nanowires and carbon nanotubes. *Nat. Nanotechnol.* **2007**, *2*, 372–377. [CrossRef]
136. Yu, G.; Li, X.; Lieber, C.M.; Cao, A. Nanomaterial-incorporated blown bubble films for large-area, aligned nanostructures. *J. Mater. Chem.* **2008**, *18*, 728–734. [CrossRef]
137. Zhang, J.; Cui, J.; Wang, X.; Wang, W.; Mei, X.; Yi, P.; Yang, X.; He, X. Recent Progress in the Preparation of Horizontally Ordered Carbon Nanotube Assemblies from Solution. *Phys. Status Solidi* **2018**, *215*, 1700719. [CrossRef]
138. Krebs, F.C. Roll-to-roll fabrication of monolithic large-area polymer solar cells free from indium-tin-oxide. *Sol. Energy Mater. Sol. Cells* **2009**, *93*, 1636–1641. [CrossRef]
139. Aziz, F.; Ismail, A.F. Spray coating methods for polymer solar cells fabrication: A review. *Mater. Sci. Semicond. Process.* **2015**, *39*, 416–425. [CrossRef]
140. Kopola, P.; Aernouts, T.; Guillerez, S.; Jin, H.; Tuomikoski, M.; Maaninen, A.; Hast, J. High efficient plastic solar cells fabricated with a high-throughput gravure printing method. *Sol. Energy Mater. Sol. Cells* **2010**, *94*, 1673–1680. [CrossRef]
141. Hoth, C.N.; Choulis, S.A.; Schilinsky, P.; Brabec, C.J. High Photovoltaic Performance of Inkjet Printed Polymer:Fullerene Blends. *Adv. Mater.* **2007**, *19*, 3973–3978. [CrossRef]
142. Voigt, M.M.; MacKenzie, R.; King, S.P.; Yau, C.P.; Atienzar, P.; Dane, J.; Keivanidis, P.; Zadrzil, I.; Bradley, D.D.; Nelson, J. Gravure printing inverted organic solar cells: The influence of ink properties on film quality and device performance. *Sol. Energy Mater. Sol. Cells* **2012**, *105*, 77–85. [CrossRef]
143. Roßkopf, D.; Strehle, S. Surface-controlled contact printing for nanowire device fabrication on a large scale. *Nanotechnology* **2016**, *27*, 185301. [CrossRef]
144. Yao, J.; Yan, H.; Lieber, C.M. A nanoscale combing technique for the large-scale assembly of highly aligned nanowires. *Nat. Nanotechnol.* **2013**, *8*, 329–335. [CrossRef]
145. Bensimon, A.; Simon, A.; Chiffaudel, A.; Croquette, V.; Heslot, F. Alignment and Sensitive Detection of DNA by a Moving Interface. *Science* **1994**, *265*, 2096–2098. [CrossRef]
146. Yao, J.; Yan, H.; Das, S.; Klemic, J.F.; Ellenbogen, J.C.; Lieber, C.M. Nanowire nanocomputer as a finite-state machine. *Proc. Natl. Acad. Sci. USA* **2014**, *111*, 2431–2435. [CrossRef]
147. Holland, L.; Bateman, S.K. Effects of oil vapour contamination on the adhesion of zinc sulphide films to glass and silica. *Br. J. Appl. Phys.* **1960**, *11*, 382–385. [CrossRef]
148. Wu, Z.; Chen, Z.; Du, X.; Logan, J.M.; Sippel, J.; Nikolou, M.; Kamaras, K.; Reynolds, J.R.; Tanner, D.B.; Hebard, A.F.; et al. Transparent, Conductive Carbon Nanotube Films. *Science* **2004**, *305*, 1273–1276. [CrossRef]
149. Aguirre, C.M.; Auvray, S.; Pigeon, S.; Izquierdo, R.; Desjardins, P.; Martel, R. Carbon nanotube sheets as electrodes in organic light-emitting diodes. *Appl. Phys. Lett.* **2006**, *88*, 183104. [CrossRef]
150. Ferrer-Anglada, N.; Kaempgen, M.; Skakalova, V.; Dettlaf-Weglikowska, U.; Roth, S. Synthesis and characterization of carbon nanotube-conducting polymer thin films. *Diam. Relat. Mater.* **2004**, *13*, 256–260. [CrossRef]
151. Muhl, S.; Aguilar Osorio, R.; Martínez Huitle, U.A. Transparent conductive carbon nanotube films. *Rev. Mex. Fis.* **2014**, *63*, 439–447.
152. Hu, L.; Hecht, D.S.; Grüner, G. Percolation in Transparent and Conducting Carbon Nanotube Networks. *Nano Lett.* **2004**, *4*, 2513–2517. [CrossRef]
153. Zhang, D.; Ryu, K.; Liu, X.; Polikarpov, E.; Ly, J.; Tompson, M.E.; Zhou, C. Transparent, Conductive, and Flexible Carbon Nanotube Films and Their Application in Organic Light-Emitting Diodes. *Nano Lett.* **2006**, *6*, 1880–1886. [CrossRef]
154. Serre, P.; Ternon, C.; Chapron, P.; Durlin, Q.; Francheteau, A.; Lantreibeq, A. Role of nanowire length in morphological and electrical properties of silicon nanonets. In Proceedings of the 2014 10th Conference on Ph. D. Research in Microelectronics and Electronics (PRIME), Grenoble, France, 30 June–3 July 2014; pp. 9–12. [CrossRef]
155. Demes, T.; Ternon, C.; Morisot, F.; Riassetto, D.; Legallais, M.; Roussel, H.; Langlet, M. Mechanisms involved in the hydrothermal growth of ultra-thin and high aspect ratio ZnO nanowires. *Appl. Surf. Sci.* **2017**, *410*, 423–431. [CrossRef]
156. Aksoy, B.; Coskun, S.; Kucukyildiz, S.; Unalan, H.E. Transparent, highly flexible, all nanowire network germanium photodetectors. *Nanotechnology* **2012**, *23*, 325202. [CrossRef]
157. Wang, Y.; Feng, T.; Wang, K.; Qian, M.; Chen, Y.; Sun, Z. A Facile Method for Preparing Transparent, Conductive, and Paper-Like Silver Nanowire Films. *J. Nanomater.* **2011**, *2011*, 1–5. [CrossRef]
158. Assad, O.; Leshansky, A.M.; Wang, B.; Stelzner, T.; Christiansen, S.; Haick, H. Spray-Coating Route for Highly Aligned and Large-Scale Arrays of Nanowires. *ACS Nano* **2012**, *6*, 4702–4712. [CrossRef]
159. Kim, T.; Canlier, A.; Kim, G.H.; Choi, J.; Park, M.; Han, S.M. Electrostatic Spray Deposition of Highly Transparent Silver Nanowire Electrode on Flexible Substrate. *ACS Appl. Mater. Interfaces* **2012**, *5*, 788–794. [CrossRef]
160. Wang, M.C.; Gates, B.D. Directed assembly of nanowires. *Mater. Today* **2009**, *12*, 34–43. [CrossRef]
161. Thelander, C.; Agarwal, P.; Brongersma, S.; Eymery, J.; Feiner, L.; Forchel, A.; Scheffler, M.; Riess, W.; Ohlsson, B.; Gösele, U.; et al. Nanowire-based one-dimensional electronics. *Mater. Today* **2006**, *9*, 28–35. [CrossRef]
162. Chen, L.J. Silicon nanowires: The key building block for future electronic devices. *J. Mater. Chem.* **2007**, *17*, 4639–4643. [CrossRef]

163. Valizadeh, P. Field Effect Transistors, A Comprehensive Overview: From Basic Concepts to Novel Technologies. *F. Eff. Transistors A Compr. Overv. Basic Concepts Nov. Technol.* **2016**, 1–457. [CrossRef]
164. Moore, G.M. Cramming more components onto integrated circuits with unit cost. *Electronics* **1965**, *38*, 114. Available online: <https://newsroom.intel.com/wp-content/uploads/sites/11/2018/05/moores-law-electronics.pdf> (accessed on 9 February 2022).
165. Inaba, S.; Okano, K.; Matsuda, S.; Fujiwara, M.; Hokazono, A.; Adachi, K.; Ohuchi, K.; Suto, H.; Fukui, H.; Shimizu, T.; et al. High performance 35 nm gate length CMOS with NO oxynitride gate dielectric and Ni salicide. *IEEE Trans. Electron Devices* **2002**, *49*, 2263–2270. [CrossRef]
166. Iwai, H.; Ohguro, T.; Ohmi, S.-I. NiSi salicide technology for scaled CMOS. *Microelectron. Eng.* **2002**, *60*, 157–169. [CrossRef]
167. Hu, J.; Odom, T.W.; Lieber, C.M. Chemistry and Physics in One Dimension: Synthesis and Properties of Nanowires and Nanotubes. *Accounts Chem. Res.* **1999**, *32*, 435–445. [CrossRef]
168. Lu, W.; Xie, P.; Lieber, C.M. Nanowire Transistor Performance Limits and Applications. *IEEE Trans. Electron Devices* **2008**, *55*, 2859–2876. [CrossRef]
169. Patolsky, F.; Zheng, G.; Lieber, C.M. Fabrication of silicon nanowire devices for ultrasensitive, label-free, real-time detection of biological and chemical species. *Nat. Protoc.* **2006**, *1*, 1711–1724. [CrossRef]
170. McIntyre, P.; Morral, A.F. Semiconductor nanowires: To grow or not to grow? *Mater. Today Nano* **2019**, *9*, 100058. [CrossRef]
171. Fasoli, A.; Milne, W. Overview and status of bottom-up silicon nanowire electronics. *Mater. Sci. Semicond. Process.* **2012**, *15*, 601–614. [CrossRef]
172. Aouida, S.; Zaghouni, R.B.; Bachtouli, N.; Bessais, B. Hydrogen passivation of silicon nanowire structures. *Appl. Surf. Sci.* **2016**, *370*, 49–52. [CrossRef]
173. Yuan, W.; Tutuncuoglu, G.; Mohabir, A.T.; Thorpe, R.; Feldman, L.C.; Filler, M.A.; Shan, J.W. Reducing Conductivity Variability in Si Nanowires via Surface Passivation for Nanoelectronics. *ACS Appl. Nano Mater.* **2021**, *4*, 3852–3860. [CrossRef]
174. Chen, K.-I.; Li, B.-R.; Chen, Y.-T. Silicon nanowire field-effect transistor-based biosensors for biomedical diagnosis and cellular recording investigation. *Nano Today* **2011**, *6*, 131–154. [CrossRef]
175. Weber, W.M.; Geelhaar, L.; Graham, A.P.; Unger, E.; Duesberg, G.S.; Liebau, M.; Pamler, W.; Chèze, C.; Riechert, H.; Lugli, P.; et al. Silicon-Nanowire Transistors with Intruded Nickel-Silicide Contacts. *Nano Lett.* **2006**, *6*, 2660–2666. [CrossRef]
176. Dellas, N.S.; Schuh, C.J.; Mohny, S.E. Silicide formation in contacts to Si nanowires. *J. Mater. Sci.* **2012**, *47*, 6189–6205. [CrossRef]
177. Shkunov, M.; Rigas, G.; Constantinou, M. Solution-Processable Nanowire Field-Effect Transistors. In *Nanowires-New Insights*; IntechOpen: London, UK, 2017. [CrossRef]
178. Pregl, S.; Weber, W.M.; Nozaki, D.; Kunstmann, J.; Baraban, L.; Opitz, J.; Mikolajick, T.; Cuniberti, G. Parallel arrays of Schottky barrier nanowire field effect transistors: Nanoscopic effects for macroscopic current output. *Nano Res.* **2013**, *6*, 381–388. [CrossRef]
179. Islam, A.E. Variability and Reliability of Single-Walled Carbon Nanotube Field Effect Transistors. *Electronics* **2013**, *2*, 332–367. [CrossRef]
180. Shin, S.H.; Masuduzzaman, M.; Gu, J.; Wahab, M.A.; Conrad, N.; Si, M.; Ye, P.D.; Alam, A. Impact of nanowire variability on performance and reliability of gate-all-around III-V MOSFETs. *2013 IEEE Int. Electron Devices Meet.* **2013**, *7*, 188–191. [CrossRef]
181. Zheng, G.; Lu, W.; Jin, S.; Lieber, C.M. Synthesis and Fabrication of High-Performance n-Type Silicon Nanowire Transistors. *Adv. Mater.* **2004**, *16*, 1890–1893. [CrossRef]
182. Byon, K.; Tham, D.; Fischer, J.E.; Johnson, A.T. Systematic study of contact annealing: Ambipolar silicon nanowire transistor with improved performance. *Appl. Phys. Lett.* **2007**, *90*, 143513. [CrossRef]
183. Hayden, O.; Björk, M.T.; Schmid, H.; Riel, H.; Drechsler, U.; Karg, S.F.; Lörtscher, E.; Riess, W. Fully Depleted Nanowire Field-Effect Transistor in Inversion Mode. *Small* **2007**, *3*, 230–234. [CrossRef] [PubMed]
184. Rajeev, K.P.; Stolojan, C.O.V.; Constantinou, M.; Shkunov, M. Effect of Nanowire-dielectric Interface on the Hysteresis of Solution Processed Silicon Nanowire FETs. *Nanosci. Nanoeng.* **2017**, *5*, 17–24. [CrossRef]
185. Van, N.H.; Lee, J.-H.; Whang, D.; Kang, D.J. Low-Programmable-Voltage Nonvolatile Memory Devices Based on Omega-shaped Gate Organic Ferroelectric P(VDF-TrFE) Field Effect Transistors Using p-type Silicon Nanowire Channels. *Nano-Micro Lett.* **2014**, *7*, 35–41. [CrossRef] [PubMed]
186. Jung, Y.; Vacic, A.; Perea, D.E.; Picraux, S.T.; Reed, M. Minority carrier lifetime and surface effects in VLS-grown axial p-n junction silicon nanowires. *Adv. Mater.* **2011**, *23*, 4306–4311. [CrossRef]
187. Heo, K.; Park, J.W.; Yang, J.-E.; Koh, J.; Kwon, J.-H.; Jhon, Y.M.; Kim, M.; Jo, M.-H.; Hong, S. Large-scale assembly of highly flexible low-noise devices based on silicon nanowires. *Nanotechnology* **2010**, *21*, 145302. [CrossRef]
188. Celle, C.; Carella, A.; Mariolle, D.; Chevalier, N.; Rouvière, E.; Simonato, J.-P. Highly end-doped silicon nanowires for field-effect transistors on flexible substrates. *Nanoscale* **2010**, *2*, 677–680. [CrossRef]
189. McAlpine, M.; Friedman, R.; Lieber, C. High-Performance Nanowire Electronics and Photonics and Nanoscale Patterning on Flexible Plastic Substrates. *Proc. IEEE* **2005**, *93*, 1357–1363. [CrossRef]
190. Knopfmacher, O.; Tarasov, A.; Fu, W.; Wipf, M.; Niesen, B.; Calame, M.; Schönenberger, C. Nernst Limit in Dual-Gated Si-Nanowire FET Sensors. *Nano Lett.* **2010**, *10*, 2268–2274. [CrossRef]
191. Liu, Y.; Zhu, L.; Guo, L.; Zhang, H.; Xiao, H. Surface Passivation Performance of Atomic-Layer-Deposited Al₂O₃ on p-type Silicon Substrates. *J. Mater. Sci. Technol.* **2014**, *30*, 835–838. [CrossRef]
192. Liang, S.; He, G.; Wang, D.; Qiao, F. Atomic-layer-deposited (ALD) Al₂O₃ passivation dependent interface chemistry, band alignment and electrical properties of HfYO/Si gate stacks. *J. Mater. Sci. Technol.* **2018**, *35*, 769–776. [CrossRef]

193. Noor, M.O.; Krull, U.J. Silicon nanowires as field-effect transducers for biosensor development: A review. *Anal. Chim. Acta* **2014**, *825*, 1–25. [CrossRef] [PubMed]
194. Reddy, B.; Dorvel, B.R.; Go, J.; Nair, P.R.; Elibol, O.H.; Credo, G.M.; Daniels, J.S.; Chow, E.K.C.; Su, X.; Varma, M.; et al. High-k dielectric Al₂O₃ nanowire and nanoplate field effect sensors for improved pH sensing. *Biomed. Microdevices* **2011**, *13*, 335–344. [CrossRef] [PubMed]
195. Zhou, W.; Dai, X.; Fu, T.-M.; Xie, C.; Liu, J.; Lieber, C.M. Long Term Stability of Nanowire Nanoelectronics in Physiological Environments. *Nano Lett.* **2014**, *14*, 1614–1619. [CrossRef]
196. Klinghammer, S.; Rauch, S.; Pregl, S.; Uhlmann, P.; Baraban, L.; Cuniberti, G. Surface Modification of Silicon Nanowire Based Field Effect Transistors with Stimuli Responsive Polymer Brushes for Biosensing Applications. *Micromachines* **2020**, *11*, 274. [CrossRef]
197. Nikonov, A.M.; Naumova, O.V.; Generalov, V.M.; Safatov, A.S.; Fomin, B.I. Surface Preparation as a Step in the Fabrication of Biosensors Based on Silicon Nanowire Field-Effect Transistors: Review. *J. Surf. Investig. X-ray Synchrotron. Neutron. Tech.* **2020**, *14*, 337–346. [CrossRef]
198. Demes, T.; Morisot, F.; Legallais, M.; Calais, A.; Pernot, E.; Pignot-Paintrand, I.; Ternon, C.; Stambouli, V. DNA grafting on silicon nanonets using an eco-friendly functionalization process based on epoxy silane. *Mater Today Proc.* **2019**, *6*, 333–339. [CrossRef]
199. Nguyen, T.T.T.; Legallais, M.; Morisot, F.; Cazimajou, T.; Stambouli, V.; Mouis, M.; Ternon, C. First evidence of superiority of Si nanonet field effect transistors over multi-parallel Si nanowire ones in view of electrical DNA hybridization detection. *Mater. Res. Express* **2018**, *6*, 016301. [CrossRef]
200. Vallejo-Perez, M.; Ternon, C.; Spinelli, N.; Morisot, F.; Theodorou, C.; Jayakumar, G.; Hellström, P.-E.; Mouis, M.; Rapenne, L.; Mescot, X.; et al. Optimization of GOPS-Based Functionalization Process and Impact of Aptamer Grafting on the Si Nanonet FET Electrical Properties as First Steps towards Thrombin Electrical Detection. *Nanomaterials* **2020**, *10*, 1842. [CrossRef]
201. Celle, C.; Suspene, C.; Simonato, J.; Lenfant, S.; Ternisien, M.; Vuillaume, D. Self-assembled monolayers for electrode fabrication and efficient threshold voltage control of organic transistors with amorphous semiconductor layer. *Org. Electron.* **2009**, *10*, 119–126. [CrossRef]
202. Celle, C.; Suspène, C.; Ternisien, M.; Lenfant, S.; Guerin, D.; Smaali, K.; Lmimouni, K.; Simonato, J.-P.; Vuillaume, D. Interface dipole: Effects on threshold voltage and mobility for both amorphous and poly-crystalline organic field effect transistors. *Org. Electron.* **2014**, *15*, 729–737. [CrossRef]
203. Robert, D.; Yoshio, N. Front Matter. In *Handbook of Semiconductor Manufacturing Technology*, 2nd ed.; CRC Press: Boca Raton, FL, USA, 2007. [CrossRef]
204. Bhaskaran, M.; Sriram, S.; Holland, A.S.; du Plessis, J. Nickel silicide and titanium silicide formation: A comparison. *Smart Struct. Devices Syst. III* **2006**, *6414*, 64141B. [CrossRef]
205. Chen, L.J. *Institution of Electrical Engineers. Silicide Technology for Integrated Circuits*; Institution of Electrical Engineers: London, UK, 2004.
206. Lavoie, C.; D’Heurle, F.; Detavernier, C.; Cabral, C. Towards implementation of a nickel silicide process for CMOS technologies. *Microelectron. Eng.* **2003**, *70*, 144–157. [CrossRef]
207. Murarka, S.P. *Silicides for VLSI Applications*; Academic Press: Cambridge, MA, USA, 1983.
208. Sze, S.M. *Physics of Semiconductor Devices*, 3rd ed.; Wiley: New York, NY, USA, 2006.
209. Connétable, D.; Thomas, O. First-principles study of nickel-silicides ordered phases. *J. Alloys Compd.* **2011**, *509*, 2639–2644. [CrossRef]
210. Zhang, S.; Östling, M.; Zhang, S.; Östling, M. Metal Silicides in CMOS Technology: Past, Present, and Future Trends Metal Silicides in CMOS Technology: Past, Present, and Future Trends. *Crit. Rev. Solid State Mater. Sci.* **2003**, *28*, 1–129. [CrossRef]
211. Ryuji, T. A Study on Formation of High Resistivity Phases of Nickel Silicide at Small Area and its Solution for Scaled CMOS Devices. Ph.D. Thesis, Tokyo Institute of Technology, Tokyo, Japan, 2013.
212. Mongillo, M. Transport Properties and Functional Devices on CVD Grown Silicon Nanowires. Ph.D. Thesis, Université Joseph-Fourier-Grenoble I, Grenoble, France, 2010.
213. Chou, Y.-C.; Wu, W.-W.; Chen, L.-J.; Tu, K.-N. Homogeneous Nucleation of Epitaxial CoSi₂ and NiSi in Si Nanowires. *Nano Lett.* **2009**, *9*, 2337–2342. [CrossRef] [PubMed]
214. Chou, Y.-C.; Lu, K.-C.; Tu, K. Nucleation and growth of epitaxial silicide in silicon nanowires. *Mater. Sci. Eng. R Rep.* **2010**, *70*, 112–125. [CrossRef]
215. Katsman, A.; Beregovsky, M.; Yaish, Y.E. Formation and Evolution of Nickel Silicide in Silicon Nanowires. *IEEE Trans. Electron Devices* **2014**, *61*, 3363–3371. [CrossRef]
216. Katsman, A.; Yaish, Y.; Beregovsky, M. From Contact to Diffusion Controlled Growth of Nickel Silicides in Silicon Nanowires. *Defect Diffus. Forum* **2012**, *323–325*, 427–432. [CrossRef]
217. Hsu, H.-F.; Huang, W.-R.; Chen, T.-H.; Wu, H.-Y.; Chen, C.-A. Fabrication of Ni-silicide/Si heterostructured nanowire arrays by glancing angle deposition and solid state reaction. *Nanoscale Res. Lett.* **2013**, *8*, 224. [CrossRef]
218. Dellas, N.S.; Liu, B.Z.; Eichfeld, S.M.; Eichfeld, C.M.; Mayer, T.S.; Mohny, S.E. Orientation dependence of nickel silicide formation in contacts to silicon nanowires. *J. Appl. Phys.* **2009**, *105*, 94309. [CrossRef]
219. Lin, Y.-C.; Chen, Y.; Xu, D.; Huang, Y. Growth of Nickel Silicides in Si and Si/SiO_x Core/Shell Nanowires. *Nano Lett.* **2010**, *10*, 4721–4726. [CrossRef]

220. Otaga, K.; Sutter, E.; Zhu, X.; Hofmann, S. Ni-Silicide growth kinetics in Si and Si/SiO₂core/shell nanowires. *Nanotechnology* **2011**, *22*, 365305. [CrossRef]
221. Chen, Y.; Lin, Y.-C.; Zhong, X.; Cheng, H.-C.; Duan, X.; Huang, Y. Kinetic Manipulation of Silicide Phase Formation in Si Nanowire Templates. *Nano Lett.* **2013**, *13*, 3703–3708. [CrossRef] [PubMed]
222. Tang, W.; Dayeh, S.A.; Picraux, S.T.; Huang, J.Y.; Tu, K.-N. Ultrashort Channel Silicon Nanowire Transistors with Nickel Silicide Source/Drain Contacts. *Nano Lett.* **2012**, *12*, 3979–3985. [CrossRef] [PubMed]
223. Weber, W.M.; Geelhaar, L.; Unger, E.; Chèze, C.; Kreupl, F.; Riechert, H.; Lugli, P. Silicon to nickel-silicide axial nanowire heterostructures for high performance electronics. *Phys. Status Solidi* **2007**, *244*, 4170–4175. [CrossRef]
224. Chou, Y.C.; Wu, W.W.; Lee, C.Y.; Liu, C.Y.; Chen, L.J.; Tu, K.N. Heterogeneous and Homogeneous Nucleation of Epitaxial NiSi₂ in [110] Si Nanowires. *J. Phys. Chem. C* **2011**, *115*, 397–401. [CrossRef]
225. Song, J.; Matsumoto, K.; Kakushima, K.; Kataoka, Y.; Nishiyama, A.; Sugii, N.; Wakabayashi, H.; Tsutsui, K.; Natori, K.; Iwai, H. Resistivity of Ni silicide nanowires and its dependence on Ni film thickness used for the formation. *ECS Trans.* **2013**, *58*, 87–91. [CrossRef]
226. Legallais, M.; Nguyen, T.; Mouis, M.; Salem, B.; Robin, E.; Chenevier, P.; TERNON, C. An innovative large scale integration of silicon nanowire-based field effect transistors. *Solid-State Electron.* **2018**, *143*, 97–102. [CrossRef]
227. Mongillo, M.; Spathis, P.; Katsaros, G.; Gentile, P.; Sanquer, M.; De Franceschi, S. Joule-Assisted Silicidation for Short-Channel Silicon Nanowire Devices. *ACS Nano* **2011**, *5*, 7117–7123. [CrossRef]
228. Yan, H.; Xing, Y.; Hang, Q.; Yu, D.; Wang, Y.; Xu, J.; Xi, Z.; Feng, S. Growth of amorphous silicon nanowires via a solid–liquid–solid mechanism. *Chem. Phys. Lett.* **2000**, *323*, 224–228. [CrossRef]
229. Um, H.-D.; Solanki, A.; Jayaraman, A.; Gordon, R.G.; Habbal, F. Electrostatically Doped Silicon Nanowire Arrays for Multispectral Photodetectors. *ACS Nano* **2019**, *13*, 11717–11725. [CrossRef] [PubMed]
230. Li, Q.; Koo, S.-M.; Edelstein, M.D.; Suehle, J.S.; Richter, C.A. Silicon nanowire electromechanical switches for logic device application. *Nanotechnology* **2007**, *18*, 315202. [CrossRef]
231. Zhu, H.; Bonevich, J.E.; Li, H.; Richter, C.A.; Yuan, H.; Kirillov, O.; Li, Q. Discrete charge states in nanowire flash memory with multiple Ta₂O₅ charge-trapping stacks. *Appl. Phys. Lett.* **2014**, *104*, 233504. [CrossRef]
232. Baraban, L.; Ibarlucea, B.; Baek, E.; Cuniberti, G. Hybrid Silicon Nanowire Devices and Their Functional Diversity. *Adv. Sci.* **2019**, *6*, 1900522. [CrossRef]
233. Park, S.J.; Jeon, D.-Y.; Piontek, S.; Grube, M.; Ocker, J.; Sessi, V.; Heinzig, A.; Trommer, J.; Kim, G.-T.; Mikolajick, T.; et al. Reconfigurable Si Nanowire Nonvolatile Transistors. *Adv. Electron. Mater.* **2017**, *4*, 1700399. [CrossRef]
234. Yoo, J.; Kim, Y.; Lim, D.; Kim, S. Electrical characteristics of silicon nanowire CMOS inverters under illumination. *Opt. Express* **2018**, *26*, 3527–3534. [CrossRef]
235. Singh, P.; Delhi, N. Properties and Transistor Applications of Silicon Nanowires. *Int. J. Phys. Appl.* **2020**, *12*, 11–19.
236. Chen, Z.H.; Jie, J.S.; Luo, L.B.; Wang, H.; Lee, C.-S.; Lee, S.T. Applications of silicon nanowires functionalized with palladium nanoparticles in hydrogen sensors. *Nanotechnology* **2007**, *18*, 345502. [CrossRef]
237. Pourkiaei, S.M.; Ahmadi, M.H.; Sadeghzadeh, M.; Moosavi, S.; Pourfayaz, F.; Chen, L.; Pour Yazdi, M.A.; Kumar, R. Thermoelectric cooler and thermoelectric generator devices: A review of present and potential applications, modeling and materials. *Energy* **2019**, *186*, 115849. [CrossRef]
238. Fonseca, L.; Donmez-Noyan, I.; Dolcet, M.; Estrada-Wiese, D.; Santander, J.; Salleras, M.; Gadea, G.; Pacios, M.; Sojo, J.-M.; Morata, A.; et al. Transitioning from Si to SiGe Nanowires as Thermoelectric Material in Silicon-Based Microgenerators. *Nanomaterials* **2021**, *11*, 517. [CrossRef] [PubMed]



Review

Recent Progress of Black Silicon: From Fabrications to Applications

Zheng Fan ¹, Danfeng Cui ¹, Zengxing Zhang ¹, Zhou Zhao ¹, Hongmei Chen ¹, Yanyun Fan ¹, Penglu Li ¹, Zhidong Zhang ¹ , Chenyang Xue ^{1,*} and Shubin Yan ^{2,3,*}

- ¹ Key Laboratory of Instrumentation Science & Dynamic Measurement, Ministry of Education, North University of China, Taiyuan 030051, China; s1906119@st.nuc.edu.cn (Z.F.); cuidanfeng@nuc.edu.cn (D.C.); zengxingzhang88@163.com (Z.Z.); Zzzzhou95@163.com (Z.Z.); lmxchm@126.com (H.C.); 18103510614@163.com (Y.F.); lipenglu98@163.com (P.L.); zdzhang@nuc.edu.cn (Z.Z.)
- ² The School of Electrical Engineering, Zhejiang University of Water Resources and Electric Power, Hangzhou 310018, China
- ³ Zhejiang-Belarus Joint Laboratory of Intelligent Equipment and System for Water Conservancy and Hydropower Safety Monitoring, Zhejiang University of Water Resources and Electric Power, Hangzhou 310018, China
- * Correspondence: xuechenyang@nuc.edu.cn (C.X.); yanshb@zjweu.edu.cn (S.Y.)

Abstract: Since black silicon was discovered by coincidence, the special material was explored for many amazing material characteristics in optical, surface topography, and so on. Because of the material property, black silicon is applied in many spheres of a photodetector, photovoltaic cell, photo-electrocatalysis, antibacterial surfaces, and sensors. With the development of fabrication technology, black silicon has expanded in more and more applications and has become a research hotspot. Herein, this review systematically summarizes the fabricating method of black silicon, including nanosecond or femtosecond laser irradiation, metal-assisted chemical etching (MACE), reactive ion etching (RIE), wet chemical etching, electrochemical method, and plasma immersion ion implantation (PIII) methods. In addition, this review focuses on the progress in multiple black silicon applications in the past 10 years. Finally, the prospect of black silicon fabricating and various applications are outlined.

Keywords: black silicon; light absorption enhanced; micro-nano manufacturing; nanometer surface

Citation: Fan, Z.; Cui, D.; Zhang, Z.; Zhao, Z.; Chen, H.; Fan, Y.; Li, P.; Zhang, Z.; Xue, C.; Yan, S. Recent Progress of Black Silicon: From Fabrications to Applications. *Nanomaterials* **2021**, *11*, 41. <https://doi.org/10.3390/nano11010041>

Received: 19 November 2020

Accepted: 23 December 2020

Published: 26 December 2020

Publisher's Note: MDPI stays neutral with regard to jurisdictional claims in published maps and institutional affiliations.



Copyright: © 2020 by the authors. Licensee MDPI, Basel, Switzerland. This article is an open access article distributed under the terms and conditions of the Creative Commons Attribution (CC BY) license (<https://creativecommons.org/licenses/by/4.0/>).

1. Introduction

Black silicon material is a silicon material with a micro-scale, nano-scale, and both micro-nano scales, including various structures such as holes, needles, and columns structures on the surface of wafers [1–5]. Compared with polished silicon, due to the micro-nano structure and impurity doping of the black silicon surface, it has ultralow light reflection in the visible and near-infrared bands, especially in the near-infrared band. Because of the limitation of the forbidden bandwidth of the polished silicon itself, when the wavelength is greater than 1100 nm [6], the light absorption ability is extremely reduced. The black silicon material has a light absorption rate of more than 90% in the range of 1100 nm to 2500 nm [7,8]. While extending the absorption range of materials in the longer band, it also improves the light absorption capacity. Black silicon has high absorption of light, as even the absorption rate is close to 100%. It is dark black to the naked eye. The micro-nano structure on the surface is the crucial factor to improving the absorption of this unusual material in the visible light band. Figure 1 explains the high absorption principle of the material. The incident light will be reflected multiple times between the tapered structures. Each reflection process is accompanied by transmission at the interface. Each transmission increases the number and probability of absorption of incident light by black silicon so that the light seems to be trapped in the micro-awl of the material surface. The existence of the light trapping effect is the main reason why black silicon has not only extreme low reflex in a broad spectral range, but also high absorption in the visible light band.

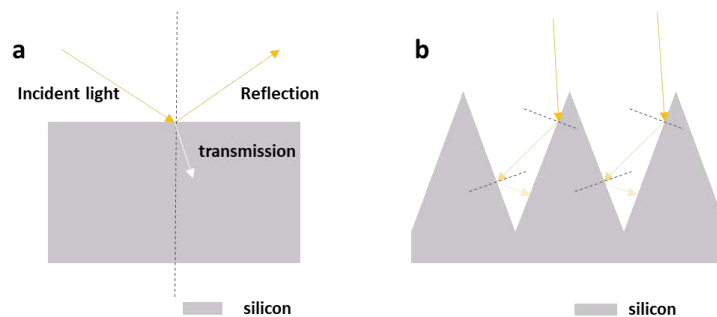


Figure 1. The reflection performance of (a) polished silicon and (b) black silicon.

Since the discovery of black silicon materials in the late 20th century [9], after more than 20 years of development, black silicon has been fabricated in a variety of ways. Since the black silicon was discovered, common fabricating methods include nanosecond or femtosecond laser irradiation [8–11], metal-assisted chemical etching (MACE) [12–15], reactive ion etching (RIE) [16–18], wet chemical etching [19], and plasma immersion ion implantation (PIII) methods. Each fabrication method can fabricate black silicon with a micro-nano surface structure. However, the surface structure of the black silicon fabricated is also different using different fabrication processes. Furthermore, the material exhibits different optical characteristics and electrical characteristics. The choice of micro-nano processing technology also determines the performance of the device.

The development of black silicon materials has a lot of applications in different fields while the fabricating process is developing. In solar cells [20–24], the low reflectivity of black silicon and the high absorption of visible light is of great help to promote the performance of solar cells. In catalysis [25,26], the use of black silicon as a photoelectric catalytic substrate can synergize the light absorption characteristics of black silicon and the redox characteristics of photocatalysts to improve the performance of photocatalytic materials. In photodetectors [27–31], due to the excellent light absorption capabilities of black silicon in the visible and near-infrared bands, it can fabricate the silicon-based photodetectors with high responsivity and wide response ranges in the near-infrared band. In sensing applications, high-sensitivity detection can be achieved in surface-enhanced Raman scattering (SERS), biochemical sensing, gas sensing, etc. [32–35]. Figure 2 shows an overview of the entire review, including fabrication methods and characteristics and corresponding applications.

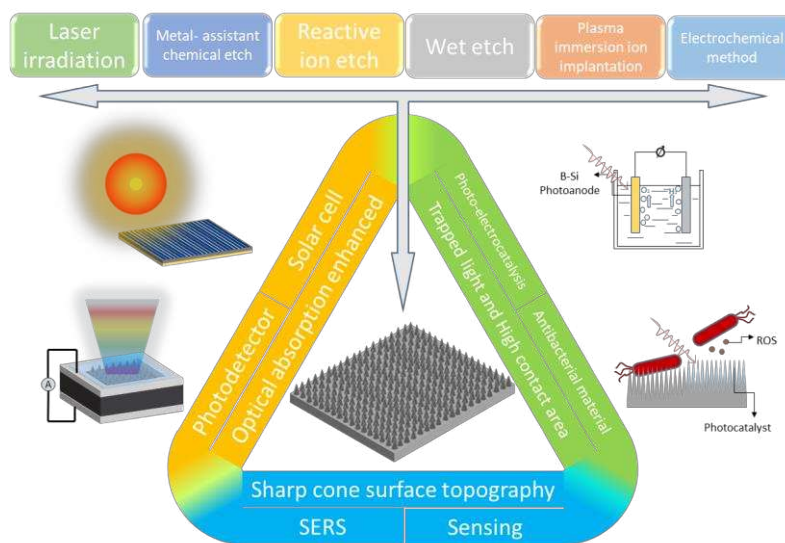


Figure 2. A figure overview of this review.

In this paper, we review the fabrication methods and applications of this special material over the last decade. The paper compares the complexity, cost, and suitable conditions of different fabricating processes. In addition, this paper also summarizes the researches on the optical properties of black silicon samples. Finally, we propose the outlook in fabrication methods and multiple applications.

2. Fabrication Techniques

2.1. Femtosecond/Nanosecond Laser Irradiation

The fabrication of black silicon by laser irradiation is one of the most frequently used methods. According to different laser pulse lengths, the laser irradiation methods of preparing black silicon can be divided into femtosecond laser irradiation and nanosecond laser irradiation. Figure 3 shows the principle of femtosecond/nanosecond laser irradiation in the black silicon fabrication process [36]. In 1998, professor E. Mazur [9] and his team fabricated black silicon materials for the first time by using femtosecond lasers to irradiate the silicon surface under the corrosive gas SF_6 .

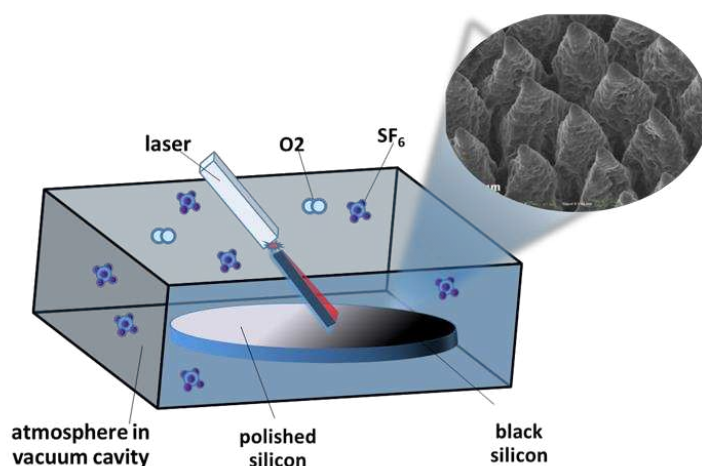


Figure 3. The fabrication principle of black silicon using femtosecond/nanosecond laser irradiation. Adapted from reference [37], with permission from Elsevier © 2020.

In the last decade, the method of making black silicon by laser irradiation has been further developed. However, the atmosphere of the laser irradiation process is an extraordinarily important factor for the light absorption of black silicon, especially the absorption range. Due to the doping of element Sulphur, the light absorption range of black silicon was expanded to the near-infrared band in the Sulphur-bearing atmosphere. H. Mei [37] et al. developed a new type of black silicon with flexible properties by femtosecond laser irradiation in corrosive gas atmosphere. Figure 4a shows the SEM image of black silicon using femtosecond laser irradiation in corrosive gas atmosphere. When manufacturing black silicon, the silicon wafer is placed on a programmable three-dimensional mobile platform, and the automatic irradiation can be realized through programming control. The surface nanostructures of black silicon are more regular, with an absorption rate of up to 97% in visible light, and they are insensitive to changes in incidence angle. Usually, the irradiation is done in the existence of corrosive gases to expand the light absorption range. However, A. Viorobyev [10] et al. fabricated black silicon by irradiating a high-intensity femtosecond laser directly on the silicon surface in an air atmosphere. Figure 4b shows the SEM and absorption of black silicon using femtosecond laser irradiation in air atmosphere. The black silicon has low reflectance and an equidistant parallel nanostructured textured micro-slot array. The black silicon formed was a black velvet color, and the surface nanostructure was similar to the ridge shape when observed under SEM images. The reflectivity of black silicon under visible light is very good, only 3–4%.

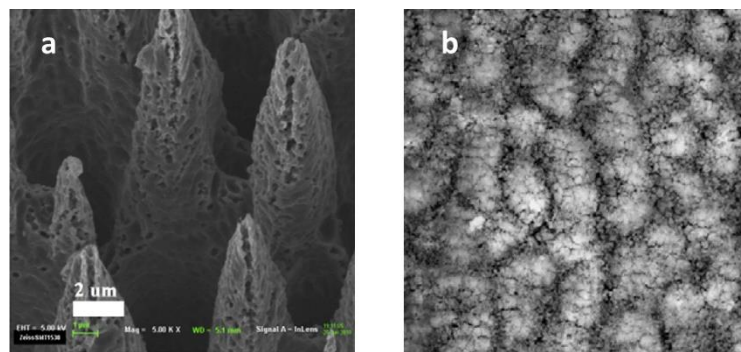


Figure 4. SEM image of black silicon fabricated by femtosecond laser irradiation in corrosive gas or air. (a) Corrosive gas atmosphere. Adapted from reference [37], with permission from Elsevier © 2020. (b) Air atmosphere. Adapted from reference [10], with permission from Elsevier © 2020.

In recent years, the effect of black silicon materials with different fabrication details on the absorptivity was also studied [38], such as the different doping elements, different irradiation power, and surface metal influence. In 2016, C. Li [39] et al. used phosphorus-doped silicon instead of sulfur-doped silicon to fabricate black silicon. Black silicon was fabricated by femtosecond laser irradiation under the SF_6 atmosphere. After thermal annealing at 873 K in argon for 30 min, the black silicon still has a 70% absorptivity in the band from 1100 nm to 2000 nm. In 2017, X. Yu et al. [40] fabricated black silicon by femtosecond pulse laser irradiation on silicon wafers coated with gold film. The absorptivity of black silicon fabricated under different irradiation powers was researched. The results showed that the black silicon fabricated under different irradiation powers had no significant effect on the absorptivity. In a certain power range, the sample absorption rate increases with the increase of laser power. In 2018, Y. Su et al. [41] used a femtosecond laser to directly irradiate silicon wafers with the Al membrane on the surface to fabricate in the atmosphere. In the visible light region, the presence or absence of the Al membrane has little influence on the absorption rate, which is about 95%. However, at longer wavelengths, silicon wafers with an Al film have better absorptivity.

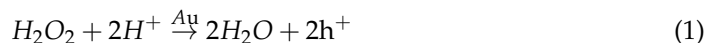
Black silicon is produced likewise by irradiating the surface of a silicon wafer with a nanosecond laser [42]. The fabricated black silicon sample also has very good optical and electrical properties. In 2015, B. Franta et al. [43] fabricated high-doped black silicon with high crystallization and high absorption by irradiating high-doped silicon wafers with nanosecond laser pulses. By comparing SEM images, the nanoscale surface of black silicon irradiated by a nanosecond laser is smoother than that irradiated by a femtosecond laser. The absorptivity of the black silicon sample is about 95% in the visible band. In 2018, L. Zhang et al. [44] fabricated black silicon by ablating silicon wafers with an infrared nanosecond pulse laser, and the researchers investigated the corresponding relation between the laser burning period and the surface morphology. The results showed that the black silicon microcolumn was formed by the accumulation of irradiation, instead of directly forming a columnar microstructure.

The material fabricated by laser irradiation can control the nanostructure on the surface to a certain extent by different time and laser power. More importantly, the laser irradiation method can dope the element to limit impurity level, which can improve adsorption in the near-infrared band. This method can fabricate high-performance black silicon to apply to wideband photodetectors. However, the femtosecond laser and nanosecond laser instruments are expensive and not suitable for manufacture and mass production.

2.2. Metal Assisted Chemical Etching

The fabrication of black silicon by MACE has been common in recent years. The researchers fabricate black silicon by etching wafers with different metals, most commonly gold and silver. In general, metal nanoparticles are formed on the surface in different ways

after the surface is cleaned and deoxidized. Then, the sample was put into the etching solution, and the nano-conical structure was formed on the material surface through the catalytic action of surface metal nanoparticles. The noble metal nanoparticles accomplish a vertical shield machine-like action. Figure 5 shows this activity, where black silicon formed in the MACE method [45]. Equations (1) and (2) explain the chemical process of the MACE method with gold nanoparticles as an example.



The main methods used to deposit metal nanoparticles are thermal evaporation, post-coating heat treatment, and chemical solution formation. Then, the MACE method is introduced in different deposition methods of noble metal nanoparticles.

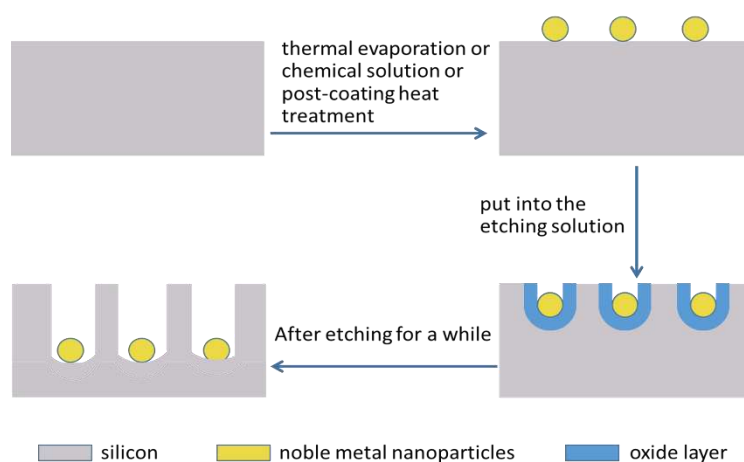


Figure 5. The fabrication principle of black silicon using metal assisted chemical etching (MACE).

The thermal evaporation method requires the use of thermal evaporation instruments to complete the evaporation of noble metal nanoparticles. Y. Liu et al. [24] fabricated black silicon by MACE. Surface noble metal nanoparticles are first formed by thermal evaporation. After the sample was immersed in the etching solution for a few minutes, a nano-tapered structure is created on the silicon chip. Figure 6a shows the SEM of the thermal evaporation method using thermal evaporation instruments. The reflectivity of the fabricated black silicon ranges from 300 nm to 1000 nm and is about 8%.

In 2019, N. Noor et al. [46] used a post-coating heat treatment method to form noble metal nanoparticles. Silver assisted etching was used as the fabrication method. Researchers studied the influence of annealing temperature on the surface morphology and optical properties of the material. After removing the natural oxide from the monocrystalline silicon sheet, 15 nm Ag film was formed on the silicon wafer using radio frequency sputtering. Figure 6b,c show the cross-section and top-view SEM of black silicon using a post-coating heat treatment method. The silver nanoparticles were formed by hot annealing at 200 °C, 230 °C, and 260 °C for 40 min in a nitrogen environment. Finally, black silicon was prepared by placing the sample in an etching solution. The reflectance of black silicon was only 3% at the 600 nm wavelength of the sample annealed at 230 °C.

The formation of noble metal nanoparticles from chemical solutions is one of the most common and low-cost methods. To fabricate black silicon materials using this method, the cleaned silicon wafers are first put into a mixture of noble metallic ions to model noble metal nanoparticles on the surface. After that, the sample was placed into the etching solution for a while, and the nanostructure was formed on the surface through the catalysis of nanoparticles. Figure 6d shows SEM of black silicon fabricated by the MACE method in different etching time in high concentration Ag^+ solution.

Y. Su et al. [47] fabricated black silicon by MACE. The researchers first used alkaline etching to form micro columnar structures on the surface of silicon wafers. The sample was immersed in etching mixed solution for 8 min at no heating situation. After gold nanoparticles were formed, the solution was further etched to form a microporous structure on the surface. At 200 nm to 1000 nm, the absorption rate was about 85%. In 2014, C. Wang et al. [48] also fabricated double-layered black silicon by alkaline anisotropic etching and MACE. In 2014, Z. Zhao et al. [49] fabricated black silicon by MACE. It was also the first to use an alkaline etching method to form a micro pyramid morphology on the surface, and then to form micro holes in the micro pyramid structure by etching solution with silver ions. In the presence of an antireflection layer, black silicon has a reflectivity of less than 5% in the 400 nm to 1000 nm band. In 2016, H. Zhong et al. [50] fabricated nanostructured black silicon by MACE. In the production, the alkaline etching is eliminated, and the MACE is directly used. The nanostructure was etched on the material, and the absorptivity reached 95% at the band of 400 nm to 1100 nm. In 2019, I. Putra et al. [51] used alkaline etching to form tiny pyramidal structures on the surface. Micro-pores were formed in the micro-pyramid structure by the silver ion etching solution. The reflectance of the sample was less than 5% in the band of 300 nm to 900 nm. In 2019, F. Hu et al. [52] fabricated black silicon by MACE. First, the silver is formed on the surface of the silicon by heating it under low pressure. Then, the black silicon was immersed in a mixture etching solution at room temperature. Under the catalysis of silver, a micro-conical surface structure is formed. The absorptivity of black silicon with silver film at 400 nm to 1000 nm is more than 75%. The absorptivity of black silicon with Ag-NPs from 400 nm to 1000 nm is about 90%. Due to the non-impurity-doped, the absorptivity decreases seriously at the wavelength of 1000 nm to 2200 nm.

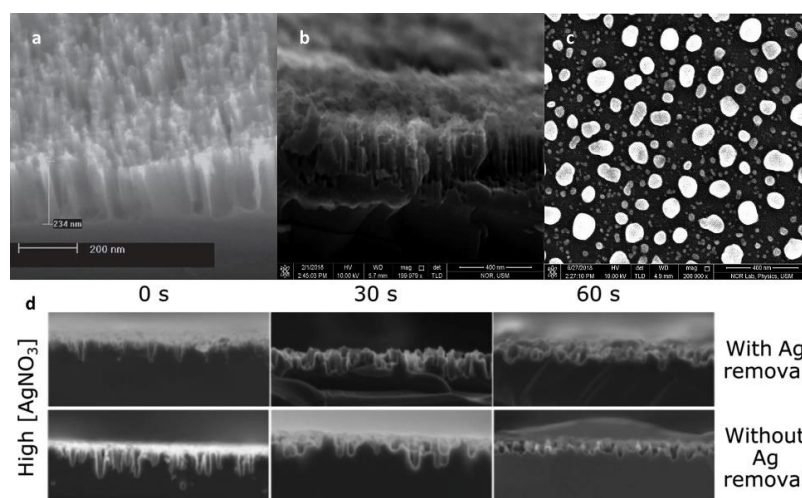


Figure 6. SEM of using different nanoparticles deposited methods to fabricate black silicon. (a) The thermal evaporation method using thermal evaporation instruments. Adapted from reference [24], with permission from John Wiley and Sons © 2020. (b,c) Using a post-coating heat treatment method to form noble metal nanoparticles. Adapted from reference [46], with permission from Elsevier © 2020. (d) Different etching time in high concentration Ag^+ solution. Adapted from reference [53], with permission from IEEE © 2020.

The researchers not only used MACE to fabricate black silicon, but also explored the optimization of the preparation process [46] through experiments. When a different etching time [54,55], solution metal ion density [53], or substrate thickness are used, the fabricated black silicon sample will have different optical properties.

In 2009, H. Branz et al. [56] fabricated black silicon materials by mixing 5 nm colloidal gold particles or HAuCl_4 solution in the etching solution. The results showed that the black silicon made of colloidal gold particles mixed with 5 nm solution had better anti-reflection ability, and the reflectivity was less than 8% between 300 nm and 1000 nm.

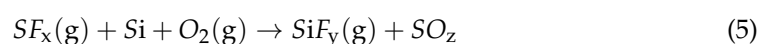
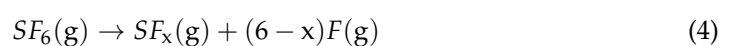
Moreover, the formation mechanism of nanopores on the black silicon surface is catalyzed by Au. The catalytic decomposition of hydrogen peroxide on the gold nanoparticles leads to rapid local oxidation of Si. Then hydrofluoric acid etches SiO₂ to form it. In 2015, S. Marthi et al. [57] fabricated black silicon by MACE, and the researchers studied the effects of metal-assisted chemical etching at different times and substrate thickness on the optical properties of the material. The results express that the longer the time from 20 s to 180 s, the lower the reflectivity of the sample. Additionally, the thickness has little influence on the reflectivity, but the increase of thickness will increase the stability of the reflectivity. In 2019, K. Chen et al. [53] fabricated black silicon by MACE, and the researchers studied the effect of silver ion concentration on the optical and electrical performances of the material in the etching solution. The results show that the silver ion concentration has an effect on the porosity of black silicon samples, and the lower concentration of silver ion can improve the electrical performance, but has some damage to the optical performance.

In addition to the precious metals silver and gold, copper and nickel can be used in the catalytic metal nanoparticles of the MACE method. Due to the advantages of copper being cheaper and easily available, when compared with silver and gold metals, copper has a greater application prospect in the industrial application of black silicon production. Compared with wet chemical etching, black silicon fabricated by copper-assisted chemical etching has better optical absorption characteristics. B. Lee et al. [58] used Cu-assisted chemical etching to fabricate black silicon in 2020. First, Cu particles were deposited on the cleaned silicon wafer by CuCl₂ and HF. Then, black silicon is fabricated in HF, H₂O₂, and H₂O. The author optimized the Cu-ACE fabrication process of black silicon through a 100 W UV lamp. By comparing the black silicon prepared under different lighting environments, the black silicon prepared under the UV lamp environment has larger micropores and better light absorption. Ni-assisted chemical etching can also be used to fabricate black silicon materials. The researchers optimized the process steps by studying factors such as different etching time, different UV light illumination [59], and different etching solution ratios [60,61].

Compared to previous years, ultra-high aspect ratios and ultra-large pores have been fabricated on the surface of silicon in recent years. With recent development, the black silicon can achieve more special application through the unattainable process manufacture method. The black silicon fabricated by MACE has good performance in optical properties. In the fabrication process, the steps are simple, but the controllability of the surface morphology of black silicon is poor compared with the laser irradiation method. The cost of the MACE method is low, and it is expected to be used to fabricate black silicon on a mass scale to apply to black silicon solar cells.

2.3. Reactive Ion Etching

RIE [62] is a dry etching technique with strong anisotropy and high selectivity. The method uses an ion-induced chemical reaction to achieve anisotropic etching. That is to use the ionic energy to make the surface of the etched layer to form a damage layer that is easy to etch and to promote the chemical reaction. To fabricate black silicon with this method, the silicon wafer is first put into a vacuum chamber, and a corrosion gas is introduced to form a surface passivation layer. However, due to the instability of the passivation layer under the influence of plasma, the material surface is over-passivated, resulting in the black silicon structure. This etching method can damage the surface, pollute it, and it is difficult to form a finer structure. Equations (3)–(5) explain the chemical process of RIE method with SF₆ and O₂ as examples.



In 2013, M. Steglich et al. [63] fabricated black silicon by inductively coupled plasma reactive ion etching (ICP-RIE) in the pressure of 1 Pa or 4 Pa and a ratio of SF₆: O₂ in a gaseous environment of 1:1. Without the need for chemical pretreatment or (photolithography) masking of the chip, the optimal average reflectance of black silicon samples at the 300 nm to 1000 nm band is 5%. In 2014, M. Steglich et al. [64] used the ICP-RIE method to fabricate black silicon. The absorptivity was 99.5% at 350 nm to 2000 nm and 99.8% at 1000 nm to 1250 nm. When a layer of Al₂O₃ is formed on the black silicon by the ALD method, the absorptivity of the whole band can be improved. In 2015, H. Savin et al. [65] fabricated black silicon by deep reactive ion etching. Moreover, the surface is passivated by depositing 90 nm Al₂O₃ film, which further reduces the reflectance and the composition of surface carriers. The average reflectance of black silicon in the band of 300 nm to 1000 nm is around 3%. In 2016, M. Juntunen et al. [66] fabricated black silicon on 525 μm thick high-resistance n-type silicon wafers by ICP-RIE. The reflectivity of the black silicon material was gauged at different angles. The average reflectivity of the material at different angles from 350 nm to 1000 nm was below 10%. In 2018, K. Isakov et al. [67] fabricated broad-band absorption black silicon for niobium nitride deposition at the atomic layer using ICP-RIE technology. Black silicon was fabricated by etching the silicon surface with a mixture of SF₆ and O₂ gas at −110 °C. In the spectral region of 1100~2500 nm, the sample of niobium nitride layer coated with 15 nm achieved high absorption of 97%~99%.

After several years of technological progress, regular surface morphology and smaller-scale micro-nano structures have gradually replaced single disordered surface structures. Due to the more repeated absorption of reflection, the multilayer micro-nano structures express more excellent performance in light absorption. Recently, multiply reactive ion etching is applied to fabricate excellent performance black silicon. In 2020, Z. Zhang et al. [68,69] combined two methods to fabricate order structure black silicon that has micro-nano structures on the surface of materials to apply for photothermal conversion. The silicon wafers were etched by reactive ion etching in the mask of photoresist to fabricate regular honeycomb-likely microstructure, firstly. Then, the microstructure material was etched by plasma etching in SF₆ and O₂ to fabricate nanostructure on the surface. Finally, the gold deposited on the order micro-nano structure black silicon to enhance the absorption of near-infrared waveband. The regular micro-nano structure black silicon has an ultralow reflectance of 1% and 5% in 200 nm to 1100 nm and 1100 nm to 1700 nm, respectively. Figure 7 shows SEM of order structure black silicon. The black silicon achieves excellent photothermal conversion compared with disordered nanopore silicon.

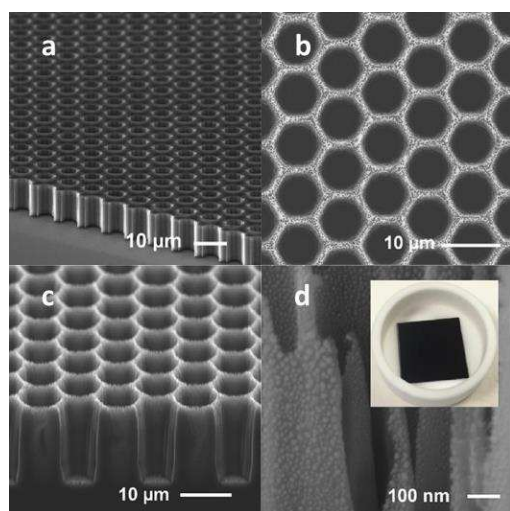


Figure 7. The SEM of order micro-nanostructure black silicon. (a) The cross-section SEM of black silicon after the first etching. (b) The top view of black silicon after the second etching. (c) The cross-section SEM of black silicon after the second etching. (d) The SEM of black silicon after Au deposition. Adapted from reference [68], with permission from Elsevier © 2020.

Compared with other methods, black silicon fabricated by the RIE method has an excellent broadband absorption rate. The black silicon fabricated by this method has a reflectance of less than 5% in both visible and near-infrared wavelengths, but it has some disadvantages in terms of cost due to the expensive equipment required.

2.4. Wet Etching

Wet etching is a technique in which the etched material is immersed in a corrosive solution. It is a pure chemical etching with excellent selectivity. The etch will stop when the current film has been etched without damaging the film of the next layer of other material. Because of the isotropy of all semiconductor wet etching, the width of transverse etching is close to the depth of vertical etching for both the oxide layer and the metal layer. Because of this isotropy, black silicon, fabricated in this way, forms tiny structures in the shape of micro pyramids on etched silicon wafers.

In 2017, Z. Qi et al. [70] fabricated black silicon material by a wet etching method. The surface of the pyramid-silicon was prepared by continuous etching for 30 min in a mixture of NaOH, NaSiO₃, and isopropyl alcohol at 80 °C using a single side polished silicon wafer as the substrate. The average absorption rate of the black silicon at the wavelength of 1000 nm to 1600 nm is 55%. In 2018, P. Agnihotri et al. [71] fabricated black silicon materials by alkaline wet chemical etching. The researchers used KOH solution to chemically etch the polished p-shaped silicon wafers for 10 min at 80 °C. The wafer was washed with DI water and blow-dried to complete the fabricated conical microstructure with a uniform and high density on the surface. The aspect ratio of the conical microstructure is 1.3, and the angle between the sidewall and the base is about 55°. Black silicon materials have a 90% absorptivity from 300 nm to 2000 nm.

The black silicon fabricated by the wet etching method is larger in the microstructure. If there is no metal layer catalytic etching, it is usually pyramidal in SEM images. The depth of the microstructure is not as deep as that of black silicon made by other methods. Therefore, the absorption of black silicon in the region of visible light is not ideal without doping. However, it is cheaper and easier to fabricate black silicon by wet etching. This black silicon fabricated by wet chemical etching has been widely used in industrial production as the most advanced industrial technology. Through further optimization and exploration of this process, the performance of black silicon produced by this method can be further improved.

2.5. Plasma Immersion Ion Implantation Etching

PIII etching is a surface modification technique in which the accelerated ions in the plasma are injected into a suitable substrate by using a high-voltage pulsed DC or pure DC power supply as dopants. In the process of plasma immersion ion implantation, firstly the dissociated fluorine group will be injected into the silicon substrate and react with the silicon to form volatile SF₄ gas, thus playing the role of etching. Then the product Si_xO_yF_z will deposit on the surface of the silicon to prevent the fluoro groups from continuing to react with the silicon, thus playing a part in passivation. Finally, the high-energy ions accelerated under the action of dc pulse bias will collide with Si_xO_yF_z deposited on the silicon surface, thus making the fluoro groups continue to react with the silicon. Under the joint action of the above three processes, the surface of the silicon wafer is formed into randomly distributed micro-spicules.

In 2011, Y. Xia et al. [21] fabricated black silicon by PIII, and the average reflectance of material at the wavelength from 300 nm to 1000 nm was 1.79%. In 2013, S. Zhong et al. fabricated black silicon with holes of different depths by PIII. Under different preparation situation, nanopores with a height of 150~600 nm were etched on the surface of the material. In the band from 350 nm to 1100 nm, the reflectance declined with the increment of the height of the nanopore, and the optimal average reflectance was 5%. In 2013, Y. Xia et al. [22] fabricated black silicon by PIII and researched the surface composition of the black silicon using XPS. The results show that the surface composition elements of the material are Si,

C, O, and F, and the different surface structure was formed from porous to needle-like in the different gas ratio between SF₆ and O₂. When the microstructure of black silicon is porous and needle-like, the reflection of the black silicon is 4.87% and 2.12% at 200 nm and 1100 nm, respectively.

This method was applied to the dope element to expand the optical absorption range. In 2018, J. Lim et al. [72] combined plasma immersion ion implantation and plasma dry etching to fabricate high-performance black silicon. The substrates of P-type silicon were doped with N by the PIII process to form a PN junction, firstly. The PIII was in the N₂ atmosphere. The second step of PDE was a sculptured nanostructure on the black silicon in H₂ and Ar. The black silicon fabricated by the two steps method has an ultra-low reflectivity of 1.8% in 300 nm to 1100 nm.

Plasma immersion ion implantation is also a dry etching method, and more importantly, it is a method that can inject impurity elements into black silicon to expand the optical absorption range and promote optical absorption. This method can combine with other fabrication methods to fabricate order structure black silicon that has high absorption in the near-infrared band.

2.6. Electrochemical Method

This method has gradually developed since the electrochemical HF etching of silicon proposed decades ago. Electrochemical HF etching of silicon usually uses silicon as an anode and immerses it in a mixed solution of HF/H₂O/ethanol. For the fabrication of black silicon, the current density, the proportion of HF, the etching time, and different light levels [73,74] are adjusted to control the morphology. According to the current density distinction, low current density and high current density will produce porous silicon and polished silicon, respectively, and the middle of these two current densities can produce random nanopillars without a mask. The exact current density of these three regions is determined by the doping type and concentration of the wafer. The n-type silicon wafer was electrochemically etched in a mixed solution of HF and MeOH to produce black silicon with low reflectance at 450 nm–1000 nm [75]. Since the black silicon produced by this method has different responses to light at different angles, the angle of incident light and the polarization-resolved reflectance coefficient of this black silicon were tested.

The above methods have their own advantages, but their methods involve toxic and corrosive chemicals that bring unknowing dangers. Recently, electrochemistry in molten salt is an emerging method of making black silicon. Another advantage of this method is that it does not involve expensive raw materials.

There are several different ways to prepare black silicon by molten salt electrochemistry. One of them is the production of black silicon by anodizing in molten salt [76]. By applying voltage between the two electrodes in the molten salt, through Si dissolution, redeposition, and Si alloying-dealloying with Ca to realize the production of black silicon. Another way [77] is to make black silicon by electro-reduction of SiO₂ with microstructure.

The technical advantages of molten salt electrochemistry are that it is relatively simple and has no toxic or corrosive chemicals, and the price is also low. These advantages can provide feasibility for further expansion of production scale and industrial production of high-performance black silicon.

2.7. Comparison of Different Fabrication Methods

Due to the different principles of fabrication methods, surface micro-nano structures with various morphologies are fabricated by diverse fabrication methods. Figure 8a,a' show the SEM and optical performance of B-Si that is fabricated by femtosecond laser irradiation method. The optical performance clearly represents the advantages of the laser irradiation method that expand the optical absorption to 2500 nanometer wavelength by element doping. Fewer fabrication steps are another advantage of the laser irradiation method. However, the system of femtosecond laser irradiation method to fabricate black silicon is very expensive, which is a serious obstacle to mass fabrication of black silicon

by this method. Figure 8b,b' show the SEM and absorptance of B-Si fabricated by MACE. The MACE method has the advantage of a compromise between price and performance. This method can realize the control of the nanostructure on the black silicon through different metal nanoparticle deposition methods and different etching solutions. Figure 8c,c' show the SEM and absorptance of B-Si fabricated by RIE. Compared with the absorption rate of polished silicon, the silicon etched by the RIE method has a very excellent improvement in the wavelength band below 1100 nm. Because there is an impurity energy level in B-Si, the absorption rate of black silicon also drops sharply. Figure 8d,d' show the SEM and absorptance of B-Si fabricated by wet chemical etching. Wet chemical etching method is the low-cost fabrication method. The pyramid-like microstructure is one of the characteristics of this method. It is precisely because of this microstructure that the optical performance of this black silicon is much worse. Figure 8e shows the SEM and absorptance of B-Si fabricated by PIIE. The reflectance is effectively suppressed in the wavelength of 300 nm to 1100 nm. However, more importantly, it is a method that can inject impurity elements into black silicon to expand the optical absorption range and promote optical absorption. The technical advantages of molten salt electrochemistry are that it is relatively simple and has no toxic or corrosive chemicals, and the price is also low.

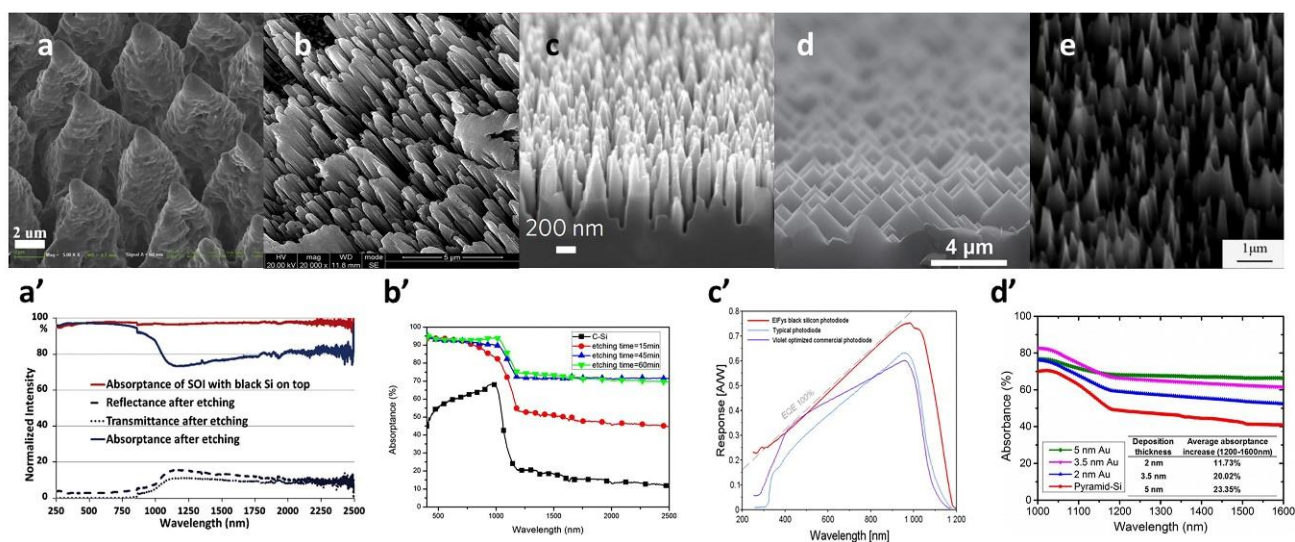


Figure 8. SEM and optical performances of using different fabrication methods. **(a,a')** Black silicon using femtosecond/nanosecond laser irradiation. Adapted from reference [37], with permission from Elsevier © 2020. **(b,b')** Black silicon using metal assistant chemical etching. Adapted from reference [50], with permission from Springer Nature © 2020. **(c,c')** Black silicon using reactive ion etching. **(d,d')** Black silicon using wet chemical. Adapted from reference [70]. **(e)** Black silicon using plasma immersion ion implantation etching. Adapted from reference [21], with permission from Elsevier © 2020.

3. Applications

3.1. Photocatalysis and Photo-Electrocatalysis

Since the discovery of the Honda-Fujishima Effect in 1967, photocatalysis has gradually become a hot topic in the field of catalysis. Photocatalysis has a very good application prospect in water purification, air purification, antifogging, degerming, and hydrogen and oxygen production. However, the existence of the electron recombination effect means the catalytic capacity is not high enough, and the efficiency of hydrogen production and oxygen production is not high enough. One of the effective methods is to weaken electron recombination by photo-electrocatalysis.

Black silicon, as one of the photo-electrocatalytic materials for hydrogen and oxygen production, has been used in recent years [78]. In 2011, the U.S. renewable energy laboratory [25] used black silicon as a cathode for photo-electrocatalytic hydrogen produc-

tion. Due to the effective reaction area between the electrode and the solution increases, the cathode provides more positions for water-splitting and reduces the overpotential for photo-electrocatalytic hydrogen production. In 2020, S. Zhao et al. [79] fabricated several black silicon using MACE and wet chemical etching to realize enhanced hydrogen generation. After the cleaning, the silicon was submerged in three different etching solutions to form a different surface morphology that has a different hydrophilic. The SiIP wafers act as a substrate to be electrodeposited metal Co, and the materials were sulfurated using CVD to finish the fabrication of photocathodes. The optimized photocathodes had a well onset potential of 0.22 V, and the photocurrent density is 10.4 mA cm^{-2} at -0.45 V . In 2020, B. Wang et al. [80] fabricated a plasmon-enhanced black silicon material to synthetic ammonia using photo-electrocatalysis. Through putting silicon into AgNO_3 and HF solution, the Ag nanoparticles and surface nanostructure of black silicon were formed, due to the catalysis of Ag^+ and the etching of HF. The fabricated Ag/b-Si photo-electrocatalytic had a superb alkaline air yield of $2.87 \mu\text{mol h}^{-1} \text{cm}^{-2}$ at -0.2 V . There are three reasons for the high yield: The excellent light absorption of black silicon, the black silicon protection of Ag nanoparticles, and the co-catalysis of Ag. In 2019, B. Wang et al. [81] fabricated a material having highly efficient photo-electrocatalysis hydrogen evolution by modifying MoS_x quantum dot on the interface of material. The substrate of black silicon used the MACE method and MoS_x quantum dot used hydrothermal for 24 h in 240, was put into liquid nitrogen, and ultrasonicated for several times to fabricate MoS_x quantum dot and black silicon synthesis by drop-casting. The material has an excellent photocurrent density of 12.2 mA cm^{-2} , an onset potential of 0.255 V, and a H_2 production rate of $226.5 \mu\text{mol h}^{-1} \text{cm}^{-2}$. In 2020, Y. Meng et al. [82] fabricated black silicon/ $(\text{Ga}_{1-x}\text{Zn}_x)(\text{N}_{1-x}\text{O}_x)$ nanorods to use as photo-electrocatalysis water splitting. Researchers used the MACE method, water bath, heating after dripping, and nitridation to fabricate the photo-electrocatalysis material. Due to the better absorption of black silicon, the grown $(\text{Ga}_{1-x}\text{Zn}_x)(\text{N}_{1-x}\text{O}_x)$ nanorods on surface structure had better performance compared with growing on polished silicon. The result shows that black silicon/ $(\text{Ga}_{1-x}\text{Zn}_x)(\text{N}_{1-x}\text{O}_x)$ nanorods have $0.55 \mu\text{A cm}^{-2}$, approximately 5 times more than $(\text{Ga}_{1-x}\text{Zn}_x)(\text{N}_{1-x}\text{O}_x)$ nanorods/polished silicon.

Since the stability of the catalyst cannot be guaranteed in the long-time reaction, researchers began to explore the protection of the black silicon photo-electro-catalyst. In 2016, the U.S. renewable energy laboratory [26] used MACE to make black silicon, and platinum nanoparticles were chemically deposited to fabricate photocathode. Figure 9b shows the framework of black silicon photo-electrocatalysis. It was found that PtNPs could enter the silicon by secondary metal-assisted etching. Moreover, due to the constancy of the Pt/Si interface, platinum nanoparticles' black silicon photocathode has a stable hydrogen evolution activity. In 2017, the University of Wisconsin–Madison used the atomic layer deposition (ALD) method to deposit titanium dioxide protective film and cobalt hydroxide film on black silicon as the photo-anode of photo-electrocatalysis [83]. Figure 9c shows the charge generation and oxygen evolution processes in photo-electrocatalysis. The nano-heterostructure has a photocurrent density of 32.3 mA cm^{-2} at an applied voltage of 1.48 v with cobalt hydroxide film under the sunlight. The titanium dioxide film passivated the defective sites on the interface without affecting the light absorption and charge transfer characteristics to improve charge separation efficiency and photocurrent density of photo-anode. Moreover, the titanium dioxide film isolates black silicon from the alkaline electrolyte, improves the catalytic stability of the black silicon, and prolongs the service time of the black silicon structure. In 2017, black silicon was fabricated by deep-reaction ion etching (DRIE) [84]. Water splitting photocatalyst was prepared by the deposition of 40 nm titanium dioxide and sputtering 40 nm gold film on the surface of the material. The wide wavelength absorption of substrate helps titanium dioxide films to have better photocatalytic capability. However, the intrinsic surface morphology of black silicon hinders the hydrophilicity of photocatalytic films. In 2019, San Diego State University fabricated black silicon from metal-assisted etching silicon wafers [85]. The researchers

sequentially deposited titanium dioxide films, platinum nanoparticles, and titanium dioxide films on the surface to achieve the protection of strong acids and strong bases. In 2019, researchers [86] fabricated the black silicon by combining with photochemical and chemical etching methods. After the formation of NiNPs and SiO_x on the material surface, NiFe was deposited to make a photoanode without a protective layer. Figure 9a shows the fabrication process of the photo-electrocatalysis material. The photoanode can produce oxygen at a steady high rate for 16 h.

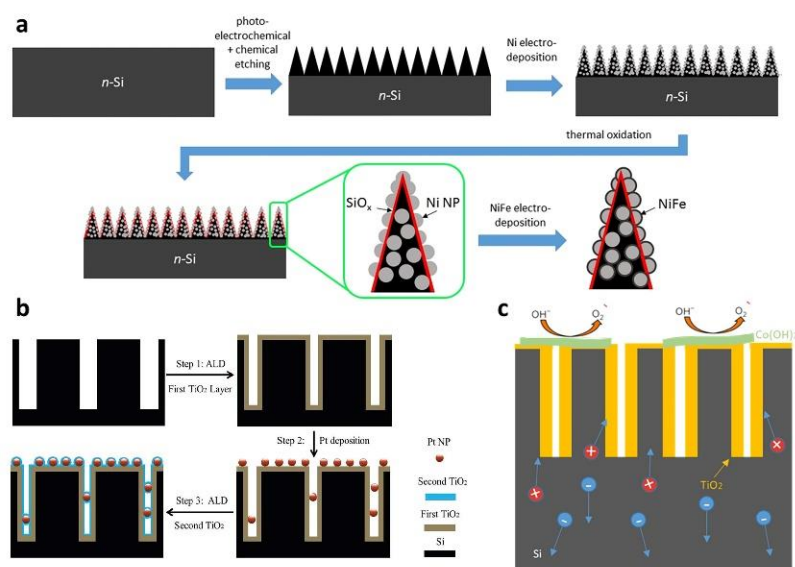


Figure 9. The applications of black silicon in photocatalysis and photo-electrocatalysis. (a) The fabrication process of NiNPs and SiO_x on the black silicon surface. (b) The fabrication process of double TiO_2 protective layers with Pt nanoparticles on black silicon. Adapted from reference [26], with permission from Royal Society of Chemistry © 2020. (c) Schematic illustration of the charge generation and oxygen evolution processes in n -Si/ TiO_2 /Co(OH) $_2$.

Photo-electrocatalysis usually has a low performance due to poor light absorption capacity. The excellent light absorption ability of black silicon can promote the performance of photo-electrocatalysis when it is used as a substrate of active material. Combined with black silicon and active material, the active material can have better efficiency due to the multiple reflections in the nanostructure of black silicon. Due to the durability of photoelectric catalysis, the micro-nano structure on black silicon can very easily cause damage after a period of photoelectric catalysis, which reduces the photoelectric catalytic ability. Therefore, researchers have used different methods to protect the surface structure of black silicon, aiming to extend the stability of photo-electrocatalysis.

3.2. Near-Infrared and Visible Light Photodetection

Near-infrared band photodetection has many applications in engineering, medical treatment, and detection. For example, near-infrared detectors can be used for non-contact temperature measurement, gas composition analysis, nondestructive flaw detection, thermal image detection, infrared remote sensing, and military target detection, search, tracking, and communication. Along with the evolution of modern technology, the application prospect of the infrared sensor will be broader. Therefore, it is very important to increase the absorption rate and absorption range of NIR detection. Black silicon has excellent absorption and low reflectance in the NIR band. Since the late 1990s, when Eric Mazur, a professor at Harvard University, discovered black silicon by accident [9], researchers have been exploring its application to infrared photodetection [47,63,82–89] and ultrahigh sensitivity in the ultraviolet band and visible light range [90–92].

Due to its low reflectivity, black silicon can be used as the surface of the absorption layer to absorb near-infrared light, to enhance the photodiode absorption of light. In 2016, M. Juntunen et al. [66] of Aalto University in Finland formed a PN-like structure by injecting boron ions and phosphorus ions into the positive/negative side of black silicon. Figure 10a shows cross-section of photodetection. Then, the researchers created photodiodes by depositing Al layers in the front/back by atomic layer deposition. The external quantum efficiency (EQE) is as high as 96% in the 250 nm to 950 nm band, and the spectral responsivity is close to the ideal photodiode.

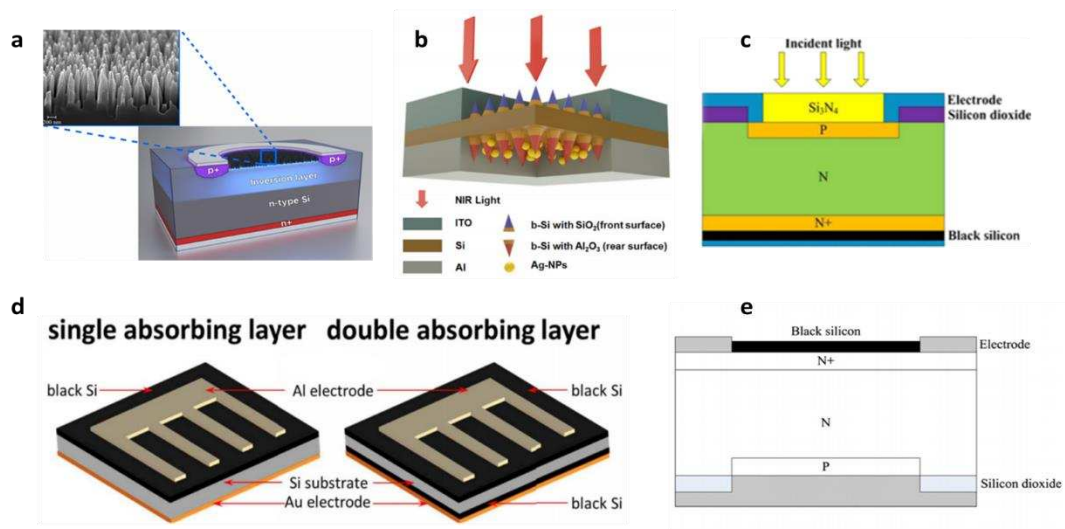


Figure 10. Photodetector based on black silicon with different principles and structures. (a) Cross-section of induced-junction b-Si photodiode structure with high EQE in the 250 nm to 950 nm. (b) Schematic of b-Si/Ag-NPs Schottky photodetector. Adapted from reference [52]. (c) Structure of Si-PIN photoelectronic detector with microstructure black silicon at the back surface. Adapted from reference [50], with permission from Springer Nature © 2020. (d) Two different schematic diagrams of nitrogen-doped black silicon photodiodes with single layer or double layers black silicon. Adapted from reference [93], with permission from IEEE © 2020. (e) Structure of Si-PIN detector based on nanostructured black silicon. Adapted from reference [94].

When black silicon fabricated by different fabrication methods is applied to photodetectors, due to the difference of surface nanostructures, the responsivity and response range will have certain differences in the near-infrared band. In 2016, H. Zhong [50] fabricated B-Si materials by MACE. The light absorption rate of black silicon is greatly enhanced, and the maximum absorption rate can reach 95% in the wide wavelength range of 400~2500 nm. Figure 10c displays the framework of Si-pin photodetection. The Si-pin photodetector based on the material has a response rate of 0.57 A/W at the 1060 nm. In 2018, H. Zhong et al. [94] fabricated black silicon using a two-step method combining DRIE and PIII. Figure 10e shows the structure of Si-pin photodetector. Si-pin photodetector using this black silicon material is 0.31 A/W and 0.53 A/W, respectively, at 1060 nm and 1100 nm. Although the second method reduces the response rate at the same wavelength, the surface nanostructures are more regular, broadening the detector's response range.

The researchers further improved the light response range of this special material detector in the near-infrared band by utilizing the surface plasmon resonance effect of the metal nanoparticles [95]. In 2017, Z. Qi et al. [70] fabricated a gold nanoparticle modified silicon pyramid-shaped material that is able to enhance thermal electron NIR light detection. The thermionic detector using this material has a wide light response spectrum in 1200~1475 nm, and the dark current is 10^{-5} Acm⁻². In 2019, F. Hu et al. [52] designed a sub-band-gap black silicon Schottky photodetector with AgNPs deposited on the back. Figure 10b shows the schematic of b-Si/Ag-NPs photodetector. At the reverse bias voltage of 3 V, the response rates of the b-Si/Ag-NPs photodetector in 1319 nm and

1550 nm were 0.277 mA/W and 0.226 mA/W, respectively. Table 1 shows the performance comparison of photodetectors based on black silicon in the past ten years.

Table 1. Performance comparison of photodetectors based on black silicon.

Year	Nation	Mechanism	Main Response Band	Performance	Ref.
2013	China	MSM-bSi	600 nm	76.8 A/W	[47]
2013	Germany	PtSi-bSi	1550 nm	EQE: 27%, 0.33 A/W	[65]
2014	China	AuNPs@graphene/CH ₃ -SiNWs	850 nm	1.5 A/W	[96]
2014	China	MSM-bSi	-	0.5 A/W@5 V	[48]
2016	China	Si-Pin	1060 nm;1100 nm	0.57 A/W; 0.37 A/W	[50]
2016	Finland	the induced-junction PD	250 nm–950 nm	EQE: 96%	[66]
2017	China	AuNPs-bSi	1200 nm–1475 nm	8.17 mA/W	[79]
2018	China	Schottky-based	1310 nm	5.3 mA/W@10 V	[93]
2018	China	Si-Pin	1060 nm	0.53 A/W	[94]
2019	China	bSi/AgVPs PD	1319 nm; 1550 nm	0.277 mA/W; 0.226 mA/W@3 V	[52]
2020	China	Schottky-based	650 nm; 808 nm; 1550 nm	445 mA/W; 56 mA/W; 15 mA/W@8 V	[89]

The thermal annealing process is a significant element that influences the light absorption rate of black silicon and the light response rate of the detector. It is also one of the research directions to study the effect of reducing the step of hot annealing on the preparation of black silicon materials. In 2018, C. Li et al. [93] fabricated a black silicon Schottky photodiode by plating Al and Au metal electrodes on the front and back of the silicon. Figure 10d show different structure Schottky photodetection. The broadband photodiode has good thermal stability, and the optical response rate at the 1330 nm band is 5.3 mA/W at 10 V reverse bias. In 2020, S. Huang et al. [88] promoted the performance of black silicon photodetection by using rapid thermal annealing and surface passivation. The a-Si:H layer is deposited on the surface of material using a plasma-enhanced chemical vapor deposition (PECVD) method to reduce dark current, and the rapid thermal annealing can diminish the diffusion of sulfur doping to lower the degree of the defect. The black silicon photodetection acquired an excellent performance, where the response rate is 0.80 A/W at 1550 nm and the dark current is 7.8 μ A at -5 V.

The photodetector based on black silicon material has a high spectral responsivity and a wider spectral response range, especially because the doped black silicon material has a much higher responsivity than silicon materials in the near-infrared band. Firstly, researchers use black silicon as the light absorption layer of the photodetector and increase the responsivity of the photodetector through the ultra-low reflectivity of black silicon. The photodetectors made by different black silicon fabrication methods usually have different response ranges and responsivity due to the different surface morphology and doping. Currently, the higher absorption of material brings the possibility of higher responsivity to black silicon-based photodetectors. Secondly, since undoped black silicon has low absorption in the NIR band, the surface plasmon resonance effect formed by noble metal nanoparticles is used to promote the absorption of undoped black silicon in the NIR band. Thirdly, the effect of annealing on black silicon is also one of the most significant research directions.

3.3. Solar Cell

The use of fossil fuels has brought about vigorous economic development to society and brought a lot of convenience to people. However, fossil energy is also limited, its combustion causes environmental pollution, and the greenhouse effect also affects the earth's ecology and climate. As people began to realize that relying on fossil fuels alone was not

feasible, researchers began to explore environmentally friendly, renewable energy sources. Solar energy can be seen everywhere on the earth, and the utilization of solar energy as new energy has become one of the research directions of researchers. The application of solar cells has already entered the fields of industry, commerce, agriculture, communication, household appliances, and public facilities from the military and aerospace fields. In particular, it can be distributed in remote areas, mountains, deserts, islands, and rural areas to save on costly transmission lines. In recent years, black silicon has become one of the materials used to make solar cells [72,97–101]. The research hotspot is to change the surface structure of black silicon [102] and passivate black silicon [103].

By changing the surface structure of the material in different ways, the researchers can improve the conversion efficiency of B-Si solar cells. Figure 11 shows the performance comparison of solar cells based on black silicon. In 2014, Z. Zhao et al. [49] fabricated black silicon by MACE. The surface treatment of B-Si by tetramethyl-ammonium hydroxide has better internal quantum efficiency than that of untreated black silicon in the short-wave region. The surface of black silicon was etched with tetramethyl-ammonium hydroxide, and the microstructure of black silicon changed slightly, resulting in a slight increase in reflectivity. The tetramethyl ammonium hydroxide (TMAH) etching treatment also changed the doping concentration of black silicon, and the depth of heavy doping concentration became shallower. This may inhibit carrier auger recombination of the b2-base cell diffusion emitter. The filling factor of the black silicon solar cell was 78.63%, and the conversion efficiency was 17.3%. In 2016, P. Li et al. [99] treated the black silicon surface with tetramethylammonium hydroxide for the 30 S, and obtained a black silicon solar cell with a better conversion efficiency, with a filling factor of 78.80% and a conversion efficiency of 19.03%. In 2018, G. Su et al. [104] fabricated black silicon material using metal-assisted chemical etching of diamond wire saw polysilicon. The researchers removed the etching process at different times to form nanostructures of different sizes on the surface. The defect removal etching (DRE) process can affect the nanometer size and reflectance of material, etc. With the increase of DRE time, the reflectance becomes larger and the passivation effect becomes better. The DWS MC-Si solar cell filling factor was 80.07%, and the conversion efficiency was 19.07%. In 2019, I. Putra et al. [51] made a B-Si solar cell by performing a silver-assisted chemical etching of the micro pyramid on a silicon wafer to form a finer nanocolumn structure on the micro pyramid. The increase in the formation time of Si nanopores led to a significant increase in photoluminescence properties. This may be because charge composition limits the efficient separation of photogenic carriers. The sample filling factor with an etching time of 8 min was 78.59%, and the conversion efficiency was 18.78%.

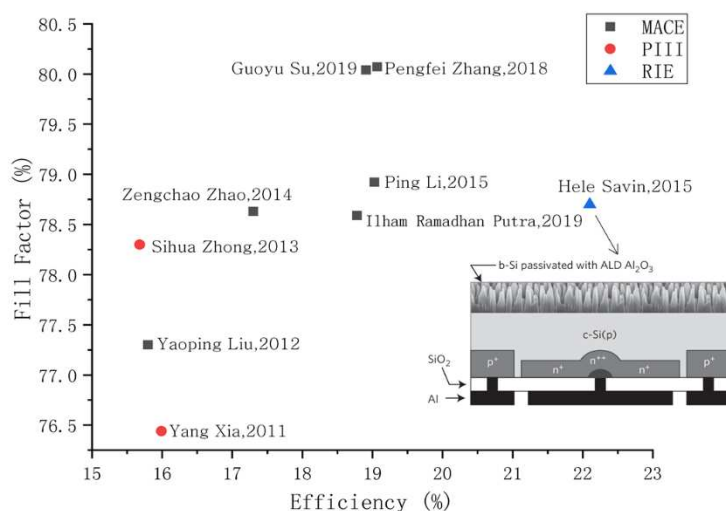


Figure 11. Performances comparison of solar cells based on black silicon, the inset shows black silicon solar cells with interdigitated back-contacts.

For solar cell, the recombination of photogenerated electrons and holes on the material surface is a major factor that limits the efficiency of solar cells. Due to the further in-depth research, how to avoid the recombination of photogenerated electrons and holes has gradually become one of the research hotspots. By surface passivation of B-Si, it reduces the surface photocarrier recombination rate and improves the conversion efficiency of B-Si solar cell. In 2015, H. Savin et al. [65] fabricated black silicon by deep reactive ion etching. Moreover, the surface was passivated by depositing 90 nm Al_2O_3 film, which further reduced the reflectance and the composition of surface carriers. The researchers chose an interdigitated back-contact back-junction (IBC) type of solar cell structure, which relies heavily on the surface composition of smaller photocarriers to improve efficiency. The Figure 10 inset illustrates the structure of a solar cell. The filling factor of the B-Si solar cells obtained by the method is 78.7%, and the conversion efficiency is 22.1%. In 2019, D. Kim et al. [105] treated black silicon materials with Al_2O_3 films by using $(\text{NH}_4)_2\text{S}$ solution. It slows down the recombination of the surface electrons. The researchers soaked black silicon with 10 nm Al_2O_3 films in $(\text{NH}_4)_2\text{S}$ solution at different times. The results showed that the sample immersed in the solution for 10 min had better conversion efficiency. The conversion efficiency reached 13.5%, the filling factor was 72.02%, and the sample conversion efficiency increased by 16% before the comparison treatment.

The surface structure of the solar cell light-absorbing material is one of the key factors to promote the performance of the solar cell. As the most widely used solar cell material with the largest market share, silicon material has a mature industrial chain in terms of processing. As a material with ultra-low reflectivity and ultra-high absorptivity in the visible light and NIR bands, black silicon is applied to solar cells, greatly improving their efficiency. Researchers have done a lot of research on the surface structure of black silicon and the surface passivation of B-Si solar cells, but further exploration is needed in terms of cost reduction and mass production.

3.4. SERS

Surface-enhanced Raman scattering (SERS) is a technique used to detect and analyze compounds. Because of its ultra-high sensitivity, resistance to photobleaching, narrow spectral bandwidth, and molecular feature detection, SERS is applied in many spheres such as food safety, biological sciences, environmental monitoring, and other fields. In general, the substrate used for SERS detection is a rough surface composed of noble metals. In recent years, due to the large surface area and/or high aspect ratio of black silicon structures, it has attracted widespread attention as the potential SERS substrate.

In 2018, E. Mitsui [106] proposed a black silicon structure that is chemically inert and consists of randomly-arranged pointed Mie resonators, used to identify low-concentration the molecular fingerprints without contact. By comparing the SERS signal of the catalytic conversion of para-aminothiophenol (PATP) to 4,4'-dimercaptoazobenzene (DMAB) between metal-coated black silicon and metal-free black silicon, it demonstrated the non-contact ultra-sensitive SERS detection of metal-free modified black silicon at concentrations as low as 10^{-6} M. Figure 12a–c show the different situation substrates detected in PATP-to-DMAB photocatalysis conversion.

In 2019, L. Liu [107] fabricated a black silicon substrate with high sensitivity of the SERS signal by using the plasma immersion ion implantation method. Testing and calibration of different concentrations of R6G show a good relationship between the fluorescence peak and the concentration, and the calibration plot coefficient is as high as 97.8%. Figure 12d–g shows the relationship between fluorescence peak and concentration. Therefore, the concentration of R6G can be detected by using a black silicon substrate to detect the change in fluorescence peak. When the concentration of R6G changed from 10^{-8} M to 10^{-3} M, the fluorescence peak shifted from 545 nm to 588 nm. The fluorescence peak shows a red-shift phenomenon with increasing concentration, which may be caused by the repulsive force field of other molecules.

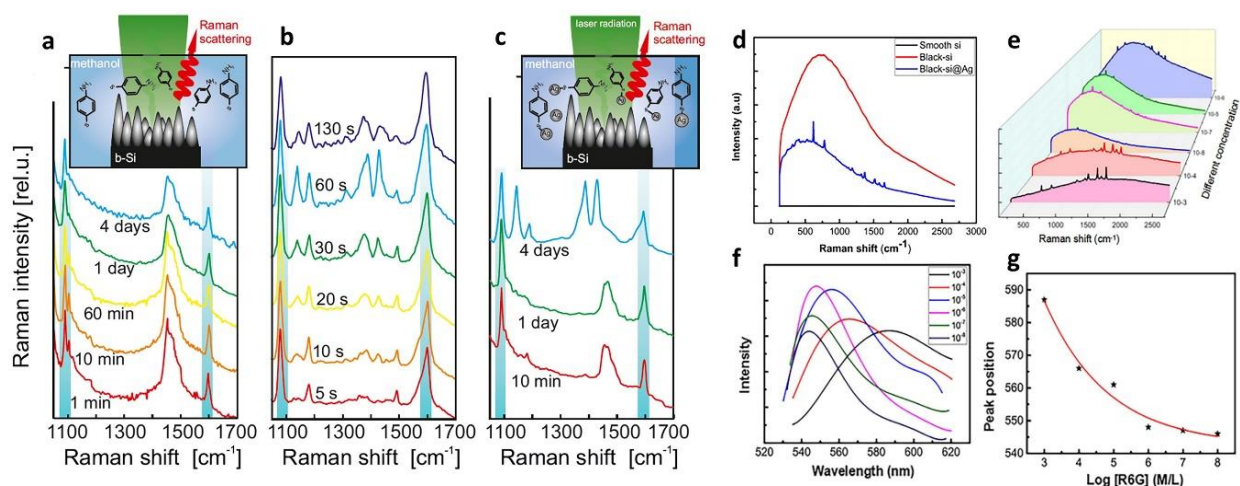


Figure 12. Application of black silicon in surface-enhanced Raman scattering (SERS). (a–c) detected PATP-to-DMAB photocatalysis conversion using different bare or Ag-coated black silicon with or without laser radiation in the aqueous methanol solution. Adapted from reference [103]. (a) Bare black silicon without laser radiation. (b) Ag-coated black silicon without laser radiation. (c) Bare black silicon without laser radiation. (d–g) Performances of R6G concentration detector based on black silicon. Adapted from reference [107], with permission from Elsevier © 2020. (d) Sensitivity of black-silicon SERS substrate. (e) Original SERS spectrum of different R6G concentration. (f) Fluorescence spectra of different concentrations of R6G. (g) The corresponding R6G sensor calibration diagram drawn by different fluorescence peaks.

Surface-enhanced Raman vanquishes the shortage of low Raman spectroscopy sensitivity and can obtain structural information that is not easily obtained by conventional Raman spectroscopy. It is widely used in surface research, adsorption interface surface state research, interface orientation, and configuration of biological large and small molecules, conformation studies, structural analysis, etc., can analyze the adsorption orientation of the compound at the interface, the change of adsorption state, and interface information. The use of black silicon as the substrate greatly enhances the SERS signal and increases the detection sensitivity.

3.5. Sensing

The application of black silicon in sensing is not as popular as solar cells and photodetectors. However, the sensitivity of sensors based on black silicon is usually very high, that is to say, sensors based on black silicon materials can detect very weak signals. Because of this unique advantage, black silicon sensors have gradually developed in recent years. Black silicon sensors are mainly used in gas sensing and imaging. In gas sensing, it is usually used in the detection of ultra-low concentration gases, such as the detection of dangerous gases. In an imaging sense, there are already products for imaging under low light conditions.

In 2018, X. Liu [108] first proposed the use of black silicon materials as gas sensing materials. Based on the excellent photoelectric characteristics of the black silicon material, the researchers realized the dual drive sensor of light and electricity by asymmetrically illuminating the two electrode regions. Figure 13a shows the structure of the ammonia sensor using b-Si material. Within a certain range of applied voltage, the sensitivity is significantly improved and tends to infinity. Foraging equipment with reduced sensitivity, the sensitivity to 500 ppm NH₃ will increase by two orders of magnitude with an additional optical drive. Finally, a mechanism based on the Demper effect explained this phenomenon.

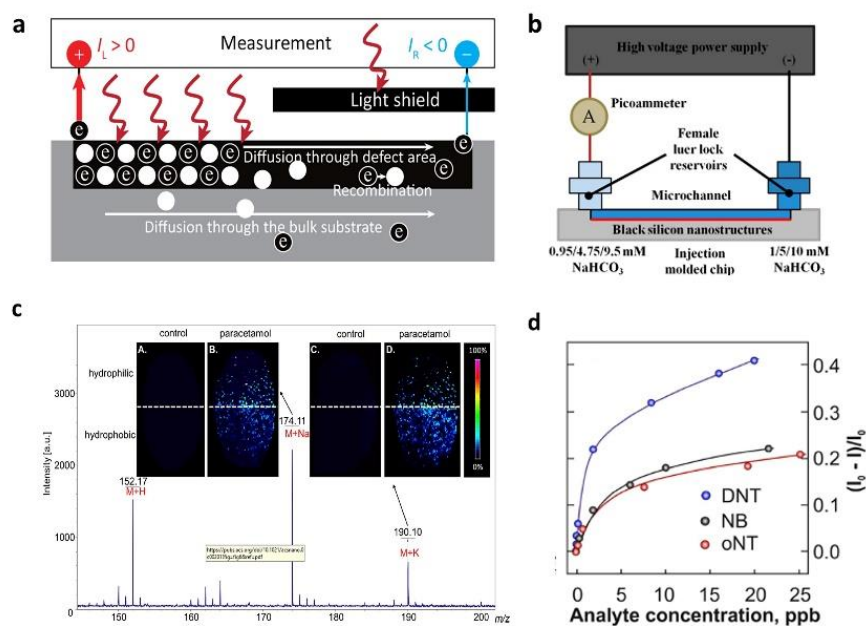


Figure 13. Serval applications based on black silicon in sensing. (a) Structure of ammonia sensor using b-Si material to realize ultrahigh Sensitivity. Adapted from reference [108], with permission from American Chemical Society © 2020. (b) Experimental setup for black silicon nanostructures current monitoring. Adapted from reference [109], with permission from Royal Society of Chemistry © 2020. (c) Using black silicon to achieve surface-assisted laser desorption/ionization mass spectrometry imaging. Adapted from reference [110], with permission from American Chemical Society © 2020. (d) Evaluate detection limits of cbz-bSi gas sensor. Adapted from reference [111], with permission from American Chemical Society © 2020.

In 2018, A. Lim et al. [109] studied the effect of nanostructured black silicon on the electroosmotic flow effect, which was used to accurately control the fluid velocity in microfluidic chips. The researchers have proposed a new technique that uses dry etching, electroplating, and molding (DEEMO) processes and RIE to fabricate long-silicon nano-silicon microchannels. The reduction of EOF is caused by the local electric field distortion on the nanostructure, and the longer the B-Si nanostructure, the better the effect of reducing the velocity. Figure 13b shows the experimental setup for black silicon nanostructures' current monitoring. The experimental results show that the EOF speed is reduced by 13.7%, which is quite close to the simulation result predicted to reduce by about 8%.

In 2019, A. Mironenko [111] fabricated a black silicon-based ultra-sensitive detector by attaching a carbazole monolayer on the surface of nanostructured black silicon. It can achieve a sensitivity test as low as 10^{-12} and a dynamic test range as high as 10 PPM. Figure 13d shows the comparison of FL quenching efficiency in different targets. Due to the presence of the carbazole monolayer, the luminescence spectrum of the reaction between the carbazole monolayer and the aromatic nitro molecule can be used to identify the presence of the aromatic nitro molecule. While the sensor has high sensitivity, it also has an ideal dynamic test range. This is precisely because the nanostructure on the surface of the B-Si substrate makes the local concentration of carbazole molecules uneven, forming surface reaction sites with different sensitivities. The sensor can be used to detect dangerous components in air or water to prevent pollution and danger.

In 2020, S. Iakab [110] fabricated a black silicon substrate modified with gold nanoparticles for surface-assisted laser desorption/ionization mass spectrometry imaging. Figure 13c shows the performance of black silicon used as SALDI-MSI. To this end, the researchers used a variety of plasma treatment methods to modify the surface of gold-modified black silicon to form hydrophilic and hydrophobic gold-modified black silicon, which can selectively adhere to molecules.

3.6. Antibacterial Material

One of the main challenges facing the biomedical industry is the development of powerful antibacterial surfaces. Due to the needle-like nanostructure of black silicon, black silicon has also been used as one of the antibacterial materials in recent years.

The researchers conducted antibacterial studies on black silicon with different nanostructures, such as the height of needle-like structures and surface density. In 2018, G. Hazell et al. [112] used the RIE method to fabricate needle-shaped black silicon surfaces with different depths and surface densities for use as antibacterial materials. The researchers studied the killing effect of black silicon and black diamond surfaces on Gram-negative (*e. coli*) and Gram-positive (*s. codon*) bacteria. All black silicon with nanostructures killed *E. coli* significantly faster than planar silicon or diamond samples. Compared with the density of the needle-shaped surface of black silicon, the length of the needle-shaped surface is a more important factor for the sterilization effect. Figure 14a,b show that the bacteria sink or are impaled by the nanostructure of black silicon. In contrast, *Gordoni* is not affected by the surface of the nanostructure. Because of their smaller size, thicker cell membranes, and lack of mobility. In 2018, C. Bhadra et al. [113] studied the effect of B-Si nano-surface structures with different heights and surface densities on antibacterial effects. The results of this work prove that although B-Si substrates have visually similar nanostructures, the sterilization efficiency of these substrates is different. For different bacteria, different structures of black silicon have different bactericidal effects, and the specific laws need further research.

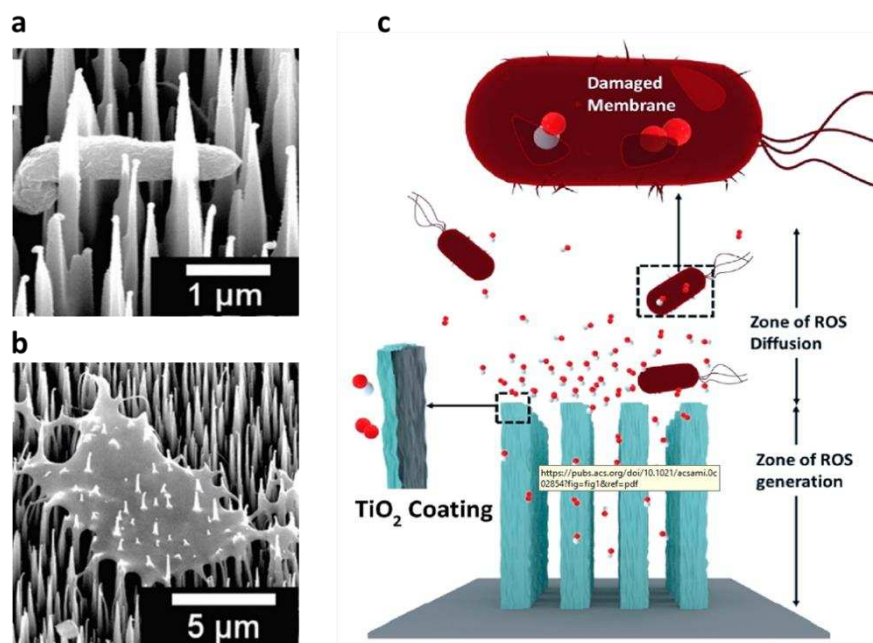


Figure 14. Applications of black silicon as antibacterial material. (a) SEM of bacteria trapped in black silicon. Adapted from reference [112], with permission from Royal Society of Chemistry © 2020. (b) SEM of bacterium punctured by nanostructures on black silicon surface. Adapted from reference [113]. (c) Reactive oxygen species (ROS) is produced by the photocatalysis of TiO₂ to decompose bacteria. Adapted from reference [114].

In 2020, J. Singh et al. [114] studied the antibacterial ability of black silicon and black silicon oxide deposited with a photocatalytic layer of titanium dioxide. This antibacterial material combines the good light absorption capability of black silicon and black silicon oxide with the antibacterial mechanism of photocatalytic materials. Figure 14c shows the principle of antibacterial using black silicon or black silica. Photocatalytic materials generate active oxygen by decomposing surface water molecules. Due to the strong oxidative

decomposition ability of this substance, the bacterial cell membrane is decomposed and the antibacterial ability is improved. Although high nanostructures absorb more light, finite-difference time-domain (FDTD), and finite element simulation results show that the higher the nanostructures are, the higher the ROS concentration is not a certainty. It may be because the nanostructure exceeds 5 microns in height, the ROS cannot diffuse out of the nanostructure.

The B-Si with a needle-like structure on the surface can puncture bacteria with a sharp tip, destroying the bacterial structure and inactivating it. However, smaller-scale bacteria are not easily destroyed by the needle-like structure. By combining the antibacterial ability of the photocatalytic material with the needle-like structure of black silicon, the better antibacterial ability can be achieved.

4. Summary and Future Directions

Along with the quick progress of the semiconductor industry, silicon is becoming one of the most popular semiconductor materials, due to its small size, wide range applications, easy integration, and long life. However, silicon materials have some disadvantages, such as high reflectivity and wide-bandgap. The black silicon remedies these disadvantages to realize low reflectivity at 350 nm to 2500 nm and excellent optical and electrical properties. After the discovery of black silicon, researchers began to study the application of black silicon in the photodetector. At the same time, they began to study the different methods to fabricate black silicon and the factors affecting the properties of black silicon materials. After more than 20 years of development, the fabrication process of black silicon materials has gradually developed through several different technologies, such as femtosecond laser pulse irradiation, RIE, MACE, wet chemical etching, and plasma immersion ion implantation etching. In recent years, with the development of the fabrication technology of black silicon materials, the application of black silicon materials has also been explored by researchers. Black silicon material has many applications in the fields of photoelectric detection, photothermal conversion, solar cell, photoelectric catalysis, and sensing.

In terms of the fabrication of black silicon material, it will proceed towards mass production and order surface morphology. Instead of simply etching the silicon wafer surface, it will design the surface micro-nano structure and produce high-performance black silicon through accurate fabrication methods. For example, photolithography is combined with plasma injection reactive ion etching or Bosch etching with deep reactive ion etching to fabricate order micron structures and nanostructures on micron structures. There are a lot of literatures on the optical properties of black silicon. In terms of electrical characteristics research, there is a lack of systematic and unified research. In some applications of black silicon, such as photocatalytic applications and photodetection applications, the research on the photoelectric properties of black silicon is involved, but there is still a lack of special research on the electrical properties of the material. We believe that the research on the electrical characteristics of black silicon also needs further exploration in the future.

There will also be more and more efficient applications. In the field of the photodetector, because the black silicon with micro-nano structure breaks through the inherent optical absorption wavelength limit of silicon materials, it will have high absorption in the near-infrared band. Therefore, achieving high responsiveness in optical communication bands such as 1330 nm and 1550 nm will be one of the development trends of photodetectors using black silicon. Due to the mature micro-nano processing technology of silicon material and highly integrated, the great absorption of black silicon can fabricate high highly responsive photodetector in visible light to near-infrared to use as wide spectrum detection. In solar cells, because silicon is cheaper than other solar cell materials, black silicon has a large market in the future as a solar cell material. Research is advancing towards the mass production of large black silicon solar cells. In polycrystalline solar cells, black silicon material also has great advantages. So, it has great development and application potential in polycrystalline black silicon solar cells. In catalysis, black silicon will combine the high-absorption structure of near-infrared and visible light with the high-efficiency

photoelectric catalytic material to produce hydrogen and oxygen efficiently and synthesize ammonia with nitrogen. Besides, researches will be carried out on the long-lasting efficacy of catalysis. There will be more breakthroughs and applications in other directions, such as photoluminescence, antibacterial materials, and high-sensitivity sensing.

Author Contributions: Z.F. wrote the entire manuscript and reviewed black silicon through reference and collection, combined with our research experience. D.C. and Z.Z. (Zengxing Zhang) revised and reviewed the black silicon fabricating methods and applications. Z.Z. (Zhou Zhao), H.C., Y.F., P.L. investigated relevant materials, and Z.Z. (Zhidong Zhang) optimized the language and grammar. S.Y. and C.X. guided the overall direction of the manuscript. All authors have read and agreed to the published version of the manuscript.

Funding: This work was funded by the Natural Science Foundation of Shanxi Province, China, grant number 201801D221212 and 201801D221197. This research was also funded by the Fund for Key Laboratory of Equipment Pre-research, grant number 6142001190409. This work was supported in part by the Zhejiang Provincial Natural Science Foundation of China under Grant LD21F050001 and Development Project of Zhejiang Province under Grant 2021C03019.

Institutional Review Board Statement: Not applicable.

Informed Consent Statement: Not applicable.

Data Availability Statement: The data presented in this study are available on request from the corresponding author.

Acknowledgments: We greatly appreciate the Natural Science Foundation of Shanxi Province and the Key Laboratory.

Conflicts of Interest: The authors declare no conflict of interest.

References

1. Lv, J.; Zhang, T.; Zhang, P.; Zhao, Y.; Li, S. Review Application of Nanostructured Black Silicon. *Nanoscale Res. Lett.* **2018**, *13*, 1–10. [CrossRef]
2. Tan, Q.; Lu, F.; Xue, C.; Zhang, W.; Lin, L.; Xiong, J. Physical Nano-fabrication methods and novel applications of black silicon. *Sensors Actuators A Phys.* **2019**, *295*, 560–573. [CrossRef]
3. Otto, M.; Algasinger, M.; Branz, H.; Gesemann, B.; Gimpel, T.; Füchsel, K.; Käsebier, T.; Kontermann, S.; Koynov, S.; Li, X.; et al. Black silicon photovoltaics. *Adv. Opt. Mater.* **2015**, *3*, 147–1642.
4. Juzeliūnas, E.; Fray, D.J. Silicon Electrochemistry in Molten Salts. *Chem. Rev.* **2020**, *120*, 1690–1709. [CrossRef]
5. Liu, X.; Coxon, P.R.; Peters, M.; Hoex, B.; Cole, J.M.; Fray, D.J. Black silicon: Fabrication methods, properties and solar energy applications. *Energy Environ. Sci.* **2014**, *7*, 3223–3263. [CrossRef]
6. Casalino, M. Near-Infrared Sub-Bandgap All-Silicon Photodetectors: A Review. *Int. J. Opt. Appl.* **2012**, *2*, 1–16. [CrossRef]
7. Loudon, A.Y.; Hiskett, P.A.; Buller, G.S.; Carline, R.T.; Herbert, D.C.; Leong, W.Y.; Rarity, J.G. Enhancement of the infrared detection efficiency of silicon photon-counting avalanche photodiodes by use of silicon germanium absorbing layers. *Opt. Lett.* **2002**, *27*, 219–221. [CrossRef] [PubMed]
8. Younkin, R.; Carey, J.E.; Mazur, E.; Levinson, J.A.; Friend, C.M. Infrared absorption by conical silicon microstructures made in a variety of background gases using femtosecond-laser pulses. *J. Appl. Phys.* **2003**, *93*, 2626–2629. [CrossRef]
9. Her, T.-H.; Finlay, R.J.; Wu, C.; Deliwala, S.; Mazur, E. Microstructuring of silicon with femtosecond laser pulses. *Appl. Phys. Lett.* **1998**, *73*, 1673–1675. [CrossRef]
10. Vorobyev, A.Y.; Guo, C. Direct creation of black silicon using femtosecond laser pulses. *Appl. Surf. Sci.* **2011**, *257*, 7291–7294. [CrossRef]
11. Zhao, J.-H.; Lv, Z.-H.; Li, C.-H.; Yu, X.-Y.; Li, X.-B. The Infrared Photodiode of Textured Silicon Irradiated Under Mixed Gas by Femtosecond Laser. *IEEE Sens. J.* **2016**, *17*, 1. [CrossRef]
12. Cheng, S.; Cai, B.; Zhu, Y. Black Silicon as Absorber for Near-Infrared Photo-Thermal Conversion. In Proceedings of the 2015 Opto-Electronics and Communications Conference (OECC), Shanghai, China, 28 June–2 July 2015; pp. 1–3. [CrossRef]
13. Jurecka, S.; Matsumoto, T.; Imamura, K.; Kobayashi, H. Multifractal analysis and optical properties of nanostructured silicon layers. *Appl. Surf. Sci.* **2017**, *395*, 150–156. [CrossRef]
14. Zhang, P.; Sun, H.; Tao, K.; Jia, R.; Su, G.; Dai, X.; Jin, Z.; Liu, X. An 18.9% efficient black silicon solar cell achieved through control of pretreatment of Ag/Cu MACE Screen printing. *J. Mater. Sci. Mater. Electron.* **2019**, *30*, 8667–8675. [CrossRef]
15. Phan, T.L.; Yu, W.J. CVD-Grown Carbon Nanotube Branches on Black Silicon Stems for Ultrahigh Absorbance in Wide Wavelength Range. *Sci. Rep.* **2020**, *10*, 1–7. [CrossRef]
16. Qiu, Y.; Hao, H.-C.; Zhou, J.; Lu, M. A close to unity and all-solar-spectrum absorption by ion-sputtering induced Si nanocone arrays. *Opt. Express* **2012**, *20*, 22087–22094. [CrossRef] [PubMed]

17. Hildebrandt, M.; Zhou, J.; Lu, M. Self-organized antireflecting nano-cone arrays on Si (100) induced by ion bombardment. *J. Appl. Phys.* **2011**, *109*, 053513. [CrossRef]
18. Steglich, M.; Käsebier, T.; Schrepel, F.; Kley, E.-B.; Tünnermann, A. Infrared Physics & Technology Self-organized, effective medium Black Silicon for infrared antireflection. *Infrared Phys. Technol.* **2015**, *69*, 218–221. [CrossRef]
19. Tan, Q.; Tang, L.; Mao, H.; Chen, Y.; Ren, Y.; Lei, C.; Yuan, F.; Ou, W.; Xiong, J. Nanoforest of black silicon fabricated by AIC and RIE method. *Mater. Lett.* **2016**, *164*, 613–617. [CrossRef]
20. Bilyalov, R.; Stalmans, L.; Schirone, L.; Levy-Clement, C. Use of porous silicon antireflection coating in multicrystalline silicon solar cell processing. *IEEE Trans. Electron Devices* **1999**, *46*, 2035–2040. [CrossRef]
21. Yang, X.; Liu, B.; Liu, J.; Shen, Z.; Li, C. A novel method to produce black silicon for solar cells. *Sol. Energy* **2011**, *85*, 1574–1578. [CrossRef]
22. Yang, X.; Liu, B.; Zhong, S.; Li, C. X-ray photoelectron spectroscopic studies of black silicon for solar cell. *J. Electron Spectrosc. Relat. Phenom.* **2012**, *184*, 589–592. [CrossRef]
23. Murias, D.; Reyes-Betanzo, C.; Moreno, M.; Torres, A.; Itzmoyotl, A.; Ambrosio, R.; Soriano, M.; Lucas, J.; I Cabarrocas, P.R. Black Silicon formation using dry etching for solar cells applications. *Mater. Sci. Eng. B* **2012**, *177*, 1509–1513. [CrossRef]
24. Liu, Y.; Lai, T.; Li, H.; Wang, Y.; Mei, Z.; Liang, H.; Li, Z.; Zhang, F.; Wang, W.; Kuznetsov, A.Y.; et al. Nanostructure Formation and Passivation of Large-Area Black Silicon for Solar Cell Applications. *Small* **2012**, *8*, 1392–1397. [CrossRef] [PubMed]
25. Oh, J.; Deutsch, T.G.; Yuan, H.-C.; Branz, H.M. Nanoporous black silicon photocathode for H₂ production by photoelectrochemical water splitting. *Energy Environ. Sci.* **2011**, *4*, 1690–1694. [CrossRef]
26. Aguilar, J.A.; Anderson, N.; Neale, N.R. Revealing the semiconductor–catalyst interface in buried platinum black silicon photocathodes. *J. Mater. Chem. A* **2016**, *4*, 8123–8129. [CrossRef]
27. Meng, W.; Zhong, H.; Hou, W.; Gou, Y.; Song, Y.; Li, W. Comparison of different etching methods on the morphology and semiconductor characters of black silicon. *IOP Conf. Ser. Mater. Sci. Eng.* **2017**, *250*, 12015. [CrossRef]
28. Lee, M.-K.; Chu, C.-H.; Wang, Y.-H.; Sze, S.M. 155- μm and infrared-band photoresponsivity of a Schottky barrier porous silicon photodetector. *Opt. Lett.* **2001**, *26*, 160–162. [CrossRef]
29. Huang, Z.; Carey, J.E.; Liu, M.; Guo, X.; Mazur, E.; Campbell, J.C. Microstructured silicon photodetector. *Appl. Phys. Lett.* **2006**, *89*, 033506. [CrossRef]
30. Casalino, M.; Coppola, G.; Iodice, M.; Rendina, I.; Sirleto, L. Near-Infrared Sub-Bandgap All-Silicon Photodetectors: State of the Art and Perspectives. *Sensors* **2010**, *10*, 10571–10600. [CrossRef]
31. Said, A.J.; Recht, D.; Sullivan, J.T.; Warrander, J.M.; Buonassisi, T.; Persans, P.D.; Aziz, M.J. Extended infrared photoresponse and gain in chalcogen-supersaturated silicon photodiodes. *Appl. Phys. Lett.* **2011**, *99*, 073503. [CrossRef]
32. Kwon, B.; Jiang, J.; Schulmerich, M.V.; Xu, Z.; Bhargava, R.; Liu, G.L.; King, W.P. Bimaterial microcantilevers with black silicon nanocone arrays. *Sensors Actuators A Phys.* **2013**, *199*, 143–148. [CrossRef]
33. Pralle, M.U.; Vineis, C.; Palsule, C.; Jiang, J.; Carey, J.E. Extending black silicon imaging to backside illumination. In Proceedings of the Infrared Technology and Applications XLII, International Society for Optics and Photonics, Baltimore, MD, USA, 17–21 April 2016; Volume 9819, pp. 1–5. [CrossRef]
34. Liu, W.; Ming, A.; Tan, Z.; Tan, Q.; Sun, X.; Li, C.; Yang, C.; Mao, H.; Wang, W.; Xiong, J.; et al. Development of MEMS IR source by compound release process with nano-scale silicon forest radiation layer. In Proceedings of the 2016 IEEE SENSORS, Orlando, FL, USA, 30 October–3 November 2016; pp. 1–3. [CrossRef]
35. Sait, M.; Mazzone, V.; Fratolocchi, A. Broadband Holography via Structured Black Silicon Nano-Antennas. *Appl. Sci.* **2019**, *9*, 1378. [CrossRef]
36. Takamura, S.; Aota, T.; Iwata, H.; Maenaka, S.; Fujita, K.; Kikuchi, Y.; Uesugi, Y. Black silicon with nanostructured surface formed by low energy helium plasma irradiation. *Appl. Surf. Sci.* **2019**, *487*, 755–765. [CrossRef]
37. Mei, H.; Wang, C.; Yao, J.; Chang, Y.-C.; Cheng, J.; Zhu, Y.; Yin, S.; Luo, C. Development of novel flexible black silicon. *Opt. Commun.* **2011**, *284*, 1072–1075. [CrossRef]
38. Wen, C.; Chen, W.; Chen, Y.; Liu, K.; Li, X.; Hu, S.; Yang, Y. Thermal annealing performance of sulfur-hyperdoped black silicon fabricated using a Nd:YAG nanosecond-pulsed laser. *Mater. Res. Bull.* **2017**, *93*, 238–244. [CrossRef]
39. Li, C.-H.; Zhao, J.-H.; Yu, X.-Y.; Chen, Q.-D.; Feng, J.; Sun, H.-B. Fabrication of Black Silicon with Thermostable Infrared Absorption by Femtosecond Laser. *IEEE Photonics J.* **2016**, *8*, 1–9. [CrossRef]
40. Yu, X.-Y.; Zhao, J.-H.; Li, C.-H.; Chen, Q.-D.; Sun, H.-B. Gold-Hyperdoped Black Silicon with High IR Absorption by Femtosecond Laser Irradiation. *IEEE Trans. Nanotechnol.* **2017**, *16*, 502–506. [CrossRef]
41. Su, Y.; Zhan, X.; Zang, H.; Fu, Y.; Li, A.; Xu, H.; Chin, S.-L.; Polynkin, P. Direct and stand-off fabrication of black silicon with enhanced absorbance in the short-wavelength infrared region using femtosecond laser filament. *Appl. Phys. A* **2018**, *124*, 223. [CrossRef]
42. Huang, Z.-M.; Huang, W.-Q.; Jiang, Z.-M.; Liu, S.-R.; Wu, X.-K.; Qin, C.-J. Electronic states of defect with impurity and infrared emission on black silicon prepared by an ns-laser. *Opt. Lett.* **2017**, *42*, 358–361. [CrossRef]
43. Franta, B.; Pastor, D.; Gandhi, H.H.; Rekemeyer, P.H.; Gradečak, S.; Aziz, M.J.; Mazur, E. Simultaneous high crystallinity and sub-bandgap optical absorptance in hyperdoped black silicon using nanosecond laser annealing. *J. Appl. Phys.* **2015**, *118*, 225303. [CrossRef]

44. Zhang, L.; Wei, Q.; Huang, H.; Zhang, T.; Liang, Y.Q.; Yang, X. Formation and evolution of black silicon microcolumns with array distribution after IR nanosecond-pulsed laser ablation. *Ferroelectrics* **2018**, *528*, 51–57. [CrossRef]
45. Elsayed, A.A.; Sabry, Y.M.; Marty, F.; Bourouina, T.; Khalil, D. Optical modeling of black silicon using an effective medium/multi-layer approach. *Opt. Express* **2018**, *26*, 13443–13460. [CrossRef] [PubMed]
46. Noor, N.A.M.; Mohamad, S.K.; Hamil, S.S.; Devarajan, M.; Pakhuruddin, M.Z. Effects of annealing temperature towards surface morphological and optical properties of black silicon fabricated by silver-assisted chemical etching. *Mater. Sci. Semicond. Process.* **2019**, *91*, 167–173. [CrossRef]
47. Su, Y.; Li, S.; Wu, Z.; Yang, Y.; Jiang, Y.; Jiang, J.; Xiao, Z.; Zhang, P.; Zhang, T. High responsivity MSM black silicon photodetector. *Mater. Sci. Semicond. Process.* **2013**, *16*, 619–624. [CrossRef]
48. Wang, C.; Jiang, J.; Zhang, C.; Jiang, Y.; Li, S.; Wu, Z. Influence of two-tier structuring on the performance of black silicon-based MSM photodetectors. *J. Mater. Sci. Mater. Electron.* **2014**, *25*, 1542–1546. [CrossRef]
49. Zhao, Z.; Li, P.; Wei, Y.; Lu, C.; Tan, X.; Liu, A. 17.3% efficient black silicon solar cell without dielectric antireflection coating. *Sol. Energy* **2014**, *110*, 714–719. [CrossRef]
50. Zhong, H.; Guo, A.; Guo, G.; Li, W.; Jiang, Y. The Enhanced Light Absorptance and Device Application of Nanostructured Black Silicon Fabricated by Metal-assisted Chemical Etching. *Nanoscale Res. Lett.* **2016**, *11*, 322. [CrossRef]
51. Putra, I.R.; Li, J.-Y.; Chen, C.-Y. 18.78% hierarchical black silicon solar cells achieved with the balance of light-trapping and interfacial contact. *Appl. Surf. Sci.* **2019**, *478*, 725–732. [CrossRef]
52. Hu, F.; Dai, X.-Y.; Zhou, Z.-Q.; Kong, X.-Y.; Sun, S.; Zhang, R.-J.; Wang, S.-Y.; Lu, M.; Sun, J. Black silicon Schottky photodetector in sub-bandgap near-infrared regime. *Opt. Express* **2019**, *27*, 3161–3168. [CrossRef]
53. Chen, K.; Pasanen, T.P.; Vähänissi, V.; Savin, H. Effect of MACE Parameters on Electrical and Optical Properties of ALD Passivated Black Silicon. *IEEE J. Photovolt.* **2019**, *9*, 974–979. [CrossRef]
54. Noor, N.A.M.; Mohamad, S.K.; Hamil, S.S.; Devarajan, M.; Pakhuruddin, M.Z. Effects of etching time towards broadband absorption enhancement in black silicon fabricated by silver-assisted chemical etching. *Optik* **2019**, *176*, 586–592. [CrossRef]
55. Abdulkadir, A.; Aziz, A.B.A.; Pakhuruddin, M.Z. Optimization of etching time for broadband absorption enhancement in black silicon fabricated by one-step electroless silver-assisted wet chemical etching. *Optik* **2019**, *187*, 74–80. [CrossRef]
56. Branz, H.M.; Yost, V.E.; Ward, S.; Jones, K.M.; To, B.M.; Stradins, P. Nanostructured black silicon and the optical reflectance of graded-density surfaces. *Appl. Phys. Lett.* **2009**, *94*, 231121. [CrossRef]
57. Marthi, S.R.; Sekhri, S.; Ravindra, N.M. Optical Properties of Black Silicon: An Analysis. *JOM J. Miner. Met. Mater. Soc.* **2015**, *67*, 2154–2159. [CrossRef]
58. Kuo, K.-H.; Ku, W.-H.; Lee, B.T.-H. Photoluminescent or Blackened Silicon Surfaces Synthesized with Copper-assisted Chemical Etching: For Energy Applications. *ECS J. Solid State Sci. Technol.* **2020**, *9*, 024006. [CrossRef]
59. Volovlikova, O.; Gavrilov, S.; Lazarenko, P.; Kukin, A.; Dudin, A.; Tarhanov, A. Influence of Etching Regimes on the Reflectance of Black Silicon Films Formed by Ni-Assisted Chemical Etching. *Key Eng. Mater.* **2019**, *806*, 24–29. [CrossRef]
60. Volovlikova, O.; O Silakov, G.; Gavrilov, S.; A Dudin, A.; O Diudbin, G.; I Shilyaeva, Y. Investigation of the Morphological Evolution and Etching Kinetics of black Silicon During Ni-Assisted Chemical Etching. *J. Phys. Conf. Ser.* **2018**, *987*, 012039. [CrossRef]
61. Kamarauskas, M.; Treideris, M.; Agafonov, V.; Mironas, A.; Strazdienė, V.; Rėza, A.; Šetkus, A. Black silicon quality control by conditions of nickel-assisted etching of crystalline silicon surfaces in photovoltaic devices. *Lith. J. Phys.* **2020**, *60*. [CrossRef]
62. Wang, Z.Y.; Zhang, R.; Lu, M.; Chen, X.; Zheng, Y.X.; Chen, L.Y.; Ye, Z.; Wang, C.Z.; Ho, K.M. Broadband optical absorption by tunable Mie resonances in silicon nanocone arrays. *Sci. Rep.* **2015**, *5*, 7810. [CrossRef]
63. Steglich, M.; Zilk, M.; Bingel, A.; Patzig, C.; Käsebier, T.; Schrempel, F.; Kley, B.; Tünnermann, A. A normal-incidence PtSi photoemissive detector with black silicon light-trapping. *J. Appl. Phys.* **2013**, *114*, 183102. [CrossRef]
64. Steglich, M.; Lehr, D.; Ratzsch, S.; Käsebier, T.; Schrempel, F.; Kley, E.-B.; Tünnermann, A. An ultra-black silicon absorber. *Laser Photonics Rev.* **2014**, *8*, L13–L17. [CrossRef]
65. Savin, H.; Repo, P.; Von Gastrow, G.; Ortega, P.; Calle, E.; Garín, M.; Alcubilla, R. Black silicon solar cells with interdigitated back-contacts achieve 22.1% efficiency. *Nat. Nanotechnol.* **2015**, *10*, 624–628. [CrossRef] [PubMed]
66. Juntunen, M.A.; Heinonen, J.; Vähänissi, V.; Repo, P.; Valluru, D.; Savin, H. Near-unity quantum efficiency of broadband black silicon photodiodes with an induced junction. *Nat. Photonics* **2016**, *10*, 777–781. [CrossRef]
67. Isakov, K.; Perros, A.P.; Shah, A.; Lipsanen, H. Wide-band ‘black silicon’ with atomic layer deposited NbN. *Nanotechnology* **2018**, *29*, 335303. [CrossRef] [PubMed]
68. Zhang, Z.; Wang, Y.; Hansen, P.A.S.; Du, K.; Gustavsen, K.R.; Liu, G.; Karlsen, F.; Nilsen, O.; Xue, C.; Wang, K. Black silicon with order-disordered structures for enhanced light trapping and photothermal conversion. *Nano Energy* **2019**, *65*, 103992. [CrossRef]
69. Wang, K.; Martinsen, T.; Liu, G.; Tayyib, M.; Cui, D.; De Boer, M.J.; Karlsen, F.; Jakobsen, H.; Xue, C.; Wang, K. Ultralow Broadband Reflectivity in Black Silicon via Synergy between Hierarchical Texture and Specific-Size Au Nanoparticles. *Adv. Opt. Mater.* **2020**, *8*, 202000668. [CrossRef]
70. Zhou, Z.-Q.; Wang, L.-X.; Shi, W.; Sun, S.-L.; Lu, M. A synergetic application of surface plasmon and field effect to improve Si solar cell performance. *Nanotechnology* **2016**, *27*, 145203. [CrossRef]
71. Agnihotri, P.K.; Ghai, V.; Singh, H. Optically Graded Ultra Dark Absorber for Visible and Near-infrared Wavelength Range. *Sci. Rep.* **2018**, *8*, 12312. [CrossRef]

72. Lim, J.; Huang, S.; Xu, L.; Lim, Y.; Loh, Y.; Chan, C.; Bazaka, K.; Levchenko, I.; Xu, S. Ultra-low reflective black silicon photovoltaics by high density inductively coupled plasmas. *Sol. Energy* **2018**, *171*, 841–850. [CrossRef]
73. Zhang, X.G.; Collins, S.D.; Smith, R.L. Porous Silicon Formation and Electropolishing of Silicon by Anodic Polarization in HF Solution. *J. Electrochem. Soc.* **1989**, *136*, 1561–1565. [CrossRef]
74. Zhang, X.G. Morphology and Formation Mechanisms of Porous Silicon. *J. Electrochem. Soc.* **2004**, *151*, C69–C80. [CrossRef]
75. Müllerová, J.; Scholtz, L.; Ďurišová, J.; Pinčík, E.; Solanská, M.; Pudiš, D. Angle- and polarization resolved antireflection properties of black silicon prepared by electrochemical etching supported by external electric field. *Appl. Surf. Sci.* **2018**, *461*, 182–189. [CrossRef]
76. Juzeliūnas, E.; Coxon, P.; Fray, D.; Kalinauskas, P.; Valsiūnas, I.; Miečinskis, P. Photoelectrochemical activity of microporous silicon formed in molten calcium chloride. *Chemija* **2016**, *27*, 11–16.
77. Coxon, P.R.; Coto, M.; Juzeliūnas, E.; Fray, D.J. The use of electro-deoxidation in molten salts to reduce the energy consumption of solar grade silicon and increase the output of PV solar cells. *Prog. Nat. Sci.* **2015**, *25*, 583–590. [CrossRef]
78. Alexander, F.; Almheiri, M.; Dahal, P.; Abed, J.; Rajput, N.; Aubry, C.; Viegas, J.; Jouiad, M. Water splitting TiO₂ composite material based on black silicon as an efficient photocatalyst. *Sol. Energy Mater. Sol. Cells* **2018**, *180*, 236–242. [CrossRef]
79. Zhao, S.; Yuan, G.; Wang, Q.; Liu, W.; Wang, R.; Yang, S. Quasi-hydrophilic black silicon photocathodes with inverted pyramid arrays for enhanced hydrogen generation. *Nanoscale* **2020**, *12*, 316–325. [CrossRef]
80. Wang, B.; Yao, L.; Xu, G.; Zhang, X.; Wang, D.; Shu, X.; Lv, J.; Wu, Y. Highly Efficient Photoelectrochemical Synthesis of Ammonia Using Plasmon-Enhanced Black Silicon under Ambient Conditions. *ACS Appl. Mater. Interfaces* **2020**, *12*, 20376–20382. [CrossRef]
81. Wang, B.; Wu, H.; Xu, G.; Zhang, X.; Shu, X.; Lv, J.; Wu, Y. MoS_x Quantum Dot-Modified Black Silicon for Highly Efficient Photoelectrochemical Hydrogen Evolution. *ACS Sustain. Chem. Eng.* **2019**, *7*, 17598–17605. [CrossRef]
82. Meng, Y.; An, L.; Han, X.; Li, Y.; Hou, C.; Zhang, Q.; Wang, H. Controllable (Ga_{1-x}Zn_x)(N_{1-x}O_x) nanorods grown on black silicon as anodes for water splitting. *Appl. Surf. Sci.* **2020**, *502*, 144174. [CrossRef]
83. Yu, Y.; Zhang, Z.; Yin, X.; Kvit, A.; Liao, Q.; Kang, Z.; Yan, X.; Zhang, Y.; Wang, X. Enhanced photoelectrochemical efficiency and stability using a conformal TiO₂ film on a black silicon photoanode. *Nat. Energy* **2017**, *2*, 17045. [CrossRef]
84. Dahal, P.; Pereira, D.; Elamurugu, E.; Viegas, J. Photocurrent enhancement in nanocoatings of cerium oxide and platinum on black silicon. In Proceedings of the SPIE OPTO. Optical Components and Materials XIV, San Francisco, CA, USA, 28 January–2 February 2017; Volume 10100, pp. 1–5. [CrossRef]
85. Yang, F.; Aguiar, J.A.; Fairchild, M.; Vakki, W.; Younan, S.; Zhou, Y.; Zhuo, L.; Gu, J. Dual Protection Layer Strategy to Increase Photoelectrode–Catalyst Interfacial Stability: A Case Study on Black Silicon Photoelectrodes. *Adv. Mater. Interfaces* **2019**, *6*, 6. [CrossRef]
86. Oh, K.; Joanny, L.; Gouttefangeas, F.; Fabre, B.; Lassalle-Kaiser, B.; Lassalle-Kaiser, B.; Vacher, A.; Mériadec, C.; Ababou-Girard, S.; Loget, G. Black Silicon Photoanodes Entirely Prepared with Abundant Materials by Low-Cost Wet Methods. *ACS Appl. Energy Mater.* **2019**, *2*, 1006–1010. [CrossRef]
87. Li, C.-H.; Zhao, J.-H.; Chen, Q.-D.; Feng, J.; Sun, H.-B. Sub-bandgap photo-response of non-doped black-silicon fabricated by nanosecond laser irradiation. *Opt. Lett.* **2018**, *43*, 1710–1713. [CrossRef] [PubMed]
88. Huang, S.; Wudeng, W.; Jia, Z.; Jin, X.; Fu, X.; Huang, H.; Zhang, X.; Yao, J.; Xu, J. Black Silicon Photodetector with Excellent Comprehensive Properties by Rapid Thermal Annealing and Hydrogenated Surface Passivation. *Adv. Opt. Mater.* **2020**, *8*. [CrossRef]
89. Su, Y.; Yao, D.; Wang, S.; Zhan, X.; Xu, H. Broadband n+–n photodiode based on tellurium-doped black silicon fabricated by femtosecond laser filament. *Opt. Laser Technol.* **2020**, *123*, 105913. [CrossRef]
90. Juntunen, M.A.; Heinonen, J.; Laine, H.S.; Vähänissi, V.; Repo, P.; Vaskuri, A.; Savin, H. N-type induced junction black silicon photodiode for UV detection. In Proceedings of the Integrated Photonics: Materials, Devices, and Applications IV, Barcelona, Spain, 8–10 May 2017. [CrossRef]
91. Garin, M.; Heinonen, J.; Werner, L.; Pasanen, T.P.; Vähänissi, V.; Haarahiltunen, A.; Juntunen, M.A.; Savin, H. Black-Silicon Ultraviolet Photodiodes Achieve External Quantum Efficiency above 130%. *Phys. Rev. Lett.* **2020**, *125*, 117702. [CrossRef]
92. Tsang, T.; Bolotnikov, A.; Haarahiltunen, A.; Heinonen, J. Quantum efficiency of black silicon photodiodes at VUV wavelengths. *Opt. Express* **2020**, *28*, 13299–13309. [CrossRef]
93. Li, C.-H.; Wang, X.-P.; Zhao, J.-H.; Zhang, D.-Z.; Yu, X.-Y.; Li, X.-B.; Feng, J.; Chen, Q.-D.; Ruan, S.-P.; Sun, H.-B. Black Silicon IR Photodiode Supersaturated With Nitrogen by Femtosecond Laser Irradiation. *IEEE Sens. J.* **2018**, *18*, 3595–3601. [CrossRef]
94. Zhong, H.; Ilyas, N.; Song, Y.; Li, W.; Jiang, Y. Enhanced near-infrared absorber: Two-step fabricated structured black silicon and its device application. *Nanoscale Res. Lett.* **2018**, *13*, 316. [CrossRef]
95. Song, Y.; Liu, T.; Liu, S.; Huang, J.; Li, J.; Tian, C.; Yu, T.; He, Y.; Liu, Y.; Zhong, Z. A plasmon-enhanced broadband absorber fabricated by black silicon with self-assembled gold nanoparticles. *J. Mater. Sci. Mater. Electron.* **2020**, *31*, 4696–4701. [CrossRef]
96. Luo, L.-B.; Zeng, L.-H.; Xie, C.; Yu, Y.-Q.; Liang, F.-X.; Wu, C.-Y.; Wang, L.; Hu, J.-G. Light trapping and surface plasmon enhanced high-performance NIR photodetector. *Sci. Rep.* **2014**, *4*, 3914. [CrossRef] [PubMed]
97. Guenther, K.-M.; Baumann, A.; Gimpel, T.; Kontermann, S.; Schade, W. Tandem Solar Cell Concept Using Black Silicon for Enhanced Infrared Absorption. *Energy Procedia* **2012**, *27*, 555–560. [CrossRef]
98. Zhong, S.; Liu, B.; Xia, Y.; Liu, J.; Liu, J.; Shen, Z.; Xu, Z.; Li, C. Influence of the texturing structure on the properties of black silicon solar cell. *Sol. Energy Mater. Sol. Cells* **2013**, *108*, 200–204. [CrossRef]

99. Li, P.; Wei, Y.; Zhao, Z.; Tan, X.; Bian, J.; Wang, Y.; Lu, C.; Liu, A. Highly efficient industrial large-area black silicon solar cells achieved by surface nanostructured modification. *Appl. Surf. Sci.* **2015**, *357*, 1830–1835. [CrossRef]
100. Abdullah, M.; Alghoul, M.A.; Naser, H.; Asim, N.; Ahmadi, S.; Yatim, B.; Sopian, K. Research and development efforts on texturization to reduce the optical losses at front surface of silicon solar cell. *Renew. Sustain. Energy Rev.* **2016**, *66*, 380–398. [CrossRef]
101. Pasanen, T.P.; Modanese, C.; Vähänissi, V.; Laine, H.S.; Wolny, F.; Oehlke, A.; Kusterer, C.; Heikkinen, I.; Wagner, M.; Savin, H. Impact of black silicon on light- and elevated temperature-induced degradation in industrial passivated emitter and rear cells. *Prog. Photovolt. Res. Appl.* **2019**, *27*, 918–925. [CrossRef]
102. Li, X.; Gao, Z.; Zhang, D.; Tao, K.; Jia, R.; Jiang, S.; Wang, B.; Ji, Z.; Jin, Z.; Liu, X. High-efficiency multi-crystalline black silicon solar cells achieved by additive assisted Ag-MACE. *Sol. Energy* **2020**, *195*, 176–184. [CrossRef]
103. Özkol, E.; Procel, P.; Zhao, Y.; Mazzarella, L.; Medlin, R.; Sütta, P.; Isabella, O.; Zeman, M. Effective Passivation of Black Silicon Surfaces via Plasma-Enhanced Chemical Vapor Deposition Grown Conformal Hydrogenated Amorphous Silicon Layer. *Phys. Status Solidi (RRL)—Rapid Res. Lett.* **2019**, *14*. [CrossRef]
104. Su, G.; Dai, X.; Tao, K.; Sun, H.; Jia, R.; Jin, Z.; Liu, X.; Liu, H.; Liu, S.; Xu, C.; et al. The study of the defect removal etching of black silicon for diamond wire sawn multi-crystalline silicon solar cells. *Sol. Energy* **2018**, *170*, 95–101. [CrossRef]
105. Kim, D.W.; Song, J.-W.; Jin, H.S.; Yoo, B.; Lee, J.-H.; Park, T.J. Sulfur-Enhanced Field-Effect Passivation using (NH₄)₂S Surface Treatment for Black Si Solar Cells. *ACS Appl. Mater. Interfaces* **2019**, *11*, 25140–25146. [CrossRef]
106. Kuchmizhak, A.; Kuchmizhak, A.; Pustovalov, E.; Sergeev, A.; Mironenko, A.; Bratskaya, S.; Linklater, D.P.; Balcytis, A.; Ivanova, E.P.; Juodkazis, S. Chemically non-perturbing SERS detection of a catalytic reaction with black silicon. *Nanoscale* **2018**, *10*, 9780–9787. [CrossRef]
107. Liu, L.-H.; Cui, S.-H.; Fu, T.-Z.; Yuan, Y.; Li, C.-B. Effect of concentration on the position of fluorescence peak based on black-silicon SERS substrate. *Appl. Surf. Sci.* **2019**, *464*, 337–343. [CrossRef]
108. Liu, X.-L.; Zhu, S.-W.; Sun, H.-B.; Hu, Y.; Ma, S.-X.; Ning, X.-J.; Zhao, L.; Zhuang, J. “Infinite Sensitivity” of Black Silicon Ammonia Sensor Achieved by Optical and Electric Dual Drives. *ACS Appl. Mater. Interfaces* **2018**, *10*, 5061–5071. [CrossRef] [PubMed]
109. Lim, A.E.; Lim, C.Y.; Lam, Y.; Taboryski, R. Electroosmotic Flow in Microchannel with Black Silicon Nanostructures. *Micromachines* **2018**, *9*, 229. [CrossRef]
110. Iakab, S.A.; Ràfols, P.; Tajés, M.; Correig-Blanchar, X.; García-Altare, M. Gold Nanoparticle-Assisted Black Silicon Substrates for Mass Spectrometry Imaging Applications. *ACS Nano* **2020**, *14*, 6785–6794. [CrossRef]
111. Mironenko, A.Y.; Tutov, M.V.; Sergeev, A.A.; Mitsai, E.V.; Ustinov, A.Y.; Zhizhchenko, A.Y.; Linklater, D.P.; Bratskaya, S.Y.; Juodkazis, S.; Kuchmizhak, A. Ultratrace Nitroaromatic Vapor Detection via Surface-Enhanced Fluorescence on Carbazole-Terminated Black Silicon. *ACS Sensors* **2019**, *4*, 2879–2884. [CrossRef]
112. Hazell, G.; May, P.W.; Taylor, P.; Nobbs, A.H.; Welch, C.C.; Su, B. Studies of black silicon and black diamond as materials for antibacterial surfaces. *Biomater. Sci.* **2018**, *6*, 1424–1432. [CrossRef]
113. Bhadra, C.M.; Werner, M.; Baulin, V.A.; Truong, V.K.; Al Kobaisi, M.; Nguyen, S.H.; Balcytis, A.; Juodkazis, S.; Wang, J.Y.; Mainwaring, D.E.; et al. Subtle Variations in Surface Properties of Black Silicon Surfaces Influence the Degree of Bactericidal Efficiency. *Nano-Micro Lett.* **2018**, *10*, 1–8. [CrossRef]
114. Singh, J.; Jadhav, S.; Avasthi, S.; Sen, P. Designing Photocatalytic Nanostructured Antibacterial Surfaces: Why Is Black Silica Better than Black Silicon? *ACS Appl. Mater. Interfaces* **2020**, *12*, 20202–20213. [CrossRef]



Review

Recent Advances in Functionalized Mesoporous Silica Frameworks for Efficient Desulfurization of Fuels

Shruti Mendiratta * and Ahmed Atef Ahmed Ali *

Department of Chemical and Petroleum Engineering, University of Calgary, Calgary, AB T2N1N4, Canada

* Correspondence: shruti.mendiratta@ucalgary.ca (S.M.); ahmed.atef.dr@gmail.com or ahmed.atef1@ucalgary.ca (A.A.A.A.)

Received: 29 April 2020; Accepted: 3 June 2020; Published: 5 June 2020

Abstract: Considerable health and climate benefits arising from the use of low-sulfur fuels has propelled the research on desulfurization of fossil fuels. Ideal fuels are urgently needed and are expected to be ultra-low in sulfur (10–15 ppm), with no greater than 50 ppm sulfur content. Although several sulfur removal techniques are available in refineries and petrochemical units, their high operational costs, complex operational needs, low efficiencies, and higher environmental risks render them unviable and challenging to implement. In recent years, mesoporous silica-based materials have emerged as promising desulfurizing agents, owing to their high porosity, high surface area, and easier functionalization compared to conventional materials. In this review, we report on recent progress in the synthesis and chemistry of new functionalized mesoporous silica materials aiming to lower the sulfur content of fuels. Additionally, we discuss the role of special active sites in these sorbent materials and investigate the formulations capable of encapsulating and trapping the sulfur-based molecules, which are challenging to remove due to their complexity, for example the species present in JP-8 jet fuels.

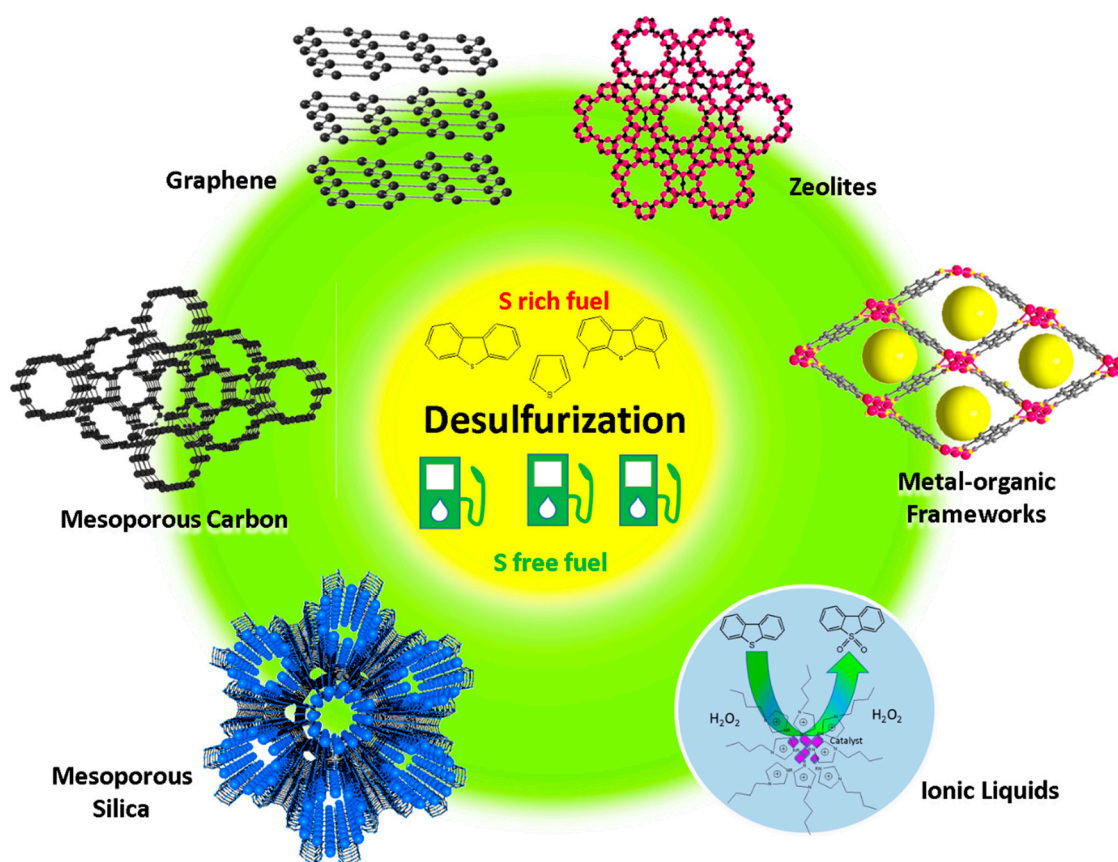
Keywords: mesoporous silica; nanomaterials; desulfurization; fuel; JP-8

1. Introduction

According to the World Health Organization (WHO), exposure to air pollution is the topmost environmental health risk factor, having led to one in eight global deaths in 2016 [1]. Reducing the greenhouse gas emissions is listed as one of the sustainable goals of the United Nations which directed their climate change mitigation efforts to apply stringent regulations, promote intelligent transport systems and innovative construction techniques, and invest in cleaner energy from fossil fuels through greenhouse gas capture, storage, and sequestration [2]. As per the 2016 Climate and Clean Air Coalition (CCAC) report, fine particles ($PM_{2.5}$) present in the air, arising as a consequence of high sulfur content in fuels, are among the major contributors to air pollution. The presence of sulfur in fuels is linked directly to increased air pollution through direct emissions of harmful sulfur oxide (SO_x) compounds in the atmosphere, resulting in acid rain, as well as indirectly by deactivating/poisoning the catalysts used in the refining systems and decreasing the efficiencies of emission control devices [3]. For example, black carbon released from the combustion of diesel can be captured through filters; however, these filters perform well only in the presence of low sulfur concentrations. Therefore, desulfurization of fuels becomes imperative for the preservation of environment, protection of health, and for increasing the lifetime of components playing essential roles in power generation systems.

High chemical affinity of sulfur atoms for metallic cations have made metal-oxide loaded solid sorbents to play vital role in removing sulfur content at mid, as well as high, temperatures. Hydrodesulfurization (HDS) is one of the conventional methods to desulfurize fuel in refineries where organic sulfur is converted to H_2S employing transition metal catalysts loaded on alumina substrates.

Low cost transition metal oxides of Mn, Zn, Fe, Co, and Mo act as active components of these catalysts due to their high thermal stability [4–9]. However, energy demanding operating conditions involving high temperatures and pressures, low octane/cetane values, and selectivity towards simple refractory sulfur compounds in comparison to more complex aromatic species makes this process less efficient and makes room for new alternatives. Although few companies, like Akzo Nobel, ExxonMobil, and Nippon Ketjen, have come forward with a new trimetallic HDS catalyst (Mo-W-Ni, NEBULA) capable of producing diesel oil with a sulfur content as low as 10 ppm sulfur content, this process is still very energy intensive and requires hydrogen. Much effort is now being directed towards low temperature purification systems with high adsorption capacities for sulfur by exploring the efficiency of adsorbents, such as zeolites, metal–organic frameworks (MOFs), carbonaceous materials, ionic liquids (IL), and silica (Scheme 1). However, the efficiency of conventional adsorptive desulfurization methods can only be enhanced in the presence of better adsorbents or by using a combination of sulfur removal platforms.



Scheme 1. Various porous materials reported for desulfurization of fuels.

The discovery of mesoporous molecular sieves (MCM-41) possessing hexagonal porous channels was a hallmark in materials science, not only in terms of opening avenues of new materials, such as mesoporous silica nanoparticles, mesoporous carbon nanosheets, and MOFs, for catalysis, gas adsorption, and drug delivery but also towards creation of new zeolites and their derivatives [10–20]. Structural marvels of mesoporous silica (MS) have also motivated researchers in recent years to investigate their performance in desulfurization of fuels, and they are being investigated as supports for metal oxides, owing to their high porosities, large surface areas, structural flexibility, and easy functionalization. High pore volumes and confined pore characteristics of one dimensional MCM-41 (with a 2–4 nm pore diameter) and two dimensional Santa Barbara Amorphous (SBA)-15 (with a 4.5–30 nm pore diameter) and their derivatives make them ideal representatives for adsorbing common aromatic S-based molecules present in fuels, such as benzothiophene (BT), dibenzothiophene (DBT), or

4,6-dimethyldibenzothiophene (4,6-DMDBT). To the best of our knowledge, this review article is the first to focus on the design and performance of mesoporous silica frameworks and the corresponding nanoparticles for desulfurization of fuels.

In this review, we discuss the synthesis, functionalization, and desulfurization performance of various MS frameworks. We focus our attention on the promising adsorption techniques using MS frameworks containing photocatalytic, redox, magnetic, ionic liquid, and carbonaceous active sites. A brief account of the synthetic strategies for preparing a MS catalytic host framework is given, along with commercial, as well as developing, desulfurization strategies. In addition, we discuss the mechanisms for removal of sulfur rich species wherever possible and make efforts to understand the role of special active sites in such sorbents. Finally, we investigate the formulations capable of encapsulating and trapping the sulfur-based molecules that are more complex and difficult to remove, such as the ones present in JP-8 and JP-5 jet fuels. In our opinion, this review will be beneficial for a wide audience working in the fields of energy production and environmental remediation.

2. Strategies to Synthesize Mesoporous Silica Catalytic Host Materials

High surface area of MS makes it a very promising material for the adsorptive desulfurization and hydrothermal methods. The meso-templates method is one of the conventional methods for MS catalyst preparation. A typical MS synthesis involves the self-organization of surfactant species, followed by their treatment with silica precursors. Condensation of the precursors around surfactants and their consecutive removal via reflux or calcination generates perfect MS frameworks. However, the hydrothermal method using various cationic, anionic, and neutral surfactants makes this process expensive and non-ecofriendly. Fortunately, these shortcomings can be overcome by incorporating new green and economical synthetic strategies using renewable templates. In recent years, sustainable development methods involve new templating strategies using nanocellulose, triblock copolymers, and task-specific ionic liquids as templates, instead of conventional surfactants. Some methods mentioned in this section even bypass the traditional templating strategies by using molecular imprinting techniques and single or dual phase hydrolytic conditions.

2.1. Templating Strategies

2.1.1. Nanocellulose Template

One of the most abundant biomaterial present in nature is cellulose, which is a low cost, reusable, and biodegradable material. Upon acid hydrolysis, this material can be transformed to form nanocellulose fibers with lengths ranging from 50 nm to a micron [21]. Nanocellulose has the potential to become an environmentally benign templating alternative. It can offer benefits of both soft and hard templates, owing to its unique structural and chemical features, including high aspect ratio and low density, as well as presence of hydrophilic surface hydroxyl groups [22,23]. Recently, nanocellulose was used as a template by Shen et al. for the development of tungsten-impregnated mesoporous silica catalysts [24]. The resulting disordered worm-like mesoporous catalysts had highly dispersed tungsten species and high surface areas in the range of 344–535 m²/g. It was observed that the pore diameter (2.3 nm to 10 nm) and pore volume (0.32 cm³/g to 0.95 cm³/g) increased significantly when the dosage of nanocellulose templates was increased in the precursor solution.

2.1.2. Triblock Copolymer (P123) as a Template

Several types of triblock copolymers are used in the synthesis of porous materials as the pore-directing agents. One widely used symmetric triblock copolymer with favorable characteristics is Pluronic P123, which comprises poly(ethylene oxide)–poly(propylene oxide)–poly(ethylene oxide) repeating units. P123 exhibits high hydrothermal stability, as well as amphiphilic properties, that can form stable micelles [25]. Generally, P123 can be used to form 2-D hexagonal mesoporous silica structures using acidic conditions and room temperature [26]. However, alteration of the synthesis

conditions, such as the addition of sodium dodecyl sulfate (SDS) [27], n-butanol [28], or NaI [29], can result in the formation of cubic *Ia3d* mesoporous silica structures. In 2020, Tagaya et al. successfully synthesized novel biocompatible slit-shaped mesoporous silica/hydroxyapatite hybrid particles using P123 and Cetyl trimethylammonium bromide (CTAB) for biological applications. [30]. It was found that the use of P123 as a template was beneficial in increasing the pore size of the mesoporous structure of synthesized particles. Moreover, the use of P123 imparted dispersion stability for the particles at the monodisperse state.

2.1.3. Task-Specific Ionic Liquid Strategy

Task-specific ionic liquids (TSIL) have gained significant attention in recent years for their role in synthesizing nanoparticles and chiral moieties with tailorable characteristics (physical, chemical, and biological) [31]. A series of mesoporous silicas (which were further loaded with zirconium derived nanoparticles) was successfully synthesized from hydrolysis of the precursor material tetraethoxysilane (TEOS) in acidic medium in the presence of the ionic liquid 1-hexadecyl-3-methylimidazolium bromide, which acted as a template material for the mesoporous silicas. The synthesized mesoporous silica structures showed high capacity to be impregnated with the zirconium derived nanoparticles [32]. Similarly, high-surface-area mesoporous silicas were fabricated using the task-specific ionic liquid 1-alkyl-3-methylimidazolium hydrogen sulfate as the template material from the precursor material TEOS [33]. In addition, it was reported that the use of the long-chain ionic liquid 1-hexadecyl-3-methylimidazolium chloride can produce two-dimensional hexagonal *p6mm* and cubic *Ia3d* mesoporous silica structures, depending on the synthesis conditions from the precursor material TEOS [34].

2.1.4. Polystyrene Colloidal Crystal Template

The use of colloidal crystals as templates for the synthesis of various mesoporous structures has gained adequate recognition due to their ordered interparticle pores and other desirable characteristics [35]. Yang et al. prepared bimodal ordered porous silica structures with mesoporous macropore walls, which were formed from polystyrene colloidal crystal templates. They used the seed emulsion polymerization method to prepare the polystyrene template films, which were used to prepare the silica structures from the precursor material TEOS [36]. Míguez and coworkers reported the successful fabrication of bimodal mesoporous silica structures within polystyrene colloidal crystal films that were formed on the surface of glass substrate from the precursor material TEOS using the spin-coating method [37]. In 2019, Peng et al. could achieve the synthesis of a hybrid nanostructure composed of a core of hollow mesoporous silica nanoparticles coated with a shell of pH-responsive and thermo-sensitive moieties as a model of drug delivery platform [38]. The authors used the soap-free emulsion polymerization method to prepare monodisperse polystyrene microspheres as a template for the fabrication of their hollow mesoporous silica nanoparticles, which were monodispersed with adjustable mesoporous silica shell thickness and particle size (depending on the fabrication parameters). The synthesis of ordered macroporous silica particles from the precursor material tetramethyl orthosilicate (TMOS) using polystyrene colloidal crystal as a template was also reported [39].

2.2. Molecular Imprinting Polymer Technology

Molecular imprinting technique offers an alternative method for deep desulfurization, where refractory organosulfur species can be easily removed under mild conditions [40]. In this technique, functionalized monomers are made to react and crosslink with template molecules. After the reaction, the template molecules are extracted leaving behind well-defined arrangement of ligands structures and tailor-made binding pockets. Compared to other structurally similar compounds, surface molecularly imprinted polymers have distinct affinity towards their templates. There are several benefits associated with their usage, such as high guest absorption and access, reduced mass transfer resistance, feasible

extraction of template molecules, rapid adsorption kinetics, structural tenability, and easy synthetic protocols [41–43]. As binding capacity of these polymers critically depends on surface area of templates, new materials with high porosity and surface areas are in demand and mesoporous silica materials are ideal candidates for this role, thanks to their high surface areas, uniform pores, and structural and chemical tunability, as well as diverse morphologies, which makes them suitable materials for molecular imprinting technology.

2.3. 1D Silica Fibers and Nanowires

Development of carbon nanotube mimicking one dimensional mesoporous silica micro and nanostructures have gained much attention in recent years for applications, such as waveguides and laser components, and several different strategies are being implemented to make these materials with a diameter less than 50 nm. Electrospinning methods can generate silica fibers with an average diameter of 40 μm [26], while anodic aluminium membrane strategy [27] can help in growing fibers that have small diameters of about 250 nm. In contrast, two-phase solution methods have shown the growth of mesoporous silica fibers with average diameters in the range of 1–15 μm [28], and this method can even be extended to one-phase (aqueous) hydrolysis method in the presence or absence of acidic environment to produce 1D fibrous silica-based materials with 50–300 nm diameters [29]. Transforming 1D silica fibers into materials with unique pore architecture is of prime importance for materials scientists. Judicious design of mesoporous silica materials with hierarchical pores is associated with benefits, such as efficient host guest interactions, high catalytic performance, and better mass transport properties [30]. Although high porosity and large surface areas are recognized as key features for their implementation, orientation of mesopores should also be given equal importance. Studies have shown that mesopores that are parallel with the length of 1D silica fibers can limit catalyst loading and decrease active catalytic sites by blocking the longitudinal channels, whereas mesopores aligned perpendicular to the axial direction of 1D channels permit easy catalyst access and higher effective surface area [31,32].

3. Strategies to Desulfurize Fuel

3.1. Hydrodesulfurization (HDS)

Hydrodesulfurization is one of the conventional methods to desulfurize crude oil where concentration of the sulfur containing compounds is reduced. However, HDS takes place in the presence of harsh operating conditions requiring elevated temperatures in the range of 300–450 $^{\circ}\text{C}$, hydrogen, catalysts, and high pressures ranging from 3–5 MPa, making it an expensive desulfurization technique [44]. HDS is certainly effective in removing simple thiols, thioethers, and disulfides; however, it is not successful in removing other complex heterocyclic molecules, such as dibenzothiophene (DBT), 4,6-dimethyldibenzothiophene (4,6-DMDBT), and their derivatives [44]. A typical HDS catalysis generates H_2S gas which is converted to elemental sulfur through a Claus process [45]. Harsh catalytic conditions cause hydrogenation of olefins, followed by a negative octane rating and increased H_2 consumption, whereas a mild HDS environment generates recombinant mercaptans through the reaction of H_2S with olefins and are responsible for retained sulfur in final fuel. Desulfurization mechanism of DBT using hydrogen at 300 $^{\circ}\text{C}$ and 102 atm is suggested to proceed via two major pathways, direct desulfurization (DDS) and hydro desulfurization (HYD) pathways. The DDS pathway involves elimination of sulfur without hindering the aromatic rings, while HYD proceeds via selective hydrogenation of DBT aromatic rings, followed by desulfurization [44]. Molybdenum-, nickel-, cobalt-, and tungsten-based catalysts are commonly used and incorporated in the HDS process to reduce sulfur content in the form of disulfides, thioethers, and mercaptans. Performance of HDS process is greatly influenced by the choice of catalyst, and the efficiency has been found to be high in case of second and third row elements in the periodic table, owing to their unique electronic and structural characteristics. Several bimetallic blended catalysts, including alumina supported NiMo,

NiW, CoW, CoMo, NiMo, and PtPd, have shown better catalytic activity in the past through highly selective and efficient hydrogenation [44,46–48]. In particular, nano-sized noble metals catalysts, including Pd, Pt, and Rh, have shown superior hydrogenation performance and high activities for deep hydrodesulfurization. However, their high susceptibility to sulfur poisoning due to the adsorption of H₂S on noble metals restricts their widespread usage [49,50]. Additional drawbacks of using noble metals in hydroprocessing catalysts have been summarized by Marafi and Furimsky that include deactivation by coke deposition, inhibition by sulfur and oxygenates, poisoning by nitrogen and chlorides, deposition of contaminant metals, agglomeration of active metals, and leaching of active metals [51]. Different modes of deactivation may take place simultaneously, and adverse efforts are made for catalyst recovery by regeneration. The issue of sulfur poisoning is overcome by using phosphides of noble metals (Rh₂P, Ru₂P, Pd₅P₂), by using transition metal phosphides (Co₂P, CoP, Ni₂P, MoP, WP), or by using acidic supports (Al-SBA-15) [49,50]. Among various supports, SBA-15 has been used widely as a hydrodesulfurization support. Bimetallic catalysts impregnated SBA-15 (CoMo-SBA-15, NiMo-SBA-15) have shown better thiophene conversion compared to γ -Al₂O₃ supported catalysts [52,53]. Some excellent reports and reviews are available on this topic and reveal that mesoporous silica frameworks, including SBA-15, MCM-41, MCM-48, and KIT-6, are promising HDS agents when they are incorporated with active species, such as WS₂, NiW, Ni_{2-x}M_xP (M = Co, Fe), MoS₂, and NiMoO₄, or with heteropolyacids, like H₃PW₁₂O₄₀, H₃PMo₁₂O₄₀, and (NH₄)₆Mo₇O₂₄·4H₂O [50,54–56]. Cost associated with HDS and stringent fuel specifications in recent times have motivated researchers to explore new innovative strategies.

3.2. Oxidative Desulfurization (ODS)

ODS has emerged as a promising desulfurization technology, owing to its mild operating conditions requiring ambient temperatures and atmospheric pressures, no H₂ prerequisites, and high efficiency towards the refractory thiophenic sulfides (DBTs). In a typical ODS process, oxidation of heavy sulfides takes place by incorporation of oxygen atoms at sulfur sites, without rupturing C–S bonds in the presence of judiciously selected oxidants, such as H₂O₂, O₃, NO₂, peroxy salts, or tertbutyl-H₂O₂. Out of these, H₂O₂ is the most widely used oxidant; however, in recent years, transition metal-based oxidizing agents (Re, Mo/W oxides, tungstophosphoric acid, MPcS and persulfates, tetra-amido macrocyclic ligands) have become popular and have been investigated in combination with hydrogen peroxide [57–60]. The success of an ODS process depends on the textural, structural, surface, and chemical properties of an active catalyst, combined with an appropriate oxidant. Other methods of oxidative desulfurization involve irradiation techniques, ultrasonic methods, direct photo-oxidation, and photocatalytic, electrocatalytic, and plasma techniques [44,61]. Oxidation is accompanied by liquid extraction to separate the oxidized components because of their enhanced polarities. The efficiency of extraction is influenced by solvent polarity, boiling point, and freezing point, as well as surface tension. In addition to common water-soluble polar solvents, ionic liquids are employed to extract S-compounds directly or after they have been oxidized. Recently, a combination of extractive and oxidative desulfurization called extractive catalytic oxidative desulfurization (ECODS) has gained recognition as a technique for producing ultra-low sulfur clean fuels, making use of ionic liquids as extractants and H₂O₂ as the oxidant, easily converting organosulfur compounds to sulfoxides and sulfones [62]. Issues associated with ODS, such as lack of oxidant selectivity, unwanted side reactions, undesirable residual S-containing aromatic moieties due to incorrect choice of extraction solvent, and high cost, are carefully weighed against the benefits linked with this process that cannot be achieved in conventional HDS process. For more information, we direct our readers to some new reviews that have appeared in literature focusing on ODS catalysts for clean environment, ODS of heavy oils with high sulfur contents, ODS using heteropolyacid-based catalysts, and ultrasound assisted ODS of hydrocarbon fuels [63–67].

3.3. Adsorptive Desulfurization (ADS)

There is a direct link between microporosity and adsorption capacity for efficient desulfurization. There has been a quest for materials with pores larger than 10 Å and adsorbents, such as zeolites, activated carbon, metal-organic frameworks (MOFs), aluminosilicates, and ZnO, have been tested for capturing and eliminating organosulfur compounds present in high value fuels. In addition to having excellent porosity, an ideal adsorbent has high available surface area, high selectivity, good surface chemistry, and recyclability for efficient removal of S-compounds. ADS can proceed through two main approaches: physical adsorption, a less energy intensive pathway where the S-based compounds are not chemically modified on separation; and reactive adsorption that offers benefits of both catalytic HDS and physisorption. A chemical reaction taking place between S-based moieties and solid adsorbent in the latter approach releases sulfur in the form of H₂S, Sox, or elemental S. For practical industrial applications, more studies and engineering at a molecular scale is required to adjust the size of host pores to match the guest size and to avoid any steric hindrance between guest molecules.

3.4. Biodesulfurization (BDS)

With advancement in biotechnology, green processing of fossil fuels has become possible, and microorganisms with an affinity for sulfur are playing an important role in metabolizing organosulfur compounds in fuels. This technology has potential to become cost effective and efficient. Microorganisms, such as *Pantoea agglomerans*, *Alcaligenes xylosoxidans*, *Rhodococcus erythropolis*, *Mycobacterium*, and thermophilic *Paenibacillus*, have been identified for aerobic BDS, while *Desulfovibrio desulfuricans*, *Desulfomicrobium scambium*, and *Desulfovibrio longreachii* have been for anaerobic BDS. Kirkwood et al. indicated in their studies that specificity for sulfur and metabolic pathways may not be dependent only on sulfur but, rather, on the type of species used [68–70]. Metabolism of organosulfur compounds and C–S bond cleavage by bacteria is suggested to proceed either through reduction of C–S bond and oxidation of C–S bond, or through oxidation of C–C bond (Kodama pathway) [71,72]. Although BDS has several advantages over conventional desulfurization processes, it can be uneconomical due to the additional cost associated with culturing the bacteria [73]. Other important drawbacks include phase change (fuel-aqueous phase) and stability of cells in the presence of fuel species.

3.5. Other Forms of Desulfurization

British Petroleum had developed and tested alkylation-based desulfurization on light oils, where acid catalysed aromatic alkylation is performed on thiophenic compounds with an aim to upgrade olefinic gasoline by increasing the molecular weight and boiling point of alkylated sulfur compounds, so that their separation becomes feasible [74]. Another simplified form of alkylation is S-alkylation, where thiophenic molecules are made to reaction with methyl iodide and fluoroborate salts of silver, leading to alkylated sulfonium salts which are precipitated and easily eliminated without distillation [75]. However, S-alkylation is not selective in these reagents, owing to their affinity to aromatic hydrocarbons, making this process challenging in carbon rich heavy oils.

C–S and S–S bonds can also be cleaved by chlorinolysis, where chlorine is able to bind at sulfur sites. This process takes place under moderate operating conditions (25–80 °C, atmospheric pressure) in fuels that can be easily homogenized with chlorine and which are corrosion resistant in the presence of chlorine. In order to remove impurities, additional steps comprising hydrolysis, oxidation of sulfur, and several aqueous and caustic washes are usually performed after chlorination.

Supercritical aqueous desulfurization or supercritical water desulfurization (SCW) has been shown to break C–S bonds in non-aromatic sulfur molecules through free radical pathway. However, some studies have shown that SCW independently cannot desulfurize fuels when not in the presence of H₂ and conventional HDS catalysts. There are indeed some benefits associated with SCW, such as increase in liquid yield, precipitation of sulfur saturated compounds, and H₂ generation through water

gas shift. To discuss further on industrially applicable methods for desulfurization is beyond the scope of this review; thus, for more information, we direct readers to some excellent reviews on this topic provided by Javadli et al. [61] and Srivastava et al. [44], as well as advances in biodesulfurization by Sadare et al. [73].

4. Mesoporous Silica and Mesoporous Silica Nanoparticles in Desulfurization

4.1. Photocatalytic MSs

Photocatalytic adsorption desulfurization (PADS) has emerged as a form of oxidative desulfurization method due to the low cost, high stability, and recyclability of photocatalytic materials [76,77]. Solar power is capable of exciting the photocatalysts and generating holes that are great oxidants. Certain aromatic sulfurous molecules, including DBT, DBTO (dibenzothiophene sulfoxide), and DBTO₂, can be oxidized in the presence of free radicals, such as •OH and •O₂⁻, and PADS is useful in deep desulfurization requirements. Recently, Zhou et al. reported on the use of mesoporous ZnO/TiO₂-SiO₂ (ZTS) as a photocatalyst and adsorbing material towards organic sulphides [78]. ZnO is known for its high photocatalytic activity and has a bandwidth of 3.2 eV (380 nm) [79]. Previous studies have shown that performance of ZnO can be enhanced dramatically in the presence of TiO₂ by inhibiting the recombination of electrons and holes, extending their lifetime and enlarging the photoresponse range [80]. Inspired by these findings, Zhou et al. implemented these studies for synthesising effective desulfurizing agents [78]. ZnO were chosen as active sites in the mesoporous TiO₂-SiO₂ catalyst, and the TiO₂-SiO₂ precursor materials were synthesized hydrothermally in the presence of triblock copolymer (P123) as a template, so as to tune the pore size. ZnO was incorporated using impregnation techniques, and the ratio of Si/Ti was adjusted in order to achieve optimized adsorption PADS capacity. The authors showed that ZTS-3 with Si/Ti = 3 exhibited the best photocatalytic desulfurization activity. The DBT conversion rate was found to be 97% in 4 h, and maximum adsorption of DBT over ZTS-3 was 47 mgS per gram of catalyst used and the adsorption rate was much higher than mesoporous TiO₂-SiO₂-40 (13.7 mg S/g-cat) [81]. The photocatalytic activity of ZTS was attributed to the heterojunction formed through the interactions of ZnO with TiO₂, leading to the expansion of sunlight absorption, enhancing the efficiency of charge separation, and inhibiting electron-hole recombination. Interestingly, this desulfurization could proceed without involving extra oxidants, such as hydrogen peroxide, O₂, or organic oxidants, making it a cost-effective process that exhibits high PADS performance and excellent adsorption capacity. As shown in Figure 1, the photocatalytic mechanism is suggested to proceed through the formation of •O₂⁻, which is capable of oxidizing DBT to DBTO₂ [78].

TiO₂ in varying structures and morphologies are among the most promising photocatalytic agents for different applications, such as fuel desulfurization and degradation of contaminants in various systems. In 2017, Meizhen et al. prepared a photocatalytic TiO₂-modified bimodal mesoporous silica structure (TiO₂/BMMS) and compared its desulfurization of dibenzothiophene efficiency to that of the mono-modal mesoporous (TiO₂/SBA-15) catalyst and pure TiO₂ [82]. They found that the photocatalytic activity and desulfurization efficiency of TiO₂/BMMS was the highest, achieving a desulfurization rate of 99.2%, followed by TiO₂/SBA-15 and then pure TiO₂. In 2014, Zaccariello et al. found that TiO₂ nanoparticles confined within mesoporous silica nanospheres exhibited enhanced photocatalytic activity due to the added adsorptive effects and thermal stability of the mesoporous silica nanospheres [83].

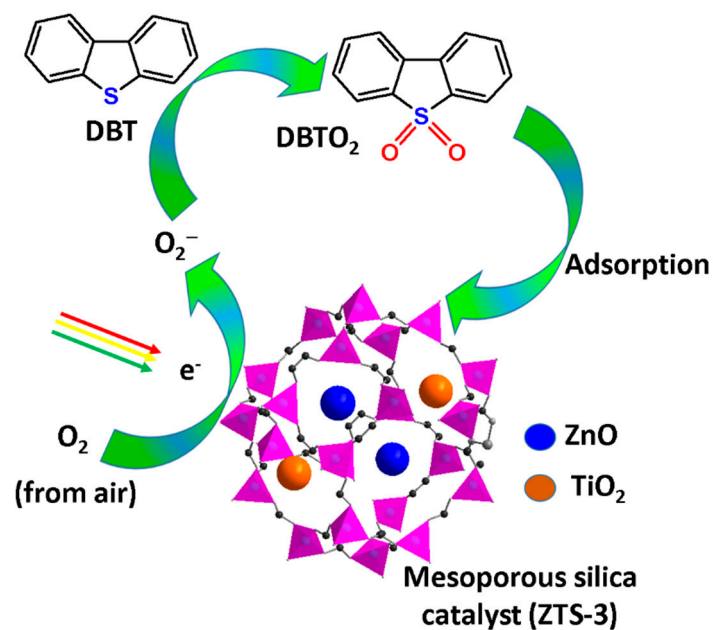


Figure 1. Photocatalytic desulfurization mechanism of ZnO/TiO₂-SiO₂ (ZTS-3) catalyst under solar light [78].

4.2. Redox Active MSNs

Conventional desulfurization strategies are associated with issues that hinder their implementation in desulfurization industry, and these problems include high concentration of oxidants, such as hydrogen peroxide, and elongated reaction times [84]. In order to overcome these issues, it becomes essential to formulate suitable catalysts for an eco-friendly and efficient oxidative desulfurization process. Polyoxometalates (POMs) belong to a category of transition metal-based oxygenated anionic clusters, which have emerged in recent years as promising materials for homogeneous oxidation desulfurization (HOD) process, owing to their unique structural and chemical characteristics and their redox potential. Advances in nanotechnology has made possible the immobilization of POMs onto solid supports, such as metal organic frameworks (MOFs), zeolites, porous carbons, and porous silica materials [85–88]. This addition not only imparts stability and reusability to the POMs but also enhances their catalytic activity towards refractory S-based molecules. Specially designed dendritic mesoporous silica nanospheres with center-radial oriented large mesopores were reported earlier by Zhao et al. as potential carriers or substrates for development of new functional materials [89,90]. Interestingly, Zhang et al. took advantage of the above materials to design a molybdenum-embedded dendritic mesoporous silica sphere using Stöber approach [91]. As shown in Figure 2, they introduced active molybdenum species with a concomitant use of ionic liquid (IL) as a metal source into the mesopores of dendritic silica spheres (DSSs). The DSSs featured large specific surface areas and high pore volumes and possessed a highly dispersed molybdenum species. The authors explored optimum synthetic conditions and characterized ODS products using gas chromatography–mass spectrometry GC-MS analysis. The judiciously designed catalyst showed rapid and high catalytic activity in oxidizing 4,6-DMDBT, and the catalyst could be easily separated from a heterogeneous mixture after fulfilling its role. Under optimal conditions, elimination of 4,6-DMDBT could reach 100% in 40 min, and a low dosage of oxidant was required. The recycling performance of the DSS revealed that they could be reused nine times without an appreciable decrease in catalytic activity [91].

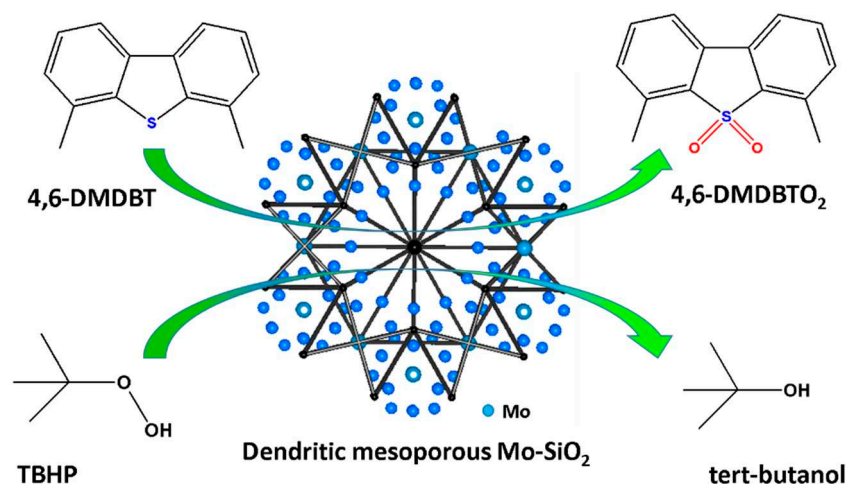


Figure 2. Schematic representation of dendritic mesoporous Mo-SiO₂ catalyst and its desulfurization mechanism [91].

Exemplary performance of monolacunary [PW₁₁O₃₉]⁷⁻ Keggin polyoxometalates in oxidative reactions [92–96] has inspired a few researchers to explore their performance in ODS process, too [97–99]. For example, Ribeiro et al. have worked extensively on Keggin-type materials, including PW₁₁ embedded on amine decorated SBA-15 (PW₁₁@aptSBA-15 and PW₁₁@tbaSBA-15), and on cationic tma functionalized mesoporous silica supports for the desulfurization of model and real diesels (Figure 3) [100]. Oxidative desulfurization studies on amine functionalized SBA-15 supports revealed high performance in case of PW₁₁@aptSBA-15, which could completely desulfurize simulated diesel in solvent-free conditions with half the oxidant amount (H₂O₂/S = 4), whereas it showed 83.4% efficiency in case of real unthread diesel (in a biphasic system, 1:1 diesel/acetonitrile) with a recycle capacity for eight consecutive cycles. Their recent work involved impregnation of PW₁₁ on cationic group (*N*-trimethoxysilypropyl-*N,N,N*-trimethylammonium, TMA) functionalized MS supports [101]. Here, two kinds of MS supports were selected (ordered MS, SBA-15, and an ethylene-bridged periodic mesoporous organosilica, PMOE) and two catalysts were prepared, PW₁₁@TMA-SBA-15 and PW₁₁@TMA-PMOE. Oxidative desulfurization was carried out on simulat diesel under biphasic (1:1 diesel/acetonitrile) and solvent-free conditions. A remarkable desulfurization performance was exhibited by the PW₁₁@TMA-SBA-15 catalyst, which could achieve ultra-low sulfur levels (<10 ppm) in both biphasic, as well as solvent-free conditions, and could be recycled six consecutive times without appreciable loss of catalytic activity. This promising catalyst was also tested on untreated real diesel provided by Spanish petroleum company, CEPSA (1335 ppm S) under biphasic system and demonstrated 90% desulfurization efficiency for 3 consecutive cycles [101].

Recently, Ribeiro et al. reported on zinc-incorporated polyoxotungstates [PW₁₁Zn(H₂O)₃₉]⁵⁻, PW₁₁Zn for ODS of real, as well as model, diesels, where active species were embedded in periodic mesoporous organosilicas (PMOs) composed of walls with ethane-bridges and benzene bridges [102]. These compounds showed high desulfurization efficiency under solvent-free conditions and in the presence of H₂O₂ with a H₂O₂/S ratio of 4, where ultra-low levels of sulfur could be obtained in just 1 h. PW₁₁Zn@aptPMOE catalyst was further investigated due to its robust nature for sulfur removal of real diesel, and an efficiency of 75.9% could be achieved after 2 h, and the catalyst could be reused.

A heteropolyacid-based adsorbent catalyst was reported by Yuzbashi et al. with an aim to decrease the leaching of active components and to increase the ODS kinetics of DBT present in model diesel fuel [59]. Phosphotungstic acid (HPW) was incorporated in a zirconium-modified hexagonal mesoporous silica (Zr-HMS) to give HPW/Zr-HMS catalyst, and its DBT removal ability was compared with Zr-HMS, HPW-HMS. Zr-HMS showed only 15% S-removal efficiency, whereas the efficiency of the two others was found to be similar; however, an efficiency of 99.4% was observed within 120 min when the composition of prepared catalyst was 20% HPW/Zr-HMS. An increase in the catalyst dosage

from 0.03 to 0.05 g drastically increased S-removal efficiency from 10% to 99.4%. In the presence of H_2O_2 , the model fuel was oxidized in less than 30 min and achieved an efficiency greater than 95% of the 350 ppm DBT. The formulated catalyst was recovered and was reused at least five times, and the leaching of HPW species was inhibited, indicating the promising nature of catalyst for ultra-deep desulfurization process [59].

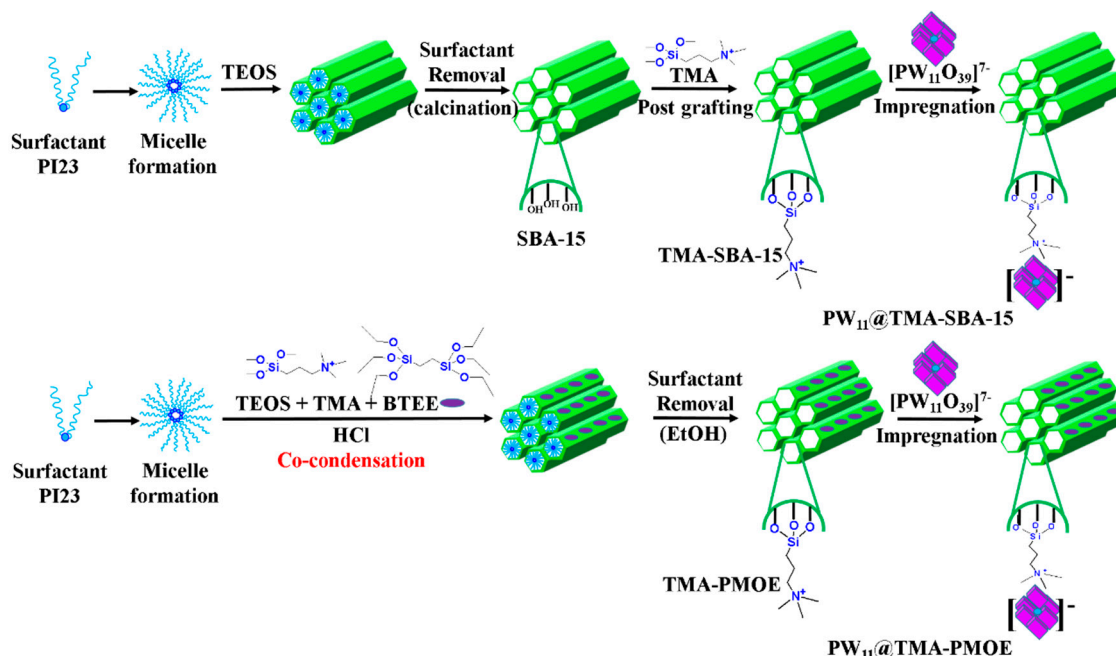


Figure 3. Synthetic strategy to prepare Keggin's polyoxometalate anion incorporated $PW_{11}@TMA-SBA-15$ and $PW_{11}@TMA-PMOE$ [101].

There have been cases where, instead of using heteropolyacids, silicotungstic acids have been used directly for the preparation of mesoporous tungsten-silica catalysts. For example, Shen et al. reported on the formation of disordered worm-like mesoporous silica catalysts with well dispersed tungsten species using nanocellulose as templates [24]. High surface area of the formed catalysts in the range of 344–535 m^2/g , their narrow pore size distributions (2 nm to 10 nm), and an optimum Si/W ratio supported high catalytic activity towards DBT and its elimination at 60 °C in just ten min. The catalytic activity towards S-compounds was found to increase in the following order: $BT < 4,6-DMDBT < BT$. GC-MS analysis of oxidized species showed that the catalyst formulations not only played their role as catalysts but also acted as efficient adsorbents. This catalyst could be recovered and be reused at least five times and still retain its desulfurization efficiency up to 94% [24]. The authors of this report had proposed a mechanism for the oxidation of DBT where the first step involves the adsorption of DBT in the pores of the catalysts, followed by its reaction with active peroxy-tungsten complex, which in turn is a direct consequence of reaction between tungsten species and H_2O_2 as oxidant. The interactions between DBT and peroxy-tungsten complex converts DBT to $DBTO_2$, which gets adsorbed in the mesopores of the catalyst, with the simultaneous reduction of peroxy-tungsten complex to tungsten oxide.

With advances in nanoscience, unique properties have been observed for particles with an average diameter lying in the range of 0.1 nm to 1.0 nm. This size range sets them apart from their nano counterparts, and some refer them as subnanoclusters [103,104]. A large number of catalysts are being developed using metal oxide subnanoclusters, and many materials have shown promising catalytic behavior for a large number of organic reactions. Along the same lines, the size of mesoporous silica materials is also decreasing, and new ultras-small MSNs (UMSNs) with particle size less than 25 nm are being developed in order to reduce mass transfer resistance and enhance the catalytic activity. Some

researchers, like Wang et al., reported on the synthesis of subnano-MoO₃ supported on ultrasmall MSN particles (~14 nm) with a peculiar “raisin-bun” structure, using reverse microemulsion technique (Figure 4a) [105]. This hybrid catalyst, subnano-MoO₃/ultrasmall MSN (UMSN), was then used for ODS of a model diesel comprising of benzothiophenes, where they were oxidized to DBTO₂ with a 100% efficiency within 15 min (Time of flight, TOF of ODS: 53.3/h) (Figure 4b) [106]. Percentage of catalyst, reaction time, and temperature influenced the DBT conversion; however, the percentage of oxidant did not play a significant role. Surprisingly, performance of nano-MoO₃/UMSN tested under similar operating conditions showed a DBT to DBTO₂ conversion of only 25.7% (TOF was 10.2/h), proving that subnano-MoO₃ was more active than nano-MoO₃. It is well known that smaller size generates high catalytic active sites with higher ratio of surface to bulk atoms; however, an 80% efficiency drop was attributed to the higher binding energy associated with subnano particles (1.1 eV higher than bulk), appearing as a result of lowered core-hole screening existing in small clusters. This indicates that electronic properties show significant variation with size and can show unusual response at subnano level.

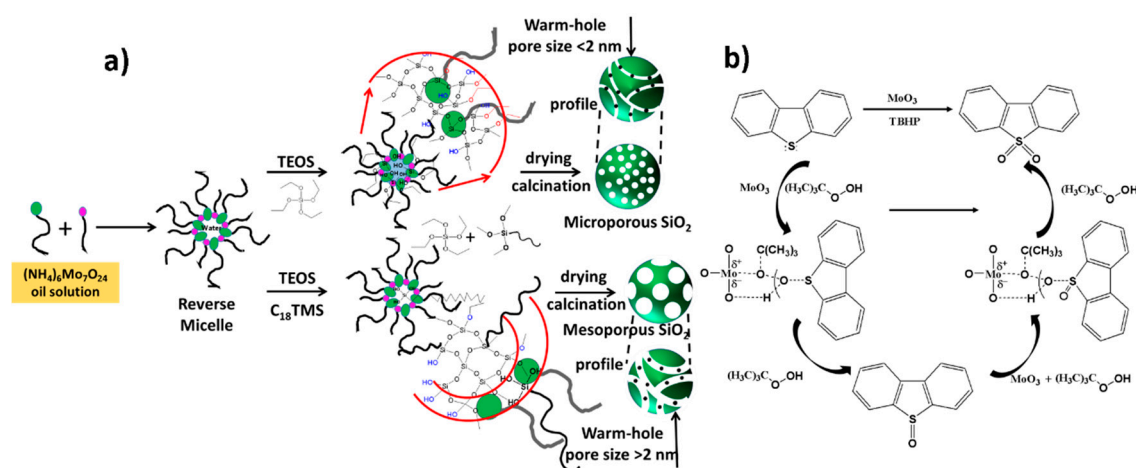


Figure 4. (a) Schematic representation for the formation of subnano-MoO₃/ultrasmall mesoporous silica nanoparticles (UMSN); (b) catalytic mechanism of MoO₃ catalyzing dibenzothiophene (DBT) oxidation in the presence of TBHP (tert-butyl hydro peroxide) [106].

Development of 1D silica fibers with diameters of about 50 nm or less and their transformation into materials with unique pore architectures, especially with pores aligned perpendicular to the direction of fibers, has become of paramount importance for materials scientists. Aiming to improve catalytic and sorption properties of silica materials, Dou and Zeng developed interconnected mesoporous silica nanowires with a 3D network having shallow wormhole channels aligned perpendicular to the axis of nanowires using a simple synthetic strategy, where TEOS hydrolysis took place under basic conditions (Figure 5) [107]. They explored synthetic parameters, including the effect of cosolvents, surfactants, alkalinity, duration of reaction, and optimum aging temperatures, to get an insight on the formation mechanism. α -MoO₃ species were immobilized on the interconnected mesoporous SiO₂ nanowires to form a Mo/mSiO₂ catalyst–adsorbent system and was examined in ODS of model diesels.

Although, in these studies, the diameter of Mo/mSiO₂ nanowires was significantly reduced and reached in the range of 10–20 nm, the authors were able to increase the final dimensions of the catalyst to a micron level, allowing easy recovery and separation after being used. The BET surface area of Mo/mSiO₂ reduced from 852 to 503 m²/g on increasing the Mo loading from 2 to 15%. The recipes containing 5 to 10% Mo showed highest conversions of DBT, owing to an optimum balance between total working catalyst and effective surface area. For a 10% Mo/mSiO₂ nanowire recipe, a DBT conversion efficiency remained as high as 95.4% in the first 30 min, even after seven cycles, and the sulfur concentration was 33 ppm after the seventh run.

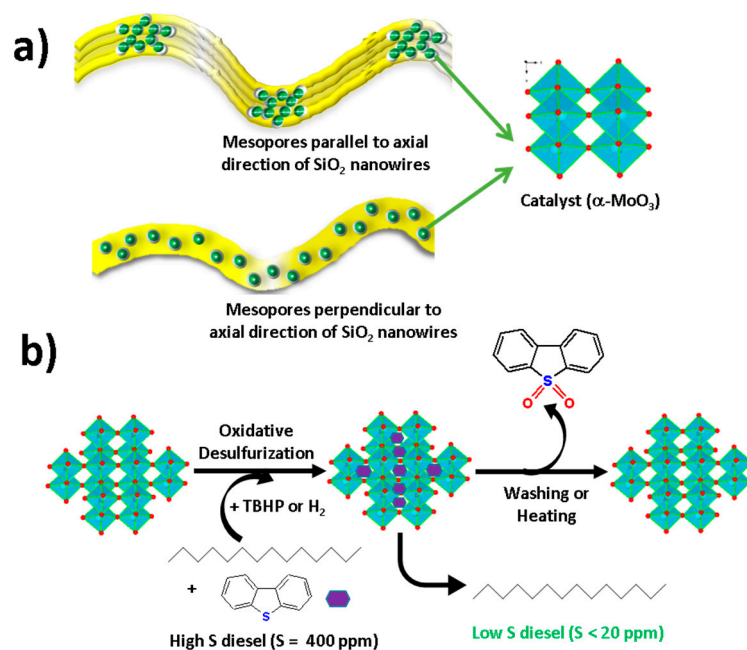


Figure 5. (a) Structure of mesoporous silica nanowires with mesopores aligned parallel or aligned perpendicular to the axial direction of nanowires; (b) desulfurization mechanism showing reaction of DBT unit with catalytic species and removal of DBTO₂ molecules after oxidation [107].

4.3. Ionic Liquid MSN Catalysts

Ionic liquids (ILs) have emerged in the past few years as green solvents and catalysts, thanks to their unique properties that include high thermal stability, feasible design, and synthesis, as well as a wide liquid range [108]. These features allow dissolution of several catalysts in the ionic liquids providing a biphasic liquid system beneficial not only in esterification [109] and fructose dehydration [110] but also in oxidation of sulphides [111,112]. However, necessity for large amounts of ILs and difficult catalyst recovery makes it challenging to apply them in wide range of organic reactions, except when these ILs can be heterogenized. Therefore, many attempts have been exerted towards fabrication of “supported ionic liquid catalysts” (SILCs) that can immobilize homogeneous ILs on appropriate host materials, which can range from silica-based materials and MOFs to carbon nanotubes [113–118]. Advantages associated with use of mesoporous silica have compelled researchers to use impregnation and grafting methods to prepare SILCs, but these efforts are accompanied by other issues, like reduction in surface area of supports, leaching of active components, or confinement in the degree of freedom of ILs [119,120]. These limitations can be overcome by incorporation of functionalized ILs in the grafting matrix, by performing one pot hydrothermal synthesis in architectural supports, and by removing templates in subsequent reactions [121–123]. In our opinion, it is worth discussing examples where ionic liquids have been immobilized on mesoporous silica materials to be used for desulfurization process.

A few years ago, Gu et al. reported on the synthesis of hybrid mesoporous silica material using task-specific ionic liquid (TSIL) templating strategy, where POM-based IL [(n-C₈H₁₇)₃-NCH₃]₂ [W₂O₃(O₂)₄] (termed as T₈W₂O₁₁) was used as template [124]. The authors blended the amphiphilic T₈W₂O₁₁ with silicate source tetraethyl orthosilicate (TEOS). Silicate condensation lead to the entrapment of T₈W₂O₁₁ species, and subsequent calcination eliminated the organic cations, leaving behind a functionalized mesoporous silica framework. Catalytic activity of the resulting product was tested in oxidative desulfurization process, where 99.6% efficiency was observed in the case of DBT sulfur removal using low catalyst dose and without using organic solvents. The efficiency of catalytic oxidation of organosulfur compounds decreased in the following order: DT > 4,6-DMDBT > DBT > BT. The efficiency of the catalyst could be retained, even after recycling eight times [124].

This work was followed by Zhang et al., who reported encapsulation of polyoxometalate-based ILs with the formula $[C_x\text{mim}]_3\text{PW}_{12}\text{O}_{40}$ ($C_x\text{-IL}$, $x = 4, 8, \text{ and } 16$) into the pores of ordered mesoporous silica through a one-pot hydrothermal reaction (Figure 6a) [125]. The as-prepared catalytic material ($C_x\text{-IL@OMS}$) was systematically characterized using multiple chemical and physical techniques, proving its high specific surface area and uniform dispersion in silica supports. These catalysts were employed in the desulfurization of organosulfur compounds, and $[C_4\text{mim}]_3\text{PW}_{12}\text{O}_{40}\text{@OMS}$ was a winner among the series (Figure 6b). It showed high catalytic activity, high stability, and could be recycled multiple times. When compared with other IL@OMS , catalytic oxidation of DBT decreased in the following order: $C_4\text{-IL@OMS}$ (99.5%) > $C_8\text{-IL@OMS}$ (76.7%) > $C_{16}\text{-IL@OMS}$ (30.5%). High performance of $C_4\text{-IL@OMS}$ could be ascribed to its large surface area providing highly exposed active sites for oxidation of DBT and short IL chain imparting low steric hindrance and enough platform for peroxide species to interact with DBT molecule. Interestingly, catalytic oxidative desulfurization efficiency of pure $C_4\text{-IL}$ (S removal:12.7%) was much lower in comparison with $C_4\text{-IL@OMS}$ (S removal:99.5%). Additionally, even after recycling seven times, the removed sulfur in case of $C_4\text{-IL@OMS}$ exhibited an impressive 93% efficiency [125].

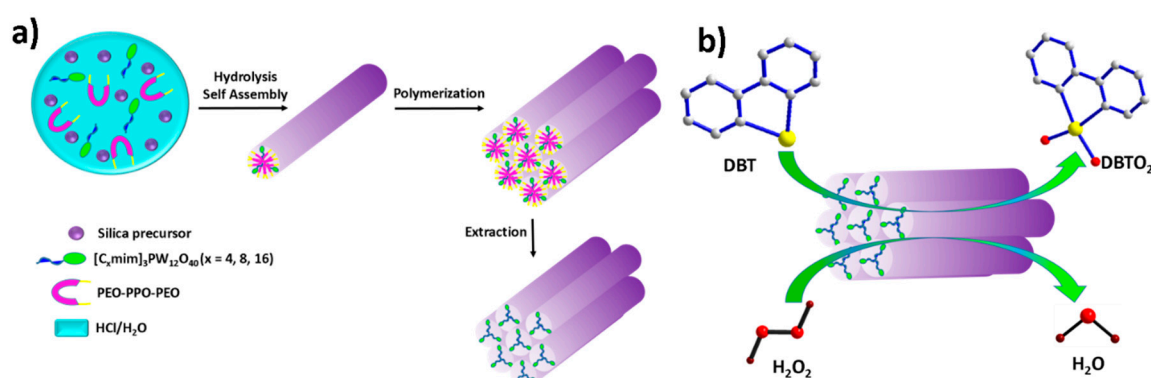


Figure 6. (a) Fabrication of ordered mesoporous silica encapsulating polyoxometalates (POMs)-based ionic liquids (IL); (b) possible desulfurization mechanism for the oxidation of DBT to DBTO_2 with concomitant transformation of hydrogen peroxide to water [125].

Prior studies have also shown lanthanide-based POM clusters $\text{Na}_7\text{H}_2\text{LaW}_{10}\text{O}_{36}\cdot 32\text{H}_2\text{O}$ (LaW_{10}) as promising catalysts for ECODS process [126,127]. However, new materials are required to make ECODS more efficient and highly selective in terms catalyst separation, recovery, and reusability. As shown in Figure 7, Chen and Song impregnated LaW_{10} on dihydroimidazolium (ionic liquid) modified mesoporous silica supports, forming $\text{LaW}_{10}/\text{IL-SiO}_2$ [128]. The new catalyst exhibited deep desulfurization of several organosulfur compounds, including DBT, BT, and 4,6-DMBT, under mild operating conditions and in less than 30 min.

Ultra-deep desulfurization (<100 ppm) could be achieved for DBT in just 1 min for small batches, whereas scaled-up studies (1 litre model oil with S content of 1000 ppm) showed 100% sulfur removal in 25 min and at 70 °C. Additionally, the process was cost-effective as reusability of catalyst did not require simultaneous use of ionic liquid each time, recovery of $\text{LaW}_{10}/\text{IL-SiO}_2$ catalyst was easy, and it could be reused at least ten times without degrading its efficiency, making it a promising material for ultra-low sulfur fuels [128].

Although some mesoporous silicas, such as MCM-41 and SBA-15, possess uniform pore size and a large internal surface area, their small pore size at times can lead to blocking and collapsing of pores during the desulfurization process, eventually giving poor recycling performance. In order to overcome these challenges, three-dimensional ordered macroporous (3DOM) materials with well-connected pores, large pore size sufficient to catalyze most fuel related organosulfur compounds, better mass transfer properties, and high surface areas are being developed [129,130]. Silica-based meso-macroporous materials ($\text{H}_3\text{PW}_{12}\text{O}_{40}/\text{SiO}_2$) synthesized via polystyrene colloidal crystal template

and using evaporation-induced self-assembly (EISA) have been reported by Lei et al. and applied in the ODS process [131,132]. In both cases, hierarchically meso/macroporous catalysts exhibit superior catalytic activity than their purely mesoporous and macroporous counterparts. This enhanced performance can be attributed to the larger mesoporous specific surface area, peculiar hierarchically meso/macrochannels structural characteristics and shorter length of mesoporous channels that facilitate mass transfer of precursors and products. Recently, Chen et al. reported on a POM-based ionic liquid supported 3DOM silica (IL-3DOM SiO₂) as a catalyst for heterogeneous oxidative desulfurization [58]. The catalyst exhibited high porosity, as well as, a high specific surface area. This catalyst was prepared using the colloidal crystal template assembled from polymethylmethacrylate (PMMA), having a mean diameter of approximately 240 nm. The 3D crosslinked structure of catalyst allows guest diffusion, capture, and exposure of the active species. Sulfur removal efficiency of an IL-3DOM SiO₂ catalyst in the absence of H₂O₂ was only 5.7%, while it was 100% in its presence, indicating the ability of 3D crosslinked structure to effectively adsorb organo sulfur molecules and essential presence of tungsten-based IL to activate H₂O₂ to oxidize S-compounds. The desulfurization performance of IL-3DOM SiO₂ catalyst decreased in the following order: 4-MDBT > DBT > 4,6-DMDBT > 3-MBT > BT. Additionally, even after recycling 17 times, the sulfur removal efficiency could still reach 94% in the absence of a regeneration process [58]. The mechanism of DBT desulfurization by IL-3DOM SiO₂ is shown to proceed, firstly via adsorption of DBT in the macropores and then its reaction with peroxy species formed in turn from the combination of POM-IL with H₂O₂. Subsequent steps involve the oxidation of DBT to the corresponding sulfones (DBTO₂), their precipitation, and presence in the catalyst phase. Towards the end of cycle, the peroxy species convert into active species, which further combine with H₂O₂, forming species for the next cycle [58].

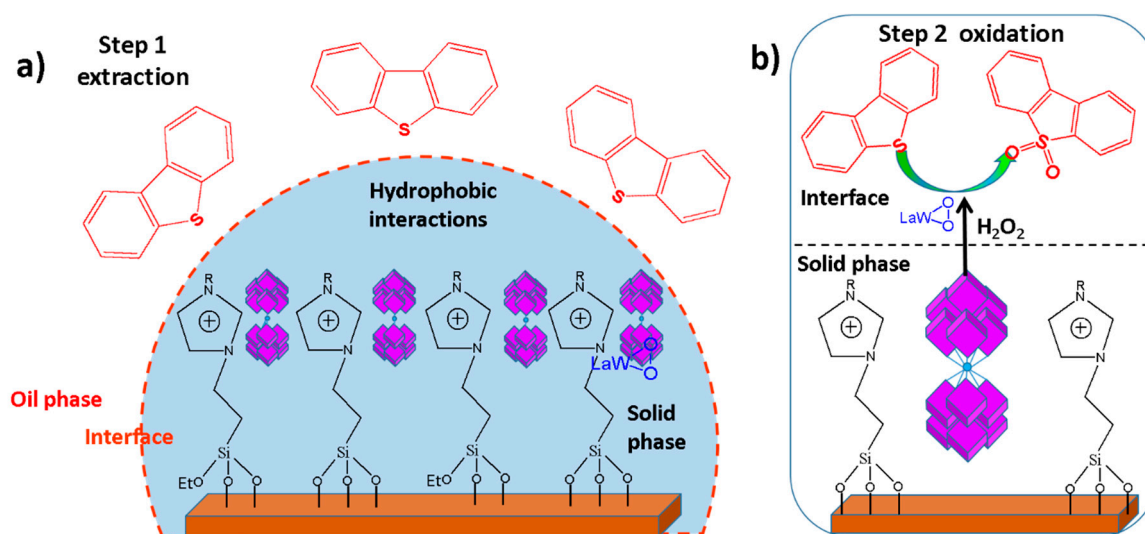


Figure 7. Schematic illustration for the highly selective and efficient removal of sulfur species using LaW₁₀/IL-SiO₂ nanocomposites. (a) Extraction of the substrate by ionic liquid, (b) catalytic oxidation of DBT to DBTO₂ by LaW₁₀ in the presence of H₂O₂ (R = -C₈H₁₇) [128].

Compared to conventional mesoporous silicas, such as MCM-41 or SBA-15, the reports on the corresponding nanoparticles as adsorbents for desulfurization are very limited. Last year, Mirante et al. reported on composite materials prepared through the immobilization of Keggin polyoxomolybdate [PMo₁₂O₄₀]³⁻ anion on MCM-48 type mesoporous silica nanoparticles functionalized with surface-tethered tributylammonium (TBA) groups [133]. The composite catalyst PMo₁₂@TBA-MSN had high stability and was highly efficient in the oxidative desulfurization (ECODS) of a diesel simulant in the presence of H₂O₂ (oxidant) and [BMIM]PF₆ (IL and solvent). The shorter channels of MSNs and cubic mesoporous framework of MCM-48 nanoparticles with branched networks seem to allow mass transfer in comparison to conventional porous silica materials with unidirectional

structures. The ECODS studies were carried out on a model diesel composed of BT, DBT, 4-MDBT, and 4,6-DMBT in n-octane with a total sulfur content of 2016 ppm. For the first ECODS cycle, the efficiency of $\text{PMo}_{12}@TBA\text{-MSN}$ was high and comparable to the homogeneous catalyst PMo_{12} , where desulfurization could be achieved in 2 h. However, PMo_{12} could not be reused in the subsequent cycles, while the hybrid catalyst $\text{PMo}_{12}@TBA\text{-MSN}$ exhibited higher stability and could be reused, along with ionic liquid, several times. The impregnation of PMo_{12} on MSNs proved to be beneficial in enhancing the stability of polyoxomolybdate and in obtaining not only a robust and effective catalyst but also a recyclable material [133].

In comparison to polyoxometalates (POMs), Keggin-type heteropolyacids (HPAs) have shown high catalytic activity for oxidation studies, owing to their high chemical resistance and mechanical robustness, making them suitable for desulfurization reactions as mentioned earlier, when they were combined with meso/macroporous silica [58]. Heteropolyacids have octahedral MO_6 units, and their lowest unoccupied molecular orbitals (LUMO) are mainly the non-bonding metal orbitals, allowing easy participation in redox reactions [134,135]. A heterogeneous catalyst (HPMo-IL/SBA-15) was reported by Xiong et al. via impregnation of phosphomolybdic acid on the IL functionalized SBA-15 and used for the ODS process [136]. The hydrophilicity of SBA-15 was conquered by functionalization with imidazole-based IL, and the heterogeneous HPMo-IL/SBA-15 catalyst exhibited good wettability for the model oil while providing sufficient active sites for the access of organosulfur compounds. The catalytic system involved the use of H_2O_2 with a H_2O_2 /sulfur mole ratio of 2, which is much less in comparison to other desulfurization systems, and, in the presence of 0.05HPMo-IL/SBA-15, a S-removal efficiency of 90% could be achieved. High catalytic performance of HPMo-IL/SBA-15 is attributed to its (a) high surface area and good IL dispersion; (b) uniform pore channels allowing efficient mass transfer; and (c) high wettability towards model oil [136].

4.4. Magnetic MS Catalysts

Catalytic materials synthesized using surface molecular imprinting techniques have shown promise for deep desulfurization reactions. Surface imprinted polymers are beneficial in terms of high guest inclusion rates, reduced mass transport resistance, rapid adsorption kinetics, and feasible template extraction. Additionally, as far as complex fuel samples are concerned, magnetic separation can help to separate impurities and purify the process by adsorption of organosulfur compounds on magnetic catalysts. If molecular imprinted polymers (MIPs) are embedded with magnetic nanoparticles or porous materials doped with magnetic nanoparticles, these adsorbents can be separated in the presence of applied magnetic field [137,138]. Few researchers, including Li et al. and Men et al., have applied this strategy to prepare surface imprinted core-shell magnetic beads and magnetic MIPs for the adsorption of template molecules and their separation from the matrix [139,140]. However, there are only few reports of this strategy used for desulfurization of fuels. With an aim to develop efficient materials for deep-desulfurization of fuels, Wang et al. reported on the synthesis of molecularly imprinted polymer (MIP) coated magnetic mesoporous silica, $\text{Fe}_3\text{O}_4@m\text{SiO}_2@DT\text{-MIP}$, using double-template strategy for desulfurization of DBT and 4-MDBT in model and real gasoline fuels (Figure 8) [141]. The adsorption studies revealed that $\text{Fe}_3\text{O}_4@m\text{SiO}_2@DT\text{-MIP}$ followed pseudo-second-order kinetics in the case of DBT and 4-MDBT, with an adsorption amount of 104.2 mg g^{-1} for DBT, whereas it showed an amount of 113.6 mg g^{-1} towards 4-MDBT, respectively. When the performance of molecular imprinted polymer was compared with non-imprinted polymer (NIP), it revealed that $\text{Fe}_3\text{O}_4@m\text{SiO}_2@DT\text{-MIP}$ had higher binding ability and significant recognition capacity for DBT and 4-MDBT, and it could be regenerated and reused at least eight times more than $\text{Fe}_3\text{O}_4@m\text{SiO}_2@NIP$. When adsorption experiments were carried out on real fuel (92#gasoline), $\text{Fe}_3\text{O}_4@m\text{SiO}_2@DT\text{-MIP}$ catalyst was able to reduce the amounts of DBT and 4-MDBT by at least by 69% [141].

The catalytic activity of materials is of prime importance in biphasic reaction of oil and water and most hydrophilic catalysts can be hindered on interactions with hydrophobic aromatic sulfur compounds. Ionic liquids can come to rescue in these situations by providing active sites and also

making the carriers hydrophobic. An ideal ionic liquid has optimum length of carbon chain which does not cause steric hindrance and easy leaching of active species. Inspired by the superhydrophobic lotus leaves, it can be concluded that rough surfaces on carriers can change their wettability, and Zhao et al. demonstrated this by synthesizing core-shell mesoporous silica structures which had cauliflower mimicking morphology [142]. These materials were modified using kinetic-controlled interface co-assembly to produce magnetic mesoporous microspheres (MMSs) which acted as supports for POM-based short chain ionic liquids ($[(C_4H_9)_3NCH_3]_3PMO_{12}O_{40}$). The contact angle measurements substantiated the wettability of these materials and their desulfurization capacity, which in turn could be regulated by their surface morphology. The catalyst, $[(C_4H_9)_3NCH_3]_3PMO_{12}O_{40}/RS-MMS$ was used for the ODS of diesel in the presence of H_2O_2 as an oxidant and showed highest catalytic activity towards most refractory sulfur compounds.

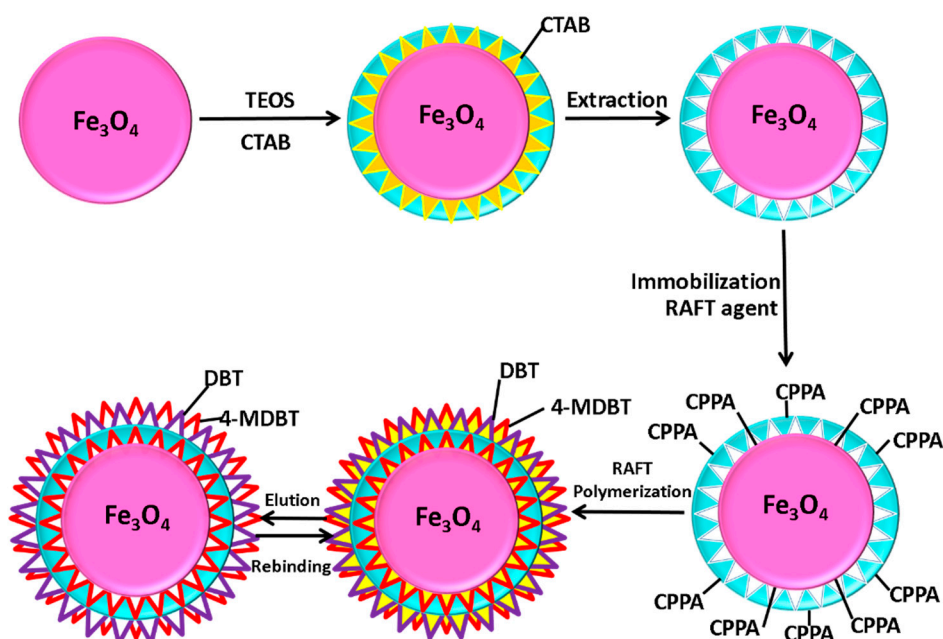


Figure 8. Schematic illustration for the preparation of functionalized magnetic mesoporous silica ($Fe_3O_4@mSiO_2@DT-MIP$) covered with double template molecular imprinted polymer (MIP) [141].

A model oil consisting of 4,6-DMDBT as a representative was chosen to investigate the desulfurization efficiency of POM incorporating IL and IL/RS-MMS, and the results revealed that IL showed only 16.3% sulfur removal efficiency, whereas IL/RS-MMS showed 98.3% sulfur removal efficiency at equal time intervals and the same temperatures, which may be attributed to high surface area and better dispersion of active components in IL/RS-MMS catalyst. Sulfur removal followed the order: $DBT > 4-MDBT > 4,6-DMDBT$, and the effect of ODS reaction temperature for 4,6-DMDBT by IL/RS-MMS revealed an increase in desulfurization efficiency from 41.1% at 40 °C to 98.3% at 60 °C and a reduction in sulfur concentration in model oil to as low as 3.4 mg kg^{-1} . When ODS activity of smooth surface (SS) catalysts were compared to those with superhydrophobic rough surfaces, only the catalysts with suitable amphiphilicity displayed good catalytic activity. The recyclability of ODS of 4,6-DMDBT using a IL/RS-MMS catalyst showed that the catalyst could be recovered and be reused at least five times [143].

There have been reports on using triblock copolymer templating strategy to synthesize 2D-hexagonal mesoporous silica structures under acidic conditions [26]. Recently, this method has also been used to create POM-IL-incorporated mesoporous silica nanocomposites (PMS) for desulfurization of fuels. For example, Zhang et al. used triblock copolymer P123, PMO-based IL ($[C_{16}mim]_3PMO_{12}O_{40}$), and TEOS to synthesize PMS, which was further impregnated with iron oxide nanoparticles using an equivalent-volumetric ultrasonic impregnation method to form magnetic PMS

(MPMS) [26]. The catalysts were used desulfurize and remove multiple refractory sulfur compounds (BT, 3-MBT, DBT, 4-MDBT, 4,6-DMDBT) and showed double-edged influence due to iron oxide, where the catalysts were superparamagnetic and were easily attracted by external magnets, laying the platform for magnetic fixation in the recovery steps. In particular, the 0.5-MPMS recipe exhibited excellent catalytic activity, and the desulfurization performance displayed the following order: DBT > 4-MDBT > 3-MBT > 4,6-DMDBT > BT. Furthermore, using this recipe, a desulfurization efficiency of 94% could be achieved, even after ten cycles, making it, so far, the highest recycled compound and a potential candidate for industrial applications [26].

4.5. Spinel Embedded Silicoaluminophosphate Catalysts

Spinel phase oxides with the formula AB_2O_4 (A and B are metals) are known for their high stability and diverse framework architectures. In particular, Zn-based spinel adsorbents (ZnB_2O_4) with periodical $[B_4O_4]^{4-}$ cubical secondary building units have been reported to considerably subdue vaporization of zinc atoms during hot gas desulfurization when temperatures of the reactors were $<600\text{ }^\circ\text{C}$ and demonstrates the synergistic effects of ZnO as B_2O_3 units on reaction with H_2S in desulfurization steps [144–146]. Additionally, zeolites are high porosity green materials that can prevent sintering of active guest species and have been used in multiple applications, including ion exchange, catalysis, and gas adsorption [147–151]. Silicoaluminophosphates (SAPO) belong to a series of crystalline zeolites, which contain repeating tetrahedral AlO_4 and SiO_4 units creating well-defined channels and microporous cavities and have received recent attention in desulfurization process. For example, this year, Liu et al. reported on the fabrication of SAPO-34 zeolites embedded with Zn-based spinels with the formula $ZnB_xB'_{2-x}O_4$ ($B = Co, Mn, Fe; x = 0-2$) with an aim for H_2S removal from simulated coal gas (Figure 9) [152]. The authors prepared SAPO-34@SBA-15 (SS), SAPO-34@ZSM-5 (SZ), SAPO-34-P123 (SP123), and SAPO-34-PAA (S-PAA) as solid supports for spinel inclusion. SS had a BET surface area of $323\text{ m}^2/\text{g}$ and was used as a representative for multiple examinations. Lattice substitution in B-sites of Zn spinels indicated the stability of $ZnCo_2/SS$ structure and efficiency in desulfurization process with a high breakthrough S capacity of 138.08 mg/g when compared to other supports impregnated with Fe or Mn. The best recipe for effective desulfurization was found to be 50 wt% $ZnCo_2/SS$ with a reaction proceeded at $550\text{ }^\circ\text{C}$. With successive regeneration of catalyst, the breakthrough S capacity decreased from 138.08 to 118.69 mg/g , owing to the evaporation of Zn species, generation of highly stable sulfides (ZnS and Co_9S_8), and partial sintering of the catalyst [152].

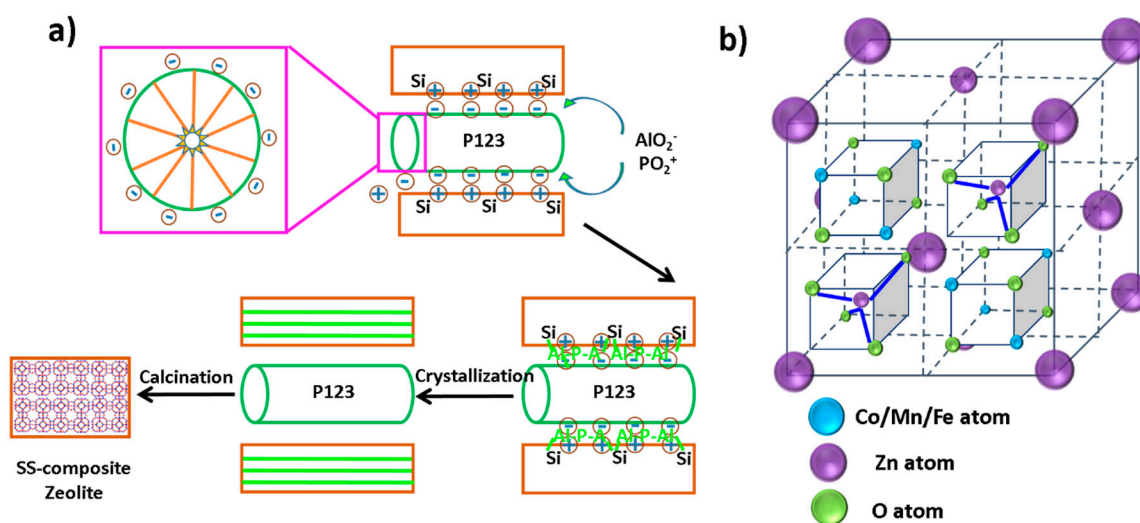


Figure 9. Schematic illustration of (a) synthesis of silicoaluminophosphates (SAPO)-34@as-synthesized SBA-15 (silica sphere (SS) composite zeolite) using triblock copolymer (P123) templates; (b) $ZnCo_2O_4$ structure [152].

4.6. MSN-Carbon Composites

In addition to mesoporous silica usage, hydrophobic carbonaceous materials can play an important role in desulfurization due to their high adsorption capacity, high specific surface areas and feasible recovery. Moreover, the wide abundance of carbon materials from biomass to rubber tires makes them low cost adsorbents [153,154]. Combination of catalytic metal sites on carbonaceous materials embedded on mesoporous silica supports can provide a synergistic effect to the materials for adsorption desulfurization (ADS); however, only a few reports exist in literature on this topic. Recently, Liu et al. reported on the synthesis of monodispersed dendritic mesoporous silica/carbon nanospheres (DMS/CNs) impregnated with Ag ions and used them as sorbents for selective desulfurization of DBT (Figure 10). AgNO_3 was included in the catalyst through wet impregnation and thermal dispersion techniques. Adsorption dynamics simulation studies indicated that the adsorption rate increased with an increase in the carbon content of DMS/CNs and with a decrease in the particle size of the catalyst, whereas Ag impregnation improved the efficiency of desulfurization, owing to the sulfur and Ag interactions and formation of S–Ag bonds and π -complexation with thiophene rings present in DBT. When compared to non-impregnated S-100-HC (adsorption capacity, 4.02 mg S/g (no toluene), 2.71 mg S/g (toluene)), Ag/S-100-HC was a promising candidate giving an equilibrium adsorption capacity of 6.88 mg S/g without using toluene and 4.22 mg S/g in the presence of toluene. Its enhanced sulfur selectivity could be attributed to its ordered dendritic mesoporous silica/carbon nature with large center-radial mesoporous channels, providing easy access to active metal sites and a synergistic effect between carbonaceous species and embedded silver ions [155].

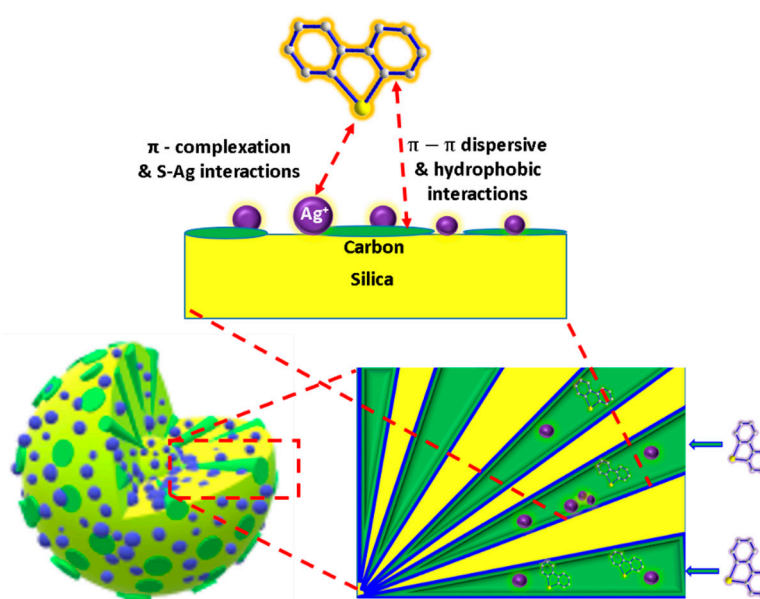


Figure 10. Schematic representation of the synergistic effect of DBT adsorption on doped carbonaceous mesoporous silica supports, Ag/dendritic mesoporous silica/carbon nanosphere (DMS/CN) structure [155].

4.7. Silica Gels

High porosity, low cost, and wide availability of silica gels compared to well-ordered MS frameworks have also motivated researchers to explore these materials for desulfurization of fuels. Although few in number, some interesting examples exist in literature where efficiency of silica gel has been explored. For example, Song and co-workers reported on desulfurization of diesel fuel using silica gel impregnated with 5.0 wt% of undisclosed metal species, and a reduction in S content was demonstrated using GC chromatographic analysis by studying the composition of fuel before and after treatment [156]. The authors claimed that JP-8 fuel was used in further studies, and similar results

were obtained. Molecular orbital calculations were performed on sulfur rich species, like thiophene, BT, and DBT, and they revealed the presence of HOMO (highest occupied molecular orbital) on sulfur atoms. These studies indicate direct interactions of HOMO orbitals with the LUMO (lowest unoccupied molecular orbital), belonging to the active species present in silica gel, are responsible for selective elimination of sulfur rich molecules in fuel. Wang et al. reported on Ni-heteropolyacids supported on silica gel and used them for removal of thiophene, alkyl thiophene, BT, and DBT under Ultrasound and Ultraviolet irradiation conditions [157]. Soon after this report, Zheng et al. reported on the entrapment of polyoxometalate precursor ($[C_{16}H_{33}(CH_3)_2NOH]_3[PO_4[WO(O_2)_2]_4]$) in the channels of silica gel and used this heterogenous catalyst to oxidize DBT in the presence of hydrogen peroxide [158]. A few years ago, Xun et al. reported on ionic liquid catalysts ($[Bmim]FeCl_4$) embedded in silica gel, and various conditions were investigated for the removal of DBT using the catalytic oxidative desulfurization process, where the desulfurization efficiency was over 90%, even after recycling the catalyst six times [159]. This study marked a new era for the emergence of ionic liquid supported silica gels and interesting examples were reported by Zhao et al. and Safa et al. The former study reported on using ether functionalized ionic liquid/silica gel catalysts to adsorb SO_2 and the adsorption capacities ranged from 2.621 mol of SO_2 /mol for $[C_3O_1Mim][H_3CSO_3]$ to 3.453 mol of SO_2 /mol for $[C_7O_3Mim][H_3CSO_3]$, indicating an increase in adsorption capacity with elongation in chain length of the cation [160]. The latter study reported on using 1-octyl-3-methylimidazolium hydrogen sulfate ($[Omim][HSO_4]$) in the silica-gel matrix for ODS of a model oil composed of DBT and real diesel fuel. The highest DBT removal efficiency of 99.1% was achieved when 17 wt% of ionic liquid embedded catalyst was used, and 75.7% S-removal efficiency was observed in case of desulfurization of the hydrotreated real diesel fuel [161].

5. MS Frameworks and Nanomaterials in Desulfurization of JP-8 and JP-5 Aviation Fuel

Fossil fuels are not only used in combustion engines but also as a source of hydrogen for solid-oxide fuel cells (SOFCs) to be used in vehicles, stationary power generators, or military purpose silent watch units [162]. JP-8 jet fuel is a popular fuel for military applications, where it not only functions as a hydrogen source for SOFCs but also to power the aircrafts, and it is used a fuel for heaters, stoves, and tanks. An ideal fuel should be widely available, hydrogen rich, and potentially safe to transport and stock [163]. However, presence of high content of sulfurous compounds in JP-8 fuel poison the anodes of SOFCs and cylinder heads and exhaust valves in supercharged diesel engines. Lifetime of SOFCs can be enhanced with the use of JP-8 fuel with a concentration of <1ppmWS. Deep desulfurization of lighter fuels, such as gasoline, is usually carried out using hydrodesulfurization (HDS) [162,164]. However, several issues associated with HDS, including demanding operating conditions, requiring high temperatures and elevated pressures; non-selective hydrogenation; inefficiency for less reactive aromatic sulfur compounds (DMBT, TMBT); and low octane levels, call for new methods of desulfurization that are low cost and less energy intensive [165].

Mesoporous hierarchical MCM-41 or SBA-15 frameworks embedded with metallic active species and even metal oxides have been investigated in the past for adsorptive desulfurization of JP-5 aviation fuel. MCM-41 and SBA-15 were impregnated with Cu^+ and Pd^{2+} ions by heating at 550 °C followed by spontaneous dispersion of monolayers. Under such synthetic conditions, the formed $CuCl$ or $PdCl_2$ coatings get homogenized with supporting frameworks [166]. The performance of $Pd^{2+}/MCM-41$ was found to be better than $Cu^+/MCM-41$ towards JP-5 as the breakthrough S capacity was 10.9 mg S/g for the former composite, while it was 7.7 mg S/g for the latter composite, and the saturation capacity of Pd^{2+} composite was 16.0 mg S/g and 14.4 mg S/g for the Cu^+ composite. High desulfurization performance and better selectivity of Pd^{2+} composite can be attributed to its strong π interactions with the aromatic organosulfur compounds than Cu^+ . Interestingly, breakthrough capacity of $Pd^{2+}/SBA-15$ (32.1 mg S/g) composites were much higher than the MCM-41 composites (10.9 mg S/g), even when the impregnation had 16% less Pd^{2+} in the former composites, and this higher performance can be correlated to the higher porosity and large pore size of SBA-15 compared to MCM-41 [166].

This work was followed by exploration of cuprous oxide impregnated mesoporous silica materials (MCM-41 and SBA-15) for ADS; however, the results contradicted with the previous work and claimed that large pore size and volume of SBA-15 was not beneficial [166]. Here, MCM-41 with a specific surface area of 523 m²/g outperformed as an adsorbent in comparison to SBA-15 with a lower surface area (400 m²/g) [167]. In these studies, a higher reduction temperature (700 °C) was perceived to be better in converting active species to Cu₂O, leading to a greater adsorption capacity in case of MCM composite (12.8 mg S/g) compared to SBA-15 composite (9.6 mg S/g). The results also indicate that free transition metal ions exhibit higher performance in terms of saturation capacity and breakthrough capacity when compared to transition metal oxides. The saturation capacity of Cu⁺/SBA-15 was thrice that of Cu₂O/SBA-15, and its breakthrough capacity was four times that of Cu₂O/SBA-15. However, metal oxides could be regenerated more successfully in comparison to free metal ions due to their higher stability and strong bonding with surfaces via covalent interactions [167].

With the advent of studies on palladium catalysts, new efforts were exerted towards using precious metals ions like silver for desulfurization, and Ag⁺ impregnated mesoporous silicas were achieved through wet impregnation techniques [168]. In this case, the catalytic activity of Ag⁺/MCM-41 applied on JP-5 fuel was compared with Ag⁺/SBA-15, and breakthrough capacity of 15.7 mg S/g was achieved for the formed composite, and a value of 10.3 mg S/g was achieved for the latter. Saturation capacity, on the other hand, was 32.1 mg S/g for the MCM composite, whereas it was 29.2 mg S/g for the SBA composite. This data corroborates with the findings presented earlier by Wang et al., proving the high surface area of MCM-41 [166]. It was observed that Ag⁺/MCM-41 could be thermally recovered in air and could maintain 50% of its initial desulfurization efficiency, even after second and third cycles [168].

This work on silver-containing frameworks acted as a platform for further research on these materials and similar compounds have been evaluated for desulfurization of real, as well as model, fuels. Researchers have reported on the use of Ag-impregnated bulk MCM-41 for JP-5 fuel; however, there is still a huge demand for high edge adsorbents to be applied in advanced JP-8 fuel. A few years ago, Palomino et al. reported on using mesoporous silica nanoparticles as an extension to bulk MCM-41 for ADS of JP-8 aviation fuel with a sulfur concentration of 516 ppmw S [169]. This report was the first of its kind to compare commercial bulk MCM-41 with MCM-41 nanoparticles (MSNs) for JP-8 desulfurization. The prepared nanoparticles were spherical in shape and had an average diameter of 80 nm. Ag-impregnated composite catalytic materials were prepared using MCM-41 and MSN and their adsorption capacities were compared. Adsorption capacity of Ag–MCM-41 (24.5 mg S/g) was found to be lower than Ag–MSN (32.6 mg S/g) [169]. Maximum model fuel capacity was achieved when a silver loading of 18 wt% was used for Ag-MCM-41 and 20 wt% for Ag-MSN. Adsorption capacity and breakthrough S capacity of Ag-MSN (32.6 mg S/g, 0.98 mg S/g) were much higher than that of Ag-MCM-41 (25.4 mg S/g, 0.21 mg S/g), owing to the high surface area of nanomaterials. Ag-MSN could also be recovered with diethyl ether and be reused with 70% efficiency [169]. To go in depth on other materials for jet fuels is beyond the scope of this review. For more details on catalytic materials for desulfurization of aviation fuels, we direct our readers to one excellent review provided by Tran et al. [165].

6. Summary

Key qualities that are widely present among ideal desulfurization materials include: (i) high porosity and large surface areas offering significant area and numerous active sites for adsorption within small volumes; (ii) catalytic materials and their precursors are economical; (iii) porous catalysts are usually embedded with active metal sites (in zerovalent, ionic, or oxide forms) for enriched adsorption; and (iv) finally, they are highly stable and can be recycled without significant loss of catalytic efficiency. These desulfurizing agents have unique surface and structural properties, including surface acidity, magnetic nature, photocatalytic activity, or the ability to homogeneously disperse active sites and aiding the adsorption process.

Table 1 provides a summary of various functionalized mesoporous silica frameworks and their desulfurization performance. According to this table, it is clear that: (1) the sulfur adsorption capacity of MS frameworks impregnated with core-shell magnetic nanoparticles is significantly higher than that of MS frameworks embedded with photocatalytic nanoparticles; (2) although complete DBT conversion occurs within short period of time using subnano-MoO₃/UMSN structure, LaW₁₀/IL-SiO₂ structure outperforms in terms of time and quantity for both small and large batches; (3) conversion performance of PW₁₁@TMA-SBA-15 is remarkable in comparison to 0.05HPMo-IL/SBA-15, which shows lower desulfurization efficiency for various organosulfur compounds with higher reaction time; (4) the desulfurization performance of the hybrid periodic mesoporous silica (PW₁₁@TMA-PMOE) is lower than that of the hybrid ordered mesoporous silica (PW₁₁@TMA-SBA-15); and (5) a high conversion rate of an ideal catalyst should be accompanied by its high recyclability without significant loss in its efficiency.

Table 1. Desulfurization efficiency of different functionalized mesoporous silica materials.

Catalyst	Sulfur Species	Conversion % (time, min)	qm (mg-S per g-Cat)	Ref.
ZnO-Mesoporous TiO ₂ -SiO ₂	DBT	97%	46.1	[78]
Mesoporous TiO ₂ -SiO ₂ -40	DBT	99%	13.7	[81]
Mo/10SiO ₂ -550	4,6-DMDBT	100% (40 m)	-	[91]
WO ₃ /SBA-15	4,6-DMDBT	100% (60 m)	-	[170]
15%MoO ₃ /SBA-15	4,6-DMDBT	100% (60 m)	-	[171]
PW ₁₁ @aptes-SBA-15	1-BT, DBT, 4-MDBT, 4,6-DMDBT	100% (60 m)	-	[100]
PW ₁₁ @TMA-SBA-15	DBT	100% (30 m)	-	[101]
PW ₁₁ @TMA-SBA-15	4-MDBT	100% (30 m)	-	[101]
PW ₁₁ @TMA-SBA-15	4,6-DMDBT	100% (30 m)	-	[101]
PW ₁₁ @TMA-SBA-15	1-BT	93.9% (30 m)	-	[101]
PW ₁₁ @TMA-PMOE	DBT	98.2% (60 m)	-	[101]
PW ₁₁ @TMA-PMOE	4-MDBT	99.0% (60 m)	-	[101]
PW ₁₁ @TMA-PMOE	4,6-DMDBT	99.3% (60 m)	-	[101]
PW ₁₁ @TMA-PMOE	1-BT	92.8% (60 m)	-	[101]
20%HPW/Zr-HMS	DBT	95.0% (30 m)	-	[59]
Mesoporous W-SiO ₂	BT, DBT, 4,6-MDBT	100% (60 m)	-	[24]
subnano-MoO ₃ /UMSN	DBT	100% (15 m)	-	[106]
10% Mo/mSiO ₂ nanowire	DBT	100% (30 m)	-	[107]
W-mSiO ₂ -450	DBT	99.6% (30 m)	-	[124]
[C ₄ mim] ₃ PW ₁₂ O ₄₀ @OMS	DBT	99.5% (60 m)	-	[125]
LaW ₁₀ /IL-SiO ₂	DBT	100% (1 m, small batch)100% (25 m, large scale)	-	[128]
IL-3DOM SiO ₂	BT, DBT, 3-MBT, 4-MDBT, 4,6-DMDBT	100% (60 m)	-	[58]
PMo ₁₂ @TBA-MSN	BT, DBT, 3-MBT, 4-MDBT, 4,6-DMDBT	98% (70 m)	-	[133]
PMo ₁₂ @TMA-MSN	4,6-DMDBT	92% (70 m)	-	[133]
0.05HPMo-IL/SBA-15	DBT	90% (90 m)	-	[136]
0.05HPMo-IL/SBA-15	BT	71% (90 m)	-	[136]
0.05HPMo-IL/SBA-15	4,6-DMDBT	69.8% (90 m)	-	[136]
Fe ₃ O ₄ @mSiO ₂ @DT-MIP	DBT	-	104.2	[141]
Fe ₃ O ₄ @mSiO ₂ @DT-MIP	4-MDBT	-	113.6	[141]
Fe ₃ O ₄ @SiO ₂ -IL/RS-MMS	4,6-DMDBT	98.3% (50 m)	-	[143]
Fe ₃ O ₄ @SiO ₂ -IL/RS-MMS	4-MDBT	99.5% (50 m)	-	[143]
Fe ₃ O ₄ @SiO ₂ -IL/RS-MMS	DBT	99.7% (50 m)	-	[143]

7. Conclusions

Mesoporous silica frameworks and nanoparticles are the third generation of Si-based nanoporous materials that are promising for clean fuel applications. With increased research interest in the use of specialized MS frameworks for desulfurization of fuels, in this review, we discussed appropriate functionalization strategies vital to adsorb the sulfur rich molecules present in fuels and their oxidation to easily removable species. We examined how uniquely designed MS formulations are capable of encapsulating not only simple sulfur species but also bulky aromatic compounds, like 4,6-DMDBT. We compiled various templating technologies, as well as other methods, like molecular imprinted polymers, to generate catalytic MS frameworks and examined the diverse nature of how surface modification with ionic liquids, photocatalytic active species, magnetic core-shell nanoparticles, and carbonaceous active sites can significantly affect the outcome of sulfur adsorption and removal. Ultra-deep desulfurization of fuels, especially JP-8 type of aviation fuels for fuel cell applications, demand judicious methods of catalysis, where currently precious metal ions are used in the desulfurization process, and stability of porous frameworks is essential to make recovery and reuse of these materials viable. A thorough examination of not only the pore size but also the size of the bulk material, as well as their competitive and interfering interactions in the presence of other compounds in fuels, such as asphaltenes, remains to be explored and can provide insights on the performance of these particles and may provide valuable information related to the criteria of MS material design.

Author Contributions: S.M. and A.A.A.A. sketched the outline of the manuscript, collected the scientific materials, reviewed the literature and wrote the manuscript. S.M. drew all the figures in the manuscript. S.M. and A.A.A.A. revised the manuscript for content and scientific quality. Both authors reviewed and approved the submitted manuscript and its revisions. All authors have read and agreed to the published version of the manuscript.

Acknowledgments: Authors wish to thank the University of Calgary's Canada First Research Excellence Fund (CFREF) program, the Global Research Initiative for Sustainable Low-Carbon Unconventional Resources, for financial support.

Conflicts of Interest: The authors declare no conflict of interest.

References

1. Available online: https://www.who.int/gho/publications/world_health_statistics/2018/en/ (accessed on 4 June 2020).
2. Available online: <https://www.unec.org/info/about-unece/mission/unece-and-the-sdgs.html> (accessed on 4 June 2020).
3. Available online: <https://ccacoalition.org/en/resources/global-strategy-introduce%2%A0low-sulfur-fuels-and-cleaner-diesel-vehicles> (accessed on 4 June 2020).
4. Li, H.; Su, S.; Peng, Y.; Wu, L.; Xu, K.; Liu, L.; Qing, M.; Hu, S.; Wang, Y.; Xiang, J. Effect of La-Modified Supporter on H₂S Removal Performance of Mn/La/Al₂O₃ Sorbent in a Reducing Atmosphere. *Ind. Eng. Chem. Res.* **2019**, *58*, 8260–8270. [CrossRef]
5. Liu, D.; Zhou, W.; Wu, J. CeO₂-MnOx/ZSM-5 sorbents for H₂S removal at high temperature. *Chem. Eng. J.* **2016**, *284*, 862–871. [CrossRef]
6. Guo, L.F.; Pan, K.L.; Lee, H.M.; Chang, M.B. High-temperature gaseous H₂S removal by Zn-Mn-based sorbent. *Ind. Eng. Chem. Res.* **2015**, *54*, 11040–11047. [CrossRef]
7. Wu, M.; Chang, B.; Lim, T.-T.; Oh, W.-D.; Lei, J.; Mi, J. High-sulfur capacity and regenerable Zn-based sorbents derived from layered double hydroxide for hot coal gas desulfurization. *J. Hazard. Mater.* **2018**, *360*, 391–401. [CrossRef]
8. Zeng, B.; Yue, H.; Liu, C.; Huang, T.; Li, J.; Zhao, B.; Zhang, M.; Liang, B. Desulfurization behavior of Fe-Mn-based regenerable sorbents for high-temperature H₂S removal. *Energy Fuels* **2015**, *29*, 1860–1867. [CrossRef]
9. Xia, H.; Liu, B.; Li, Q.; Huang, Z.; Cheung, A.S.-C. High capacity Mn-Fe-Mo/FSM-16 sorbents in hot coal gas desulfurization and mechanism of elemental sulfur formation. *Appl. Catal. B Environ.* **2017**, *200*, 552–565. [CrossRef]

10. Chen, C.-S.; Budi, C.S.; Wu, H.-C.; Saikia, D.; Kao, H.-M. Size-tunable Ni nanoparticles supported on surface-modified, cage-type mesoporous silica as highly active catalysts for CO₂ hydrogenation. *ACS Catal.* **2017**, *7*, 8367–8381. [CrossRef]
11. Liang, J.; Liang, Z.; Zou, R.; Zhao, Y. Heterogeneous catalysis in zeolites, mesoporous silica, and metal–organic frameworks. *Adv. Mater.* **2017**, *29*, 1701139. [CrossRef]
12. Manzano, M.; Vallet-Regí, M. Mesoporous Silica Nanoparticles for Drug Delivery. *Adv. Funct. Mater.* **2019**, *30*, 1902634. [CrossRef]
13. Mendiratta, S.; Hussein, M.; Nasser, H.A.; Ali, A.A.A. Multidisciplinary Role of Mesoporous Silica Nanoparticles in Brain Regeneration and Cancers: From Crossing the Blood–Brain Barrier to Treatment. *Part. Part. Syst. Charact.* **2019**, *36*, 1900195. [CrossRef]
14. Niu, M.; Yang, H.; Zhang, X.; Wang, Y.; Tang, A. Amine-impregnated mesoporous silica nanotube as an emerging nanocomposite for CO₂ capture. *ACS Appl. Mater. Interfaces* **2016**, *8*, 17312–17320. [CrossRef] [PubMed]
15. Kankala, R.K.; Han, Y.H.; Na, J.; Lee, C.H.; Sun, Z.; Wang, S.B.; Kimura, T.; Ok, Y.S.; Yamauchi, Y.; Chen, A.Z. Nanoarchitected Structure and Surface Biofunctionality of Mesoporous Silica Nanoparticles. *Adv. Mater.* **2020**, 1907035. [CrossRef] [PubMed]
16. Shieh, F.-K.; Wang, S.-C.; Yen, C.-I.; Wu, C.-C.; Dutta, S.; Chou, L.-Y.; Morabito, J.V.; Hu, P.; Hsu, M.-H.; Wu, K.C.-W. Imparting functionality to biocatalysts via embedding enzymes into nanoporous materials by a de novo approach: Size-selective sheltering of catalase in metal–organic framework microcrystals. *J. Am. Chem. Soc.* **2015**, *137*, 4276–4279. [CrossRef] [PubMed]
17. Sue, Y.-C.; Wu, J.-W.; Chung, S.-E.; Kang, C.-H.; Tung, K.-L.; Wu, K.C.-W.; Shieh, F.-K. Synthesis of hierarchical micro/mesoporous structures via solid–aqueous interface growth: Zeolitic imidazolate framework-8 on siliceous mesocellular foams for enhanced pervaporation of water/ethanol mixtures. *ACS Appl. Mater. Interfaces* **2014**, *6*, 5192–5198. [CrossRef]
18. Wang, J.; Xu, Y.; Ding, B.; Chang, Z.; Zhang, X.; Yamauchi, Y.; Wu, K.C.W. Confined Self-Assembly in Two-Dimensional Interlayer Space: Monolayered Mesoporous Carbon Nanosheets with In-Plane Orderly Arranged Mesopores and a Highly Graphitized Framework. *Angew. Chem. Int. Ed.* **2018**, *57*, 2894–2898. [CrossRef]
19. Liao, Y.-T.; Matsagar, B.M.; Wu, K.C.-W. Metal–organic framework (MOF)-derived effective solid catalysts for valorization of lignocellulosic biomass. *ACS Sustain. Chem. Eng.* **2018**, *6*, 13628–13643. [CrossRef]
20. Kaneti, Y.V.; Dutta, S.; Hossain, M.S.; Shiddiky, M.J.; Tung, K.L.; Shieh, F.K.; Tsung, C.K.; Wu, K.C.W.; Yamauchi, Y. Strategies for improving the functionality of zeolitic imidazolate frameworks: Tailoring nanoarchitectures for functional applications. *Adv. Mater.* **2017**, *29*, 1700213. [CrossRef]
21. Klemm, D.; Kramer, F.; Moritz, S.; Lindström, T.; Ankerfors, M.; Gray, D.; Dorris, A. Nanocelluloses: A New Family of Nature-Based Materials. *Angew. Chem. Int. Ed.* **2011**, *50*, 5438–5466. [CrossRef]
22. Lin, N.; Dufresne, A. Nanocellulose in biomedicine: Current status and future prospect. *Eur. Polym. J.* **2014**, *59*, 302–325. [CrossRef]
23. Moon, R.J.; Martini, A.; Nairn, J.; Simonsen, J.; Youngblood, J. Cellulose nanomaterials review: Structure, properties and nanocomposites. *Chem. Soc. Rev.* **2011**, *40*, 3941–3994. [CrossRef]
24. Shen, D.; Dai, Y.; Han, J.; Gan, L.; Liu, J.; Long, M. A nanocellulose template strategy for the controllable synthesis of tungsten-containing mesoporous silica for ultra-deep oxidative desulfurization. *Chem. Eng. J.* **2018**, *332*, 563–571. [CrossRef]
25. Chen, S.-Y.; Cheng, S. Acid-free synthesis of mesoporous silica using triblock copolymer as template with the aid of salt and alcohol. *Chem. Mater.* **2007**, *19*, 3041–3051. [CrossRef]
26. Zhao, D.; Huo, Q.; Feng, J.; Chmelka, B.F.; Stucky, G.D. Nonionic triblock and star diblock copolymer and oligomeric surfactant syntheses of highly ordered, hydrothermally stable, mesoporous silica structures. *J. Am. Chem. Soc.* **1998**, *120*, 6024–6036. [CrossRef]
27. Chen, D.; Li, Z.; Yu, C.; Shi, Y.; Zhang, Z.; Tu, B.; Zhao, D. Nonionic block copolymer and anionic mixed surfactants directed synthesis of highly ordered mesoporous silica with bicontinuous cubic structure. *Chem. Mater.* **2005**, *17*, 3228–3234. [CrossRef]
28. Kim, T.-W.; Kleitz, F.; Paul, B.; Ryoo, R. MCM-48-like large mesoporous silicas with tailored pore structure: Facile synthesis domain in a ternary triblock copolymer– butanol– water system. *J. Am. Chem. Soc.* **2005**, *127*, 7601–7610. [CrossRef] [PubMed]

29. Flodström, K.; Alfredsson, V.; Källrot, N. Formation of a New Ia3-d Cubic Meso-Structured Silica via Triblock Copolymer-Assisted Synthesis. *J. Am. Chem. Soc.* **2003**, *125*, 4402–4403. [CrossRef] [PubMed]
30. Yamada, S.; Motozuka, S.; Tagaya, M. Synthesis of nanostructured silica/hydroxyapatite hybrid particles containing amphiphilic triblock copolymer for effectively controlling hydration layer structures with cytocompatibility. *J. Mater. Chem. B* **2020**, *8*, 1524–1537. [CrossRef] [PubMed]
31. Sawant, A.; Raut, D.; Darvatkar, N.; Salunkhe, M. Recent developments of task-specific ionic liquids in organic synthesis. *Green Chem. Lett. Rev.* **2011**, *4*, 41–54. [CrossRef]
32. Ward, A.J.; Pujari, A.A.; Costanzo, L.; Masters, A.F.; Maschmeyer, T. Ionic liquid-templated preparation of mesoporous silica embedded with nanocrystalline sulfated zirconia. *Nanoscale Res. Lett.* **2011**, *6*, 192. [CrossRef]
33. Pujari, A.A.; Chadbourne, J.J.; Ward, A.J.; Costanzo, L.; Masters, A.F.; Maschmeyer, T. The use of acidic task-specific ionic liquids in the formation of high surface area mesoporous silica. *New J. Chem.* **2009**, *33*, 1997–2000. [CrossRef]
34. Wang, T.; Kaper, H.; Antonietti, M.; Smarsly, B. Templating behavior of a long-chain ionic liquid in the hydrothermal synthesis of mesoporous silica. *Langmuir* **2007**, *23*, 1489–1495. [CrossRef] [PubMed]
35. Yamamoto, E.; Mori, S.; Shimojima, A.; Wada, H.; Kuroda, K. Fabrication of colloidal crystals composed of pore-expanded mesoporous silica nanoparticles prepared by a controlled growth method. *Nanoscale* **2017**, *9*, 2464–2470. [CrossRef] [PubMed]
36. Yang, Z.; Qi, K.; Rong, J.; Wang, L.; Liu, Z.; Yang, Y. Template synthesis of 3-D bimodal ordered porous silica. *Chin. Sci. Bull.* **2001**, *46*, 1785–1789. [CrossRef]
37. Villaescusa, L.A.; Mihi, A.; Rodríguez, I.; García-Bennett, A.E.; Míguez, H. Growth of mesoporous materials within colloidal crystal films by spin-coating. *J. Phys. Chem. B* **2005**, *109*, 19643–19649. [CrossRef] [PubMed]
38. Peng, W.; Zhang, Z.; Rong, M.; Zhang, M. Core-Shell Structure Design of Hollow Mesoporous Silica Nanospheres Based on Thermo-Sensitive PNIPAM and pH-Responsive Catechol-Fe³⁺ Complex. *Polymers* **2019**, *11*, 1832. [CrossRef] [PubMed]
39. Yi, G.-R.; Moon, J.H.; Yang, S.-M. Ordered macroporous particles by colloidal templating. *Chem. Mater.* **2001**, *13*, 2613–2618. [CrossRef]
40. Qin, L.; Shi, W.; Liu, W.; Yang, Y.; Liu, X.; Xu, B. Surface molecularly imprinted polymers grafted on ordered mesoporous carbon nanospheres for fuel desulfurization. *RSC Adv.* **2016**, *6*, 12504–12513. [CrossRef]
41. Wang, Y.; Yang, Y.; Xu, L.; Zhang, J. Bisphenol A sensing based on surface molecularly imprinted, ordered mesoporous silica. *Electrochim. Acta* **2011**, *56*, 2105–2109. [CrossRef]
42. Pan, S.-D.; Shen, H.-Y.; Zhou, L.-X.; Chen, X.-H.; Zhao, Y.-G.; Cai, M.-Q.; Jin, M.-C. Controlled synthesis of pentachlorophenol-imprinted polymers on the surface of magnetic graphene oxide for highly selective adsorption. *J. Mater. Chem. A* **2014**, *2*, 15345–15356. [CrossRef]
43. Zhang, Z.; Li, J.; Fu, L.; Liu, D.; Chen, L. Magnetic molecularly imprinted microsensor for selective recognition and transport of fluorescent phycoerythrin in seawater. *J. Mater. Chem. A* **2015**, *3*, 7437–7444. [CrossRef]
44. Chandra Srivastava, V. An evaluation of desulfurization technologies for sulfur removal from liquid fuels. *RSC Adv.* **2012**, *2*, 759–783. [CrossRef]
45. Austin, G.T. *Shreve's Chemical Process Industries*; McGraw-Hill Companies: New York, NY, USA, 1984.
46. Bej, S.K.; Maity, S.K.; Turaga, U.T. Search for an efficient 4, 6-DMDBT hydrodesulfurization catalyst: A review of recent studies. *Energy Fuels* **2004**, *18*, 1227–1237. [CrossRef]
47. Egorova, M.; Prins, R. Competitive hydrodesulfurization of 4, 6-dimethyldibenzothiophene, hydrodenitrogenation of 2-methylpyridine, and hydrogenation of naphthalene over sulfided NiMo/γ-Al₂O₃. *J. Catal.* **2004**, *224*, 278–287. [CrossRef]
48. Li, X.; Wang, A.; Egorova, M.; Prins, R. Kinetics of the HDS of 4, 6-dimethyldibenzothiophene and its hydrogenated intermediates over sulfided Mo and NiMo on γ-Al₂O₃. *J. Catal.* **2007**, *250*, 283–293. [CrossRef]
49. Layan Savithra, G.H.; Bowker, R.H.; Carrillo, B.A.; Bussell, M.E.; Brock, S.L. Mesoporous matrix encapsulation for the synthesis of monodisperse Pd₅P₂ nanoparticle hydrodesulfurization catalysts. *ACS Appl. Mater. Interfaces* **2013**, *5*, 5403–5407. [CrossRef]
50. Huirache-Acuña, R.; Nava, R.; Peza-Ledesma, C.L.; Lara-Romero, J.; Alonso-Núñez, G.; Pawelec, B.; Rivera-Muñoz, E.M. SBA-15 mesoporous silica as catalytic support for hydrodesulfurization catalysts. *Materials* **2013**, *6*, 4139–4167. [CrossRef]

51. Marafi, M.; Furimsky, E. Hydroprocessing catalysts containing noble metals: Deactivation, regeneration, metals reclamation, and environment and safety. *Energy Fuels* **2017**, *31*, 5711–5750. [CrossRef]
52. Kumaran, G.M.; Garg, S.; Soni, K.; Kumar, M.; Sharma, L.; Rama Rao, K.; Dhar, G.M. Effect of Al-SBA-15 support on catalytic functionalities of hydrotreating catalysts. II. Effect of variation of molybdenum and promoter contents on catalytic functionalities. *Ind. Eng. Chem. Res.* **2007**, *46*, 4747–4754. [CrossRef]
53. Soni, K.; Rana, B.; Sinha, A.; Bhaumik, A.; Nandi, M.; Kumar, M.; Dhar, G. 3-D ordered mesoporous KIT-6 support for effective hydrodesulfurization catalysts. *Appl. Catal. B Environ.* **2009**, *90*, 55–63. [CrossRef]
54. Sorensen, A.C.; Fuller, B.L.; Eklund, A.G.; Landry, C.C. Mo-Doped mesoporous silica for thiophene hydrodesulfurization: Comparison of materials and methods. *Chem. Mater.* **2004**, *16*, 2157–2164. [CrossRef]
55. Danforth, S.J.; Liyanage, D.R.; Hitihami-Mudiyanselage, A.; Ilic, B.; Brock, S.L.; Bussell, M.E. Probing hydrodesulfurization over bimetallic phosphides using monodisperse Ni₂-xM_xP nanoparticles encapsulated in mesoporous silica. *Surf. Sci.* **2016**, *648*, 126–135. [CrossRef]
56. Chiranjeevi, T.; Kumar, P.; Maity, S.; Rana, M.; Dhar, G.M.; Rao, T.P. Characterization and hydrodesulfurization catalysis on WS₂ supported on mesoporous Al-HMS material. *Microporous Mesoporous Mater.* **2001**, *44*, 547–556. [CrossRef]
57. Campos-Martin, J.; Capel-Sanchez, M.; Fierro, J. Highly efficient deep desulfurization of fuels by chemical oxidation. *Green Chem.* **2004**, *6*, 557–562. [CrossRef]
58. Chen, X.; Zhang, M.; Wei, Y.; Li, H.; Liu, J.; Zhang, Q.; Zhu, W.; Li, H. Ionic liquid-supported 3DOM silica for efficient heterogeneous oxidative desulfurization. *Inorg. Chem. Front.* **2018**, *5*, 2478–2485. [CrossRef]
59. Yuzbashi, S.; Mousazadeh, M.; Ramezani, N.; Sid Kalal, H.; Sabour, B. Mesoporous zirconium–silica nanocomposite modified with heteropoly tungstophosphoric acid catalyst for ultra-deep oxidative desulfurization. *Appl. Organomet. Chem.* **2020**, *34*, e5326. [CrossRef]
60. Gao, M.; Zhang, G.; Tian, M.; Liu, B.; Chen, W. Oxidative desulfurization of dibenzothiophene by central metal ions of chlorophthalocyanines-tetracarboxyl complexes. *Inorg. Chim. Acta* **2019**, *485*, 58–63. [CrossRef]
61. Javadli, R.; De Klerk, A. Desulfurization of heavy oil. *Appl. Petrochem. Res.* **2012**, *1*, 3–19. [CrossRef]
62. Zhu, W.; Li, H.; Jiang, X.; Yan, Y.; Lu, J.; He, L.; Xia, J. Commercially available molybdc compound-catalyzed ultra-deep desulfurization of fuels in ionic liquids. *Green Chem.* **2008**, *10*, 641–646. [CrossRef]
63. Rajendran, A.; Cui, T.-Y.; Fan, H.-X.; Yang, Z.; Feng, J.; Li, W. A comprehensive review on oxidative desulfurization catalysts targeting clean energy and environment. *J. Mater. Chem. A* **2020**, *8*, 2246–2285. [CrossRef]
64. Hossain, M.N.; Park, H.C.; Choi, H.S. A comprehensive review on catalytic oxidative desulfurization of liquid fuel oil. *Catalysts* **2019**, *9*, 229. [CrossRef]
65. Houda, S.; Lancelot, C.; Blanchard, P.; Poinel, L.; Lamonier, C. Oxidative desulfurization of heavy oils with high sulfur content: A review. *Catalysts* **2018**, *8*, 344. [CrossRef]
66. Li, J.; Yang, Z.; Li, S.; Jin, Q.; Zhao, J. Review on oxidative desulfurization of fuel by supported heteropolyacid catalysts. *J. Ind. Eng. Chem.* **2020**, *82*, 1–16. [CrossRef]
67. Ja'fari, M.; Ebrahimi, S.L.; Khosravi-Nikou, M.R. Ultrasound-assisted oxidative desulfurization and denitrogenation of liquid hydrocarbon fuels: A critical review. *Ultrason. Sonochem.* **2018**, *40*, 955–968. [CrossRef] [PubMed]
68. Kirkwood, K.; Ebert, S.; Foght, J.; Fedorak, P.; Gray, M. Bacterial biodegradation of aliphatic sulfides under aerobic carbon-or sulfur-limited growth conditions. *J. Appl. Microbiol.* **2005**, *99*, 1444–1454. [CrossRef]
69. Kirkwood, K.M.; Foght, J.M.; Gray, M.R. Selectivity among organic sulfur compounds in one-and two-liquid-phase cultures of *Rhodococcus* sp. strain JVH1. *Biodegradation* **2007**, *18*, 473–480. [CrossRef]
70. Kirkwood, K.M.; Andersson, J.T.; Fedorak, P.M.; Foght, J.M.; Gray, M.R. Sulfur from benzo thiophene and alkylbenzo thiophenes supports growth of *Rhodococcus* sp. strain JVH1. *Biodegradation* **2007**, *18*, 541–549. [CrossRef]
71. McFarland, B.L.; Boron, D.J.; Deever, W.; Meyer, J.; Johnson, A.R.; Atlas, R.M. Biocatalytic sulfur removal from fuels: Applicability for producing low sulfur gasoline. *Crit. Rev. Microbiol.* **1998**, *24*, 99–147. [CrossRef]
72. Gupta, N.; Roychoudhury, P.; Deb, J. Biotechnology of desulfurization of diesel: Prospects and challenges. *Appl. Microbiol. Biotechnol.* **2005**, *66*, 356–366. [CrossRef]
73. Sadare, O.O.; Obazu, F.; Daramola, M.O. Biodesulfurization of petroleum distillates—Current status, opportunities and future challenges. *Environments* **2017**, *4*, 85. [CrossRef]

74. Xu, W.; Li, Y. Alkylation desulfurization of the C9 fraction over Amberlyst 36 resin. *RSC Adv.* **2015**, *5*, 2908–2913. [CrossRef]
75. Han, D.Y.; Chen, C.J.; Zhang, F.J. Deep Desulfurization of Light Oil Using the Imitating Silver Salt ILs Method. *Petrol. Sci. Technol.* **2011**, *29*, 2487–2493. [CrossRef]
76. He, J.; Wu, P.; Wu, Y.; Li, H.; Jiang, W.; Xun, S.; Zhang, M.; Zhu, W.; Li, H. Taming interfacial oxygen vacancies of amphiphilic tungsten oxide for enhanced catalysis in oxidative desulfurization. *ACS Sustain. Chem. Eng.* **2017**, *5*, 8930–8938. [CrossRef]
77. Wang, X.-S.; Huang, Y.-B.; Lin, Z.-J.; Cao, R. Phosphotungstic acid encapsulated in the mesocages of amine-functionalized metal–organic frameworks for catalytic oxidative desulfurization. *Dalton Trans.* **2014**, *43*, 11950–11958. [CrossRef] [PubMed]
78. Zhou, K.; Ding, Y.; Zhang, L.; Wu, H.; Guo, J. Synthesis of mesoporous ZnO/TiO₂-SiO₂ composite material and its application in photocatalytic adsorption desulfurization without the addition of an extra oxidant. *Dalton Trans.* **2020**, *49*, 1600–1612. [CrossRef] [PubMed]
79. Saravanan, R.; Karthikeyan, S.; Gupta, V.; Sekaran, G.; Narayanan, V.; Stephen, A. Enhanced photocatalytic activity of ZnO/CuO nanocomposite for the degradation of textile dye on visible light illumination. *Mater. Sci. Eng. C* **2013**, *33*, 91–98. [CrossRef] [PubMed]
80. Wang, Z.; Hu, T.; He, H.; Fu, Y.; Zhang, X.; Sun, J.; Xing, L.; Liu, B.; Zhang, Y.; Xue, X. Enhanced H₂ production of TiO₂/ZnO nanowires Co-using solar and mechanical energy through piezo-photocatalytic effect. *ACS Sustain. Chem. Eng.* **2018**, *6*, 10162–10172. [CrossRef]
81. Qin, B.; Shen, Y.; Xu, B.; Zhu, S.; Li, P.; Liu, Y. Mesoporous TiO₂-SiO₂ adsorbent for ultra-deep desulfurization of organic-S at room temperature and atmospheric pressure. *RSC Adv.* **2018**, *8*, 7579–7587. [CrossRef]
82. Meizhen, X.; Lina, Y.; Jian, L. Photocatalytic oxidative desulfurization of dibenzothiophene on TiO₂ modified bimodal mesoporous silica. *China Pet. Process. Petrochem. Technol.* **2017**, *19*, 59–67.
83. Zaccariello, G.; Moretti, E.; Storaro, L.; Riello, P.; Canton, P.; Gombac, V.; Montini, T.; Rodriguez-Castellon, E.; Benedetti, A. TiO₂-mesoporous silica nanocomposites: Cooperative effect in the photocatalytic degradation of dyes and drugs. *RSC Adv.* **2014**, *4*, 37826–37837. [CrossRef]
84. Julião, D.; Gomes, A.C.; Pillinger, M.; Valença, R.; Ribeiro, J.C.; de Castro, B.; Gonçalves, I.S.; Cunha Silva, L.; Balula, S.S. Zinc-Substituted Polyoxotungstate@ amino-MIL-101 (Al)-An Efficient Catalyst for the Sustainable Desulfurization of Model and Real Diesels. *Eur. J. Inorg. Chem.* **2016**, *2016*, 5114–5122. [CrossRef]
85. Genovese, M.; Lian, K. Polyoxometalate modified pine cone biochar carbon for supercapacitor electrodes. *J. Mater. Chem. A* **2017**, *5*, 3939–3947. [CrossRef]
86. Ghahramaninezhad, M.; Soleimani, B.; Shahrak, M.N. A simple and novel protocol for Li-trapping with a POM/MOF nano-composite as a new adsorbent for CO₂ uptake. *New J. Chem.* **2018**, *42*, 4639–4645. [CrossRef]
87. Xun, S.; Zhu, W.; Chang, Y.; Li, H.; Zhang, M.; Jiang, W.; Zheng, D.; Qin, Y.; Li, H. Synthesis of supported SiW₁₂O₄₀-based ionic liquid catalyst induced solvent-free oxidative deep-desulfurization of fuels. *Chem. Eng. J.* **2016**, *288*, 608–617. [CrossRef]
88. Li, S.-W.; Li, J.-R.; Gao, Y.; Liang, L.-L.; Zhang, R.-L.; Zhao, J.-S. Metal modified heteropolyacid incorporated into porous materials for a highly oxidative desulfurization of DBT under molecular oxygen. *Fuel* **2017**, *197*, 551–561. [CrossRef]
89. Shen, D.; Yang, J.; Li, X.; Zhou, L.; Zhang, R.; Li, W.; Chen, L.; Wang, R.; Zhang, F.; Zhao, D. Biphasic stratification approach to three-dimensional dendritic biodegradable mesoporous silica nanospheres. *Nano Lett.* **2014**, *14*, 923–932. [CrossRef] [PubMed]
90. Shen, D.; Chen, L.; Yang, J.; Zhang, R.; Wei, Y.; Li, X.; Li, W.; Sun, Z.; Zhu, H.; Abdullah, A.M. Ultradispersed palladium nanoparticles in three-dimensional dendritic mesoporous silica nanospheres: Toward active and stable heterogeneous catalysts. *ACS Appl. Mater. Interfaces* **2015**, *7*, 17450–17459. [CrossRef]
91. Zhang, M.; Liu, J.; Yang, J.; Chen, X.; Wang, M.; Li, H.; Zhu, W.; Li, H. Molybdenum-containing dendritic mesoporous silica spheres for fast oxidative desulfurization in fuel. *Inorg. Chem. Front.* **2019**, *6*, 451–458. [CrossRef]
92. Casuscelli, S.; Crivello, M.; Perez, C.; Ghione, G.; Herrero, E.; Pizzio, L.; Vázquez, P.; Cáceres, C.; Blanco, M. Effect of reaction conditions on limonene epoxidation with H₂O₂ catalyzed by supported Keggin heteropolycompounds. *Appl. Catal. A Gen.* **2004**, *274*, 115–122. [CrossRef]

93. Granadeiro, C.M.; Barbosa, A.D.; Silva, P.; Paz, F.A.A.; Saini, V.K.; Pires, J.; de Castro, B.; Balula, S.S.; Cunha-Silva, L. Monovacant polyoxometalates incorporated into MIL-101 (Cr): Novel heterogeneous catalysts for liquid phase oxidation. *Appl. Catal. A Gen.* **2013**, *453*, 316–326. [CrossRef]
94. Ribeiro, S.; Barbosa, A.D.; Gomes, A.C.; Pillinger, M.; Gonçalves, I.S.; Cunha-Silva, L.; Balula, S.S. Catalytic oxidative desulfurization systems based on Keggin phosphotungstate and metal-organic framework MIL-101. *Fuel Process. Technol.* **2013**, *116*, 350–357. [CrossRef]
95. Singh, S.; Patel, A.; Prakashan, P. One pot oxidative esterification of aldehyde over recyclable cesium salt of nickel substituted phosphotungstate. *Appl. Catal. A Gen.* **2015**, *505*, 131–140. [CrossRef]
96. Coronel, N.C.; da Silva, M.J. Lacunar keggins heteropolyacid salts: Soluble, solid and solid-supported catalysts. *J. Clust. Sci.* **2018**, *29*, 195–205. [CrossRef]
97. Abdalla, Z.E.A.; Li, B. Preparation of MCM-41 supported $(\text{Bu}_4\text{N})_4\text{H}_3(\text{PW}_{11}\text{O}_{39})$ catalyst and its performance in oxidative desulfurization. *Chem. Eng. J.* **2012**, *200*, 113–121. [CrossRef]
98. Abdalla, Z.E.A.; Li, B.; Tufail, A. Direct synthesis of mesoporous $(\text{C}_{19}\text{H}_{42}\text{N})_4\text{H}_3(\text{PW}_{11}\text{O}_{39})/\text{SiO}_2$ and its catalytic performance in oxidative desulfurization. *Colloids Surf. A Physicochem. Eng. Asp.* **2009**, *341*, 86–92. [CrossRef]
99. Wu, N.; Li, B.; Liu, Z.; Han, C. Synthesis of Keggin-type lacunary 11-tungstophosphates encapsulated into mesoporous silica pillared in clay interlayer galleries and their catalytic performance in oxidative desulfurization. *Catal. Commun.* **2014**, *46*, 156–160. [CrossRef]
100. Ribeiro, S.O.; Granadeiro, C.M.; Almeida, P.L.; Pires, J.; Capel-Sanchez, M.C.; Campos-Martin, J.M.; Gago, S.; De Castro, B.; Balula, S.S. Oxidative desulfurization strategies using Keggin-type polyoxometalate catalysts: Biphasic versus solvent-free systems. *Catal. Today* **2019**, *333*, 226–236. [CrossRef]
101. Ribeiro, S.O.; Granadeiro, C.M.; Corvo, M.C.; Pires, J.; Campos-Martin, J.M.; de Castro, B.; Balula, S.S. Mesoporous Silica vs. Organosilica Composites to Desulfurize Diesel. *Front. Chem.* **2019**, *7*, 756. [CrossRef] [PubMed]
102. Ribeiro, S.O.; Almeida, P.; Pires, J.; de Castro, B.; Balula, S.S. Polyoxometalate@ Periodic mesoporous organosilicas as active materials for oxidative desulfurization of diesels. *Microporous Mesoporous Mater.* **2020**, 110193. [CrossRef]
103. Ni, B.; Wang, X. Chemistry and properties at a sub-nanometer scale. *Chem. Sci.* **2016**, *7*, 3978–3991. [CrossRef]
104. Lu, Y.; Chen, W. Sub-nanometre sized metal clusters: From synthetic challenges to the unique property discoveries. *Chem. Soc. Rev.* **2012**, *41*, 3594–3623. [CrossRef]
105. Wang, J.; Li, X.; Zhang, S.; Lu, R. Facile synthesis of ultrasmall monodisperse “raisin-bun”-type $\text{MoO}_3/\text{SiO}_2$ nanocomposites with enhanced catalytic properties. *Nanoscale* **2013**, *5*, 4823–4828. [CrossRef] [PubMed]
106. Wang, J.; Wu, W.; Ye, H.; Zhao, Y.; Wang, W.-H.; Bao, M. MoO_3 subnanoclusters on ultrasmall mesoporous silica nanoparticles: An efficient catalyst for oxidative desulfurization. *RSC Adv.* **2017**, *7*, 44827–44833. [CrossRef]
107. Dou, J.; Zeng, H.C. Integrated Networks of Mesoporous Silica Nanowires and Their Bifunctional Catalysis–Sorption Application for Oxidative Desulfurization. *ACS Catal.* **2014**, *4*, 566–576. [CrossRef]
108. Ma, Z.; Yu, J.; Dai, S. Preparation of inorganic materials using ionic liquids. *Adv. Mater.* **2010**, *22*, 261–285. [CrossRef]
109. Leng, Y.; Wang, J.; Zhu, D.; Ren, X.; Ge, H.; Shen, L. Heteropolyanion-based ionic liquids: Reaction-induced self-separation catalysts for esterification. *Angew. Chem. Int. Ed.* **2009**, *48*, 168–171. [CrossRef] [PubMed]
110. Ma, Y.; Qing, S.; Wang, L.; Islam, N.; Guan, S.; Gao, Z.; Mamat, X.; Li, H.; Eli, W.; Wang, T. Production of 5-hydroxymethylfurfural from fructose by a thermo-regulated and recyclable Brønsted acidic ionic liquid catalyst. *RSC Adv.* **2015**, *5*, 47377–47383. [CrossRef]
111. Jiang, W.; Zhu, W.; Chang, Y.; Chao, Y.; Yin, S.; Liu, H.; Zhu, F.; Li, H. Ionic liquid extraction and catalytic oxidative desulfurization of fuels using dialkylpiperidinium tetrachloroferrates catalysts. *Chem. Eng. J.* **2014**, *250*, 48–54. [CrossRef]
112. Lü, H.; Wang, S.; Deng, C.; Ren, W.; Guo, B. Oxidative desulfurization of model diesel via dual activation by a protic ionic liquid. *J. Hazard. Mater.* **2014**, *279*, 220–225. [CrossRef]
113. Ding, Y.; Zhang, B.; Gupta, N.; Su, D.S. Heterogenization of homogenous reaction system on carbon surface with ionic liquid as mediator. *Green Chem.* **2015**, *17*, 1107–1112. [CrossRef]
114. Liu, C.; Zhang, G.; Zhao, C.; Li, X.; Li, M.; Na, H. MOFs synthesized by the ionothermal method addressing the leaching problem of IL–polymer composite membranes. *Chem. Commun.* **2014**, *50*, 14121–14124. [CrossRef]

115. Wan, H.; Chen, C.; Wu, Z.; Que, Y.; Feng, Y.; Wang, W.; Wang, L.; Guan, G.; Liu, X. Encapsulation of heteropolyanion-based ionic liquid within the metal–organic framework MIL-100 (Fe) for biodiesel production. *ChemCatChem* **2015**, *7*, 441–449. [CrossRef]
116. Patil, J.D.; Patil, S.A.; Pore, D.M. A polymer supported ascorbate functionalized task specific ionic liquid: An efficient reusable catalyst for 1, 3-dipolar cycloaddition. *RSC Adv.* **2015**, *5*, 21396–21404. [CrossRef]
117. Sharma, P.; Gupta, M. Silica functionalized sulphonic acid coated with ionic liquid: An efficient and recyclable heterogeneous catalyst for the one-pot synthesis of 1, 4-dihydropyridines under solvent-free conditions. *Green Chem.* **2015**, *17*, 1100–1106. [CrossRef]
118. Sidhpuria, K.B.; Daniel-da-Silva, A.L.; Trindade, T.; Coutinho, J.A. Supported ionic liquid silica nanoparticles (SILnPs) as an efficient and recyclable heterogeneous catalyst for the dehydration of fructose to 5-hydroxymethylfurfural. *Green Chem.* **2011**, *13*, 340–349. [CrossRef]
119. Zhang, J.; Wang, A.; Li, X.; Ma, X. Oxidative desulfurization of dibenzothiophene and diesel over [Bmim] 3PMo12O40. *J. Catal.* **2011**, *279*, 269–275. [CrossRef]
120. Virtanen, P.; Mikkola, J.-P.; Toukoniitty, E.; Karhu, H.; Kordas, K.; Eränen, K.; Wärnå, J.; Salmi, T. Supported ionic liquid catalysts—From batch to continuous operation in preparation of fine chemicals. *Catal. Today* **2009**, *147*, S144–S148. [CrossRef]
121. Bordoloi, A.; Sahoo, S.; Lefebvre, F.; Halligudi, S. Heteropoly acid-based supported ionic liquid-phase catalyst for the selective oxidation of alcohols. *J. Catal.* **2008**, *259*, 232–239. [CrossRef]
122. Sadeghzadeh, S.M. A heteropolyacid-based ionic liquid immobilized onto fibrous nano-silica as an efficient catalyst for the synthesis of cyclic carbonate from carbon dioxide and epoxides. *Green Chem.* **2015**, *17*, 3059–3066. [CrossRef]
123. Eguizábal, A.; Lemus, J.; Urbiztondo, M.; Moschovi, A.; Ntais, S.; Soler, J.; Pina, M. Ammonium based ionic liquids immobilized in large pore zeolites: Encapsulation procedures and proton conduction performance. *J. Power Sources* **2011**, *196*, 4314–4323. [CrossRef]
124. Gu, Q.; Zhu, W.; Xun, S.; Chang, Y.; Xiong, J.; Zhang, M.; Jiang, W.; Zhu, F.; Li, H. Preparation of highly dispersed tungsten species within mesoporous silica by ionic liquid and their enhanced catalytic activity for oxidative desulfurization. *Fuel* **2014**, *117*, 667–673. [CrossRef]
125. Zhang, M.; Li, M.; Chen, Q.; Zhu, W.; Li, H.; Yin, S.; Li, Y.; Li, H. One-pot synthesis of ordered mesoporous silica encapsulated polyoxometalate-based ionic liquids induced efficient desulfurization of organosulfur in fuel. *RSC Adv.* **2015**, *5*, 76048–76056. [CrossRef]
126. Xu, J.; Zhao, S.; Chen, W.; Wang, M.; Song, Y.F. Highly efficient extraction and oxidative desulfurization system using Na₇H₂LaW₁₀O₃₆·32H₂O in [bmim] BF₄ at room temperature. *Chem. Eur. J.* **2012**, *18*, 4775–4781. [CrossRef] [PubMed]
127. Xu, J.; Zhao, S.; Ji, Y.; Song, Y.F. Deep Desulfurization by Amphiphilic Lanthanide-Containing Polyoxometalates in Ionic-Liquid Emulsion Systems under Mild Conditions. *Chem. Eur. J.* **2013**, *19*, 709–715. [CrossRef]
128. Chen, Y.; Song, Y.F. Immobilization of LaW10 onto Ionic-Liquid-Modified Mesoporous Silica: Deep Desulfurization with Zero-Order Reaction Kinetics. *ChemPlusChem* **2014**, *79*, 304–309. [CrossRef] [PubMed]
129. Wang, Z.; Fan, X.; Han, D.; Gu, F. Structural and electronic engineering of 3DOM WO₃ by alkali metal doping for improved NO₂ sensing performance. *Nanoscale* **2016**, *8*, 10622–10631. [CrossRef]
130. Wang, J.; Zhang, W.; Zheng, Z.; Gao, Y.; Ma, K.; Ye, J.; Yang, Y. Enhanced thermal decomposition properties of ammonium perchlorate through addition of 3DOM core-shell Fe₂O₃/Co₃O₄ composite. *J. Alloys Compd.* **2017**, *724*, 720–727. [CrossRef]
131. Yue, D.; Lei, J.; Lina, Z.; Zhenran, G.; Du, X.; Li, J. Oxidation desulfurization of fuels by using amphiphilic hierarchically meso/macroporous phosphotungstic acid/SiO₂ catalysts. *Catal. Letters* **2018**, *148*, 1100–1109. [CrossRef]
132. Du, Y.; Yang, P.; Zhou, S.; Li, J.; Du, X.; Lei, J. Direct synthesis of ordered meso/macrostructured phosphotungstic acid/SiO₂ by EISA method and its catalytic performance of fuel oil. *Mater. Res. Bull.* **2018**, *97*, 42–48. [CrossRef]
133. Mirante, F.; Gomes, N.; Branco, L.C.; Cunha-Silva, L.; Almeida, P.L.; Pillinger, M.; Gago, S.; Granadeiro, C.M.; Balula, S.S. Mesoporous nanosilica-supported polyoxomolybdate as catalysts for sustainable desulfurization. *Microporous Mesoporous Mater.* **2019**, *275*, 163–171. [CrossRef]

134. Kozhevnikov, I.V. Catalysts for fine chemical synthesis. In *Catalysis by Polyoxometalates*; John Wiley & Sons Inc.: New York, NY, USA, 2002; Volume 2.
135. Okuhara, T.; Mizuno, N.; Misono, M. Catalytic chemistry of heteropoly compounds. In *Advances in Catalysis*; Academic Press; Elsevier: Amsterdam, The Netherlands, 1996; Volume 41, pp. 113–252.
136. Xiong, J.; Zhu, W.; Ding, W.; Yang, L.; Zhang, M.; Jiang, W.; Zhao, Z.; Li, H. Hydrophobic mesoporous silica-supported heteropolyacid induced by ionic liquid as a high efficiency catalyst for the oxidative desulfurization of fuel. *RSC Adv.* **2015**, *5*, 16847–16855. [CrossRef]
137. Huang, W.; Xu, P.; Yang, W.; Xu, W. Thermosensitive molecularly imprinted polymers based on magnetic nanoparticles for the recognition of sulfamethazine. *RSC Adv.* **2016**, *6*, 74734–74741. [CrossRef]
138. Gao, R.; Mu, X.; Hao, Y.; Zhang, L.; Zhang, J.; Tang, Y. Combination of surface imprinting and immobilized template techniques for preparation of core-shell molecularly imprinted polymers based on directly amino-modified Fe₃O₄ nanoparticles for specific recognition of bovine hemoglobin. *J. Mater. Chem. B* **2014**, *2*, 1733–1741. [CrossRef] [PubMed]
139. Li, Y.; Li, X.; Chu, J.; Dong, C.; Qi, J.; Yuan, Y. Synthesis of core-shell magnetic molecular imprinted polymer by the surface RAFT polymerization for the fast and selective removal of endocrine disrupting chemicals from aqueous solutions. *Environ. Pollut.* **2010**, *158*, 2317–2323. [CrossRef] [PubMed]
140. Men, H.-F.; Liu, H.-Q.; Zhang, Z.-L.; Huang, J.; Zhang, J.; Zhai, Y.-Y.; Li, L. Synthesis, properties and application research of atrazine Fe₃O₄@ SiO₂ magnetic molecularly imprinted polymer. *Environ. Sci. Pollut. Res.* **2012**, *19*, 2271–2280. [CrossRef] [PubMed]
141. Wang, J.; Wei, J. Selective and simultaneous removal of dibenzothiophene and 4-methylthiophene using double-template molecularly imprinted polymers on the surface of magnetic mesoporous silica. *J. Mater. Chem. A* **2017**, *5*, 4651–4659. [CrossRef]
142. Yue, Q.; Zhang, Y.; Jiang, Y.; Li, J.; Zhang, H.; Yu, C.; Elzatahry, A.A.; Alghamdi, A.; Deng, Y.; Zhao, D. Nanoengineering of core-shell magnetic mesoporous microspheres with tunable surface roughness. *J. Am. Chem. Soc.* **2017**, *139*, 4954–4961. [CrossRef]
143. Jiang, W.; Jia, H.; Fan, X.; Dong, L.; Guo, T.; Zhu, L.; Zhu, W.; Li, H. Ionic liquid immobilized on magnetic mesoporous microspheres with rough surface: Application as recyclable amphiphilic catalysts for oxidative desulfurization. *Appl. Surf. Sci.* **2019**, *484*, 1027–1034. [CrossRef]
144. Bian, L.; Li, Y.-J.; Li, J.; Nie, J.-N.; Dong, F.-Q.; Song, M.-X.; Wang, L.-S.; Dong, H.-L.; Li, H.-L.; Nie, X.-Q. Photovoltage response of (XZn) Fe₂O₄-BiFeO₃ (X= Mg, Mn or Ni) interfaces for highly selective Cr³⁺, Cd²⁺, Co²⁺ and Pb²⁺ ions detection. *J. Hazard. Mater.* **2017**, *336*, 174–187. [CrossRef]
145. Ko, T.-H.; Wang, S.; Chang, F.-H.; Chu, C.-Y. Performance of ZnMn₂O₄/SiO₂ sorbent for high temperature H₂S removal from hot coal gas. *RSC Adv.* **2017**, *7*, 35795–35804. [CrossRef]
146. Liu, Q.; Zhang, Z.; Liu, B.; Xia, H. Rare earth oxide doping and synthesis of spinel ZnMn₂O₄/KIT-1 with double gyroidal mesopores for desulfurization nature of hot coal gas. *Appl. Catal. B Environ.* **2018**, *237*, 855–865. [CrossRef]
147. Babaahamdi-Milani, M.; Nezamzadeh-Ejhieh, A. A comprehensive study on photocatalytic activity of supported Ni/Pb sulfide and oxide systems onto natural zeolite nanoparticles. *J. Hazard. Mater.* **2016**, *318*, 291–301. [CrossRef] [PubMed]
148. Ejhieh, A.N.; Khorsandi, M. Photodecolorization of Eriochrome Black T using NiS-P zeolite as a heterogeneous catalyst. *J. Hazard. Mater.* **2010**, *176*, 629–637. [CrossRef] [PubMed]
149. Sheikh-Mohseni, M.H.; Nezamzadeh-Ejhieh, A. Modification of carbon paste electrode with Ni-clinoptilolite nanoparticles for electrocatalytic oxidation of methanol. *Electrochim. Acta* **2014**, *147*, 572–581. [CrossRef]
150. Tamiji, T.; Nezamzadeh-Ejhieh, A. A comprehensive study on the kinetic aspects and experimental design for the voltammetric response of a Sn (IV)-clinoptilolite carbon paste electrode towards Hg (II). *J. Electroanal. Chem.* **2018**, *829*, 95–105. [CrossRef]
151. Radko, M.; Rutkowska, M.; Kowalczyk, A.; Mikrut, P.; Świąś, A.; Díaz, U.; Palomares, A.E.; Macyk, W.; Chmielarz, L. Catalytic oxidation of organic sulfides by H₂O₂ in the presence of titanasilicate zeolites. *Microporous Mesoporous Mater.* **2020**, *302*, 110219. [CrossRef]
152. Liu, Q.; Liu, B.; Liu, Q.; Xu, R.; Xia, H. Lattice substitution and desulfurization kinetic analysis of Zn-based spinel sorbents loading onto porous silicoaluminophosphate zeolites. *J. Hazard. Mater.* **2020**, *383*, 121151. [CrossRef]

153. Chao, Y.; Ju, H.; Luo, J.; Jin, Y.; Wang, C.; Xiong, J.; Wu, P.; Ji, H.; Zhu, W. Synthesis of porous carbon via a waste tire leavening strategy for adsorptive desulfurization. *RSC Adv.* **2019**, *9*, 30575–30580. [CrossRef]
154. Shi, Y.; Zhang, X.; Wang, L.; Liu, G. MOF-derived porous carbon for adsorptive desulfurization. *AIChE J.* **2014**, *60*, 2747–2751. [CrossRef]
155. Liu, C.; Yuan, P.; Duan, A.; Mei, J.; Zheng, P.; Meng, Q.; Cai, A.; Cheng, T.; Gong, Y. Monodispersed dendritic mesoporous silica/carbon nanospheres with enhanced active site accessibility for selective adsorptive desulfurization. *J. Mater. Sci.* **2019**, *54*, 8148–8162. [CrossRef]
156. Ma, X.; Sun, L.; Song, C. A new approach to deep desulfurization of gasoline, diesel fuel and jet fuel by selective adsorption for ultra-clean fuels and for fuel cell applications. *Catal. Today* **2002**, *77*, 107–116. [CrossRef]
157. Wang, L.; Chen, Y.; Du, L.; Li, S.; Cai, H.; Liu, W. Nickel-heteropolyacids supported on silica gel for ultra-deep desulfurization assisted by Ultrasound and Ultraviolet. *Fuel* **2013**, *105*, 353–357. [CrossRef]
158. Zheng, H.; Sun, Z.; Chen, X.; Zhao, Q.; Wang, X.; Jiang, Z. A micro reaction-controlled phase-transfer catalyst for oxidative desulfurization based on polyoxometalate modified silica. *Appl. Catal. A Gen.* **2013**, *467*, 26–32. [CrossRef]
159. Xun, S.; Zhu, W.; Zheng, D.; Zhang, L.; Liu, H.; Yin, S.; Zhang, M.; Li, H. Synthesis of metal-based ionic liquid supported catalyst and its application in catalytic oxidative desulfurization of fuels. *Fuel* **2014**, *136*, 358–365. [CrossRef]
160. Zhao, Y.; Wang, J.; Jiang, H.; Hu, Y. Desulfurization performance of ether-functionalized imidazolium-based ionic liquids supported on porous silica gel. *Energy Fuels* **2015**, *29*, 1941–1945. [CrossRef]
161. Safa, M.; Mokhtarani, B.; Mortaheb, H.R.; Tabar Heidar, K.; Sharifi, A.; Mirzaei, M. Oxidative desulfurization of diesel fuel using a Brønsted acidic ionic liquid supported on silica gel. *Energy Fuels* **2017**, *31*, 10196–10205. [CrossRef]
162. Samokhvalov, A.; Tatarchuk, B.J. Review of experimental characterization of active sites and determination of molecular mechanisms of adsorption, desorption and regeneration of the deep and ultradeep desulfurization sorbents for liquid fuels. *Catal. Rev.* **2010**, *52*, 381–410. [CrossRef]
163. Hernández-Maldonado, A.J.; Yang, R.T. Desulfurization of transportation fuels by adsorption. *Catal. Rev.* **2004**, *46*, 111–150. [CrossRef]
164. Yang, R.T.; Hernández-Maldonado, A.J.; Yang, F.H. Desulfurization of transportation fuels with zeolites under ambient conditions. *Science* **2003**, *301*, 79–81. [CrossRef] [PubMed]
165. Tran, D.T.; Palomino, J.M.; Oliver, S.R. Desulfurization of JP-8 jet fuel: Challenges and adsorptive materials. *RSC Adv.* **2018**, *8*, 7301–7314. [CrossRef]
166. Wang, Y.; Yang, R.T.; Heinzl, J.M. Desulfurization of jet fuel by π -complexation adsorption with metal halides supported on MCM-41 and SBA-15 mesoporous materials. *Chem. Eng. Sci.* **2008**, *63*, 356–365. [CrossRef]
167. Wang, Y.; Yang, R.T.; Heinzl, J.M. Desulfurization of jet fuel JP-5 light fraction by MCM-41 and SBA-15 supported cuprous oxide for fuel cell applications. *Ind. Eng. Chem. Res.* **2009**, *48*, 142–147. [CrossRef]
168. Chen, H.; Wang, Y.; Yang, F.H.; Yang, R.T. Desulfurization of high-sulfur jet fuel by mesoporous π -complexation adsorbents. *Chem. Eng. Sci.* **2009**, *64*, 5240–5246. [CrossRef]
169. Palomino, J.M.; Tran, D.T.; Hauser, J.L.; Dong, H.; Oliver, S.R. Mesoporous silica nanoparticles for high capacity adsorptive desulfurization. *J. Mater. Chem. A* **2014**, *2*, 14890–14895. [CrossRef]
170. Gonzalez, J.; Wang, J.; Chen, L.; Manriquez, M.; Dominguez, J. Structural defects, Lewis acidity, and catalysis properties of mesostructured WO₃/SBA-15 nanocatalysts. *J. Phys. Chem. C* **2017**, *121*, 23988–23999. [CrossRef]
171. González, J.; Wang, J.A.; Chen, L.; Manriquez, M.; Salmones, J.; Limas, R.; Arellano, U. Quantitative determination of oxygen defects, surface lewis acidity, and catalytic properties of mesoporous MoO₃/SBA-15 catalysts. *J. Solid State Chem.* **2018**, *263*, 100–114. [CrossRef]





Article

Derivation of Luminescent Mesoporous Silicon Nanocrystals from Biomass Rice Husks by Facile Magnesiothermic Reduction

Sankar Sekar^{1,2} and Sejoon Lee^{1,2,*}

¹ Division of Physics & Semiconductor Science, Dongguk University-Seoul, Seoul 04620, Korea; sanssekar@dongguk.edu

² Quantum-Functional Semiconductor Research Center, Dongguk University-Seoul, Seoul 04620, Korea

* Correspondence: sejoon@dongguk.edu

Abstract: High-quality silicon (Si) nanocrystals that simultaneously had superior mesoporous and luminescent characteristics were derived from sticky, red, and brown rice husks via the facile and cost-effective magnesiothermic reduction method. The Si nanocrystals were confirmed to comprise an aggregated morphology with spherical nanocrystals (e.g., average sizes of 15–50 nm). Due to the surface functional groups formed at the nanocrystalline Si surfaces, the Si nanocrystals clearly exhibited multiple luminescence peaks in visible-wavelength regions (i.e., blue, green, and yellow light). Among the synthesized Si nanocrystals, additionally, the brown rice husk (BRH)-derived Si nanocrystals showed to have a strong UV absorption and a high porosity (i.e., large specific surface area: 265.6 m²/g, small average pore diameter: 1.91 nm, and large total pore volume: 0.5389 cm³/g). These are indicative of the excellent optical and textural characteristics of the BRH-derived Si nanocrystals, compared to previously reported biomass-derived Si nanocrystals. The results suggest that the biomass BRH-derived Si nanocrystals hold great potential as an active source material for optoelectronic devices as well as a highly efficient catalyst or photocatalyst for energy conversion devices.

Citation: Sekar, S.; Lee, S. Derivation of Luminescent Mesoporous Silicon Nanocrystals from Biomass Rice Husks by Facile Magnesiothermic Reduction. *Nanomaterials* **2021**, *11*, 613. <https://doi.org/10.3390/nano11030613>

Academic Editors: Céline TERNON and Sotirios BASKOUTAS

Received: 31 December 2020

Accepted: 22 February 2021

Published: 1 March 2021

Publisher's Note: MDPI stays neutral with regard to jurisdictional claims in published maps and institutional affiliations.



Copyright: © 2021 by the authors. Licensee MDPI, Basel, Switzerland. This article is an open access article distributed under the terms and conditions of the Creative Commons Attribution (CC BY) license (<https://creativecommons.org/licenses/by/4.0/>).

Keywords: biomass rice husk; silicon; nanocrystals; luminescence; high porosity

1. Introduction

Silicon (Si) is one of the most powerful semiconductors that have led to the strong advancement of modern electronics. However, bulk Si is inadequate as an active material (i.e., a core part for visible light emission or detection) in optoelectronic devices because of its indirect bandgap with an infrared energy gap of 1.12 eV at 300 K [1,2]. One effective way to overcome this issue is the nanocrystallization of Si, which can allow us to create visible light emission and detection characteristics, attributable to the quantum confinement effect and the size effect in Si nanocrystals [3–7]. Therefore, the fabrication of Si nanocrystals has attracted tremendous attention in wide scientific and technologic communities because of their vast application fields in optoelectronics as well as electronics. For instance, nanofloating gate flash memory devices [8–11], field-effect electroluminescence devices [12,13], tandem solar cells [14], and optical waveguides [15,16] are typical examples that can use the quantum-confined electronic energy system in Si nanocrystals. Owing to the high porosity of Si nanocrystals, furthermore, they are also very useful as an active source material in energy storage and conversion devices. For example, Si nanocrystals could be used as an effective catalyst for the hydrogen evolution reaction [17], and be utilized as an anodic source material for highly energy-efficient lithium-ion and sodium-ion batteries [18–20].

To obtain highly porous and/or highly luminescent Si nanocrystals, many researchers have contrived and designed various experimental methods, e.g., laser ablation [21], non-thermal plasma processes [22], pulsed laser deposition [23], chemical doping [24], electrochemical etching [25], chemical vapor deposition [26], annealing of borophosphosilicate

glasses [27], and laser pyrolysis [28]. However, these methods require expensive equipment, complex procedures, and high thermal budgets (also see Table S1, Supplementary Materials). Therefore, a facile and cost-effective approach is necessary for the mass production of Si nanoparticles. Considering both the cost-effectiveness and the eco-friendliness, biomass wastes are truly fascinating resources that can provide us with natural siliceous constituents. Accordingly, various biomass resources (e.g., sugarcane bagasse [29], bamboo leaves [29,30], beach sand [31], corn leaves [32], and rice husks (RHs) [33–37]) were used in earlier studies for the derivation of high-quality Si nanocrystals (also see Table S2 for the comparison of Si production from various biomass resources by using several experimental techniques, Supplementary Materials). Among them, RHs are one of the most prominent siliceous precursors because of their huge availability and high silica contents [18,38,39]. These provide us with a good hint to produce a large amount of Si nanocrystals via the recycling of biomass RHs. Despite such benefits, to our best knowledge, the synthesis of RH-derived high-quality Si nanocrystals with both high porosity and high luminescence has not been reported to date. Furthermore, the coexistence of both mesoporous and luminescent characteristics in a single material system is truly helpful for future energy technology; for example, the photocatalytic hydrogen evolution reaction [40–42] and oxygen evolution reaction [43–45].

We, therefore, investigated the facile derivation of mesoporous-and-luminescent Si nanocrystals from various RHs (i.e., sticky RHs, red RHs, and brown RHs) through the magnesiothermic reduction process, which can be simply performed in an inert atmosphere without toxic gases and vacuum facilities. Herein, we report on a comprehensive study from the synthesis to the characterization of RH-derived mesoporous luminescent Si nanocrystals. The kinetics of magnesiothermic reduction for Si nanocrystal production is discussed, and the structural, morphological, optical, and textural properties of the synthesized Si nanocrystals are thoroughly examined in detail.

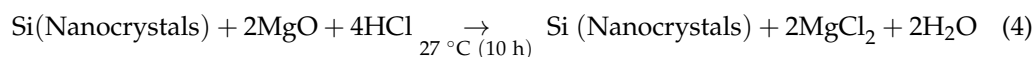
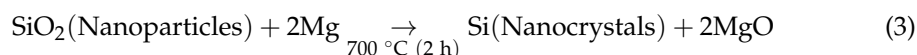
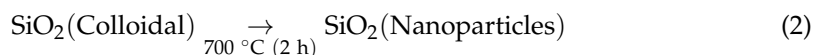
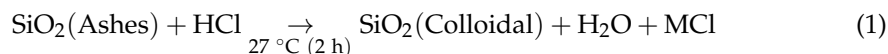
2. Experimental Section

2.1. Material Preparation

The biomass sticky rice husks (S-RHs) were collected from Gyeonggi, South Korea, and the red rice husks (R-RHs) and brown rice husks (B-RHs) were collected from Perambalur, Tamil Nadu, India. Hydrochloric acid (HCl, 37%), hydrofluoric acid (HF, 48%), and magnesium (Mg, 99% purity) powders were purchased from Sigma-Aldrich (St. Louis, MO, USA) and used with no additional purification.

2.2. Synthesis of Si Nanocrystals

The derivation of the Si nanocrystals via magnesiothermic reduction can be described by the following chemical reactions:



M in Equation (1) is the possible precipitates from raw bio-silica in the biomass RHs (e.g., Na, K, Ca, Fe, and Mg), which are normally removed as MCl after the HCl treatment. To investigate the dependence of the biomass RH resources, we used three different types of RHs, i.e., S-RHs, R-RHs, and B-RHs. As schematically illustrated in Figure 1, initially, all three types of RHs were carbonized at 500 °C for 2 h under an air atmosphere to obtain their ashes. Then, 3 g of each RH ash was stirred in a 10% HCl solution for 2 h to eliminate metal ions and contamination (e.g., Equation (1)). After HCl leaching, the

samples were rinsed with deionized water (DI), filtered, and dried at 150 °C for 15 h in an electric oven. Subsequently, the samples were transferred to an alumina crucible and were further calcinated at 700 °C for 2 h under an air atmosphere in a muffle furnace (e.g., Equation (2)). During this calcination step, the silica nanopowders were obtained from the HCl-leached RH ashes. Next, the SiO₂ nanopowders were reduced into the Si nanocrystals through magnesiothermic reduction. To achieve the reduction reaction, as a primary task, each type of SiO₂ nanopowder (2 g) was mixed with the Mg powders (0.5 g). Then, the mixture powders were annealed at 700 °C for 2 h under an Ar atmosphere in a tube furnace (e.g., Equation (3)). The obtained products were stimulated with 1 M HCl (HCl:H₂O:EtOH = 0.66:4.72:8.88 molar ratio) for 10 h to remove MgO (e.g., Equation (4)). After the HCl treatment, the colloidal solutions were reacted with 5% HF for 1 h to eliminate the residual SiO₂ inside the magnesiothermally reduced Si nanopowders. Finally, the obtained Si nanopowders were washed in DI water, filtered, and dried at 80 °C for 12 h under vacuum. Through these sequences, we were able to obtain the powder type of the Si nanocrystals. For convenience, we denote the three different types of the Si nanocrystals as S-Si, R-Si, and B-Si, which were derived from S-RHs, R-RHs, and B-RHs, respectively.

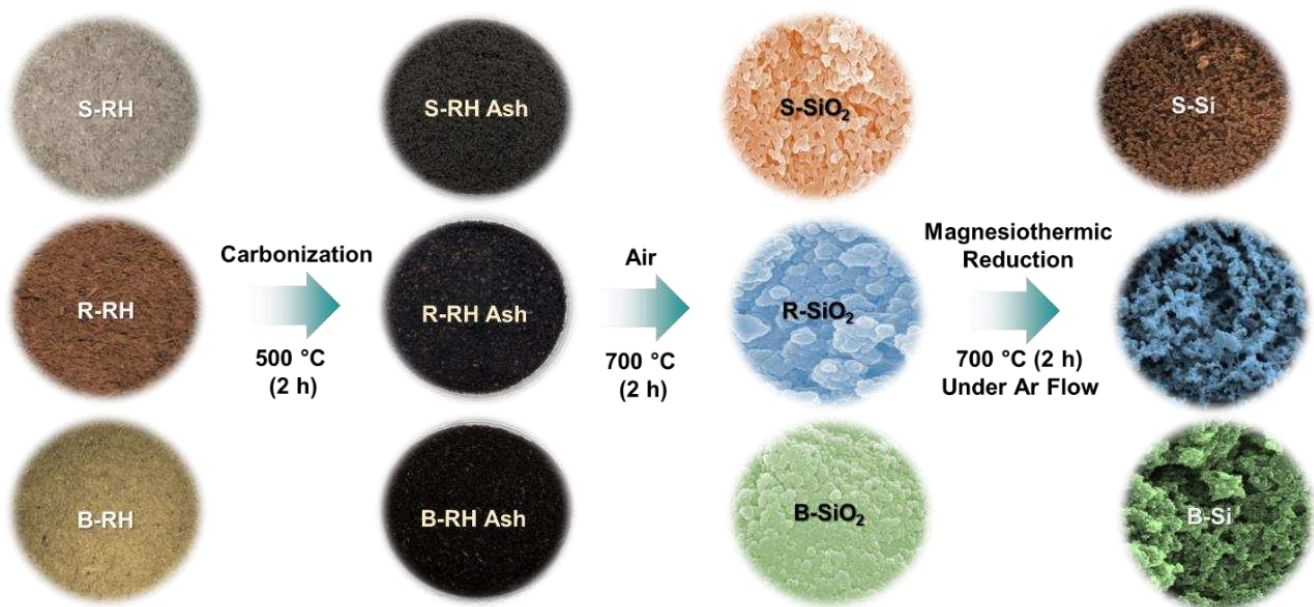


Figure 1. Schematic illustration of the magnesiothermic reduction process for synthesizing the Si nanocrystals by using biomass sticky rice husks (S-RHs), red rice husks (R-RHs), and brown rice husks (B-RHs).

2.3. Characterization of Material Properties

The morphological and the compositional properties of the Si nanocrystals were monitored by field-emission scanning electron microscopy (FE-SEM) using an Inspect F50 system (FEI Co., Mahwah, NJ, USA) and its in situ energy dispersive X-ray (EDX) spectroscopy, respectively. The structural and the vibrational properties of the samples were characterized by Raman scattering spectroscopy using a LabRAM HR800 system (HORIBA Jobin Yvon Inc., Edison, NJ, USA) and X-ray diffractometry (XRD) using a D2 Phaser system (Bruker, Madison, WI, USA), respectively. The functional groups of the nanocrystals were examined by Fourier transform infrared (FTIR) spectroscopy using a Spectrum-100 system (Perkin Elmer, Shelton, CT, USA). The optical absorption and emission characteristics were evaluated by UV–VIS spectroscopy using an S-3100 system (Scinco, Seoul, Republic of Korea) and photoluminescence (PL) spectroscopy using a Cary Eclipse Fluorescence Spectrophotometer (Agilent Technologies, Santa Clara, CA, USA), respectively. The textural properties were analyzed by nitrogen adsorption–desorption isotherms (N₂-ADI) using a BELSORP-mini II system (MicrotracBEL, Osaka, Japan).

3. Results and Discussion

3.1. Morphological and Compositional Properties

Figure 2 shows the FE-SEM images of the S-Si, R-Si, and B-Si nanocrystals. The S-Si sample exhibited cylindrically interconnected spherical nanocrystals (Figure 2a). However, the R-Si and the B-Si samples displayed a nanosponge-like morphology, where a lot of small spherical nanocrystals were densely aggregated (Figure 2b,c).

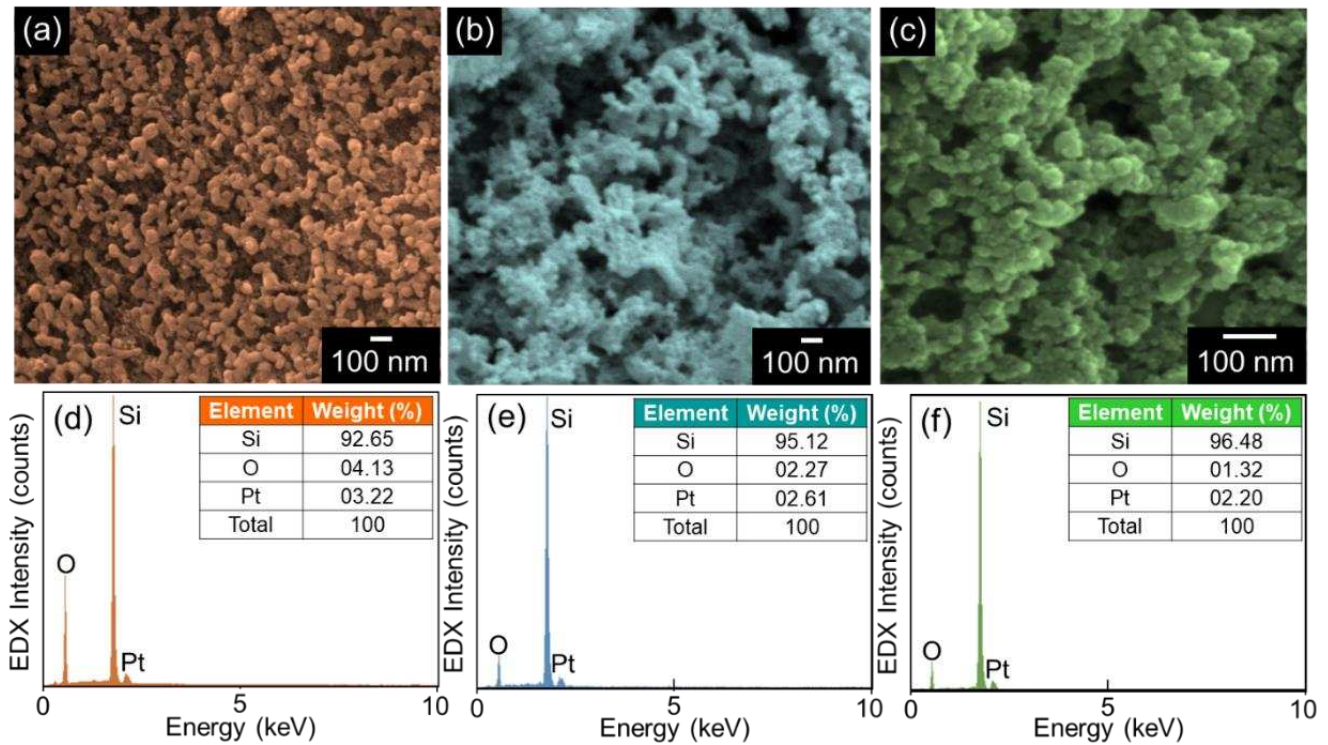


Figure 2. Field-emission scanning electron microscopy (FE-SEM) images of the (a) S-Si, (b) R-Si, and (c) B-Si nanocrystals and energy dispersive X-ray (EDX) spectra of the (d) S-Si, (e) R-Si, and (f) B-Si nanocrystals. The inset in each EDX graph summarizes the compositional properties of the Si nanoparticles.

Here, it should be noticed that the average crystal size of B-Si (~15 nm) is much smaller than those of R-Si (~35 nm) and S-Si (~50 nm). We believe such a discrepancy is attributable to the smaller contents of Si species in the raw sources of the B-RH ashes (Si~2.46%) than the R-RH (Si~5.95%) and S-RH ashes (Si~24.62%) (see Figure S1, Supplementary Materials). In other words, during the acid treatment and the calcination step (i.e., Equations (1) and (2)), the size of the colloidal SiO₂ should be smaller for the B-RH case than the others because the lower quantity of Si species in B-RH (i.e., raw bio-silica in the biomass resource) may increase the segregation of the silica nanoparticles [46]. According to previous literature [47,48], using the Fokker–Planck equation [49–51], the size distribution of the Si nanoparticles ($C(i,t)$) can be described as follows:

$$\frac{\partial C(i,t)}{\partial t} = -(N(t) - N_e) \frac{\partial(k(i)C(i,t))}{\partial i} + (N(t) + N_e) \frac{\partial^2(k(i)C(i,t))}{\partial^2 i^2}, \quad (5)$$

where i is the number of Si atoms, N_e is the equilibrium concentration of impurity atoms in the substance matrix, and $N(t)$ is the number of Si atoms in the nanocrystal at each moment of time. The kinetic coefficient $k(i)$ in Equation (5) is proportional to both the diffusion coefficient of the Si atoms in the matrix D and the Si nanocrystal radius ($R(i)$):

$$k(i) = 4\pi DR(i) \quad (6)$$

$$R(i) = b(i + m)^\alpha, \quad (7)$$

where b is the distance parameter of the nanocrystals, m is the size homogeneity factor, and α is the geometry factor ($= 1/3$ for spherical nanocrystals). Hence, the smaller size of B-Si can be interpreted as resulting from the lower concentration of Si species in B-RH. We therefore conjecture that the size of the Si nanocrystals could be automatically controlled by choosing the type of the biomass raw resources.

Next, the compositional properties of the samples were evaluated by EDX. As shown in Figure 2d–f, all the prepared samples were composed of the main species of Si and O, arising from the body and the surface of the nanocrystals, respectively. The additional component of Pt is thought of as sprouting from the conductive coating layer for the FE-SEM measurements.

3.2. Structural and Vibrational Properties

The crystallographic properties of the S-Si, R-Si, and B-Si samples were characterized by XRD. As shown in Figure 3a, all of the three samples exhibited the typical diffraction patterns of crystalline Si at 28.4° , 47.4° , 56.1° , 69.1° , 76.4° , and 88.2° , which correspond to the (111), (220), (311), (400), (331), and (422) Si planes (JCPDS No. 27-1402 [18,33,52,53]), respectively. This means that all three, S-Si, R-Si, and B-Si, were well crystallized via magnesiothermic reduction from the biomass resources of the S-RH, R-RH, and B-RH ashes, respectively. By using the Scherer formula [54–56], the average crystallite sizes of the S-Si, R-Si, and B-Si nanocrystals were determined to be 33, 28, and 22 nm, respectively. This corroborates the dependence of the Si nanocrystal size on the kind of biomass raw source; i.e., the Si nanocrystal size relies on the different Si contents in each RH, as confirmed in Figure 2. The nanocrystallization of the samples was further elucidated by Raman spectroscopy measurements. As shown in Figure 3b, the Raman spectra of all three samples revealed a similar feature of the typical Raman vibration modes from crystalline Si. Namely, the sharp peak at 519 cm^{-1} (i.e., the first-order transversal optical (TO) mode [18,57,58]) and the broad hump at 957 cm^{-1} (i.e., the second-order TO mode [18,57,58]) are clearly observable in all the samples, while no other Raman bands are visible. This demonstrates that the high-purity Si nanocrystals were effectively derived from the biomass RHs through the magnesiothermic reduction process.

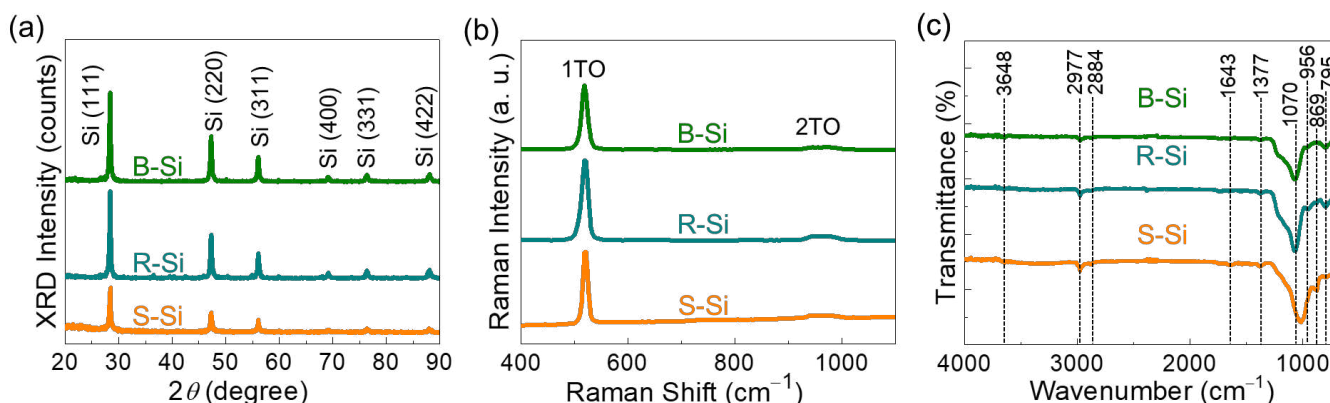


Figure 3. (a) X-ray diffractometry (XRD) patterns, (b) Raman spectra, and (c) Fourier transform infrared (FTIR) spectra of the S-Si, R-Si, and B-Si nanocrystals.

For the nanostructured materials, the functional groups of the elemental species and molecular states depend on the shape and the size of the nanomaterials because they rely on the bonding states at the surface terminals. To examine the functional groups of the samples, FTIR measurements were carried out. As shown in Figure 3c, the samples displayed several FTIR features at 795 , 869 , 956 , 1070 , 1377 , 1643 , 2884 , 2977 , and 3648 cm^{-1} , all of which are closely relevant to the Si nanostructure. In other words, the transmission band at 795 cm^{-1} is ascribed to the Si–C stretching mode [36], and the vibrational band at

869 cm^{-1} is attributed to the Si–N stretching mode [59,60]. Similarly, the band at 956 cm^{-1} arose from the Si–H bending mode [61]. Additionally, the bands at 1070, 1377, 2884, and 2977 cm^{-1} correspond to the Si–O bending, CH_3 bending, symmetric CH_2 vibration, and CH_3 stretching modes, respectively [59,62,63]. The bands at 3648 and 1643 cm^{-1} are responsible for the Si–OH vibrations [64].

3.3. Optical Properties

Figure 4a shows the UV–VIS absorption spectra of the S-Si, R-Si, and B-Si samples. The B-Si nanocrystals revealed strong UV adsorption, while the S-Si and the R-Si nanocrystals exhibited predominant visible-light adsorption characteristics. For B-Si, particularly, two distinct Si nanocrystal-related absorption bands are observable at $A_1 \sim 270$ nm and $A_2 \sim 340$ nm. Namely, the A_1 peak and the A_2 shoulder are associated with the $L-L$ and the $\Gamma-\Gamma$ transitions in nanocrystalline Si, respectively [6,36]. Since both the A_1 and A_2 adsorption intensities indicate the degree of nanocrystallization [65], one can observe that the B-Si sample was well crystallized with a smaller size than the others, as confirmed by FE-SEM and XRD.

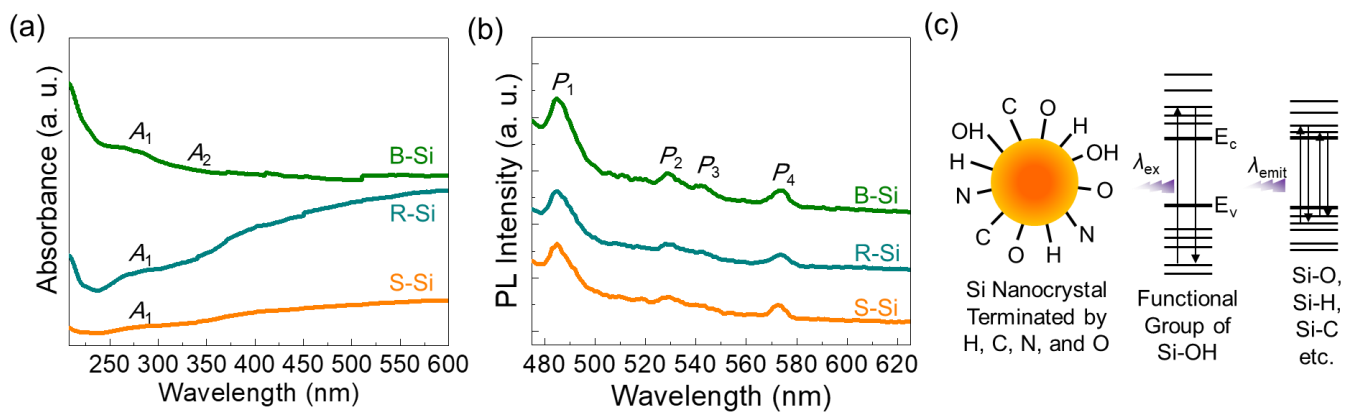


Figure 4. (a) UV–VIS absorption spectra, (b) photoluminescence (PL) spectra, and (c) light emission mechanism of the rice husk (RH)-derived biomass Si nanocrystals.

According to earlier literature [3–5], those transitions originate from the discrete energy states within the modified electronic band structure of the Si nanocrystal. In other words, when the nanocrystal size becomes smaller than the exciton Bohr radius (~ 4 nm for Si), the subbands above the conduction band and below the valence band could be altered because of the quantum confinement effect. Then, discrete energy states would be created inside the modified electronic band structure. Furthermore, since the Si nanocrystal surface is typically terminated by H, C, and O (also see the FTIR for our samples in Figure 3c), the overlap of electron and hole wave-functions would become significant [65]. These subband modulation effects can be elucidated by PL. As shown in Figure 4b, the samples emitted visible light at $P_1 \sim 485$ nm, $P_2 \sim 530$ nm, $P_3 \sim 545$ nm, and $P_4 \sim 573$ nm. The strong P_1 emission is reported to emerge from the radiative optical transitions between the discrete energy states that are created at the Si–OH surface functional groups [66] (also see Figure 4c). The other peaks at P_2 , P_3 , and P_4 are also well known to arise from the radiative optical transitions between the energy states that are created by the surface functional groups of Si–O [67], Si–C [5], and Si–H [68,69], respectively. Figure 5 shows the excitation-dependent PL spectra of the S-Si, R-Si, and B-Si samples. As the excitation wavelength (λ_{ex}) increased, the peak position of the light emission (λ_{emit}) tended to shift to the longer wavelength region (i.e., red shift). Such a λ_{emit} dependence on λ_{ex} was present in all the samples, and the λ_{emit} positions were almost identical, regardless of the raw source of the RHs. These findings depict that the PL emission in all the samples originated from the surface functional group-related subband modulation rather than the quantum confinement effect.

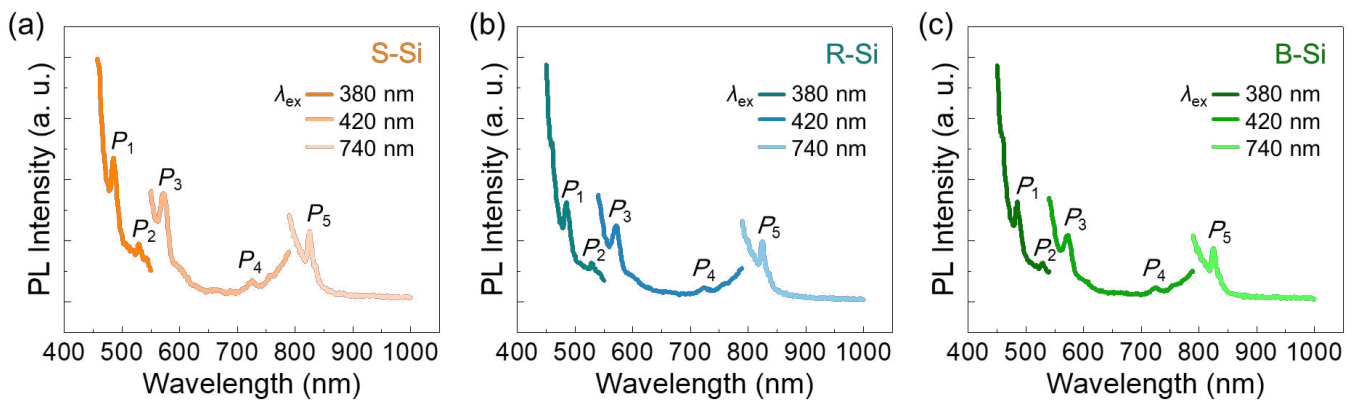


Figure 5. Excitation-dependent PL spectra of the (a) S-Si, (b) R-Si, and (c) B-Si nanocrystals.

3.4. Textural Properties

The nanocrystallization of Si would have sturdily affected the porosity of the entire material system because the locally crystallized small nanocrystal has a high surface-to-volume ratio. In short, the nanocrystals must form structural voids at the surface area, giving rise to an increase in the porosity of the material. To assess the porosity of the S-Si, R-Si, and B-Si samples, thus, the textural characteristics were evaluated by the Brunauer–Emmett–Teller (BET) and the Barrett–Joyner–Halenda (BJH) analysis methods. Firstly, the specific surface area (S_{ss}) was determined by N_2 -ADI measurements. As shown in Figure 6, all the samples exhibited Type-IV isotherm curves (classified according to IUPAC), representing the distinctive mesoporous characteristics of the materials [33,70]. Through the BET analysis, the S_{ss} values of the S-Si, R-Si, and B-Si nanocrystals were calculated to be 168.1, 212.4, and 265.6 m^2/g , respectively.

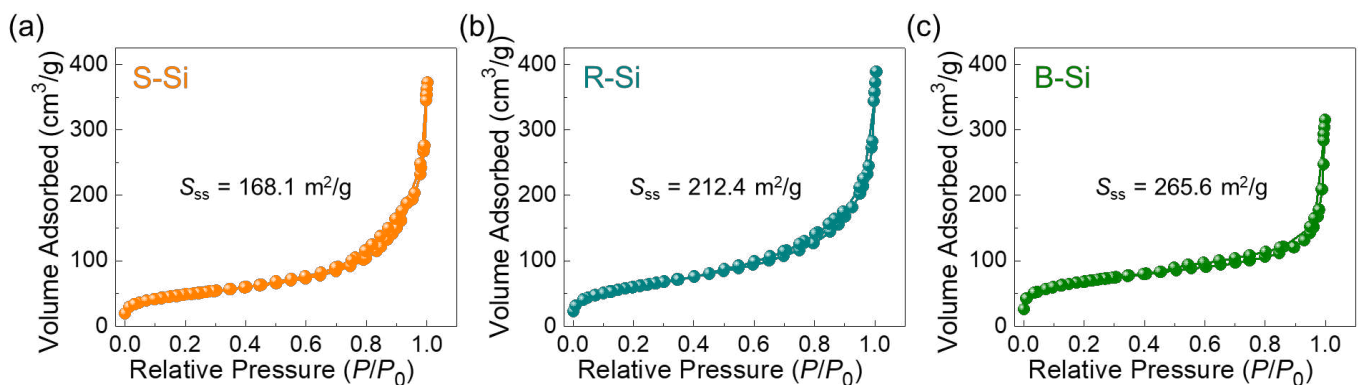


Figure 6. Nitrogen adsorption–desorption isotherm (N_2 -ADI) characteristics of the (a) S-Si, (b) R-Si, and (c) B-Si nanocrystals.

Next, the pore distribution characteristics were examined by BJH measurements (Figure 7). The pore surface areas (S_{ps}) were determined to be 149.3, 196.9, and 218.5 m^2/g for the S-Si, R-Si, and B-Si nanocrystals, respectively, and the total pore volumes (V_{tp}) were calculated to be 0.4103, 0.4201, and 0.5389 cm^3/g for S-Si, R-Si, and B-Si, respectively. Compared to S-Si and R-Si, the B-Si sample had larger magnitudes of S_{ps} and V_{tp} because of both the smaller nanocrystal size and the uniform distribution. Accordingly, the average pore diameter of B-Si ($d_{ap} \sim 4.91$ nm) was also smaller than those of S-Si ($d_{ap} \sim 9.76$ nm) and R-Si ($d_{ap} \sim 7.82$ nm).

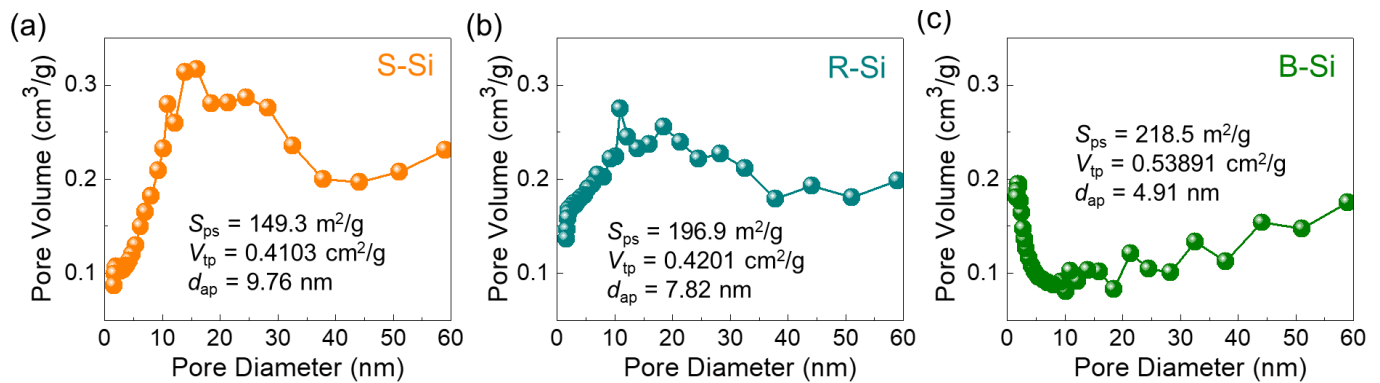


Figure 7. Pore size characteristics of the (a) S-Si, (b) R-Si, and (c) B-Si nanocrystals.

Finally, we compared the textural and the optical characteristics of our samples with various biomass-derived Si nanocrystals previously reported. As can be confirmed from Tables 1 and 2, the B-Si nanocrystals possessed a superior porosity compared to the others, and had a great potential for multiple light emissions. Based on all the above results, therefore, one can surmise that the magnesiothermally reduced biomass B-Si nanocrystals hold great promise in various applications such as energy storage/conversion devices and optoelectronic devices.

Table 1. Comparison of the luminescence characteristics for various biomass-derived Si nanostructures.

Biomass	Nanostructures	Light Emission Color	References
Brown Rice Husks	Spherical Si Nanocrystals	Blue, Green, Yellow	This Work
Red Rice Husks	Spherical Si Nanocrystals	Blue, Green, Yellow	This Work
Sticky Rice Husks	Spherical Si Nanocrystals	Blue, Green, Yellow	This Work
Rice Husks	Si Nanoparticles	Green	[36]
Wheat Straws	Si Nanoparticles	Blue	[37]
Sugarcane Bagasse	Si Nanoparticles	Blue	[37]
Rice Husks	Si Nanoparticles	Blue	[37]

Table 2. Comparison of the pore characteristics for various biomass-derived Si nanostructures.

Biomass	S_{ss} (m ² /g)	V_{tp} (cm ³ /g)	References
Brown Rice Husks	265.6	0.5389	This Work
Red Rice Husks	212.4	0.4201	This Work
Sticky Rice Husks	168.1	0.4103	This Work
Bamboo Leaves	302.13	0.526	[30]
Beach Sand	323	-	[31]
Corn Leaves	64	-	[32]
Rice Husks	288.4	0.35	[53]
Rice Husks	47.3	0.18	[34]
Rice Husks	127.05	0.2306	[71]
Waste Glass Microfiber Filter	66.12	0.64	[72]
Rice Husks	57.9	-	[73]

4. Conclusions

High-quality Si nanocrystals that simultaneously showed both strong luminescence and high porosity were successfully derived from various RHs through the facile magnesiothermic reduction method. Owing to the different quantities of raw bio-silica in each RH, the size of the Si nanoparticles could be automatically varied from 15 to 50 nm. Due to the existence of the surface functional groups at the nanocrystals, the samples showed multiple light emissions in the visible-wavelength regions (i.e., blue, green, and yellow). Among the prepared samples, the B-Si nanocrystals exhibited a higher UV absorption and

a superior porosity. The results depict that the B-RH-derived Si nanocrystals can play a crucial role as high-performance electrocatalysts, photocatalysts, and light emitters.

Supplementary Materials: The Supplementary Materials are available online at <https://www.mdpi.com/2079-4991/11/3/613/s1>: Chemical Composition of Rice Husk Ashes; Comparison of Various Methods for Silicon Production; Figure S1. EDX spectra of (a) S-RH, (b) R-RH, and (c) B-RH ashes. Note that Pt in each raw source material arose from the conductive coating of Pt for better focusing and imaging during SEM and EDX measurements, Table S1. Summary of silicon synthesized from various resources through several experimental methods, Table S2. Summary of silicon synthesized from various biomass resources through several experimental methods.

Author Contributions: Investigation and writing—original draft, S.S.; conceptualization, supervision, funding acquisition, and writing—review and editing, S.L. All authors have read and agreed to the published version of the manuscript.

Funding: This research was supported by the National Research Foundation (NRF) of Korea through the Basic Science Research Programs (2016R1A6A1A03012877 and 2019R1A2C1085448) funded by the Korean Government.

Conflicts of Interest: The authors declare no conflict of interest.

References

- Grim, J.Q.; Manna, L.; Moreels, I. A sustainable future for photonic colloidal nanocrystals. *Chem. Soc. Rev.* **2015**, *44*, 5897–5914. [CrossRef]
- Berencén, Y.; Prucnal, S.; Liu, F.; Skorupa, I.; Hübner, R.; Rebohle, L.; Zhou, S.; Schneider, H.; Helm, M.; Skorupa, W. Room-temperature short-wavelength infrared Si photodetector. *Sci. Rep.* **2017**, *7*, 43688. [CrossRef] [PubMed]
- Klimov, V.I.; Ivanov, S.A.; Nanda, J.; Achermann, M.; Bezel, I.; McGuire, J.A.; Piryatinski, A. Single-exciton optical gain in semiconductor nanocrystals. *Nature* **2007**, *447*, 441–446. [CrossRef]
- Barbagiovanni, E.G.; Lockwood, D.J.; Simpson, P.J.; Goncharova, L.V. Quantum confinement in Si and Ge nanostructures. *J. Appl. Phys.* **2012**, *111*, 034307. [CrossRef]
- Montalti, M.; Cantelli, A.; Battistelli, G. Nanodiamonds and silicon quantum dots: Ultrastable and biocompatible luminescent nanoprobes for long-term bioimaging. *Chem. Soc. Rev.* **2015**, *44*, 4853–4921. [CrossRef] [PubMed]
- Li, Q.; Luo, T.-Y.; Zhou, M.; Abroshan, H.; Huang, J.; Kim, H.J.; Rosi, N.L.; Shao, Z.; Jin, R. Silicon Nanoparticles with Surface Nitrogen: 90% Quantum Yield with Narrow Luminescence Bandwidth and the Ligand Structure Based Energy Law. *ACS Nano* **2016**, *10*, 8385–8393. [CrossRef] [PubMed]
- Wolf, O.; Dasog, M.; Yang, Z.; Balberg, I.; Veinot, J.G.C.; Millo, O. Doping and Quantum Confinement Effects in Single Si Nanocrystals Observed by Scanning Tunneling Spectroscopy. *Nano Lett.* **2013**, *13*, 2516–2521. [CrossRef] [PubMed]
- Ma, Z.; Wang, W.; Yang, H.; Jiang, X.; Yu, J.; Qin, H.; Xu, L.; Chen, K.; Huang, X.; Li, W.; et al. Performance and retention characteristics of nanocrystalline Si floating gate memory with an Al₂O₃ tunnel layer fabricated by plasma-enhanced atomic layer deposition. *J. Appl. Phys.* **2016**, *119*, 075702. [CrossRef]
- Kang, Y.M.; Lee, S.J.; Kim, D.Y.; Kim, T.W.; Woo, Y.D.; Wang, K.L. Formation of Si nanocrystals utilizing a Au nanoscale island etching mask. *Mater. Res. Bull.* **2005**, *40*, 193–198. [CrossRef]
- Lee, S.; Shim, Y.S.; Cho, H.Y.; Kang, T.W.; Kim, D.Y.; Lee, Y.H.; Wang, K.L. Fabrication and characterization of silicon-nanocrystal using platinum-nanomask. *Thin Solid Films* **2004**, *451–452*, 379–383. [CrossRef]
- Lee, S.; Shim, Y.S.; Cho, H.Y.; Kim, D.Y.; Kim, T.W.; Wang, K.L. Optical and Electrical Properties of Si Nanocrystals Embedded in SiO₂ Layers. *Jpn. J. Appl. Phys.* **2003**, *42*, 7180–7183. [CrossRef]
- Walters, R.J.; Bourianoff, G.I.; Atwater, H.A. Field-effect electroluminescence in silicon nanocrystals. *Nat. Mater.* **2005**, *4*, 143–146. [CrossRef]
- Cheng, C.-H.; Lin, G.-R. Si-QD Synthesis for Visible Light Emission, Color Conversion, and Optical Switching. *Materials* **2020**, *13*, 3635. [CrossRef]
- Hou, Y.; Aydin, E.; De Bastiani, M.; Xiao, C.; Isikgor, F.H.; Xue, D.-J.; Chen, B.; Chen, H.; Bahrami, B.; Chowdhury, A.H.; et al. Efficient tandem solar cells with solution-processed perovskite on textured crystalline silicon. *Science* **2020**, *367*, 1135–1140. [CrossRef] [PubMed]
- Alberucci, A.; Alasgarzade, N.; Chambonneau, M.; Blothe, M.; Kämmer, H.; Matthäus, G.; Jisha, C.P.; Nolte, S. In-Depth Optical Characterization of Femtosecond-Written Waveguides in Silicon. *Phys. Rev. Appl.* **2020**, *14*, 24078. [CrossRef]
- Yang, Y.; Guo, Y.; Huang, Y.; Pu, M.; Wang, Y.; Ma, X.; Li, X.; Luo, X. Crosstalk reduction of integrated optical waveguides with nonuniform subwavelength silicon strips. *Sci. Rep.* **2020**, *10*, 4491. [CrossRef]
- Ryu, J.; Jang, Y.J.; Choi, S.; Kang, H.J.; Park, H.; Lee, J.S.; Park, S. All-in-one synthesis of mesoporous silicon nanosheets from natural clay and their applicability to hydrogen evolution. *NPG Asia Mater.* **2016**, *8*, e248. [CrossRef]

18. Sekar, S.; Aqueel Ahmed, A.T.; Kim, D.Y.; Lee, S. One-Pot Synthesized Biomass C-Si Nanocomposites as an Anodic Material for High-Performance Sodium-Ion Battery. *Nanomaterials* **2020**, *10*, 1728. [CrossRef] [PubMed]
19. Loaiza, L.C.; Monconduit, L.; Seznec, V. Si and Ge-Based Anode Materials for Li-, Na-, and K-Ion Batteries: A Perspective from Structure to Electrochemical Mechanism. *Small* **2020**, *16*, 1905260. [CrossRef]
20. Chae, S.; Choi, S.-H.; Kim, N.; Sung, J.; Cho, J. Integration of Graphite and Silicon Anodes for the Commercialization of High-Energy Lithium-Ion Batteries. *Angew. Chem. Int. Ed.* **2020**, *59*, 110–135. [CrossRef]
21. Tsuchimoto, Y.; Yano, T.-A.; Hada, M.; Nakamura, K.G.; Hayashi, T.; Hara, M. Controlling the Visible Electromagnetic Resonances of Si/SiO₂ Dielectric Core–Shell Nanoparticles by Thermal Oxidation. *Small* **2015**, *11*, 4844–4849. [CrossRef]
22. Kramer, N.J.; Schramke, K.S.; Kortshagen, U.R. Plasmonic Properties of Silicon Nanocrystals Doped with Boron and Phosphorus. *Nano Lett.* **2015**, *15*, 5597–5603. [CrossRef]
23. Iannotti, V.; Ausanio, G.; Campana, C.; D’Orazio, F.; Hison, C.; Lucari, F.; Lanotte, L. Magnetic anisotropy in Ni–Si nanoparticle films produced by ultrashort pulsed laser deposition. *J. Magn. Magn. Mater.* **2008**, *320*, e594–e598. [CrossRef]
24. Ge, M.; Rong, J.; Fang, X.; Zhang, A.; Lu, Y.; Zhou, C. Scalable preparation of porous silicon nanoparticles and their application for lithium-ion battery anodes. *Nano Res.* **2013**, *6*, 174–181. [CrossRef]
25. Joo, J.; Liu, X.; Kotamraju, V.R.; Ruoslahti, E.; Nam, Y.; Sailor, M.J. Gated Luminescence Imaging of Silicon Nanoparticles. *ACS Nano* **2015**, *9*, 6233–6241. [CrossRef]
26. Yang, R.; Buonassisi, T.; Gleason, K.K. Organic Vapor Passivation of Silicon at Room Temperature. *Adv. Mater.* **2013**, *25*, 2078–2083. [CrossRef] [PubMed]
27. Hori, Y.; Kano, S.; Sugimoto, H.; Imakita, K.; Fujii, M. Size-Dependence of Acceptor and Donor Levels of Boron and Phosphorus Codoped Colloidal Silicon Nanocrystals. *Nano Lett.* **2016**, *16*, 2615–2620. [CrossRef] [PubMed]
28. Erogbogbo, F.; Lin, T.; Tucciarone, P.M.; LaJoie, K.M.; Lai, L.; Patki, G.D.; Prasad, P.N.; Swihart, M.T. On-Demand Hydrogen Generation using Nanosilicon: Splitting Water without Light, Heat, or Electricity. *Nano Lett.* **2013**, *13*, 451–456. [CrossRef] [PubMed]
29. Praneetha, S.; Murugan, A.V. Development of Sustainable Rapid Microwave Assisted Process for Extracting Nanoporous Si from Earth Abundant Agricultural Residues and Their Carbon-based Nanohybrids for Lithium Energy Storage. *ACS Sustain. Chem. Eng.* **2015**, *3*, 224–236. [CrossRef]
30. Wang, L.; Gao, B.; Peng, C.; Peng, X.; Fu, J.; Chu, P.K.; Huo, K. Bamboo leaf derived ultrafine Si nanoparticles and Si/C nanocomposites for high-performance Li-ion battery anodes. *Nanoscale* **2015**, *7*, 13840–13847. [CrossRef]
31. Favors, Z.; Wang, W.; Bay, H.H.; Mutlu, Z.; Ahmed, K.; Liu, C.; Ozkan, M.; Ozkan, C.S. Scalable Synthesis of Nano-Silicon from Beach Sand for Long Cycle Life Li-ion Batteries. *Sci. Rep.* **2014**, *4*, 5623. [CrossRef]
32. Su, A.; Li, J.; Dong, J.; Yang, D.; Chen, G.; Wei, Y. An Amorphous/Crystalline Incorporated Si/SiO_x Anode Material Derived from Biomass Corn Leaves for Lithium-Ion Batteries. *Small* **2020**, *16*, 2001714. [CrossRef]
33. Sekar, S.; Aqueel Ahmed, A.T.; Inamdar, A.I.; Lee, Y.; Im, H.; Kim, D.Y.; Lee, S. Activated carbon-decorated spherical silicon nanocrystal composites synchronously-derived from rice husks for anodic source of lithium-ion battery. *Nanomaterials* **2019**, *9*, 1055. [CrossRef] [PubMed]
34. Jung, D.S.; Ryou, M.-H.; Sung, Y.J.; Park, S.B.; Choi, J.W. Recycling rice husks for high-capacity lithium battery anodes. *Proc. Natl. Acad. Sci. USA* **2013**, *110*, 12229–12234. [CrossRef] [PubMed]
35. Marchal, J.C.; Krug Iii, D.J.; McDonnell, P.; Sun, K.; Laine, R.M. A low cost, low energy route to solar grade silicon from rice hull ash (RHA), a sustainable source. *Green Chem.* **2015**, *17*, 3931–3940. [CrossRef]
36. Bose, S.; Ganayee, M.A.; Mondal, B.; Baidya, A.; Chennu, S.; Mohanty, J.S.; Pradeep, T. Synthesis of Silicon Nanoparticles from Rice Husk and their Use as Sustainable Fluorophores for White Light Emission. *ACS Sustain. Chem. Eng.* **2018**, *6*, 6203–6210. [CrossRef]
37. Wu, Y.; Zhong, Y.; Chu, B.; Sun, B.; Song, B.; Wu, S.; Su, Y.; He, Y. Plant-derived fluorescent silicon nanoparticles featuring excitation wavelength-dependent fluorescence spectra for anti-counterfeiting applications. *Chem. Commun.* **2016**, *52*, 7047–7050. [CrossRef]
38. Sankar, S.; Kaur, N.; Lee, S.; Kim, D.Y. Rapid sonochemical synthesis of spherical silica nanoparticles derived from brown rice husk. *Ceram. Int.* **2018**, *44*, 8720–8724. [CrossRef]
39. Sankar, S.; Lee, H.; Jung, H.; Kim, A.; Aqueel Ahmed, A.T.; Inamdar, A.I.; Kim, H.; Lee, S.; Im, H.; Kim, D.Y. Ultrathin graphene nanosheets derived from rice husks for sustainable supercapacitor electrodes. *New J. Chem.* **2017**, *41*, 13792–13797. [CrossRef]
40. Jin, X.; Wang, R.; Zhang, L.; Si, R.; Shen, M.; Wang, M.; Tian, J.; Shi, J. Electron Configuration Modulation of Nickel Single Atoms for Elevated Photocatalytic Hydrogen Evolution. *Angew. Chem. Int. Ed.* **2020**, *59*, 6827–6831. [CrossRef] [PubMed]
41. Liao, G.; Gong, Y.; Zhang, L.; Gao, H.; Yang, G.-J.; Fang, B. Semiconductor polymeric graphitic carbon nitride photocatalysts: The “holy grail” for the photocatalytic hydrogen evolution reaction under visible light. *Energy Environ. Sci.* **2019**, *12*, 2080–2147. [CrossRef]
42. Zhang, J.-W.; Gong, S.; Mahmood, N.; Pan, L.; Zhang, X.; Zou, J.-J. Oxygen-doped nanoporous carbon nitride via water-based homogeneous supramolecular assembly for photocatalytic hydrogen evolution. *Appl. Catal. B* **2018**, *221*, 9–16. [CrossRef]
43. Zhao, D.; Dong, C.-L.; Wang, B.; Chen, C.; Huang, Y.-C.; Diao, Z.; Li, S.; Guo, L.; Shen, S. Synergy of Dopants and Defects in Graphitic Carbon Nitride with Exceptionally Modulated Band Structures for Efficient Photocatalytic Oxygen Evolution. *Adv. Mater.* **2019**, *31*, 1903545. [CrossRef]

44. Yang, X.; Tian, L.; Zhao, X.; Tang, H.; Liu, Q.; Li, G. Interfacial optimization of g-C₃N₄-based Z-scheme heterojunction toward synergistic enhancement of solar-driven photocatalytic oxygen evolution. *Appl. Catal. B* **2019**, *244*, 240–249. [CrossRef]
45. Wang, D.; Sheng, T.; Chen, J.; Wang, H.-F.; Hu, P. Identifying the key obstacle in photocatalytic oxygen evolution on rutile TiO₂. *Nat. Catal.* **2018**, *1*, 291–299. [CrossRef]
46. Sankar, S.; Sharma, S.K.; Kaur, N.; Lee, B.; Kim, D.Y.; Lee, S.; Jung, H. Biogenerated silica nanoparticles synthesized from sticky, red, and brown rice husk ashes by a chemical method. *Ceram. Int.* **2016**, *42*, 4875–4885. [CrossRef]
47. Bulyarskii, S.V.; Svetukhin, V.V.; Prikhod'ko, O.V. Spatially inhomogeneous oxygen precipitation in silicon. *Semiconductors* **1999**, *33*, 1157–1162. [CrossRef]
48. Bulyarskiy, S.V.; Svetukhin, V.V. A Kinetic Model of Silicon Nanocrystal Formation. *Silicon* **2020**. [CrossRef]
49. Fokker, A.D. Die mittlere Energie rotierender elektrischer Dipole im Strahlungsfeld. *Ann. Phys.* **1914**, *348*, 810–820. [CrossRef]
50. Planck, M. Über einen Satz der statistischen Dynamik und seine Erweiterung in der Quantentheorie. *Sitz. Preuss. Akad. Wiss. Berl.* **1917**, *24*, 324–341.
51. Rosenbluth, M.N.; MacDonald, W.M.; Judd, D.L. Fokker-Planck Equation for an Inverse-Square Force. *Phys. Rev.* **1957**, *107*, 1–6. [CrossRef]
52. Choi, J.-H.; Kim, H.-K.; Jin, E.-M.; Seo, M.W.; Cho, J.S.; Kumar, R.V.; Jeong, S.M. Facile and scalable synthesis of silicon nanowires from waste rice husk silica by the molten salt process. *J. Hazard. Mater.* **2020**, *399*, 122949. [CrossRef]
53. Zhang, Y.-C.; You, Y.; Xin, S.; Yin, Y.-X.; Zhang, J.; Wang, P.; Zheng, X.-s.; Cao, F.-F.; Guo, Y.-G. Rice husk-derived hierarchical silicon/nitrogen-doped carbon/carbon nanotube spheres as low-cost and high-capacity anodes for lithium-ion batteries. *Nano Energy* **2016**, *25*, 120–127. [CrossRef]
54. Sankar, S.; Sharma, S.K.; An, N.; Lee, H.; Kim, D.Y.; Im, Y.B.; Cho, Y.D.; Ganesh, R.S.; Ponnusamy, S.; Raji, P.; et al. Photocatalytic properties of Mn-doped NiO spherical nanoparticles synthesized from sol-gel method. *Optik* **2016**, *127*, 10727–10734. [CrossRef]
55. Kaur, N.; Lee, Y.; Kim, D.Y.; Lee, S. Optical bandgap tuning in nanocrystalline ZnO:Y films via forming defect-induced localized bands. *Mater. Des.* **2018**, *148*, 30–38. [CrossRef]
56. Lee, S.; Kang, T.W.; Kim, D.Y. Correlation of Magnetic Properties with Microstructural Properties for Columnar-Structured (Zn_{1-x}Mn_x)O/Al₂O₃ (0001) Thin Films. *J. Cryst. Growth* **2005**, *284*, 6–14. [CrossRef]
57. Mishra, P.; Jain, K.P. First- and second-order Raman scattering in nanocrystalline silicon. *Phys. Rev. B* **2001**, *64*, 073304. [CrossRef]
58. Krause, A.; Tkacheva, O.; Omar, A.; Langklotz, U.; Giebel, L.; Dörfler, S.; Fauth, F.; Mikolajick, T.; Weber, W.M. In Situ Raman Spectroscopy on Silicon Nanowire Anodes Integrated in Lithium Ion Batteries. *J. Electrochem. Soc.* **2019**, *166*, A5378–A5385. [CrossRef]
59. Tan, D.; Ma, Z.; Xu, B.; Dai, Y.; Ma, G.; He, M.; Jin, Z.; Qiu, J. Surface passivated silicon nanocrystals with stable luminescence synthesized by femtosecond laser ablation in solution. *Phys. Chem. Chem. Phys.* **2011**, *13*, 20255–20261. [CrossRef]
60. Zhong, Y.; Sun, X.; Wang, S.; Peng, F.; Bao, F.; Su, Y.; Li, Y.; Lee, S.-T.; He, Y. Facile, Large-Quantity Synthesis of Stable, Tunable-Color Silicon Nanoparticles and Their Application for Long-Term Cellular Imaging. *ACS Nano* **2015**, *9*, 5958–5967. [CrossRef] [PubMed]
61. Llansola Portolés, M.J.; Rodriguez Nieto, F.; Soria, D.B.; Amalvy, J.I.; Peruzzo, P.J.; Mártire, D.O.; Kotler, M.; Holub, O.; Gonzalez, M.C. Photophysical Properties of Blue-Emitting Silicon Nanoparticles. *J. Phys. Chem. C* **2009**, *113*, 13694–13702. [CrossRef]
62. Shirahata, N.; Linford, M.R.; Furumi, S.; Pei, L.; Sakka, Y.; Gates, R.J.; Asplund, M.C. Laser-derived one-pot synthesis of silicon nanocrystals terminated with organic monolayers. *Chem. Commun.* **2009**, 4684–4686. [CrossRef] [PubMed]
63. Buriak, J.M.; Stewart, M.P.; Geders, T.W.; Allen, M.J.; Choi, H.C.; Smith, J.; Rafferty, D.; Canham, L.T. Lewis Acid Mediated Hydrosilylation on Porous Silicon Surfaces. *J. Am. Chem. Soc.* **1999**, *121*, 11491–11502. [CrossRef]
64. Bateman, J.E.; Horrocks, B.R.; Houlton, A. Reactions of water and methanol at hydrogen-terminated silicon surfaces studied by transmission FTIR. *J. Chem. Soc. Faraday Trans.* **1997**, *93*, 2427–2431. [CrossRef]
65. Liu, Y.; Ji, G.; Wang, J.; Liang, X.; Zuo, Z.; Shi, Y. Fabrication and photocatalytic properties of silicon nanowires by metal-assisted chemical etching: Effect of H₂O₂ concentration. *Nanoscale Res. Lett.* **2012**, *7*, 663. [CrossRef] [PubMed]
66. Shen, X.-B.; Song, B.; Fang, B.; Jiang, A.-R.; Ji, S.-J.; He, Y. Excitation-wavelength-dependent photoluminescence of silicon nanoparticles enabled by adjustment of surface ligands. *Chem. Commun.* **2018**, *54*, 4947–4950. [CrossRef] [PubMed]
67. He, Y.; Su, Y.; Yang, X.; Kang, Z.; Xu, T.; Zhang, R.; Fan, C.; Lee, S.-T. Photo and pH Stable, Highly-Luminescent Silicon Nanospheres and Their Bioconjugates for Immunofluorescent Cell Imaging. *J. Am. Chem. Soc.* **2009**, *131*, 4434–4438. [CrossRef]
68. Pi, X.D.; Liptak, R.W.; Deneen Nowak, J.; Wells, N.P.; Carter, C.B.; Campbell, S.A.; Kortshagen, U. Air-stable full-visible-spectrum emission from silicon nanocrystals synthesized by an all-gas-phase plasma approach. *Nanotechnology* **2008**, *19*, 245603. [CrossRef]
69. Hua, F.; Erogbogbo, F.; Swihart, M.T.; Ruckenstein, E. Organically Capped Silicon Nanoparticles with Blue Photoluminescence Prepared by Hydrosilylation Followed by Oxidation. *Langmuir* **2006**, *22*, 4363–4370. [CrossRef] [PubMed]
70. Ma, Q.; Zhao, Z.; Zhao, Y.; Xie, H.; Xing, P.; Wang, D.; Yin, H. A self-driven alloying/dealloying approach to nanostructuring micro-silicon for high-performance lithium-ion battery anodes. *Energy Storage Mater.* **2021**, *34*, 768–777. [CrossRef]
71. Azadeh, M.; Zamani, C.; Ataie, A.; Morante, J.R. Three-dimensional rice husk-originated mesoporous silicon and its electrical properties. *Mater. Today Commun.* **2018**, *14*, 141–150. [CrossRef]

72. Kang, W.; Kim, J.-C.; Kim, D.-W. Waste glass microfiber filter-derived fabrication of fibrous yolk-shell structured silicon/carbon composite freestanding electrodes for lithium-ion battery anodes. *J. Power Sources* **2020**, *468*, 228407. [CrossRef]
73. Sakamoto, M.; Terada, S.; Mizutani, T.; Saitow, K.-I. Large Field Enhancement of Nanocoral Structures on Porous Si Synthesized from Rice Husks. *ACS Appl. Mater. Interfaces* **2020**, *13*, 1105–1113. [CrossRef] [PubMed]



Article

Ultrabright Fluorescent Silica Nanoparticles for Dual pH and Temperature Measurements

Saquib Ahmed M. A. Peerzade¹, Nadezhda Makarova² and Igor Sokolov^{1,2,3,*}

¹ Department of Biomedical Engineering, Tufts University, Medford, MA 02155, USA; Saquib.Peerzade@tufts.edu

² Department of Mechanical Engineering, Tufts University, Medford, MA 02155, USA; Nadezhda.Makarova@tufts.edu

³ Department of Physics, Tufts University, Medford, MA 02155, USA

* Correspondence: igor.sokolov@tufts.edu; Tel.: +1-(617)-627-2548

Abstract: The mesoporous nature of silica nanoparticles provides a novel platform for the development of ultrabright fluorescent particles, which have organic molecular fluorescent dyes physically encapsulated inside the silica pores. The close proximity of the dye molecules, which is possible without fluorescence quenching, gives an advantage of building sensors using FRET coupling between the encapsulated dye molecules. Here we present the use of this approach to demonstrate the assembly of ultrabright fluorescent ratiometric sensors capable of simultaneous acidity (pH) and temperature measurements. FRET pairs of the temperature-responsive, pH-sensitive and reference dyes are physically encapsulated inside the silica matrix of ~50 nm particles. We demonstrate that the particles can be used to measure both the temperature in the biologically relevant range (20 to 50 °C) and pH within 4 to 7 range with the error (mean absolute deviation) of 0.54 °C and 0.09, respectively. Stability of the sensor is demonstrated. The sensitivity of the sensor ranges within 0.2–3% °C⁻¹ for the measurements of temperature and 2–6% pH⁻¹ for acidity.

Citation: Peerzade, S.A.M.A.; Makarova, N.; Sokolov, I. Ultrabright Fluorescent Silica Nanoparticles for Dual pH and Temperature Measurements. *Nanomaterials* **2021**, *11*, 1524. <https://doi.org/10.3390/nano11061524>

Academic Editor: Céline Ternon

Received: 17 May 2021

Accepted: 5 June 2021

Published: 9 June 2021

Publisher's Note: MDPI stays neutral with regard to jurisdictional claims in published maps and institutional affiliations.



Copyright: © 2021 by the authors. Licensee MDPI, Basel, Switzerland. This article is an open access article distributed under the terms and conditions of the Creative Commons Attribution (CC BY) license (<https://creativecommons.org/licenses/by/4.0/>).

Keywords: pH sensor; temperature sensor; dual sensor

1. Introduction

Knowledge of temperature and acidity at the nanoscale is of interest from both applied and fundamental points of view. For example, understanding the distribution of those parameters inside of the biological cell is key to understanding complex biochemical processes that are occurring in a highly heterogeneous environment of the cell. Cellular functions like gene and protein expression and protein stability are strongly temperature-dependent [1]. It is also known that cell migration, cell proliferation, wound healing [2], protein denaturation, protein folding and protein stability [3] are strongly pH-dependent. From a fundamental point of view, physical and chemical processes in the nanoscale are still not well understood in general because temperature and acidity were not measured at that scale.

Using fluorescence as an indication of pH and temperature is an attractive option because it can be accessed remotely and in three dimensions across a volume of interest. There were attempts to make a complex fluorescent molecule that would be sensitive to the change in both pH and temperature [4]. However, the fluorescence of this molecule was excessively sensitive to the changes in the ionic composition of the medium. This effectively prohibits the direct use of this molecule as a sensor. Encapsulation of sensitive molecules inside nanoparticles can decrease the dependence of the fluorescence from the medium surrounding nanoparticles, and thus, make it a sensor.

There were multiple attempts to measure both pH and temperature sequentially. For example, it was done to study biological cells, specifically, the investigation of mitochondrial acidification due to real-time monitoring of mitochondrial pH using fluorescent

probes [5]. In this study, for measuring intracellular pH, the fluorescent probe was used that shows pH response based on a single peak [5]. For making measurements ratiometric, cells were post-stained with mitotracker. Measurements of pH were done by using a ratio of mitotracker and molecular probe. It was assumed that mitotracker and fluorescent probe both are homogeneously distributed. Here the concentration of mitotracker should be known and kept constant with calibration and cell measurements. The cell density on the glass-bottomed dishes for both calibration and temperature distribution measurements should be constant. Moreover, two wavelengths were used for exciting mitotracker and molecular probe. Local heat production by mitochondria inside the living cells has also been detected before using intracellular fluorescent temperature mapping [6]. Temperature mapping was performed using fluorescence lifetime imaging microscopy (FLIM), which is typically a time-consuming imaging.

Fluorescent nanoparticles changing their fluorescence spectrum as a function of acidity have previously been reported [7]. FITC, a pH-sensitive dye, and rhodamine B was used as a reference. Although rhodamine B shows a temperature dependent fluorescence, it was not discussed, and only pH measurements were demonstrated. In another study, two dyes FITC and Rb were used for measuring both pH and temperature simultaneously [8]. However, only relative changes in the pH and temperature were measured in this approach. In addition, the reported particles were of micron size, not nano. As a result, the particles have a rather limited range of applications. The fluorescent nanosensors capable of simultaneous measurements of actual accurate values of the pH and temperature have not been reported (see more comparison to the state-of-the-art in the Discussion section).

Here we report on the synthesis of fluorescent nanoparticles that can serve as nanoscopic sensors capable of measuring the values of both temperature and acidity simultaneously. The sensors are based on the encapsulation of three fluorescent dyes within the mesoporous silica matrix of nanoparticles. As was shown previously [9–11], such encapsulation results in obtaining ultrabright fluorescence of nanoparticles. The phenomenon of ultrabrightness was attributed to preserving the quantum yield of the encapsulated dyes while attaining a very high concentration of the dye inside the particles. The close proximity of the encapsulated dye molecules allows for the Förster's resonance energy transfer (FRET) between the neighbor dye molecules. This allows us to build effective ultrabright fluorescent ratiometric sensors, which are excited with just one excitation wavelength. The possibility to use the FRET approach to build ultrabright fluorescent nanosensors of temperature has been recently demonstrated [12]. Our fluorescent nanosensors are ratiometric to avoid dependence on the intensity of the excitation light. This is important because it is practically impossible to control the intensity of the excitation light in an optically inhomogeneous medium. It should be noted that we previously demonstrated encapsulation of multiple organic dyes in the reported nanoparticles [13] for the purpose of multiplexed detection. To the best of the authors' knowledge, the present work is the first report on ultrabright mesoporous silica nanoparticles for sensing both pH and temperature simultaneously.

In the presentation here, nanosensors were allowed to find the temperature and pH by using two fluorescent ratios. It should be noted that such an approach was reported for a silica-based pH and oxygen sensor [14]. Both fluorescent ratios reported in that work were independent of each other. In our approach, we do observe crosstalk between the two ratios used. To define both temperature and pH independently, we developed an algorithm that allows for decoupling the crosstalk, and as a result, minimizes the error in the definition of temperature and pH. Our algorithm allows for finding the particular wavelengths of the fluorescence spectrum to maximize the signal to noise ratio of the spectral signal. We demonstrated that using our approach, one can attain quite small errors (mean absolute deviation, or the average of residuals at different pH and temperature) of 0.54 °C and 0.09 in the definition of temperature and pH, respectively. The sensitivity of the sensor ranges within 0.2–3% for °C and 2–6% for pH^{-1} . This is comparable with ranges reported in the literature [15].

2. Materials and Methods

2.1. Materials

Tetraethylorthosilicate (TEOS, $\geq 99\%$, GC, Acros Organics, Fair Lawn, NJ, USA), triethanolamine (TEA, reagent grade 98%, Sigma Aldrich, St. Louis, MO, USA), cetyltrimethylammonium bromide (CTAB, High Purity Grade, Amresco, Solon, OH, USA), ethyltriethoxysilane (ETES, 96%, Frontier Scientific, Logan, UT, USA), fluorescein isothiocyanate (FITC, Exciton, Dayton, OH, USA), rhodamine B (Rb, Exciton, Dayton, OH, USA) and Nile blue perchlorate (Nb, 95%, Sigma Aldrich) were used. RC membrane (RC membrane, Spectra/Pore, Rancho Dominguez, CA, USA) with 10–15 kDa MW was used. Deionized water was used in all synthesis.

2.2. Synthesis of Nanosensors

The previously reported procedure [13,16] was modified to assemble the presented pH and temperature sensor based on mesoporous silica particles. The molar ratio of chemicals in the synthesizing bath was 1 TEOS: 8.2 TEA: 0.23 CTAB: 142 H₂O: 0.1 ETES. The ratio of FITC: Rb: Nb was 1:4:55. The mixture of TEOS (1.71 g, 8.2 mmol) and TEA (10 g, 67 mmol) was stirred for one minute and kept at 90 °C under quiescent conditions for 20 min. Another mixture of CTAB (0.69 g, 1.9 mmol), FITC (0.001 g, 0.0026 mmol), Rb (0.005 g, 0.013 mmol) and Nb (0.05 g, 0.14 mmol) and H₂O (21 mL) was stirred for 1 min in 21 mL water and kept at 60 °C for 40 min. The CTAB, dye and water mixture were stirred at room temperature for another 15 min and kept in a cold bath for 5 min. After 5 min the mixture of TEOS and TEA was then added to the aqueous solution of CTAB and dye. ETES (130 μ L, 0.8 mmol) was added after 10–15 min and stirred for another 40 min in the cold bath. After 40 min, the synthesis mixture was diluted with 30 mL water and the excess reagents were removed by dialyzing with water using the membrane of MW 10–15 kDa until no fluorescence was obtained from the dialysate (several (2–3) days). The pH of the mixture after dialysis was ~ 9 . HCl was added to neutralize the mixture.

2.3. Characterization Techniques

Dynamic light scattering (DLS): DLS was used to measure the particle size and zeta potential of the nanoparticles using Zetasizer Nano ZS by Malvern Instruments Ltd., Malvern, UK. DLS uses the laser light of 633 nm and the backscattered light is monitored at an angle of 173°. The intensity-average size (Z-average) and most probable size (mean of number weighted distribution) was the average of three measurements.

Optical measurements: Cary 60 UV–Vis spectrometer (Agilent, Santa Clara, CA, USA) was used to measure the absorbance with an averaging time of 0.1 s and a scan rate of 600 nm/min. Fluorescence was measured using a Horiba Fluorelog 3 (Horiba, Japan) using a 2 nm slit width with an integration time of 0.1 s and a scan rate of 600 nm/min.

AFM imaging of sensors: An Icon Atomic Force Microscopy (AFM, Bruker, Inc., Santa Barbara, CA, USA) with NanoScope V controller with a ringing mode add-on (NanoScience Solutions, Inc., Arlington, VA, USA) was used to image the nanoparticles.

3. Results

3.1. Characterization of the Nanosensors

The DLS measurements of the particle size are shown in Figure 1a. The most probable particle size is ~ 51 nm. This is confirmed by direct imaging of the particles with AFM, Figure 1b. From the material point of view, the synthesized particles are identical to those previously reported by us in [11,13,16,17]. As was shown there, the internal structure of the particles is not changed when dyes are added, while the overall size of the particles can change. Thus, one can check the internal structure (measured by TEM and N₂ absorbance) of these particles in [11,13,16,17].

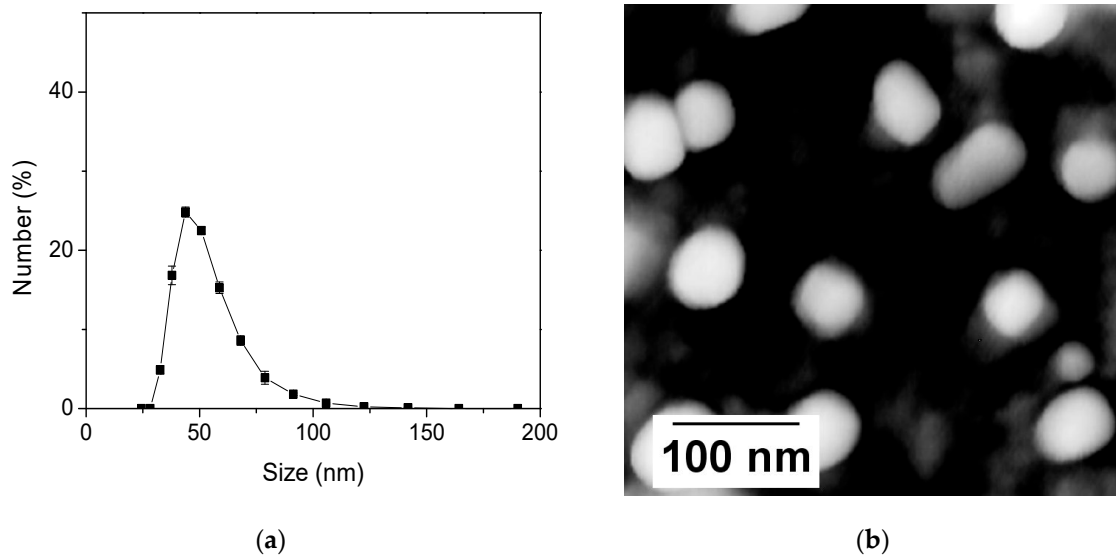


Figure 1. (a) Dynamic Light Scattering (DLS) measurements of the particle size distribution and (b) Atomic Force Microscopy (AFM) of nanosensors.

Three fluorescent dyes were encapsulated inside each nanosensor. Nile blue (Nb) was used as the reference, FITC was used for pH sensing, and rhodamine B (Rb) for temperature sensing. The spectral characteristics of synthesized nanosensors are shown in Figure 2 together with the spectral characteristics of individually encapsulated dyes. Figure 2 shows the (A) absorbance and (B) fluorescence spectra (excited at 488 nm) of the nanosensors. The dotted black line represents the fitting after demultiplexing (the addition of the individual dye components). Normalized absorbance and fluorescence spectra of individual FITC, Rb and Nb dyes are shown in Figure 2C.

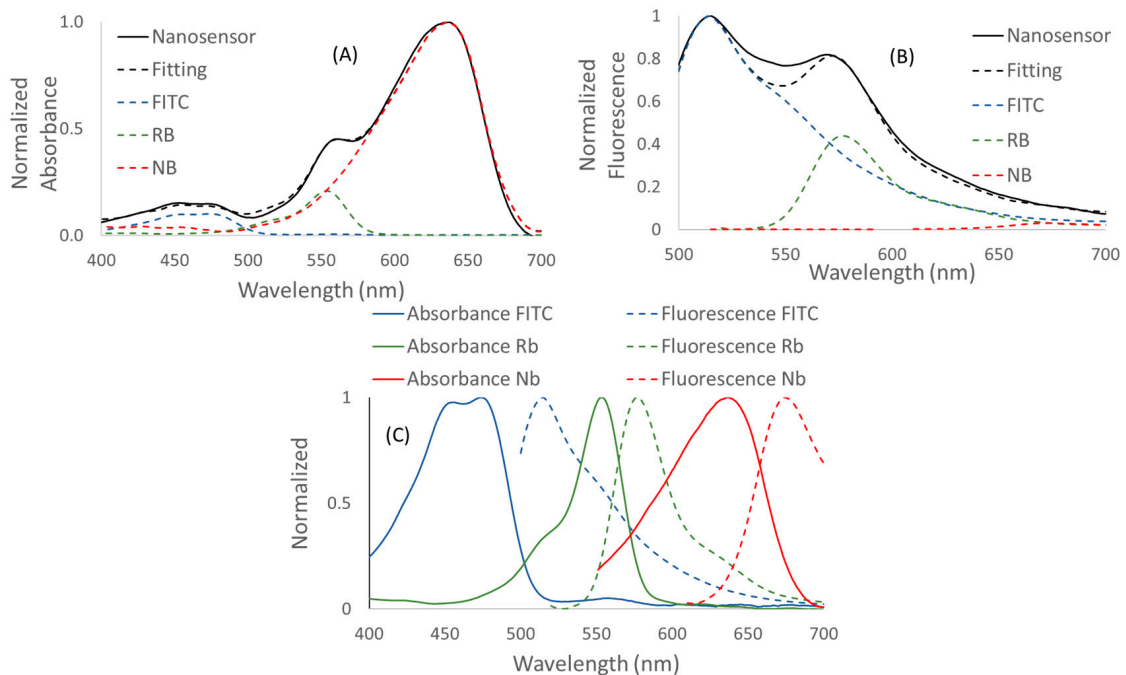


Figure 2. Spectral characteristics of nanosensors. (A) Normalized absorbance and (B) normalized fluorescence spectra of nanosensors. Individual component spectra of dyes used for fitting are shown. (C) Normalized absorbance/emission spectra of FITC, Rb and Nb dyes.

The fluorescence brightness of the synthesized nanosensors was measured as described in the Equations (S15) and (S18), see reference [18] for detail. Because of the complex fluorescence composition, the brightness is calculated with respect to each of the three encapsulated dyes. The results are presented in Table 1, which shows the fluorescence characteristics of the synthesized particles, including the fluorescent brightness and quantum yield. It should be noted that the definition of the quantum yield of a fluorescent nanoparticle is somewhat ambiguous. Here we use the definition in which the quantum yield is assigned per single encapsulated dye molecule, see references [9,10] for detail. Brightness is given in the relative MESF (Molecules of Equivalent Soluble Fluorochrome) and absolute $M^{-1} \text{ cm}^{-1}$ units. MESF units relative to the corresponding dye are broadly used in flow cytometry and the characterization of particle brightness [19–24]. The absolute units are used to compare the brightness with the particles with any other fluorophore.

Table 1. Fluorescence properties of ultrabright pH and temperature-sensing nanoparticles. Relative fluorescence brightness of ultrabright mesoporous silica nanoparticles in both MESF units (relative to one free dye molecule) and $M^{-1} \text{ cm}^{-1}$, and the number of dye molecules per particle. Note that all the calculations were performed using the number weighted average particle size of 51 nm.

Contributing Dye	Excitation	Emission Range	Absolute Brightness ($M^{-1} \text{ cm}^{-1}$)	Relative Brightness (MESF Units)	Number of Dye Molecules Per Particle	Volume Per One Dye Molecule (nm^3)
FITC	490 nm	500–700 nm	$(10 \pm 1) \times 10^6$	150 ± 10	178 ± 12	390
Rb	550 nm	560–700 nm	$(12 \pm 1) \times 10^6$	387 ± 30	385 ± 30	180
Nb	630 nm	640–700 nm	$(40 \pm 3) \times 10^6$	1965 ± 135	2475 ± 170	28

One can see that particles showed the brightness of ~ 150 and 390 relative to the free FITC and Rb dye molecules, respectively, when exciting with 490 and 550 nm. Brightness relative to Nile blue is the highest (~ 2000 in MESF units) when particles are excited with 630 nm wavelength. The number of FITC, Rb and Nb molecules encapsulated per particle is 180 ± 10 , 390 ± 30 and 2500 ± 200 , respectively. FRET efficiency and distance between dye molecules are given in Table S4 [25,26].

To find the absolute fluorescent brightness, the brightness in MESF units was multiplied by the absolute brightness of corresponding fluorescent molecules. The values of the extinction coefficient of FITC dye at 490 nm, Rb dye at 550 nm and Nb dye at 630 nm wavelength were taken from the literature, $70,000 M^{-1} \text{ cm}^{-1}$ [27], $\sim 100,000 M^{-1} \text{ cm}^{-1}$ [28] and $\sim 76,000 M^{-1} \text{ cm}^{-1}$ [29,30], respectively. The quantum yields of free FITC, Rb and Nb dyes were used as reported in the literature 0.93 [31], 0.31 [32] and 0.27 [29], respectively. The quantum yield of the encapsulated dye was calculated in the Supplementary Information (S16) and (S17). Thus, the absolute brightness of nanosensors was $(10 \pm 1) \times 10^6$, $(12 \pm 1) \times 10^6$ and $(40 \pm 3) \times 10^6 M^{-1} \text{ cm}^{-1}$, respectively.

The number of Nile blue dye molecules is the highest, 2500 ± 200 Nile blue dye molecules per particle. This corresponds to a 60 mM concentration of Nb dye molecules inside the particles. Thus, it corresponds to the ratio of the number of the dye molecules inside the particles FITC: Rb: Nb 1:2:14. It is interesting to compare the ratio of dyes used for synthesis, FITC: Rb: Nb 1:5:55. The difference is presumably due to the different solubility of the dyes inside the silica matrix.

When considering fluorescence sensing, it is important to verify that the fluorescence does not depend on the other parameters of the environment. In the case of the most probable use of the sensors, biomedical applications, the environment can contain complex ions, which potentially can influence the fluorescence of the encapsulated dye. Figure 3 shows the ratio of fluorescent intensities, which are used for the determination of temperature and pH (see later), in the presence of various ions typical for physiological buffers. For this purpose, the selectivity measurements were done in the presence of monovalent (K^+ and Na^+) and divalent (Ca^{2+} and Mg^{2+}) ions. The stability of the ratios for determining pH and temperature in the presence of ions is shown in Figure 3. Ratios $I(525 \text{ nm})/I(537 \text{ nm})$ and

$I(581\text{ nm})/I(611\text{ nm})$ were used for calculating temperature and pH, as shown in Figure S3. The ions K^+ , Ca^{2+} , Mg^{2+} and Na^+ were added consecutively. It can be seen that the ratios stayed virtually constant after the addition of the ions. The standard deviations across all the different addition of ions were $\pm 0.2\text{ }^\circ\text{C}$ and ± 0.03 for temperature and pH, respectively.

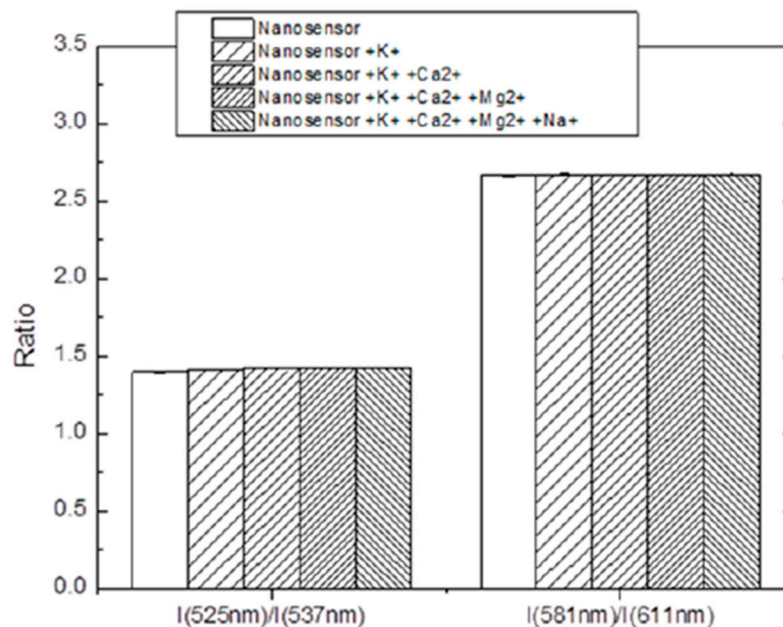


Figure 3. Stability of the ratios for nanosensors toward metal ions (1 mM) K^+ , Ca^{2+} , Mg^{2+} and Na^+ .

3.2. Temperature and pH Calibration

Figure 4 demonstrates the changes in the fluorescence spectral behavior of the nanosensors to the change of pH in the range of 4–7 and the temperature in the range of 25–45 $^\circ\text{C}$. FITC dye is known to be sensitive to both temperature and pH while rhodamine B dye is sensitive to only temperature [8,33]. One can see that the rhodamine B peak ($\sim 570\text{ nm}$) decreases with the increase in temperature, whereas the FITC peak at 515 nm decreases with the decrease of pH (increase in acidity) and increased with increase in temperature at pH 6.8 and 6.3 (Figure 4a,b). This is consistent with the reported response of FITC and rhodamine B dyes to the change of pH and temperature, respectively.

It should be noted that the presence of FRET can be seen through a relatively high fluorescence of rhodamine B and Nile blue dyes. The excitation wavelength was 488 nm. The absorbance of rhodamine B and Nile blue dyes at this wavelength is much lower compared to the absorbance of FITC. In the present configuration, FITC plays the role of the donor dye. The change of the fluorescence spectra shown in Figure 4 are due to the change of fluorescent properties of the dyes as described above, and presumably not due to the change in FRET efficiency. The latter might happen due to the change of distances between the dye molecules because of the temperature expansion of the silica matrix. However, a simple estimation shows that this effect is negligible.

The calibration of the sensors was done for a number of fixed conditions: five different temperatures (24.17, 29.63, 34.74, 39.77 and 44.8 $^\circ\text{C}$) and six different acidity (pH 6.8, 6.3, 5.8, 5.3, 4.8 and 4.3). The fluorescence spectra were recorded for each of these 30 conditions. These calibration points were used to fit the polynomial functions of the algorithm as described in the next sections.

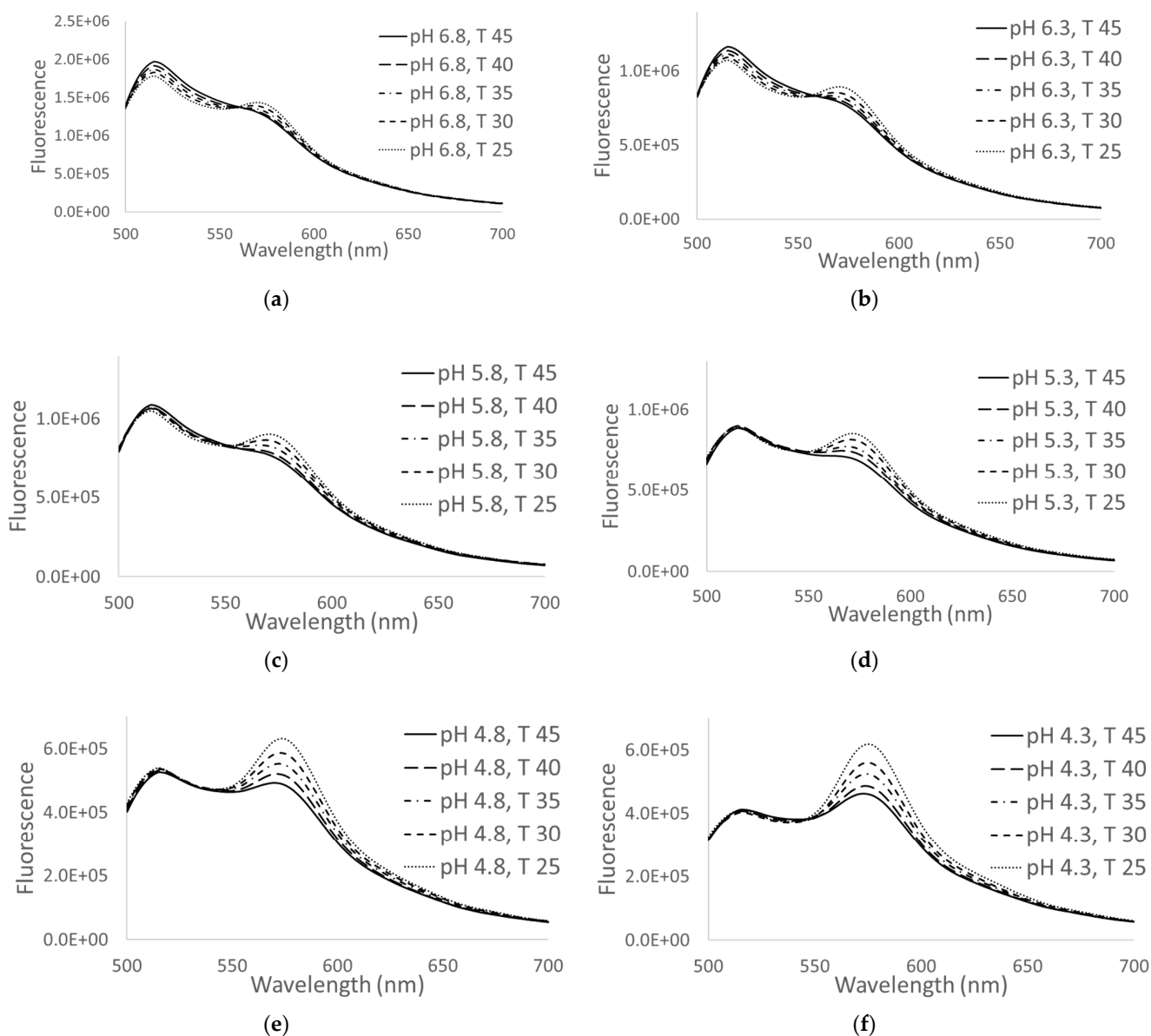


Figure 4. Temperature and pH responses of nanosensors to the change in temperature (shown for 25, 30, 35, 40 and 45 °C and the change in pH: (a) 6.8, (b) 6.3, (c) 5.8, (d) 5.3, (e) 4.8 and (f) 4.3, respectively. The excitation wavelength is 488 nm.

3.3. Method of Simultaneous Measurements of Temperature and Acidity

As one can see in Figure 4, the combination of encapsulated dyes shows a rather nontrivial dependence on both temperature and pH. There is substantial crosstalk between the responses to the change of temperature and pH. Here we present an algorithm, which allows us to decouple this complex behavior of the fluorescent spectra to define the temperature and acidity separately and with relatively high precision. We demonstrate that it is sufficient to have two ratios of fluorescence intensities at different wavelengths to determine the temperature and acidity quite accurately. To do it, first, we will find the optimal values of the wavelengths to be used to calculate the intensity ratios. Then we suggest simple polynomial functions to determine the temperature and acidity using those ratios.

3.4. Finding the Optimal Values of Wavelengths to Measure Temperature and Acidity Simultaneously

To define both pH and temperature in a ratiometric manner, two different fluorescence ratios corresponding to two different wavelengths should be chosen. Our approach is based

on Equation (1) minimization of the ambiguity of finding both pH and temperature (due to existing crosstalk between responses to the change in pH and temperature) and Equation (2) minimization of the error of the measurements (because the fluorescence intensities have different signal-to-noise ratio at different wavelengths). To minimize the complexity of such an analysis, it is preferable to have a linear relationship between the sought ratios and pH and temperature. To find the linear relations, regression analysis was used [34]. The Pearson correlation coefficient r indicates the proportion of variance in variable Y represented by a linear function of X . This coefficient is given by the following formula:

$$r^2 = \frac{S_{xy}^2}{S_x S_y} = \frac{(\sum_{i=1}^n (X_i - \bar{X})(Y_i - \bar{Y}))^2}{\sum_{i=1}^n (X_i - \bar{X})^2 \sum_{i=1}^n (Y_i - \bar{Y})^2} \quad (1)$$

where, S_{xy} is the covariance of X and Y , S_x is the standard deviation of X , S_y is the standard deviation of Y . The linear relation implies this coefficient to be close to 1.

Combining the standard deviation of pH and the ratio R and covariance of pH and R , as given in Equations (S2), (S3) and (S5), one can find the Pearson correlation coefficient for pH as follows:

$$r_{pH}^2 = \frac{S_{pH,R}^2}{S_{pH} S_R} r_{pH}^2 = \frac{S_{pH,R}^2}{S_{pH} S_R} = \frac{\left(\sum_{pH_1}^{pH_n} \left((pH - pH_{mean}) \left(\sum_{T_1}^{T_n} \left(\frac{R}{n_T} \right) - \bar{R} \right) \right) \right)^2}{\sum_{pH_1}^{pH_n} (pH - pH_{mean})^2 \sum_{pH_1}^{pH_n} \left(\sum_{T_1}^{T_n} \left(\frac{R}{n_T} \right) - \bar{R} \right)^2} \quad (2)$$

Similarly, combining the standard deviation of T , R and covariance of T and R given by Equations (S6), (S7) and (S9), one can find the Pearson correlation coefficient for temperature T given by the following formula:

$$r_T^2 = \frac{S_{T,R}^2}{S_T S_R} = \frac{\left(\sum_{T_1}^{T_n} \left((T - T_{mean}) \left(\sum_{pH_1}^{pH_n} \left(\frac{R}{n_{pH}} \right) - \bar{R} \right) \right) \right)^2}{\sum_{T_1}^{T_n} (T - T_{mean})^2 \sum_{T_1}^{T_n} \left(\sum_{pH_1}^{pH_n} \left(\frac{R}{n_{pH}} \right) - \bar{R} \right)^2} \quad (3)$$

Figure 5 shows the plots of the values of the Pearson coefficients for pH and temperature calculated using the fluorescence spectra shown in Figure 4. Using Equations (2) and (3), the Pearson coefficients are calculated for different wavelengths used to calculate the ratio of fluorescent intensities. One can see that Figure 5a,b shows linearity (the Pearson coefficients close to 1) for both pH and temperature for a wavelength range of 500–550 nm. The range of 550–650 nm is also highly linear with respect to the change of temperature with the Pearson coefficient >0.996 (Figure 5b). Comparing Figure 5a,b, one can see that the ratio dependencies are more linear for temperature ($r_T^2 > 0.996$) compared to pH ($r_{pH}^2 > 0.95$). This is in agreement with previously reported FITC-based pH sensors, which are known to be nonlinear with respect to the change in pH [35]. The regions of wavelengths, in which the dependence of temperature and pH on the corresponding fluorescence ratios is quite linear are considered further to choose the wavelengths for the ratio to obtain the minimum error of measurements.

Although we see the linear relation between the parameters, pH and temperature, and the intensity ratios, it is instructive to add a few nonlinear polynomial terms because the Pearson coefficient is not exactly 1, which indicates it may be small, but still a deviation from linearity. In addition, it will help us to verify that the nonlinear terms are small. Hereafter, we suggest the Equations (4)–(9) comprising the polynomial of the third order and a linear crosstalk product of two ratios:

$$T(R_T, R_{pH}) = At \times (R_{pH})^3 + Bt \times (R_{pH})^2 + Ct \times R_{pH} + Dt \times R_T \times R_{pH} + Et, \quad (4)$$

$$pH(R_T, R_{pH}) = ApH \times (R_{pH})^3 + BpH \times (R_{pH})^2 + CpH \times R_{pH} + DpH \times R_T \times R_{pH} + EpH, \quad (5)$$

where $A_t, B_t, C_t, D_t, E_t, A_{pH}, B_{pH}, C_{pH}, D_t$ and E_t are constants, R_{pH} and R_T are ratios of fluorescence intensities of the chosen reflexes (i.e., $R_{pH} = I(\lambda_1)/I(\lambda_2)$ and $R_T = I(\lambda_3)/I(\lambda_4)$).

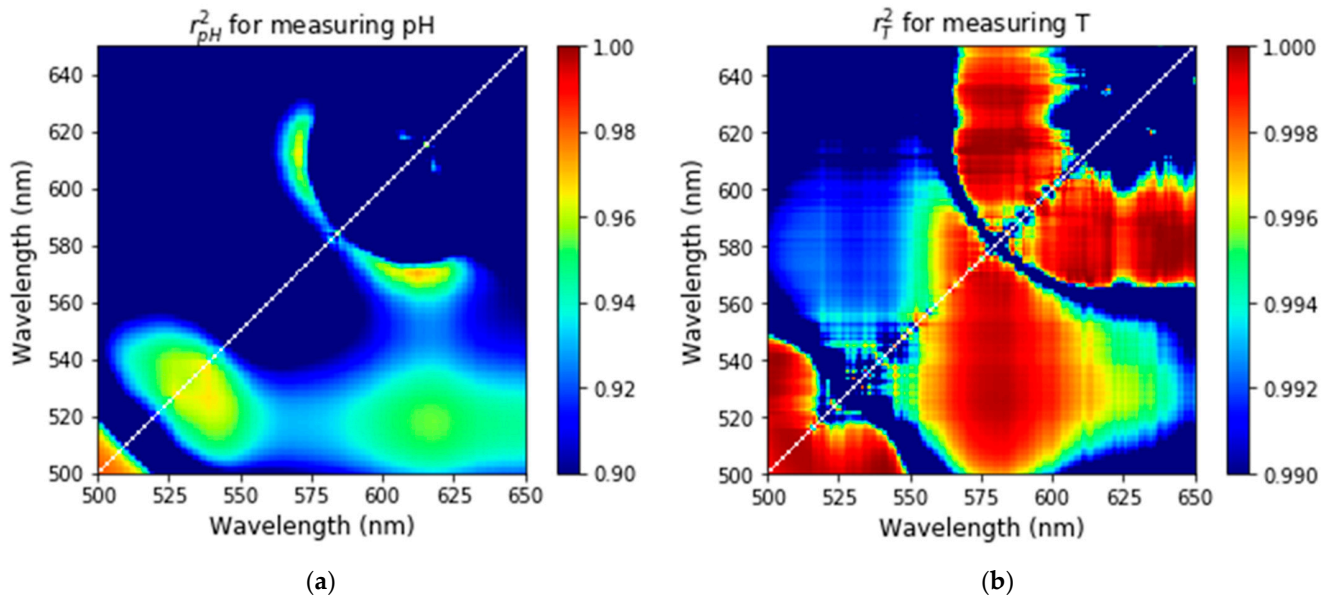


Figure 5. The Pearson correlation coefficients are shown for different wavelengths used to calculate the ratio of fluorescent intensities. The dependence between the model parameters (temperature and pH) and the corresponding ratios is close to linear when the Pearson coefficient is close to 1. The results are shown for pH (a) and temperature (b) measurements.

Now we can focus on maximizing the signal-to-noise ratio of the fluorescence signal that is used to find temperature and pH, i.e., the ratio of the fluorescence intensities. It is useful to simultaneously maximize the sensitivity to the change of temperature and pH. Therefore, we suggest maximizing the signal-to-noise ratio of the following signal:

$$S(A, B) = \left| \frac{\left(\left(\frac{I_1}{I_2} \right)_{T_1} - \left(\frac{I_1}{I_2} \right)_{T_2} \right)}{\left(\frac{\left(\frac{I_1}{I_2} \right)_{T_1} + \left(\frac{I_1}{I_2} \right)_{T_2}}{2} \right)} \right| = \left| \left(\frac{A - B}{\left(\frac{A+B}{2} \right)} \right) \right|, \quad (6)$$

where I_1 and I_2 are the fluorescence intensities at wavelength 1 and 2, respectively, A and B are the ratio of intensity at temperatures T_1 and T_2 , respectively.

According to the formula of error propagation, the error in signal $S(A, B)$ is given by

$$\delta S(A, B) = \sqrt{(\partial_A S(A, B))^2 (\delta A)^2 + (\partial_B S(A, B))^2 (\delta B)^2}, \quad (7)$$

$$= \sqrt{\left(\partial_A \left(\frac{A - B}{\left(\frac{A+B}{2} \right)} \right) \right)^2 (\delta A)^2 + \left(\partial_B \left(\frac{A - B}{\left(\frac{A+B}{2} \right)} \right) \right)^2 (\delta B)^2} = 4 \sqrt{\frac{B^2 (\delta A)^2 + A^2 (\delta B)^2}{(A + B)^4}}, \quad (8)$$

where,

$$\delta A(I_1, I_2) = A \sqrt{\left(\frac{\delta I_1}{I_1} \right)^2 + \left(\frac{\delta I_2}{I_2} \right)^2}, \quad \delta B(I_1, I_2) = B \sqrt{\left(\frac{\delta I_1}{I_1} \right)^2 + \left(\frac{\delta I_2}{I_2} \right)^2} \quad (9)$$

Similar formulas can be derived for the signal defining pH.

Pearson correlation coefficient (PCC) and signal-to-noise ratios (SNR), $S(A, B) / \delta S(A, B)$ calculated for the fluorescent nanosensors are shown in Figure 6 and Figure S2. One can see still a sufficiently broad range of wavelengths to choose from when PCC is close to 1.

The freedom of choice of the optimal wavelengths can further be reduced by finding the regions of the wavelengths in which the Pearson correlation coefficient is sufficiently close to 1 and the signal-to-noise ratio is sufficiently high. In addition, to reduce the ambiguity and cross-correlation between pH and temperature, one ratio should depend on only one parameter and should be independent of the other parameter. For finding the two ratios, where one ratio depends on only one parameter and is independent of the other, the region of interest was identified such that the ratio of two wavelengths have high linearity (or dependence) to pH and low linearity (or independence) for temperature, and similarly, the region of interest for temperature was identified such that the second ratio of other two wavelengths has high linearity (or dependence) to temperature and low linearity (or less dependence) to pH. Specifically, we find two wavelengths for pH such that the PCC of pH was taken greater than 0.7 while that of temperature was taken less than 0.5 (Figure 6c). Figure 6e shows the SNR of pH for the region of interest where PCC of pH is greater than 0.7 while PCC of temperature is less than 0.5. Similarly, for finding two wavelengths for temperature, for PCC of temperature were set such that the PCC of temperature was taken greater than 0.95 while that of pH was taken less than 0.5 (Figure 6d), and Figure 6f shows the SNR of temperature for the region of interest where PCC of temperature is greater than 0.95 while PCC of pH is less than 0.5. The ratio of intensities at wavelength 582 to 614 nm showed high SNR and PCC for temperature while the ratio of intensities at wavelength 523 to 536 nm showed high SNR and PCC for pH. Hence R_T and R_{pH} were taken as the ratio of intensities at wavelength 582 to 614 nm and 523 to 536 nm, respectively.

3.5. Algorithm for Further Finding the Optimal Values of Wavelength

In principle, the accuracy of the measuring temperature and acidity could further be improved using the algorithm shown in Figure 7. According to the algorithm, for the wavelengths in the range of $\lambda_1 - n$ to $\lambda_1 + n$, $\lambda_2 - n$ to $\lambda_2 + n$, $\lambda_3 - n$ to $\lambda_3 + n$ and $\lambda_4 - n$ to $\lambda_4 + n$, the first four wavelengths (i.e., $\lambda_1 - n$, $\lambda_2 - n$, $\lambda_3 - n$ and $\lambda_4 - n$) were chosen and fitted to Equation (4) and values of temperature were determined. The residual (the absolute difference between the actual values of temperature and the values measured using our nanosensors) was calculated for 30 data points (i.e., five data points for different temperatures and six data points for different pH) and the maximum of all the residuals were calculated. If the maximum residual was less than 1.2 °C for temperature, the four wavelengths and their residual were stored and displayed, and if it was greater then, one of the wavelengths was iterated and the loop continued until all the range of the wavelengths were iterated (i.e., until $\lambda_1 + n$, $\lambda_2 + n$, $\lambda_3 + n$ and $\lambda_4 + n$). In this way, the four wavelengths that show a maximum residual of less than 1.2 °C were identified. For finding temperature, since the wavelengths determined using PCC and SNR were 523, 536, 582 and 614 nm for λ_1 , λ_2 , λ_3 and λ_4 , respectively, the range of the wavelengths used was 519–527 nm for λ_1 , 532–540 nm for λ_2 , 578–586 nm for λ_3 and 610–618 nm for λ_4 (considering $n = 4$). The range was four wavelengths below and above the wavelengths determined using regression and SNR analysis. Since the temperature error should be less than 1.2 °C, the expected residual in temperature was chosen to be less than 1.2 °C. Out of all the wavelengths, the wavelengths 525, 537, 581 and 611 nm showed the lowest maximum residual of ~1.1 °C for temperature. Using the same four wavelengths, the maximum residual for pH was determined to be equal to 0.3.

Table S1 shows the ratios at different pH and temperature. These ratios were further used for multiparametric fitting. From Figure S1, it can be seen that the ratios change repeatably when pH is constant and the temperature is changed and also vice versa. This makes the pH and temperature sensor repeatable.

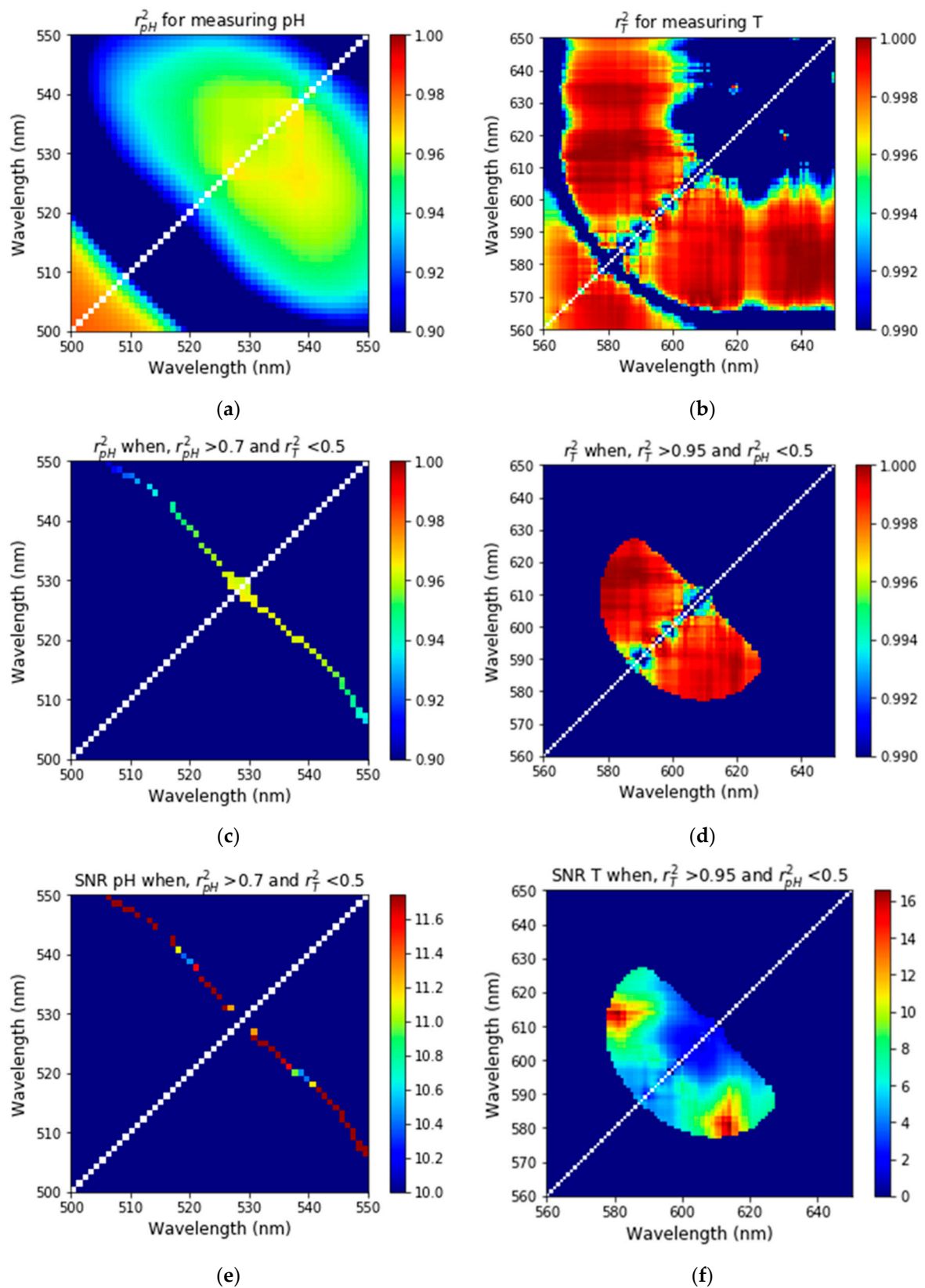


Figure 6. The Pearson correlation coefficient and signal-to-noise ratios for different wavelengths. The Pearson correlation coefficients for pH (a) and temperature (b) measurements. Pearson correlation coefficient for (c) pH when PCC of pH is greater than 0.7 while PCC of temperature is less than 0.5 and for (d) T when PCC of temperature is greater than 0.95 while PCC of pH is less than 0.5. SNR for (e) pH when PCC of pH is greater than 0.7 while PCC of temperature is less than 0.5 and for (f) T when PCC of temperature is greater than 0.95 while PCC of pH is less than 0.5.

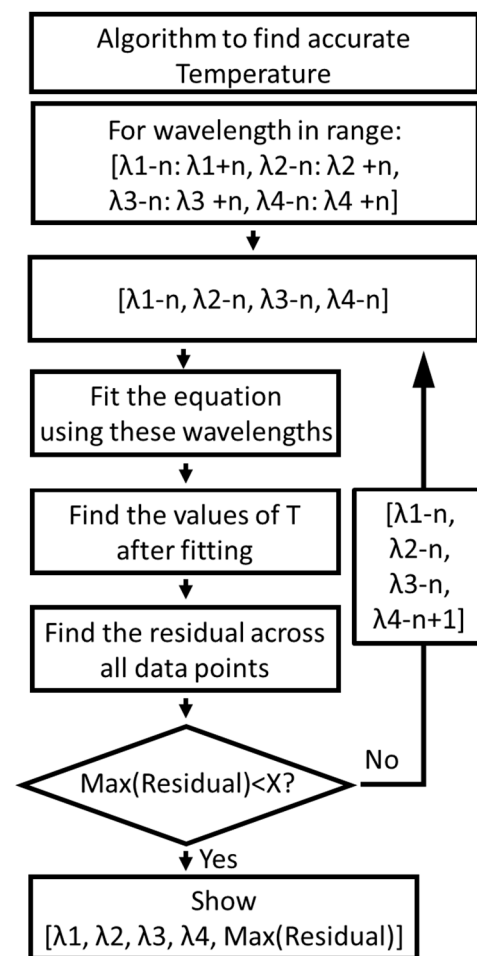


Figure 7. Flowchart outlining the procedure for obtaining four wavelengths for temperature. Note that the fitting for temperature was performed using Equation (4) and R_{pH} and R_T represent $I(\lambda_1)/I(\lambda_2)$ and $I(\lambda_3)/I(\lambda_4)$, respectively; X represents $1.2\text{ }^\circ\text{C}$ for temperature.

3.6. Multiparametric Fit for pH and Temperature

Using the wavelengths that were found, we fit the experimental data (shown in Figure 4 for a set of different temperatures and pH) with the help of Equations (4) and (5). Table 2 shows the fitted coefficients used in Equations (4) and (5). One can see that the coefficients corresponding to the nonlinear terms are indeed rather small. Both the results of the fitting and the experimental data are shown in Figure 8. One can see a rather good fit.

Table 2. Fitted coefficients used in Equations (4) and (5) when using the optimal wavelengths of 525, 537, 581 and 611 nm.

Coefficients for Equation (4)	Value	Coefficients for Equation (5)	Value
At	51,470	ApH	2498
Bt	−166,817	BpH	−8089
Ct	180,264	CpH	8747
Dt	−91.5	DpH	1.04
Et	−64,712	EpH	−3156

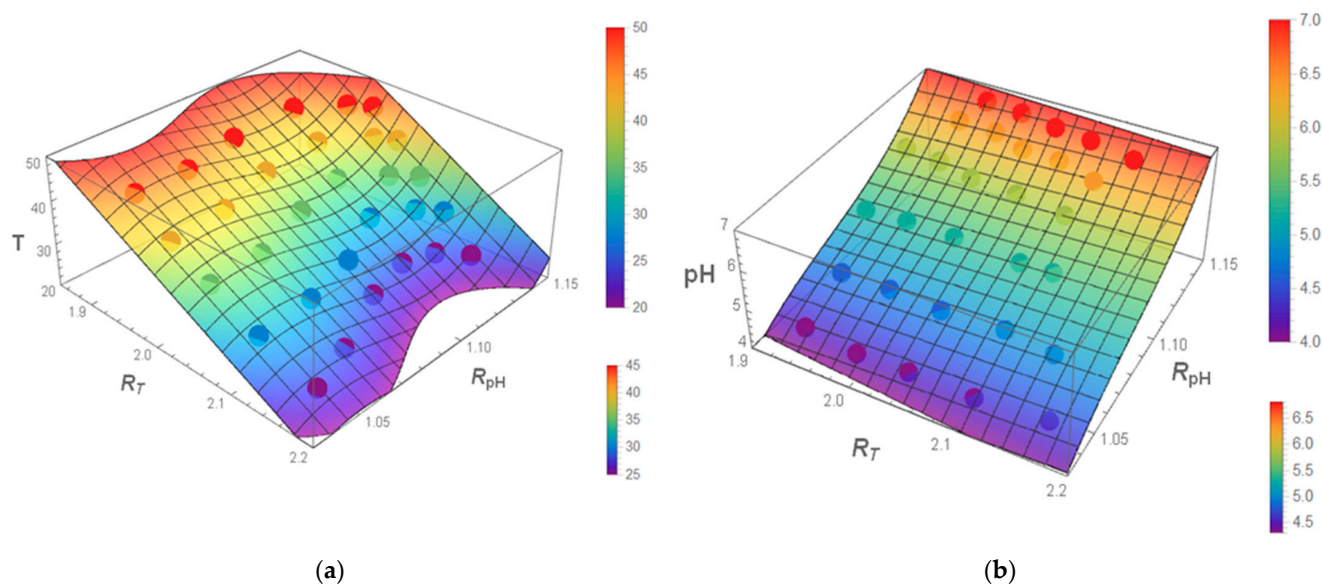


Figure 8. The results of the multiparametric fitting of experimental data (shown by dots) using Equations (4) and (5) to measure measuring temperature and pH, respectively. The measurements of the (a) temperature and (b) pH as a function of two ratios, R_T and R_{pH} .

To estimate the errors of the measurements of temperature and pH using the functions of fitted Equations (4) and (5), we conducted four independent measurements of fluorescence at temperature 24.17, 29.63, 34.74, 39.77 and 44.8 °C and pH 6.8, 6.3, 5.8, 5.3, 4.8 and 4.3. Measuring multiple spectra and using the error propagation (see the Supplementary Information), we find the errors of measurements of both temperature and pH. The examples are shown in Table S2 (assuming fixed pH) and Table S3 (assuming fixed temperature). Corresponding ratios R_T and R_{pH} are shown in the Supplementary Information.

Table S1 shows the ratios that are calculated using the intensities at wavelengths 525 to 537 nm, and 581 to 611 nm wavelengths for pH and temperature, respectively. The accuracy determined using this formula was 98.4% and 98.36% for pH and temperature, respectively.

4. Discussion

Here we discuss the results obtained in comparison with the current state-of-the-art. Because the achievement reported is based on multiple pillars, we describe each of them separately below.

4.1. Use of Mesoporous Silica Versus Solid Silica as the Material of the Nanothermometers

Gold–FITC encapsulation of dye molecules in solid silica matrix has been previously reported. For example, silica nanoparticles had physically encapsulated rhodamine B dye while the silica shell was modified with APTES followed by conjugation with FITC [7]. This post-conjugation of silica particles with APTES and further attachment with FITC is not only an additional and time-consuming process, but it also reduces the quantum yield of the encapsulated dye molecules. The particles obtained served as a pH sensor due to the presence of pH-sensitive FITC dye, whereas rhodamine B served as a reference [7]. Although rhodamine B is temperature-sensitive, no temperature measurements were reported for that work because there was no third reference dye involved (a third dye is needed to make the sensor ratiometric). In another paper, a ratiometric pH sensor using FITC and Nile blue was reported [36]. Nile blue was used as a reference. FITC and Nb were conjugated on the surface of carbon dots. However, ratiometric pH and dual temperature sensors based on two ratios (three dyes) have not been made before.

The use of mesoporous silica particles as hosts for dye molecules creates a novel possibility to create ratiometric fluorescent sensors coupling two different dyes with FRET [12,13]. For extending the application of sensors to understand cellular processes, it is important

that the sensors can operate at the nanoscale. Physical encapsulation of dyes in mesoporous silica could be used for encapsulating multiple dyes that are sensitive to different parameters (for example, pH and temperature in this case) in a single nanoparticle. In this work, sensor-based on ultrabright mesoporous silica nanoparticles is synthesized incorporating three dyes. Herein, FITC and rhodamine B were used for pH and temperature sensing, respectively, while Nile blue was used as a reference. This is the first demonstration of pH and temperature nanosensors based on the physical encapsulation of three dyes. The particles reported here are free of the issues mentioned above and can be used as sensors.

4.2. The Problem of Ambiguity of Simultaneous Measurement of Temperature and Acidity

Gold-FITC based nanoclusters have been reported for pH and temperature sensing [37]. This dual sensor was built using two fluorescence peaks coming from gold and FITC. However, for unambiguous determination of both pH and temperature, the magnitude of the intensity ratio or the initial values of pH and temperature should be known. In other work, a pH and temperature sensor was made using a co-assembly of temperature-sensitive polymer PNIPAM, pH-sensitive polymer PNIPAM-co-PAA, photoluminescence sources europium and quaternary ammonium tetraphenyl ethylene derivatives [38]. However, simultaneous temperature and pH measurements were not conducted due to the ambiguity of cross-correlation between the fluorescence dependence of the temperature and pH. The temperature measurements were performed at a constant pH 7 only. As we demonstrated in the present work, we use two different fluorescence ratios to avoid the need of the above ad hoc knowledge and solve the problem of cross-correlation.

4.3. Multiparametric Sensor

The other pillar used in this work is the use of multiparametric algorithms, in particular, the use of polynomial sensing Equations (4) and (5). Ideally, in a dual sensor, the two parameters should be independent of each other. Linear multiparametric sensors, a polynomial of the order of one, have been studied in [39]. Nonlinear polynomial fit for calibrating pH sensor is reported [35]. However, to the best of our knowledge, a nonlinear polynomial fit for sensing both pH and temperature has not been previously reported. In addition, the multiparametric sensor, in which the two parameters are related to each other, has not been previously reported. In this study, a nonlinear multiparametric sensor in which the two parameters are cross-correlated but avoid ambiguity in measuring both parameters (temperature and pH) is reported.

4.4. Stability of the Sensor

Because of a potential concern of leakage of the encapsulated dye and photobleaching, it is important to demonstrate that the sensor is stable and the readings are repeatable. The repeatability of the described sensors is shown in Figure S1. Fluorescent spectra from nanosensors were measured at pH 7 for temperatures 35 and 50 °C and, similarly, at pH 4 for temperatures 35 and 50 °C for four cycles of temperature. The errors defined as the standard deviation across four measurement cycles are shown in Figure S1. One can see that the error to signal ratio is less than 1%, Table S5.

Spectral stability with respect to the presence of different ions in the solution is shown in Figure 3 and Figure S3. Measurements were done in the presence of monovalent (K^+ and Na^+) and divalent (Ca^{2+} and Mg^{2+}) ions. The choice of these particular ions was dictated by the immediate application of the reported sensors to measure the temperature and pH in biological tissues and cells. These ions are the most abundant in biological buffers. It should be noted that the applicability of sensors to other environments has to be tested for each specific environment. Because the number of cases in which the sensors described can be used is practically unlimited, the study of spectral stability in other buffers is beyond the scope of this work. Furthermore, if this problem appears, it could potentially be addressed by additional nonporous silica coating.

5. Conclusions

In the present work, we describe a dual acidity (pH) and temperature sensor based on ultrabright fluorescent nanoparticles. Simultaneous, multiparametric and nonlinear pH and temperature sensing were successfully demonstrated using FITC (a pH-sensitive dye), rhodamine B (a temperature-sensitive dye) and Nile blue (a reference dye) physically mixed in mesoporous silica particle.

To measure both pH and temperature simultaneously, using two ratios of fluorescent intensities measured at four wavelengths was suggested. A regression analysis was used to find regions of four wavelengths that are (almost) linear with pH and temperature. This allowed us to find the wavelengths to optimize the signal-to-noise ratio and reduce cross-correlation between acidity and temperature dependencies, which in turn decreased the error of the measurements when using the sensors. The regression analysis and algorithm described may further be used in multiparametric systems or sensors in which the parameters are cross-correlated and there is a need to reduce the cross-correlation. The analysis of the discrepancy between the equations and experimentally measured pH and temperature showed that the method suggested can be used to measure pH and temperature with an accuracy of greater than 98%. The repeatability of measuring pH and temperature was demonstrated by multiple cycling of temperature and acidity. Finally, the stability of the sensor in the presence of different ions typical for biological media was demonstrated. Due to a high brightness, sensing with ultrabright nanoparticles could be done at a low dosage and low intensity of the excitation light. When applied to biomedical detection, this will decrease not only the chemotoxicity but also the phototoxicity.

Supplementary Materials: The following are available online at <https://www.mdpi.com/article/10.3390/nano11061524/s1>, Figure S1: Repeatability of measurements at (a and b) constant pH and different temperature and at (c and d) constant temperature and different pH. Figure S2: (a) PCC of pH when PCC of pH is greater than 0.7 while PCC of temperature is less than 0.5, PCC of temperature when PCC of temperature is greater than 0.95 while PCC of temperature is less than 0.5 and (b) SNR of pH when PCC of pH is greater than 0.7 while PCC of temperature is less than 0.5, (c) PCC and (d) SNR of temperature when PCC of temperature is greater than 0.95 while PCC of pH is less than 0.5. Figure S3: Temperature and pH response of nanosensors towards metal ions (1 mM) K⁺, Ca²⁺, Mg²⁺ and Na⁺. Table S1: Ratios of fluorescence intensity at wavelengths of 525 and 537 nm (RpH) and 581 and 611 nm (RT) for measuring pH and temperature. Error represents the standard deviation of four measurements. Table S2: Temperature and standard deviation calculated using Equation (4) (considering pH fixed). Both temperature and pH in the table headings are measured using standard tools (a thermocouple and pH meter). Table S3: pH and standard deviation calculated using Equation (5) (considering temperature fixed). Table S4: FRET efficiency and distance between different dye molecules. Both temperature and pH in the table headings are measured using standard tools (a thermocouple and pH meter). Table S5: Repeatability of the sensor ratios.

Author Contributions: Conceptualization, I.S. and S.A.M.A.P.; methodology, S.A.M.A.P.; synthesis, S.A.M.A.P.; data analysis, S.A.M.A.P.; AFM measurements, N.M.; writing—original draft preparation, S.A.M.A.P.; writing—review and editing, I.S.; supervision, I.S.; funding acquisition, I.S. All authors have read and agreed to the published version of the manuscript.

Funding: The study was funded by NSF grants CBET 1605405 and CMMI 1937373 (I.S.).

Acknowledgments: Authors would like to thank Kyle Monahan for help with Python code.

Conflicts of Interest: The authors declare no conflict of interest. The funders had no role in the design of the study; in the collection, analyses, or interpretation of data; in the writing of the manuscript, or in the decision to publish the results.

References

1. Somero, G.N. Proteins and temperature. *Annu. Rev. Physiol.* **1995**, *57*, 43–68. [CrossRef]
2. Kruse, C.R.; Singh, M.; Targosinski, S.; Sinha, I.; Sørensen, J.A.; Eriksson, E.; Nuutila, K. The effect of pH on cell viability, cell migration, cell proliferation, wound closure, and wound reepithelialization: In vitro and in vivo study. *Wound Repair Regen.* **2017**, *25*, 260–269. [CrossRef]

3. O'Brien, E.P.; Brooks, B.R.; Thirumalai, D. Effects of pH on proteins: Predictions for ensemble and single-molecule pulling experiments. *J. Am. Chem. Soc.* **2011**, *134*, 979–987. [CrossRef] [PubMed]
4. Sarkar, T.; Selvakumar, K.; Motiei, L.; Margulies, D. Message in a molecule. *Nat. Commun.* **2016**, *7*, 11374. [CrossRef]
5. Lee, M.H.; Park, N.; Yi, C.; Han, J.H.; Hong, J.H.; Kim, K.P.; Kang, D.H.; Sessler, J.L.; Kang, C.; Kim, J.S. Mitochondria-Immobilized pH-Sensitive Off-On Fluorescent Probe. *J. Am. Chem. Soc.* **2014**, *136*, 14136–14142. [CrossRef]
6. Okabe, K.; Inada, N.; Gota, C.; Harada, Y.; Funatsu, T.; Uchiyama, S. Intracellular temperature mapping with a fluorescent polymeric thermometer and fluorescence lifetime imaging microscopy. *Nat. Commun.* **2012**, *3*, 705. [CrossRef] [PubMed]
7. Fu, J.; Ding, C.; Zhu, A.; Tian, Y. An efficient core-shell fluorescent silica nanoprobe for ratiometric fluorescence detection of pH in living cells. *Analyst* **2016**, *141*, 4766–4771. [CrossRef] [PubMed]
8. Liu, H.; Maruyama, H.; Masuda, T.; Honda, A.; Arai, F. Multi-fluorescent micro-sensor for accurate measurement of pH and temperature variations in micro-environments. *Sens. Actuators B Chem.* **2014**, *203*, 54–62. [CrossRef]
9. Kalaparthi, V.; Palantavida, S.; Sokolov, I. The nature of ultrabrightness of nanoporous fluorescent particles with physically encapsulated fluorescent dyes. *J. Mater. Chem. C* **2016**, *4*, 2197–2210. [CrossRef]
10. Sokolov, I.; Volkov, D.O. Ultrabright fluorescent mesoporous silica particles. *J. Mater. Chem.* **2010**, *20*, 4247–4250. [CrossRef]
11. Cho, E.B.; Volkov, D.O.; Sokolov, I. Ultrabright Fluorescent Mesoporous Silica Nanoparticles. *Small* **2010**, *6*, 2314–2319. [CrossRef]
12. Kalaparthi, V.; Peng, B.; Peerzade, S.A.M.; Palantavida, S.; Maloy, B.; Dokukin, M.E.; Sokolov, I. Ultrabright fluorescent nanothermometers for absolute measurements of temperature. 2021; under review.
13. Wang, X.-d.; Stolwijk, J.A.; Lang, T.; Sperber, M.; Meier, R.J.; Wegener, J.; Wolfbeis, O.S. Ultra-small, highly stable, and sensitive dual nanosensors for imaging intracellular oxygen and pH in cytosol. *J. Am. Chem. Soc.* **2012**, *134*, 17011–17014. [CrossRef] [PubMed]
14. Zhou, J.; Del Rosal, B.; Jaque, D.; Uchiyama, S.; Jin, D. Advances and challenges for fluorescence nanothermometry. *Nat Methods* **2020**, *17*, 967–980. [CrossRef]
15. Peerzade, S.A.M.A.; Qin, X.; Laroche, F.J.F.; Palantavida, S.; Dokukin, M.; Peng, B.; Feng, H.; Sokolov, I. Ultrabright fluorescent silica nanoparticles for in vivo targeting of xenografted human tumors and cancer cells in zebrafish. *Nanoscale* **2019**, *11*, 22316–22327. [CrossRef]
16. Peerzade, S.A.M.A.; Makarova, N.; Sokolov, I. Ultrabright Fluorescent Silica Nanoparticles for Multiplexed Detection. *Nanomaterials* **2020**, *10*, 905. [CrossRef] [PubMed]
17. Lim, S.J.; Zahid, M.U.; Le, P.; Ma, L.; Entenberg, D.; Harney, A.S.; Condeelis, J.; Smith, A.M. Brightness-equalized quantum dots. *Nat. Commun.* **2015**, *6*, 8210. [CrossRef] [PubMed]
18. Chan, W.C.W.; Maxwell, D.J.; Gao, X.H.; Bailey, R.E.; Han, M.Y.; Nie, S.M. Luminescent quantum dots for multiplexed biological detection and imaging. *Curr. Opin. Biotechnol.* **2002**, *13*, 40–46. [CrossRef]
19. Chan, W.C.W.; Nie, S.M. Quantum dot bioconjugates for ultrasensitive nonisotopic detection. *Science* **1998**, *281*, 2016–2018. [CrossRef]
20. Lei, J.; Wang, L.; Zhang, J. Superbright multifluorescent core-shell mesoporous nanospheres as trackable transport carrier for drug. *ACS Nano* **2011**, *5*, 3447–3455. [CrossRef]
21. Medintz, I.L.; Uyeda, H.T.; Goldman, E.R.; Mattoussi, H. Quantum dot bioconjugates for imaging, labelling and sensing. *Nat. Mater.* **2005**, *4*, 435–446. [CrossRef]
22. Palantavida, S.; Tang, R.; Sudlow, G.P.; Akers, W.J.; Achilefu, S.; Sokolov, I. Ultrabright NIR fluorescent mesoporous silica nanoparticles. *J. Mater. Chem. B* **2014**, *2*, 3107–3114. [CrossRef]
23. Santra, S.; Zhang, P.; Wang, K.; Tapeç, R.; Tan, W. Conjugation of Biomolecules with Luminophore-Doped Silica Nanoparticles for Photostable Biomarkers. *Anal. Chem.* **2001**, *73*, 4988–4993. [CrossRef]
24. Chigaev, A.; Smagley, Y.; Haynes, M.K.; Ursu, O.; Bologa, C.G.; Halip, L.; Oprea, T.; Waller, A.; Carter, M.B.; Zhang, Y. FRET detection of lymphocyte function-associated antigen-1 conformational extension. *Mol. Biol. Cell* **2015**, *26*, 43–54. [CrossRef] [PubMed]
25. Lu, P.; Yu, Z.; Alfano, R.; Gersten, J. Picosecond studies of energy transfer of donor and acceptor dye molecules in solution. *Phys. Rev. A* **1982**, *26*, 3610. [CrossRef]
26. Iwabuchi, M.F.; Hetu, M.M.; Tong, W.G. Sensitive analysis of α -synuclein by nonlinear laser wave mixing coupled with capillary electrophoresis. *Anal. Biochem.* **2016**, *500*, 51–59. [CrossRef]
27. Birtalan, E.; Rudat, B.; Kölmel, D.K.; Fritz, D.; Vollrath, S.B.; Schepers, U.; Bräse, S. Investigating rhodamine B-labeled peptoids: Scopes and limitations of its applications. *Pept. Sci.* **2011**, *96*, 694–701. [CrossRef] [PubMed]
28. Rahavendran, S.V.; Karnes, H.T. A high sensitivity laboratory constructed HPLC-VDLIF detector evaluated with an oxazine reagent. *Instrum. Sci. Technol.* **1997**, *25*, 121–131. [CrossRef]
29. Link, M.; Kele, P.; Achatz, D.E.; Wolfbeis, O.S. Brightly fluorescent purple and blue labels for amines and proteins. *Bioorg. Med. Chem. Lett.* **2011**, *21*, 5538–5542. [CrossRef]
30. Cheng, D.; Xu, Q.-H. Separation distance dependent fluorescence enhancement of fluorescein isothiocyanate by silver nanoparticles. *Chem. Commun.* **2007**, 248–250. [CrossRef] [PubMed]
31. Gaigalas, A.K.; Wang, L. Measurement of the fluorescence quantum yield using a spectrometer with an integrating sphere detector. *J. Res. Natl. Inst. Stand. Technol.* **2008**, *113*, 17. [CrossRef] [PubMed]

32. Liu, H.; Maruyama, H.; Masuda, T.; Arai, F. Sensitivity compensation of multi-fluorescence sensor toward on-chip cell measurement. In Proceedings of the MHS2013, Nagoya, Japan, 10–13 November 2013; pp. 1–2.
33. Bewick, V.; Cheek, L.; Ball, J. Statistics review 7: Correlation and regression. *Crit. Care* **2003**, *7*, 451. [CrossRef] [PubMed]
34. Ma, J.; Ding, C.; Zhou, J.; Tian, Y. 2D ratiometric fluorescent pH sensor for tracking of cells proliferation and metabolism. *Biosens. Bioelectron.* **2015**, *70*, 202–208. [CrossRef] [PubMed]
35. Leng, Y.K.; Wu, W.J.; Li, L.; Lin, K.; Sun, K.; Chen, X.Y.; Li, W.W. Magnetic/Fluorescent Barcodes Based on Cadmium-Free Near-Infrared-Emitting Quantum Dots for Multiplexed Detection. *Adv. Funct. Mater.* **2016**, *26*, 7581–7589. [CrossRef]
36. Zhao, Y.; Shi, C.; Yang, X.; Shen, B.; Sun, Y.; Chen, Y.; Xu, X.; Sun, H.; Yu, K.; Yang, B. pH-and temperature-sensitive hydrogel nanoparticles with dual photoluminescence for bioprobes. *ACS Nano* **2016**, *10*, 5856–5863. [CrossRef]
37. Huang, T.; Fu, S.; Ke, C.; Shum, P.P.; Liu, D. Characterization of fiber Bragg grating inscribed in few-mode silica-germanate fiber. *IEEE Photonics Technol. Lett.* **2014**, *26*, 1908–1911. [CrossRef]
38. Deng, Z.J.; Morton, S.W.; Bonner, D.K.; Gu, L.; Ow, H.; Hammond, P.T. A plug-and-play ratiometric pH-sensing nanoprobe for high-throughput investigation of endosomal escape. *Biomaterials* **2015**, *51*, 250–256. [CrossRef]
39. Cho, E.B.; Volkov, D.O.; Sokolov, I. Ultrabright Fluorescent Silica Mesoporous Silica Nanoparticles: Control of Particle Size and Dye Loading. *Adv. Funct. Mater.* **2011**, *21*, 3129–3135. [CrossRef]



Article

Effect of Size and Shape on Electrochemical Performance of Nano-Silicon-Based Lithium Battery

Caroline Keller^{1,2}, Antoine Desrues³, Saravanan Karuppiah^{1,2}, Eléa Martin¹, John P. Alper^{2,3}, Florent Boismain³, Claire Villevieille¹, Nathalie Herlin-Boime³, Cédric Haon² and Pascale Chenevier^{1,*}

- ¹ CEA, CNRS, IRIG, SYMMES, STEP, University Grenoble Alpes, 38000 Grenoble, France; caroline.keller@univ-grenoble-alpes.fr (C.K.); krsaro87@gmail.com (S.K.); elea.martin@etu.unistra.fr (E.M.); claire.villevieille@cea.fr (C.V.)
- ² CEA, LITEN, DEHT, University Grenoble Alpes, 38000 Grenoble, France; johnalper@googlemail.com (J.P.A.); cedric.haon@cea.fr (C.H.)
- ³ CEA, CNRS, IRAMIS, NIMBE, LEDNA, University Paris Saclay, 91191 Gif-sur-Yvette, France; antoine.desrues@cea.fr (A.D.); florent.boismain@insa-lyon.fr (F.B.); nathalie.herlin@cea.fr (N.H.-B.)
- * Correspondence: pascale.chenevier@cea.fr

Abstract: Silicon is a promising material for high-energy anode materials for the next generation of lithium-ion batteries. The gain in specific capacity depends highly on the quality of the Si dispersion and on the size and shape of the nano-silicon. The aim of this study is to investigate the impact of the size/shape of Si on the electrochemical performance of conventional Li-ion batteries. The scalable synthesis processes of both nanoparticles and nanowires in the 10–100 nm size range are discussed. In cycling lithium batteries, the initial specific capacity is significantly higher for nanoparticles than for nanowires. We demonstrate a linear correlation of the first Coulombic efficiency with the specific area of the Si materials. In long-term cycling tests, the electrochemical performance of the nanoparticles fades faster due to an increased internal resistance, whereas the smallest nanowires show an impressive cycling stability. Finally, the reversibility of the electrochemical processes is found to be highly dependent on the size/shape of the Si particles and its impact on lithiation depth, formation of crystalline $\text{Li}_{15}\text{Si}_4$ in cycling, and Li transport pathways.

Keywords: silicon nanoparticles; silicon nanowires; synthesis; high energy density; lithium-ion batteries; high-capacity anode; VLS; laser pyrolysis; size effect; shape effect

Citation: Keller, C.; Desrues, A.; Karuppiah, S.; Martin, E.; Alper, J.P.; Boismain, F.; Villevieille, C.; Herlin-Boime, N.; Haon, C.; Chenevier, P. Effect of Size and Shape on Electrochemical Performance of Nano-Silicon-Based Lithium Battery. *Nanomaterials* **2021**, *11*, 307. <http://doi.org/10.3390/nano11020307>

Academic Editor: Jie Wang
Received: 23 December 2020
Accepted: 21 January 2021
Published: 25 January 2021

Publisher's Note: MDPI stays neutral with regard to jurisdictional claims in published maps and institutional affiliations.



Copyright: © 2021 by the authors. Licensee MDPI, Basel, Switzerland. This article is an open access article distributed under the terms and conditions of the Creative Commons Attribution (CC BY) license (<https://creativecommons.org/licenses/by/4.0/>).

1. Introduction

High energy density in lithium-ion batteries (LiB) requires active materials with enhanced lithium absorption capacity and a large potential gap. On the anode side, silicon appears as the most promising material to enhance the specific capacity for several reasons [1]. Si is an earth-abundant, low-cost, and non-toxic element, with a mature industrial knowledge base from its application in electronics, optics, and photovoltaics. Furthermore, its low potential, close to Li/Li^+ , makes it suitable for composites with graphite, the current commercial anode material [2–4]. Finally, Si shows a high Li-alloying capacity but, consequently, an undesired high volume change in cycling [5]. This deleterious volume change stimulated the development of Si nanomaterials, because Si at the nano scale can withstand swelling without fracture during LiB cycling. This has been demonstrated for a variety of morphologies including Si nanoparticles (SiNP) [6–11], Si nanowires (SiNW) [3,12–14], Si nanotubes [15,16], and Si porous nanomaterials [17–19]. However, nanostructuring can be a costly process that needs to be carefully optimized for a dedicated application.

The size of the nano-Si and its impact on lithiation mechanisms has been the subject of numerous papers. Several in situ TEM investigations have shown that fracture of crystalline SiNWs [20,21] and SiNPs [21,22] occurs above a critical diameter of ≈ 150 nm. A critical diameter was also predicted by a mechanical numerical model [23] at 90 nm for SiNPs

and 70 nm for SiNWs. By contrast, several electrochemical studies in LiB investigated the impact of particle size on Si-based anode cycling for small [6,8] and large [7–9] SiNPs, with the best results at diameters of 20–50 nm. As for SiNWs, some studies have suggested the optimal diameter as being around 30 nm [10,24]. These size limits in batteries look much lower than the safe nano-silicon size inferred from calculations or TEM observations. However, these electrochemical studies use different sources of Si with heterogeneous size distributions and within a narrow range of average sizes, making the optimum estimation quite challenging. Additionally, to date, no study has compared different shapes of nano-silicon cycled in the same conditions to enable direct comparison of 0D and 1D structures.

SiNPs and SiNWs can be obtained with a very high control on diameter from well-described synthesis methods, such as colloidal nanocrystal synthesis [25] and chemical vapor deposition (CVD) growth [26,27]. However, these highly controlled growth processes produce insufficient (~1 mg) quantities of material for assembling a lithium-ion battery (requiring >100 mg for typical coin cell electrodes). Typical scalable processes developed for industrial synthesis of SiNPs [28,29] and SiNWs [9,30,31] produce nanomaterial either with a very wide size distribution or with a limited ability to change the diameter. The synthesis of a series of nano-silicon materials of fine-tuned size in a large scale is, thus, a challenge for materials chemists.

In the present paper, we present optimized, scalable processes to obtain large batches of SiNPs and SiNWs allowing a comparison of Si nanomaterials in shape (spherical or cylindrical) and size. All materials were tested in half-cell Li-ion batteries in the same conditions to investigate the impact of shape/size on the electrochemical performance and reaction mechanisms.

2. Materials and Methods

Chemicals: Calcium carbonate (CaCO₃ nanopowder, 50 nm), sodium citrate, ascorbic acid, and carboxymethylcellulose sodium (CMC) were purchased from Sigma Aldrich. Gold tetrachloroauric acid (HAuCl₄), tetraoctylammonium bromide (TOAB), dodecanethiol, and sodium chloride were purchased from Alfa Aesar. Carbon black Super-P (CB) was purchased from Imerys. Diphenylsilane was purchased from Chemical Point. Silane (high purity, 98%) was purchased from Messer.

Silicon nanoparticle synthesis: The silicon nanoparticles (NPs) were synthesized by laser pyrolysis as already described [28,32]. Briefly, a flow of gaseous silane intersects with the beam of a high power CO₂ laser. In the interaction zone, silane absorbs the laser radiation. Dissociation of the precursor followed by nucleation and growth of Si nanoparticles occurs with appearance of a flame. Key parameters to control the nanoparticle size are the residence time in the laser beam, the nucleation, and the flame temperatures. The main control parameters are the gas flow rates, the dilution of active gases, and the laser power.

Gold nanoparticle synthesis for silicon nanowire growth: 1–2 nm gold nanoparticles (AuNP) are synthesized by the Brust method [33]. Briefly, HAuCl₄·xH₂O dissolved in water is transferred in toluene using tetraoctylammonium bromide, then reduced with NaBH₄ and stabilized with dodecanethiol (dodecanethiol/gold molar ratio 2:1), leading to 1.5–2 nm diameter AuNPs quantitatively. The organic gold nanoparticles are purified by precipitation in ethanol and redispersed in chloroform. Twelve nanometers AuNPs are synthesized using the Turkevich method [34]. Briefly, HAuCl₄·xH₂O dissolved in water is mixed with a sodium citrate solution at 100 °C and agitated for 30 min. Higher diameter AuNPs are made following the Ziegler and Eychmüller method [35], by regrowing from the 12 nm AuNPs used as gold seeds. Briefly, a suspension of 12 nm AuNPs in water (120 mL, 90 mg/L) is slowly mixed with an aqueous solution of HAuCl₄ (60 mL, 3.4 mM), sodium citrate, and ascorbic acid (60 mL, 6.3 and 4.6 mM, respectively). The aqueous AuNPs are purified by centrifugation after precipitation with ethanol.

Silicon nanowire synthesis: SiNWs are synthesized in a 150 cm³ home-built stainless-steel reactor designed to withstand pressure above 50 bars and temperatures above 500 °C.

AuNPs are deposited by drop drying either on a NaCl micropowder if the colloid solvent is organic, or on a CaCO₃ nanopowder if the colloid is in aqueous solution (50 mg AuNPs on 25 g NaCl or 3 g CaCO₃). After drying, the powder is placed in a 2 cm diameter alumina crucible in the reactor with 12 mL diphenylsilane under vacuum. The reactor is heated to 430 °C within 40 min and kept at 430 °C for 80 min. After cooling, the powder is washed with water if grown on NaCl, or with 4 M aqueous HCl if grown on CaCO₃, and with dichloromethane. To check for the effect of NaCl or CaCO₃ on the growth process, some 12 nm AuNPs were transferred in toluene using ligand exchange with hexadecylamine in toluene [36], then replacing hexadecylamine with dodecanethiol and subsequently depositing on NaCl powder by centrifugation. The SiNWs grown from 12 nm AuNPs on NaCl did not show any change in shape and size as compared to the SiNWs grown from 12 nm AuNPs on CaCO₃.

Materials characterization: Phase identification was performed with powder X-ray diffraction (XRD) technique on a Bruker D8 advance diffractometer θ – 2θ configuration with a Cu anticathode (Bruker AXS, Karlsruhe, Germany). The scanning step used was 0.02° with a counting time of 1.2 s per step. Scanning electron microscopy (SEM) was performed on a Zeiss Ultra 55 microscope (Zeiss, Oberkochen, Germany) at an accelerating voltage of 5 kV and working distance of 5 mm. A JEOL 2010 (JEOL, Tokyo, Japan) high-resolution transmission electron microscope (HRTEM) operated at 200 kV was used for TEM and HRTEM observations. For TEM measurements, the powder was dispersed in ethanol and nanoparticles separated with intensive ultrasound using the Hielscher Ultrasound Technology VialTweeter UIS250V (Hielscher, Teltow, Germany). Then, the dispersion was dropped on a grid made of a Lacey Carbon Film (300 mesh Copper—S166-3H). The Brunauer, Emmet, and Teller (BET) method was used to measure the SBET specific surface of the different samples using Micromeritic apparatus Tristar II and Flowsorb 2300 (Micromeritics, Norcross, GA, USA). Electrochemical studies, including electrochemical impedance spectroscopy, were carried out using a Biologic VMP3 multichannel potentiostat (Biologic, Seyssinet-Pariset, France) and an ARBIN charge–discharge cycle life tester (Arbin, College Station, TX, USA).

Lithium battery assembly and test: SiNPs or SiNWs are mixed in an ink containing 50 wt. % of active material, 25 wt. % of carbon black, and 25 wt. % of CMC dispersed in distilled water. The resultant slurry is coated using the doctor blade method on thin copper foil (12 μ m), dried at 80 °C overnight (mass loading 0.19–0.46 mg_{Si} cm^{−2}, dry thickness around 20 μ m), and calendared at 1 ton. A celgard separator was soaked with 150 μ L electrolyte of ethylenecarbonate/diethylenecarbonate 1/1 v/v containing 1M LiPF₆, 10 wt. % fluoroethylene carbonate, and 2 wt. % vinylenecarbonate. Two thousand and thirty-two coin cells were assembled with lithium metal as reference and counter electrode in an argon-filled glove box and crimp sealed. Electrochemical properties of the half-cells were evaluated in the potential window between 0.01 and 1.0 V vs. Li⁺/Li. All potentials reported below were measured in a half cell configuration in reference to the Li metal counter electrode and are, thus, expressed as vs. Li⁺/Li. The first cycle rate is C/20. Later, cycles are performed at C/5 rate, with a floating time at the end of lithiation until a current of C/100 and C/50, respectively, under 0.01 V. All the capacity values shown in this paper are based on the mass of silicon in the electrode.

3. Results

3.1. Tuning the Size of SiNPs: Silane Concentration and Residence Time

Batches of SiNPs with different diameters were synthesized by laser pyrolysis. Table 1 presents the main experimental parameters and size measurements of the samples used in this study. The samples are labeled SiNP_X where X states the average SiNP diameter. A flow of silane (silicon precursor) is diluted in He with slightly different ratios to control the nucleation and growth. The silane flow rate is varied from 50 to 200 sccm with a total gas flow rate of 1100 ± 100 sccm. Increasing the SiH₄ to He ratio results in samples with diameters regularly increasing from 30 to 87 nm. The samples SiNP₄₃ and SiNP₅₃ were

synthesized with the same SiH₄ flow and differ by the He flow rate (1000 vs. 1100 sccm). Finally, in order to reach higher SiNP diameters, we modified the reactor to increase the residence time. The reactant inlet tube close to the laser beam was enlarged from 2 to 4 mm diameter, thus dividing the gas velocity by a factor of 4 and increasing the time of residence in the reaction zone. The synthesis of SiNPs with a diameter of 110 nm could, thus, be achieved, although with a broader size distribution.

Table 1. Main experimental parameters and characterizations of the Si nanoparticles (SiNP) samples.

Sample	SiH ₄ (sccm)	BET Specific Area (m ² /g)	Diameter (nm)		Crystallite Size (nm) from XRD
			From BET	From TEM	
SiNP ₃₀	50	88	29	22	6
SiNP ₄₃	100	60	43	33	25
SiNP ₅₃	100	49	53	32	18
SiNP ₇₁	150	36	71	50	35
SiNP ₈₇	200	30	87	62	44
SiNP ₁₀₇	234	24	107	114	63

The typical morphology and size analysis of the different samples presented in Figure 1 shows the quality of this synthesis approach, with a very narrow size dispersion obtained for most SiNP samples. The SiNP size was measured both from the BET specific area and estimated from TEM images. The BET diameter is consistently larger than the TEM average diameter because of the morphology of the SiNPs forming small agglomerates. The surface area lost in interparticle contacts decreases the measured BET surface and, therefore, increases the estimated diameter. In the same way, the crystallite size deduced from XRD measurements (Figure S1) is always smaller than TEM indicating that the SiNPs are not monocrystalline, as also seen by HRTEM in Figure S2.

3.2. Tuning the SiNW Diameter: Catalyst Size and Silane Partial Pressure

Free-standing SiNW growth is achieved by a process similar to the vapor–liquid–solid (VLS) mechanism, using a sacrificial porous support as described in our previous work [30]. The SiNWs are grown at low temperature (430 °C) using gold nanoparticles (AuNPs) as a catalyst. The sacrificial powder of NaCl or CaCO₃ covered with the AuNPs is heated in a closed stainless-steel reactor with diphenylsilane as a Si source. At the end of the synthesis, the sacrificial template is removed by washing with water or aqueous HCl, respectively. The optimized process yields up to 0.5 g of SiNWs of 10 nm diameter with a low size dispersion, from AuNPs of 2 nm [30].

It has been demonstrated that diameter control in similar CVD processes can be realized by controlling the catalyst size as was demonstrated for carbon nanotubes [37,38] and for SiNWs [39,40]. Mechanistic studies on SiNW CVD growth show that thermodynamic constraints control the nanowire diameter. It was demonstrated that a high partial pressure of silane (90 Pa) at 400–500 °C induces the growth of small diameter SiNWs (2–20 nm), whereas a low partial pressure (5 Pa) at 550–650 °C allows the growth of SiNWs of 50 to 1000 nm diameter [26,27,41,42]. However, our closed reactor does not allow for a direct control on the silane partial pressure.

In our process, the diphenylsilane evaporates then decomposes into silane and tetraphenylsilane, following a disproportionation reaction [43–45]. The silane partial pressure is, therefore, controlled by the kinetic balance between its formation from diphenylsilane and its consumption by the SiNW growth. The diphenylsilane disproportionation is slower but starts at a low temperature [44] (from 200 °C), while the silane decomposition on gold is fast but requires a high enough temperature to form the Au–Si eutectic [27] at 363 °C. Thus, a SiH₄ stock has time to build up in the reactor before the AuNP catalyst turns active for silane decomposition. From diphenylsilane disproportionation rate estimates [44], we can infer a partial pressure of SiH₄ of 100–500 Pa at the onset of gold catalyzed silane

decomposition. At such a high silane pressure, SiNWs can grow as fast as 200 nm/min, and the thinnest SiNWs are favored [26].

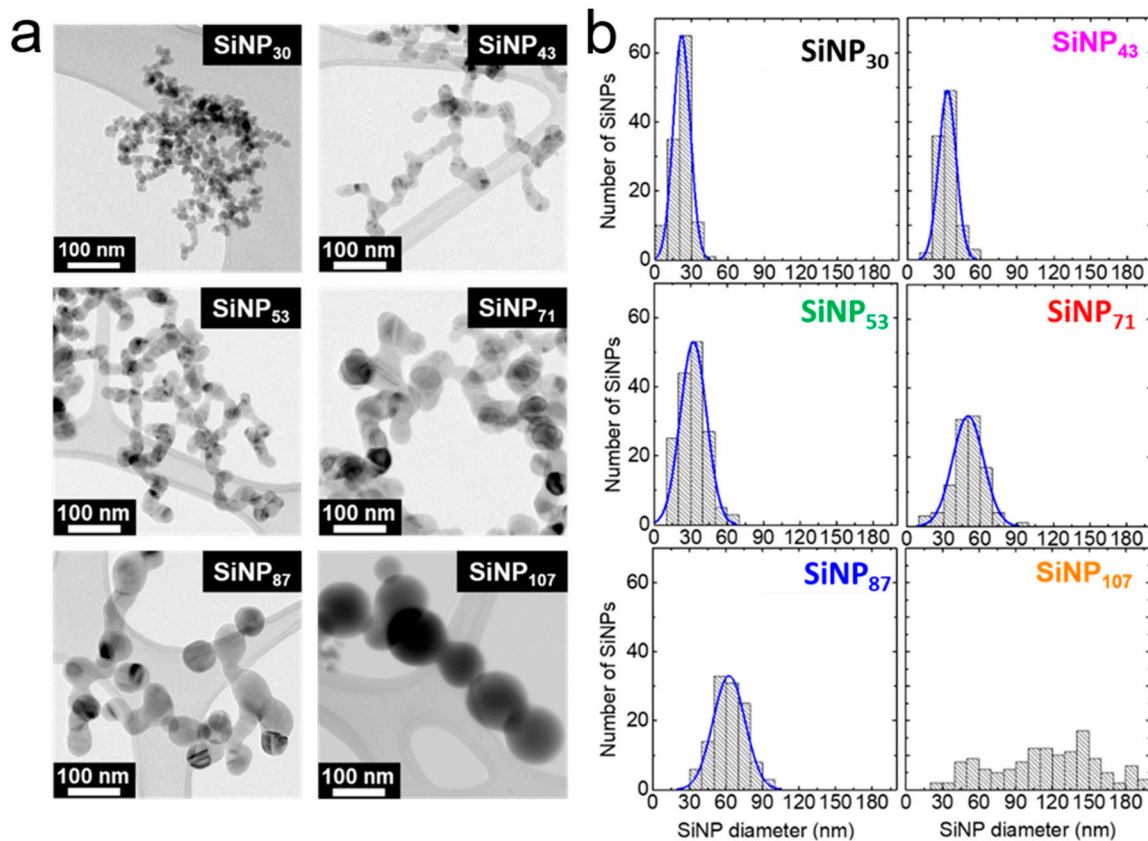


Figure 1. TEM images (a) and corresponding size analysis (b) of the SiNPs samples described in Table 1. The histograms were obtained from at least 100 particle measurements.

We, therefore, developed a novel strategy to achieve size tuning of SiNWs by locally reducing the silane partial pressure. The dense CaCO_3 nanopowder (50 nm) used as a porous growth support is placed in a cylindrical crucible. The powder compacity generates a gradient of partial pressure from the surface to the bottom of the crucible, as illustrated in Figure 2a. Silane entering the crucible is quickly consumed by the top AuNPs, so that only limited silane can diffuse down in the powder. Therefore, the average silane partial pressure inside the powder is lower than at the surface, which drives the growth of bigger SiNWs if proper catalysts are present. We first demonstrated this effect using a 1 cm^3 carbon foam cube (Figure 2b). Analysis of the SiNW diameters at the cube surface and deep in the cube show a significant difference of 30%, as presented in Figure 2c. It can be concluded that the chemical rate of silane consumption for SiNW growth is much faster than the rate of silane gas diffusion, although the porosity of the carbon foam is very large ($400 \mu\text{m}$ pores). A much higher silane depletion is expected in the CaCO_3 nanopowder, in which the pores are thinner ($<100 \text{ nm}$) and the pathway more tortuous.

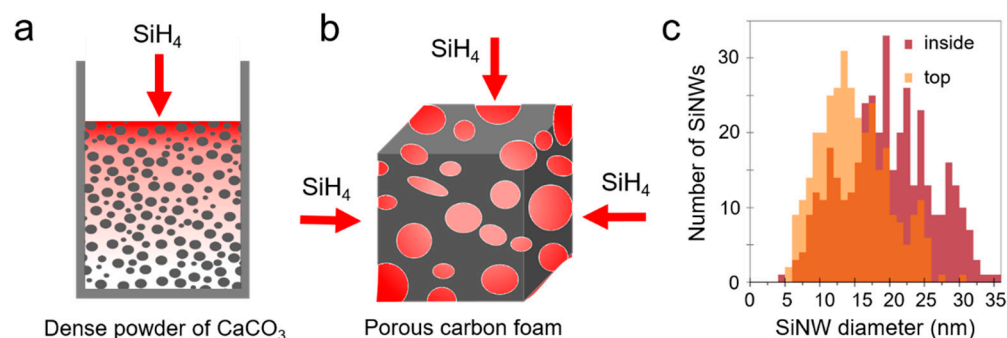


Figure 2. Scheme of the partial pressure reduction in the porous growth support, CaCO_3 powder (a) and carbon foam cube (b). The SiH_4 pressure is represented in red shades. (c) Diameters of Si nanowires (SiNWs) grown from 1–2 nm gold nanoparticles (AuNPs) in a 1 cm^3 carbon foam cube on the surface (“top”) and 2 mm below the surface (“inside”). Inside, SiNWs had the same diameter distribution at all depths down to the center.

Once able to lower the silane pressure, gold catalysts with the right size are still needed for large SiNW growth. Three colloidal AuNP growth methods [33–35] were necessary to access AuNPs with a wide range of sizes. Small AuNPs (1–3 nm) are efficiently grown by dodecanethiol stabilization [33] in an organic solvent, while bigger AuNPs (12 nm) can only be obtained stabilized by citrate [34] in aqueous solution. The latter can be enlarged in a controlled way using an established regrowth method [35] in water in the range 15 to 120 nm (see SEM images of the AuNPs in insets Figure 3a and Figure S3).

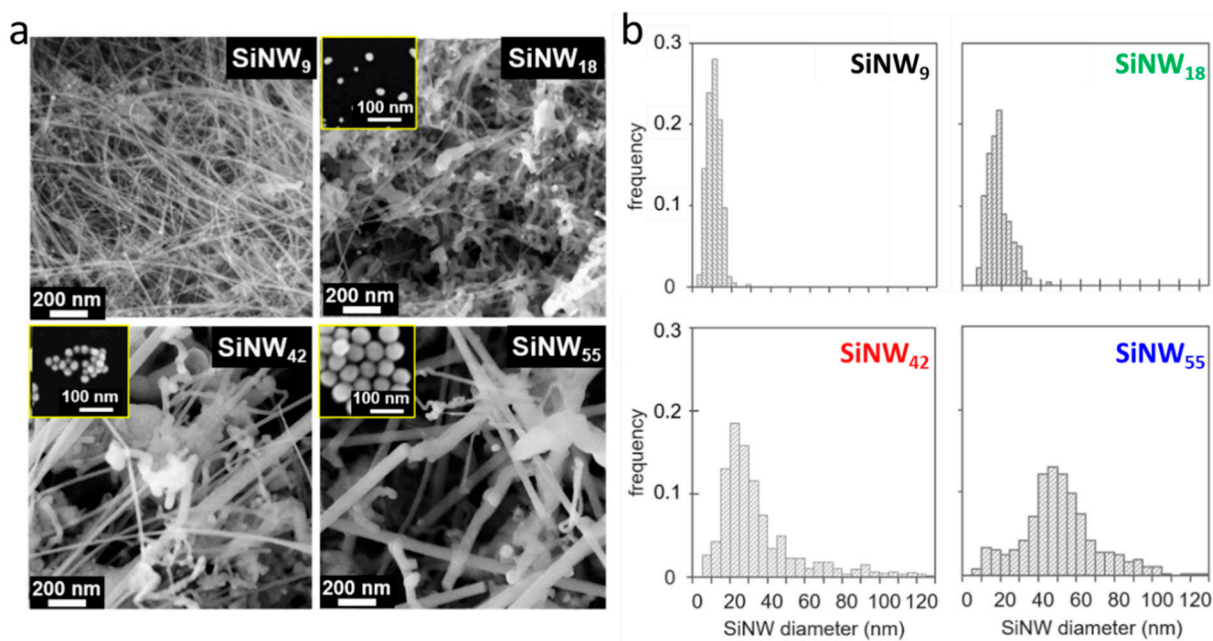


Figure 3. SEM images (a) and corresponding diameter histograms (b) of SiNWs. Insets: SEM images of the AuNP catalysts used for each SiNW growth. Histograms are calculated on >250 counts.

We could check the combined effect of AuNP size and thin porosity of the support on the growth of SiNWs from the 12 nm AuNPs (Table 2, Figure S4): SiNWs grown in the CaCO_3 nanopowder have a diameter of 18 nm, 35% higher than the 13 nm SiNWs grown in the carbon foam. Then, by using AuNP catalysts of increasing size, it was possible to obtain a series of SiNWs of increasing diameter (Figure 3, Figure S3). Note that the growth is not homogeneous, as the thin SiNWs grown on the top constitute a minor population in all samples. This is clearly shown in Figure 3b for SiNW₅₅ with a small population at 10 nm, aside the main population at 50 nm. Although numerous, the thin SiNWs represent

only a small fraction of the Si volume in the material. Some large SiNWs show a more tortuous shape, and the number of kinks in the SiNWs increases with their diameter. This worm-like morphology, already described in SiNW CVD growth, is typical of an unfavored growth [46,47].

Table 2. Characteristics of the SiNW samples.

Sample	AuNP Size (nm)	BET Specific Area (m ² /g)	Diameter from SEM (nm)	
			Small Population	Large Population
SiNW ₉	1–2	194	-	9
SiNW ₁₈	12	86	-	18
SiNW ₂₀	18	76	-	20
SiNW ₄₂	22	108	20	42
SiNW ₅₅	51	85	23	55
SiNW ₉₃	120	25	31	93

Figure 4a displays the SiNW diameter distribution as a function of the size of the AuNPs used as catalyst. The minor population of small SiNWs is shown with circles. The diameter of the main population of SiNWs nearly matches the size of the AuNPs, as reported for the VLS mechanism [47]. Our strategy for a catalyst-size-directed growth of SiNW, thus, proves efficient, as the SiNW diameter increased over a decade by this method. The distribution width of the main population (measured as the full width at half maximum) is 30–40% for all samples.

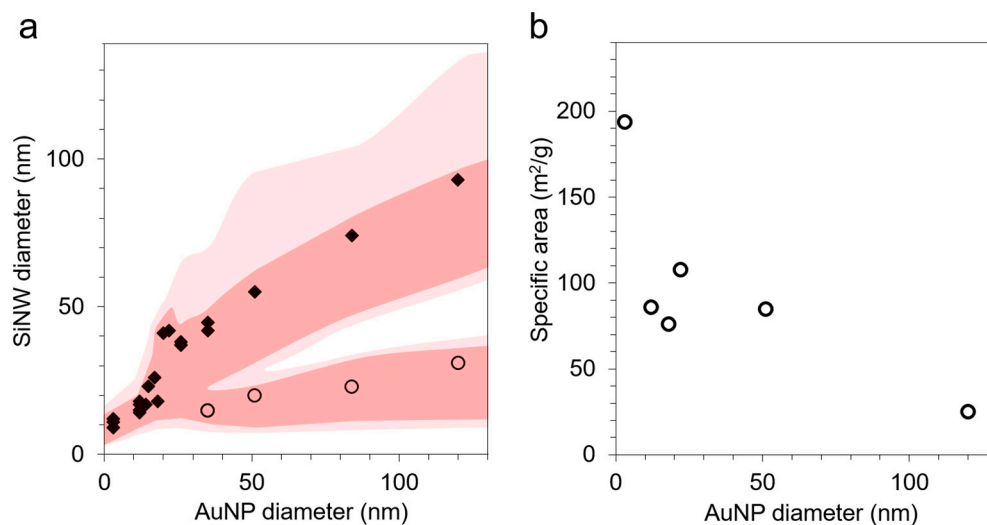


Figure 4. (a) Average diameter of the main (diamond) and minority (circles) SiNW populations as a function of the size of the catalyst AuNPs, as measured by SEM (diameter histograms in Figure 3 and Figure S3). The shaded zones show the full width at half maximum and the 90% limit for both SiNW diameter peaks. (b) Specific area of the SiNWs as measured by the BET method as a function of the size of the AuNP catalysts.

The specific area measured by the BET method on the SiNW samples (Figure 4b) drops consistently when increasing the size. The BET and SEM data are in agreement for the smallest SiNWs (SEM estimated specific area of 150 m²/g for a BET surface of 194 m²/g). However, for larger SiNW samples, they diverge, showing an underestimated count of the small SiNW population by SEM.

3.3. Electrochemical Performance in Li-Ion Batteries

The electrochemical performance of SiNPs and SiNWs in lithium batteries are displayed in Figure 5. All materials were tested with 50 wt. % active material in the anode. The

quantity of carbon black (25 wt. %) and binder (25 wt. %) were quite high to ensure good electronic conductivity and mechanical stability during electrochemical measurements for all materials. The contribution of the carbon black to the specific capacity, measured independently, is a constant 100 mAh/g.

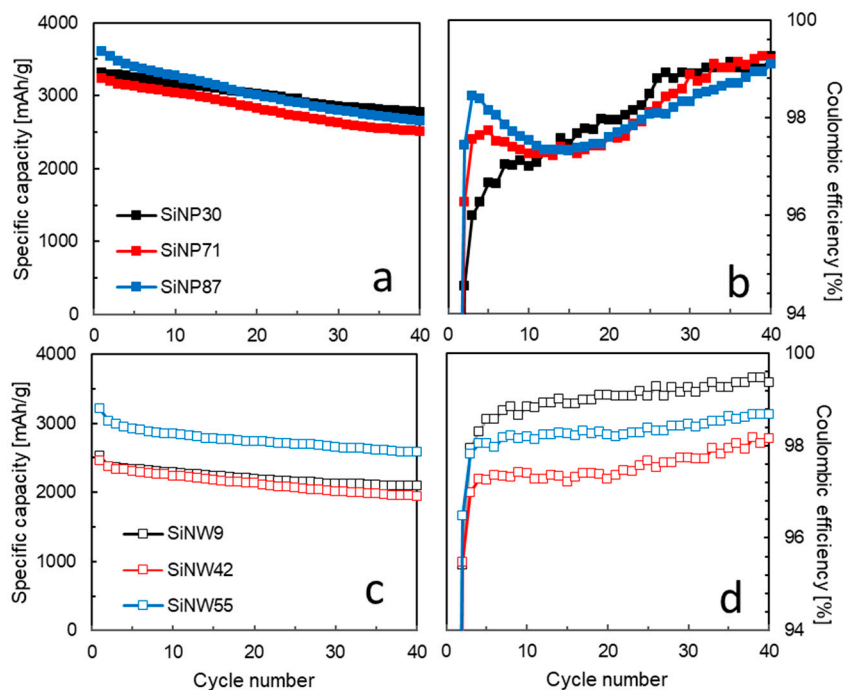


Figure 5. Electrochemical performance of SiNPs and SiNWs measured in half-cell configuration at C/20 rate (activation), then C/5. Specific charge capacity (mAh per gram of silicon) as a function of the cycle number obtained from (a) SiNP and (c) SiNW electrodes. Corresponding Coulombic efficiency for (b) SiNP and (d) SiNW electrodes. The results presented here are the most representative of at least 3 repeatable cells (standard deviation 10%). Data for all SiNP sizes are available in Figure S5.

The specific capacity is higher and more repeatable for SiNPs (3000–3500 mAh/g) than for SiNWs (2500–3000 mAh/g). All SiNP anodes give a similar specific capacity. For SiNWs, we observe a minimum of specific capacity for the medium size, SiNW₄₂. The most favorable trade-off between specific capacity and first irreversible capacity is observed for the largest size, SiNW₅₅ (Figure 5c and Figure S5). However, among all samples, only the smallest SiNW anode, SiNW₉, attains the Coulombic efficiency of 99.5% required for long term cycling (Figure 5d). The lower specific capacity of the SiNWs may be due to difficulties in dispersion of the material during the slurry preparation. The growth in a porous support favors SiNW entanglement, and the obtained 1–10 μm sized agglomerates do not fully separate during slurry process, thus leading to a poorer wetting by the electrolyte in the agglomerates (Figure S6). During the potentiostatic step applied at the end of full lithiation, the equilibrium is not reached, especially for large SiNWs (Figure S7). This indicates residual capacity still available in the SiNW electrode and a kinetic limitation to lithiation in the agglomerates.

The loss in the first Coulombic efficiency (CE) is due to irreversible processes happening in the first lithiation (also called activation). For nano-silicon anodes, it is mostly related to the solid–electrolyte interphase (SEI) formation. It depends on the surface area of the material as demonstrated for graphite particles [48]. Figure 6a presents the first and fifth CE as a function of the BET surface measured for SiNPs and SiNWs. As can be seen for the SiNP electrodes, the excellent correlation shows that the first CE depends linearly on the specific area. The capacity loss in the first cycle is, thus, due to the homogeneous coverage of the silicon surface by a SEI passivation layer. SiNWs follow the same trend, but with a poorer correlation due to a less controlled wetting in the SiNW agglomerates.

To the best of our knowledge, this linear correlation has never been reported for silicon. In the subsequent cycles (fifth CE shown on Figure 6a), the CE rises above 95%, and the linear correlation with specific area fades away. On Figure 6b, the first CE is presented as a function of SEM/TEM diameters, d , and shows the expected $1/d$ evolution. The SiNW diameter reported here is the average of the most abundant SiNW population. The presence of the small SiNWs brings a large additional surface area and, thus, a higher irreversible capacity in the first cycle.

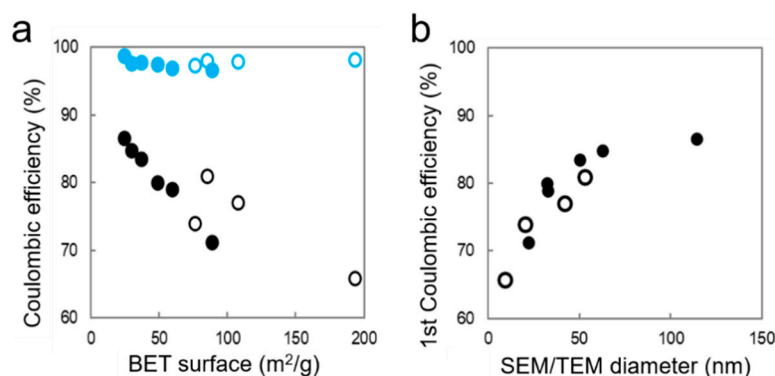


Figure 6. Coulombic efficiency as a function of BET specific area (a) and statistical SEM/TEM diameter (b) for SiNPs (full circles) and SiNWs (empty circles) on the 1st cycle (black) and the 5th cycle (blue).

Upon long-term cycling, the SiNW₉ electrodes outperform the other materials due to their enhanced stability and very high CE (Figure 5d). On the contrary, the SiNP specific capacity suffers from a faster fading. The size of SiNPs also has a strong impact on the evolution of the Coulombic efficiency upon cycling. Indeed, for the smallest SiNPs, the CE presents a progressive increase, whereas the larger SiNPs show a fast initial increase then a decrease with a minimum around 10 cycles. This phenomenon could be attributed to an electrochemical sintering [49–51] leading to larger SiNPs. Microscopy studies on SiNP anodes in cycling showed general sintering, forming large networks of sintered SiNPs in the anode [49]. Such large Si structures are sensitive to mechanical pulverization in the subsequent cycles, leading to a loss in Coulombic efficiency.

To better assess the impact of the Si shape and size during electrochemical cycling, we plotted the normalized galvanostatic cycle as a function of the cycle number. During the first lithiation (Figure S8), the very long potential plateau at ca. 100 mV is shifted toward lower potential for larger SiNPs, indicating polarization. This is in agreement with a slower Li diffusion along longer distances within large SiNPs [52]. In the following cycles (Figure 7), we can see that polarization during lithiation is increasing as a function of the cycling number for the large SiNPs. For the SiNWs, the potential plateau in the first cycle is also low, indicating anode polarization, which is independent of size (Figure S8), and in the subsequent cycles, polarization does not increase (Figure 8). This discrepancy indicates an influence of the Si shape on the Li diffusion.

Stronger differences can be seen during the delithiation. For SiNPs, a very long potential plateau at ca. 450 mV appears during the first cycles (second or third depending of the samples) and disappears after more than 30 cycles. This potential plateau is generally ascribed to the biphasic delithiation of the crystalline Li₁₅Si₄ phase [53] and was reported to be size-dependent (appearing with large particles [50,54,55]) or linked to the stress distribution in the case of thin films [56]. The appearance of this plateau indicates that a large part of the Si is fully lithiated to the crystalline Li₁₅Si₄, even if the crystallization of this phase is reported to be more difficult in small SiNPs [50,54,57]. According to the literature, this phase also reduces the Coulombic efficiency [58], which is in agreement with the observed CE evolution of the SiNPs in our study (Figure 5b).

Thus, the CE fluctuations observed for larger SiNPs would correlate with the pronounced potential plateaus in delithiation, i.e., with the larger amount of crystalline $\text{Li}_{15}\text{Si}_4$ formed during lithiation. Deep lithiation has been reported to favor the electrochemical sintering of SiNPs in lithium battery anodes, because the swelling of Si in the form of an amorphous Li alloy induces the formation of necks between neighboring particles [49,51,59]. Within this soft structure, the crystallization of $\text{Li}_{15}\text{Si}_4$ in the points of deepest lithiation might strengthen these simple contacts by growing crystals through the necks. Indeed, our SiNPs are connected in a necklace morphology from the growth (Figure 1a), which could enhance this phenomenon.

Surprisingly, this crystalline $\text{Li}_{15}\text{Si}_4$ delithiation process is much less visible in the SiNW electrodes, with very small potential plateaus at 450 mV (Figure 8d–f). This shows that the crystalline $\text{Li}_{15}\text{Si}_4$ phase is present in a much smaller quantity, or that the lithiated phase remains mostly amorphous [53]. Only the mid-sized SiNW_{42} shows a significant plateau, a fact that can be correlated with its low Coulombic efficiency as compared to the other SiNW samples (Figure 5d). A reason why SiNWs do not undergo electrochemical sintering as easily as SiNPs might be related to their elastic “spring” behavior. Even after grinding and calendaring, SiNWs in the anode remain stiff. Agglomerates of SiNWs contain a nanoscale porosity that was clearly imaged in our recent FIB-SEM study [3]. Such porosity allows swelling during lithiation with a low risk of sintering with neighboring SiNWs.

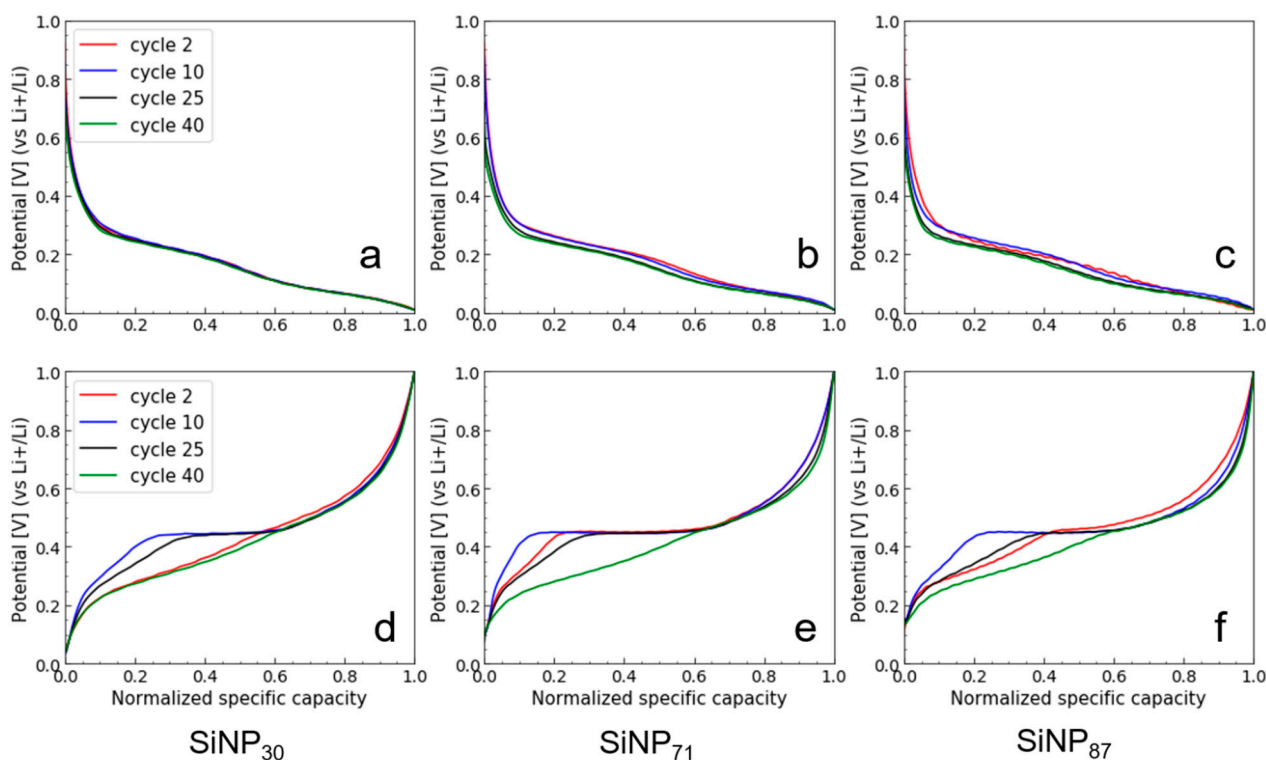


Figure 7. Normalized galvanostatic curves in lithiation (a–c) and delithiation (d–f) as a function of the cycle numbers for SiNP_{30} (a,d), SiNP_{71} (b,e), and SiNP_{87} (c,f).

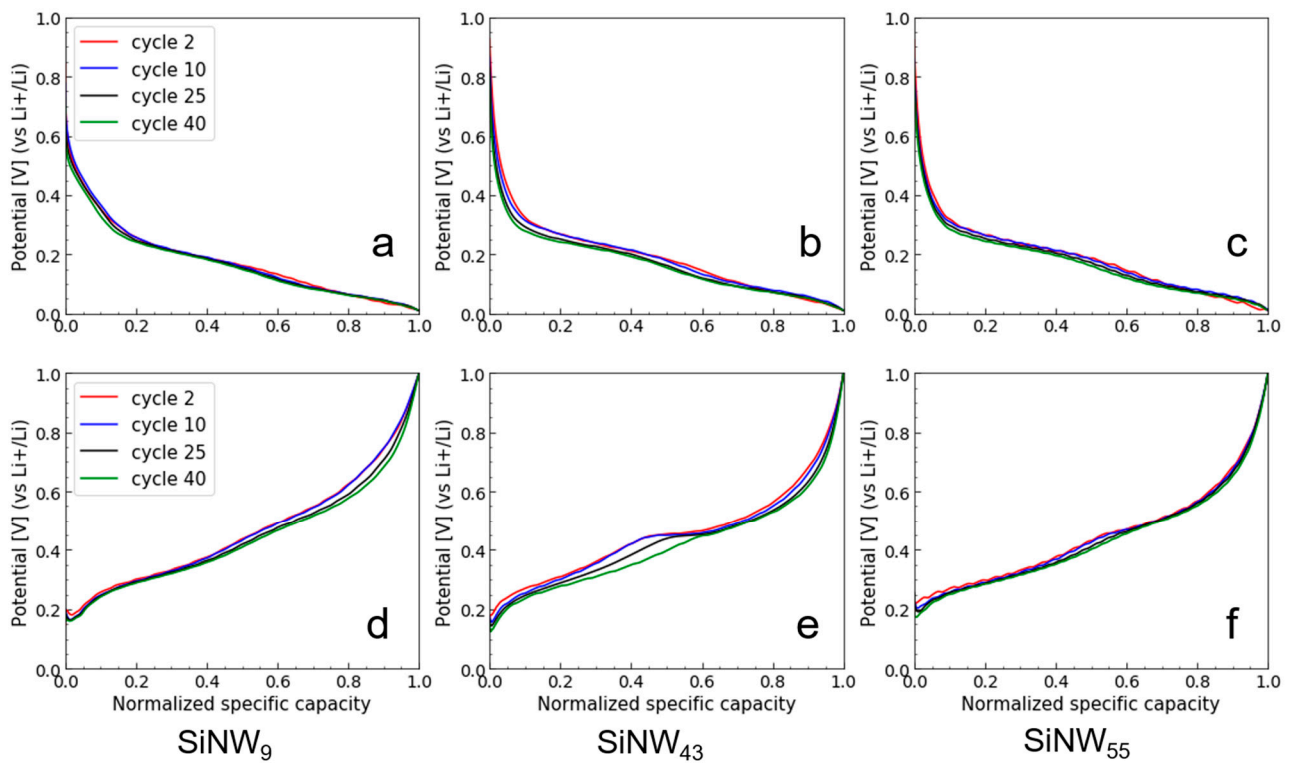


Figure 8. Normalized galvanostatic curves in lithiation (a–c) and delithiation (d–f) as a function of the cycle numbers for SiNW₉ (a,d), SiNW₄₂ (b,e), and SiNW₅₅ (c,f).

4. Discussion

The discrepancy in the ability of the nano-silicon material to lithiate into crystalline Li₁₅Si₄ may have a direct impact on the specific capacity retention of the LiB, as shown on Figure 9. The smallest SiNWs show a much higher specific capacity retention over the fourth to 80th cycles, while most of the capacity fading for the SiNPs happens in the cycles 4–30, i.e., when lithiation into crystalline Li₁₅Si₄ is observed.

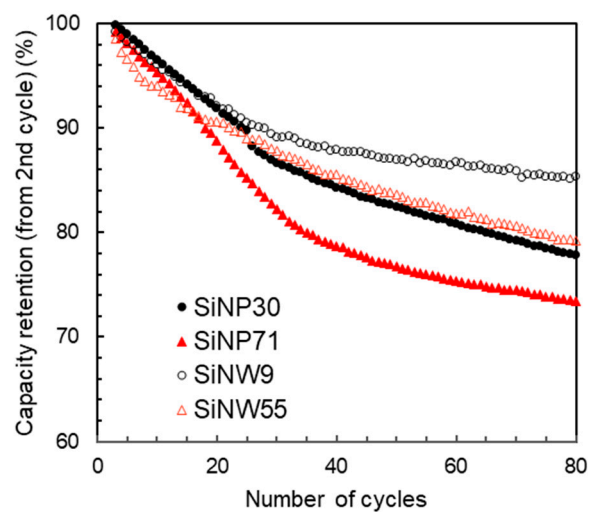


Figure 9. Capacity retention for small (black circles) and large (red triangles) SiNPs (full symbols) and SiNWs (empty symbols).

The influence of the shape/size of the nano-silicon on the reaction mechanisms in cycling and the electrochemical performance can be summarized as follows:

- First, the irreversible capacity loss in the first cycle increases linearly with the specific area, in a similar trend for SiNPs and SiNWs (Figure 6). This clear correlation indicates that a similar homogeneous SEI layer passivates the silicon surface, independently of Si size and shape.
- For the SiNPs, the gas-flow process of pyrolysis produces a fine powder, which is easily incorporated in a homogeneous anode and ensures a high specific capacity independent of the SiNP size. The size strongly affects the electrochemical performance, as polarization builds up in cycling over the first 40 cycles. A crystalline $\text{Li}_{15}\text{Si}_4$ phase develops in the 2nd–30th cycles, having an impact on the CE behavior and enhancing capacity fade. Polarization, crystalline $\text{Li}_{15}\text{Si}_4$ formation, and lower CE might be attributed to electrochemical sintering [49]. The phenomenon is less apparent at lower size, thus small SiNPs should be favored for long term cycling. Alternatively, sintering is efficiently prevented by a carbon coating, conveniently obtained in the same reactor just after pyrolysis, as we recently reported [60].
- When comparing SiNWs to SiNPs, it appears that the initial specific capacity of SiNWs is lower due to their micron-sized agglomerate form, while the CE of SiNWs is more stable and can be very high for the smallest size. It seems that the 1D shape of SiNWs brings a significant advantage in maintaining a 3D porous structure in the material, because stiff wires do not pack as tightly as particles. This 3D structure has a strong impact both on lithium diffusion and on avoiding Si electrochemical sintering.
- The effect of size for SiNWs is more complex than for SiNPs. It seems to reflect a trade-off between specific area (decreasing with diameter) and SiNW stiffness and pore size of agglomerates (increasing with diameter). We observe a minimum performance for the mid-sized SiNW_{42} : a low specific capacity and a low Coulombic efficiency, which correlates with the formation of a higher quantity of crystalline $\text{Li}_{15}\text{Si}_4$ during lithiation. The larger sized SiNW_{55} with a smaller specific area (thus a lower irreversible capacity) and probably a larger size of pores in the agglomerates have a higher specific capacity. On the other hand, the smallest SiNW_9 offer the highest Coulombic efficiency in the long run, probably due to fast Li diffusion. Additional electrode engineering is, thus, required to take full advantage of the promising performances of SiNWs. An alternative strategy consists of growing SiNWs at the surface of graphite flakes to produce directly a composite anode material [3]. This way, we could reduce micron-sized aggregation and attain full Si capacity cycling. Passivation of the SiNW surface to avoid large irreversible capacity at first cycle is another strategy to explore.

5. Conclusions

This paper presents the first extensive comparison of size/shape of nano-silicon (nanoparticles and nanowires) used as anode materials in lithium-ion batteries. The main challenge was to obtain each nanomaterial with a good size and shape control, and in gram-scale quantities for reliable LiB electrochemical tests. We used two independent synthesis processes: laser pyrolysis for SiNPs (now an industrial process) and gold-catalyzed VLS growth in porous media for SiNWs (a scalable patented process). Tuning the synthesis parameters, we obtained SiNPs in a 25–110 nm diameter range. By tuning the gold catalyst size and the porosity of the support, SiNWs with diameters ranging 9–93 nm were realized. An important difference between the two nano-silicon morphologies is that the SiNP material, grown in a gas flow, consists of a fine nanopowder, while the SiNW material, grown in a porous support, consists mostly of 1–10 μm sized agglomerates. Although an advantage in dealing with nano safety, this turns to a disadvantage in the making the electrode, leading to a less homogeneous slurry and to a part of the Si being inaccessible to the electrolyte. Unsurprisingly, the 1D shape appears more difficult than 0D to control and produce at a large scale.

The matching series of SiNP and SiNW materials was implemented in lithium batteries in the same conditions and cycled the same way. Their electrochemical behavior shows several consistent effects of size and shape. First, the initial specific capacity of the material

depends on its shape: it is close to the theoretical 3579 mAh/g for SiNPs, while SiNWs provide an about 25% lower capacity due to the entanglement of SiNWs during the growth. Second, the irreversible specific capacity at the first cycle is linearly correlated to the specific surface area of the materials, thus to the nano-silicon size. Third, the SiNPs prove much more prone to lithiation down to the crystalline $\text{Li}_{15}\text{Si}_4$ phase, and probably to electrochemical sintering, than SiNWs. Finally, in the long run, the smallest SiNW electrodes show a better capacity retention, with a Coulombic efficiency above 99.5% after 43 cycles. A size effect is again observed as smaller SiNWs and SiNPs show a lower polarization and, therefore, a better capacity retention. Improvements are currently under investigation, using carbon coating in the case of SiNPs to reduce irreversible capacity and using direct growth on graphite in the case of SiNWs to make more efficient composites.

Supplementary Materials: The following are available online at <https://www.mdpi.com/2079-4991/11/2/307/s1>, Figure S1: X-ray diffractograms of the SiNPs; Figure S2: HRTEM images of SiNP₃₀; Figure S3 SEM images of AuNPs and SiNWs; Figure S4: SEM images/diameters of SiNWs grown from 12 nm AuNPs on CaCO₃ nanopowder or in carbon foam cube; Figure S5: Specific capacity and coulombic efficiency for all SiNPs; Figure S6: SEM image of an electrode with SiNW₉; Figure S7: Specific capacity in the galvanostatic/potentiostatic steps; Figure S8: Cell potential vs. normalized galvanostatic capacity.

Author Contributions: A.D., F.B. performed synthesis of SiNPs; C.K., E.M., P.C. performed synthesis of SiNWs; A.D., N.H.-B., C.H., J.P.A. performed characterization and analysis of results on SiNPs; C.K., S.K. performed characterization of SiNWs; C.K., C.V., N.H.-B., C.H., P.C. finalized the analyses and wrote the paper. All authors have read and agreed to the published version of the manuscript.

Funding: This work was funded under the CEA Silicon for Lithium-Ion Batteries (SiBaLi) project, the French National agency under the HELIOS project (ANR-13-PRGE-0006), and the H2020 European funding Flagship Graphene Core 2 (grant agreement 785219). J.P.A. is grateful for support of Eurotalents postdoctoral fellowship.

Data Availability Statement: The data presented in this study are available on request from the corresponding author.

Acknowledgments: N.H.-B., F.B., A.D. gratefully thank Dominique Porterat for his constant help in solving all kinds of experimental trouble. A.D. and N.H.-B. thank Eric Larquet at Ecole Polytechnique for TEM and HRTEM measurements. A.D. and C.H. thank Daniel Tomasi for battery making and cycling. C.K. and P.C. thank Annette Delices for AuNP size tuning and synthesis. C.K. and C.H. thank Agnès Brun for BET analysis. C.K. and P.C. thank Gérard Lapertot for his help in designing the stainless-steel reactors.

Conflicts of Interest: The authors declare no conflict of interest.

References

1. Ashuri, M.; He, Q.; Shaw, L.L. Silicon as a Potential Anode Material for Li-Ion Batteries: Where Size, Geometry and Structure Matter. *Nanoscale* **2016**, *8*, 74–103. [CrossRef]
2. Li, P.; Hwang, J.-Y.; Sun, Y.-K. Nano/Microstructured Silicon–Graphite Composite Anode for High-Energy-Density Li-Ion Battery. *ACS Nano* **2019**, *13*, 2624–2633. [CrossRef]
3. Karuppiah, S.; Keller, C.; Kumar, P.; Jouneau, P.-H.; Aldakov, D.; Ducros, J.-B.; Lapertot, G.; Chenevier, P.; Haon, C. A Scalable Silicon Nanowires-Grown-On-Graphite Composite for High-Energy Lithium Batteries. *ACS Nano* **2020**, *14*, 12006–12015. [CrossRef]
4. Berhaut, C.L.; Dominguez, D.Z.; Tomasi, D.; Vincens, C.; Haon, C.; Reynier, Y.; Porcher, W.; Boudet, N.; Blanc, N.; Chahine, G.A.; et al. Prelithiation of Silicon/Graphite Composite Anodes: Benefits and Mechanisms for Long-Lasting Li-Ion Batteries. *Energy Storage Mater.* **2020**, *29*, 190–197. [CrossRef]
5. McDowell, M.T.; Lee, S.W.; Nix, W.D.; Cui, Y. 25th Anniversary Article: Understanding the Lithiation of Silicon and Other Alloying Anodes for Lithium-Ion Batteries. *Adv. Mater.* **2013**, *25*, 4966–4985. [CrossRef]
6. Kim, H.; Seo, M.; Park, M.-H.; Cho, J. A Critical Size of Silicon Nano-Anodes for Lithium Rechargeable Batteries. *Angew. Chem. Int. Ed.* **2010**, *49*, 2146–2149. [CrossRef]
7. Schott, T.; Robert, R.; Benito, S.P.; Ulmann, P.A.; Lanz, P.; Zürcher, S.; Spahr, M.E.; Novák, P.; Trabesinger, S. Cycling Behavior of Silicon-Containing Graphite Electrodes, Part B: Effect of the Silicon Source. *J. Phys. Chem. C* **2017**, *121*, 25718–25728. [CrossRef]

8. Yu, J.; Wang, K.; Song, W.; Huang, H.; Liang, C.; Xia, Y.; Zhang, J.; Gan, Y.; Wang, F.; Zhang, W. A Low Temperature $MgH_2-AlCl_3-SiO_2$ System to Synthesize Nano-Silicon for High-Performance Li-Ion Batteries. *Chem. Eng. J.* **2021**, *406*, 126805. [CrossRef]
9. Eshraghi, N.; Berardo, L.; Schrijnemakers, A.; Delaval, V.; Shaibani, M.; Majumder, M.; Cloots, R.; Vertruyen, B.; Boschini, F.; Mahmoud, A. Recovery of Nano-Structured Silicon from End-of-Life Photovoltaic Wafers with Value-Added Applications in Lithium-Ion Battery. *ACS Sustain. Chem. Eng.* **2020**, *8*, 5868–5879. [CrossRef]
10. Sun, F.; Hu, Z.; Wu, L.; Chen, J.; Luo, J.; Wu, X.; Cheng, G.; Zheng, R. Reduced Graphene Oxide Wrapped Ultra-Thin Silicon Nanowires for Lithium Ion Battery Anodes. *J. Phys. Conf. Ser.* **2020**, *1520*, 012011. [CrossRef]
11. Favors, Z.; Bay, H.H.; Mutlu, Z.; Ahmed, K.; Ionescu, R.; Ye, R.; Ozkan, M.; Ozkan, C.S. Towards Scalable Binderless Electrodes: Carbon Coated Silicon Nanofiber Paper via Mg Reduction of Electrospun SiO_2 Nanofibers. *Sci. Rep.* **2015**, *5*, 8246. [CrossRef] [PubMed]
12. Krause, A.; Langklotz, U.; Pohl, D.; Tkacheva, O.; Pohl, D.; Nielsch, K.; Mikolajick, T.; Weber, W.M. Surface Related Differences between Uncoated versus Carbon-Coated Silicon Nanowire Electrodes on Performance in Lithium Ion Batteries. *J. Energy Storage* **2020**, *27*, 101052. [CrossRef]
13. Cui, L.-F.; Yang, Y.; Hsu, C.-M.; Cui, Y. Carbon-Silicon Core-Shell Nanowires as High Capacity Electrode for Lithium Ion Batteries. *Nano Lett.* **2009**, *9*, 3370–3374. [CrossRef]
14. Zhang, J.; Fang, S.; Qi, X.; Yu, Z.; Wu, Z.; Yang, J.; Lu, S. Preparation of High-Purity Straight Silicon Nanowires by Molten Salt Electrolysis. *J. Energy Chem.* **2020**, *40*, 171–179. [CrossRef]
15. Song, T.; Xia, J.; Lee, J.-H.; Lee, D.H.; Kwon, M.-S.; Choi, J.-M.; Wu, J.; Doo, S.K.; Chang, H.; Park, W.I.; et al. Arrays of Sealed Silicon Nanotubes As Anodes for Lithium Ion Batteries. *Nano Lett.* **2010**, *10*, 1710–1716. [CrossRef] [PubMed]
16. Wu, H.; Chan, G.; Choi, J.W.; Ryu, I.; Yao, Y.; McDowell, M.T.; Lee, S.W.; Jackson, A.; Yang, Y.; Hu, L.; et al. Stable Cycling of Double-Walled Silicon Nanotube Battery Anodes through Solid–Electrolyte Interphase Control. *Nat. Nanotechnol.* **2012**, *7*, 310–315. [CrossRef] [PubMed]
17. Li, X.; Gu, M.; Hu, S.; Kennard, R.; Yan, P.; Chen, X.; Wang, C.; Sailor, M.J.; Zhang, J.-G.; Liu, J. Mesoporous Silicon Sponge as an Anti-Pulverization Structure for High-Performance Lithium-Ion Battery Anodes. *Nat. Commun.* **2014**, *5*, 4105. [CrossRef] [PubMed]
18. Wu, Y.-J.; Chen, Y.-A.; Huang, C.-L.; Su, J.-T.; Hsieh, C.-T.; Lu, S.-Y. Small Highly Mesoporous Silicon Nanoparticles for High Performance Lithium Ion Based Energy Storage. *Chem. Eng. J.* **2020**, *400*, 125958. [CrossRef]
19. Jia, H.; Li, X.; Song, J.; Zhang, X.; Luo, L.; He, Y.; Li, B.; Cai, Y.; Hu, S.; Xiao, X.; et al. Hierarchical Porous Silicon Structures with Extraordinary Mechanical Strength as High-Performance Lithium-Ion Battery Anodes. *Nat. Commun.* **2020**, *11*, 1–9. [CrossRef]
20. Ryu, I.; Choi, J.W.; Cui, Y.; Nix, W.D. Size-Dependent Fracture of Si Nanowire Battery Anodes. *J. Mech. Phys. Solids* **2011**, *59*, 1717–1730. [CrossRef]
21. Liu, X.H.; Liu, Y.; Kushima, A.; Zhang, S.; Zhu, T.; Li, J.; Huang, J.Y. In Situ TEM Experiments of Electrochemical Lithiation and Delithiation of Individual Nanostructures. *Adv. Energy Mater.* **2012**, *2*, 722–741. [CrossRef]
22. Liu, X.H.; Zhong, L.; Huang, S.; Mao, S.X.; Zhu, T.; Huang, J.Y. Size-Dependent Fracture of Silicon Nanoparticles During Lithiation. *ACS Nano* **2012**, *6*, 1522–1531. [CrossRef]
23. Ma, Z.; Li, T.; Huang, Y.L.; Liu, J.; Zhou, Y.; Xue, D. Critical Silicon-Anode Size for Averting Lithiation-Induced Mechanical Failure of Lithium-Ion Batteries. *RSC Adv.* **2013**, *3*, 7398–7402. [CrossRef]
24. Sun, F.; Tan, Z.; Hu, Z.; Chen, J.; Luo, J.; Wu, X.; Cheng, G.; Zheng, R. Ultrathin Silicon Nanowires Produced by a Bi-Metal-Assisted Chemical Etching Method for Highly Stable Lithium-Ion Battery Anodes. *NANO* **2020**, *15*, 2050076. [CrossRef]
25. Reiss, P.; Carrière, M.; Lincheneau, C.; Vaure, L.; Tamang, S. Synthesis of Semiconductor Nanocrystals, Focusing on Nontoxic and Earth-Abundant Materials. *Chem. Rev.* **2016**, *116*, 10731–10819. [CrossRef]
26. Dhalluin, F.; Baron, T.; Ferret, P.; Salem, B.; Gentile, P.; Harmand, J.C. Silicon Nanowires: Diameter Dependence of Growth Rate and Delay in Growth. *Appl. Phys. Lett.* **2010**, *96*, 133109. [CrossRef]
27. Schmidt, V.; Wittemann, J.V.; Senz, S.; Gösele, U. Silicon Nanowires: A Review on Aspects of Their Growth and Their Electrical Properties. *Adv. Mater.* **2009**, *21*, 2681–2702. [CrossRef]
28. Lacour, F.; Guillois, O.; Portier, X.; Perez, H.; Herlin, N.; Reynaud, C. Laser Pyrolysis Synthesis and Characterization of Luminescent Silicon Nanocrystals. *Phys. E Low-Dimens. Syst. Nanostruct.* **2007**, *38*, 11–15. [CrossRef]
29. Sourice, J.; Quinsac, A.; Leconte, Y.; Sublemontier, O.; Porcher, W.; Haon, C.; Bordes, A.; De Vito, E.; Boulineau, A.; Larbi, S.J.S.; et al. One-Step Synthesis of Si@C Nanoparticles by Laser Pyrolysis: High-Capacity Anode Material for Lithium-Ion Batteries. *ACS Appl. Mater. Interfaces* **2015**, *7*, 6637–6644. [CrossRef]
30. Burchak, O.; Keller, C.; Lapertot, G.; Salaün, M.; Danet, J.; Chen, Y.; Bendiab, N.; Pépin-Donat, B.; Lombard, C.; Faure-Vincent, J.; et al. Scalable Chemical Synthesis of Doped Silicon Nanowires for Energy Applications. *Nanoscale* **2019**, *11*, 22504–22514. [CrossRef]
31. Bang, B.M.; Kim, H.; Song, H.-K.; Cho, J.; Park, S. Scalable Approach to Multi-Dimensional Bulk Si Anodes via Metal-Assisted Chemical Etching. *Energy Environ. Sci.* **2011**, *4*, 5013–5019. [CrossRef]
32. Cannon, W.R.; Danforth, S.C.; Haggerty, J.S.; Marra, R.A. Sinterable Ceramic Powders from Laser-Driven Reactions: II, Powder Characteristics and Process Variables. *J. Am. Ceram. Soc.* **1982**, *65*, 330–335. [CrossRef]
33. Brust, M.; Walker, M.; Bethell, D.; Schiffrin, D.J.; Whyman, R. Synthesis of Thiol-Derivatized Gold Nanoparticles in a Two-Phase Liquid-Liquid System. *J. Chem. Soc. Chem. Comm.* **1994**, 801–802. [CrossRef]

34. Turkevich, J.; Stevenson, P.C.; Hillier, J. A Study of the Nucleation and Growth Processes in the Synthesis of Colloidal Gold. *Discuss. Faraday Soc.* **1951**, *11*, 55–75. [CrossRef]
35. Ziegler, C.; Eychmüller, A. Seeded Growth Synthesis of Uniform Gold Nanoparticles with Diameters of 15–300 Nm. *J. Phys. Chem. C* **2011**, *115*, 4502–4506. [CrossRef]
36. Karg, M.; Schelero, N.; Oppel, C.; Gradzielski, M.; Hellweg, T.; von Klitzing, R. Versatile Phase Transfer of Gold Nanoparticles from Aqueous Media to Different Organic Media. *Chemistry* **2011**, *17*, 4648–4654. [CrossRef]
37. Jourdain, V.; Bichara, C. Current Understanding of the Growth of Carbon Nanotubes in Catalytic Chemical Vapour Deposition. *Carbon* **2013**, *58*, 2–39. [CrossRef]
38. Morjan, R.E.; Nerushev, O.A.; Sveningsson, M.; Rohmund, F.; Falk, L.K.L.; Campbell, E.E.B. Growth of Carbon Nanotubes from C60. *Appl. Phys. A* **2004**, *78*, 253–261. [CrossRef]
39. Langklotz, U.; Lein, T.; Schulze, C.; Weiser, M.; Krause, A.; Michaelis, A. Scalable Fabrication of Gold Nanoparticles with Adjustable Size Distribution as Catalytic Nuclei for the CVD Growth of Silicon Nanowires. *Appl. Surf. Sci.* **2020**, *502*, 144203. [CrossRef]
40. Krause, A.; Dorfler, S.; Piwko, M.; Wisser, F.M.; Jaumann, T.; Ahrens, E.; Giebeler, L.; Althues, H.; Schadlich, S.; Grothe, J.; et al. High Area Capacity Lithium-Sulfur Full-Cell Battery with Prelithiated Silicon Nanowire-Carbon Anodes for Long Cycling Stability. *Sci. Rep.* **2016**, *6*, 27982. [CrossRef]
41. Gentile, P.; David, T.; Dhalluin, F.; Buttard, D.; Pauc, N.; Hertog, M.D.; Ferret, P.; Baron, T. The Growth of Small Diameter Silicon Nanowires to Nanotrees. *Nanotechnology* **2008**, *19*, 125608. [CrossRef]
42. Dhalluin, F.; Desré, P.J.; den Hertog, M.L.; Rouvière, J.-L.; Ferret, P.; Gentile, P.; Baron, T. Critical Condition for Growth of Silicon Nanowires. *J. Appl. Phys.* **2007**, *102*, 094906. [CrossRef]
43. Speier, J.L.; Ruth, E. Zimmerman Disproportionation of Phenylsilanes with Aluminum Chloride as the Catalyst. *J. Am. Chem. Soc.* **1955**, *77*, 6395–6396. [CrossRef]
44. Gilman, H.; Miles, D.H. Disproportionation Reaction of Diphenylsilane in the Absence of Any Added Catalyst. *J. Org. Chem.* **1958**, *23*, 326–328. [CrossRef]
45. Lee, D.C.; Hanrath, T.; Korgel, B.A. The Role of Precursor-Decomposition Kinetics in Silicon-Nanowire Synthesis in Organic Solvents. *Angew. Chem. Int. Ed. Engl.* **2005**, *44*, 3573–3577. [CrossRef]
46. Salhi, B.; Grandidier, B.; Boukherroub, R. Controlled Growth of Silicon Nanowires on Silicon Surfaces. *J. Electroceram.* **2006**, *16*, 15–21. [CrossRef]
47. Schmidt, V.; Wittemann, J.V.; Gösele, U. Growth, Thermodynamics, and Electrical Properties of Silicon Nanowires. *Chem. Rev.* **2010**, *110*, 361–388. [CrossRef]
48. Winter, M.; Novák, P.; Monnier, A. Graphites for Lithium-Ion Cells: The Correlation of the First-Cycle Charge Loss with the Brunauer-Emmett-Teller Surface Area. *J. Electrochem. Soc.* **1998**, *145*, 428–436. [CrossRef]
49. Hovington, P.; Dontigny, M.; Guerfi, A.; Trottier, J.; Lagacé, M.; Mauger, A.; Julien, C.M.; Zaghbi, K. In Situ Scanning Electron Microscope Study and Microstructural Evolution of Nano Silicon Anode for High Energy Li-Ion Batteries. *J. Power Sources* **2014**, *248*, 457–464. [CrossRef]
50. Shen, C.; Ge, M.; Luo, L.; Fang, X.; Liu, Y.; Zhang, A.; Rong, J.; Wang, C.; Zhou, C. In Situ and Ex Situ TEM Study of Lithiation Behaviours of Porous Silicon Nanostructures. *Sci. Rep.* **2016**, *6*, 31334. [CrossRef]
51. Luo, L.; Wu, J.; Luo, J.; Huang, J.; Dravid, V.P. Dynamics of Electrochemical Lithiation/Delithiation of Graphene-Encapsulated Silicon Nanoparticles Studied by In-Situ TEM. *Sci. Rep.* **2014**, *4*, 3863. [CrossRef] [PubMed]
52. Bruce, P.G.; Scrosati, B.; Tarascon, J.-M. Nanomaterials for Rechargeable Lithium Batteries. *Angew. Chem. Int. Ed.* **2008**, *47*, 2930–2946. [CrossRef] [PubMed]
53. Obrovac, M.N.; Krause, L.J. Reversible Cycling of Crystalline Silicon Powder. *J. Electrochem. Soc.* **2006**, *154*, A103. [CrossRef]
54. Gan, C.; Zhang, C.; Wen, W.; Liu, Y.; Chen, J.; Xie, Q.; Luo, X. Enhancing Delithiation Reversibility of Li₁₅Si₄ Alloy of Silicon Nanoparticles-Carbon/Graphite Anode Materials for Stable-Cycling Lithium Ion Batteries by Restricting the Silicon Particle Size. *ACS Appl. Mater. Interfaces* **2019**, *11*, 35809–35819. [CrossRef] [PubMed]
55. Gauthier, M.; Mazouzi, D.; Reyter, D.; Lestriez, B.; Moreau, P.; Guyomard, D.; Roué, L. A Low-Cost and High Performance Ball-Milled Si-Based Negative Electrode for High-Energy Li-Ion Batteries. *Energy Environ. Sci.* **2013**, *6*, 2145–2155. [CrossRef]
56. Iaboni, D.S.M.; Obrovac, M.N. Li₁₅Si₄ Formation in Silicon Thin Film Negative Electrodes. *J. Electrochem. Soc.* **2015**, *163*, A255. [CrossRef]
57. Gao, H.; Xiao, L.; Plümel, I.; Xu, G.-L.; Ren, Y.; Zuo, X.; Liu, Y.; Schulz, C.; Wiggers, H.; Amine, K.; et al. Parasitic Reactions in Nanosized Silicon Anodes for Lithium-Ion Batteries. *Nano Lett.* **2017**, *17*, 1512–1519. [CrossRef]
58. Schmerling, M.; Fenske, D.; Peters, F.; Schwenzel, J.; Busse, M. Lithiation Behavior of Silicon Nanowire Anodes for Lithium-Ion Batteries: Impact of Functionalization and Porosity. *ChemPhysChem* **2018**, *19*, 123–129. [CrossRef]
59. Gu, M.; Li, Y.; Li, X.; Hu, S.; Zhang, X.; Xu, W.; Thevuthasan, S.; Baer, D.R.; Zhang, J.-G.; Liu, J.; et al. In Situ TEM Study of Lithiation Behavior of Silicon Nanoparticles Attached to and Embedded in a Carbon Matrix. *ACS Nano* **2012**, *6*, 8439–8447. [CrossRef]
60. Bernard, P.; Alper, J.P.; Haon, C.; Herlin-Boime, N.; Chandesris, M. Electrochemical Analysis of Silicon Nanoparticle Lithiation—Effect of Crystallinity and Carbon Coating Quantity. *J. Power Sources* **2019**, *435*, 226769. [CrossRef]



Article

Vertically Aligned *n*-Type Silicon Nanowire Array as a Free-Standing Anode for Lithium-Ion Batteries

Andika Pandu Nugroho ^{1,2} , Naufal Hanif Hawari ¹, Bagas Prakoso ³, Andam Deatama Refino ^{4,5}, Nursidik Yulianto ^{4,6}, Ferry Iskandar ⁷ , Evvy Kartini ^{2,8}, Erwin Peiner ⁴, Hutomo Suryo Wasisto ^{4,9} and Afriyanti Sumboja ^{1,*}

- ¹ Material Science and Engineering Research Group, Faculty of Mechanical and Aerospace, Institut Teknologi Bandung, Jl. Ganesha 10, Bandung 40132, Indonesia; 2landika@students.itb.ac.id (A.P.N.); 23720309@mahasiswa.itb.ac.id (N.H.H.)
- ² National Battery Research Institute, Gedung EduCenter Lt. 2 Unit 22260 BSD City, South Tangerang 15331, Indonesia; evvy.kartini@n-bri.org
- ³ Mekanisasi Perikanan, Politeknik Kelautan dan Perikanan Sorong, Jl. Kapitan Pattimura, Sorong 98411, Indonesia; bagas.prakoso@polikpsorong.ac.id
- ⁴ Institute of Semiconductor Technology (IHT) and Laboratory for Emerging Nanometrology (LENA), Technische Universität Braunschweig, Hans-Sommer-Straße 66, 38106 Braunschweig, Germany; a.refino@tu-braunschweig.de (A.D.R.); n.yulianto@tu-braunschweig.de (N.Y.); e.peiner@tu-braunschweig.de (E.P.); h.wasisto@nanosense-id.com (H.S.W.)
- ⁵ Engineering Physics Program, Institut Teknologi Sumatera (ITERA), Jl. Terusan Ryacudu, Way Huwi, Lampung Selatan 35365, Indonesia
- ⁶ Research Center for Physics, National Research and Innovation Agency (BRIN), Jl. Kawasan Puspipstek 441-442, South Tangerang 15314, Indonesia
- ⁷ Department of Physics, Faculty of Mathematics and Natural Sciences, Institut Teknologi Bandung, Jl. Ganesha 10, Bandung 40132, Indonesia; ferry@fi.itb.ac.id
- ⁸ Center for Science and Technology of Advanced Materials, National Nuclear Energy Agency (BATAN), South Tangerang 15314, Indonesia
- ⁹ PT Nanosense Instrument Indonesia, Umbulharjo, Yogyakarta 55167, Indonesia
- * Correspondence: afriyanti.sumboja@material.itb.ac.id

Citation: Nugroho, A.P.; Hawari, N.H.; Prakoso, B.; Refino, A.D.; Yulianto, N.; Iskandar, F.; Kartini, E.; Peiner, E.; Wasisto, H.S.; Sumboja, A. Vertically Aligned *n*-Type Silicon Nanowire Array as a Free-Standing Anode for Lithium-Ion Batteries. *Nanomaterials* **2021**, *11*, 3137. <https://doi.org/10.3390/nano11113137>

Academic Editors: Céline Ternon and Cheol-Min Park

Received: 13 October 2021
Accepted: 18 November 2021
Published: 20 November 2021

Publisher's Note: MDPI stays neutral with regard to jurisdictional claims in published maps and institutional affiliations.



Copyright: © 2021 by the authors. Licensee MDPI, Basel, Switzerland. This article is an open access article distributed under the terms and conditions of the Creative Commons Attribution (CC BY) license (<https://creativecommons.org/licenses/by/4.0/>).

Abstract: Due to its high theoretical specific capacity, a silicon anode is one of the candidates for realizing high energy density lithium-ion batteries (LIBs). However, problems related to bulk silicon (e.g., low intrinsic conductivity and massive volume expansion) limit the performance of silicon anodes. In this work, to improve the performance of silicon anodes, a vertically aligned *n*-type silicon nanowire array (*n*-SiNW) was fabricated using a well-controlled, top-down nano-machining technique by combining photolithography and inductively coupled plasma reactive ion etching (ICP-RIE) at a cryogenic temperature. The array of nanowires $\sim 1 \mu\text{m}$ in diameter and with the aspect ratio of ~ 10 was successfully prepared from commercial *n*-type silicon wafer. The half-cell LIB with free-standing *n*-SiNW electrode exhibited an initial Coulombic efficiency of 91.1%, which was higher than the battery with a blank *n*-silicon wafer electrode (i.e., 67.5%). Upon 100 cycles of stability testing at 0.06 mA cm^{-2} , the battery with the *n*-SiNW electrode retained 85.9% of its 0.50 mAh cm^{-2} capacity after the pre-lithiation step, whereas its counterpart, the blank *n*-silicon wafer electrode, only maintained 61.4% of 0.21 mAh cm^{-2} capacity. Furthermore, 76.7% capacity retention can be obtained at a current density of 0.2 mA cm^{-2} , showing the potential of *n*-SiNW anodes for high current density applications. This work presents an alternative method for facile, high precision, and high throughput patterning on a wafer-scale to obtain a high aspect ratio *n*-SiNW, and its application in LIBs.

Keywords: silicon nanowire; nanowire array; silicon anode; *n*-type silicon anode; Li-ion battery

1. Introduction

Lithium-ion batteries (LIBs) are among the most robust energy storage devices due to their good cycle life, low self-discharge, and high energy density [1,2]. Those superiorities drive the utilization of LIBs in many applications, such as portable electronic devices, electric vehicles (EVs), and stationary energy storage [3]. However, traditional LIBs use graphite anodes, which possess a relatively low specific capacity (372 mAh g^{-1}), limiting their achievable energy density [4]. Various materials with higher theoretical capacities have been pursued as alternatives for the graphite anode, such as Co_3O_4 (890 mAh g^{-1}), Sn (994 mAh g^{-1}), Ge (1625 mAh g^{-1}), MgH_2 (2038 mAh g^{-1}), and Si (4200 mAh g^{-1}) [5–7]. In particular, silicon has been introduced as the anode material for high energy density LIBs due to its large storage capacity, abundance, environmental friendliness, and suitable discharge voltage [8]. However, its significant volume expansion (up to 300–400%) during alloying with lithium leads to pulverization of active material and loss of electrical contact with the current collector, which restricts the performance of Si anode in LIBs, consequently [9].

Various strategies have been performed to improve the Si anode performance, e.g., introducing a dopant to enhance the conductivity, and nano-structuring to alleviate the volume expansion by providing buffer space around its structure [10–12]. In general, compared to undoped and *p*-type Si, *n*-type Si is favorable, as it can provide high conductivity derived from the high electron mobility in the silicon [13,14]. Furthermore, among various types of Si nanostructures, an array of one-dimensional (1D) Si nanowires (NWs) provides charge transport in one direction along the NW axis all the way to the current collector, enhancing the capacity and rate capability of the LIBs [15]. Proper spacing in the Si NW array enables facile strain relaxation in the NWs, which accommodates the volume changes during alloying with Li and improves the cycling stability of the Si anode [16].

Both bottom-up and top-down fabrication approaches have been employed to manufacture 1D Si nanostructures [17–19]. Bottom-up approaches may utilize deposition and templating methods that often require complex instruments, intricate methods, or toxic precursors [20]. Top-down methods, which are typically performed by combining lithography and etching processes, offer a controllable and facile procedure for large-scale fabrication of nanostructured Si. Among the nanoscale lithography techniques (e.g., nanoimprint lithography, colloidal nanosphere lithography, and electron beam lithography), photolithography is considered the most established method [21–24]. It enables the formation of a large variety of patterns with relatively short processing time, high accuracy of structural transfer, and suitability for wafer-scale production [25]. The deposited pattern will serve as a mask in the subsequent etching step, in which the exposed Si is removed, and the pattern is transferred onto the Si wafer, resulting in the formation of vertical nanostructures on the Si substrate.

Among various etching methods, reactive ion etching (RIE) utilizes a radio frequency (RF) electromagnetic field to bombard the etch target with ions and radicals produced in a plasma. Inductively coupled plasma (ICP) is introduced to the RIE system to obtain an independent control of ion density [26]. Besides that, by combining photolithography and ICP-RIE, the production cost could be potentially reduced due to the high throughput of the patterning process with homogenous shape and size. Moreover, compared to the Bosch process, which suffers from scalloping effects on the etched structures, ICP-RIE conducted at cryogenic temperatures can produce vertical Si NW arrays with high aspect ratios and smooth sidewalls [27]. Although high-aspect-ratio Si nanowires have been successfully produced by photolithography and cryogenic ICP-RIE, their use in LIBs is rarely reported [28].

Furthermore, nanostructured Si anodes have mostly been prepared by producing a slurry consisting of active materials, conductive additives, and binders, which were then coated onto a current collector [29–31]. However, the use of binders may reduce the conductivity of the anode. The interfaces among the active materials, binder, and current collector may also serve as initial crack points, which can limit the capacity and

cycling stability of the LIBs [32]. On the other hand, free-standing anodes do not require a binder, additives, or a current collector, potentially reducing the production cost and overall resistance of the LIBs [33]. Moreover, due to their robust structure, free-standing Si anodes may enhance the cycling stability of LIBs by providing strong mechanical support during repeated charge/discharge processes [34]. Nanostructured black Si anodes had been fabricated using plasma etching of an *n*-type Si substrate [35]. However, despite its small NW diameter (450 nm) and high aspect ratio (~22), the black Si showed low initial Coulombic efficiency (i.e., ~23.9%) and poor cycling stability when used in a LIB, which could be associated with its uneven surface morphology and too-dense structure.

In this work, we demonstrate the fabrication of a vertically aligned *n*-type Si nanowire array (*n*-SiNW) as a free-standing anode for LIBs by combining photolithography and cryogenic ICP-RIE. This fast and precise method can produce an NW array with smooth morphology, high areal density, and adjustable dimensions. The as-produced NWs possess a high aspect ratio and are structurally attached to the Si substrate, which also serves as the current collector. A half-cell LIB was fabricated with the *n*-SiNW electrode, and its performance was compared to a respective counterpart with a plain/blank *n*-Si wafer electrode in terms of initial Coulombic efficiency, charge and discharge capacity, cycling stability, and capacity retention at high current densities. This work provides an alternative large-scale method for obtaining free-standing Si anodes with homogeneous and easily adjustable shapes and sizes.

2. Materials and Methods

2.1. Top-Down Fabrication of *n*-SiNW

Si wafers were purchased from SIEGERT WAFER GmbH, Aachen, Germany. They are *n*-type Si wafers doped with phosphorus having a crystal orientation of $\langle 100 \rangle$, a thickness of $525 \pm 20 \mu\text{m}$, and a resistivity of 5–10 $\Omega \text{ cm}$. The *n*-SiNWs were directly carved from Si substrate by photolithography and cryogenic ICP-RIE. The Si wafers were first cleaned with acetone and dried with nitrogen blow. The wafers were then exposed to hexamethyldisilazane (HMDS) vapor during heating at 115 °C. The photoresist was deposited on the Si wafers by spin coating a diluted mixture of AZ 5214 E: AZ EBR (1:1) purchased from Merck Performance Materials Germany GmbH, Darmstadt, Germany, at 3000 rpm for 35 s on the Si wafer substrate, followed by soft-baking at 110 °C for 50 s. A photomask was used to transfer circular patterns to the substrate by exposing the sample to UV light generated by a 210 W Hg lamp for 13 s. This photolithography process was carried out by employing an MJB4 mask aligner from SÜSS MicroTec SE, Garching, Germany. The pattern was realized by dipping the substrate into AZ 726 MIF developer obtained from Merck Performance Materials Germany GmbH, Darmstadt, Germany for 25 s.

Once the circular photoresist patterns had been created on the Si wafer, cryogenic ICP-RIE was conducted using a SI 500C plasma etcher from SENTECH Instruments GmbH, Berlin, Germany. The etching was conducted using several optimized parameters: an ICP power of 500 W, an RF power of 6 W corresponding to an RF bias of -12 V , a temperature of -95 °C , a pressure of 1.0 Pa, an etch time of 5 min, an O_2 flow of 12 sccm, and an SF_6 flow of 119 sccm. To ensure good thermal dissipation during cryogenic cooling, a thermally conductive oil was applied between the Si wafer and the substrate holder, which was removed using acetone after the etching had been completed. At the same time, the remaining photoresist mask was also stripped off by acetone. To fit its size to the package of a typical coin cell Li-ion battery (LIB), the *n*-SiNW-containing wafer was then diced into a $1 \times 1 \text{ cm}^2$ piece (mass $\approx 131 \text{ mg}$).

2.2. Structural and Electrochemical Characterizations

X-ray diffraction (XRD) analysis was conducted utilizing an X-ray diffractometer (Bruker D8 Advance, Billerica, United States of America) using $\text{Cu K}\alpha$ radiation ($\lambda = 1.54060 \text{ \AA}$). The diffraction peaks were analysed using PANalytical Expert Highscore Plus software. A scanning electron microscope (SEM HITACHI SU3500, Tokyo, Japan) was used to inves-

tigate the morphologies of the Si samples. The half-cell LIBs were assembled by employing *n*-SiNW and blank *n*-Si wafer electrodes, both having a die area of $1 \times 1 \text{ cm}^2$. The Si samples were directly used as the electrode without using any binder, additives, or current collector. Other essential components, a Li metal counter electrode, a polypropylene separator (Cellgard[®] 2400), and a 1 M lithium hexafluorophosphate (LiPF₆) electrolyte with 10 %wt fluoroethylene carbonate (FEC) in a 1:1:1 volume mixture of ethylene carbonate, dimethyl carbonate, and diethyl carbonate (EC/DMC/DEC), were stacked in an appropriate sequence in a CR2032 coin shell. All components were purchased from Xiamen Tob New Energy Technology Co., Ltd., Xiamen, China, except the FEC, which was bought from Sigma Aldrich, Singapore.

The half-cell assembly was performed in a glove box (Kiyon, Seoul, Korea), in which O₂ and H₂O concentrations were maintained at less than 0.1 ppm. The fabricated half-cells were rested for 24 h prior to the test to ensure the electrolyte was fully impregnated in the separator. To prepare a surface electro-active region and enable stable cycling performance, all cells were then pre-lithiated for 10 h to 0.1 V at a current density of 0.06 mA cm^{-2} . To determine the capacity and cycling performance, the prepared cells were subsequently tested in a battery analyzer (Neware Battery Testing System, Shenzhen, China) using the galvanostatic charge–discharge method within the potential range of 0.15 V to 1.0 V, at 0.06 mA cm^{-2} for 100 cycles at room temperature. The capacities of the cells were calculated with respect to the electrode areas (1 cm^2). The rate capabilities were evaluated by charging and discharging at various current densities. The electrochemical impedance spectroscopy measurements were measured with an electrochemical workstation (GAMRY, Warminster, UK) after the pre-lithiation of the half cells in the frequency range of 1 MHz to 0.01 Hz, with an amplitude of 5 mV at room temperature. The resistance values of the cells were obtained from fitting with the ZSimpWin software.

3. Results and Discussion

Free-standing *n*-SiNW anodes were successfully fabricated by combining photolithography and cryogenic ICP-RIE (Figure 1). Photolithography was employed to create a photoresist mask pattern on a Si wafer. In the first step, the photoresist thin film was spin-coated and baked on a cleaned Si substrate (Figure 1a,b). Upon exposure to ultraviolet (UV) light, a circular pattern array was transferred to the photoresist. A developer solution was then used to selectively strip off the exposed photoresist area, leaving circular photoresist pattern arrays on the Si wafer (Figure 1c).

The cryogenic ICP-RIE enabled simultaneous passivation and etching processes (Figure 1d,e). In this process, a plasma discharge containing O₂ and SF₆ gases is generated inside a vacuum chamber to produce SF_x ions, and O and F radicals (O* and F*). The charged species (and the dragged radicals) are transported towards the Si substrate by an applied RF bias. A vertical bombardment of accelerated SF_x ions etch the Si wafer physically. Simultaneously, SiF species are desorbed due to chemical reactions between F* and the exposed Si atoms, performing chemical etching on the Si wafer. The etching removes Si from the areas of the non-masked surface, forming sidewalls around the masked area that subsequently turns into the vertical nanowire structure. At cryogenic temperatures, O* reacts with Si and F*, forming SiO_xF_y that conformally adsorbs on the wafer surface and serves as a passivation layer against chemical etching. Due to the vertical direction of ion bombardment, a stable passivation layer can only be built up on the sidewalls, which protects the NWs from lateral etching. On the bottom surface between the NWs, the passivation layer is continuously removed by the physical etching of the impinging ions. At the end of the process, after exposing the etched substrate to room temperature, SiO_xF_y becomes volatile, and the passivation layer on the NW sidewalls is removed. Cryogenic ICP-RIE enables the fabrication of Si NW arrays with various aspect ratios by adjusting the etching parameters (e.g., temperature, gas flow rate, ICP power, chamber pressure, and etching time) [27,36]. Besides, it can produce Si NWs with smooth sidewalls without a scalloping effect that may introduce stress concentration, resulting in the severe capacity

fading of LIBs [37]. Finally, in order to fit the *n*-SiNW anode into a battery coin cell, the wafer was diced into $1 \times 1 \text{ cm}^2$ pieces (Figure 1f).

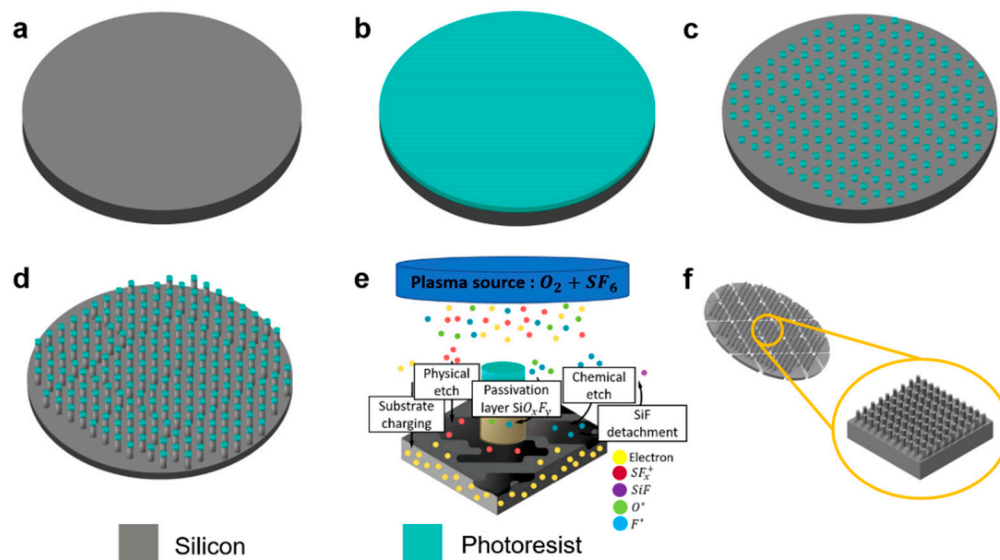


Figure 1. Schematic of the processing steps to fabricate the *n*-SiNW. (a) Preparation and cleaning of the Si wafer. (b) Spin coating of the photoresist on the wafer. (c) Circular photoresist pattern formation after photolithography. (d) ICP-RIE at cryogenic temperature resulting in an *n*-SiNW. (e) Mechanism of the etching process by ICP-RIE. (f) Photoresist removal and mechanical dicing to obtain a die area of $1 \times 1 \text{ cm}^2$.

The nanowires obtained via photolithography and cryogenic ICP-RIE are homogeneous due to the high controllability of the process and the flexibility of the etching parameters [27]. The morphology of the obtained Si NW array was examined with a scanning electron microscope (SEM). It was first conducted on a blank *n*-type Si substrate (Figure 2a). The Si substrate has no specific morphology, except the flat surface, providing a perfect area for uniform deposition of the resist film. Starting from a corresponding surface, a homogenous nanowire array with predetermined spacing distance and diameter was obtained after etching (Figure 2b). The Si NWs had a diameter of $\sim 996 \text{ nm}$ and were $\sim 3 \mu\text{m}$ from the closest wire. Side-view images further display that the nanowire was cylindrical with a height of $\sim 10.2 \mu\text{m}$, yielding an aspect ratio of ~ 10.2 (Figure 2c).

The obtained aspect ratio of *n*-SiNWs in this work is higher than that of a similar structure from another study with an aspect ratio of <7 , which can be attributed to the selected etching parameters (e.g., gas flow rate and etch time) [38]. Vertical Si NWs with a high aspect ratio possess a high surface area with a large electrode–electrolyte interface, which can enhance electrolyte permeation and Li ion transport [39]. Furthermore, a well-ordered nanowire array is more desirable than a random array or disordered distributions of nanowires, which can lead to inefficient charge storage [40,41]. Moreover, the obtained *n*-SiNWs had direct attachment to the Si wafer, which strengthened the structural integrity of the anode. Figure 2d depicts X-ray diffraction (XRD) patterns of a plain/blank *n*-Si wafer and an as-fabricated *n*-SiNW array. The diffraction peak at $2\theta = 69.13^\circ$ for the plain/blank Si wafer and the *n*-SiNW corresponds to the $\langle 400 \rangle$ crystal orientation as the first reflection from $\langle 100 \rangle$ -Si [42]. An *n*-type Si with $\langle 100 \rangle$ orientation enables faster diffusion of Li ions, which is beneficial for reducing the volume expansion of Si anodes [43].

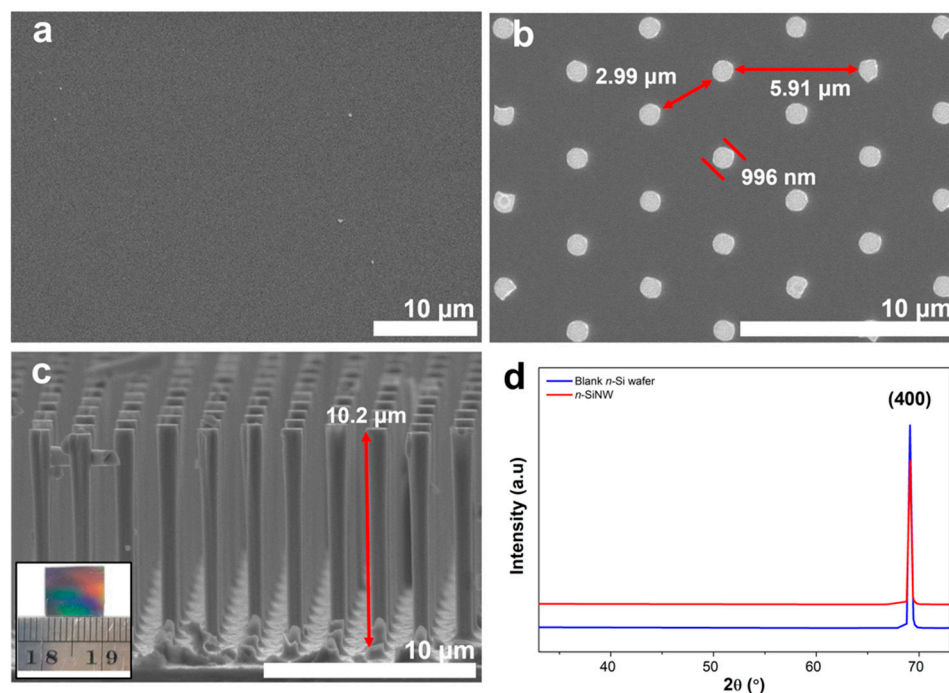


Figure 2. Top-down fabricated *n*-SiNW anode with an aspect ratio of ~ 10 compared to an unstructured *n*-Si substrate. Top view of SEM images for (a) plain/blank Si substrate and (b) *n*-SiNW. (c) The cross-sectional view of the free-standing *n*-SiNW anode (inset: the actual die dimensions of the *n*-SiNW anode). (d) X-ray diffraction (XRD) patterns of an *n*-SiNW and a plain/blank *n*-type Si wafer.

The electrochemical performance of plain/blank *n*-Si wafer and *n*-SiNW electrodes in half-cell LIBs were investigated by galvanostatic discharge–charge measurements (Figure 3). During the pre-lithiation cycle, the battery with a blank *n*-Si wafer electrode reached an initial Coulombic efficiency (ICE) of 67.5% with specific discharge and charge capacities of 0.50 mAh cm^{-2} and 0.34 mAh cm^{-2} , respectively (Figure 3a). Noticeable capacity losses were observed in the following discharge–charge cycles, resulting in discharge capacities of 0.21 mAh cm^{-2} , 0.15 mAh cm^{-2} , and 0.13 mAh cm^{-2} at the 2nd, 50th, and 100th cycles, respectively (Figure 3b). The low discharge capacity of the LIB with the blank *n*-Si wafer electrode can be attributed to incomplete Li–Si alloying during the lithiation process [44]. The Li ions could not diffuse through the thickness of the blank Si wafer ($\sim 525 \text{ }\mu\text{m}$ thick). Hence, only a small portion of the blank Si wafer could be alloyed with Li to form a Li–Si alloy, leading to the low discharge capacity of the LIB. Furthermore, during the cycling test, local volume expansion increased the internal stress of the Si electrode. That could produce cracks that would further consume active Li, generate new solid electrolyte interphase (SEI) layer, and degrade the LIB capacity, subsequently [45].

On the other hand, the half-cell LIB with *n*-SiNW electrode delivered improved specific discharge and charge capacities during the pre-lithiation cycle (0.88 and 0.80 mAh cm^{-2} , respectively), generating an ICE as high as 91.1% (Figure 3c). The value of ICE increased to $\sim 99\%$ after three cycles and stabilized at the subsequent cycles. The battery with the *n*-SiNW electrode also showed improved discharge and charge capacities in the subsequent cycles— 0.50 , 0.42 , and 0.43 mAh cm^{-2} at the 2nd, 50th, and 100th cycles, respectively (Figure 3d). In this case, lithiation in the vertical Si nanowires preferably took place in a radial orientation, providing a high surface area for the lithiation process [15,46]. Moreover, the small wire diameter of $\sim 1 \text{ }\mu\text{m}$ further shortens the diffusion path of Li ions. Therefore, a high proportion of Li ions can be effectively alloyed with Si, delivering a good discharge capacity for the LIB [15]. As the thickness of the remaining bulk Si substrate is much larger than the height of the *n*-SiNWs (i.e., ~ 50 times the *n*-SiNW height), the mass of the bulk substrate that does not contribute to the capacity is much larger than the NWs' mass.

Therefore, area-specific capacity was chosen as the more appropriate metric for comparison instead of gravimetric specific capacity. Besides that, area capacity measurements are typically performed to ensure compatibility between anode and cathode, as both electrodes face each other in battery cells [47]. Obviously, electrodes with high areal capacity are able to store more energy per unit area. Hence, it is a crucial parameter for the miniaturization of LIBs.

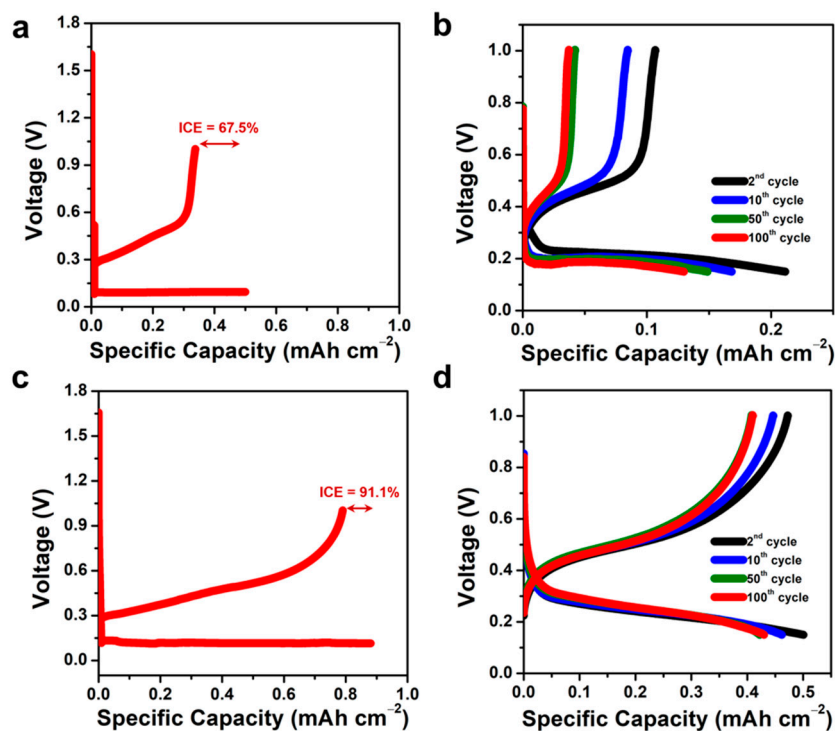


Figure 3. Galvanostatic discharge and charge profiles of the half-cell LIBs with plain/blank *n*-Si wafer and *n*-SiNW electrode. (a) Pre-lithiation cycle and (b) 2nd to 100th cycles of a LIB with blank *n*-Si wafer electrode. (c) Pre-lithiation cycle and (d) 2nd to 100th cycles of LIBs with *n*-SiNW electrode.

The cycling performances of the half-cell LIBs with blank *n*-Si wafer and *n*-SiNW electrodes and their corresponding Coulombic efficiencies are given in Figure 4a,b. After 100 cycles of discharge–charge, the LIB with the blank Si wafer electrode (Figure 4a) exhibited low discharge and charge capacities (i.e., 0.13 and 0.03 mAh cm^{−2}, respectively), and a low Coulombic efficiency (~21.2%). Furthermore, the Coulombic efficiency of the cell with a blank Si wafer was unstable throughout the cycling test, indicating the drawbacks of pristine and bulk Si as an electrode material for LIBs. The poor Coulombic efficiency of the battery could be associated with the continuous formation of an SEI, which severely consumes the active lithium in the LIB. Moreover, inhomogeneity of the formed SEI and a significant volume expansion of the blank Si wafer resulted in low capacity retention of the LIB (i.e., 61.4% after 100 cycles of the discharge–charge test). Bulk Si wafers may not be able to withstand the volume expansion, leading to plastic deformation and electrode failure upon delithiation [44].

The half-cell LIB with a *n*-SiNW electrode generated an average Coulombic efficiency of 99.5% during 100 cycles of discharge–charge at 0.06 mA cm^{−2} (Figure 4b). In addition, it also exhibited a relatively stable cycling performance, retaining 85.9% of its first discharge capacity after the pre-lithiation step. The free space between the nanowires can accommodate volume expansion, minimize internal stress, and keep the structural integrity of the electrode, resulting in high and stable Coulombic efficiency [8,48]. Moreover, the small diameter of the nanowires is able to mitigate the large volume change of the silicon, resulting in better cycling performance of the LIBs [49]. After 100 cycles, the cycling stability

of the half-cell using an *n*-SiNW electrode was better than previous reports on Si NW anodes prepared by chemical vapor deposition (CVD) and metal-assisted chemical etching (MACE) that reported capacity retention of up to only 83% [19,50,51]. Additionally, the cycling stability of the cell with an *n*-SiNW electrode remained advantageous compared to some pristine Si nanoparticle and Si thin film anodes, which had less than 50% capacity retention after 100 cycles [52–54].

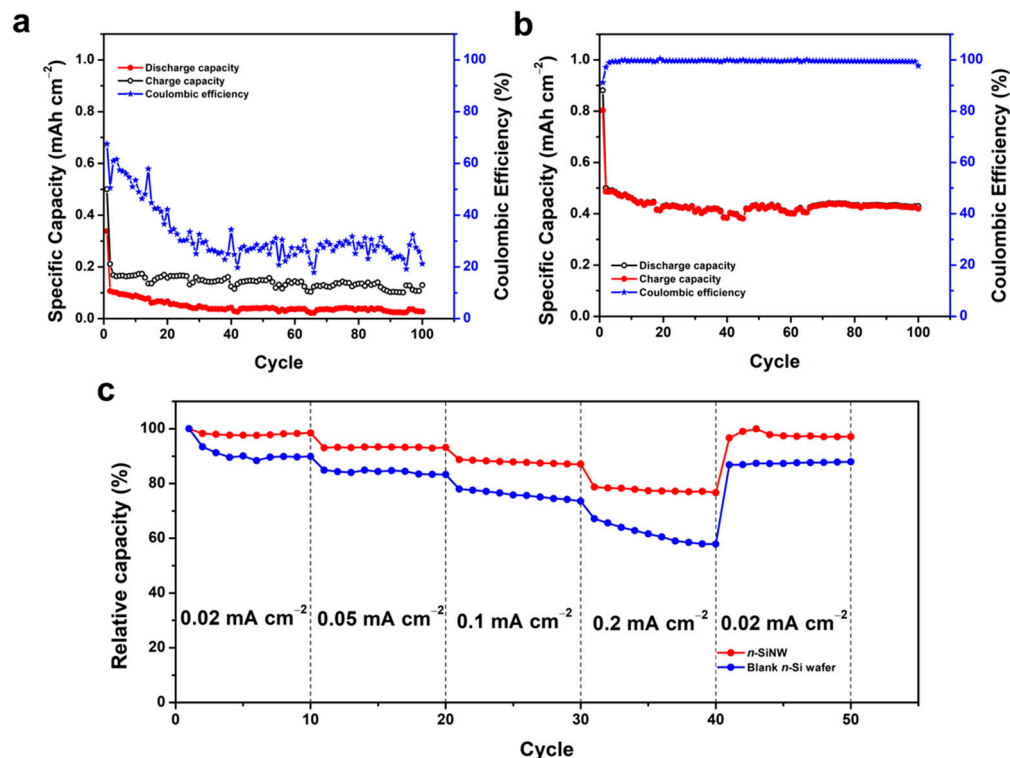


Figure 4. Electrochemical performances of LIBs with blank *n*-Si wafer or *n*-SiNW electrodes. Discharge–charge capacities and the corresponding Coulombic efficiencies at a current density of 0.06 mA cm^{-2} for 100 cycles of the batteries with (a) a blank *n*-Si wafer or (b) an *n*-SiNW electrode. (c) Capacity retention of LIBs with blank Si wafer and *n*-SiNW electrodes cycled at 0.02 , 0.05 , 0.1 , and 0.2 mA cm^{-2} .

The rate capability tests of the LIBs with blank *n*-Si wafer and *n*-SiNW electrodes at various current densities are depicted in Figure 4c. At a high discharge rate of 0.2 mA cm^{-2} , the LIB with a blank Si wafer electrode retained 57.9% of its discharge capacity at 0.02 mA cm^{-2} . The cell also exhibited capacity retention of 87.9% when the current rate was reduced back to 0.02 mA cm^{-2} . On the contrary, the capacity of the LIB with an *n*-SiNW electrode demonstrated capacity retention of 76.7% at 0.2 mA cm^{-2} , and restored 97.1% of its capacity when the discharge rate was reduced back to 0.02 mA cm^{-2} . In this case, the vertical arrangement of the nanowires provided a facile and fast Li ion diffusion pathway, resulting in the measured improved capacity retention at high current rates [15,43]. The good rate performance of LIBs with *n*-SiNW electrodes is also ascribed to the fast infiltration and circulation of the electrolyte in the nanowire array electrode, facilitating rapid ion transport during the electrochemical reactions [8]. Moreover, the high capacity retention after the current density was lowered back to 0.02 mA cm^{-2} indicates that the nanowire array is electrochemically stable and able to withstand high current charge–discharge rates.

Electrochemical impedance spectroscopy (EIS) measurements for LIBs with blank *n*-Si wafer and *n*-SiNW electrodes were carried out after the prelithiation cycle at a voltage of 0.24 V. Figure 5a shows the results of EIS measurements and the corresponding equivalent circuit model [55]. R_s is the Ohmic resistance of the whole cell, which can be expressed

by an intercept at the high-frequency region [56]. The impedance of the imperfect contact due to the newly formed interface at the electrode is composed of the interface's constant phase element (CPE_{int}) and the interface's resistance (R_{int}) [55]. The impedance related to the characteristics of SEI is given by SEI's constant phase element (CPE_{SEI}) and the SEI's resistance (R_{SEI}). The last parallel components of the impedance consist of the capacitive nature of double-layer electrode/electrolyte interphase (CPE_{DL}), charge transfer resistance at the electrode/electrolyte interface (R_{CT}), and diffusion behavior of Li ions within the electrode which is expressed by the Warburg impedance (Z_W) [57]. The fitted Nyquist plot is represented by a solid line, showing good agreement of the fitted parameters with the experimental results.

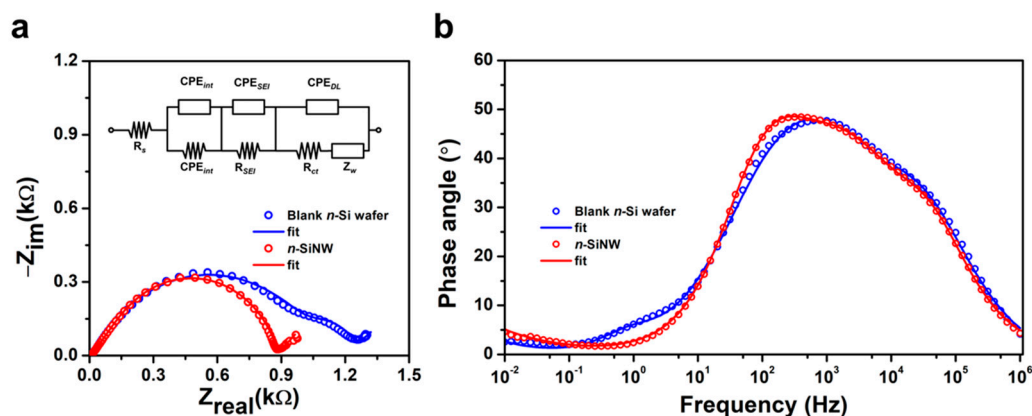


Figure 5. Electrochemical impedance spectroscopy (EIS) analysis of half-cell LIBs with blank *n*-Si wafer and *n*-SiNW electrodes after pre-lithiation cycles. (a) Nyquist plots of the cells with blank *n*-Si wafer and *n*-SiNW electrodes. The inset image is the equivalent circuit model used for fitting the EIS results. (b) Phase angle diagram of the cells with blank *n*-Si wafer and *n*-SiNW electrodes.

The similar R_S values ($\sim 10 \Omega$) for cells with blank *n*-Si wafer and *n*-SiNW electrodes can be attributed to the same half-cell systems that were used in the experiments. The cell with an *n*-SiNW electrode had a lower R_{INT} (9.87Ω) than its counterpart with a blank *n*-Si wafer electrode (14.66Ω). These results suggest the small resistance associated with the newly formed interfaces due to the volume expansion in the *n*-SiNW, further affirming the benefit of the nanowire structure in mitigating the volume changes in the Si anode. The R_{SEI} value can be influenced by the type of electrolyte and the volume expansion of Si, which affect the growth of the SEI [58]. Since both cells used the same electrolyte, the lower R_{SEI} of the cell with the *n*-SiNW electrode (784.6Ω) in comparison to the cell with the blank *n*-Si wafer (1057Ω) can be attributed to the more controlled volume expansion of Si nanowires, which stabilizes the growth of the SEI during alloying with Li [15]. Furthermore, the smaller R_{CT} of the LIB with an *n*-SiNW electrode (74.5Ω) than its counterpart with a blank *n*-Si wafer electrode (155Ω) also suggests the structural benefit of the nanowire array electrode over its bulk structure. In particular, the nanowire array structure provides facile charge transport channels, leading to fast kinetics of charge displacement at the electrode–electrolyte interface [59]. Consequently, the *n*-SiNW electrode has improved kinetics during electrochemical alloying and dealloying, resulting in a higher capacity and enhanced rate capability.

The phase angle diagram for both cells is shown in Figure 5b. At the high to the middle-frequency region (1 MHz–1 kHz), the cells with blank *n*-Si wafer and *n*-SiNW electrodes showed similar responses, as the Ohmic resistance dominates the impedance response [60]. The reversal of the phase angle at 1 kHz–10 Hz is related to the impedance of SEI in both cells. The relatively high phase angle of the cell with *n*-SiNW suggests that the *n*-SiNW electrode produced a more stable SEI compared to the blank *n*-Si wafer, which is in agreement with a higher R_{SEI} of the cell with the blank *n*-Si wafer than the cell with the *n*-SiNW electrode [61]. The charge transfer behavior of both cells in the phase angle

diagram is characterized in the frequency range of 10 Hz–0.1 Hz. At this range, the lower phase angle of the cell with *n*-SiNW indicates that the *n*-SiNW electrode is able to mobilize a higher number of electrons at the electrode–electrolyte interface compared to the blank *n*-Si wafer electrode. These data are in line with the fitting results of Nyquist plots, where the cell with the *n*-SiNW electrode has a lower R_{CT} than its counterpart with the blank *n*-Si wafer electrode.

4. Conclusions

Free-standing Li-ion battery (LIB) anodes made of *n*-SiNW were successfully realized through a combination of photolithography and cryogenic ICP-RIE. Homogeneous *n*-SiNWs with a predetermined diameter of ~996 nm and a high aspect ratio of ~10.2 were well “carved” on commercial *n*-type Si wafer substrates. A half-cell LIB with a free-standing *n*-SiNW electrode typically generated a promising ICE as high as 91.13%. A large areal capacity of 0.43 mAh cm⁻² after 100 cycles of cycling test could be maintained by the designed structure, retaining 86% of its initial capacity after the pre-lithiation. Furthermore, it exhibited high capacity retention—up to 77% of its initial value at a current density of 0.2 mA cm⁻². This promising performance is attributed to a facile and short-diffusion Li ion pathway, and fast infiltration and circulation of the electrolyte in the vertically aligned Si nanowire array anode. In the next development steps, further optimization can be expected by employing higher aspect ratio nanowires (of either larger height or smaller diameter) and combining *n*-SiNW with other active materials to form the composite electrode.

Author Contributions: Conceptualization, H.S.W. and A.S.; Methodology, A.P.N., N.H.H., B.P., A.D.R., N.Y., H.S.W. and A.S.; Validation, F.I., E.K., E.P., H.S.W. and A.S.; Formal Analysis and Investigation, A.P.N., N.H.H., B.P., A.D.R., N.Y., H.S.W. and A.S.; Resources, F.I., E.K., E.P., H.S.W. and A.S.; Data Curation, A.P.N., N.H.H., B.P., A.D.R. and N.Y.; Writing—Original Draft Preparation, A.P.N., N.H.H., B.P. and A.S.; Writing—Review and Editing, A.D.R., N.Y., F.I., E.K., E.P., H.S.W. and A.S.; Supervision, E.P., H.S.W. and A.S.; Funding Acquisition, H.S.W. and A.S. All authors have read and agreed to the published version of the manuscript.

Funding: This work is funded by the Indonesia Endowment Fund for Education (LPDP) and the German Federal Ministry of Education and Research (BMBF) under the Southeast Asia–Europe Joint Funding Scheme (SEA-EU JFS) for Research and Innovation. A.D.R. and N.Y. acknowledge the Ministry of Research, Technology and Higher Education of the Republic of Indonesia (RISTEKDIKTI) for the Ph.D. scholarships of BPP-LN under number T/912/D3.2/KD.02.01/2019 and Riset-Pro under number 34/Riset-Pro/FGS/III/2019, respectively. E.P. thanks the financial support for the EMPIR project of 19ENG05 NanoWires from the Participating States and the European Union’s Horizon 2020 research and innovation program.

Data Availability Statement: Not applicable.

Acknowledgments: The authors are grateful for the technical support from Angelika Schmidt, Juliane Breitfelder, and Aileen Michalski during the fabrication of the vertical Si nanowire array.

Conflicts of Interest: The authors declare no conflict of interest.

References

- Zubi, G.; Dufo-López, R.; Carvalho, M.; Pasaoglu, G. The lithium-ion battery: State of the art and future perspectives. *J. Renew. Sustain. Energy* **2018**, *89*, 292–308. [CrossRef]
- Dong, C.; Dong, W.; Lin, X.; Zhao, Y.; Li, R.; Huang, F. Recent progress and perspectives of defective oxide anode materials for advanced lithium ion battery. *EnergyChem* **2020**, *2*, 100045. [CrossRef]
- Manthiram, A. An outlook on lithium ion battery technology. *ACS Cent. Sci.* **2017**, *3*, 1063–1069. [CrossRef]
- Hu, Y.; Wayment, L.J.; Haslam, C.; Yang, X.; Lee, S.-h.; Jin, Y.; Zhang, W. Covalent organic framework based lithium-ion battery: Fundamental, design and characterization. *EnergyChem* **2021**, *3*, 100048. [CrossRef]
- Yuda, A.P.; Koraag, P.Y.E.; Iskandar, F.; Wasisto, H.S.; Sumboja, A. Advances of the top-down synthesis approach for high-performance silicon anodes in Li-ion batteries. *J. Mater. Chem. A* **2021**, *9*, 18906–18926. [CrossRef]
- Cheng, Q.; Sun, D.; Yu, X. Metal hydrides for lithium-ion battery application: A review. *J. Alloys Compd.* **2018**, *769*, 167–185. [CrossRef]

7. Zhu, S.; Li, J.; Deng, X.; He, C.; Liu, E.; He, F.; Shi, C.; Zhao, N. Ultrathin-Nanosheet-Induced Synthesis of 3D Transition Metal Oxides Networks for Lithium Ion Battery Anodes. *Adv. Funct. Mater.* **2017**, *27*, 1605017. [CrossRef]
8. Wang, X.; Huang, L.; Zhang, Y.; Yin, F.; Bakenov, Z.; Umirov, N.; Jin, M.; Zhou, G. Novel silicon nanowire film on copper foil as high performance anode for lithium-ion batteries. *Ionics* **2018**, *24*, 373–378. [CrossRef]
9. Kennedy, T.; Brandon, M.; Laffir, F.; Ryan, K.M. Understanding the influence of electrolyte additives on the electrochemical performance and morphology evolution of silicon nanowire based lithium-ion battery anodes. *J. Power Sources* **2017**, *359*, 601–610. [CrossRef]
10. Mukanova, A.; Nurpeissova, A.; Kim, S.S.; Myronov, M.; Bakenov, Z. N-Type Doped Silicon Thin Film on a Porous Cu Current Collector as the Negative Electrode for Li-Ion Batteries. *ChemistryOpen* **2018**, *7*, 92. [CrossRef]
11. Franco Gonzalez, A.; Yang, N.-H.; Liu, R.-S. Silicon anode design for lithium-ion batteries: Progress and perspectives. *J. Phys. Chem. C* **2017**, *121*, 27775–27787. [CrossRef]
12. Sun, F.; Tan, Z.; Hu, Z.; Chen, J.; Luo, J.; Wu, X.; Cheng, G.; Zheng, R. Ultrathin Silicon Nanowires Produced by a Bi-Metal-Assisted Chemical Etching Method for Highly Stable Lithium-Ion Battery Anodes. *Nano* **2020**, *15*, 2050076. [CrossRef]
13. Burchak, O.; Keller, C.; Lapertot, G.; Salaün, M.; Danet, J.; Chen, Y.; Bendiab, N.; Pépin-Donat, B.; Lombard, C.; Faure-Vincent, J.; et al. Scalable chemical synthesis of doped silicon nanowires for energy applications. *Nanoscale* **2019**, *11*, 22504–22514. [CrossRef]
14. Chang, N.L.; Wright, M.; Egan, R.; Hallam, B. The Technical and Economic Viability of Replacing n-type with p-type Wafers for Silicon Heterojunction Solar Cells. *Cell Rep. Phys. Sci.* **2020**, *1*, 100069. [CrossRef]
15. Song, T.; Hu, L.; Paik, U. One-dimensional silicon nanostructures for Li ion batteries. *J. Phys. Chem. Lett.* **2014**, *5*, 720–731. [CrossRef] [PubMed]
16. Casimir, A.; Zhang, H.; Ogoke, O.; Amine, J.C.; Lu, J.; Wu, G. Silicon-based anodes for lithium-ion batteries: Effectiveness of materials synthesis and electrode preparation. *Nano Energy* **2016**, *27*, 359–376. [CrossRef]
17. Schmerling, M.; Fenske, D.; Peters, F.; Schwenzel, J.; Busse, M. Lithiation Behavior of Silicon Nanowire Anodes for Lithium-Ion Batteries: Impact of Functionalization and Porosity. *ChemPhysChem* **2018**, *19*, 123–129. [CrossRef] [PubMed]
18. Wasisto, H.S.; Huang, K.; Merzsch, S.; Stranz, A.; Waag, A.; Peiner, E. Finite element modeling and experimental proof of NEMS-based silicon pillar resonators for nanoparticle mass sensing applications. *Microsyst. Technol.* **2014**, *20*, 571–584. [CrossRef]
19. Sandu, G.; Coulombier, M.; Kumar, V.; Kassa, H.G.; Avram, I.; Ye, R.; Stopin, A.; Bonifazi, D.; Gohy, J.-F.; Leclère, P.; et al. Kinked silicon nanowires-enabled interweaving electrode configuration for lithium-ion batteries. *Sci. Rep.* **2018**, *8*, 9794. [CrossRef]
20. Ge, M.; Fang, X.; Rong, J.; Zhou, C. Review of porous silicon preparation and its application for lithium-ion battery anodes. *Nanotechnology* **2013**, *24*, 422001. [CrossRef] [PubMed]
21. Hamdana, G.; Puranto, P.; Langfahl-Klabes, J.; Li, Z.; Pohlenz, F.; Xu, M.; Granz, T.; Bertke, M.; Wasisto, H.S.; Brand, U.; et al. Nanoindentation of crystalline silicon pillars fabricated by soft UV nanoimprint lithography and cryogenic deep reactive ion etching. *Sens. Actuators A* **2018**, *283*, 65–78. [CrossRef]
22. Hamdana, G.; Südkamp, T.; Descoins, M.; Mangelinck, D.; Caccamo, L.; Bertke, M.; Wasisto, H.S.; Bracht, H.; Peiner, E. Towards fabrication of 3D isotopically modulated vertical silicon nanowires in selective areas by nanosphere lithography. *Microelectron. Eng.* **2017**, *179*, 74–82. [CrossRef]
23. Mariana, S.; Gülink, J.; Hamdana, G.; Yu, F.; Stempel, K.; Spende, H.; Yulianto, N.; Granz, T.; Prades, J.D.; Peiner, E. Vertical GaN nanowires and nanoscale light-emitting-diode arrays for lighting and sensing applications. *ACS Appl. Nano Mater.* **2019**, *2*, 4133–4142. [CrossRef]
24. Feng, B.; Deng, J.; Lu, B.; Xu, C.; Wang, Y.; Wan, J.; Chen, Y. Nanofabrication of silicon nanowires with high aspect ratio for photo-electron sensing. *Microelectron. Eng.* **2018**, *195*, 139–144. [CrossRef]
25. Yulianto, N.; Refino, A.D.; Syring, A.; Majid, N.; Mariana, S.; Schnell, P.; Wahyuno, R.A.; Triyana, K.; Meierhofer, F.; Daum, W. Wafer-scale transfer route for top-down III-nitride nanowire LED arrays based on the femtosecond laser lift-off technique. *Microsyst. Nanoeng.* **2021**, *7*, 32. [CrossRef] [PubMed]
26. Shah, A.P.; Bhattacharya, A. Inductively coupled plasma reactive-ion etching of β -Ga₂O₃: Comprehensive investigation of plasma chemistry and temperature. *J. Vac. Sci. Technol. A Vac. Surf. Films* **2017**, *35*, 041301. [CrossRef]
27. Merzsch, S.; Steib, F.; Wasisto, H.; Stranz, A.; Hinze, P.; Weimann, T.; Peiner, E.; Waag, A. Production of vertical nanowire resonators by cryogenic-ICP-DRIE. *Microsyst. Technol.* **2014**, *20*, 759–767. [CrossRef]
28. Refino, A.D.; Yulianto, N.; Syamsu, I.; Nugroho, A.P.; Hawari, N.H.; Syring, A.; Kartini, E.; Iskandar, F.; Voss, T.; Sumboja, A.; et al. Versatilely tuned vertical silicon nanowire arrays by cryogenic reactive ion etching as a lithium-ion battery anode. *Sci. Rep.* **2021**, *11*, 19779. [CrossRef]
29. Yue, H.; Wang, S.; Yang, Z.; Li, Q.; Lin, S.; He, D. Ultra-thick porous films of graphene-encapsulated silicon nanoparticles as flexible anodes for lithium ion batteries. *Electrochim. Acta* **2015**, *174*, 688–695. [CrossRef]
30. Gao, S.; Sun, F.; Brady, A.; Pan, Y.; Erwin, A.; Yang, D.; Tsukruk, V.; Stack, A.G.; Saito, T.; Yang, H.; et al. Ultra-efficient polymer binder for silicon anode in high-capacity lithium-ion batteries. *Nano Energy* **2020**, *73*, 104804. [CrossRef]
31. Hansen, S.; Quiroga-González, E.; Carstensen, J.; Föll, H. Size-dependent cyclic voltammetry study of silicon microwire anodes for lithium ion batteries. *Electrochim. Acta* **2016**, *217*, 283–291. [CrossRef]
32. Zhu, J.; Wu, Y.; Huang, X.; Huang, L.; Cao, M.; Song, G.; Guo, X.; Sui, X.; Ren, R.; Chen, J. Self-healing liquid metal nanoparticles encapsulated in hollow carbon fibers as a free-standing anode for lithium-ion batteries. *Nano Energy* **2019**, *62*, 883–889. [CrossRef]

33. Youn, D.-Y.; Kim, C.; Cheong, J.Y.; Cho, S.-H.; Yoon, K.R.; Jung, J.-W.; Kim, N.-H.; Kim, I.-D. Stable and High-Capacity Si Electrodes with Free-Standing Architecture for Lithium-Ion Batteries. *ACS Appl. Energy Mater.* **2020**, *3*, 208–217. [CrossRef]
34. Zaidi, S.D.A.; Wang, C.; György, B.; Sun, C.; Yuan, H.; Tian, L.; Chen, J. Iron and silicon oxide doped/PAN-based carbon nanofibers as free-standing anode material for Li-ion batteries. *J. Colloid Interface Sci.* **2020**, *569*, 164–176. [CrossRef]
35. Lee, G.; Schweizer, S.L.; Wehrspohn, R.B. Electrochemical characteristics of plasma-etched black silicon as anodes for Li-ion batteries. *J. Vac. Sci. Technol. A* **2014**, *32*, 061202. [CrossRef]
36. Li, Z.; Chen, Y.; Zhu, X.; Zheng, M.; Dong, F.; Chen, P.; Xu, L.; Chu, W.; Duan, H. Fabrication of single-crystal silicon nanotubes with sub-10 nm walls using cryogenic inductively coupled plasma reactive ion etching. *Nanotechnology* **2016**, *27*, 365302. [CrossRef]
37. Bertini, S.; Verotti, M.; Bagolini, A.; Bellutti, P.; Ruta, G.; Belfiore, N.P. Scalping and stress concentration in DRIE-manufactured comb-drives. *Actuators* **2018**, *7*, 57. [CrossRef]
38. Mills, E.; Cannarella, J.; Zhang, Q.; Bhadra, S.; Arnold, C.B.; Chou, S.Y. Silicon nanopillar anodes for lithium-ion batteries using nanoimprint lithography with flexible molds. *J. Vac. Sci. Technol. B* **2014**, *32*, 06FG10. [CrossRef]
39. Chen, S.; Chen, Z.; Xu, X.; Cao, C.; Xia, M.; Luo, Y. Scalable 2D Mesoporous Silicon Nanosheets for High-Performance Lithium-Ion Battery Anode. *Small* **2018**, *14*, 1703361. [CrossRef]
40. Martha, R.; Nagaraja, H. Effect of current density and electrochemical cycling on physical properties of silicon nanowires as anode for lithium ion battery. *Mater. Charact.* **2017**, *129*, 24–30. [CrossRef]
41. Green, M.; Fielder, E.; Scrosati, B.; Wachtler, M.; Moreno, J.S. Structured Silicon Anodes for Lithium Battery Applications. *Electrochem. Solid-State Lett.* **2003**, *6*, A75. [CrossRef]
42. Roland, A.; Dupuy, A.; Machon, D.; Cunin, F.; Louvain, N.; Fraisse, B.; Boucherif, A.; Monconduit, L. In-depth study of annealed porous silicon: Understand the morphological properties effect on negative LiB electrode performance. *Electrochim. Acta* **2019**, *323*, 134758. [CrossRef]
43. Lau, D.; Hall, C.A.; Lim, S.; Yuwono, J.A.; Burr, P.A.; Song, N.; Lennon, A. Reduced Silicon Fragmentation in Lithium Ion Battery Anodes Using Electronic Doping Strategies. *ACS Appl. Energy Mater.* **2020**, *3*, 1730–1741. [CrossRef]
44. Li, H.; Yamaguchi, T.; Matsumoto, S.; Hoshikawa, H.; Kumagai, T.; Okamoto, N.L.; Ichitsubo, T. Circumventing huge volume strain in alloy anodes of lithium batteries. *Nat. Commun.* **2020**, *11*, 1584. [CrossRef]
45. Salah, M.; Murphy, P.; Hall, C.; Francis, C.; Kerr, R.; Fabretto, M. Pure silicon thin-film anodes for lithium-ion batteries: A review. *J. Power Sources* **2019**, *414*, 48–67. [CrossRef]
46. Chen, X.; Bi, Q.; Sajjad, M.; Wang, X.; Ren, Y.; Zhou, X.; Xu, W.; Liu, Z. One-dimensional porous silicon nanowires with large surface area for fast charge–discharge lithium-ion batteries. *Nanomaterials* **2018**, *8*, 285. [CrossRef]
47. Kim, S.J.; Naguib, M.; Zhao, M.; Zhang, C.; Jung, H.-T.; Barsoum, M.W.; Gogotsi, Y. High mass loading, binder-free MXene anodes for high areal capacity Li-ion batteries. *Electrochim. Acta* **2015**, *163*, 246–251. [CrossRef]
48. Yang, Y.; Yuan, W.; Kang, W.; Ye, Y.; Pan, Q.; Zhang, X.; Ke, Y.; Wang, C.; Qiu, Z.; Tang, Y. A review on silicon nanowire-based anodes for next-generation high-performance lithium-ion batteries from a material-based perspective. *Sustain. Energy Fuels* **2020**, *4*, 1577–1594. [CrossRef]
49. Jiang, T.; Xu, X.; Chen, G.Z. Silicon prepared by electro-reduction in molten salts as new energy materials. *J. Energy Chem.* **2020**, *47*, 46–61. [CrossRef]
50. Wang, X.; Li, G.; Seo, M.H.; Lui, G.; Hassan, F.M.; Feng, K.; Xiao, X.; Chen, Z. Carbon-Coated Silicon Nanowires on Carbon Fabric as Self-Supported Electrodes for Flexible Lithium-Ion Batteries. *ACS Appl. Mater. Interfaces* **2017**, *9*, 9551–9558. [CrossRef] [PubMed]
51. Schneier, D.; Harpak, N.; Menkin, S.; Davidi, G.; Goor, M.; Mados, E.; Ardel, G.; Patolsky, F.; Golodnitsky, D.; Peled, E. Analysis of scale-up parameters in 3D silicon-nanowire lithium-battery anodes. *J. Electrochem. Soc.* **2020**, *167*, 050511. [CrossRef]
52. Shen, T.; Xia, X.-h.; Xie, D.; Yao, Z.-j.; Zhong, Y.; Zhan, J.-y.; Wang, D.-h.; Wu, J.-b.; Wang, X.-l.; Tu, J.-p. Encapsulating silicon nanoparticles into mesoporous carbon forming pomegranate-structured microspheres as a high-performance anode for lithium ion batteries. *J. Mater. Chem. A* **2017**, *5*, 11197–11203. [CrossRef]
53. Yang, Y.; Yuan, W.; Kang, W.; Ye, Y.; Yuan, Y.; Qiu, Z.; Wang, C.; Zhang, X.; Ke, Y.; Tang, Y. Silicon-nanoparticle-based composites for advanced lithium-ion battery anodes. *Nanoscale* **2020**, *12*, 7461–7484. [CrossRef]
54. Chen, Q.; Zhang, C.; Lin, L.; Xie, Q.; Xu, W.; Qiu, Y.; Lin, J.; Wang, L.; Peng, D.-L. Electrochemically induced high ion and electron conductive interlayer in porous multilayer Si film anode with enhanced lithium storage properties. *J. Power Sources* **2021**, *481*, 228833. [CrossRef]
55. Campbell, B.; Ionescu, R.; Tolchin, M.; Ahmed, K.; Favors, Z.; Bozhilov, K.N.; Ozkan, C.S.; Ozkan, M. Carbon-Coated, Diatomite-Derived Nanosilicon as a High Rate Capable Li-ion Battery Anode. *Sci. Rep.* **2016**, *6*, 33050. [CrossRef] [PubMed]
56. Li, W.; Guo, X.; Geng, P.; Du, M.; Jing, Q.; Chen, X.; Zhang, G.; Li, H.; Xu, Q.; Braunstein, P.; et al. Rational Design and General Synthesis of Multimetallic Metal–Organic Framework Nano-Octahedra for Enhanced Li–S Battery. *Adv. Mater.* **2021**, *33*, 2105163. [CrossRef]
57. Guo, X.; Zheng, S.; Luo, Y.; Pang, H. Synthesis of confining cobalt nanoparticles within SiO_x/nitrogen-doped carbon framework derived from sustainable bamboo leaves as oxygen electrocatalysts for rechargeable Zn-air batteries. *Chem. Eng. J.* **2020**, *401*, 126005. [CrossRef]
58. Wu, B.; Lochala, J.; Taverne, T.; Xiao, J. The interplay between solid electrolyte interface (SEI) and dendritic lithium growth. *Nano Energy* **2017**, *40*, 34–41. [CrossRef]

59. Xu, Y.; Zhou, M.; Lei, Y. Nanoarchitected array electrodes for rechargeable lithium-and sodium-ion batteries. *Adv. Energy Mater.* **2016**, *6*, 1502514. [CrossRef]
60. Orazem, M.E.T.B. *Electrochemical Impedance Spectroscopy*; Wiley: Hoboken, NJ, USA, 2008.
61. Cho, J.-H.; Picraux, S.T. Silicon Nanowire Degradation and Stabilization during Lithium Cycling by SEI Layer Formation. *Nano Lett.* **2014**, *14*, 3088–3095. [CrossRef]



Article

Hydration Characteristics of Tricalcium Aluminate in the Presence of Nano-Silica

Dapeng Zheng^{1,2}, Manuel Monasterio¹ , Weipeng Feng¹, Waiching Tang³ , Hongzhi Cui^{1,*} and Zhijun Dong¹

- ¹ Key Laboratory for Resilient Infrastructures of Coastal Cities (Ministry of Education), Underground Polis Academy, College of Civil and Transportation Engineering, Shenzhen University, Shenzhen 518060, China; dpzheng2-C@my.cityu.edu.hk (D.Z.); microcanonico@gmail.com (M.M.); wp_feng@163.com (W.F.); dongzj@szit.edu.cn (Z.D.)
- ² Department of Architecture and Civil Engineering, City University of Hong Kong, Kowloon, Hong Kong 999077, China
- ³ School of Architecture and Built Environment, The University of Newcastle, Callaghan, NSW 2308, Australia; patrick.tang@newcastle.edu.au
- * Correspondence: h.z.cui@szu.edu.cn; Tel.: +86-755-26917849

Abstract: Tricalcium aluminate (C_3A) is the most reactive component of the Portland cement and its hydration has an important impact on the workability and early strength of concrete. Recently, nanomaterials such as nano-silica (nano- SiO_2) have attracted much attention in cement-based materials because of its pozzolanic reactivity and the pore-filling effect. However, its influence on the hydration of C_3A needs to be well understood. In this study, the hydration kinetics of C_3A mixed with different percentages of nano- SiO_2 were studied and compared with pure C_3A . The hydration products were examined by different characterization techniques including XRD, XPS, and NMR spectroscopy and isothermal calorimetry analyses. The XRD results showed that the addition of nano- SiO_2 promoted the conversion of the intermediate product C_4AH_{13} . The isothermal calorimetry results showed that the addition of nano- SiO_2 significantly reduced the hydration exotherm rate of C_3A from 0.34 to less than 0.1 mW/g. With the presence of nano- SiO_2 , the peaks for Q^1 were observed in ^{29}Si MAS-NMR measurements, and the content of Q^1 increased from 6.74% to 30.6% when the nano- SiO_2 content increased from 2 wt.% to 8 wt.%, whereas the proportion of Q^4 gradually decreased from 89.1% to 63.6%. These results indicated a pozzolanic reaction provoked by the nano- SiO_2 combined with aluminate structures generating C-A-S-H gel.

Keywords: nano-silica; tricalcium aluminate; pozzolanic reaction; C-A-S-H gel

Citation: Zheng, D.; Monasterio, M.; Feng, W.; Tang, W.; Cui, H.; Dong, Z. Hydration Characteristics of Tricalcium Aluminate in the Presence of Nano-Silica. *Nanomaterials* **2021**, *11*, 199. <https://doi.org/10.3390/nano11010199>

Received: 4 December 2020

Accepted: 12 January 2021

Published: 14 January 2021

Publisher's Note: MDPI stays neutral with regard to jurisdictional claims in published maps and institutional affiliations.



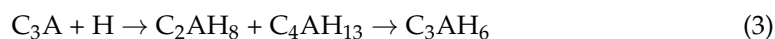
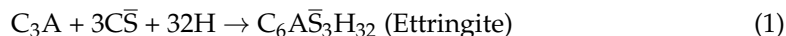
Copyright: © 2021 by the authors. Licensee MDPI, Basel, Switzerland. This article is an open access article distributed under the terms and conditions of the Creative Commons Attribution (CC BY) license (<https://creativecommons.org/licenses/by/4.0/>).

1. Introduction

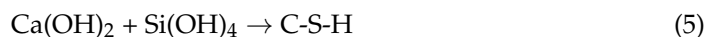
It is well known that the macroscopic properties of a cement-based material are a consequence of how the constituent particles are arranged and held together at micro- and nano-scales. Many studies have been using nanomaterials such as nano- SiO_2 , nano- Al_2O_3 , and nano- TiO_2 to improve the microstructure performance of cement-based materials [1,2]. However, most of them focused the impact of nanomaterials on the hydration of tricalcium silicate (C_3S) only [3], not on tricalcium aluminate (C_3A), which is the most intense hydration mineral component in cement. Though the typical proportion of C_3A in cement is only about 10 wt.% [4], it is the most reactive component of the Portland cement.

C_3A , together with alite (C_3S), belite (C_2S), and ferrite (C_4AF), are the main components of cement. Compared to C_3S , the hydration of C_3A is significantly faster, forming calcium hydroaluminates and other phases such as calcium hydroaluminate-ferrite, commonly called AFm [5]. However, the fast reaction, often named “flash setting” [6], will reduce the workability and strength of the final products, which is usually avoided by adding gypsum [4,5]. The sulfate in gypsum binds C_3A , generating sulfoaluminates

instead of calcium hydroaluminates [7]. The reactions of C_3A with and without calcium sulfate are expressed as Equations (1)–(3) (in cement notation) [8,9]:



It is well-known that nano-SiO₂ in cement can increase the density of the C-S-H gel and decrease the final porosity of the hydrated products [10,11]. Besides, it can reduce the amount of calcium hydroxide formation, as well as the setting time [12,13], and thus increase the hydration degree of cement [14,15] to obtain the best mechanical performance. All the above-mentioned advantages are achieved through the three mechanisms of nano-SiO₂: The nucleation reaction, pozzolanic effect, and pore-filling effect. Nano-SiO₂ can act as a nucleation site for C-S-H seeds, accelerating cement hydration. At the same time, nano-SiO₂ particles can generate C-S-H gel by undertaking pozzolanic reaction that further intensifies the growth of C-S-H gels in the matrix and consequently increases the final density [16,17]. The pozzolanic reaction is the reaction between nano-SiO₂ and calcium hydroxide, which allows the generation of C-S-H gel as expressed in Equations (4) and (5). In addition, the nano-SiO₂ particles can fill up micro-pores to reduce the overall porosity of the final products [18,19].



However, to our knowledge, research about the effect of nano-SiO₂ on C_3A hydration remains limited. A few works in the literature postulate that the pozzolanic reaction of nano-SiO₂ in a high-aluminum environment may generate C-A-S-H gel, similar to C-S-H gel, where some of the silicon tetrahedrons could be replaced by aluminum [20,21]. The main objective of this research is to study the effects of nano-SiO₂ on the hydration of C_3A and its hydrated products. It is worth noting that the Al/Si ratio used in this study was much higher than previous studies as the aluminum was not the substitute element [22].

In this research, X-ray diffraction (XRD) was used to determine the final hydration products of C_3A with different contents of nano-SiO₂. Besides, the isothermal calorimetry was chosen to examine the intensity and speed of different amounts of nano-SiO₂ on the heat flow of C_3A hydration. An X-ray photoelectron spectrometer (XPS) and nuclear magnetic resonance (NMR) were used to reveal the microstructure of the hydrated products. It is believed that the findings of this study can help to prove the existence of the C-A-S-H gel and other alterations in the hydration products of C_3A with different contents of nano-SiO₂.

2. Materials and Methods

2.1. Materials

The C_3A with a purity of 99 wt.%, employed in this experiment, was purchased from a company in Shanghai. The nano-SiO₂ with a purity of 99.5 wt.% and an average particle size of 15 ± 5 nm was provided by Shanghai Macklin Biochemical Co., Ltd. Figure 1a shows the XRD pattern of the pure C_3A with high and well-defined peaks, which proved to be cubic C_3A according to PDF#38-1429. In addition, the SEM image in Figure 1b shows that the size of the pure C_3A particle is about 10 μ m. On the other hand, as seen in Figure 1c, the curve of pure nano-SiO₂ shows a hump at 20–25°, indicating that the nano-SiO₂ used in this study had noncrystallinity and high activity [23]. Therefore, XRD analysis can confirm that both nano-SiO₂ and pure C_3A were of high purity. Although the nano-SiO₂ nanoparticles tended to agglomerate, an average size of about 10 nm could be measured from the TEM image, as shown in Figure 1d.

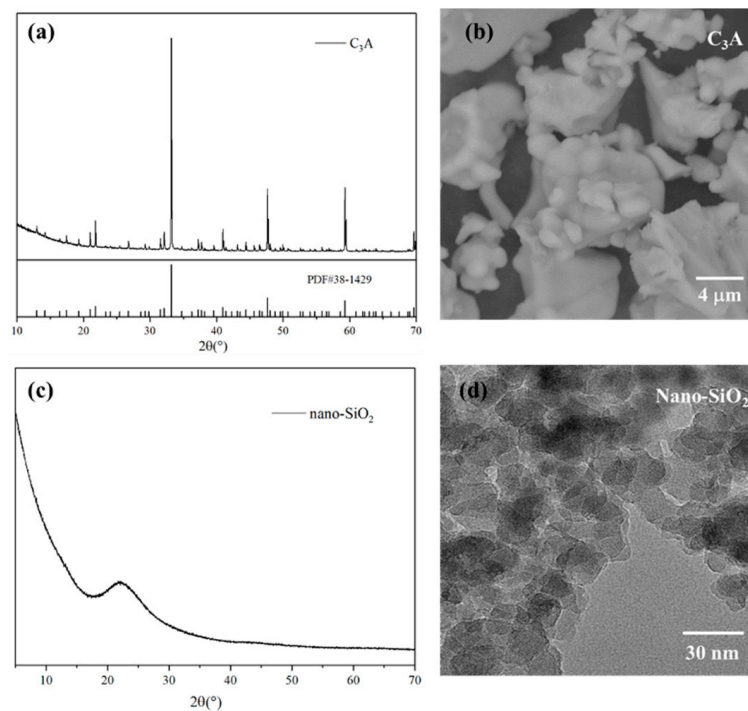


Figure 1. Mineral composition and particle characteristics of pure C_3A and nano- SiO_2 measured by (a) XRD diffraction pattern of pure C_3A ; (b) SEM photograph of C_3A ; (c) XRD diffraction pattern of nano- SiO_2 ; (d) TEM photograph of nano- SiO_2 .

2.2. Sample Preparation

In this study, five mixes of pure C_3A with different nano- SiO_2 contents (0, 2, 4, 6, and 8 wt.%) were prepared as indicated in Table 1. The samples were prepared through the following procedures: Initially, the specific amounts of C_3A and nano- SiO_2 in powder form were weighed and premixed. Then, the mixture was placed in a glass flask filled with deionized water and mixed continuously by a magnetic stirrer for 72 h. The speed of stirring was 800 rpm and the liquid-to-solid ratio (L/S) was kept constant at 50. It is worth emphasizing that the glass flask was always filled with nitrogen during the 72 h hydration process to prevent possible carbonization and impurities in the air. After 72 h, the samples were removed from the stirring platform and filtered using a 7 cm filter paper and a suction filter glass. Then, the samples were placed into a vacuum oven and allowed to dry for 7 days at a temperature of 40 °C. The dried samples were kept sealed for later testing.

Table 1. Proportion of different components used during the preparation of the samples.

Sample Name	C_3A (g)	Nano- SiO_2 (g)	Water (g)	L/S
Pure C_3A	1	0	50	50
C_3A -2 wt.% nano SiO_2	1	0.02	51	50
C_3A -4 wt.% nano SiO_2	1	0.04	52	50
C_3A -6 wt.% nano SiO_2	1	0.06	53	50
C_3A -8 wt.% nano SiO_2	1	0.08	54	50

2.3. Methods

X-ray diffraction (XRD, D8 Advance, Bruker, Germany) was used to determine the mineralogical composition of raw materials and hydration products of C_3A (with and without nano- SiO_2). A scanning rate of 0.08 °/s from 5° to 70° with Cu $K\alpha$ radiation ($\lambda = 1.5418 \text{ \AA}$) was used, as well as a screen to prevent high background at small degrees.

Transmission Electron Microscopy (TEM, TALOS F200X, Thermo Fisher Scientific, Waltham, Massachusetts, USA) and Scanning Electron Microscopy (SEM, TM 250 FEG,

Thermo Fisher Scientific, Waltham, Massachusetts, USA) were employed to determine the particle characteristics of the raw samples.

A Thermal Activity Monitor (TAM-AIR, TA Instruments, New Castle, Delaware, USA), equipment for isothermal calorimetry, was employed to analyze the heat flow produced during the hydration of the samples. The samples were prepared using 0.5 g of C_3A and the corresponding percentages of nano- SiO_2 with a water-to-solid ratio of 5. Prior to the hydration process, the samples in powder form were kept inside the device for 3–4 h until the calorimeter was stabilized. Then, the distilled water was added and the mixtures were stirred for 30 s to begin the hydration.

The solid-state Nuclear Magnetic Resonance (MAS-NMR, JEOL-600, Japan) technique was used in two different modes. The first mode was ^{29}Si MAS-NMR that employed single-pulse decoupling including 1024 scans with a relaxation delay of 60 s. The probe was 8 mm in diameter and the spinning speed was 5000 rpm. The second mode was ^{27}Al MAS-NMR, a single pulse with 1000 scans, and 10 s of relaxation time. The probe was 3.2 mm in diameter and the spinning speed was 12,000 rpm. The references used to calibrate the peaks were TSPA and AlK (SO_4) for ^{29}Si and ^{27}Al , respectively.

The X-ray photoelectron spectrometer (XPS, Thermo escalab XI+) was employed to verify the molecular structure of the hydration products and record the measurements with a monochromatic Al $K\alpha$ ($h\nu = 1486.6$ eV) X-ray source, employing a flare area of $650 \mu m$, calibrated by 284.8 eV C1s. A constant analyzer pass energy of 20 eV was applied.

3. Results and Discussion

3.1. Mineral Composition Analysis

The XRD analysis of the hydrated samples can be seen in Figure 2. In agreement with the literature [24,25], the majority of the peaks found in the results were related to Katoite (written as $Ca_3Al_2(OH)_{12}$ or C_3AH_6), which is one of the final forms of the C_3A hydration, indicating a good reaction process of C_3A . Another peak at 11.5° found in all the samples was related to C_4AH_{13} , which is an intermediate form during the hydration of C_3A . The small peak at 47.5° was only found in the hydration products of pure C_3A , which may be related to the carbonation of C_3A hydration products. Besides, another peak at 33.2° is associated with anhydrate C_3A , indicating that the hydration of pure C_3A was incomplete. The intensity of this peak was reduced after adding 2 wt.% of nano- SiO_2 and even smaller when the nano- SiO_2 content increased to 4 wt.%. Furthermore, this peak disappeared completely in the samples of C_3A with 6 wt.% and 8 wt.% nano- SiO_2 . This result substantiates the promotion effect of nano- SiO_2 on the hydration process of C_3A .

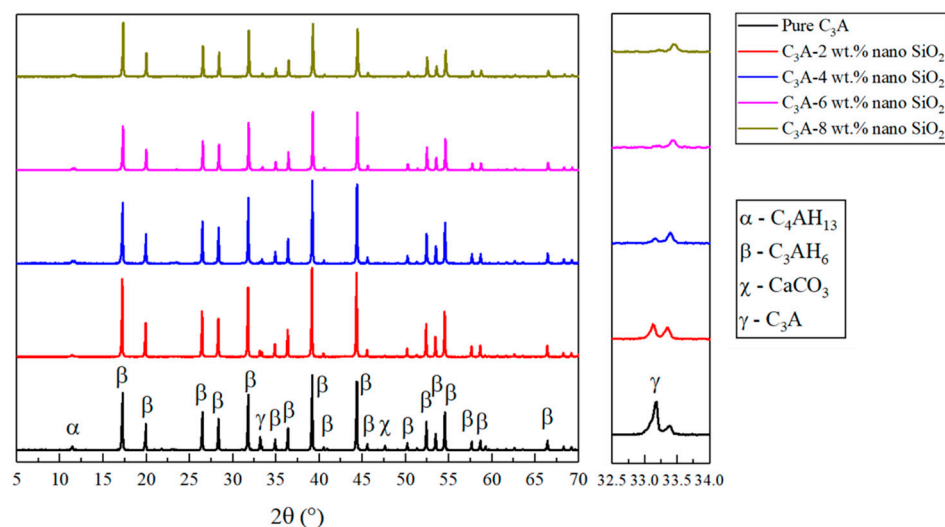


Figure 2. XRD analysis of all the samples to observe the evolution of peaks related to the hydration of the samples.

3.2. Hydration Exothermic Analysis

The effect of nano-SiO₂ on the hydration heat release rate of C₃A was studied using the isothermal calorimetry, and the results can be seen in Figure 3. De Jong et al. [26] previously found a second exothermic peak observed in the C₃A hydration process after adding amorphous silica, which appeared in the first hours of hydration but being at later stage when the amorphous silica content increased. However, as shown in Figure 3a, this study showed different results. It can be seen from Figure 3b that the pure C₃A sample showed the highest reactivity and the peak in hydration heat release rate occurred at 420 s. When 2 wt.% nano-SiO₂ was added to the C₃A hydration system, the hydration heat release rate of C₃A was greatly reduced from 0.34 to less than 0.1 mW/g. The hydration rate can be further reduced with increasing nano-SiO₂ content, but the significance is not obvious. With 2 wt.% nano-SiO₂, the hydration exothermic peak was delayed by more than 2 min. In addition, a further delay was noted with the increase in the nano-SiO₂ content. Xu et al. [3] stated that the addition of nano-SiO₂ will accelerate the rate of heat release in the early stage of C₃S hydration. However, the opposite phenomenon occurred during the C₃A hydration process. The reduction in heat release can be attributed to two reasons: (1) The hydration reaction rate of C₃A was much higher than that of C₃S, and the surface of the C₃A particles was adsorbed with a large amount of nano-SiO₂ with high specific surface area, which would reduce the contact area between C₃A and water, thus slowing down the reaction rate [27]; (2) the surface of C₃A particles was covered by the C-A-S-H gels (generated by the pozzolanic reaction of nano-SiO₂ combined with C₃A), thereby reducing the reaction rate. This is consistent with the phenomenon that the appearance time of the C₃A hydration exothermic peak continuously delayed as the amount of nano-SiO₂ increased. Hou et al. [28] explored the influence of nano-SiO₂ on the hydration process of C₃A-gypsum and C₃A-C₃S-gypsum systems, and obtained similar conclusions. They believed that the nano-SiO₂ adsorbed on the surface of C₃A due to the electrostatic effect is the reason for the delayed hydration. At the same time, the C-S-H gel generated by the pozzolanic effect of nano-SiO₂ can cover the surface of C₃A, which will also inhibit the hydration heat release rate of C₃A.

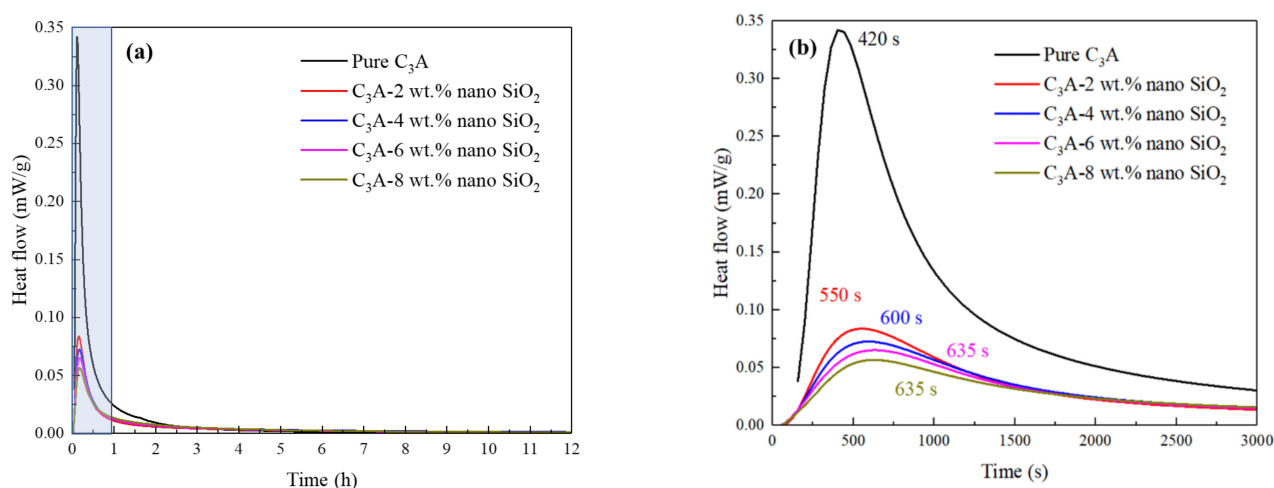


Figure 3. Heat flow rate of C₃A samples with different nano-SiO₂ contents in (a) 12 h (the blue area is enlarged and displayed as (b)) and (b) 3000 s (50 min). The number in (b) is the time needed to reach the maximum heat flow rate, in seconds.

3.3. X-ray Photoelectron Spectroscopy Results

The XPS was performed to analyze the binding energies of Al 2p and Si 2p in the hydration products of C₃A with different nano-SiO₂ contents. For Al 2p, previous work has indicated that the binding energy of octahedral coordinated aluminum is generally higher than that of the tetrahedral form [29]. It can be seen from Figure 4a that the Al

2p binding energy of the pure C_3A hydration products was around 74.1 eV, which can be related to C_3AH_6 [30,31]. All the samples containing nano SiO_2 , except C_3A -8 wt.%, gave similar results showing a unique peak around 74.1 eV. The sample of C_3A with 8 wt.% nano- SiO_2 presented a peak around 74.3 eV. It can be inferred that the amount of 8 wt.% nano- SiO_2 was enough to influence the binding energy of C_3A hydration products. It also indicated that the reaction between nano- SiO_2 and C_3A could create an Al-O-Si bond as Al would migrate to Si due to its high electronegativity, thus increasing the Al 2p binding energy [32]. On the other hand, the binding energy of Si 2p in all hydration products is shown in Figure 4b. It can be seen from the figure that the Si 2p binding energy of pure nano- SiO_2 is 103.6 eV, while the Si 2p binding energy of C_3A with 2 wt.% nano- SiO_2 , however, showed a very low intensity, almost being a plateau. This phenomenon indicates that there is Al element insertion in the silicon chain, which leads to a substantial decrease in Si 2p binding energy. Besides, the Si 2p binding energy rebounded with the amount of nano- SiO_2 increased. When the nano- SiO_2 content increased to 4 wt.%, 6 wt.%, and 8 wt.%, the Si 2p binding energy rebounded to 101.8, 101.9, and 102.3 eV, respectively, and the peaks became more obvious. This phenomenon could prove the formation of Al-O-Si bonds when nano- SiO_2 was added to C_3A . Overall, the Si 2p results are consistent with the Al 2p binding energy results, and are in good agreement with the previous findings [33,34].

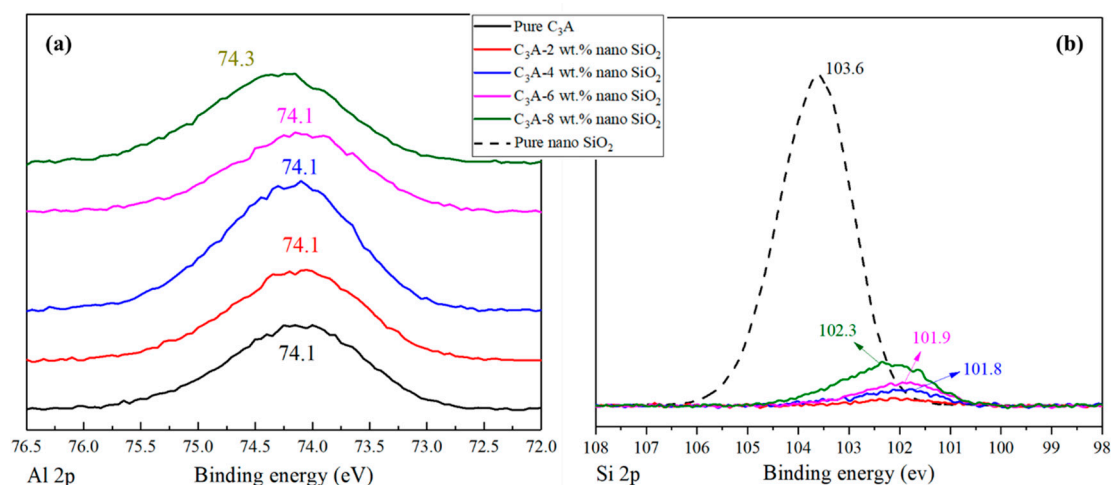


Figure 4. XPS results of (a) Al 2p and (b) Si 2p for hydration products of pure C_3A and C_3A with different nano SiO_2 contents.

3.4. Structural Changes Observed by Nuclear Magnetic Resonance

The NMR spectroscopy was performed with the intention of finding relevant information to prove a possible alteration in the hydration products structures brought by nano- SiO_2 [35]. Figure 5 shows the ^{29}Si and ^{27}Al MAS-NMR results of all samples, in order to reveal the effect of nano- SiO_2 on the structure of C_3A hydration products. As shown in Figure 5a, all the hydration samples showed similar ^{27}Al MAS-NMR results with a unique peak at 12.18 ppm, which is related to the octahedral aluminum configuration in the C_3AH_6 component [8,36,37]. The absence of any shift in the peak can lead to the conclusion that the presence of nano- SiO_2 would not alter the original structure formed by the C_3A hydration [35].

However, the ^{29}Si MAS-NMR results shown in Figure 5b are different from the ^{27}Al MAS-NMR results. The peaks were labeled as Q^n , where “n” is the number of similar tetrahedrons connected in the molecule. For example, Q^0 refers to a silicon tetrahedral configuration completely insulated to other silicon, whereas Q^2 refers to a silicon tetrahedral configuration connected with another two silicon tetrahedrons, forming a chain of silicon, as illustrated in Figure 6. According to the ^{29}Si MAS-NMR results, the two peaks observed around -79.2 and -112.5 ppm were Q^1 and Q^4 , respectively. In this context, Q^1 implies the existence of a silicon tetrahedron in the final position of a chain [38–41]. Sometimes,

this peak is found in a more negative value (around -81 ppm) [39,42]. This chemical shift is in agreement with the presence of aluminum in the environment of silicon tetrahedra to reach more positive ppm values [42,43]. This is a good indicator of the generation of dimers, combining silicon and aluminum tetrahedra. The intensity of this peak grew considerably with nano-SiO₂ content, owing to the larger amount of dimers generated within the structure. The peak Q⁴ refers to the presence of a “three-dimensional” net of silicon tetrahedra in the sample [44,45], and is strongly related to nano-SiO₂ [23,46]. In the Q¹ peak, there is a shift to more positive values due to the presence of aluminum within the close environment of the silicon tetrahedron. Additionally, new peaks were found in some of the samples. The Q⁰ peak appeared in hydration products of C₃A with 6 wt.% and 8 wt.% nano SiO₂, which is associated with silicon tetrahedra completely insolated. Due to this peak only being found in samples with a high percentage of nano-SiO₂, this could imply that some silicon ions from the dissolution of the nano-SiO₂ were not integrated into the C-A-S-H structure.

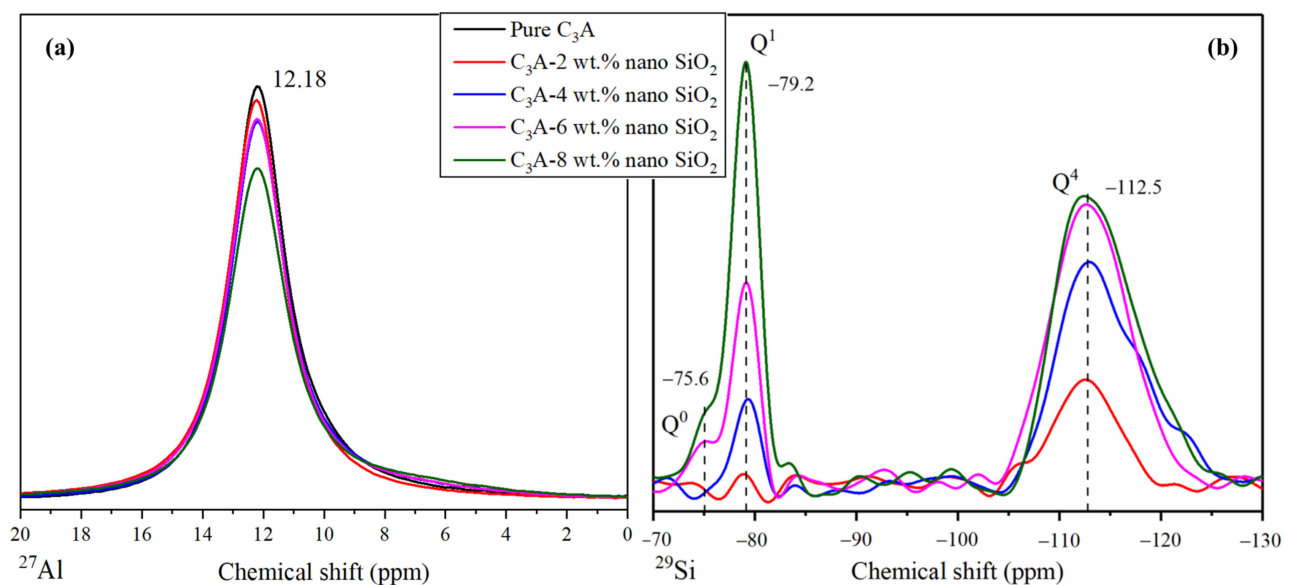


Figure 5. MAS-NMR signal obtained for (a) ²⁷Al and (b) ²⁹Si. ²⁹Si measurement shows a large number of peaks; meanwhile, ²⁷Al shows one peak uniquely.

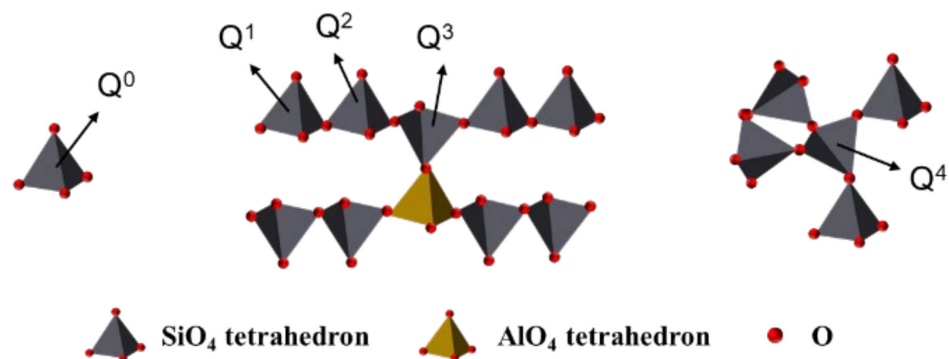


Figure 6. Silicon chain structure in C-S-H gel.

The percentages of different Qⁿ peaks obtained by Gaussian deconvolution are shown in Figure 7. It is quite clear to show that the existence of Q⁰ depends on nano-SiO₂ content. On the other hand, the proportion of Q¹ increased rapidly from 6.74% to 30.6% when the amount of nano-SiO₂ increased from 2 wt.% to 8 wt.%. However, the proportion of

Q^4 gradually decreased from 89.1% to 63.6% correspondingly. This finding implies that the higher the nano-SiO₂ content, the more silicon dimers in hydration products can be formed. Additionally, the positions of the Q^4 peaks were slightly shifted to more negative values from -112.63 to -113.53 ppm as the nano-SiO₂ content increased from 2 to 8 wt.%. This observation is in agreement with the trend of the position of the pure nano-SiO₂ Q^4 peak, around -115 ppm [23]. In addition, not all the silicon tetrahedra would be influenced by aluminum with a high content of nano-SiO₂, and the shift to more positive values created by the aluminum would become weaker.

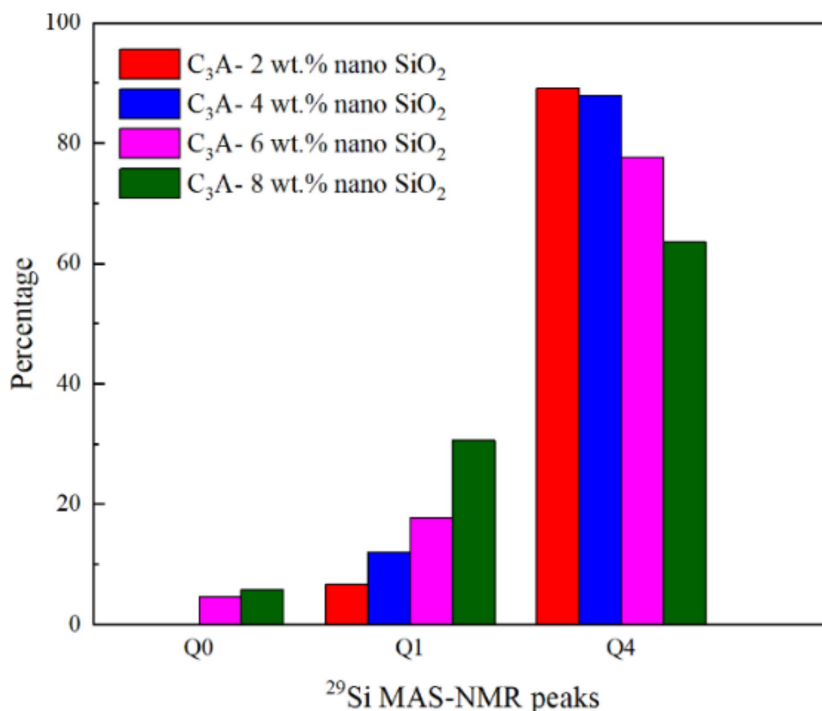


Figure 7. Percentages of different Q^n peaks, calculated by Gaussian deconvolution from the ^{29}Si MAS-NMR measurements.

Owing to the C-A-S-H gel being amorphous, its presence can only be revealed by the apparition of the Q^1 ^{29}Si MAS NMR peak and the shifted Q^4 to more positive values under the influence of aluminum. Based on the findings from this study, it is safe to say that nano-SiO₂ can promote the apparition of C-A-S-H gel in the final hydration products of C₃A, besides the C₃AH₆ structure.

4. Conclusions and Recommendations

This study examined the effect of nano-SiO₂ on the hydration of C₃A in cement. According to the test results, the following conclusions are drawn:

- (1) The addition of nano-SiO₂ can promote the hydration degree of C₃A while significantly reducing the heat release rate of C₃A hydration from 0.34 to less than 0.1 mW/g, and the occurrence time of the hydration exothermic peak was delayed by more than 2 min. The main reasons are probably the surface of C₃A being adsorbed by nano-SiO₂ and/or covered by the C-A-S-H gel (formed by the pozzolanic hydration reaction of nano-SiO₂ and C₃A) at an early age, thereby reducing the contact area of C₃A with water.
- (2) The reaction between nano-SiO₂ and C₃A can establish Si-O-Al bonds and generate C-A-S-H gels. The chemical shifts in Al 2p and Si 2p both confirm this conclusion. In addition, ^{29}Si MAS-NMR results showed that Q^1 appeared after the nano-SiO₂ was added to the C₃A hydration system. With the nano-SiO₂ content increased,

the proportion of Q^1 in the hydration product increased from 6.74% to 30.6%, while the proportion of Q^4 gradually decreased from 89.1% to 63.6%.

- (3) The addition of nano-silica can promote the hydration reaction rate of C_3S while delaying the hydration of C_3A . For the two hydration systems of C_3A and C_3S , the addition of nano- SiO_2 has shown completely different effects, and the influence mechanism of nano- SiO_2 in the two different hydration processes needs further exploration.

Author Contributions: D.Z.: Methodology, data analysis, writing; M.M.: Experiments, data and image processing, writing; W.F.: Tests; W.T.: Language correction; H.C.: Research plan formulation, draft reviewing; Z.D.: Draft reviewing and editing. All authors have read and agreed to the published version of the manuscript.

Funding: Nature Science Foundation of China (Grant No: 51708363) and National Key Research and Development Program of China (2019YFC1907203).

Data Availability Statement: Data is contained within the article.

Acknowledgments: The authors gratefully acknowledge the financial supports of the National Nature Science Foundation of China (Grant No: 51708363) and National Key Research and Development Program of China (2019YFC1907203).

Conflicts of Interest: The authors declare no conflict of interest.

Abbreviations

C_3A	Tricalcium aluminate
C_3S	Tricalcium silicate, alite
C_2S	Dicalcium silicate, belite
C_4AF	Tetracalcium aluminate, ferrite
CS	Calcium sulfate, $CaSO_4$
C-S-H	Calcium silicate hydrate
C-A-S-H	Calcium silicoaluminate hydrate
$C_6A\bar{S}_3H_{32}$, Aft	Ettringite
$3C_4A\bar{S}H_{12}$, AFm	Monosulfate
$Ca_3Al_2(OH)_{12}$, or C_3AH_6	Calcium aluminium hydrate
C_4AH_{13}/C_2AH_8	Calcium aluminium hydrate

References

- Li, H.; Du, T.; Xiao, H.; Zhang, Q. Crystallization of calcium silicate hydrates on the surface of nanomaterials. *J. Am. Ceram. Soc.* **2017**, *100*, 3227–3238. [CrossRef]
- Borrmann, T.; Johnston, J.H.; McFarlane, A.J.; Richardson, M.J.; O'Connor, S.J. Nano-structured calcium silicate hydrate functionalised with iodine. *J. Colloid Interface Sci.* **2009**, *339*, 175–182. [CrossRef] [PubMed]
- Xu, Z.; Zhou, Z.; Du, P.; Cheng, X. Effects of nano-silica on hydration properties of tricalcium silicate. *Constr. Build. Mater.* **2016**, *125*, 1169–1177. [CrossRef]
- Hewlett, P.; Liska, M. *Lea's Chemistry of Cement and Concrete*; Butterworth-Heinemann: Oxford, UK, 2019.
- Quennoz, A.; Scrivener, K.L. Hydration of C_3A -gypsum systems. *Cem. Concr. Res.* **2012**, *42*, 1032–1041. [CrossRef]
- Maier, A.-K.; Dezmirean, L.; Will, J.; Greil, P. Three-dimensional printing of flash-setting calcium aluminate cement. *J. Mater. Sci.* **2011**, *46*, 2947–2954. [CrossRef]
- Manzano, H.; Dolado, J.S.; Ayuela, A. Structural, mechanical, and reactivity properties of tricalcium aluminate using first-principles calculations. *J. Am. Ceram. Soc.* **2009**, *92*, 897–902. [CrossRef]
- Skibsted, J.; Henderson, E.; Jakobsen, H.J. Characterization of calcium aluminate phases in cements by aluminum-27 MAS NMR spectroscopy. *Inorg. Chem.* **1993**, *32*, 1013–1027. [CrossRef]
- Gismera-Diez, S.; Manchobas-Pantoja, B.; Carmona-Quiroga, P.M.; Blanco-Varela, M. Effect of $BaCO_3$ on C_3A hydration. *Cem. Concr. Res.* **2015**, *73*, 70–78. [CrossRef]
- Nunes, C.; Sližková, Z.; Stefanidou, M.; Němeček, J. Microstructure of lime and lime-pozzolana pastes with nanosilica. *Cem. Concr. Res.* **2016**, *83*, 152–163. [CrossRef]
- Singh, L.; Ali, D.; Sharma, U. Studies on optimization of silica nanoparticles dosage in cementitious system. *Cem. Concr. Compos.* **2016**, *70*, 60–68. [CrossRef]

12. Chen, Y.; Deng, Y.-F.; Li, M.-Q. Influence of nano-SiO₂ on the consistency, setting time, early-age strength, and shrinkage of composite cement pastes. *Adv. Mater. Sci. Eng.* **2016**, *1*, 1–8.
13. Shih, J.-Y.; Chang, T.-P.; Hsiao, T.-C. Effect of nanosilica on characterization of Portland cement composite. *Mater. Sci. Eng. A* **2006**, *424*, 266–274. [CrossRef]
14. Gu, Y.; Ran, Q.; Shu, X.; Yu, C.; Chang, H.; Liu, J. Synthesis of nanoSiO₂@PCE core-shell nanoparticles and its effect on cement hydration at early age. *Constr. Build. Mater.* **2016**, *114*, 673–680. [CrossRef]
15. Wu, Z.; Shi, C.; Khayat, K.H.; Wan, S. Effects of different nanomaterials on hardening and performance of ultra-high strength concrete (UHSC). *Cem. Concr. Compos.* **2016**, *70*, 24–34. [CrossRef]
16. Wu, Z.-Q.; Young, J. The hydration of tricalcium silicate in the presence of colloidal silica. *J. Mater. Sci.* **1984**, *19*, 3477–3486. [CrossRef]
17. Singh, L.; Bhattacharyya, S.; Shah, S.P.; Mishra, G.; Ahalawat, S.; Sharma, U. Studies on early stage hydration of tricalcium silicate incorporating silica nanoparticles: Part I. *Constr. Build. Mater.* **2015**, *74*, 278–286. [CrossRef]
18. Bentz, D.P.; Hansen, A.S.; Guynn, J.M. Optimization of cement and fly ash particle sizes to produce sustainable concretes. *Cem. Concr. Compos.* **2011**, *33*, 824–831. [CrossRef]
19. Kong, D.; Corr, D.J.; Hou, P.; Yang, Y.; Shah, S.P. Influence of colloidal silica sol on fresh properties of cement paste as compared to nano-silica powder with agglomerates in micron-scale. *Cem. Concr. Compos.* **2015**, *63*, 30–41. [CrossRef]
20. Puertas, F.; Palacios, M.; Manzano, H.; Dolado, J.; Rico, A.; Rodríguez, J. A model for the CASH gel formed in alkali-activated slag cements. *J. Eur. Ceram. Soc.* **2011**, *31*, 2043–2056. [CrossRef]
21. Garcia-Lodeiro, I.; Palomo, A.; Fernández-Jiménez, A.; Macphee, D. Compatibility studies between NASH and CASH gels. Study in the ternary diagram Na₂O–CaO–Al₂O₃–SiO₂–H₂O. *Cem. Concr. Res.* **2011**, *41*, 923–931. [CrossRef]
22. Pardal, X.; Pochard, I.; Nonat, A. Experimental study of Si–Al substitution in calcium-silicate-hydrate (CSH) prepared under equilibrium conditions. *Cem. Concr. Res.* **2009**, *39*, 637–643. [CrossRef]
23. Singh, L.; Bhattacharyya, S.; Mishra, G.; Ahalawat, S. Reduction of calcium leaching in cement hydration process using nanomaterials. *Mater. Technol.* **2012**, *27*, 233–238. [CrossRef]
24. Lin, T.T.; Lin, C.F.; Wei, W.C.J. Mechanisms of metal stabilization in cementitious matrix: Interaction of dicalcium silicate (C₂S) paste and copper oxide. *Toxicol. Environ. Chem.* **1994**, *43*, 51–62. [CrossRef]
25. Myers, R.J.; Geng, G.; Rodriguez, E.D.; da Rosa, P.; Kirchheim, A.P.; Monteiro, P.J. Solution chemistry of cubic and orthorhombic tricalcium aluminate hydration. *Cem. Concr. Res.* **2017**, *100*, 176–185. [CrossRef]
26. De Jong, J.; Stein, H.; Stevels, J. Influence of amorphous silica on the hydration of tricalcium aluminate. *J. Appl. Chem.* **1969**, *19*, 25–28. [CrossRef]
27. Hou, P.; Wang, X.; Cheng, X. Effects of nanosilica on C₃A hydration. In Proceedings of the 73rd RILEM Annual Week & the International Conference on Innovative Materials for Sustainable Civil Engineering, Nanjing, China, 25–30 August 2019; p. 119.
28. Hou, P.; Wang, X.; Zhao, P.; Wang, K.; Kawashima, S.; Li, Q.; Xie, N.; Cheng, X.; Shah, S.P. Physicochemical effects of nanosilica on C₃A/C₃S hydration. *J. Am. Ceram. Soc.* **2020**, *103*, 6505–6518. [CrossRef]
29. Barr, T. ESCA studies of the coordination state of aluminium in oxide environments. *J. Chem. Soc. Faraday Trans.* **1997**, *93*, 181–186. [CrossRef]
30. Dubina, E.; Plank, J.; Black, L. Impact of water vapour and carbon dioxide on surface composition of C₃A polymorphs studied by X-ray photoelectron spectroscopy. *Cem. Concr. Res.* **2015**, *73*, 36–41. [CrossRef]
31. Dubina, E.; Black, L.; Sieber, R.; Plank, J. Interaction of water vapour with anhydrous cement minerals. *Adv. Appl. Ceram.* **2010**, *109*, 260–268. [CrossRef]
32. Li, J.; Liu, Y.; Wang, Y.; Wang, W.; Wang, D.; Qi, T. Hydrous alumina/silica double-layer surface coating of TiO₂ pigment. *Colloids Surf. A Physicochem. Eng. Asp.* **2012**, *407*, 77–84. [CrossRef]
33. Barr, T.; Hoppe, E.; Hardcastle, S.; Seal, S. X-ray photoelectron spectroscopy investigations of the chemistries of soils. *J. Vac. Sci. Technol. A Vac. Surf. Film.* **1999**, *17*, 1079–1085. [CrossRef]
34. Seyama, H.; Soma, M. Bonding-state characterization of the constituent elements of silicate minerals by X-ray photoelectron spectroscopy. *J. Chem. Soc. Faraday Trans. 1 Phys. Chem. Condens. Phases* **1985**, *81*, 485–495. [CrossRef]
35. Pardal, X.; Brunet, F.; Charpentier, T.; Pochard, I.; Nonat, A. ²⁷Al and ²⁹Si solid-state NMR characterization of calcium-aluminosilicate-hydrate. *Inorg. Chem.* **2012**, *51*, 1827–1836. [CrossRef] [PubMed]
36. Woessner, D.E. Characterization of clay minerals by ²⁷Al nuclear magnetic resonance spectroscopy. *Am. Mineral.* **1989**, *74*, 203–215.
37. Slade, R.; Southern, J.; Thompson, I. ²⁷Al Nuclear magnetic resonance spectroscopy investigation of thermal transformation sequences of alumina hydrate. PT. 1. GIBBSITE, GAMMA-Al(OH)₃. *J. Mater. Chem.* **1991**, *1*, 563–568. [CrossRef]
38. Monasterio, M.; Gaitero, J.J.; Erkizia, E.; Bustos, A.M.G.; Miccio, L.A.; Dolado, J.S.; Cervený, S. Effect of addition of silica-and amine functionalized silica-nanoparticles on the microstructure of calcium silicate hydrate (C–S–H) gel. *J. Colloid Interface Sci.* **2015**, *450*, 109–118. [CrossRef]
39. Yang, H.; Monasterio, M.; Cui, H.; Han, N. Experimental study of the effects of graphene oxide on microstructure and properties of cement paste composite. *Compos. Part A Appl. Sci. Manuf.* **2017**, *102*, 263–272. [CrossRef]
40. Klur, I.; Pollet, B.; Virlet, J.; Nonat, A. CSH structure evolution with calcium content by multinuclear NMR. In *Nuclear Magnetic Resonance Spectroscopy of Cement-Based Materials*; Springer: Berlin, Germany, 1998; pp. 119–141.

41. Richardson, I.G. The calcium silicate hydrates. *Cem. Concr. Res.* **2008**, *38*, 137–158. [CrossRef]
42. Richardson, I.; Brough, A.; Groves, G.; Dobson, C. The characterization of hardened alkali-activated blast-furnace slag pastes and the nature of the calcium silicate hydrate (CSH) phase. *Cem. Concr. Res.* **1994**, *24*, 813–829. [CrossRef]
43. Schilling, P.J.; Butler, L.G.; Roy, A.; Eaton, H.C. ²⁹Si and ²⁷Al MAS-NMR of NaOH-activated blast-furnace slag. *J. Am. Ceram. Soc.* **1994**, *77*, 2363–2368. [CrossRef]
44. Škvára, F.; Jílek, T.; Kopecký, L. Geopolymer materials based on fly ash. *Ceram. Silik.* **2005**, *49*, 195–204.
45. Justnes, H.; Meland, I.; Bjoergum, J.; Krane, J.; Skjetne, T. Nuclear magnetic resonance (NMR)—A powerful tool in cement and concrete research. *Adv. Cem. Res.* **1990**, *3*, 105–110. [CrossRef]
46. Gaitero, J.J.; Campillo, I.; Guerrero, A. Reduction of the calcium leaching rate of cement paste by addition of silica nanoparticles. *Cem. Concr. Res.* **2008**, *38*, 1112–1118. [CrossRef]



Article

Soil Application of Nano Silica on Maize Yield and Its Insecticidal Activity Against Some Stored Insects After the Post-Harvest

Mehrez E. El-Naggar ^{1,*}, Nader R. Abdelsalam ^{2,*}, Moustafa M.G. Fouda ^{1,*},
Marwa I. Mackled ³, Malik A.M. Al-Jaddadi ⁴, Hayssam M. Ali ^{5,6}, Manzer H. Siddiqui ⁵ and
Essam E. Kandil ⁷

¹ Pre-Treatment and Finishing of Cellulosic based Fibers Department, Textile Industries Research Division, National Research Center, 33 El- Behooth St, Dokki, Giza 12311, Egypt

² Agricultural Botany Department, Faculty of Agriculture, Saba Basha, Alexandria University, Alexandria P.O. Box 21531, Egypt

³ Department of Stored Product Pests, Plant Protection Institute, Agriculture Research Center (ARC), Sabahia, Alexandria P.O. Box 21616, Egypt; Mazennour2@yahoo.com

⁴ Ministry of Commerce, Trade and Financial Control Department, Trade Control Department, Division Quality Control, Baghdad 13201, Iraq; malekmutalk@gmail.com

⁵ Botany and Microbiology Department, College of Science, King Saud University, P.O. Box 2455, Riyadh 11451, Saudi Arabia; hayhassan@ksu.edu.sa (H.M.A.); mhsiddiqui@ksu.edu.sa (M.H.S.)

⁶ Timber Trees Research Department, Sabahia Horticulture Research Station, Horticulture Research Institute, Agriculture Research Center, Alexandria 21526, Egypt

⁷ Plant Production Department, Faculty of Agriculture (Saba Basha), Alexandria University, Alexandria P.O. Box 21531, Egypt; essam.kandil@alexu.edu.eg

* Correspondence: mehrez_chem@yahoo.com (M.E.E.-N.); nader.wheat@alexu.edu.eg (N.R.A.); m_gaballa@yahoo.com (M.M.G.F.); Tel.: +20-11-2601-8116 (M.E.E.-N); +20-10-6632-9045 (N.R.A.); +20-10-9266-1554 (M.M.G.F.)

Received: 9 March 2020; Accepted: 7 April 2020; Published: 12 April 2020

Abstract: Maize is considered one of the most imperative cereal crops worldwide. In this work, high throughput silica nanoparticles (SiO₂-NPs) were prepared via the sol-gel technique. SiO₂-NPs were attained in a powder form followed by full analysis using the advanced tools (UV-vis, HR-TEM, SEM, XRD and zeta potential). To this end, SiO₂-NPs were applied as both nanofertilizer and pesticide against four common pests that infect the stored maize and cause severe damage to crops. As for nanofertilizers, the response of maize hybrid to mineral NPK, “Nitrogen (N), Phosphorus (P), and Potassium (K)” (0% = untreated, 50% of recommended dose and 100%), with different combinations of SiO₂-NPs; (0, 2.5, 5, 10 g/kg soil) was evaluated. Afterward, post-harvest, grains were stored and fumigated with different concentrations of SiO₂-NPs (0.0031, 0.0063, 0.025, 0.05, 0.1, 0.2, 0.5, 1, 2, 5, 10 g/kg) in order to identify LC₅₀ and mortality % of four common insects, namely *Sitophilus oryzae*, *Rhizopertha dominica*, *Tribolium castaneum*, and *Orizaephilus surinamensis*. The results revealed that, using the recommended dose of 100%, mineral NPK showed the greatest mean values of plant height, chlorophyll content, yield, its components, and protein (%). By feeding the soil with SiO₂-NPs up to 10 g/kg, the best growth and yield enhancement of maize crop is noticed. Mineral NPK interacted with SiO₂-NPs, whereas the application of mineral NPK at the rate of 50% with 10 g/kg SiO₂-NPs, increased the highest mean values of agronomic characters. Therefore, SiO₂-NPs can be applied as a growth promoter, and in the meantime, as strong unconventional pesticides for crops during storage, with a very small and safe dose.

Keywords: maize; NPK; SiO₂-NPs; productivity; fertilizer; mineral; weevils; LC₅₀; toxicity

1. Introduction

The global population will rise to 9 billion by the year of 2050, and the existing agricultural practices cannot satisfy this growing demand for food without variations in the fertilizer's application. Nanotechnology is currently being applied in abundant fields such as medicine, pharmaceuticals, electronics, and agriculture. The size and purity of nanomaterials results significantly in various procedures as well as improvements in the physical and chemical properties of any materials due to their small size which in turn, caused very large surface area [1,2].

Worldwide, *Zea mays* L. is considered as one of the most important cereal crops [3–5]. The area of maize cultivation in Egypt is 1.1 million hectares (average yield about 7.4 t/ha) and in the world 188 million hectares (an average yield about 5.6 t/ha) reported by (FAO, 2007).

Elements such as Nitrogen, Phosphor, and Potassium, abbreviated as NPK, are considered vital macronutrients for meristematic production and several physiological processes in plant [6–15] for instance, shoot, root system, flowers etc., moreover, leading to effective water translocation and nutrition, improve the process of photosynthesis [16]. On the other hand, silicon can be considered as a micro nutrient and it is supportive for plant growth, mainly in dry environments, in order to hold water and bind other nutrients, in addition to increasing the cell strength [17]. Moreover, the utilization of silicon makes the plant shoot system more erect as the effect of a high dose of nitrogen fertilizers, which will improve plant photosynthesis, chlorophyll content, and product quality [18,19] evaluated the effectiveness of nano fertilizers relative to their conventional analogues and the results displayed that nano fertilizers has the largest increase in median efficacy increase (29%). Thus, using SiO₂-NPs, as nanofertilizer together with NPK will increase the absorbability of fertilizers by plants and, hence, it will be more effective than conventional chemical fertilizers [20]. Prihastanti et al. [21] noticed that SiO₂-NPs are an important nanofertilizer which contains silicon which is essential to the monocotyl plants, such as maize, to increase the growth and productivity as well, rather than, NPK alone, that comprises N, P, and K (macronutrient). The combination between NPK and SiO₂-NPs limits the utilization of hazard chemical fertilizers besides its capability to improve maize production [22,23].

There are many ways that extensively used for the production of silica nanoparticles (SiO₂-NPs) such as electrochemical, hydrothermal, plasma–metal hydrogen reaction, micro-emulsion, arc discharge, chemical vapor condensation, vapor phase laser pyrolysis, radiation, sonication, laser, biological, and chemical methods [12,24–36]. One of these chemical methods is the sol–gel process which is extensively used in order to produce homogenous silica products in a powder form. The produced silica gels are non-toxic and suitable to be used for several domains particularly, agricultural applications.

As far as post-harvest is concerned, maize grains are considered one of the identical hosts for many stored products insects such as, *Sitophilus* and *Rhizopertha dominica*, *Tribolium castaneum*, and *Orizaephilus surinamensis*, which resulted in a loss of more than 25%. Fumigants and residual pesticides are widely used to protect the stored grains from infestation by plague [37].

Hereby, this current research work aimed to prepare silica nanoparticles (SiO₂-NPs) in high concentration with small size and distribution to be used as an alternative and effective nanomaterial for the protection of stored grains. It is expected that these nanoparticles will reduce the utilization of hazardous chemical pesticides which, in turn, will reduce the health hazard from residual toxicity. Additionally, the prepared SiO₂-NPs enhances to solve the insect resistance to the conventional insecticides (phosphine and pyrethroids) too [38–41].

Overall, the main objectives of this current research are divided into three key subjects: a) preparation and characterization of SiO₂-NPs using the sol–gel method, b) evaluation of the influence of the combination between SiO₂-NPs and mineral NPK, as soil application and their interaction with the plant characteristics of maize, and c) application of SiO₂-NPs as an alternative pesticide to combat pests infested maize grains through post-harvest, as well as to resolve insect resistance to the conventional pesticides.

2. Materials and Methods

2.1. Experiment Place and Design

The present investigation was carried out at the Experimental Farm, Faculty of Agriculture (Saba Basha), Alexandria University, Alexandria, Egypt and Department of Stored Product Pests, Agriculture Research Center, Sabahia, Alexandria, Egypt, cooperated with Botany and Microbiology Department, College of Science, King Saud University, Riyadh, Saudi Arabia through the two successive summer seasons of 2018 and 2019, in split plot design with 3 replications. The major plot was mineral NPK fertilizers rates ((0% (0:0:0:0), 50% (144:30:30), and 100% (288:60:60)/ha), while sub plots were allocated by silica NPs concentration (0.0, 2.5, 5.0 and 10.0 g/kg autoclaved soil) in both seasons.

2.2. Sol-Gel Synthesis of Silica Nanoparticles (SiO_2 -NPs)

For the preparation of SiO_2 -NPs via sol-gel method, 35 mL of H_2O was mixed with 65 mL of absolute alcohol for 5 min under mechanical stirring. After that, 25 mL of tetraethyl orthosilicate (TEOS) was added dropwise to the previous ethanol/water solution and kept under mechanical stirring for 60 min at room temperature. To this end, ammonia solution was added dropwise until the complete formation of gel. Thus, it was noted that the solution was converted to gel (sol-gel process). The formed gel was submitted to ultra-centrifugation for 2 h at 7000 rpm. Finally, the precipitated wet gel was collected and washed three times with distilled water in order to remove the undesired/unreacted compound (TEOS). The wet gel was subjected again to ultracentrifugation. At the end, the obtained gel was left for calcination at 700 °C for 5-7 h.

2.3. Physical Characterization of Silica Nanoparticles (SiO_2 -NPs)

The sample for transmission electron microscope (TEM) examination was prepared by placing the dispersed SiO_2 -NPS on a carbon-coated copper grid and left for drying at room temperature before being characterized via TEM instrument (JEOL 200 kV, Tokyo, Japan). The particle size and zeta potential of SiO_2 -NPs in its colloidal solution and after submission for 15 min of sonication were assessed using particle size analyzer (Nano-Sizer SZ90, Malvern instruments Ltd., Cambridge, UK). The size distribution and zeta potential of the as prepared SiO_2 -NPs was measured at pH = 7 and 25 °C. Scanning Electron Microscopy (SEM; JEOL, JSM-6360LA, Tokyo, Japan) instrument was used to investigate the internal structure and surface morphology of SiO_2 -NPS. X-ray diffraction (XRD) analysis was performed to examine the crystallinity and the specific peaks for the formed SiO_2 -NPs using an XRD device (Panalytical Emperian, Istanbul, Turkey) having $\text{Cu}_{K\alpha}$ radiation and operating with 40 kV and a 2-theta range of 10–80.

2.4. Soil Characterization and Preparing Materials

A surface sample of soil (0-30 cm) was collected before planting to identify some soil physical and chemical properties, as shown in Table 1. According to Keeney et al. [42], the previous crop was clover (berseem) in both seasons. Nano silica powder were mixed well with autoclaved soil and applied at two times, the first time before the first irrigation (after thinning) and the second time before the second irrigation. The recommended dose of NPK as following; the recommended dose of phosphorus fertilizer was used at rate of 60 kg P_2O_5 /ha (where ha = 0.42 feddan) from calcium super phosphate (12.5% P_2O_5) and potassium rate of 60 kg K_2O /ha from potassium sulphate (48% K_2O) with soil preparation. The recommended dose of mineral N at the different rate of 288 kg N/ha was fully given in the form of urea (46.5% N) such as previous adding. Each plot size was 12.60 m², included 6 ridges, each 3 m in length and 0.70 m in width, with the distance between hills of 25 cm. The grains of maize hybrid (TWC 1100) were taken from Maize Research Division, Agriculture Research Center, Ministry of Agriculture, Cairo, Egypt. Theses grains were sown on May 15th and 14th of 2018 and 2019 seasons, respectively.

Table 1. Soil physical and chemical properties during both seasons.

Soil Properties	Season	
	2018	2019
A) Mechanical analysis:		
Clay%	41	40
Sand%	29	28
Silt%	30	32
Soil texture	Clay loam soil	
B) Chemical properties		
pH (1:1)	8	8.01
E.C. (dS/m) (1:2)	2.6	2.5
1) Soluble cations (1:2) (cmol/kg soil)		
K ⁺	1.52	1.44
Ca ⁺⁺	8.4	9.11
Mg ⁺⁺	12	12.2
Na ⁺⁺	11.5	10.5
2) Soluble anions (1:2) (cmol/kg soil)		
CO ₃ ⁻² + HCO ₃ ⁻	1.9	1.8
Cl ⁻	19.4	18.9
SO ₄ ⁻²	12	12.5
Calcium carbonate (%)	6.5	6
Total nitrogen%	1.5	1.91
Available phosphate (mg/kg)	3.3	3.45
Available K (mg/kg)	2.9	2.88
Organic matter (%)	1.41	1.4

2.5. Maize Yield and Yield Compound Characteristics

The maize yield and yield compound parameters were calculated after harvest and the data were obtained as an average of two ridges from middle of each plot. The protein% was concluded according to the methods of Helrich (1990) by assessing the total nitrogen in the grains and multiplied by 6.25 to obtain the percentage according of grains protein% [43].

2.6. Post-Harvest Experiment

2.6.1. Insect Culture

Two insects, *Sitophilus oryzae* and *Rhizopertha dominica*, were reared under laboratory conditions (27 ± 1 °C and 65 ± 5% R.H.) using autoclaved maize grains which obtained from the first experiment after storage two months in dry conditions, *T. castaneum* and *O. surinamensis* was reared on maize flour mixed with yeast (10:1, w/w), in 1-L glass jars, which were covered by fine mesh cloth for ventilation as reported by [44]. Adult insects used in toxicity tests were about 1-2 weeks old. All investigational procedures were conducted under the identical conditions as culture.

2.6.2. Contact Film Toxicity Bioassay

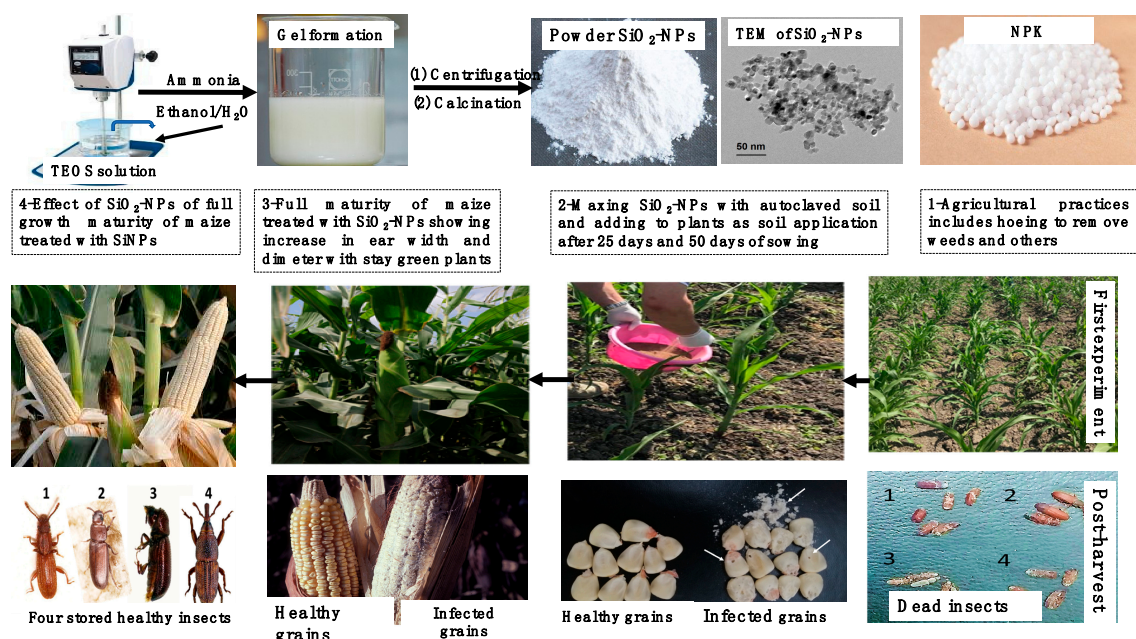
The previous SiO₂-NPs was evaluated (2.5, 5, and 10 g/kg) and the mortality percentage was 100%, so we decreased the concentrations to the lower doses for obtaining the LC₅₀ to the four stored insects. Toxicity of the nine evaluated SiO₂-NPs (0.0031, 0.0063, 0.25, 0.5, 1.0, 2.0, 2.5, 5, and 10 g/kg) against the weevils of *S. oryzae*, *R. domonica*, *T. castanum*, and *O. surinamensis* (adults) were examined by transferring 20 adults into glass jars (250 mL) containing 100 g of sterilized maize grains and admixed them well with different doses of SiO₂-NPs according to the method of Su and Zabik (1972) [45]. Control jars continues maize grains alone. Three replicates were used for all treatment and control. The mortality percentage (M%) were measured according to Finney (1971) after one, two, and three days and LC₅₀ values were determined according to the method of [46].

2.7. Statistical Analysis

Obtained data were subjected to the proper system of statistical analysis of variance as defined by [47]. The means were compared using L.S.D. test at 5% probability using a split model as found in CoStat 6.311 program, PMB320, Monterey, CA93940, and USA [48].

3. Results

In this current research work, it is aimed to develop a new strategy for the soil applications in term of feeding or fertilizing, and at the same time, as pesticide for combating the different kinds of pests that are found through storing maize grains. Nanotechnology in this research work is implemented through the production of silica nanoparticles, SiO₂-NPs, which serve as enhancement agents for the soil application as well as a pesticide agent in post-harvest, for maize grains during storage for long time. As reported previously in the literature; the production of SiO₂-NPs is depending on two major chemical steps: the first one is nucleation that occurs by the hydrolysis of tetraethyl orthosilicate to form silanol groups, which is followed by the second step, growth stage, that takes place by the condensation between the silanol groups formed leading to the construction of siloxane bridges (Si–O–Si) that, yield at the end the entire silica nanoparticle formula. The hydrolysis step is carried out in the presence of alkali like ammonia (NH₃) that acts as a reaction enhancement for the formation of the end product. Scheme 1, represents the preparation of SiO₂-NPs and their application as soil nanofertilizer for maize, as well as an insecticide for the stored maize insects.



Scheme 1. steps for the preparation and utilization of SiO₂-NPs as feeding or fertilizing and in the same time, as pesticide for combating the different kinds of pests that are found thru storing maize grains.

Below is the full analysis for the formed SiO₂-NPs by means of TEM, particle size analyzer, zeta potential, SEM, and XRD techniques.

Firstly, TEM was represented for the formed SiO₂-NPs in order to clarify the particles shape and their distributions. The TEM images of SiO₂-NPs are taken at three different magnifications to clarify the actual shape of the synthesized particles. Figure 1A-C shows that the particles shape is spherical with low disparity which may be attributed to the cluster effect of silica particles. However, these aggregated particles are less than 50 nm.

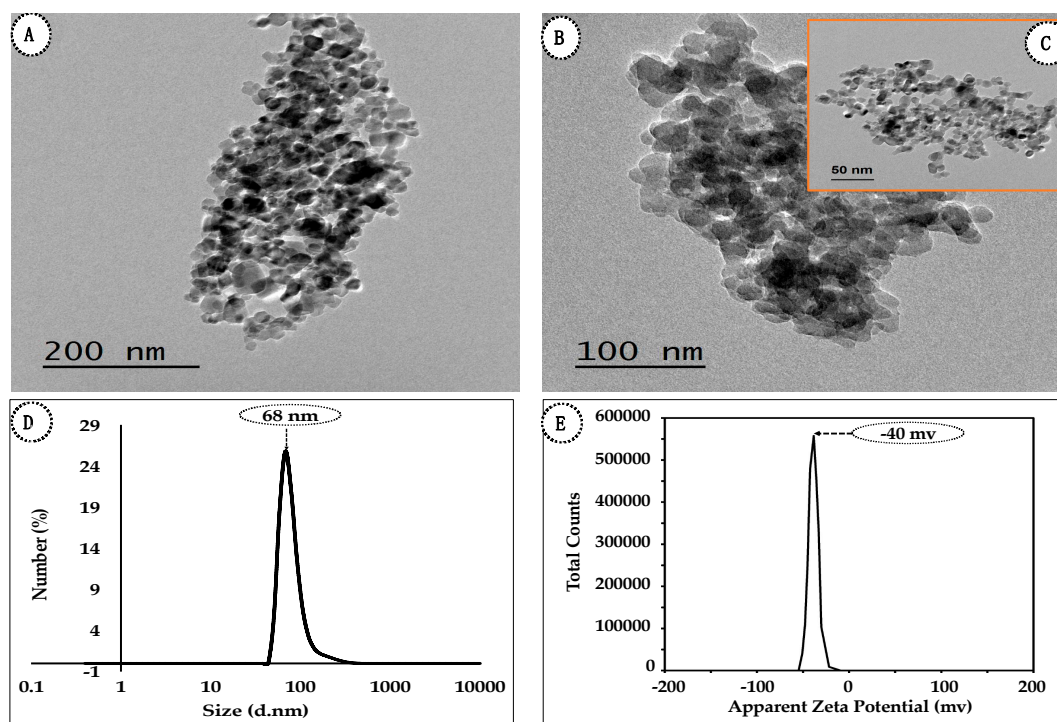


Figure 1. (A, B, C) TEM at low and high magnifications, (D) average particle size and (E) zeta potential of SiO₂-NPs.

To confirm the particle size and stability, hydrodynamic average size was examined using dynamic light scattering (DLS) as represented in Figure 1D. It is observed that the average size is around 68 nm. As can be clearly seen, the particle size obtained from DLS is little bit larger than that obtained from TEM figures. This can be claimed in terms of a swelling effect. For the DLS technique, the sample during examination is kept in distilled water for a long time (duration of measurements; 18 run). In this case, the particles are marginally swelled, which, in turn, leads to a slight increase in the size of the examined particles.

In light of stability of surface charge of the produced SiO₂-NPs, zeta potential (Figure 1E) was carried out to provide us an information about the particle stability against aggregation. It is well known that value of Zeta potential above +30 mV or -30 mV is considered as good stabilized sample and already protected from further aggregation or agglomeration. Thus, the nominated examination is very important to stand out for the sample stability after its preparation. Therefore, the average zeta potential of SiO₂-NPs is evaluated and plotted in Figure 2B. It is depicted that the zeta potential value of SiO₂-NPs is recorded as -40 mV. Such a value means that the particles are kept away from further aggregation, even after a long time.

In order to clarify the morphological surface structure of SiO₂-NPs, the sample was scanned at different magnifications using SEM. The scanned SiO₂-NPs sample is displayed in Figure 2A,B. As shown in the SEM images, the prepared powder consists of spherical particles with well-defined borders. The calcination process at high temperature (600–700 °C) is an important factor for purification and the formation of particles with spherical morphology and regular shape.

In order to outline the crystallinity and purity of the aforementioned powder sample, X-ray diffraction pattern (XRD) was utilized. XRD analysis was carried about between 2 theta degree (10–80). It is disclosed from Figure 3 that SiO₂-NPs exhibit three major peaks at 21.88°, 38.5° and 45.9° which correspond to (100), (110), and (201) planes. The obtained peak value is in accordance with that of JCPDS Card #850335 for SiO₂-NPs. Based on the aforementioned peaks, SiO₂-NPs can be prepared successfully using the sol-gel technique.

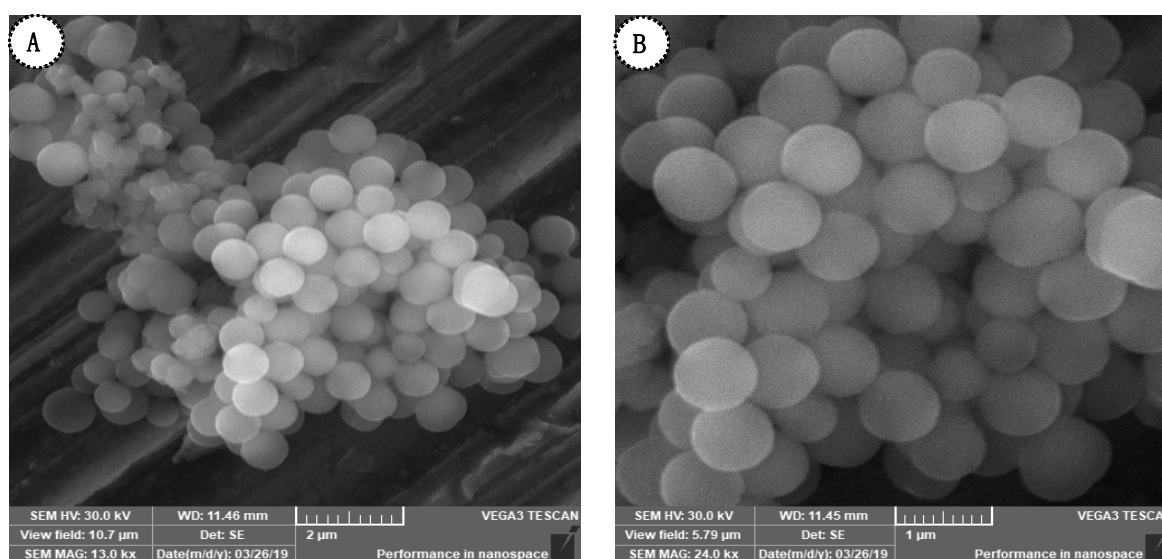


Figure 2. SEM of SiO₂-NPs at different magnifications (A) 13 kx, (B) 24 kx.

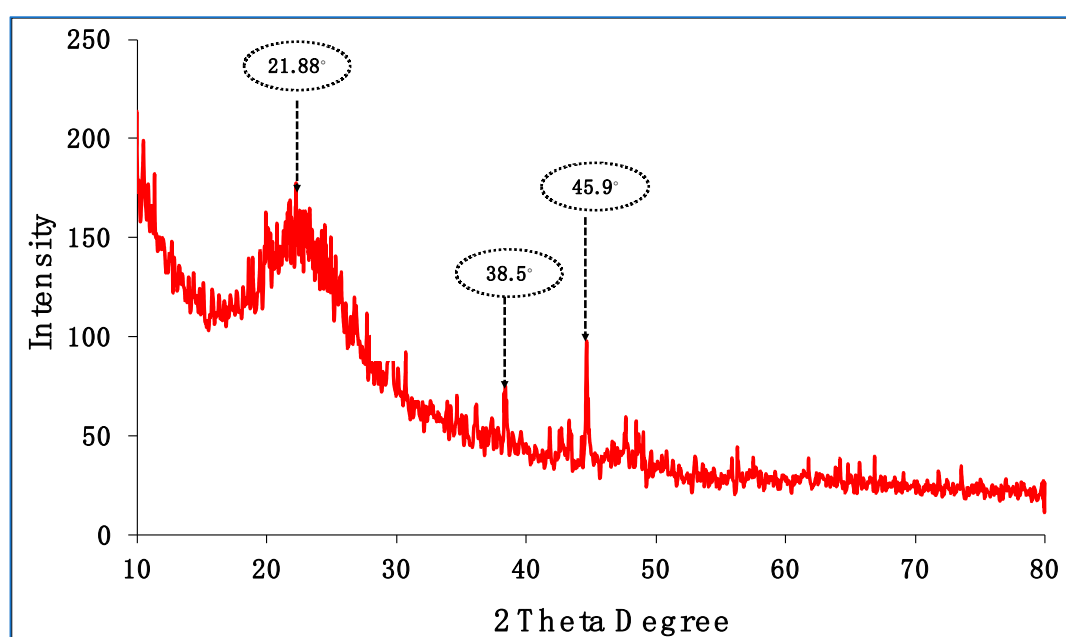


Figure 3. XRD of SiO₂-NPs.

3.1. Growth and Yield Compounds

The growth and yield characters, such as leaf chlorophyll content, plant height, ear length, grains number/row, grains number/ear, weight of 100 grains, grain yield, straw yield, biological yield, harvest index, and protein content of maize hybrid were significantly affected by a combination of NPK fertilizers and SiO₂-NPs concentrations in an average of both 2018 and 2019 seasons as found in Table 2. The results verified that the application of NPK at the recommended dose (RD = 100%) recorded the maximum mean values of leaf chlorophyll content (38.72 SPAD), plant height (195.79 cm), ear length (20.17 cm), grains number/row (41.67 grains/row), grains number /ear (583.33 grains/ear), weight of 100 grains (43.00 g), grains yield (4.79 t/fed), straw yield (6.29 t/fed), biological yield (11.08 t/fed), harvest index (43.23%) and content of protein in grain (10.18%) followed by fertilization by 50% of recommended dose from mineral NPK, while the lowest ones were given by untreated treatment (NPK = 0).

Table 2. Plant attributes of maize as affected by mineral NPK fertilizers, Nano silica (SiO₂-NPs) concentrations and their interaction in an average of the two seasons 2018 and 2019.

Treatment	Plant Attributes										
	Leaf Chlorophyll Content	Plant Height (cm)	Ear Length (cm)	No. of Grains/Row	No. of Grains/Ear	100- Grain Weight	Grain Yield (t/fed)	Straw Yield (t/fed)	Biological Yield(t/fed)	Harvest Index (%)	Grain Protein (%)
A) Mineral NPK Fertilizers											
0% RD	33.03	172.38	18.50	37.42	523.83	38.23	3.86	4.90	8.76	44.06	7.99
50% RD	38.35	191.17	19.92	40.00	560.00	42.38	4.57	6.07	10.64	42.95	9.85
100% RD	38.72	195.79	20.17	41.67	583.33	43.00	4.79	6.29	11.08	43.23	10.18
LSD _{0.05} (A)	1.49	13.22	0.68	0.60	8.36	2.39	0.18	0.29	0.22	1.84	0.21
B) Nano Silica (SiO₂-NPs) Concentration (g/kg)											
0.0 ppm	32.07	161.61	17.56	36.22	507.11	36.22	3.60	5.04	8.64	41.67	7.91
2.5 ppm	36.24	185.11	19.28	39.33	550.67	41.39	4.27	5.80	10.07	42.40	9.24
5.0 ppm	40.27	198.07	20.50	41.56	581.78	42.63	4.76	5.93	10.69	44.53	9.83
10.0 ppm	38.21	201.0	20.78	41.77	584.00	44.56	5.00	6.24	11.24	44.48	10.37
LSD _{0.05} (B)	3.03	8.45	1.08	1.21	16.93	1.19	0.23	0.38	0.50	2.02	0.46
Interaction											
AB	*	*	*	*	*	*	*	*	*	*	*

*: significant difference at LSD at 0.05% level of probability.

Regarding, effect soil application of SiO₂-NPs on maize yield and components characters, the results detected that with the increase of SiO₂-NPs concentrations from 0 up to 10 g/kg, there is an increase in all the studied characters (Table 2). The highest concentration of SiO₂-NPs verified the greatest mean values of leaf chlorophyll content (40.27 SPAD), plant height (201 cm), ear length (20.78 cm), grains number /row (41.77 grains/row), grains number /ear (583.35 grains/ear), weight of 100- grains (44.56 g), grain yield (5.00 t/fed), straw yield (6.24 t/fed), biological yield (11.24 t/fed), harvest index (44.48%) and protein content in grain (10.37%) followed by the concentration 5 g/kg Nano silica as compared with the other concentration.

Combinations between NPK and SiO₂-NPs showed a highly significant interaction, as found in Table 2 for all the studied characters. The significant interaction shows that the response of effect of treatments of the first factor dependable on the levels of the other factor.

The results in Table 3 presented the interaction effect between mineral NPK and SiO₂-NPs, where the highest mean values of chlorophyll content (45.13 SPAD), plant height (222.33 cm), ear length (22.33 cm), grains number/row (44.00 grains/row), grains number /ear (616.00 grains/ear), weight of 100 grains (47.67 g), grain yield (5.59 t/fed), straw yield (7.09 t/fed), biological yield (12.68 t/fed), and content of protein in grain (12.69%) were attained from fertilizing maize plants by the rate of 50% of recommended dose from mineral NPK and soil application of SiO₂-NPs (10 g/kg) except the highest mean of harvest index (46.30%) recorded with 50% of recommended dose from mineral NPK and 5g/kg SiO₂-NPs.

In comparison with the other treatments, meanwhile the lowest ones were given with untreated plots (0 NPK + 0 SNPs), that cleared the role of SiO₂-NPs in the response of maize crop to NPK. The data found in Table 3 demonstrate the interaction impact of mineral NPK fertilizer and SiO₂-NPs application of some maize characters, where the highest values of the studied characters recorded with 50% recommended dose of mineral NPK + 10 g/kg SiO₂-NPs.

SiO₂-NPs with high surface area produced in the commercial way are employed for the growth and productivity of maize as an unconventional source of fertilizer. Physiological transformations that are due to SiO₂-NPs fertilization considerably increase the growth and yield characters in maize plants.

Table 3. The interaction effect between mineral NPK fertilizers and nano silica (SiO₂-NPs) concentrations on plant attributes of maize in an average of the two seasons 2018 and 2019.

NPK	Nano Silica (g/kg)	Leaf Chlorophyll Content	Plant Height (cm)	Ear Length (cm)	No. of Grains/Row	No. of Grains/Ear	100- Grain Weight	Grain Yield (t/fed)	Straw Yield (t/fed)	Biological Yield(t/fed)	Harvest Index (%)	Grain Protein (%)
0%	0.0	28.20	160.00	17.00	34.00	476.00	31.67	3.30	4.50	7.80	42.31	7.80
	2.5	34.00	171.00	19.00	36.33	508.67	39.33	3.94	5.03	8.97	43.92	8.97
	5.0	35.93	173.53	21.33	39.00	546.00	40.57	4.07	5.07	9.14	44.53	9.14
	10.0	34.00	185.00	22.31	40.33	564.67	41.33	4.13	5.03	9.16	45.09	9.17
50%	0	29.03	151.00	17.00	34.33	480.67	36.67	3.33	5.13	8.46	39.36	8.47
	2.5	37.13	185.00	19.00	39.67	555.33	41.83	4.17	6.00	10.17	41.00	10.17
	5.0	42.07	206.33	21.33	42.00	588.00	43.33	5.20	6.03	11.23	46.30	11.23
	10.0	45.13	222.33	22.33	44.00	616.00	47.67	5.59	7.09	12.68	44.09	12.69
100%	0	38.97	173.83	18.67	40.33	564.67	40.33	4.17	5.50	9.67	43.12	9.67
	2.5	37.60	199.33	19.83	42.00	588.00	43.00	4.70	6.37	11.07	42.46	11.07
	5.0	42.80	214.33	21.17	43.67	611.33	44.00	5.02	6.69	11.71	42.87	11.71
	10.0	35.50	195.67	21.00	40.67	569.33	44.67	5.27	6.60	11.87	44.40	11.87
LSD _{0.05 (AB)}		5.25	14.64	1.87	2.09	29.32	2.05	0.40	0.66	0.86	3.19	0.80

0% Recommended Dose of NPK = (0:0:0), 50% Recommended Dose of NPK = (60:12.5:12) and 100% Recommended Dose of NPK = (120:25:24).

3.2. Toxicity of SiO₂-NPs against Stored Products Insects

Nine concentrations of SiO₂-NPs were appraised against four stored products insects *S. oryzae*, *R. dominica*, *T. castaneum* and *O. surinamensis* (Figure 4), the initial results obtained by the application of SiO₂-NPs; 2-10 g/kg displayed 100% mortality %, thus we decreased the concentrations used to get the LC₅₀ for the SiO₂-NPs and three exposer time.



Figure 4. Four stored products used in current study (1) *O. surinamensis*, (2) *T. castaneum*, (3) *R. dominica*, and (4) *S. oryzae*.

Figure 5 shows the difference between healthy and infected maize grains by different stored insects.



Figure 5. Difference between healthy and infected maize grains used in the current study.

The data in Figures 6–8 show that, after 24 h of the treatment, *R. Dominica* became more sensitive to SiO₂-NPs followed by *O. surinamensis*; LC₅₀ were 0.336 (range, 0.177–0.521) and 0.768 (range, 0.438–1.495) g/kg respectively. While the other LC₅₀ was 1.240 (range, 0.995–1.662) and 1.450 (range, 0.971–3.290) g/kg registered for *S. Oryzae*, *T. Castañea*. With respect to mortality percentage after 24 h, the lowest concentrations of SiO₂-NPs such as 0.0031 and 0.0063 were not successful in the case of four species, while the M% increased with concentration changes.



Figure 6. Morphological effect and mortality of SiO₂-NPs on the four stored products insects i.e., (1) *T. castaneum*, (2) *R. dominica*, (3) *O. surinamensis* and (4) *S. oryzae* showing that SiO₂-NPs covering the insects and caused death.

Compared with LC₅₀ of *R. dominica* and *O. surinamensis* with M%, findings showed that for both insects, these values ranged from 0.25 to 0.5 g/kg and ranged from 11.66–63.3% and 1036.65% respectively (Figures 6–8). After 24 h, 2 g/kg SiO₂- NPs displayed that 100% of mortality for all the species. Meanwhile, 1 g/kg of SiO₂- NPs showed 86.6% mortality for *R. dominica* comparing with 5% for *S. oryzae*; 10% for *T. castaneum* and 36.65% for *O. surinamensis*.

Results for both *R. dominica* and *O. surinamensis* recorded the lowest LC₅₀; 0.014 (range, 0.005–0.035) g/kg and 0.008 (range, 0.004–0.006) g/kg comparing with the other two insects; 0.270 (range, 0.114–0.676) g/kg for *T. castaneum* and 0.388 (range, 0.158–1.087) g/kg for *S. oryzae* (Figures 6–8). *S. oryzae* showed 30% mortality % at 1.0 g/kg of SiO₂-NPs, *R. dominica* (90%); *T. castaneum* (68.3%) and 100% for *O. surinamensis*. After 48 h of treatments, the data showed that *O. surinamensis* was very highly sensitive to the SiO₂-NPs compared with other insects.

After 72 h, the effect of SiO₂-NPs in Figures 6–8 impact posed that, *R. dominica* and *O. surinamensis* recorded the lowest LC₅₀ values were 0.002 (range, 0.0004–0.006) and 0.002 (range, 0.0005–0.007) g/kg, while *T. castaneum* (0.034) (range, 0.015–0.072 g/kg) and *S. oryzae* (0.263) (range, 0.055–0.014). From 0.25 to 2.0 g/kg of SiO₂-NPs, the *O. surinamensis* displayed 100% mortality %, while *S. oryzae* was more

resistance to SiO₂-NPs which exhibited 93.3% under 1.0 g/kg (Figure 8) compared to the other insects that disclosed 100%.

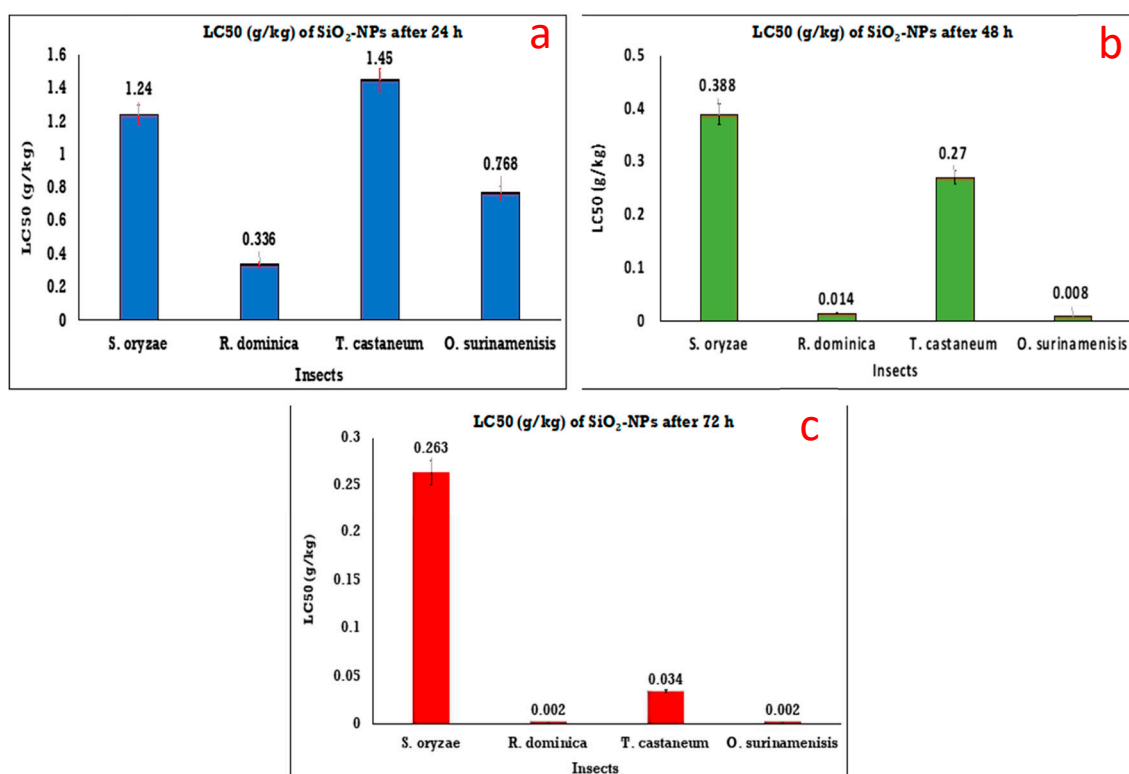


Figure 7. Insecticidal activity of the Nano silica (SiO₂-NPs) against *S. oryzae*, *R. dominica*, *T. castaneum* and *O. surinamensis* as recorded (a) after 24 h; (b) after 48 h and (c) after 72 h.

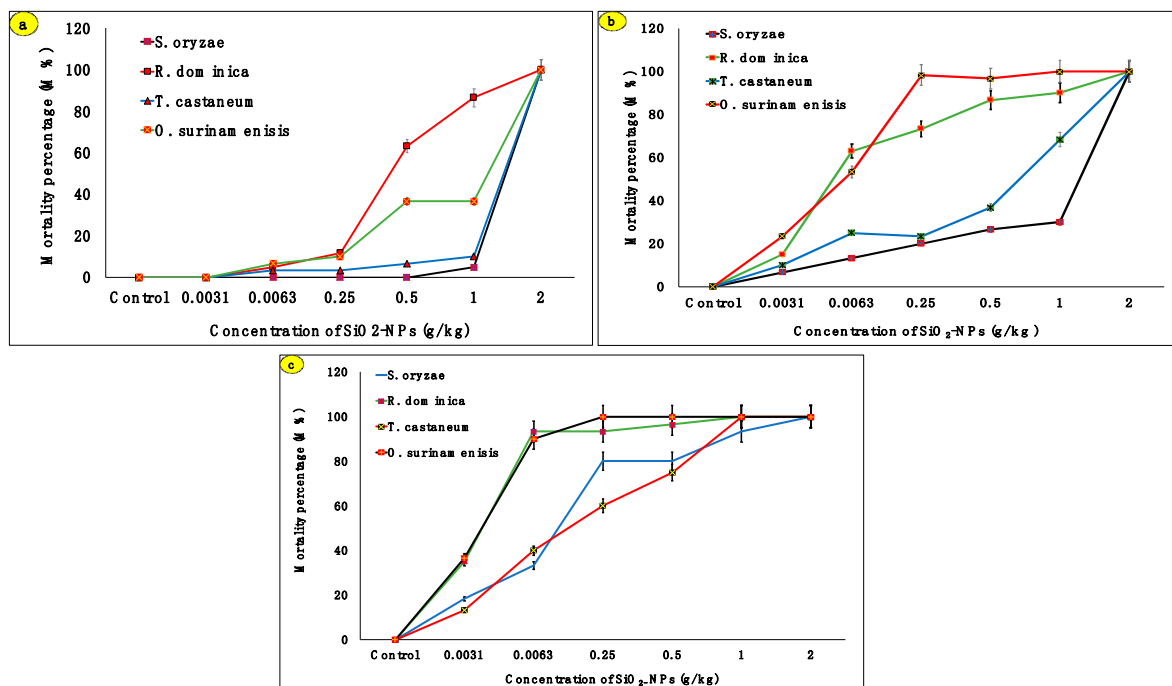


Figure 8. Mortality % of SiO₂-NPs against *S. oryzae*, *R. dominica*, *T. castaneum* and *O. surinamensis* (a) after 24 h; (b) after 48 h and (c) after 72 h.

4. Discussion

The main significance of this current work is to prepare silica nanoparticles in a very high concentration using the sol-gel technology. The prepared silica nanoparticles in their current form are not toxic, since our aim in this current work was to prepare them in a pure form without any impurities. Thus, the calcination process has been carried out to degrade the undesired and unreactive compounds of TEOS or ammonia, ethanol substances. The next step is to use this industrial scale up, of silica nanoparticle in agricultural domain, as both growth promoter for soil and in the meantime, as an alternative nano pesticide, to combat pests infested maize grains thru post-harvest, in order to resolve the insect resistance to the conventional pesticides, which reflect the novelty of this work compared with the traditional relevance, for the pests control. The results concluded and assured that, by feeding the soil with silica nanoparticles up to 10 g/kg, the best growth and yield enhancement of maize crop is noticed. Moreover, the combination between mineral NPK and silica nanoparticles on soil application, had a beneficial effect on photosynthesis, yield enhancement and increased productivity of maize plants too. Also, silica nanoparticles displayed great success in combating the stored maize insects, which reached a 100% mortality rate.

In this current research work, we aimed to develop a new strategy for soil applications in terms of feeding or fertilizing, and at the same time, as a pesticide for combating the different kinds of pests that are found through storing maize grains. These results agree with Kyuma and Suriyaprabha et al. [49,50] and Sommer et al. [17] who showed the role of Si (Silicon) as a micronutrient for helping plants achieve the optimal use of water and other nutrients from soil. Also, was agreeing with [16] who detect the effect of NPK fertilizer on the yield and yield compounds in maize.

The current results observe the same trend as [51], who presented that growth and yield characteristics were much influenced with increasing concentration of SiO₂-NPs [51]. They observed that the physiological changes showed that the expression of organic compounds such as proteins, chlorophyll, and phenols, as well as the growth and yield of maize increased by using SiO₂-NPs. Also, Farooq and Dietz (2015) showed the role of Silicon as a versatile player in plants [52].

The results are in accordance with Dung et al. (2016) that used SiO₂-NPs in different doses and reported that 60 ppm caused an increase in fresh weight, dry weight, and chlorophyll content in chili plants [53]. Another study [54] reported that SiO₂-NPs play a great role in the physiological components of maize, thus supporting the use of mineral fertilizers based on the distribution of roots and shoots. In addition, SiO₂-NPs are essential in increasing the detailed functional properties of mineral fertilizers [54].

These results in an agreement with [55,56] whose reported that the application of Nano silica (8 g/L) showed significantly increased the growth traits of tomato plants [55,56]. Also, [57–59] presented that SiO₂-NPs nutrition decreased the inhibitory outcome of salinity on plant growth by decreasing the Na⁺ content, nutrient uptake, increasing the cell wall peroxidase activities.

The results showing the efficiency of SiO₂ in maize growth and productivity and these results were the same observation detected for SiO₂-NPs that increased plant growth as reported by [55], and plant resistance to hydroponic conditions as reported by [51], as well as increased root length in plants, as stated by [60,61], and induced an improvement in photosynthesis as mentioned by [62].

Our results observed the same trend as other studies which showed the effects of Silica NPs with mineral fertilizers in many crop plants, such as maize as stated by [51,55], common bean as reported by [63], tall wheatgrass as described by [64], tomato as outlined by [65], faba bean as mentioned by [66], wheat as described by [67], rice as disclosed by [68], Glycine max as mentioned by [69], and sweet pepper as displayed by [70]. Also, others showed the effectiveness role of nanomaterial fertilizers on plant growth and productivity [21]. On the other hand, several research works have been carried out to prove the positive impact of silica nanoparticles to the crops, such as Rastogi et al. (2019) who reported the benefits of SiO₂-NPs on physiological features of the plant in which that, they allow them to enter plants and affect its metabolic activities [71]. The same group also claim that the mesoporous nature of

silica nanoparticles can also direct them to be good applicants as nano carriers for several molecules that may support in agriculture [71].

The current results showed that SiO₂-NPs disclosed effectiveness against the stored products insects, which reached to 100% (M%). These data are in agreement with [41], [72,73], and [37] who reported the impact of nanomaterials as an alternative pesticide against stored grains insects. Our results designated that nanoparticles could help to produce new insecticides and this finding agreed with [74] who reported the same fact in addition to yield pesticides and insect repellants. Few researches have been carried out to study the toxicity effect of nanoparticles on insects especially storage insects, [75] stated that nanoparticles loaded with garlic essential oil is useful against *Tribolium castaneum* (Herbst) [75]. So, the use of nanoparticles as unconventional pesticide constitutes a new approach to combat pests which have become resistant to chemical conventional pesticides.

Silicon nanoparticles have enormous application as insecticides on different insects such as aphids, cotton leaf worm, *Sitophilus oryzae* L., *Tribolium castaneum* (Herbst) and *Rhizopertha dominica* F under laboratory conditions [76]. The insect control mechanism is dependent on the structure of cuticular lipids for defending their water barrier, and in that way, prohibit death through dehydration. Meanwhile, silica nanoparticles get absorbed into the cuticular lipids by physio sorption and thus causes insects death. Moreover, Barik et al. [77] also verified the use of SiO₂-NPs as a nano-pesticide and clarified the same control mechanism of combating insects

5. Conclusions

High throughput silica nanoparticles (SiO₂-NPs) were synthesized via the sol-gel technique. The SiO₂-NPs were obtained in a powder form followed by full characterization using state of the art analysis. TEM displayed that the particle shape was spherical with low disparity due to the cluster effect of silica particles. However, these aggregated particles are less than 50 nm. Dynamic light scattering (DLS) confirmed the particle size and stability, where the average size was around 68 nm. In addition, the zeta potential value of the prepared SiO₂-NPs was -40 mV, which affirms the stability of these particles against aggregation, even after long time. Moreover, XRD ascertained that SiO₂-NPs were prepared successfully using the sol-gel technique, in pure form and free from any other impurities or unreacted compounds.

To this end, the SiO₂-NPs were applied successfully as both nanofertilizer and pesticide against four common pests that infect the stored maize and cause severe damage to them. The results obtained demonstrate that, by feeding the soil with SiO₂-NPs up to 10 g/kg, the best growth and yield enhancement of maize crop is noticed. Mineral NPK interacted significantly with SiO₂-NPs, whereas the application of mineral NPK at the rate of 50% with 10 g/kg SiO₂-NPs, increased the highest mean values of agronomic features. Consequently, it can be concluded that the combination of mineral NPK and SiO₂-NPs by soil application, had a beneficial effect on photosynthesis, yield enhancement, and increased the productivity of maize plants. In addition, it improved protein content (%) to 12.59% and chlorophyll content to (45.13 SPAD). This increase emphasizes the metabolic balance between induction of chlorophyll and proteins and cell wall transporters, damping off stress-responsive enzyme activities as a function of SiO₂-NPs application in maize plants. Also, SiO₂-NPs exhibited effectiveness against the stored products insects, which reached a 100% mortality rate.

Finally, SiO₂-NPs can be easily applied as growth promoter and can work as strong unconventional pesticides for crops during storage, with a very small and safe dose in order to combat all kinds of pests harmful to maize during storage.

Author Contributions: Data curation, N.R.A.; Formal analysis, M.E.E.-N. and M.M.F.; Funding acquisition, N.R.A.; Investigation, N.R.A. and H.M.A.; Methodology, M.E.E.-N., M.I.M., M.A.A.-J. and E.E.K.; Resources, M.I.M., M.A.A.-J. and E.K.; Software, M.M.F., H.M.A. and M.H.S.; Visualization, E.K.; Writing – original draft, M.E.E.-N. and M.H.S.; Writing—review and editing, N.R.A. and M.M.F. All authors have read and agreed to the published version of the manuscript.

Funding: This research was funded by King Saud University, Researchers Supporting Project number (RSP-2019/123), King Saud University, Riyadh, Saudi Arabia.

Acknowledgments: The authors gratefully acknowledge the Researchers Supporting Project number (RSP-2019/123) King Saud University, Riyadh, Saudi Arabia.

Conflicts of Interest: The authors declare no conflict of interest.

References

1. Rani, A.; Reddy, R.; Sharma, U.; Mukherjee, P.; Mishra, P.; Kuila, A.; Sim, L.C.; Saravanan, P. A review on the progress of nanostructure materials for energy harnessing and environmental remediation. *J. Nanostructure Chem.* **2018**, *8*, 255–291. [CrossRef]
2. Lee, S.H.; Jun, B.-H. Silver nanoparticles: Synthesis and application for nanomedicine. *Int. J. Mol. Sci.* **2019**, *20*, 865. [CrossRef] [PubMed]
3. Kumar, A.; Gali, S.; Hebsur, N. Effect of different levels of npk on growth and yield parameters of sweet corn. *Karnataka J. Agric. Sci.* **2010**, *20*.
4. Orosz, F.; Jakab, S.; Losak, T.; Slezak, K. Effect of fertilizer application to sweet corn (zea mays) grown on sandy soil. *J. Environ. Biol.* **2009**, *30*, 933–938.
5. Mohammadi, G.R.; Ghobadi, M.E.; Sheikheh-Poor, S. Phosphate biofertilizer, row spacing and plant density effects on corn (zea mays l.) yield and weed growth. *Am. J. Plant Sci.* **2012**, *3*, 425. [CrossRef]
6. Abass, N.Y.; Elwakil, H.E.; Hemeida, A.A.; Abdelsalam, N.R.; Ye, Z.; Su, B.; Alsaqufi, A.S.; Weng, C.C.; Trudeau, V.L.; Dunham, R.A. Genotype-environment interactions for survival at low and sub-zero temperatures at varying salinity for channel catfish, hybrid catfish and transgenic channel catfish. *Aquaculture* **2016**, *458*, 140–148. [CrossRef]
7. Abdelsalam, N.R. Marker assisted-selection of major traits in egyptian bread wheat (triticum aestivum l.) and wild wheat (aegilops ventricosa tausch). *Plant Cell Biotechnol. Mol. Biol.* **2014**, *15*, 67–74.
8. Abdelsalam, N.R.; Abdel-Megeed, A.; Ali, H.M.; Salem, M.Z.M.; Al-Hayali, M.F.A.; Elshikh, M.S. Genotoxicity effects of silver nanoparticles on wheat (triticum aestivum l.) root tip cells. *Ecotoxicol. Environ. Saf.* **2018**, *155*, 76–85. [CrossRef]
9. Abdelsalam, N.R.; Awad, R.M.; Ali, H.M.; Salem, M.Z.M.; Abdel Latif, K.F.; Elshikh, M.S. Morphological, pomological, and specific molecular marker resources for genetic diversity analyses in fig (ficus carica l.). *HortScience* **2019**, *54*, 1299–1309. [CrossRef]
10. Abdelsalam, N.R.; Botros, W.A.; Khaled, A.E.; Ghonema, M.A.; Hussein, S.G.; Ali, H.M.; Elshikh, M.S. Comparison of uridine diphosphate-glycosyltransferase ugt76g1 genes from some varieties of stevia rebaudiana bertonii. *Sci. Rep.* **2019**, *9*. [CrossRef]
11. Abdelsalam, N.R.; Elshikh, M.S.; Ibrahim, E.G.; Salem, M.Z.M.; Ali, H.M. Genetic and morphological characterization of mangifera indica l. Growing in egypt. *HortScience* **2018**, *53*, 1266–1270. [CrossRef]
12. Abdelsalam, N.R.; Fouda, M.M.G.; Abdel-Megeed, A.; Ajarem, J.; Allam, A.A.; El-Naggar, M.E. Assessment of silver nanoparticles decorated starch and commercial zinc nanoparticles with respect to their genotoxicity on onion. *Int. J. Biol. Macromol.* **2019**, *133*, 1008–1018. [CrossRef] [PubMed]
13. Abdelsalam, N.R.; Kandil, E.E.; Al-Msari, M.A.F.; Al-Jaddadi, M.A.M.; Ali, H.M.; Salem, M.Z.M.; Elshikh, M.S. Effect of foliar application of npk nanoparticle fertilization on yield and genotoxicity in wheat (triticum aestivum l.). *Sci. Total Environ.* **2019**, *653*, 1128–1139. [CrossRef] [PubMed]
14. Abdelsalam, N.R.; Salem, M.Z.M.; Ali, H.M.; Mackled, M.I.; El-Hefny, M.; Elshikh, M.S.; Hatamleh, A.A. Morphological, biochemical, molecular, and oil toxicity properties of taxodium trees from different locations. *Ind. Crop. Prod.* **2019**, *139*. [CrossRef]
15. Zhao, J.; Abdelsalam, N.R.; Khalaf, L.; Chuang, W.P.; Zhao, L.; Smith, C.M.; Carver, B.; Bai, G. Development of single nucleotide polymorphism markers for the wheat curl mite resistance gene cmc4. *Crop Sci.* **2019**, *59*, 1567–1575. [CrossRef]
16. Jaliya, M.; Falaki, A.; Mahmud, M.; Sani, Y. Effect of sowing date and npk fertilizer rate on yield and yield components of quality protein maize (zea mays l.). *Arpn J. Agric. Biol. Sci.* **2008**, *3*, 23–29.
17. Sommer, M.; Kaczorek, D.; Kuzyakov, Y.; Breuer, J. Silicon pools and fluxes in soils and landscapes—a review. *J. Plant Nutr. Soil Sci.* **2006**, *169*, 310–329. [CrossRef]

18. Mattson, N.S.; Leatherwood, W.R. Potassium silicate drenches increase leaf silicon content and affect morphological traits of several floriculture crops grown in a peat-based substrate. *HortScience* **2010**, *45*, 43–47. [CrossRef]
19. Kah, M.; Kookana, R.S.; Gogos, A.; Bucheli, T.D. A critical evaluation of nanopesticides and nanofertilizers against their conventional analogues. *Nat. Nanotechnol.* **2018**, *13*, 677. [CrossRef]
20. Ranjbar, M.; Shams, G. Applications of nanotechnology. *J. Green Environ.* **2009**, *34*, 85–87.
21. Prihastanti, E.; Subagyo, A.; Ngadiwiyan, N. Effect of combination of npk and nano silica on the levels of β -carotene and nutritional value of corn (zea mays l.). In Proceedings of the IOP Conference Series: Materials Science and Engineering, Bandung, Indonesia, 18 April 2018; IOP Publishing: Bristol, UK, 2018; p. 012117.
22. Rains, D.; Epstein, E.; Zasoski, R.; Aslam, M. Active silicon uptake by wheat. *Plant Soil* **2006**, *280*, 223–228. [CrossRef]
23. Suriyaprabha, R.; Karunakaran, G.; Kavitha, K.; Yuvakkumar, R.; Rajendran, V.; Kannan, N. Application of silica nanoparticles in maize to enhance fungal resistance. *Iet Nanobiotechnology* **2013**, *8*, 133–137. [CrossRef] [PubMed]
24. Dahlous, K.A.; Abd-Elkader, O.H.; Fouda, M.M.G.; Al Othman, Z.; El-Faham, A. Eco-friendly method for silver nanoparticles immobilized decorated silica: Synthesis & characterization and preliminary antibacterial activity. *J. Taiwan Inst. Chem. Eng.* **2019**, *95*, 324–331.
25. El-Aassar, M.R.; Fouda, M.M.G.; Kenawy, E.R. Electrospinning of functionalized copolymer nanofibers from poly(acrylonitrile-co-methyl methacrylate). *Adv. Polym. Technol.* **2013**, *32*. [CrossRef]
26. El-Aassar, M.R.; Hafez, E.E.; Fouda, M.M.G.; Al-Deyab, S.S. Synthesis, characterization, and antimicrobial activity of poly(acrylonitrile-co-methyl methacrylate) with silver nanoparticles. *Appl. Biochem. Biotechnol.* **2013**, *171*, 643–654. [CrossRef]
27. El-Naggar, M.E.; Shaheen, T.I.; Fouda, M.M.G.; Hebeish, A.A. Eco-friendly microwave-assisted green and rapid synthesis of well-stabilized gold and core-shell silver-gold nanoparticles. *Carbohydr. Polym.* **2016**, *136*, 1128–1136. [CrossRef]
28. Fouda, M.M.G.; Abdel-Mohsen, A.M.; Ebaid, H.; Hassan, I.; Al-Tamimi, J.; Abdel-Rahman, R.M.; Metwalli, A.; Alhazza, I.; Rady, A.; El-Faham, A.; et al. Wound healing of different molecular weight of hyaluronan; in-vivo study. *Int. J. Biol. Macromol.* **2016**, *89*, 582–591. [CrossRef]
29. Fouda, M.M.G.; EL Naggar, M.E.; Shaheen, T.I.; Al Deyab, S.S. Composition Comprising Nanoparticles and a Method for the Preparation Thereof. U.S. Patent No. 9,562,151, 7 February 2017.
30. Fouda, M.M.G.; El-Aassar, M.R.; Al-Deyab, S.S. Antimicrobial activity of carboxymethyl chitosan/polyethylene oxide nanofibers embedded silver nanoparticles. *Carbohydr. Polym.* **2013**, *92*, 1012–1017. [CrossRef] [PubMed]
31. Fouda, M.M.G.; El-Aassar, M.R.; El Fawal, G.F.; Hafez, E.E.; Masry, S.H.D.; Abdel-Megeed, A. K-carrageenan/poly vinyl pyrrolidone/polyethylene glycol/silver nanoparticles film for biomedical application. *Int. J. Biol. Macromol.* **2015**, *74*, 179–184. [CrossRef]
32. Hebeish, A.; El-Naggar, M.E.; Fouda, M.M.G.; Ramadan, M.A.; Al-Deyab, S.S.; El-Rafie, M.H. Highly effective antibacterial textiles containing green synthesized silver nanoparticles. *Carbohydr. Polym.* **2011**, *86*, 936–940. [CrossRef]
33. El-Naggar, M.A.; Alrajhi, A.M.; Fouda, M.M.; Abdelkareem, E.M.; Thabit, T.M.; Bouqellah, N.A. Effect of silver nanoparticles on toxigenic fusarium spp. And deoxynivalenol secretion in some grains. *J. Aoac Int.* **2018**, *101*, 1534–1541.
34. Přichystalová, H.; Almonasy, N.; Abdel-Mohsen, A.M.; Abdel-Rahman, R.M.; Fouda, M.M.G.; Vojtova, L.; Kobera, L.; Spatz, Z.; Burgert, L.; Jancar, J. Synthesis, characterization and antibacterial activity of new fluorescent chitosan derivatives. *Int. J. Biol. Macromol.* **2014**, *65*, 234–240. [CrossRef] [PubMed]
35. Shaheen, T.I.; El-Naggar, M.E.; Hussein, J.S.; El-Bana, M.; Emara, E.; El-Khayat, Z.; Fouda, M.M.G.; Ebaid, H.; Hebeish, A. Antidiabetic assessment; in vivo study of gold and core-shell silver-gold nanoparticles on streptozotocin-induced diabetic rats. *Biomed. Pharmacother.* **2016**, *83*, 865–875. [CrossRef]
36. Textor, T.; Fouda, M.M.G.; Mahltig, B. Deposition of durable thin silver layers onto polyamides employing a heterogeneous tollens' reaction. *Appl. Surf. Sci.* **2010**, *256*, 2337–2342. [CrossRef]
37. Debnath, N.; Das, S.; Seth, D.; Chandra, R.; Bhattacharya, S.C.; Goswami, A. Entomotoxic effect of silica nanoparticles against sitophilus oryzae (l.). *J. Pest Sci.* **2011**, *84*, 99–105. [CrossRef]

38. Heather, N. Sex-linked resistance to pyrethroids in sitophilus oryzae (l.)(coleoptera: Curculionidae). *J. Stored Prod. Res.* **1986**, *22*, 15–20. [CrossRef]
39. Rajendran, S. Responses of phosphine-resistant strains of two stored-product insect pests to changing concentrations of phosphine. *Pestic. Sci.* **1994**, *40*, 183–186. [CrossRef]
40. Daglish, G.J.; Collins, P.J.; Pavic, H.; Kopittke, R.A. Effects of time and concentration on mortality of phosphine-resistant sitophilus oryzae (l) fumigated with phosphine. *Pest Manag. Sci. Former. Pestic. Sci.* **2002**, *58*, 1015–1021. [CrossRef] [PubMed]
41. Benhalima, H.; Chaudhry, M.; Mills, K.; Price, N. Phosphine resistance in stored-product insects collected from various grain storage facilities in morocco. *J. Stored Prod. Res.* **2004**, *40*, 241–249. [CrossRef]
42. Keeney, D.R.; Nelson, D.W. Nitrogen—inorganic forms 1. *Methods Soil Anal. Part 2. Chem. Microbiol. Prop.* **1982**, 643–698.
43. AOAC. *Official methods of analysis of the association of official analytical chemists*; Keneth, H., Ed.; AOAC: Arlington, VA, USA, 1990.
44. Chakraborty, S.; Mondal, P. Specific and age female fecundity life table of callosobruchus chinensis linn. On green gram. *Int. J. Pure Appl. Biosci.* **2015**, *3*, 284–291.
45. Su, G.C.; Zabik, M.J. Photochemistry of bioactive compounds. Photolysis of m-(n, n-dimethylformamidine) phenyl n-methylcarbamate hydrochloride in water. *J. Agric. Food Chem.* **1972**, *20*, 642–644. [CrossRef] [PubMed]
46. Finney, D. Statistical logic in the monitoring of reactions to therapeutic drugs. *Methods Inf. Med.* **1971**, *10*, 237–245. [CrossRef] [PubMed]
47. Gomez, K.; Gomez, A. *Statistical procedures for agricultural research*; John wiley & sons: New York, NY, USA, 1984; Volume 680.
48. Ver, C. 6.311 (2005). Cohort software798 light house Ave. PMB320, Monterey, CA93940, and USA. Available online: <http://www.cohort.com/DownloadCoStatPart2.html>.
49. Sumida, H. Plant-available silicon in paddy soils. In Proceedings of the Second Silicon in Agriculture Conference, Tsuruoka, Yamagata, Japan, 22–26 August 2002; pp. 43–49.
50. Kyuma, K. *Paddy Soil Science*; Kyoto University Press: Kyoto, Japan, 2004.
51. Suriyaprabha, R.; Karunakaran, G.; Yuvakkumar, R.; Prabu, P.; Rajendran, V.; Kannan, N. Growth and physiological responses of maize (zea mays l.) to porous silica nanoparticles in soil. *J. Nanoparticle Res.* **2012**, *14*, 1294. [CrossRef]
52. Farooq, M.A.; Dietz, K.-J. Silicon as versatile player in plant and human biology: Overlooked and poorly understood. *Front. Plant Sci.* **2015**, *6*, 994. [CrossRef]
53. Dung, P.D.; Ngoc, L.S.; Duy, N.N.; Thuy, N.N.; Truc, L.T.M.; Van Le, B.; Van Phu, D.; Hien, N.Q. Effect of nanosilica from rice husk on the growth enhancement of chili plant (capsicum frutescens l.). *Vietnam J. Sci. Technol.* **2016**, *54*, 607. [CrossRef]
54. Miao, B.-H.; Han, X.-G.; Zhang, W.-H. The ameliorative effect of silicon on soybean seedlings grown in potassium-deficient medium. *Ann. Bot.* **2010**, *105*, 967–973. [CrossRef]
55. Yuvakkumar, R.; Elango, V.; Rajendran, V.; Kannan, N.S.; Prabu, P. Influence of nanosilica powder on the growth of maize crop (zea mays l.). *Int. J. Green Nanotechnol.* **2011**, *3*, 180–190. [CrossRef]
56. Siddiqui, M.H.; Al-Whaibi, M.H. Role of nano-sio2 in germination of tomato (lycopersicum esculentum seeds mill.). *Saudi J. Biol. Sci.* **2014**, *21*, 13–17. [CrossRef]
57. Epstein, E. Silicon in plants: Facts vs. Concepts. In *Studies in plant science*; Elsevier: Amsterdam, The Netherlands, 2001; Volume 8, pp. 1–15.
58. Hashemi, A.; Abdolzadeh, A.; Sadeghipour, H.R. Beneficial effects of silicon nutrition in alleviating salinity stress in hydroponically grown canola, brassica napus l., plants. *Soil Sci. Plant Nutr.* **2010**, *56*, 244–253. [CrossRef]
59. Li, B.; Tao, G.; Xie, Y.; Cai, X. Physiological effects under the condition of spraying nano-sio2 onto the indocalamus barbatus mcclure leaves. *J. Nanjing For. Univ. (Nat. Sci. Ed.)* **2012**, *36*, 161–164.
60. Haghghi, M.; Afifipour, Z.; Mozafarian, M. The effect of n-si on tomato seed germination under salinity levels. *J. Biol. Env. Sci.* **2012**, *6*, 87–90.
61. Sabaghnia, N.; Janmohammadi, M. Graphic analysis of nano-silicon by salinity stress interaction on germination properties of lentil using the biplot method. *Agric. For./Poljopr. I Sumar.* **2014**, *60*.

62. Liang, Y.; Chen, Q.; Liu, Q.; Zhang, W.; Ding, R. Exogenous silicon (si) increases antioxidant enzyme activity and reduces lipid peroxidation in roots of salt-stressed barley (*hordeum vulgare*l.). *J. Plant Physiol.* **2003**, *160*, 1157–1164. [CrossRef] [PubMed]
63. Alsaeedi, A.H.; El-Ramady, H.; Alshaal, T.; El-Garawani, M.; Elhawat, N.; Almohsen, M. Engineered silica nanoparticles alleviate the detrimental effects of na⁺ stress on germination and growth of common bean (*phaseolus vulgaris*). *Environ. Sci. Pollut. Res.* **2017**, *24*, 21917–21928. [CrossRef] [PubMed]
64. Azimi, R.; Borzelabad, M.J.; Feizi, H.; Azimi, A. Interaction of sio₂ nanoparticles with seed prechilling on germination and early seedling growth of tall wheatgrass (*agropyron elongatum* l.). *Pol. J. Chem. Technol.* **2014**, *16*, 25–29. [CrossRef]
65. Lu, M.M.; De Silva, D.M.; Peralta, E.; Fajardo, A.; Peralta, M. Effects of nanosilica powder from rice hull ash on seed germination of tomato (*lycopersicon esculentum*). *Philipp. E-J. Appl. Res. Dev. (Pejard)* **2015**, *5*, 11–22.
66. Qados, A.M.A. Effects of salicylic acid on growth, yield and chemical contents of pepper (*capsicum annum* l) plants grown under salt stress conditions. *Int. J. Agric. Crop Sci.* **2015**, *8*, 107.
67. Tahir, M.A.; Rahmatullah, T.; Aziz, M.; Ashraf, S.; Kanwal, S.; Maqsood, M.A. Beneficial effects of silicon in wheat (*triticum aestivum* l.) under salinity stress. *Pak. J. Bot.* **2006**, *38*, 1715–1722.
68. Yeo, A.; Flowers, S.; Rao, G.; Welfare, K.; Senanayake, N.; Flowers, T. Silicon reduces sodium uptake in rice (*oryza sativa* l.) in saline conditions and this is accounted for by a reduction in the transpirational bypass flow. *PlantCell Environ.* **1999**, *22*, 559–565. [CrossRef]
69. Lu, C.; Zhang, C.; Wen, J.; Wu, G.; Tao, M. Research of the effect of nanometer materials on germination and growth enhancement of glycine max and its mechanism. *Soybean Sci.* **2002**, *21*, 168–171.
70. Tantawy, A.; Salama, Y.; El-Nemr, M.; Abdel-Mawgoud, A. Nano silicon application improves salinity tolerance of sweet pepper plants. *Int. J. Chemtech Res.* **2015**, *8*, 11–17.
71. Rastogi, A.; Tripathi, D.K.; Yadav, S.; Chauhan, D.K.; Živčák, M.; Ghorbanpour, M.; El-Sheery, N.I.; Brestic, M. Application of silicon nanoparticles in agriculture. *3 Biotech* **2019**, *9*, 90. [CrossRef] [PubMed]
72. Park, J.Y.; Baek, M.J.; Choi, E.S.; Woo, S.; Kim, J.H.; Kim, T.J.; Jung, J.C.; Chae, K.S.; Chang, Y.; Lee, G.H. Paramagnetic ultrasmall gadolinium oxide nanoparticles as advanced t 1 mri contrast agent: Account for large longitudinal relaxivity, optimal particle diameter, and in vivo t 1 mr images. *Acs Nano* **2009**, *3*, 3663–3669. [CrossRef]
73. Stadler, T.; Buteler, M.; Weaver, D.K. Novel use of nanostructured alumina as an insecticide. *Pest Manag. Sci. Former. Pestic. Sci.* **2010**, *66*, 577–579. [CrossRef]
74. Onyeka, T.; Owolade, O.; Ogunjobi, A.; Dixon, A.G.; Okechukwu, R.; Bamkefa, B. Prevalence and severity of bacterial blight and anthracnose diseases of cassava in different agro-ecological zones of nigeria. *Afr. J. Agric. Res.* **2008**, *3*, 297–304.
75. Yang, F.-L.; Li, X.-G.; Zhu, F.; Lei, C.-L. Structural characterization of nanoparticles loaded with garlic essential oil and their insecticidal activity against *tribolium castaneum* (herbst)(coleoptera: Tenebrionidae). *J. Agric. Food Chem.* **2009**, *57*, 10156–10162. [CrossRef]
76. Amal, M.; Hamza, M.; Asmaa, M.; El, G.; El-Samahy, M. A new silica nanoparticles formulation as stored product protectant. *Egy. J. Plant Pro. Res.* **2015**, *3*, 88–103.
77. Barik, T.K.; Sahu, B.; Swain, V. Nanosilica-from medicine to pest control. *Parasitol. Res.* **2008**, *103*, 253–258. [CrossRef]





Article

Optimization of Metal-Assisted Chemical Etching for Deep Silicon Nanostructures

Rabia Akan * and Ulrich Vogt

KTH Royal Institute of Technology, Department of Applied Physics, Albanova University Center, 106 91 Stockholm, Sweden; ulrich.vogt@biox.kth.se

* Correspondence: rabiaa@kth.se

Abstract: High-aspect ratio silicon (Si) nanostructures are important for many applications. Metal-assisted chemical etching (MACE) is a wet-chemical method used for the fabrication of nanostructured Si. Two main challenges exist with etching Si structures in the nanometer range with MACE: keeping mechanical stability at high aspect ratios and maintaining a vertical etching profile. In this work, we investigated the etching behavior of two zone plate catalyst designs in a systematic manner at four different MACE conditions as a function of mechanical stability and etching verticality. The zone plate catalyst designs served as models for Si nanostructures over a wide range of feature sizes ranging from 850 nm to 30 nm at 1:1 line-to-space ratio. The first design was a grid-like, interconnected catalyst (brick wall) and the second design was a hybrid catalyst that was partly isolated, partly interconnected (fishbone). Results showed that the brick wall design was mechanically stable up to an aspect ratio of 30:1 with vertical Si structures at most investigated conditions. The fishbone design showed higher mechanical stability thanks to the Si backbone in the design, but on the other hand required careful control of the reaction kinetics for etching verticality. The influence of MACE reaction kinetics was identified by lowering the oxidant concentration, lowering the processing temperature and by isopropanol addition. We report an optimized MACE condition to achieve an aspect ratio of at least 100:1 at room temperature processing by incorporating isopropanol in the etching solution.

Keywords: metal-assisted chemical etching; Si nanostructures; high aspect ratio; zone plate

Citation: Akan, R.; Vogt, U. Optimization of Metal-Assisted Chemical Etching for Deep Silicon Nanostructures. *Nanomaterials* **2021**, *11*, 2806. <https://doi.org/10.3390/nano11112806>

Academic Editor: Céline Ternon

Received: 30 September 2021

Accepted: 19 October 2021

Published: 22 October 2021

Publisher's Note: MDPI stays neutral with regard to jurisdictional claims in published maps and institutional affiliations.



Copyright: © 2021 by the authors. Licensee MDPI, Basel, Switzerland. This article is an open access article distributed under the terms and conditions of the Creative Commons Attribution (CC BY) license (<https://creativecommons.org/licenses/by/4.0/>).

1. Introduction

Nanostructured Si is the material of choice for a variety of applications such as photonics [1], lithium ion batteries [2], solar cells [3], biosensors [4], microfluidic channels [5] and X-ray optics [6]. Many of these applications require devices with highly vertical and deep Si nanostructures, i.e., high aspect ratios. The smaller the structures are, the more challenging it gets to fabricate high-aspect ratio nanostructures that are mechanically stable.

Both dry and wet etching processes are used for the fabrication of Si devices. Reactive ion etching (RIE) [7] is an example of a commonly used dry etching technique. For Si devices with nanostructures, maintaining a vertical etching profile becomes challenging with RIE and thus limits the achievable aspect-ratios [8]. Therefore, RIE is more suitable for the fabrication of devices with structures in the micrometer range or when extreme aspect ratios are not needed.

A wet etching process that overcomes fabrication challenges is MACE. MACE is an electroless method that is gaining a lot of attention as a pattern transfer technique for the fabrication of deep high-aspect ratio Si nanostructures [9,10]. In MACE, a noble metal catalyst (e.g., gold (Au) that is lithographically defined or in nanoparticle form) is etching its way into a Si substrate in an electrolyte (etching solution) composed of hydrofluoric acid (HF) and a strong oxidizer (e.g., hydrogen peroxide (H₂O₂)). The noble metal (cathode) catalyzes the reduction of the oxidizer and consequently electrical holes are formed. The holes are injected into the Si substrate (anode) locally on the noble metal site and oxidizes

the substrate. The HF then dissolves the oxidized Si and the catalyst pattern is transferred into the Si substrate.

Although conceptually simple, MACE can become complicated since many parameters influence the process like etching solution composition [11], etching temperature [12], doping concentration of the Si substrate [13,14], catalyst thickness [15] or catalyst morphology [16,17]. These parameters have to be carefully adjusted to obtain the desired etching performance. In the literature, there are numerous studies investigating many of these parameters and their effects on micro- and nanostructure etching. However, comparing results is often difficult due to the variation in active etching areas and structure sizes. There is a lack of systematic studies that make direct comparison of etching behavior possible.

For etching of catalyst structures in the nanometer range two main challenges exist. Firstly, maintaining a vertical etching direction and secondly, keeping a good mechanical stability for deep etching when reaching extreme aspect ratios. Especially, the catalyst design has a great impact on these two challenges [11]. In this work we choose zone plate structures as model catalyst patterns to find the morphological parameters and etching conditions that are best suited for MACE processing of sub-100 nm high-aspect ratio Si structures.

Zone plates are diffractive imaging and focusing optics commonly used in X-ray microscopes [18]. Their circular grating structures are decreasing in width with the zone plate radii. Two parameters are key for the zone plate performance: imaging resolution and diffraction efficiency. The zone plate resolution is defined by the outermost zone width, whereas the diffraction efficiency is defined by the zone thickness [19]. The X-ray energy and zone plate material will define the required zone thickness. For the use in the hard X-ray regime, thicknesses of several micrometers are often needed. In order to fabricate a high-resolution and high-efficient zone plate, very high aspect ratios are therefore required. Since X-ray zone plates contain structures ranging from micron-sized features in the center to nanometer-sized features in the outer parts, they are ideal model patterns to systematically investigate the MACE process. The obtained results are applicable to other Si devices with nanostructured, lithographically defined catalyst patterns.

We systematically investigate MACE of two catalyst pattern designs at four different MACE conditions in order to find optimum process conditions for obtaining vertical, mechanically stable deep high-aspect ratio Si nanostructures. The first design, called “brick wall” (Figure 1a), is a grid catalyst with all zones interconnected, whereas the second design, called “fishbone” (Figure 1b) is a hybrid catalyst with partly interconnected and partly isolated zones. Both designs have smallest feature sizes of 30 nm (width of the outermost zones), which are as far as we are aware the smallest lithographically defined catalyst structures reported for MACE. To our knowledge, this is the first study that combines the brick wall and fishbone type catalyst designs on the same chip, using the same active catalyst area and exposes them to the same exact reaction conditions, including cold etching and IPA addition. This makes direct comparisons of etching behavior possible.

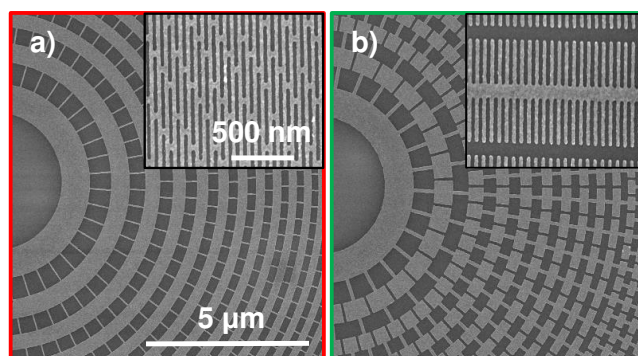


Figure 1. Top-view SEM micrographs of Au zone plate catalyst patterns on Si illustrating (a) brick wall (red frame) and (b) fishbone designs (green frame). The insets show the outermost parts of the zone plate designs. The zone plates designs have a 150 μm diameter, 1:1 line-to-space ratio and the outermost zone widths are 30 nm. Same scale bars apply to the micrographs.

2. Motivation for the Selection of Catalyst Designs and MACE Conditions

In the literature, there are several studies reporting the fabrication of Si zone plate nanostructures using MACE [11,20–24]. None of the reported studies contain a detailed motivation for their choice of catalyst design and MACE processing conditions, instead, the MACE pattern transfer has been presented as one in a series of steps for a complete device fabrication. Some of the studies used grid catalyst designs [11,20,24] while others preferred fishbone catalyst designs [21–23,25]. It has to be noted that it is difficult to etch isolated catalyst structures in a controlled way, so some kind of connected catalyst design is necessary in order to achieve vertical etching.

There are benefits and challenges with both grid and fishbone designs. A grid catalyst design has the advantage of maintaining a vertical etching profile owing to the interconnected zones, however, resulting in isolated Si nanostructures. The isolated Si structures will limit the achievable etch depths due to collapse, especially in smallest features [20]. In the fishbone design, the noble metal rings are interrupted forming sections with perpendicular lines crossing each section, resulting in partly interconnected Si after MACE. This interconnection will contribute with mechanical stability, but at the expense of etching verticality. It was recently reported that the fishbone design deviates from its vertical etching path at thicknesses beyond 1 μm due to the free Au ends in the design [23]. It should be noted that the results were obtained for a specific MACE processing condition, and it is therefore not possible to identify if this behavior is due to the catalyst design or the reaction conditions. Here, our aim is to directly compare these two types of catalyst designs by processing them on the same substrate and studying their etching behavior at different MACE conditions.

We base our choices of different MACE conditions on reaction kinetics. We want to control the hole injection rate into the Si, and thus, the overall etching rate by lowering the processing temperature and H_2O_2 concentration from our previously optimized MACE condition [11]. In our previous study, a grid catalyst design was used and the MACE condition was optimized based on etch depth and silicon zone roughness. The aim here is to investigate if a slower MACE reaction is beneficial for the etching directionality, as cold etching was used in several other studies without further explanation but showing nice vertical structures [21–23]. We further investigate the effect of isopropanol (IPA) which should also lower the etch rate [26]. Additionally, previous work suggests that the transport of generated gas from the etching location will be improved with the addition of IPA due to lower surface tension [27]. All MACE conditions are studied for different etching times to gain an understanding of to what etch depths the two designs are mechanically stable and if the different reaction conditions affect the mechanical stability of the zones. Our goal is to provide benchmark results for researchers in various fields that want to find optimum MACE processes for Si nanostructure fabrication.

3. Materials and Methods

Si p-type (100) wafers with resistivity of 1–5 Ω -cm were used for all samples. The zone plate fabrication procedure consisted of a sequence of steps: (1) Ultrasonic cleaning of wafer pieces followed by an oxygen plasma cleaning step, (2) resist spinning and patterning via electron-beam lithography, (3) resist development, (4) short oxygen plasma treatment, (5) electron beam evaporation of catalyst layer, (6) resist lift-off, (7) oxygen plasma cleaning for removal of organics, (8) MACE and (9) critical point drying. An overview of the experimental procedure is presented in Figure 2.

The Si wafers were cut into 1.5 cm \times 1.5 cm chips and cleaned ultrasonically in acetone and IPA for removal of Si dust and by an oxygen plasma step (PlasmaLab 80 Plus RIE/ICP system, Oxford Instruments, Abingdon, UK) for removal of organics and further oxidising the Si surface (each cleaning step was typically 5 min). We used 80 nm of the positive resist CSAR 62 (Allresist GmbH, Strausberg, Germany) for the electron beam lithography step (50 kV Voyager EBL system, Raith GmbH, Dortmund, Germany) and the zone plate catalyst designs investigated in this study (brick wall and fishbone) were patterned on each substrate. The zone plate designs had a diameter of 150 μ m, 1:1 line-to-space ratio and zone widths ranging from 850 nm (innermost zones) to 30 nm (outermost zones). The interconnects in the brick wall design were 40 nm and brick length of the outermost zones were 460 nm. In the fishbone design, the backbone was 95 nm and free ends were 360 nm of the outermost zones. The resist development was performed in amyl acetate (60 s) followed by rinsing in IPA and n-pentane (10 and 15 s, respectively). The short oxygen plasma treatment step (13 s) after development was to ensure removal of any resist residues in the zone plate patterns. For the catalyst layer, 10 nm Au was electron beam evaporated (in-house Eurovac/Thermionics deposition system) at 1 \AA /s on a 2 nm adhesive Ti layer. The resist lift-off was performed in dimethyl succinate under ultrasonication. The final oxygen plasma step (3 min) was necessary to remove any organics on the sample surfaces that might prevent the MACE process.

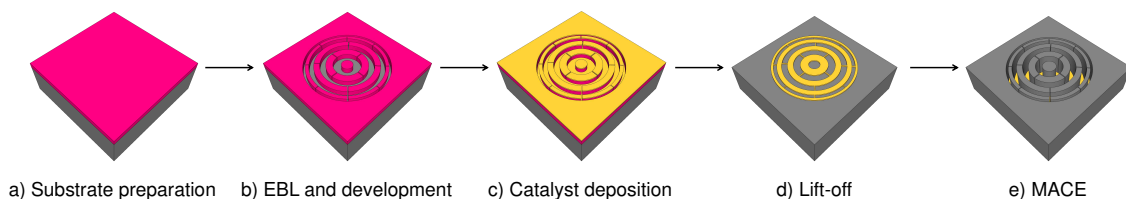


Figure 2. Overview of the experimental procedure. (a) Si substrate (grey) preparation by spin-coating 80 nm CSAR 62 resist (pink). (b) Zone plate patterning by EBL and development for removal of resist residues. (c) Deposition of 2 nm Ti and 10 nm Au (yellow) by evaporation. (d) Resist lift-off, leaving the metal zone plate pattern. (e) Etching the metal zone plate pattern into the Si via MACE.

The MACE experiments were all performed in a polytetrafluoroethylene (PTFE) container under light protection. Four different MACE conditions were used to investigate the etching behavior of the two designs (Table 1).

Table 1. Investigated MACE conditions.

Condition	[H ₂ O ₂] : [HF] : [IPA] (M)	Temperature (°C)
C1	0.68 : 4.7 : 0	25
C2	0.068 : 4.7 : 0	25
C3	0.68 : 4.7 : 0	8
C4	0.68 : 4.7 : 0.91	25

To understand the reproducibility of the MACE process, eight substrates with three zone plates per design were processed and each MACE condition was repeated twice. The etching solution compositions were based on previously reported studies [11,27]. The

cold MACE experiments at 8 °C (C2) were performed using pre-cooled chemicals in a surrounding cooling bath. Both the patterned Si chips and etching solutions were kept in the cooling bath prior MACE to ensure temperature stabilization. To carefully investigate the etching direction and mechanical stability at different etch depths, the processing time was set to 3, 6, 9 and 12 min for each MACE condition. The samples were transferred to ethanol after MACE processing and further critical point dried (Leica EM CPD300, Leica Microsystems GmbH, Wetzlar, Germany). For etch depth analysis, cross-sections were prepared using FIB milling (Nova 200 NanoLab system, FEI Company, Hillsboro, OR, USA). Additionally, some samples were cleaved manually for a better visualization of cross sections. Unfortunately, this is a complicated procedure and cleaved cross-sections could not be obtained for all etching conditions and designs.

4. Results and Discussion

We characterize the etching behavior of our catalyst designs based on mechanical stability and etching verticality. The MACE conditions that are favorable for each design in terms of these two characteristics are identified and discussed.

4.1. Mechanical Stability

As previously reported, a grid-like catalyst design resulted in vertically etched Si structures, almost independently of the used MACE condition [11]. While its strength lay in maintaining etching verticality, the mechanical stability of the remaining Si structures became a limitation at too small structural widths and large etch depths. Zone plates were therefore ideal catalyst structures to identify at what point the mechanical instability started thanks to their broad size range of zones.

Figure 3 shows cross-section micrographs of a $\approx 1.4 \mu\text{m}$ (average thickness over the zone plate radius) thick brick wall zone plate at three points with different zone widths. The zone width in Figure 3a was 60 nm and no collapse of zones were apparent. At 50 nm zone width, as shown in Figure 3b, some tendency of collapse was starting to show suggesting that a stability limit for the etch depth was reached at this point. At the outermost parts of the zone plate where the zone widths were 30 nm most of the Si nanostructures had collapsed (Figure 3c). It should be noted that the etch depth varied over the zone plate, where the innermost zones were less deep than the outermost parts. The exact depth where the collapse started appearing at 50 nm zone width was $1.5 \mu\text{m}$, suggesting that the achievable aspect ratio of a stable brick wall design was 30:1.

The etching behavior of the catalysts at the investigated conditions C1–C4 are summarized in Figure 4, a common etching time point of 6 min was chosen for comparison. The average etch rates for the different conditions are presented in Table 2. Room temperature processing with the higher H_2O_2 concentration gave the fastest etch rate (C1) which, based on the well accepted MACE theory [9,28], suggested the highest hole injection rate into the Si. The deepest etching of $\approx 2.4 \mu\text{m}$ was obtained at this condition and especially the outermost zones of both the brick wall (Figure 4a) and the fishbone (Figure 4e) design showed deformation.

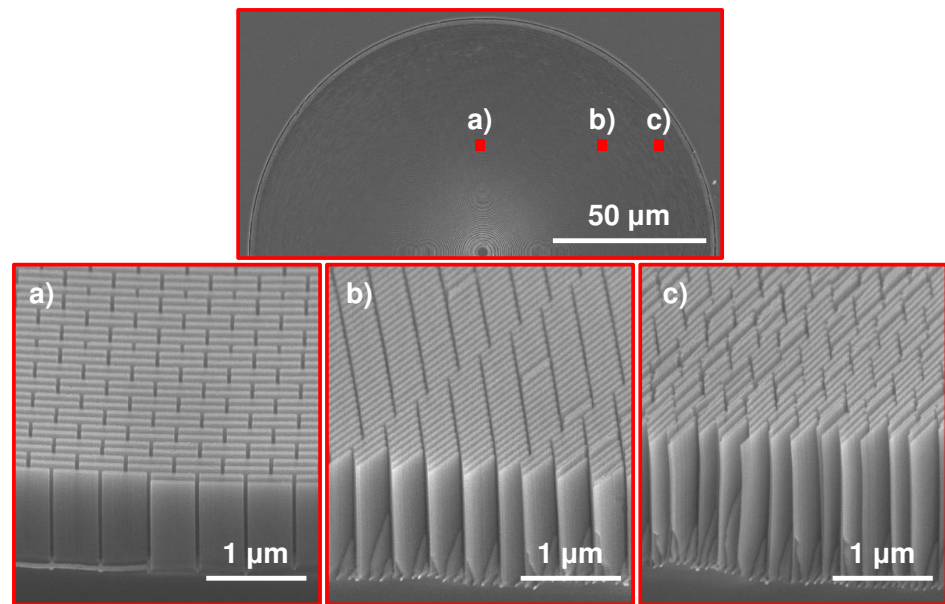


Figure 3. Brick wall catalyst design processed at MACE condition C1. The top micrograph shows where the three micrographs labeled (a–c) are localized on the zone plate. The cross-sections were prepared by manual cleaving.

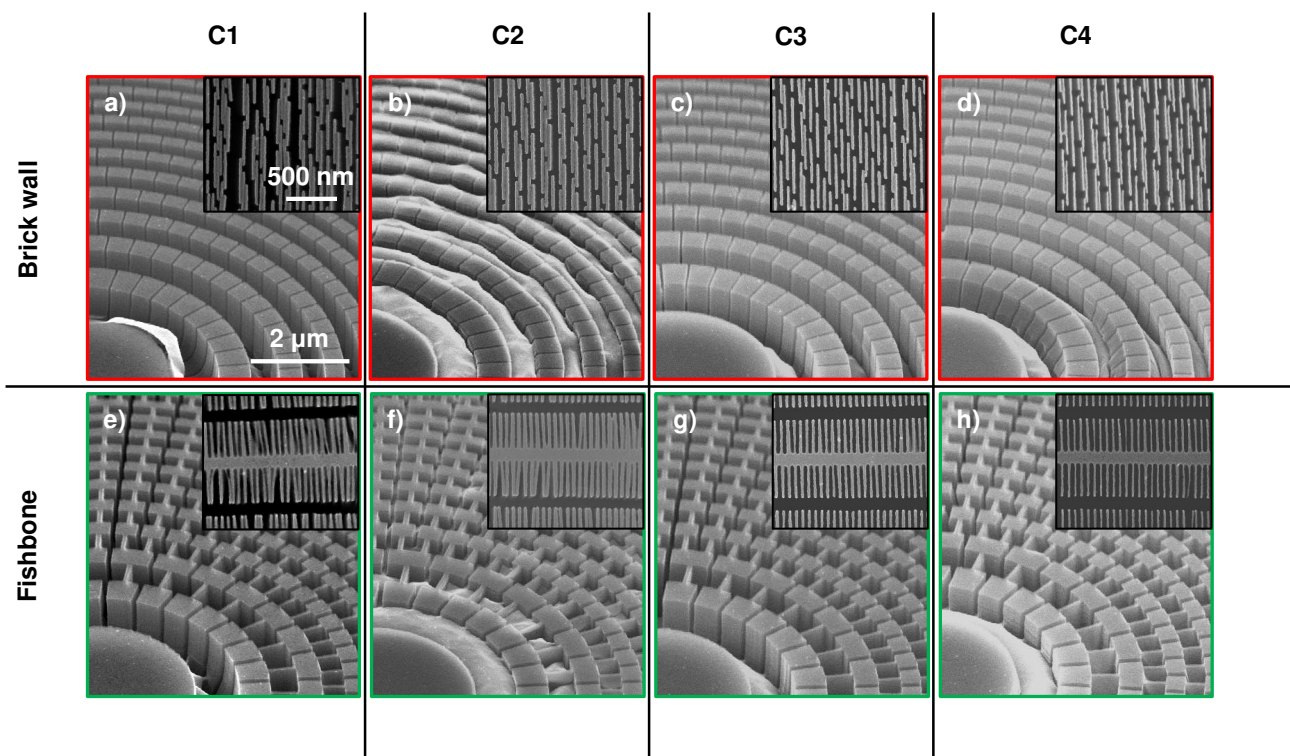


Figure 4. Brick wall (red frame) and fishbone (green frame) zone plate designs etched for 6 min at MACE conditions (a) C1, (b) C2, (c) C3 and (d) C4 and (e) C1, (f) C2, (g) C3 and (h) C4, respectively. The two designs shown per MACE condition were processed on the same Si chip. Same scale bars apply to main SEM micrographs and the insets. The insets show the outermost zones.

Table 2. Average etch rates for the investigated MACE conditions.

Condition	Rate [$\mu\text{m}/\text{min}$]
C1	0.45
C2	0.090
C3	0.26
C4	0.28

Interestingly, a 10 times lower H_2O_2 concentration (C2), and consequently a slower etch rate (Table 2), did not result in a homogeneous and controlled etching. An uneven etching with both catalyst designs was more apparent here than with any other investigated MACE condition (Figure 4b,f). Especially for the fishbone design, local differences in etching within neighboring structures was observed suggesting an uneven H_2O_2 distribution over the catalyst area (see Figure 5a). The etch depth was $\approx 0.5 \mu\text{m}$ and surprisingly, at this shallow etch depth collapse of the outermost zone plate structures was observed for the brick wall catalyst (Figure 4b). A homogeneous and vertical etching was thus key for mechanical stability of the Si structures. Furthermore, these results showed that verticality was a prerequisite for the stability of the Si structures. It should be noted that we did not implement any stirring of the etching solution during MACE to avoid any disturbance of the process.

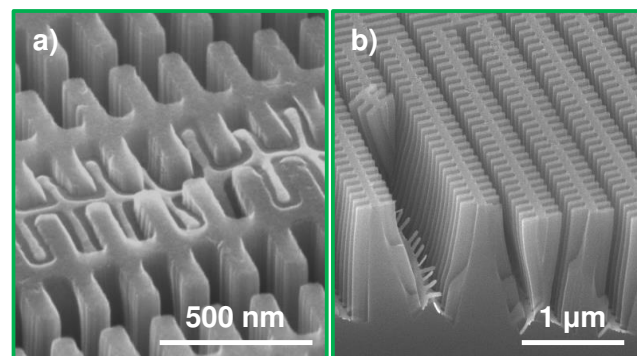


Figure 5. Fishbone zone plate catalyst etched at MACE condition C2. SEM micrographs show (a) local etching differences (6 min MACE) and (b) non-vertical etching (12 min MACE). The cross-section in (b) was prepared by manual cleaving.

Lowering the processing temperature (C3) and adding IPA (C4) to the etching solution resulted as expected in slower etch rates [12,24,29] (Table 2). At etch depths of $\approx 1.7 \mu\text{m}$ and $\approx 1.4 \mu\text{m}$ with MACE conditions C3 and C4, respectively, a positive impact on the overall etching uniformity of both the brick wall (Figure 4c,d) and the fishbone (Figure 4g,h) catalysts was observed. With the IPA addition, slight broadening of the innermost Si structures could be seen (Figure 4d), but nonetheless, both conditions contributed to a better mechanical stability of the outermost structures.

4.2. Etching Verticality

Maintaining a vertical etch direction for isolated catalyst structures of nanometer sizes is challenging [30,31]. The fishbone design with partly isolated structures was also found to require more careful control of the MACE chemistry and reaction kinetics to maintain a vertical etching direction throughout the process. At the highest investigated etch rate (C1) deformation of the outermost zones of the fishbone catalyst indicated a deviated etch direction (Figure 4e). This was confirmed from the cross-section micrograph in Figure 6a, where the non-vertical etch profile as well as catalyst deformation is shown ($\approx 2 \mu\text{m}$ etch depth). The brick wall design processed on the same Si chip maintained a vertical but collapsed etching profile ($\approx 3 \mu\text{m}$ etch depth, Figure 6b). Similarly to the negative effect on

the Si structure stability, the uneven or limited access of H_2O_2 to the catalyst surface also negatively impacted the etching verticality, although etch rates were significantly lowered. This is illustrated in Figure 4f (outermost zones) and Figure 5b.

Compared to conditions C1 and C2, conditions C3 and C4 indicated a more even etching, especially at the outermost parts of the fishbone catalyst design (Figure 4g,h). The impact IPA addition (C4) had on the etching verticality is illustrated in Figure 6c, where the zones are vertical and the etching profile is uniform. As for most other conditions, the brick wall catalyst processed on the same chip also kept a vertical etching profile at C4 (Figure 6d). The etch depth of both zone plate designs in Figure 6c,d was $\approx 3 \mu\text{m}$. This suggests that aspect ratios of at least 100:1 with a maintained vertical etching profile that can be obtained by IPA addition.

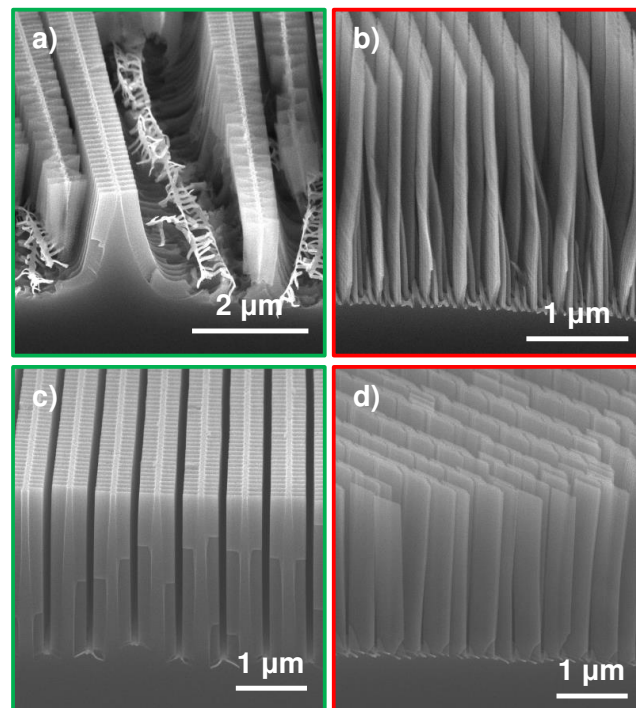


Figure 6. The effect of IPA on etching verticality. (a) fishbone and (b) brick wall catalyst designs etched at condition C1 (no IPA, same Si chip), and (c) fishbone and (d) brick wall catalysts etched at condition C4 (with IPA, same Si chip). The MACE time was 9 min for both samples. The cross-sections were prepared by cleaving.

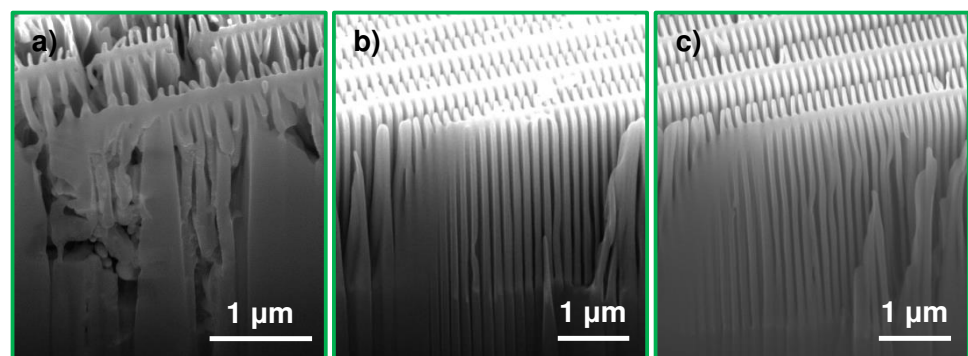


Figure 7. Cross-section SEM micrographs of the fishbone design catalyst processed at MACE condition (a) C1 for 9 min, (b) C3 for 12 min and (c) C4 for 12 min. The cross-sections were made by FIB milling.

Figure 7 shows micrographs of cross-sections prepared by FIB milling comparing the original MACE condition (C1, Figure 7a) with the relatively low processing temperature (C3, Figure 7b) and the addition of IPA (C4, Figure 7c) at average etch depths of $\approx 4.2 \mu\text{m}$, $\approx 3.2 \mu\text{m}$ and $\approx 4 \mu\text{m}$, respectively. It should be noted that FIB milling caused deformation of the finer structures, but still could give an indication of the etching directionality and depth. From these micrographs, it is obvious that both C3 and C4 were beneficial with regards to the etching direction. We draw the conclusion that controlling the MACE kinetics by lower processing temperature or by addition of IPA in the etching solution had similar, positive impacts on the etching verticality. However, the effect of IPA addition on the MACE process was not completely clear. If the effect of IPA was limited to reduction of the etch rate or if other mechanisms like easier release of formed gases were important is an open question. From a process handling point of view, we recommend adding IPA to the etching solution instead of temperature regulation of the etching solution. Temperature stabilization using a large volume of etching solution was time consuming and needed pre-cooling of the chemicals. The low heat conductivity of the PTFE container was altering the temperature of the chemicals and limited the number of MACE experiments that could be performed due to long temperature stabilization times in between samples. Therefore, to avoid uneven etch rates due to temperature elevation, room temperature processing with IPA is preferable.

4.3. Process Reproducibility

Many reports on MACE either use the process as one in a series of steps for micro- and nanofabrication, or investigate the process performance for a given application. As far as we are aware, there are no reports that discuss the reproducibility of the process. In this study, we explored four different MACE conditions and examined the etching behavior at four time points per condition, which in turn was repeated twice. We believe this large set of experiments gave a good indication of the reproducibility of the MACE process.

Figure 8 shows the average etch depth of one brick wall and one fishbone zone plate catalyst design processed on the same chip as a function of processing time at conditions C1–C4. The error bars represent the standard deviation and indicate the variation in depth between the two zone plates. As previously reported, the decreasing width of the zones over the zone plate radius resulted in relatively deeper etching of the smallest, outermost zones than the largest, innermost zones. This gave a local variation of a few per cent over the same zone plate [11,20]. This variation is not shown here, but was present for all devices. Overall, all conditions gave larger zone thicknesses with longer processing time. However, the etch depth did not increase linearly with time. Even though both zone plates had the same active catalyst area, etch depth variations could be observed for certain time points.

Furthermore, differences in etch depths of zone plates on two different Si chips processed at identical conditions are shown in Figure 9. The error bars represent the standard deviation of the measurements. The variations in etch depth were largest for samples processed at conditions C1 and C2, and smaller for C3 and C4. Even though identical samples with same sizes and same active catalyst areas were processed at identical conditions, etching behavior differed depending on condition.

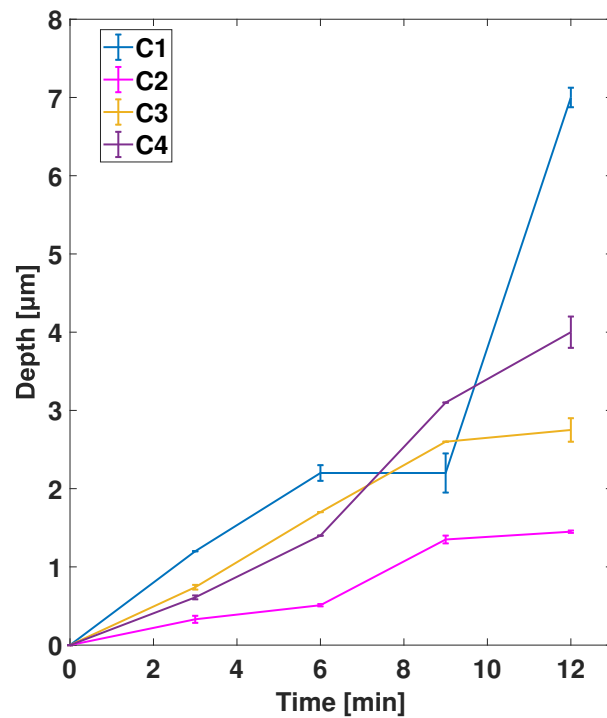


Figure 8. Average etch depths of brick wall and fishbone catalysts processed on the same Si chip as a function of etching time at MACE conditions C1–C4. The error bars show the standard deviation of the measurements.

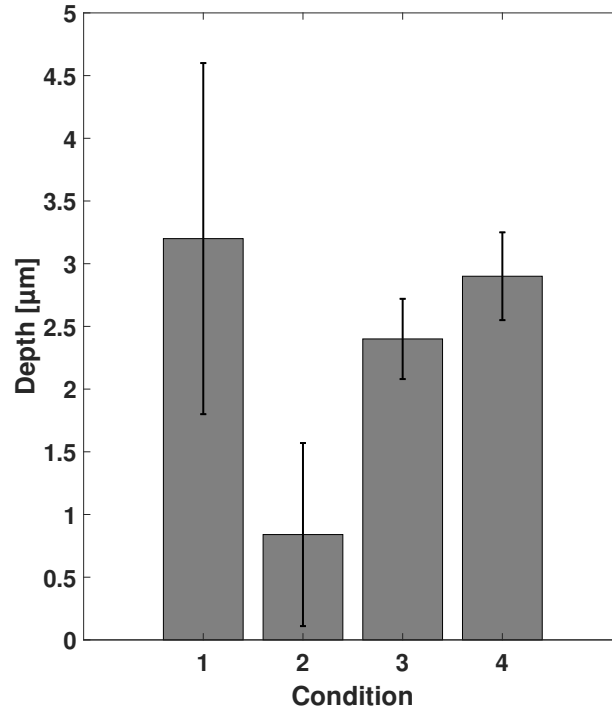


Figure 9. Average etch depths of zone plates on different Si chips processed at conditions C1–C4 for 9 min. The error bars indicate the depth variation between different chips.

With these results, we want to highlight that precise control of the etching process was challenging and that the depth might vary not only between samples from run to run, but between structures on the same Si chip. The outcome of our experiments indicated that conditions C3 and C4 were also preferable for good reproducibility.

5. Conclusions

We demonstrated the MACE effect of catalyst design and reaction kinetics on fabrication of high-aspect ratio Si structures as a function of mechanical stability and etching verticality. Two zone plate catalyst designs with structural sizes ranging from 850 nm down to 30 nm have been used, brick wall (interconnected) and fishbone (partly connected and partly isolated), and their etching behavior at four different conditions has been systematically studied. Our findings reveal that the Si structures of the brick wall design were mechanically stable up to an aspect ratio of 30:1, while deeper etching resulted in collapse of the outermost zones with the smallest structures. Furthermore, etching verticality could be maintained with the brick wall design, independently of the MACE condition. The fishbone design required more careful control of the reaction kinetics for the catalyst to translate linearly into the Si. Addition of IPA and a lowered processing temperature showed a significant improvement in etching verticality of the fishbone design as opposed to room temperature processing without any additive in the etching solution. The cold MACE required a rather complicated cooling setup, and therefore, we recommend IPA addition to the etching solution for controlled kinetics at room temperature processing. For the future, the influence of other alcohols on the processing of Si nanostructures should be investigated. We also show data indicating the sensitivity of the MACE process. These are the first results showing the reproducibility of the process and more statistics are needed for further characterization.

We think our findings provide relevant information for micro- and nanofabrication of high-aspect ratio Si structures with MACE. The easy processing without any need of complicated experimental setups or tools will be beneficial for applications that require controlled Si fabrication with lithographically defined morphology.

Author Contributions: R.A. and U.V. conceived the idea for the study. R.A. performed all lab work. R.A. and U.V. wrote the manuscript together. All authors have read and agreed to the published version of the manuscript.

Funding: This research was funded by the Swedish Research Council grant number 2018-04237 and 2019-06104.

Data Availability Statement: The data presented in this study are available on request from the corresponding author.

Acknowledgments: We thank Thomas Frisk for his help with designing the zone plates and Hanna Ohlin and Mattias Åstrand for their help with the MACE experiments. Part of this work was performed at the Albanova Nanolab.

Conflicts of Interest: The authors declare no conflict of interest.

References

1. Karabchevsky, A.; Katiyi, A.; Ang, A.S.; Hazan, A. On-chip nanophotonics and future challenges. *Nanophotonics* **2020**, *9*, 3733–3753. [CrossRef]
2. Yang, Y.; Yuan, W.; Kang, W.; Ye, Y.; Pan, Q.; Zhang, X.; Ke, Y.; Wang, C.; Qiu, Z.; Tang, Y. A review on silicon nanowire-based anodes for next-generation high-performance lithium-ion batteries from a material-based perspective. *Sustain. Energy Fuels* **2020**, *4*, 1577–1594. [CrossRef]
3. Sahoo, M.K.; Kale, P. Integration of silicon nanowires in solar cell structure for efficiency enhancement: A review. *J. Mater.* **2019**, *5*, 34–48. [CrossRef]
4. Xu, Y.; Hu, X.; Kundu, S.; Nag, A.; Afsarimanesh, N.; Sapra, S.; Mukhopadhyay, S.C.; Han, T. Silicon-Based Sensors for Biomedical Applications: A Review. *Sensors* **2019**, *19*, 2908. [CrossRef] [PubMed]
5. Gale, B.; Jafek, A.; Lambert, C.; Goenner, B.; Moghimifam, H.; Nze, U.; Kamarapu, S. A Review of Current Methods in Microfluidic Device Fabrication and Future Commercialization Prospects. *Inventions* **2018**, *3*, 60. [CrossRef]
6. Romano, L.; Stampanoni, M. Microfabrication of X-ray Optics by Metal Assisted Chemical Etching: A Review. *Micromachines* **2020**, *11*, 589. [CrossRef]
7. Wu, B.; Kumar, A.; Pamarthy, S. High aspect ratio silicon etch: A review. *J. Appl. Phys.* **2010**, *108*, 51101. [CrossRef]
8. Huff, M. Recent Advances in Reactive Ion Etching and Applications of High-Aspect-Ratio Microfabrication. *Micromachines* **2021**, *12*, 991. [CrossRef]

9. Huang, Z.; Geyer, N.; Werner, P.; De Boor, J.; Gösele, U. Metal-assisted chemical etching of silicon: A review. *Adv. Mater.* **2011**, *23*, 285–308. [CrossRef]
10. Han, H.; Huang, Z.; Lee, W. Metal-assisted chemical etching of silicon and nanotechnology applications. *Nano Today* **2014**, *9*, 271–304. [CrossRef]
11. Akan, R.; Parfeniukas, K.; Vogt, C.; Toprak, M.S.; Vogt, U. Reaction control of metal-assisted chemical etching for silicon-based zone plate nanostructures. *RSC Adv.* **2018**, *8*, 12628–12634. [CrossRef]
12. Backes, A.; Leitgeb, M.; Bittner, A.; Schmid, U. Temperature Dependent Pore Formation in Metal Assisted Chemical Etching of Silicon. *ECS J. Solid State Sci. Technol.* **2016**, *5*, P653–P656. [CrossRef]
13. Geyer, N.; Wollschläger, N.; Fuhrmann, B.; Tonkikh, A.; Berger, A.; Werner, P.; Jungmann, M.; Krause-Rehberg, R.; Leipner, H.S. Influence of the doping level on the porosity of silicon nanowires prepared by metal-assisted chemical etching. *Nanotechnology* **2015**, *26*, 245301. [CrossRef] [PubMed]
14. Aca-López, V.; Quiroga-González, E.; Gómez-Barojas, E.; Światowska, J.; Luna-López, J.A. Effects of the doping level in the production of silicon nanowalls by metal assisted chemical etching. *Mater. Sci. Semicond. Process.* **2020**, *118*, 105206. [CrossRef]
15. Um, H.D.; Kim, N.; Lee, K.; Hwang, I.; Hoon Seo, J.; Yu, Y.J.; Duane, P.; Wober, M.; Seo, K. Versatile control of metal-assisted chemical etching for vertical silicon microwire arrays and their photovoltaic applications. *Sci. Rep.* **2015**, *5*, 11277. [CrossRef] [PubMed]
16. Hildreth, O.J.; Lin, W.; Wong, C.P. Effect of Catalyst Shape and Etchant Composition on Etching Direction in Metal-Assisted Chemical Etching of Silicon to Fabricate 3D Nanostructures. *ACS Nano* **2009**, *3*, 4033–4042. [CrossRef] [PubMed]
17. Xia, W.; Zhu, J.; Wang, H.; Zeng, X. Effect of catalyst shape on etching orientation in metal-assisted chemical etching of silicon. *CrystEngComm* **2014**, *16*, 4289–4297. [CrossRef]
18. Attwood, D.; Sakdinawat, A. *X-Rays and Extreme Ultraviolet Radiation*; Cambridge University Press: Cambridge, UK, 2016. [CrossRef]
19. Lider, V.V. Zone Plates for X-Ray Focusing (Review). *J. Surf. Investig.* **2017**, *11*, 1113–1127. [CrossRef]
20. Akan, R.; Frisk, T.; Lundberg, F.; Ohlin, H.; Johansson, U.; Li, K.; Sakdinawat, A.; Vogt, U. Metal-Assisted Chemical Etching and Electroless Deposition for Fabrication of Hard X-ray Pd/Si Zone Plates. *Micromachines* **2020**, *11*, 301. [CrossRef]
21. Chang, C.; Sakdinawat, A. Ultra-high aspect ratio high-resolution nanofabrication for hard X-ray diffractive optics. *Nat. Commun.* **2014**, *5*, 1–7. [CrossRef]
22. Li, K.; Wojcik, M.J.; Divan, R.; Ocola, L.E.; Shi, B.; Rosenmann, D.; Jacobsen, C. Fabrication of hard X-ray zone plates with high aspect ratio using metal-assisted chemical etching. *J. Vac. Sci. Technol. B Nanotechnol. Microelectron. Mater. Process. Meas. Phenom.* **2017**, *35*, 06G901. [CrossRef]
23. Li, K.; Ali, S.; Wojcik, M.; De Andrade, V.; Huang, X.; Yan, H.; Chu, Y.; Nazaretski, E.; Pattammattel, A.; Jacobsen, C. Tunable hard X-ray nanofocusing with Fresnel zone plates fabricated using deep etching. *Optica* **2020**, *7*, 410–416. [CrossRef] [PubMed]
24. Romano, L.; Kagias, M.; Vila-Comamala, J.; Jefimovs, K.; Tseng, L.T.; Guzenko, V.A.; Stampanoni, M. Metal assisted chemical etching of silicon in the gas phase: A nanofabrication platform for X-ray optics. *Nanoscale Horizons* **2020**. [CrossRef]
25. Tiberio, R.C.; Rooks, M.J.; Chang, C.; F. Knollenberg, C.; Dobisz, E.A.; Sakdinawat, A. Vertical directionality-controlled metal-assisted chemical etching for ultrahigh aspect ratio nanoscale structures. *J. Vac. Sci. Technol. B Nanotechnol. Microelectron. Mater. Process. Meas. Phenom.* **2014**, *32*, 06F101. [CrossRef]
26. Kim, Y.; Tsao, A.; Lee, D.H.; Maboudian, R. Solvent-induced formation of unidirectionally curved and tilted Si nanowires during metal-assisted chemical etching. *J. Mater. Chem. C* **2013**, *1*, 220–224. [CrossRef]
27. Romano, L.; Vila-Comamala, J.; Jefimovs, K.; Stampanoni, M. Effect of isopropanol on gold assisted chemical etching of silicon microstructures. *Microelectron. Eng.* **2017**, *177*, 59–65. [CrossRef]
28. Chartier, C.; Bastide, S.; Lévy-Clément, C. Metal-assisted chemical etching of silicon in HF-H₂O₂. *Electrochim. Acta* **2008**, *53*, 5509–5516. [CrossRef]
29. Cheng, S.L.; Chung, C.H.; Lee, H.C. A Study of the Synthesis, Characterization, and Kinetics of Vertical Silicon Nanowire Arrays on (001)Si Substrates. *J. Electrochem. Soc.* **2008**, *155*, D711. [CrossRef]
30. Kong, L.; Zhao, Y.; Dasgupta, B.; Ren, Y.; Hippalgaonkar, K.; Li, X.; Chim, W.K.; Chiam, S.Y. Minimizing Isolate Catalyst Motion in Metal-Assisted Chemical Etching for Deep Trenching of Silicon Nanohole Array. *ACS Appl. Mater. Interfaces* **2017**, *9*, 20981–20990. [CrossRef] [PubMed]
31. Lianto, P.; Yu, S.; Wu, J.; Thompson, C.V.; Choi, W.K. Vertical etching with isolated catalysts in metal-assisted chemical etching of silicon. *Nanoscale* **2012**, *4*, 7532–7539. [CrossRef]

MDPI
St. Alban-Anlage 66
4052 Basel
Switzerland
Tel. +41 61 683 77 34
Fax +41 61 302 89 18
www.mdpi.com

Nanomaterials Editorial Office
E-mail: nanomaterials@mdpi.com
www.mdpi.com/journal/nanomaterials



MDPI
St. Alban-Anlage 66
4052 Basel
Switzerland
Tel: +41 61 683 77 34
www.mdpi.com



ISBN 978-3-0365-4765-7